

ADVANCED TOPICS IN SCIENCE AND TECHNOLOGY IN CHINA

Chee-Kiong Soh • Yaowen Yang
Suresh Bhalla *Editors*

Smart Materials in Structural Health Monitoring, Control and Biomechanics



ZHEJIANG UNIVERSITY PRESS
浙江大学出版社



Springer

**ADVANCED TOPICS
IN SCIENCE AND TECHNOLOGY IN CHINA**

ADVANCED TOPICS IN SCIENCE AND TECHNOLOGY IN CHINA

Zhejiang University is one of the leading universities in China. In *Advanced Topics in Science and Technology in China*, Zhejiang University Press and Springer jointly publish monographs by Chinese scholars and professors, as well as invited authors and editors from abroad who are outstanding experts and scholars in their fields. This series will be of interest to researchers, lecturers, and graduate students alike.

Advanced Topics in Science and Technology in China aims to present the latest and most cutting-edge theories, techniques, and methodologies in various research areas in China. It covers all disciplines in the fields of natural science and technology, including but not limited to, computer science, materials science, life sciences, engineering, environmental sciences, mathematics, and physics.

Chee-Kiong Soh
Yaowen Yang
Suresh Bhalla

Smart Materials in Structural Health Monitoring, Control and Biomechanics

With 363 figures

 ZHEJIANG UNIVERSITY PRESS
浙江大学出版社

 Springer

Editors

Prof. Chee-Kiong Soh
School of Civil & Environmental Engineering
Nanyang Technological University
50 Nanyang Avenue, Singapore 639798
E-mail: csohck@ntu.edu.sg

Prof. Yaowen Yang
School of Civil & Environmental Engineering
Nanyang Technological University, 50
Nanyang Avenue, Singapore 639798
E-mail: cywyang@ntu.edu.sg

Prof. Suresh Bhalla
Department of Civil Engineering, Indian
Institute of Technology Delhi, Hauz Khas
New Delhi 110016 India
E-mail: sbhalla@civil.iitd.ac.in

ISSN 1995-6819

e-ISSN 1995-6827

Advanced Topics in Science and Technology in China

ISBN 978-7-308-08266-2

Zhejiang University Press, Hangzhou

ISBN 978-3-642-24462-9

Springer Heidelberg New York Dordrecht London

ISBN 978-3-642-24463-6 (eBook)

Library of Congress Control Number: 2011937174

© Zhejiang University Press, Hangzhou and Springer-Verlag Berlin Heidelberg 2012

This work is subject to copyright. All rights are reserved by the Publishers, whether the whole or part of the material is concerned, specifically the rights of translation, reprinting, reuse of illustrations, recitation, broadcasting, reproduction on microfilms or in any other physical way, and transmission or information storage and retrieval, electronic adaptation, computer software, or by similar or dissimilar methodology now known or hereafter developed. Exempted from this legal reservation are brief excerpts in connection with reviews or scholarly analysis or material supplied specifically for the purpose of being entered and executed on a computer system, for exclusive use by the purchaser of the work. Duplication of this publication or parts thereof is permitted only under the provisions of the Copyright Law of the Publishers' locations, in its current version, and permission for use must always be obtained from Springer. Permissions for use may be obtained through RightsLink at the Copyright Clearance Center. Violations are liable to prosecution under the respective Copyright Law.

The use of general descriptive names, registered names, trademarks, service marks, etc. in this publication does not imply, even in the absence of a specific statement, that such names are exempt from the relevant protective laws and regulations and therefore free for general use.

While the advice and information in this book are believed to be true and accurate at the date of publication, neither the authors nor the editors nor the publishers can accept any legal responsibility for any errors or omissions that may be made. The publishers make no warranty, express or implied, with respect to the material contained herein.

Printed on acid-free paper

Springer is part of Springer Science+Business Media (www.springer.com)

Preface

Smart materials, perhaps the most fascinating category of materials developed in the 20th Century, possess responsive capabilities to external stimuli, enabling them to change their physical properties according to the stimulus. The feedback functions within the materials are combined with the properties and functions of the materials. Smart materials can be either “*active*” or “*passive*”. Active smart materials, one hand are those which possess the capacity to modify their geometric or material properties under the application of electric, thermal or magnetic fields, thus acquiring an inherent capacity to transduce energy. Piezoelectric materials, shape memory alloys, electro-rheological fluids and magneto-strictive materials are active smart materials which can be used as force transducers and actuators. Additionally, piezoelectric materials can convert mechanical force into electrical energy, enabling them as sensors or energy harvesters. Passive smart materials, on the other hand, lack the inherent capability to transduce energy, *e.g.*, fiber optic material. Such materials can act as sensors but not as actuators. This book examines both active and passive smart materials in structural health monitoring (SHM), control and bio-mechanics. The book starts with the fundamentals and takes the readers gradually through the mathematical formulations and experimental details.

Chapters 1 to 7 of the book are primarily concerned with the lead zirconate titanate (PZT) piezoelectric material and the electro-mechanical impedance (EMI) technique for SHM. The different impedance models, derived by the book’s authors, for health monitoring and damage quantification using PZT transducers are presented. This includes three approaches: extraction of structural mechanical impedance from signatures; identification of higher natural frequencies from signatures; and the use of evolutionary programming. Furthermore, strength and damage assessment of concrete using both surface-bonded and embedded PZT transducers are examined. The extracted equivalent stiffness is used in a framework of fuzzy set theory to spell out a damage quantification approach for real-world concrete structures. An approach to integrate the EMI technique with global vibration techniques is also presented. It is shown that the same PZT patch can serve as the sensor for both techniques. Whereas incipient-level damages can be identified using the EMI technique, the global vibration response of the

structure acquired from the same patch with minimal hardware and data processing tools can facilitate the detection, localization and quantification of moderate to severe damage. Finally, several practical issues involving the application of PZT transducers and EMI technique for SHM such as sensing region and load monitoring are discussed.

Chapters 8 to 10 of this book focus on the control and excitation of structural vibration using piezoelectric transducers. Analytical and semi-analytical solutions for vibration control of smart beams, subjected to axial loads, are derived under different control strategies. The integrated optimization of the control system for smart plates and shells is then formulated and implemented using a modified genetic algorithm (GA). Numerical results illustrate that vibration suppression could be significantly enhanced with the appropriate distribution of piezoelectric transducers and selection of control parameters. Subsequently, the optimal excitation of plates and shells using PZT transducers is demonstrated and a simple, yet general, procedure to determine the optimal excitation locations of the PZT actuators is presented. Finally, the dynamic response of a fully coupled hybrid piezo-elastic cylindrical shell with piezoelectric shear actuators is presented, followed by investigation of the active vibration control of the cylindrical shell.

Use of the passive smart material, fiber optic, as sensors for SHM is covered in Chapters 11 to 13. After a presentation of the theoretical details, real-life applications of fiber Bragg grating (FBG) sensors—the most successful type of fiber optic sensor in the health monitoring of highway bridges and rock and underground structures—are presented. In addition, comparisons between monitoring of rock and underground structures using FBG and electrical strain gauges (ESGs), and FBG and PZT are made.

Use of another active smart material, ionic polymer-metal composite (IPMC), in bio-mechanics is discussed in Chapters 14 to 16. The bending capacity of IPMC is first derived and validated under both dynamic and static electric potentials, followed by the modeling of an IPMC beam on human tissue, an IPMC ring with elastic medium and an IPMC shell with flowing fluid, which represent possible applications of IPMC materials in biomedical engineering. Examples are also used to illustrate the viability of the models. Lastly, application of PZT transducers as bio-medical sensors to characterize bones is presented. The study is verified with finite element (FE) simulation of the EMI technique on bones.

Chapter 17 completes the book by looking into the future use of smart materials. Based on preliminary works done by the book's authors, the future application of IPMC as artificial muscles and organs, and the future application of PZT, macro-fiber composite (MFC) and IPMC for harvesting of ambient energy are envisaged.

Chee-Kiong Soh
Yaowen Yang
Suresh Bhalla
Jan. 2012

Contents

1	Introduction	1
1.1	Overview.....	1
1.2	Concept of Smart Systems/Structures for SHM.....	5
1.3	Smart Materials.....	6
1.4	Piezoelectricity and Piezoelectric Materials.....	7
	References.....	14
2	Electro-Mechanical Impedance Technique	17
2.1	Introduction.....	17
2.2	Mechanical Impedance of Structures.....	18
2.3	Impedance Modeling for EMI Technique.....	21
2.4	Mechanical Impedance of PZT Patches.....	27
2.5	PZT-Structure Interaction.....	29
2.6	Practical Aspects of EMI Technique.....	35
2.7	Signal Processing Techniques and Conventional Damage Quantification.....	39
2.8	Major Technological Developments During the Last One and a Half Decades.....	41
2.9	Advantages of EMI Technique.....	46
2.10	Limitations of EMI Technique.....	47
	References.....	47
	Exercise 2.1.....	50
3	Impedance Models for Structural Health Monitoring Using Piezo-Impedance Transducers	53
3.1	Introduction.....	53
3.2	Early PZT-Structure Interaction Models.....	53
3.3	2D Effective Mechanical Impedance.....	56

3.4	2D Formulation Based on Effective Impedance.....	58
3.5	Experimental Verification.....	62
3.5.1	Details of Experimental Set-up	62
3.5.2	Determination of Structural EDP Impedance by FEM.....	63
3.5.3	Modeling of Structural Damping.....	67
3.5.4	Wavelength Analysis and Convergence Test.....	67
3.5.5	Comparison between Theoretical and Experimental Signatures	69
3.6	Refining the 2D Impedance Model	70
3.7	3D Interaction of PZT Transducer with Host Structure.....	77
3.7.1	Necessity of 3D Formulation	77
3.7.2	Issues in 1D and 2D Impedance Models	77
3.7.3	Issues to Consider in 3D Impedance Model.....	78
3.8	3D Model in Presence of Thick Adhesive Bonding	81
3.8.1	Impedance Formulation.....	81
3.8.2	Stress-Strain Relationship of PZT Patch Subjected to 3D Loading	85
3.8.3	3D Differential Equations	86
3.8.4	Solution to 3D Differential Equations.....	87
3.8.5	Active Part of Solution.....	89
3.8.6	Stress-Strain Relationships in Presence of Electric Fields	90
3.8.7	Formulation of Structural Responses and Impedances.....	91
3.8.8	EM Admittance Formulation for <i>M</i> -Functioning PZT Patches ...	96
3.8.9	Modifications of Linear Impedance Formulations for Case Studies	98
3.8.10	Results and Discussions	104
3.9	FE Modeling of EMI Technique Using Coupled Field Element	106
3.9.1	Review on FE Modeling of PZT-Structure Interaction	106
3.9.2	Inclusion of Induced Strain Actuator in FE Model.....	108
3.9.3	Comparison of FE Model with Existing Impedance-Based Analytical Model and Experimental Tests.....	109
3.9.4	FE Modeling of PZT-Structure Interaction.....	115
	References.....	124
	Exercise 3.1	126
	Exercise 3.2.....	127
	Exercise 3.3.....	128
4	Damage Quantification Using EMI Technique.....	129
4.1	Extraction of Structural Mechanical Impedance from Admittance Signatures	129

4.2	System Parameter Identification from Extracted Impedance Spectra	132
4.3	Damage Diagnosis in Aerospace and Mechanical Systems	137
4.4	Extension to Damage Diagnosis in Civil-Structural Systems	144
4.5	Identification of Higher Modal Frequencies from Conductance Signatures.....	146
4.6	Numerical Example.....	150
4.7	Experimental Verification.....	155
4.7.1	Damage Location Identification.....	158
4.7.2	Effect of Number of Sensitive Modes	159
4.7.3	Effect of Frequency Range.....	161
4.8	Advantages of Modal Approach.....	163
4.9	Limitations and Concerns of Modal Approach.....	163
4.10	Damage Identification Using EMI and Evolutionary Programming ...	164
4.11	EMI of PZT Transducers	165
4.12	Mechanical Impedance of Damaged Structure.....	167
4.13	Damage Identification Method.....	173
4.13.1	EP Algorithm.....	173
4.13.2	Fitness Function	174
4.14	Experimental Set-up.....	175
4.15	Experimental Results and Numerical Predictions	177
4.15.1	Damage Identification Results	181
4.15.2	Summary	184
	References	184
	Exercise 4.1	186
	Exercise 4.2	186
5	Strength and Damage Assessment of Concrete	187
5.1	Introduction.....	187
5.2	Conventional NDE Techniques for Concrete	187
5.3	Concrete Strength Evaluation Using EMI Technique.....	190
5.4	Extraction of Damage-Sensitive Concrete Parameters from Admittance Signatures.....	194
5.5	Monitoring Concrete Curing Using Extracted Impedance Parameters.....	198
5.6	Establishment of Impedance-Based Damage Model for Concrete.....	201
5.6.1	Definition of Damage Variable.....	201
5.6.2	Damage Variable Based on the Theory of Fuzzy Sets.....	204
5.6.3	Fuzzy Probabilistic Damage Calibration of Piezo-Impedance Transducers.....	207
5.7	Embedded PZT Patches and Issues Involved	210

5.8	Experimental Set-up	211
5.8.1	Methods to Fabricate Embeddable PZT	211
5.8.2	Fabrication of Robust Embeddable PZT Patch	213
5.9	Efficiency of Embedded PZT	216
5.9.1	Comparison Test.....	216
5.9.2	Monitoring Test	217
5.10	Damage Analysis Using Statistical Method	218
	References	220
6	Integration of EMI Technique with Global Vibration Techniques	223
6.1	Introduction	223
6.2	Piezoelectric Materials as Dynamic Strain Sensors.....	224
6.3	Determination of Strain Mode Shapes Using Surface-Bonded PZT Patches	226
6.4	Identification and Localization of Incipient Damage	230
6.5	Localization of Moderate and Severe Damages Using Global Vibration Techniques	234
6.5.1	For 1D Structures (Beams).....	234
6.5.2	For 2D Structures (Plates)	236
6.6	Severity of Damage	239
	References	243
7	Sensing Region, Load Monitoring and Practical Issues.....	245
7.1	Sensing Region of PZT Patches	245
7.1.1	Introduction	245
7.1.2	Theoretical Modeling	246
7.1.3	Experimental Verification.....	258
7.1.4	Results and Discussions	259
7.1.5	Summary	264
7.2	PZT Patches for Load Monitoring.....	265
7.2.1	Introduction	265
7.2.2	Effect of Stress in Structure.....	265
7.2.3	Influence of Applied Load on EM Admittance Signatures.....	266
7.2.4	Experimental Investigations and Discussions	267
7.2.5	Efficiency of EM Admittance Signatures Using Statistical Index	271
7.2.6	Summary	275
7.3	Practical Issues Related to Application of EMI Technique in SHM....	275
7.3.1	Introduction	275
7.3.2	Consistency of Admittance Signatures Acquired from PZT Patch.....	276

7.3.3	Effects of Bonding Layer and Temperature.....	282
7.3.4	Differentiating Temperature-Induced and Damage-Induced Signature Deviations.....	291
7.3.5	Differentiating Damage in Host Structure and in PZT Patch	293
7.3.6	Summary	294
	References.....	295
8	Smart Beams: A Semi-Analytical Method	299
8.1	Introduction.....	299
8.2	Analysis of a Column Coupled with Distributed Piezoelectric Actuator	302
8.2.1	Motion Equations.....	303
8.2.2	Analytical Solutions for Displacement Feedback Control	306
8.2.3	Semi-Analytical Solutions for Velocity Feedback Control	312
8.2.4	Effects of Feedback Strategies on Motion Equations.....	317
8.3	Numerical simulations.....	318
8.3.1	Numerical Results for Displacement Feedback Control	319
8.3.2	Numerical Results for Velocity Feedback Control	325
8.4	Conclusions and Recommendations.....	329
8.4.1	Conclusions.....	329
8.4.2	Recommendations	329
	References.....	330
9	Smart Plates and Shells.....	333
9.1	Optimal Vibration Control using Genetic Algorithms.....	333
9.1.1	Introduction.....	333
9.1.2	Sensing and Actuating Equations.....	335
9.1.3	Energy-Based Approach for Integrated Optimal Design.....	343
9.1.4	General Formulation and Modified Real-Encoded GA.....	345
9.1.5	Numerical Examples	348
9.2	Optimal Excitation of Piezoelectric Plates and Shells.....	362
9.2.1	Introduction.....	362
9.2.2	Piezoelectric Actuated Plates	363
9.2.3	Piezoelectric Actuated Cylindrical Shell.....	370
9.2.4	Optimal Placement of PZT Actuator on Plate	374
9.2.5	Optimal Placement of PZT Actuator on Shell.....	387
9.2.6	Discussions.....	389
9.2.7	Summary	391
	References.....	392

10	Cylindrical Shells with Piezoelectric Shear Actuators	395
10.1	Introduction	395
10.2	Governing Equations.....	397
10.3	Non-Damping Vibration of Simply Supported Shell.....	399
10.4	Active Vibration Control of Cylindrical Shell with PSAs.....	401
10.5	Numerical Results and Discussions.....	402
10.5.1	Steady-State Response Analysis.....	403
10.5.2	Active Vibration Control	407
10.6	Summary	410
	References	410
11	Fiber Bragg Grating.....	413
11.1	Introduction	413
11.2	History of FBG.....	414
11.3	Fabrication of FBG.....	415
11.4	Optical Properties of Grating.....	417
11.5	Thermal Properties of FBG	420
11.6	Mechanical Properties of FBG	421
11.7	Maximun Reflectivity of Bragg Grating.....	422
11.8	Full Width at Half Maximum	423
11.9	FBG Sensors.....	424
11.9.1	Direct Sensing Using FBG	424
11.9.2	Indirect Sensing by Embedded FBG	425
11.10	FBG-Based Pressure/Strain Sensor	427
11.11	FBG-Based Shear Force Sensor	428
	References	435
12	Applications of Fiber Bragg Grating Sensors.....	441
12.1	Introduction	441
12.2	Pressure Monitoring at Foot Sole of Diabetic Patients.....	441
12.3	Pressure and Temperature Monitoring in a Dental Splint.....	445
12.3.1	Structure of FBG-Based Splint Sensor.....	446
12.3.2	Experimental Results and Discussions.....	447
12.4	Monitoring Civil Structures.....	449
12.4.1	Sensing Approach.....	449
12.4.2	Symmetrically Bonded FBG Sensor Arrays on Rebars.....	449
12.4.3	Contact Force Measurement at Beam-Column Joint.....	458
12.5	Multi-Component Force Measurement	460
12.5.1	Basic Concept.....	461

12.5.2	Two-Component Force Measurement	462
12.5.3	2D Force Measurement	466
12.5.4	3D Force Measurement	467
12.6	Simultaneous Measurement of Pressure and Temperature	472
12.6.1	Sensor Configuration and Working Principle.....	472
12.6.2	Sensor Fabrication and Experimental Procedure.....	475
12.7	Summary	477
	References	478
13	Monitoring of Rocks and Underground Structures Using PZT and FBG Sensors	481
13.1	Introduction	481
13.2	Conventional Versus Smart Material Based Sensor Systems for LHR and SHM of Underground Structures.....	482
13.3	Experimental Investigations on Rocks	483
13.4	LHR by ESG and FBG Sensors.....	485
13.4.1	Specimen 1	485
13.4.2	Specimen 2	487
13.5	SHM by PZT Transducers	489
13.5.1	Specimen 1	489
13.5.2	Specimen 2	491
13.5.3	Specimen 3	492
13.5.4	Extraction of Structural Mechanical Impedance	493
13.5.5	Calibration of Extracted Parameters for Damage Quantification.....	494
13.6	Robustness of PZT Transducers and FBG-Based Strain Gauges	497
13.7	Potential Applications of Smart Sensors on Rock Structures	497
	References	499
14	Ionic Polymer-Metal Composite and its Actuation Characteristics	501
14.1	Introduction	501
14.1.1	History and Characterizations	501
14.1.2	Experimental Study and Physical Modeling	503
14.1.3	Implemented and Potential Applications.....	507
14.2	Bending Moment Capacity of IPMC.....	507
14.2.1	Charge Redistribution.....	507
14.2.2	Bending Moment.....	512
14.3	Validation and Discussions.....	520
14.4	Frequency Dependent Characteristics	525
14.5	Summary	529

References	530
15 IPMC-Based Biomedical Applications	533
15.1 Introduction	533
15.2 IPMC Beam on Human Tissues	534
15.2.1 Modeling of IPMC Beam on Human Tissues.....	534
15.2.2 Illustrative Examples and Discussions	536
15.3 IPMC Ring with Elastic Medium	543
15.3.1 Problem Formulation.....	543
15.3.2 Displacement Solutions.....	546
15.3.3 Illustrative Examples.....	548
15.4 IPMC Shell with Flowing Fluid	554
15.4.1 Problem Formulation.....	554
15.4.2 Wave Propagation Solutions.....	559
15.4.3 Illustrative Example and Discussion	563
15.5 Summary	565
References	567
16 Bone Characterization Using Piezo-Transducers as Bio-Medical Sensors.....	569
16.1 Introduction	569
16.2 Monitoring Changes in Bone Density	572
16.3 Monitoring Healing Process in Bones	575
16.4 FE Simulation of EMI Technique on Bones.....	577
References	580
17 Future of Smart Materials.....	583
17.1 Past and Future Developments of IPMC	583
17.2 PZT/MFC in Energy Harvesting	585
17.2.1 Current Research in Energy Harvesting using Piezoelectric Materials	585
17.2.2 Main Concerns for Future Practical Applications	587
17.3 Futuristic Applications of Smart Materials.....	591
References	592
Appendix	595
Index.....	613

Contributors

- Chee-Kiong Soh School of Civil & Environmental Engineering, Nanyang Technological University, 50 Nanyang Avenue, Singapore 639798 (Email: csohck@ntu.edu.sg)
- Yaowen Yang School of Civil & Environmental Engineering, Nanyang Technological University, 50 Nanyang Avenue, Singapore 639798 (Email: cywyang@ntu.edu.sg)
- Suresh Bhalla Department of Civil Engineering, Indian Institute of Technology Delhi, Hauz Khas, New Delhi 110016 India (Email: sbhalla@civil.iitd.ac.in)
- Ashok Gupta Department of Civil Engineering, Indian Institute of Technology Delhi, Hauz Khas, New Delhi 110016 India (Email: ashokg@civil.iitd.ac.in)
- Changkuan Ju Materials Technologies Corporation, 1950 Spectrum Circle SE, Suite B-375, Marietta, Georgia 30067, USA (Email: cju@aboutmtc.com)
- Hongyun Li Department of Engineering Mechanics, Shanghai Jiao Tong University, Shanghai 200030, P.R. China (Email: hyli@sjtu.edu.cn)
- Jianfeng Xu Shanghai Institute of Process Automation Instrumentation, 103 CaoBao Road, Shanghai 200233, P.R. China (Email: xujianfeng5@hotmail.com)
- Jianzhong Hao RF & Optical Department, Institute for Infocomm Research, A*STAR (Agency for Science, Technology and Research), 1 Fusionopolis Way, #21-01 Connexis (South Tower), Singapore 138632 (Email: haoemily@i2r.a-star.edu.sg)
- Lei Zhang Institute of Materials Research and Engineering, A*STAR (Agency for Science, Technology and Research), 3 Research Link, Singapore 117602 (Email: zhangl@imre.a-star.edu.sg)

- Lihua Tang School of Civil & Environmental Engineering, Nanyang Technological University, 50 Nanyang Avenue, Singapore 639798 (Email: tanglihua821229@gmail.com)
- Rama Shanker Department of Civil Engineering, Moti Lal Nehru National Institute of Technology, Allahbad 211004, India (Email: ramashankeriitd@yahoo.com)
- Rupali Suresh Department of Physics, Sri Venketeswara College, University of Delhi (South Campus), Benito Juarez Road, Dhaula Kuan, New Delhi 110021 India (Email: rsuresh.assoc@ntu.edu.sg)
- Swee-Chuan Tjin School of Electrical & Electronics Engineering, Nanyang Technological University, 50 Nanyang Avenue, Singapore 639798 (Email: esctjin@ntu.edu.sg)
- Venu Gopal Madhav Annamdas School of Mechanical and Aerospace Engineering, Nanyang Technological University, 50 Nanyang Avenue, Singapore 639798 (Email: annamdas@ntu.edu.sg)
- Yee-Yan Lim Civil Engineering Program, School of Engineering & Information Technology, Universiti Malaysia Sabah, Locked Bag No. 2073, 88999 Kota Kinabalu, Sabah, Malaysia (E-mail: yylim@ums.edu.my)
- Yuhang Hu School of Engineering and Applied Sciences, Harvard University, Cambridge, MA 02138, USA (Email: yuhanghu@fas.harvard.edu)
- Zhanli Jin ST Electronics (Satellite Systems) Pte Ltd, Block S2.2, Level B3-06, 50 Nanyang Avenue, Singapore 639798 (Email: jinzhanli@stee-satsys.com)

Introduction

S. Bhalla^{*}, C. K. Soh

^{*}Department of Civil Engineering, Indian Institute of Technology Delhi,
Hauz Khas, New Delhi 110016, India
Tel: 91-11-2659-1040; Fax: 91-11-2658-1117
Email: sbhalla@civil.iitd.ac.in

1.1 Overview

Civil infrastructures are important long-term investments of a nation which are crucial in supporting the nation's economic and social activities. Therefore, it is vital to continuously monitor the performance and condition of all civil infrastructures, especially the critical ones such as bridges and power plants so that any adverse changes in their performance or condition can be detected in a timely fashion and mitigated. In addition, instrumenting the structures at the time of construction, and their monitoring thereafter, could help in validating key design parameters as well as providing valuable insight into their behavior and performance under actual loadings. Ironically, whereas vast economic resources are mobilized for the construction of civil infrastructures, structural engineers in general are not too concerned with their post-construction behavior.

During the last one and a half decades, the idea of monitoring structures through appropriate instrumentation has gained wide acceptance. The approach is similar to monitoring the critical parameters of an aircraft during flight or an automobile on the road, so that any malfunctions can be detected early, thereby facilitating pre-emptive action. Hence, the need for structural health monitoring (SHM) has become widely acknowledged. Generally, SHM is defined as the measurement of the operating environment and critical responses of a structure to track and evaluate the symptoms of operational incidents, anomalies, and deterioration or damage indicators that may affect operation, serviceability, safety

or reliability (Aktan *et al.*, 2000). It implies continuous monitoring, acquisition, validation and analysis of technical data to facilitate life-cycle management decisions (Kessler *et al.*, 2002). A subset of SHM is condition assessment, which is defined as the periodic or one-time establishment of the current conditions, specifically aimed at assessing fitness for purpose. Several bridges have been instrumented for SHM or condition assessment in recent years. Most notable among them are the I-40 bridge in New Mexico (Farrar and Jauregui, 1998), the Second Link bridge connecting Malaysia and Singapore (Moyo, 2002), the Tsing Ma suspension bridge in Hong Kong (Lynch *et al.*, 2003) and the Boujnah bridge of the Tunis-Msaken Highway (El-Borgi *et al.*, 2005).

Several algorithms have been proposed to locate and determine the severity of damage in bridge structures based on their vibration response. In these techniques, essentially the test-structure is subjected to low-frequency excitations, either harmonic or impulse, and the resulting vibration responses (displacements, velocities or accelerations) are picked up at specified locations along the structure. The vibration pick-up data are processed to extract the first few mode shapes and the corresponding natural frequencies of the structure, which, when compared with the corresponding data for the healthy state, yield information pertaining to the locations and the severity of the damage. Application of this principle for damage detection can be found as early as in the 1970s (*e.g.* Adams *et al.*, 1978). Subsequently, this concept was employed for structural system identification, a mathematical model of the structure from the experimental input-output data (*e.g.* Yao, 1985; Oreta and Tanabe, 1994; Loh and Tou, 1995). It should be mentioned that several of these techniques consist of “updating” a numerical model of the structure from test measurements. In the 1990’s, with the development of improved sensors, testing hardware, and data acquisition and processing techniques, many “quick” algorithms have been proposed (mainly for bridge type structures), such as the change in *curvature mode shape* method (Pandey *et al.*, 1991), the *change in stiffness* method (Zimmerman and Kaouk, 1994), the *change in flexibility* method (Pandey and Biswas, 1994) and the *damage index* method (Stubbs and Kim, 1994). A comparative evaluation of these algorithms on an actual bridge structure, by Farrar and Jauregui (1998), revealed the *damage index* method to be the most sensitive among these methods. However, only limited studies have been conducted on buildings and offshore structures (Thompson and Harper, 2004; Sun *et al.*, 2007), which exhibit a behavior of far greater complexity. The search for more durable and cost-effective sensors and hardware is far from over on account of the limitations of existing technologies and methods, especially when applied on real-life structures (Catbas *et al.*, 2007). The main limitations of the global dynamic techniques can be summarized as follows:

- (1) These techniques typically rely on the first few mode shapes and the corresponding natural frequencies of structures, which, being global in nature, are not sensitive enough to be altered by localized incipient damages. For example, Pandey and Biswas (1994) reported that a 50% reduction in the Young’s modulus of elasticity, over the central 3% length of a 2.44 m long beam (as an example),

only resulted in about 3% reduction in the first natural frequency. Changes of such a small order of magnitude may not be considered as reliable damage indicators for real-life structures, in view of the experimental errors of approximately the same order of magnitude.

(2) These techniques demand expensive hardware and sensors, such as inertial shakers, self-conditioning accelerometers and laser velocity meters. Typically, the cost of a single accelerometer ranges from approximately \$500 to \$1,000. For a large structure, the overall cost of such sensor systems could easily run into millions of dollars. To cite an example, the Tsing Ma suspension bridge in Hong Kong was instrumented with only 350 sensors in 1997 yet cost over US\$8 million (Lynch *et al.*, 2003).

(3) A major limitation of these techniques is the interference caused by the ambient mechanical noise, in addition to the electrical and the electromagnetic noise associated with the measurement systems themselves. On account of low frequency, the techniques are highly susceptible to ambient noise, which also happens to be in the low frequency range, typically less than 100 Hz.

(4) For miniature structural components (such as precision machinery or computer parts), the sensors involved in these techniques are not only bulky, but also likely to interfere with structural dynamics owing to their own mass and stiffness. Laser vibrometers are suitable for small structures, but are expensive and need to scan the entire structure to measure mode shapes, which proves very tedious (Giurgutiu and Zagrai, 2002).

(5) The pre-requisite of a high fidelity “model” of the test structure restricts the application of the techniques to structures with relatively simple geometries and configurations. As evaluation of stiffness and damping at the supports (which often rust during service) is extremely difficult, reliable identification of a “model” is quite difficult in practice.

(6) Often, the performance of these techniques deteriorates in multiple damage scenarios (Wang *et al.*, 1998).

In addition to the vibration-based SHM techniques described above, a few static response-based techniques have also been proposed. Banan *et al.* (1994) proposed the static displacement technique for structural identification. This involves applying static forces at specific nodal points and measuring the corresponding displacements. Although conceptually feasible, measurement of static displacements on large structures is somewhat impractical. It warrants the establishment of a frame of reference, which, for contact measurement, could necessitate the construction of a secondary structure. As an alternative, Sanayei and Saletnik (1996) put forward the *static strain measurement* technique. For structural components, surface strains, which result from axial, bending and shear deformations, can capture the component’s response to external loads quite well. Unlike displacements, strains can be measured without having to establish any secondary frame of reference.

In summary, the global techniques (static/dynamic) provide little information about local damages unless very large numbers of sensors are employed. They

also require intensive computations to process the measurement data. Little information about the specifics of location/type of damage can be inferred without the use of high fidelity numerical models and intensive data processing.

Another category of damage detection approaches is the so-called local techniques, which, as opposed to the global techniques, rely on localized structural interrogation for detecting damages. Some of the techniques in this category are ultrasonic techniques, acoustic emission, eddy currents, impact echo testing, magnetic field analysis, penetrant dye testing and X-ray analysis. Table 1.1 summarizes the typical damage sensitivities of several of the local non-destructive evaluation (NDE) techniques. The most common limitation of the local techniques is that usually, probes, fixtures and other equipment need to be physically moved around the test-structure when recording data. Often, this not only prevents autonomous application of the technique, but may also demand the removal of finishes or covers such as false ceilings. As moving the probe everywhere is impractical, these techniques are often applied at selected probable damage locations (often based on preliminary visual inspection or past experience), which is almost tantamount to knowing the damage location *a priori*. Generally, they cannot be applied while the component is under service, such as in the case of an aircraft during flight. X-ray techniques, due to their high equipment cost, are thus limited to high performance components only.

Table 1.1 Sensitivities of common local NDE techniques (adapted from (Boller, 2002), with permissions of ISSS and SPIE)

Technique	Minimum detectable crack length	High probability (>95%) detectable crack length	Remarks
Ultrasonic	2 mm	5 – 6 mm	Dependent upon structure geometry and material
Eddy currents (low-frequency)	2 mm	4.5 – 8 mm	Suitable for thickness <12 mm only
Eddy currents (high-frequency)	2 mm (surface) 0.5 mm (bore holes)	2.5 mm (surface) 1.0 mm (bore holes)	
X-ray	4 mm	10 mm	Dependent upon structure configuration. Better for thickness >12 mm
Magnetic particle	2 mm	4 mm (surface)	
Dye penetrant	2 mm	10 mm (surface)	

1.2 Concept of Smart Systems/Structures for SHM

The techniques described earlier are the conventional SHM techniques. They typically rely on the measurement of stresses, strains, displacements, accelerations or other related physical responses to identify damages. The conventional sensors, which these techniques employ, are passive, often bulky, and can only extract secondary information such as load and strain history, which may not lead to any direct information about damages (Giurgiutiu *et al.*, 2000).

However, the past two decades have witnessed the emergence of “smart” materials, systems and structures, which have shown new possibilities for SHM and NDE. Smart materials, powered by their inherent “smartness” (which work on fundamentally different principles from the conventional materials), exhibit greater sensitivity to any changes in their surrounding environment. This section briefly describes the principles and the recent developments in SHM/NDE based on smart materials and structures.

The definition of smart structures was a topic of controversy from the late 1970s to the late 1980s. In order to arrive at a consensus for major terminology, a special workshop was organized by the US Army Research Office in 1988, in which “sensors”, “actuators”, “control mechanism” and “timely response” were recognized as the four qualifying features of any smart system or structure (Rogers *et al.*, 1988). The following definition of smart systems/structures was formally adopted in the workshop (Ahmad, 1988):

*A system or material which has built-in or intrinsic sensor(s), actuator(s) and control mechanism(s) whereby it is capable of **sensing** a stimulus, **responding** to it in a predetermined manner and extent, in a **short/appropriate** time, and reverting to its original state as soon as the stimulus is removed.*

According to Varadan and Varadan (2002), “smart system” refers to a device which can sense changes in its environment and can make an optimal response by changing its material properties, geometry, mechanical or electromagnetic response. Both the sensor and the actuator must function with their appropriate feedback properly integrated. It should also be noted that if the response is too slow or too fast, the system could lose its application effectiveness or could be dangerous (Takagi, 1990). Although the workshop distinguished the terms “smart” and “intelligent”, the two have still been used almost interchangeably.

In conjunction with smart structures, Rogers (1990) defined the following additional terms, which are meant to classify smart structures further, based on the level of sophistication:

- (1) **Sensory Structures:** These structures possess sensors that enable the determination or monitoring of system states/characteristics;
- (2) **Adaptive Structures:** These structures possess actuators that enable the alteration of system states/characteristics in a controlled manner;
- (3) **Controlled Structures:** These result from the intersection of the sensory

and the adaptive structures. They possess both sensors and actuators integrated in feedback architecture for the purpose of controlling the system states/characteristics;

(4) **Active Structures:** These structures possess both sensors and actuators that are highly integrated into the structure and exhibit structural functionality in addition to control functionality;

(5) **Intelligent Structures:** These structures are basically active structures possessing highly integrated control logic and electronics that provide the cognitive element of distributed or hierarchic control architecture.

It should be noted that the sensor-actuator-controller combination can be realized either at the macroscopic (structure) level or microscopic (material) level. Accordingly, we have smart structures and materials respectively.

1.3 Smart Materials

Smart materials possess adaptive capabilities to external stimuli, such as loads or the environment, with inherent intelligence. In the US Army Research Office Workshop, Rogers *et al.* (1988) defined smart materials as *materials which possess the ability to change their physical properties in a specific manner in response to specific stimulus input*. The stimuli could be pressure, temperature, electric and magnetic fields, chemicals or nuclear radiation. The associated changeable physical properties could be shape, stiffness, viscosity or damping. This kind of “smartness” is generally programmed by material composition, special processing, introduction of defects or by modifying the micro-structure, to facilitate adaptation to various levels of stimuli in a controlled fashion. Like smart structures, the terms “smart” and “intelligent” are used interchangeably for smart materials too. Takagi (1990) defined intelligent materials as those responding to environmental changes at the most optimum conditions and manifest their own functions according to the environment. The feedback functions within the materials are combined with the properties and the functions of the materials.

Smart materials include optical fibers, piezoelectric polymers and ceramics, electro-rheological (ER) fluids, magneto-strictive materials and shape memory alloys (SMAs). Fig. 1.1 shows the associated “stimulus” and “response” of the more common smart materials. Due to their special ability to respond to stimuli, numerous applications in the field of sensors and actuators are being found. A detailed description of smart materials is covered by Gandhi and Thompson (1992).

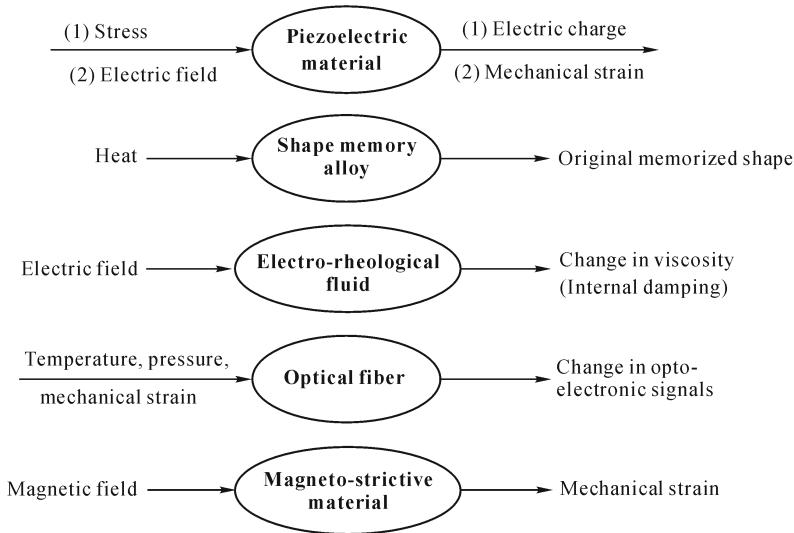


Fig. 1.1 Common smart materials and associated stimulus-response

Smart materials can be either *active* or *passive*. Fairweather (1998) defined active smart materials as those materials which possess the capacity to modify their geometric or material properties under the application of electric, thermal or magnetic fields, thereby acquiring an inherent capacity to transduce energy. Piezoelectric materials, SMAs, ER fluids and magnetostrictive materials are active smart materials, and as such, can be used as force transducers and actuators. The SMAs, for example, have a large recovery force of the order of 700 MPa (Kumar, 1991), which can be utilized for actuation. Similarly, piezoelectric materials can convert electrical energy into mechanical force. Smart materials, which are not active, are described as passive. Although smart, they lack the inherent capability to transduce energy. Fiber-optic material is a good example of a passive smart material. Such materials can act as sensors but not as actuators or transducers.

1.4 Piezoelectricity and Piezoelectric Materials

Since Part I of this book is primarily concerned with piezoelectric materials, a brief description of the phenomenon and related information is presented here. The word “piezo” is derived from a Greek word meaning “pressure”. The phenomenon of piezoelectricity was discovered in 1880 by Pierre and Paul-Jacques Curie. It occurs in non-centrosymmetric crystals, such as quartz (SiO_2), Lithium Niobate (LiNbO_3), PZT ($\text{Pb}(\text{Zr}_{1-x}\text{Ti}_x)\text{O}_3$) and PLZT ($(\text{Pb}_{1-x}\text{La}_x)(\text{Zr}_{1-y}\text{Ti}_y)\text{O}_3$), in which electric dipoles (and hence surface charges) are generated when the crystals undergo mechanical deformations. The same crystals also exhibit the converse

effect, that is, they undergo mechanical deformations when subjected to electric fields. In centrosymmetric crystals, the act of deformation does not induce any dipole moment, as shown in Fig. 1.2. However, in non-centrosymmetric crystals, this leads to a net dipole moment (Fig. 1.3). Similarly, the act of applying an electric field induces mechanical strains in the non-centrosymmetric crystals.

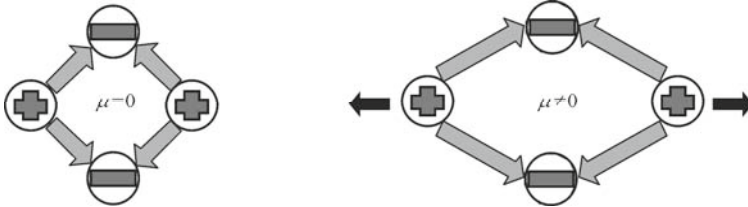


Fig. 1.2 Centrosymmetric crystals: the act of stretching does not cause any dipole moment ($\mu =$ Dipole moment)

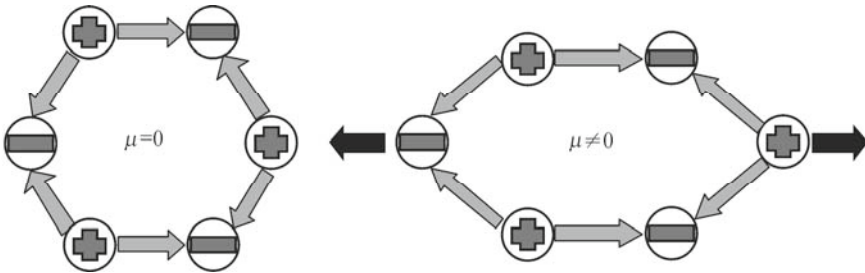


Fig. 1.3 Non-centrosymmetric crystals: the act of stretching causes dipole moment in the crystal ($\mu =$ Dipole moment)

The constitutive relations for piezoelectric materials, under small field conditions are (IEEE standard, 1987; Ikeda, 1990):

$$D_i = \overline{\epsilon}_{ij}^T E_j + d_{im}^d T_m \tag{1.1}$$

$$S_k = d_{jk}^c E_j + \overline{s}_{km}^E T_m \tag{1.2}$$

Eq. (1.1) represents the so called *direct effect* (i.e., stress induced electrical charges) whereas Eq. (1.2) represents the *converse effect* (i.e., electric field induced mechanical strains). Sensor applications are based on the direct effect and actuator applications on the converse effect. When the sensor is exposed to a stress field, it generates proportional charge in response which can be measured. On the other hand, when the actuator is bonded to the structure and an external field is applied, an induced strain field results. Generally, Eqs. (1.1) and (1.2) can be rewritten in the tensor form as (Sirohi and Chopra, 2000b):

$$\begin{bmatrix} D \\ S \end{bmatrix} = \begin{bmatrix} \overline{\epsilon^T} & \overline{d^d} \\ d^c & \overline{s^E} \end{bmatrix} \begin{bmatrix} E \\ T \end{bmatrix} \quad (1.3)$$

where $[D]_{(3 \times 1)}$ (C/m²) is the electric displacement vector, $[S]_{(3 \times 3)}$ the second order strain tensor, $[E]_{(3 \times 1)}$ (V/m) the applied external electric field vector and $[T]_{(3 \times 3)}$ (N/m²) the stress tensor. Accordingly, $[\overline{\epsilon^T}]$ (F/m) is the second order dielectric permittivity tensor under constant stress, $[\overline{d^d}]$ (C/N) and $[d^c]$ (m/V) the third order piezoelectric strain coefficient tensors, and $[\overline{s^E}]$ (m²/N) the fourth order elastic compliance tensor under constant electric field. Taking advantage of the symmetry of the stress and the strain tensors, these can be reduced from a second order (3×3) tensor form to an equivalent vector form, (6×1) in size, *i.e.*, $[S] = [S_{11}, S_{22}, S_{33}, S_{23}, S_{31}, S_{12}]^T$ and similarly, $[T] = [T_{11}, T_{22}, T_{33}, T_{23}, T_{31}, T_{12}]^T$. Accordingly, the piezoelectric strain coefficients can be reduced to second order tensors (from third order tensors), as $[\overline{d^d}]$ (3×6) and $[d^c]$ (6×3). The superscripts “*d*” and “*c*” indicate *direct* and *converse* effects, respectively. Similarly, the fourth order elastic compliance tensor $[\overline{s^E}]$ can be reduced to (6×6) second order tensor. The superscripts “*T*” and “*E*” indicate that the parameter has been measured at constant stress (free mechanical boundary) and constant electric field (short-circuited), respectively. A bar above any parameter signifies that it is complex in nature (*i.e.* measured under dynamic conditions). The piezoelectric strain coefficient d_{jk}^c defines mechanical strain per unit electric field under constant (zero) mechanical stress, and d_{im}^d defines electric displacement per unit stress under constant (zero) electric field. In practice, the two coefficients are numerically equal. Furthermore, in d_{jk}^c or d_{im}^d , the first subscript denotes the direction of the electric field and the second, the direction of the associated mechanical strain. For example, the term d_{31} signifies that the electric field is applied in direction “3” and the strain is measured in direction “1”. For a sheet of piezoelectric material (Fig. 1.4), the poling direction is usually along the thickness and is denoted as 3-axis. The 1-axis and 2-axis are in the plane of the sheet. The matrix $[d^c]$ depends on the crystal structure: for example, it is different for PZT and quartz, as given by Zhu (2003):

$$d^c = \begin{bmatrix} 0 & 0 & d_{31} \\ 0 & 0 & d_{32} \\ 0 & 0 & d_{33} \\ 0 & d_{24} & 0 \\ d_{15} & 0 & 0 \\ 0 & 0 & 0 \end{bmatrix} \text{ (PZT)}, \quad \begin{bmatrix} d_{11} & 0 & 0 \\ -d_{11} & 0 & 0 \\ 0 & 0 & 0 \\ d_{14} & 0 & 0 \\ 0 & -d_{14} & 0 \\ 0 & -2d_{11} & 0 \end{bmatrix} \text{ (quartz)} \quad (1.4)$$

where the coefficients d_{31} , d_{32} and d_{33} relate the normal strain in 1, 2 and 3 directions, respectively, to an electric field along the poling direction 3. For PZT crystals, the coefficient d_{15} relates the shear strain in the 1–3 plane to the field E_1 and d_{24} relates the shear strain in the 2–3 plane to the electric field E_2 . It is not possible to produce shear strain in the 1–2 plane purely by the application of an electric field, since all terms in the last row of the matrix $[d^E]$ are zero (see Eq. (1.4)). Conversely, shear stress in the 1–2 plane does not generate any electric response. In all poled piezoelectric materials, d_{31} is negative and d_{33} is positive. For a good sensor, the algebraic sum of d_{31} and d_{33} should be maximum and at the same time, the electric permittivity and the mechanical loss factor should be minimum (Kumar, 1991).

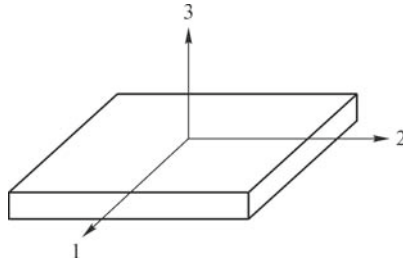


Fig. 1.4 A piezoelectric material sheet with conventional 1, 2 and 3 axes

The compliance matrix has the form:

$$\overline{s^E} = \begin{bmatrix} \overline{s_{11}^E} & \overline{s_{12}^E} & \overline{s_{13}^E} & \overline{s_{14}^E} & \overline{s_{15}^E} & \overline{s_{16}^E} \\ \overline{s_{21}^E} & \overline{s_{22}^E} & \overline{s_{23}^E} & \overline{s_{24}^E} & \overline{s_{25}^E} & \overline{s_{26}^E} \\ \overline{s_{31}^E} & \overline{s_{32}^E} & \overline{s_{33}^E} & \overline{s_{34}^E} & \overline{s_{35}^E} & \overline{s_{36}^E} \\ \overline{s_{41}^E} & \overline{s_{42}^E} & \overline{s_{43}^E} & \overline{s_{44}^E} & \overline{s_{45}^E} & \overline{s_{46}^E} \\ \overline{s_{51}^E} & \overline{s_{52}^E} & \overline{s_{53}^E} & \overline{s_{54}^E} & \overline{s_{55}^E} & \overline{s_{56}^E} \\ \overline{s_{61}^E} & \overline{s_{62}^E} & \overline{s_{63}^E} & \overline{s_{64}^E} & \overline{s_{65}^E} & \overline{s_{66}^E} \end{bmatrix} \quad (1.5)$$

Owing to energy considerations, the compliance matrix is symmetric, which leaves only 21 independent coefficients. Furthermore, for isotropic materials, there are only two independent coefficients, as expressed below (remaining terms are zero):

$$\overline{s_{11}^E} = \overline{s_{22}^E} = \overline{s_{33}^E} = \frac{1}{\gamma^E} \quad (1.6)$$

$$\overline{s_{12}^E} = \overline{s_{13}^E} = \overline{s_{21}^E} = \overline{s_{23}^E} = \overline{s_{31}^E} = \overline{s_{32}^E} = \frac{-\nu}{\gamma^E} \quad (1.7)$$

$$\overline{s_{44}^E} = \overline{s_{55}^E} = \overline{s_{66}^E} = \frac{1}{G^E} \quad (1.8)$$

where $\overline{Y^E}$ is the complex Young's modulus of elasticity (at constant electric field), $\overline{G^E}$ the complex shear modulus (at constant electric field) and ν the Poisson's ratio. It should be noted that the static moduli, Y^E and G^E , are related by:

$$G^E = \frac{Y^E}{2(1+\nu)} \quad (1.9)$$

The electric permittivity matrix is also symmetric, which reduces the number of independent coefficients to 6. Typically, it takes the following simple forms for monoclinic, cubic and orthorhombic crystals (Zhu, 2003):

$$\overline{[\varepsilon^T]} = \begin{bmatrix} \overline{\varepsilon_{11}^T} & 0 & \overline{\varepsilon_{31}^T} \\ 0 & \overline{\varepsilon_{22}^T} & 0 \\ \overline{\varepsilon_{13}^T} & 0 & \overline{\varepsilon_{33}^T} \end{bmatrix}, \begin{bmatrix} \overline{\varepsilon_{11}^T} & 0 & 0 \\ 0 & \overline{\varepsilon_{22}^T} & 0 \\ 0 & 0 & \overline{\varepsilon_{33}^T} \end{bmatrix}, \begin{bmatrix} \overline{\varepsilon_{11}^T} & 0 & 0 \\ 0 & \overline{\varepsilon_{11}^T} & 0 \\ 0 & 0 & \overline{\varepsilon_{11}^T} \end{bmatrix} \quad (1.10)$$

monoclinic orthorhombic cubic
(e.g. PZT)

It should be noted that Eqs. (1.1) and (1.2) are valid under low electric fields only. At high electric fields, the second order terms in electric fields make significant contributions. This effect is called the *electrostrictive effect*. Typically, inclusion of this effect will render Eq. (1.1) to

$$D_i = \varepsilon_{ij}^T E_j + d_{im}^d T_m + M_{mn} E_m E_n \quad (1.11)$$

where M_{mn} is the *electrostriction coefficient*, and is independent of the direction of the electric field (Sirohi and Chopra, 2000a). A very common electrostrictive crystal is PMN ($\text{Pb}(\text{Mg}_{1/3}\text{Nb}_{2/3})\text{O}_3$). The main advantage of electrostrictive materials is that they exhibit negligible hysteresis (which is significant in piezoelectric crystals), making them the first choice for high voltage applications or where precision positioning of components is warranted (Zhu, 2003). In addition, because of non-linear dependence, they can generate larger motions. It is for this reason that PMN has found its place in actuators used in the Hubble space telescope.

In initial studies, piezoelectric crystals, which are brittle and heavy, were used. However, commercial piezoelectric materials are now available as ceramics or polymers, which can be cut into a variety of convenient shapes and sizes, and can be easily bonded. PZT is the most widely used piezoceramic. It is a solid solution of lead zirconate and lead titanate, doped with other materials to obtain specific properties. It is manufactured by heating a mixture of lead, zirconium and titanium oxide powders to approximately 800 to 1,000 °C, to obtain a perovskite PZT

powder, which is then mixed with a binder and sintered into the desired shape. The resulting unit cell is elongated in one direction and exhibits a permanent dipole moment along this axis. However, since the ceramic consists of numerous randomly oriented domains, it has no net polarization. Application of a high electric field aligns the polar axes of the unit cells along the applied electric field, thereby reorienting most of the domains. This process is called **poling** and it imparts a permanent net polarization to the crystal. A permanent mechanical distortion is also created, since the polar axis of the unit cell is longer than the other two axes. Through this process, the material becomes piezoelectrically transversely isotropic in the plane normal to the poling direction, *i.e.* $d_{31} = d_{32} \neq d_{33}$; $d_{15} = d_{24}$, but remains mechanically isotropic (Sirohi and Chopra, 2000b).

PZT is a very versatile smart material. It is chemically inert and exhibits high sensitivity of about $3 \mu\text{V}/\text{Pa}$, which warrants nothing more sophisticated than a charge amplifier to buffer the extremely high-source impedance of this largely capacitive transducer. It demonstrates competitive characteristics such as light weight, low cost, small size and good dynamic performance. It also exhibits a large range of linearity (typically up to an electric field of $2 \text{ kV}/\text{cm}$ (Sirohi and Chopra, 2000a)), fast response, long term stability and high energy conversion efficiency. PZT patches can be manufactured in any shape, size and thickness (from finite rectangular shapes to complicated microelectromechanical system (MEMS) shapes) at a relatively low cost compared with the other smart materials, and can be easily used over a wide range of pressures without serious non-linearity. PZT material is also characterized by a high elastic modulus (comparable to aluminum). However, it is somewhat fragile because of its brittleness and low tensile strength. Tensile strength measured under dynamic loading is much lower (approximately one-third) than that measured under static conditions. Typically, G1195 (Piezo Systems Inc., 2003) has a compressive strength of 520 MPa and a tensile strength of 76 MPa (static) and 21 MPa (dynamic). PZT materials have negative d_{31} , which implies that a positive electric field (in the direction of polarization) results in compressive strain on the PZT sheet. If heated above a critical temperature, (the *Curie temperature*), the crystals lose their piezoelectric effect. The Curie temperature typically varies from 150 to 350°C for most commercial PZT crystals. In addition, if exposed to high electric fields ($>12 \text{ kV}/\text{cm}$), opposite to the poling direction, PZT will lose most of its piezoelectric capability. This is called *depoling* and is accompanied by a permanent change in the dimensions of the sample. Owing to high stiffness, PZT sheets are good actuators. They also exhibit high strain coefficients, and hence good sensors too. These features make PZT materials well suited for use as collocated actuators and sensors. Their uses include in deformable mirrors, mechanical micropositioners, impact devices and ultrasonic motors, sonic and ultrasonic sensors, filters and resonators, signal processing devices, igniters and voltage transformers. For achieving large displacements, multi-layered PZT systems can be manufactured, as stack, moonie and bimorph actuators. However, PZT sheets, being brittle, cannot withstand bending and also exhibit poor conformability to curved surfaces. Furthermore, PZT materials show considerable fluctuation of electrical properties with

temperature. The act of soldering wires to the electroded piezoceramics requires special skill, otherwise broken elements, unreliable connections or localized thermal depoling of the elements may result. As a solution to these problems, active piezoceramic composite actuators (by Smart Materials Corporation), active fiber composites (by Massachusetts Institute of Technology) and macro fiber composites (MFCs) (by NASA, Langley Centre) have recently been developed; MFCs have been commercially available since 2003. These new types of PZT materials are low-cost, damage tolerant, can conform to curved surfaces and are embeddable. Moreover, Active Control eXperts, Inc. (ACX), now owned by Mide Technology Corporation (2004), has developed a packaging technology in which one or more PZT elements are laminated between sheets of polymer flexible printed circuitry. This provides them with robustness, reliability and ease of use. The packaged sensors are commercially called QuickPack[®] actuators (Mide Technology Corporation, 2004). These are now widely used as vibration dampers in sporting goods, buzzer alerts, drivers for flat speakers and more recently in automotive and aerospace components (Pretorius *et al.*, 2004). However, these are currently several times more expensive than the raw PZT patches.

Contrary to piezoceramics, piezopolymers are very flexible in nature. The most common commercial piezopolymer is the Polyvinylidene Fluoride (PVDF). It is made up of long chains of repeating monomer ($-\text{CH}_2-\text{CF}_2-$), each of which has an inherent dipole moment. PVDF film is manufactured by solidification from the molten phase, then stretched in a particular direction, and poled. The stretching process aligns the chains in one single direction. Combined with poling, this imparts a permanent dipole moment to the film. As a result of stretching, the material is rendered piezoelectrically orthotropic, that is $d_{31} \neq d_{32}$, where “1” is the stretching direction. However, it still remains mechanically isotropic. The PVDF material is characterized by low stiffness (Young’s modulus typically $1/12^{\text{th}}$ that of aluminum). Hence, PVDF sensors are less likely to modify the stiffness of the host structure through their own stiffness. Also, PVDF films can be shaped as desired according to the intended application. Being a polymer, and being flexible, it can be formed into very thin sheets and adhered to curved surfaces. These characteristics make PVDF films more attractive for sensor applications, in spite of their low piezoelectric coefficients (approximately $1/10^{\text{th}}$ of PZT). It has been shown by Sirohi and Chopra (2000b) that shear lag effect (caused by the finitely thick bond layer between the patch and the host structure) is almost negligible in PVDF sensors.

Traditionally, piezoelectric materials have been well-known for their use in accelerometers, strain sensors, emitters and receptors of stress waves, vibration sensors, actuators and pressure transducers. In the last decade, piezoelectric materials, their derivative devices and structures have been increasingly employed in turbo-machinery actuators, vibration dampers and active vibration control of stationary/moving structures (*e.g.* helicopter blades). They have been shown to be very promising in active structural control of lab-sized structures and machines (*e.g.* Manning *et al.*, 2000; Song *et al.*, 2002). Structural control of large structures has also been attempted (*e.g.* Kamada *et al.*, 1997). Other new applications

include underwater acoustic absorption, robotics, precision positioning and smart skins for submarines (Kumar, 1991). Skin-like tactile sensors utilizing the piezoelectric effect for sensing temperatures and pressures have been reported. Piezoelectric materials have also been employed to produce micro- and nano-scale systems and wireless inter digital transducers (IDT) using advanced embedded system technologies, which are expected to find numerous applications in micro-electronics, bio-medical and SHM. In the field of SHM, the most striking application of piezoelectric materials has been in the form of the electro-mechanical impedance (EMI) technique. This is the main focus of Part I, and the details are covered in Chapters 2 to 7.

References

- Adams, R.D., Cawley, P., Pye, C.J. and Stone, B.J. (1978). "A Vibration Technique for Non-Destructively Assessing the Integrity of Structures", *Journal of Mechanical Engineering Science*, 20: 93-100.
- Ahmad, I. (1988). "Smart Structures and Materials", *Proceedings of U.S. Army Research Office Workshop on Smart Materials, Structures and Mathematical Issues*, September 15-16, Virginia Polytechnic Institute & State University, Technomic Publishing Co., Inc., 13-16.
- Aktan, A.E., Catbas, F.N., Grimmelsman, K.A. and Tsikos, C.J. (2000). "Issues in Infrastructure Health Monitoring for Management", *Journal of Engineering Mechanics*, 126(7): 711-724.
- Banan, M.R., Banan, M.R. and Hjelmstad, K.D. (1994). "Parameter Estimation of Structures from Static Response. I. Computational Aspects", *Journal of Structural Engineering*, 120(11): 3243- 3258.
- Boller, C. (2002). "Structural Health Management of Ageing Aircraft and Other Infrastructure", *Monograph on Structural Health Monitoring*, Institute of Smart Structures and Systems (ISSS), 1-59.
- Catbas, F.N., Ciloglu, S.K., Hasancebi, O., Grimmelsman, K. and Aktan, A.K. (2007). "Limitations in Structural Identification of Large Constructed Structures", *Journal of Structural Engineering*, 133: 1051-1066.
- El-Borgi, S., Choura, S., Ventura, C., Baccouch, M. and Cherif, F. (2005). "Modal Identification and Model Updating of a Reinforced Concrete Bridge", *Smart Structures and Systems*, 1: 83-101.
- Fairweather, J.A. (1998). "Designing with Active Materials: An Impedance Based Approach", *Ph.D. Thesis*. Rensselaer Polytechnic Institute, New York.
- Farrar, C.R. and Jauregui, D.A. (1998). "Comparative Study of Damage Identification Algorithms Applied to a Bridge: I. Experiment", *Smart Materials and Structures*, 7(5): 704-719.
- Gandhi, M.V. and Thompson, B.S. (1992). *Smart Materials and Structures*. London: Chapman and Hall.
- Giurgiutiu, V., Redmond, J., Roach, D. and Rackow, K. (2000). "Active Sensors

- for Health Monitoring of Ageing Aerospace Structures”, *Proceedings of the SPIE Conference on Smart Structures and Integrated Systems*, SPIE 3985: 294-305.
- Giurgiutiu, V. and Zagrai, A.N. (2002). “Embedded Self-Sensing Piezoelectric Active Sensors for On-Line Structural Identification”, *Journal of Vibration and Acoustics*, ASME, 124: 116-125.
- IEEE (1987). *IEEE Standard on Piezoelectricity, Std. 176*. IEEE/ANSI.
- Ikeda, T. (1990). *Fundamentals of Piezoelectricity*. Oxford: Oxford University Press.
- Kamada, T., Fujita, T., Hatayama, T., Arikabe, T., Murai, N., Aizawa, S. and Tohyama, K. (1997). “Active Vibration Control of Frame Structures with Smart Structures Using Piezoelectric Actuators (Vibration Control by Control of Bending Moments of Columns)”, *Smart Materials and Structures*, 6: 448-456.
- Kessler, S.S., Spearing, S.M., Attala, M.J., Cesnik, C.E.S. and Soutis, C. (2002). “Damage Detection in Composite Materials Using Frequency Response Methods”, *Composites, Part B: Engineering*, 33: 87-95.
- Kumar, S. (1991). “Smart Materials for Acoustic or Vibration Control”, *Ph.D. Dissertation*. Pennsylvania State University, USA.
- Loh, C.H. and Tou, I.C. (1995). “A System Identification Approach to the Detection of Changes in Both Linear and Non-linear Structural Parameters”, *Earthquake Engineering and Structural Dynamics*, 24(1): 85-97.
- Lynch, J.P., Partridge, A., Law, K.H., Kenny, T.W., Kiremidjian, A.S. and Carryer, E. (2003). “Design of Piezoresistive MEMS-Based Accelerometer for Integration with Wireless Sensing Unit for Structural Monitoring”, *Journal of Aerospace Engineering*, 16(3): 108-114.
- Manning, W.J., Plummer, A.R. and Levesley, M.C. (2000). “Vibration Control of a Flexible Beam with Integrated Actuators and Sensors”, *Smart Materials and Structures*, 9(6): 932-939.
- Mide Technology Corporation (2004) <http://www.mide.com>.
- Moyo, P. (2002). “Structural Performance Monitoring and Health Assessment of Highway Bridges”, *Ph. D. Thesis*. Nanyang Technological University, Singapore.
- Oreta, A.W.C. and Tanabe, T. (1994). “Element Identification of Member Properties of Framed Structures”, *Journal of Structural Engineering*, 120(7): 1961-1976.
- Pandey, A.K., Biswas, M. and Samman, M.M. (1991). “Damage Detection from Changes in Curvature Mode Shapes”, *Journal of Sound and Vibration*, 145(2): 321-332.
- Pandey, A.K. and Biswas, M. (1994). “Damage Detection in Structures Using Changes in Flexibility”, *Journal of Sound and Vibration*, 169(1): 3-17.
- Piezo Systems Inc. (2003) <http://www.piezo.com>.
- Pretorius, J., Hugo, M. and Spangler, R. (2004). “A Comparison of Packaged Piezoactuators for Industrial Applications”, *Technical Note*. Mide Technology Corporation, <http://www.mide.com>.
- Rogers, C.A., Barker, D.K. and Jaeger, C.A. (1988). “Introduction to Smart

- Materials and Structures”, *Proceedings of U.S. Army Research Office Workshop on Smart Materials, Structures and Mathematical Issues*, September 15-16, Virginia Polytechnic Institute & State University, Technomic Publishing Co., Inc., 17-28.
- Rogers, C.A. (1990). “Intelligent Material Systems and Structures”, *Proceedings of U.S.-Japan Workshop on Smart/Intelligent Materials and Systems*, edited by Ahmad, I., Crowson, A., Rogers C.A. and Aizawa, M., March 19-23, Honolulu, Hawaii, Technomic Publishing Co., Inc., 11-33.
- Sanayei, M. and Saletnik, M.J. (1996). “Parameter Estimation of Structures from Static Strain Measurements. I: Formulation”, *Journal of Structural Engineering*, 122(5): 555-562.
- Sirohi, J. and Chopra, I. (2000a). “Fundamental Behaviour of Piezoceramic Sheet Actuators”, *Journal of Intelligent Material Systems and Structures*, 11(1): 47-61.
- Sirohi, J. and Chopra, I. (2000b). “Fundamental Understanding of Piezoelectric Strain Sensors”, *Journal of Intelligent Material Systems and Structures*, 11(4): 246-257.
- Song, G., Qiao, P.Z., Binienda, W.K. and Zou, G.P. (2002). “Active Vibration Damping of Composite Beam Using Smart Sensors and Actuators”, *Journal of Aerospace Engineering*, 15(3): 97-103.
- Stubbs, N. and Kim, J.T. (1994). “Field Verification of a Nondestructive Damage Localization and Severity Estimation Algorithm”, *Texas A & M University Report prepared for New Mexico State University*.
- Sun, L., Li, H.N., Ren, L. And Jin, Q. (2007). “Dynamic Response Measurement of Offshore Platform Model by FBG sensors”, *Sensors and Actuators A*, 136: 572-579.
- Takagi, T. (1990). “A Concept of Intelligent Materials”, *Proceedings of U.S.-Japan Workshop on Smart/Intelligent Materials and Systems*, edited by Ahmad, I., Crowson, A., Rogers C.A. and Aizawa, M., March 19-23, Honolulu, Hawaii, Technomic Publishing Co., Inc., 3-10.
- Thompson, M. and Harper, M. (2004). “Validation of a New Approach to Condition Monitoring of Offshore Structure—Aspects of a Scale Model”, *Strain*, 40: 25-31.
- Varadan, V.K. and Varadan, V.V. (2002). “Microsensors, Micoelectromechanical Systems (MEMS) and Electronics for Smart Structures and Systems”, *Smart Materials and Structures*, 9(6): 953-972.
- Wang, M.L., Heo, G. and Satpathi, D. (1998). “A Health Monitoring System for Large Structural Systems”, *Smart Materials and Structures*, 7(5): 606-616.
- Yao, J.T.P. (1985). *Safety and Reliability of Existing Structures*. London: Pitman Publishing Programme.
- Zhu, W. (2003). *Sensors and Actuators (E6614 Lecture Notes)*. Nanyang Technological University, Singapore.
- Zimmerman, D.C. and Kaouk, M. (1994). “Structural Damage Detection Using a Minimum Rank Update Theory”, *Journal of Vibration and Accoustics*, 116: 222-231.

Electro-Mechanical Impedance Technique

S. Bhalla^{*}, C. K. Soh

^{*}Department of Civil Engineering, Indian Institute of Technology Delhi, Hauz Khas, New Delhi 110016, India
Tel: 91-11-2659-1040; Fax: 91-11-2658-1117
Email: sbhalla@civil.iitd.ac.in

2.1 Introduction

This chapter focuses on the theoretical and the practical aspects of the EMI technique for SHM/NDE. In principle, this technique is similar to the conventional global dynamic techniques described in Chapter 1. The main difference is the frequency range employed: the EMI technique typically employs 30 to 400 kHz whereas the global dynamic techniques employ less than 100 Hz.

In the EMI technique, a PZT patch is usually bonded to the surface of the structure (to be monitored) by means of a high strength epoxy adhesive, and electrically excited by means of an LCR (Inductance L, Capacitance C, and Resistance R) meter or an impedance analyzer. The LCR meter measures the electro-mechanical (EM) admittance of the bonded PZT patch (consisting of the real part, conductance, and the imaginary part, susceptance) in the user-set frequency range, at specified intervals, in sweep mode. When plotted as functions of frequency, these measurements constitute a unique signature of the structure, to be altered only by any physical change in the structure. At any future point of time, whenever the condition of the structure is to be assessed, the signatures are acquired and compared with the baseline signature. Consistency of the signature indicates the well being of the structure. Any change in the signature indicates an occurrence of damage.

Basically, the LCR meter applies a harmonic voltage signal across the PZT patch at a particular frequency. As a result, deformations are produced in the patch as well as in the local area of the host structure around it. The response of this area

to the imposed mechanical vibrations is transferred back to the PZT patch in the form of an electrical response, as conductance and susceptance signatures. As a result of this interaction, the structural characteristics are reflected in the signatures. Any damage to the structure alters the structural characteristics, and hence modifies the signatures.

Fig. 2.1 illustrates an application of the EMI technique on a steel beam. A PZT patch was bonded to the structure (a steel I-beam) at the mid-point of the bottom flange (Bhalla, 2001). The conductance signature of the patch was acquired using a HP 4192A impedance analyzer (Hewlett Packard, 1996) in the frequency range of 140 to 150 kHz, at intervals of 100 Hz. Damage was simulated by drilling a 5 mm diameter hole along section AA (Fig. 2.1(a)). The effect of the damage is shown on the conductance signature in Fig. 2.1(b). Although the induced damage was small (amounting to only 0.015% mass loss), the effect on the signature was very marked and easily recognizable. This demonstrates the high order of sensitivity of the technique. The following sections of this chapter cover the theoretical and practical aspects of the EMI technique.

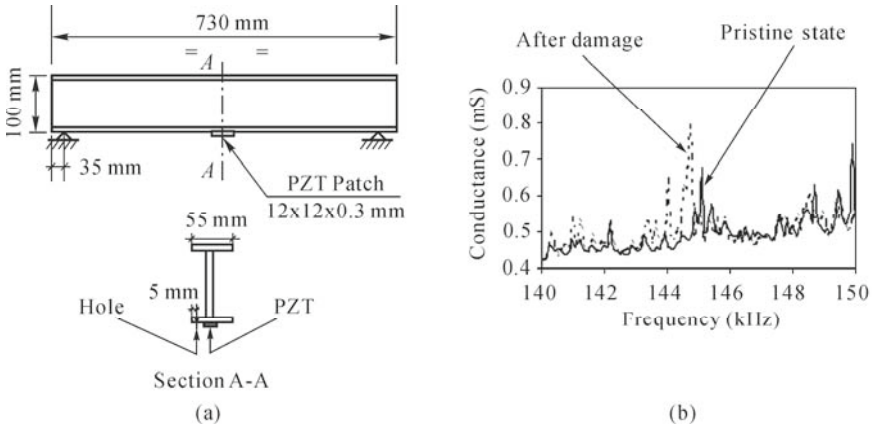


Fig. 2.1 (a) A steel beam instrumented with a PZT patch; (b) Effect of damage on conductance signature

2.2 Mechanical Impedance of Structures

A harmonic force acting on a structure can be represented by a rotating phasor on a complex plane to differentiate it from a vector (Fig. 2.2). Let F_0 be the magnitude of the phasor, and let it be rotating anti-clockwise at an angular frequency ω (same as the angular frequency of the harmonic force). At any instant of time t , the angle between the phasor and the real axis is ωt . The instantaneous force (acting on the structure) is equal to the projection of the phasor on the real axis, i.e. $F_0 \cos \omega t$. The projection on the “y” axis can be deemed as the “imaginary”

component. Hence, the phasor can be expressed using complex notation as:

$$F(t) = F_0 \cos \omega t + jF_0 \sin \omega t = F_0 e^{j\omega t} \quad (2.1)$$

The resulting velocity response, \dot{u} , at the point of application of the force, is also harmonic in nature. However, it lags behind the applied force by a phase angle ϕ due to damping inherent in the structure. Hence, velocity can also be represented as a phasor (Fig. 2.2), and expressed as:

$$\dot{u} = \dot{u}_0 \cos(\omega t - \phi) + j\dot{u}_0 \sin(\omega t - \phi) = \dot{u}_0 e^{j(\omega t - \phi)} \quad (2.2)$$

The *mechanical impedance* of a structure, at any point, is defined as the ratio of the driving harmonic force to the resulting harmonic velocity, at that point, in the direction of the applied force. Mathematically, the mechanical impedance Z can be expressed as:

$$Z = \frac{F}{\dot{u}} = \frac{F_0 e^{j\omega t}}{\dot{u}_0 e^{j(\omega t - \phi)}} = \frac{F_0}{\dot{u}_0} e^{j\phi} \quad (2.3)$$

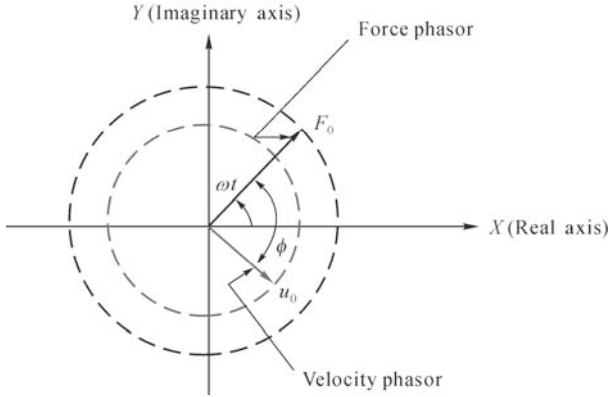


Fig. 2.2 Representation of harmonic force and velocity by rotating phasors

For a pure mass m , from Newton's second law of motion,

$$F = m\ddot{u} \quad (2.4)$$

For a harmonic motion, $\ddot{u} = j\omega\dot{u}$, the mechanical impedance of the system can be computed as:

$$Z = \frac{F}{\dot{u}} = j\omega m \quad (2.5)$$

Similarly, for a pure spring k , from Hooke's law:

$$F = ku \tag{2.6}$$

Note that, $\dot{u} = j\omega u$, the mechanical impedance is thus given by

$$Z = \frac{F}{\dot{u}} = -\frac{jk}{\omega} \tag{2.7}$$

For a pure damper c , the mechanical impedance can be directly obtained as $Z = c$ from the fact that $F = c\dot{u}$. For a parallel combination of 'n' mechanical systems, noting that velocity has to be equal for all the elements, the equivalent mechanical impedance can be derived as:

$$Z_{eq} = \sum_{i=1}^n Z_i \tag{2.8}$$

Similarly, for a series combination, owing to the transmission of the same force,

$$\frac{1}{Z_{eq}} = \sum_{i=1}^n \frac{1}{Z_i} \tag{2.9}$$

As an example, the resultant mechanical impedance of the system shown in Fig. 2.3 can be determined as:

$$Z_{ep} = c + j\left(m\omega - \frac{k}{\omega}\right) \tag{2.10}$$

Eqs. (2.8) and (2.9) are analogous to the equations for series and parallel combinations of 'electrical impedances' in the theory of classical electricity. The main advantage of the impedance approach is that the differential equations of Newtonian mechanics are reduced to simple algebraic equations, and a black-box concept is introduced. Hence, only critical forces and velocities at one or two points of interest need to be considered; the need for a complex analysis of the system is thereby eliminated.

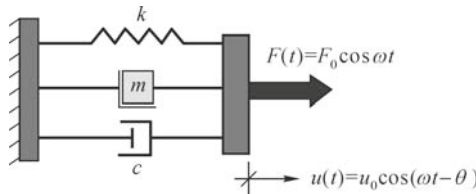


Fig. 2.3 A parallel combination of spring (k), mass (m) and damper (c)

2.3 Impedance Modeling for EMI Technique

In the EMI technique, the PZT patch is typically surface bonded onto the host structure using a high strength epoxy adhesive, and excited under harmonic voltage. In this configuration, the patch essentially behaves as a thin bar undergoing axial vibrations and interacting with the host structure (Fig. 2.4(a)). The PZT patch host-structure system can be modeled as a mechanical impedance (of the host structure) connected to an axially vibrating thin bar (the patch) as shown in Fig. 2.4(b). Here, the patch expands and contracts dynamically in

direction “1” under a uniform alternating electric field E_3 ($\frac{\partial E_3}{\partial x} = \frac{\partial E_3}{\partial y} = 0$) which

is applied in direction “3” by a LCR meter. The patch has half-length “ l ”, width “ w ” and thickness “ h ”. The host structure is assumed to be a skeletal structure, *i.e.*, composed of one-dimensional (1D) members with their sectional properties (area and moment of inertia) lumped along their neutral axes. Therefore, the vibrations of the PZT patch in direction “2” can be ignored. At the same time, the PZT loading in direction “3” is neglected by assuming the frequencies involved to be much less than the first resonant frequency for thickness vibrations. The vibrating patch is assumed to be infinitesimally small and of negligible mass and stiffness as compared to the host structure. The structure can therefore be assumed to possess uniform dynamic stiffness over the entire bonded area. The two end points of the patch can thus be assumed to encounter equal mechanical impedance, Z , from the structure (Fig. 2.4(b)). Under this condition, the PZT patch has zero displacement at the mid-point ($x=0$), irrespective of the location of the patch on the host-structure.

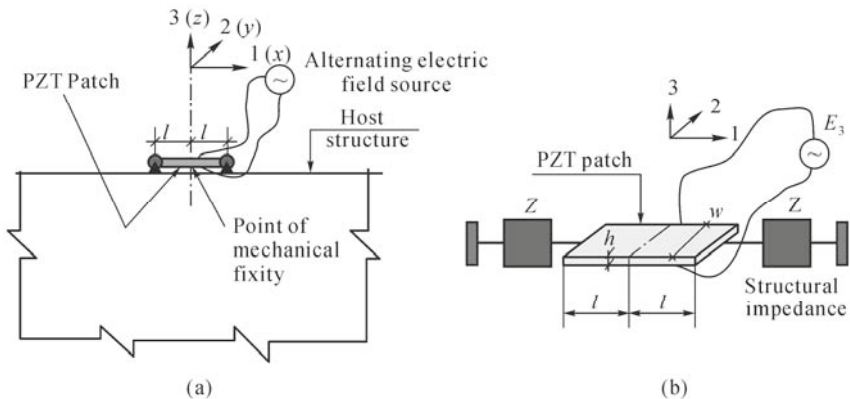


Fig. 2.4 Modeling of PZT-structure interaction. (a) PZT patch bonded to structure under electric excitation; (b) Interaction model of PZT patch and host structure

Under these assumptions, the piezoelectric constitutive relations (Eqs. (1.1) and (1.2)) can be simplified as:

$$D_3 = \overline{\epsilon_{33}^T} E_3 + d_{31} T_1 \tag{2.11}$$

$$S_1 = \frac{T_1}{\overline{Y^E}} + d_{31} E_3 \tag{2.12}$$

where D_3 is the electric displacement over the PZT patch, S_1 the strain in direction “1”, d_{31} the piezoelectric strain coefficient and T_1 the axial stress in direction “1”. $\overline{Y^E} = Y^E (1 + \eta j)$ is the complex Young’s modulus of elasticity of the PZT patch at a constant electric field, and $\overline{\epsilon_{33}^T} = \epsilon_{33}^T (1 - \delta j)$ the complex electric permittivity (in direction “3”) of the PZT material at a constant stress, where $j = \sqrt{-1}$. Here, η and δ denote respectively the mechanical loss factor and the dielectric loss factor of the PZT material.

The EM admittance formulation was analytically derived by Liang *et al.* (1994). They considered a small element of the PZT patch of length δx , situated at a distance x from the centre of the patch (Fig. 2.5), under dynamic equilibrium.

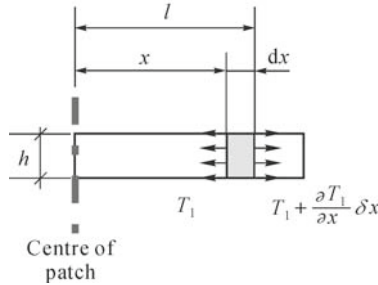


Fig. 2.5 An infinitesimal element of PZT patch under dynamic equilibrium

The infinitesimal element has a mass of

$$dm = \rho wh \delta x \tag{2.13}$$

where ρ is the density of the patch, w its width and h its thickness.

Let $u(x)$ be the displacement at any point in the actuator. Thus, application of the D’Alembert’s principle on the infinitesimal element yields

$$\left[\left(T_1 + \frac{\partial T_1}{\partial x} \delta x \right) - T_1 \right] wh = dm \frac{\partial^2 u}{\partial t^2} \tag{2.14}$$

Substituting Eq. (2.13) into Eq. (2.14) and solving, we obtain:

$$\frac{\partial T_1}{\partial x} = \rho \frac{\partial^2 u}{\partial t^2} \quad (2.15)$$

From Hooke's Law, $T_1 = \overline{Y^E} S_1$ that is

$$T_1 = \overline{Y^E} \frac{\partial u}{\partial x} \quad (2.16)$$

Substitution of Eq. (2.16) into Eq. (2.15) yields

$$\overline{Y^E} \frac{\partial^2 u}{\partial x^2} = \rho \frac{\partial^2 u}{\partial t^2} \quad (2.17)$$

Solution of the governing wave equation, by the method of separation of variables, yields

$$u = (A \sin \kappa x + B \cos \kappa x) e^{j\omega t} \quad (2.18)$$

where κ , the wave number, is related to the angular frequency of excitation ω by

$$\kappa = \omega \sqrt{\frac{\rho}{\overline{Y^E}}} \quad (2.19)$$

Application of the boundary condition that at $x=0$, $u=0$ implies $B=0$. By definition, the mechanical impedance Z of the structure can be expressed as

$$F_{(x=l)} = -Z \dot{u}_{(x=l)} \quad (2.20)$$

The use of a negative sign here simply implies that a positive u gives rise to a force in the opposite direction (compressive in nature) from the mechanical system. From Eq. (2.18), and making use of the fact that $\dot{u} = j\omega u$ (due to harmonic excitations), we get

$$F_{(x=l)} = -A j \omega Z \sin(\kappa l) e^{j\omega t} \quad (2.21)$$

Furthermore, the strain in the PZT patch can be derived as

$$S_1 = \frac{\partial u}{\partial x} = A \kappa (\cos \kappa x) e^{j\omega t} \quad (2.22)$$

Substituting Eqs. (2.21) and (2.22) into Eq. (2.12) for the case of $x=l$, noting that $T_1 = \frac{F_{(x=l)}}{wh}$ and $E_3 = (V/h)$, where V is the potential difference across the PZT patch, we get

$$A \kappa \cos(\kappa l) e^{j\omega t} = \frac{-Aj\omega Z \sin(\kappa l) e^{j\omega t}}{whY^E} + \frac{d_{31}}{h} V \quad (2.23)$$

At this juncture, the mechanical impedance of the PZT patch, similar to that of the structure is introduced. As a general practice, the mechanical impedance of the PZT patch is determined in short circuited condition (Fig. 2.6), so as to eliminate the piezoelectric effect and only invoke pure mechanical response. If F is the force applied on the PZT patch, then from Eq. (2.3), the short-circuited mechanical impedance of the patch, Z_a , can be determined as:

$$Z_a = \frac{F_{(x=l)}}{\dot{u}_{(x=l)}} = \frac{whT_{1(x=l)}}{\dot{u}_{(x=l)}} = \frac{wh\overline{Y^E} S_{1(x=l)}}{j\omega u_{(x=l)}} \quad (2.24)$$

Using Eq. (2.22) for S_1 and Eq. (2.18) for u , an expression can be derived for Z_a as:

$$Z_a = \frac{\kappa wh \overline{Y^E}}{(j\omega) \tan(\kappa l)} \quad (2.25)$$

Hence, upon solving, Eq. (2.23) yields,

$$A = \frac{Z_a V_o d_{31}}{h \kappa \cos(\kappa l) (Z + Z_a)} \quad (2.26)$$

Under general electric field conditions (that is $E_3 \neq 0$), the stress T_1 in the PZT patch is given by Eq. (2.12). Using Eqs. (2.22) and (2.26), with $V = V_o e^{j\omega t}$, an expression for T_1 can be derived as:

$$T_1 = \left[\frac{Z_a \cos \kappa x}{\cos(\kappa l) (Z + Z_a)} - 1 \right] \frac{\overline{V_o Y^E} d_{31} e^{j\omega t}}{h} \quad (2.27)$$

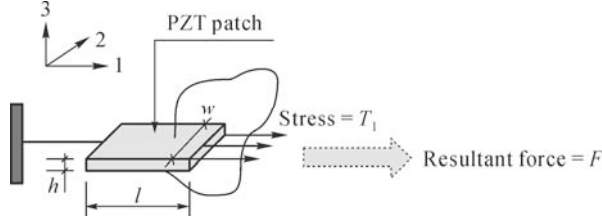


Fig. 2.6 Determination of mechanical impedance of a PZT patch

Substituting Eq. (2.27) into Eq. (2.11) and noting that $E_3 = (V/h) = (V_0/h)e^{j\omega t}$, an expression can be obtained for the electric charge density on the surfaces of the actuator as:

$$D_3 = \left[\frac{Z_a d_{31}^2 \overline{Y^E} \cos \kappa x}{(Z + Z_a) \cos(\kappa l)} + (\overline{\epsilon_{33}^T} - d_{31}^2 \overline{Y^E}) \right] \frac{V_0}{h} e^{j\omega t} \quad (2.28)$$

The electric current can be obtained by integrating the rate of change of the electric charge density over the surface of the PZT patch, that is,

$$I = \int_{y=0}^{y=w} \int_{x=-l}^{x=l} \frac{dD_3}{dt} dx dy = \int_{y=0}^{y=w} \int_{x=-l}^{x=l} D_3 j \omega dx dy \quad (2.29)$$

Substituting Eq. (2.28) and solving,

$$I = \frac{2V_0 e^{j\omega t} w l \omega j}{h} \left[\frac{Z_a d_{31}^2 \overline{Y^E} \tan \kappa l}{(Z + Z_a) \kappa} + (\overline{\epsilon_{33}^T} - d_{31}^2 \overline{Y^E}) \right] \quad (2.30)$$

Since $V_0 e^{j\omega t} = V$, the admittance $\overline{Y} = \frac{I}{V}$ is given by

$$\overline{Y} = 2\omega j \frac{wl}{h} \left[(\overline{\epsilon_{33}^T} - d_{31}^2 \overline{Y^E}) + \left(\frac{Z_a}{Z + Z_a} \right) d_{31}^2 \overline{Y^E} \left(\frac{\tan \kappa l}{\kappa} \right) \right] \quad (2.31)$$

This equation is the same as that derived by Liang *et al.* (1994), except with a multiplication factor of two, which comes into picture since the limits of integration are from $-l$ to $+l$, contrary to Liang *et al.* (1994), who had considered only one half (the right one) of the patch.

In the EMI technique, this electro-mechanical coupling between the mechanical impedance Z of the host-structure and the EM admittance \overline{Y} is utilized in damage detection. Z is a function of the structural parameters—the stiffness, the

damping and the mass distribution. Any damage to the structure will cause these structural parameters to change, and consequently alter the drive point mechanical impedance Z . Assuming that the PZT parameters remain unchanged, the EM admittance \bar{Y} will undergo change and this serves as an indicator of the state of health of the structure. Measuring Z directly may not be feasible, but \bar{Y} can be easily measured using any commercial electrical impedance analyzer or LCR meter. The common damage types which can alter Z include cracks, debondings, corrosion and loose connections (Esteban, 1996), to which the PZT admittance signatures show high sensitivity. Contrary to the low-frequency vibration techniques, damping plays a more significant role in the EMI technique due to the involvement of ultrasonic frequencies. Most conventional damage detection algorithms (in the low-frequency dynamic techniques), on the other hand, are based on damage related changes in structural stiffness and inertia, but rarely in damping (Kawiecki, 2001).

It is worthwhile mentioning that, in the early days, a complicated circuit was recommended by Dosch *et al.* (1992) for achieving self-sensing. An actuating signal was first applied, and the sensing signal was then picked up and separated from the actuating signal. Due to the high voltage and strong dependence of the capacitance on temperature, the signal was mixed with the input voltage as well as noise and was therefore not very accurate. The EMI technique, on the other hand, offers a much hassle free, simplified, and more accurate self-sensing approach.

At low frequencies ($<1/5$ of the first resonant frequency of the PZT patch), the term $\left(\frac{\tan \kappa l}{\kappa l}\right)$ tends to be close to unity. This is called “quasi-static sensor approximation” (Giurgiutiu and Zagrai, 2002), and for this condition, Eq. (2.31) can be simplified as:

$$\bar{Y} = 2\omega j \frac{wl}{h} \left[\bar{\epsilon}_{33}^T - d_{31}^2 \bar{Y}^E \left(\frac{Z}{Z + Z_a} \right) \right] \quad (2.32)$$

The EM admittance \bar{Y} (unit Siemens or ohm^{-1}) consists of the real (*conductance*, G) and imaginary (*susceptance*, B) parts. A plot of G over a sufficiently wide band of frequency serves as a diagnosis signature of the structure and is called the *conductance signature* or simply *signature*.

The signature of the bonded PZT patch is usually acquired by means of commercially available impedance analyzers, such as the HP 4192A impedance analyzer (Hewlett Packard, 1996) or the new version Agilent 4980 LCR meter (Agilent Technologies, 2009). The impedance analyzer/LCR meter imposes an alternating voltage signal of 1 volt rms (root mean square) to the bonded PZT patch over the user-specified preset frequency range (for example, 140 to 150 kHz in Fig. 2.1). The magnitude and phase of the steady state current are directly recorded in the form of conductance and susceptance signatures in the frequency domain, thereby eliminating the requirements of domain transforms. In addition,

no amplifying device is necessary. In fact, Sun *et al.* (1995) reported that higher excitation voltage has no influence on the conductance signature, though it may be helpful in amplifying the weak structural modes and increasing the sensing region.

Fig. 2.7 shows the typical conductance and susceptance plots for a PZT patch bonded on to the bottom flange of the steel beam shown in Fig. 2.1. The sharp peaks in the conductance signature correspond to the structural modes of vibration. This is how the conductance signature identifies the local structural system (in the vicinity of the patch), hence constituting a unique health-signature of the structure at the point of attachment. The imaginary part, on the other hand, is marked by very small peaks and is relatively flat. Owing to stronger interaction with the structure, the real part is traditionally preferred over the imaginary part in SHM applications. In the early days, it was believed that the imaginary part (susceptance) has very weak interaction with the structure. Therefore, most researchers considered it redundant, and solely utilized the real part (conductance) in SHM applications. However, as illustrated in the later part of this chapter, the imaginary part can also supplement the information provided by the real part in improving damage diagnosis of structures.

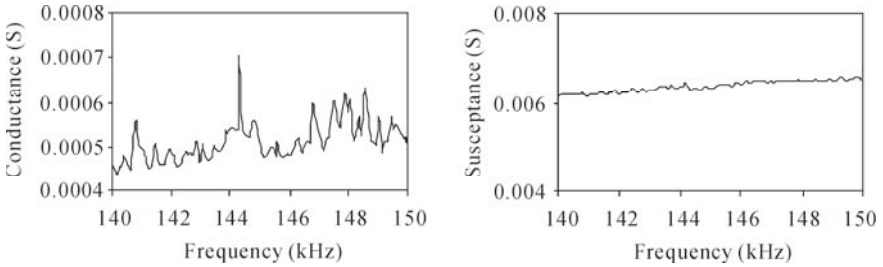


Fig. 2.7 Conductance and susceptance plots of a PZT patch bonded to the bottom flange of a steel beam

2.4 Mechanical Impedance of PZT Patches

The mechanical impedance of a PZT patch, which is a function of frequency, is a complex quantity and can be expressed as:

$$Z_a = x_a + y_a j \quad (2.33)$$

On substituting $\left(\frac{\tan \kappa l}{\kappa l}\right)$ by $(r + tj)$ and $\overline{Y^E}$ by $Y^E(1 + \eta j)$ in Eq. (2.25), and simplifying, we can obtain the following expressions for x_a and y_a

$$x_a = \frac{whY^E(\eta r - t)}{\omega l(r^2 + t^2)} \quad \text{and} \quad y_a = -\frac{whY^E(r + \eta t)}{\omega l(r^2 + t^2)} \quad (2.34)$$

The resonant frequency of the PZT patch can be determined from the condition:

$$\kappa l = \omega_{res} l \sqrt{\frac{\rho}{Y^E(1 + \eta j)}} = \frac{(2n-1)\pi}{2} \quad (2.35)$$

where n is any positive integer. At these frequencies, the term $\tan(\kappa l)$ assumes an infinitely large value, thereby reducing Z_a close to zero. Denoting $\sqrt{\rho/Y^E}$ (which is a complex number) by $(C_r + C_i j)$, and replacing ω_{res} by $2\pi f_{res}$, the following expression can be derived for the resonant frequency

$$f_{res} = \frac{(2n-1)(C_r - C_i j)}{4(C_r^2 + C_i^2)l} \quad (2.36)$$

Similarly, at frequencies where

$$\kappa l = n\pi \quad (2.37)$$

the term $\tan(\kappa l)$ approaches zero, thereby rendering the magnitude of Z_a infinitely large. This phenomenon is called “anti-resonance”, and such frequencies appear as sharp peaks in the plot of $|Z_a|$. The anti-resonance frequencies are related to the corresponding resonant frequencies by

$$f_{ar} = \left(\frac{2n}{2n-1} \right) f_{res} \quad (2.38)$$

Fig. 2.8 shows a plot of the real part (x_a), the imaginary part (y_a) and the absolute value $|Z_a|$ ($= \sqrt{x_a^2 + y_a^2}$) against frequency for a PZT patch which possesses the PZT parameters (except η) shown in Table 2.1. Two different values of mechanical loss factor, $\eta = 0$ and $\eta = 3\%$, have been considered. The points of resonance are apparent as sharp valleys in the plot of $|Z_a|$. Using Eq. (2.36), the first resonance is determined as 14.123 kHz for $\eta = 0$ and at 14.126 kHz for $\eta = 3\%$. Using Eq. (2.38), the first anti-resonance frequency is found to be 28.246 kHz for $\eta = 0$ and to be 28.252 kHz for $\eta = 3\%$.

Table 2.1 Key parameters of PZT patch

S. No.	Physical parameter	Value
1	Young's modulus at constant electric field, Y^E	$6.3 \times 10^{10} \text{ N/m}^2$
2	Piezoelectric strain coefficient, d_{31}	$-166 \times 10^{-12} \text{ m/V}$
3	Electric permittivity at constant stress, ϵ_{33}^T	$1.5 \times 10^{-8} \text{ Farad/m}$
4	Density, ρ	$7,650 \text{ kg/m}^3$
5	Dielectric loss factor, δ	0.012
6	Mechanical loss factor, η	0.001
7	Length of PZT patch, l	0.0508 m
8	Width of PZT patch, w	0.0254 m
9	Thickness of PZT patch, h	$2.54 \times 10^{-4} \text{ m}$

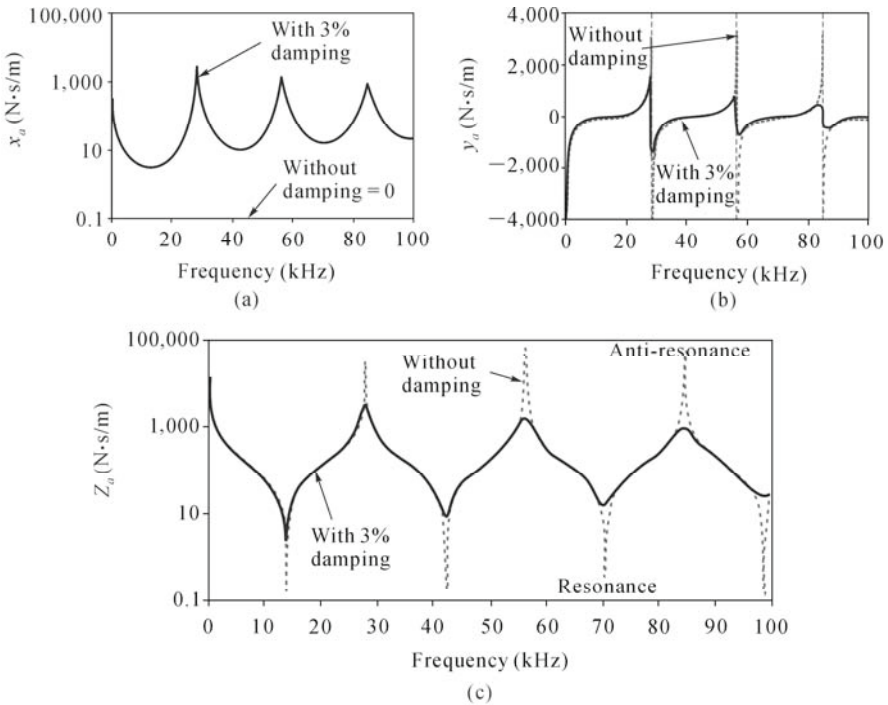


Fig. 2.8 Variation of actuator impedance with frequency. (a) Real part vs. frequency; (b) Imaginary part vs. frequency; (c) Absolute value of impedance vs. frequency

2.5 PZT-Structure Interaction

Fig. 2.9 shows a single degree of freedom (SDOF) system driven by a PZT patch, with parameters as listed in Table 2.1. The system has mass $m=2$ kg, damping

constant $c=125.7 \text{ N}\cdot\text{s/m}$ (damping ratio $\xi_d = 0.01$) and stiffness $k=1.974\times 10^7 \text{ N/m}$. This SDOF system has a natural frequency (undamped) which equals to 500 Hz. Its complex mechanical impedance, $Z=x+yj$ (x = real part and y = imaginary part) can be determined using Eq. (2.10). The conductance and susceptance plots for this system will be those given by Eq. (2.31) divided by a factor of 2 (since only one half of the patch has been considered here).

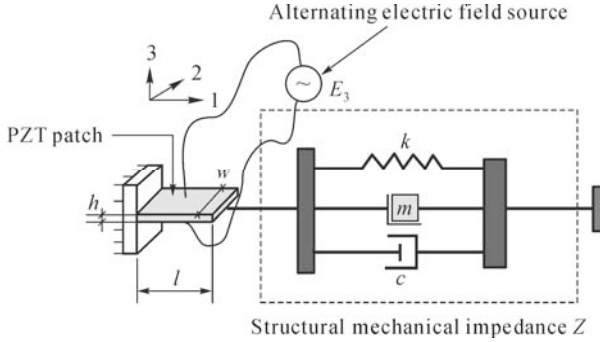


Fig. 2.9 A PZT patch coupled to a spring-mass-damper system

The structural parameters, c , k and m can be altered individually: c increased by 20%, k reduced by 20%, and m increased by 20%, so as to simulate different types of “damages” in the system. Figs. 2.10(a) and (b) respectively show the plots of conductance (G) and susceptance (B) for the pristine state as well as for the various damage states. Figs. 2.10(c) and (d) respectively show the real part (x , x_a) and the imaginary part (y , y_a) of the mechanical impedances of the structure and the PZT patch. Fig. 2.10(e) shows the variation of the absolute mechanical impedance, $|Z|$ of the structure and $|Z_a|$ of the PZT patch.

It can be observed from Fig. 2.10(a) that the G -plot for the pristine state exhibits a peak at the frequency 593 Hz. At this point, it can also be observed from Fig. 2.10(d) that a special condition “ $y = -y_a$ ” occurs, *i.e.*, the imaginary components of the mechanical impedance of the host-structure and of the patch counteract each other. At 593 Hz, the imaginary part of $(Z+Z_a)$ in Eq. (2.31) vanishes and thus G -plot exhibits a peak.

Furthermore, any variation in the structural parameters *viz.* k , c or m (*i.e.*, any “damage” inflicted on the host structure) causes detectable changes in the G -plot as well as in the B -plot. Whereas any reduction in k or any increase of m manifests itself as a leftward shift of the peaks of the G -plot and B -plot, any increase in “ c ” reflects as a suppression of the peak response. Increase in c also leads to marginal increase in the peak frequency, though hardly discernible from the figures. It should be noted that the absolute value of Z (Fig. 2.10(e)), is of comparable magnitude to that of Z_a in the frequency range under consideration.

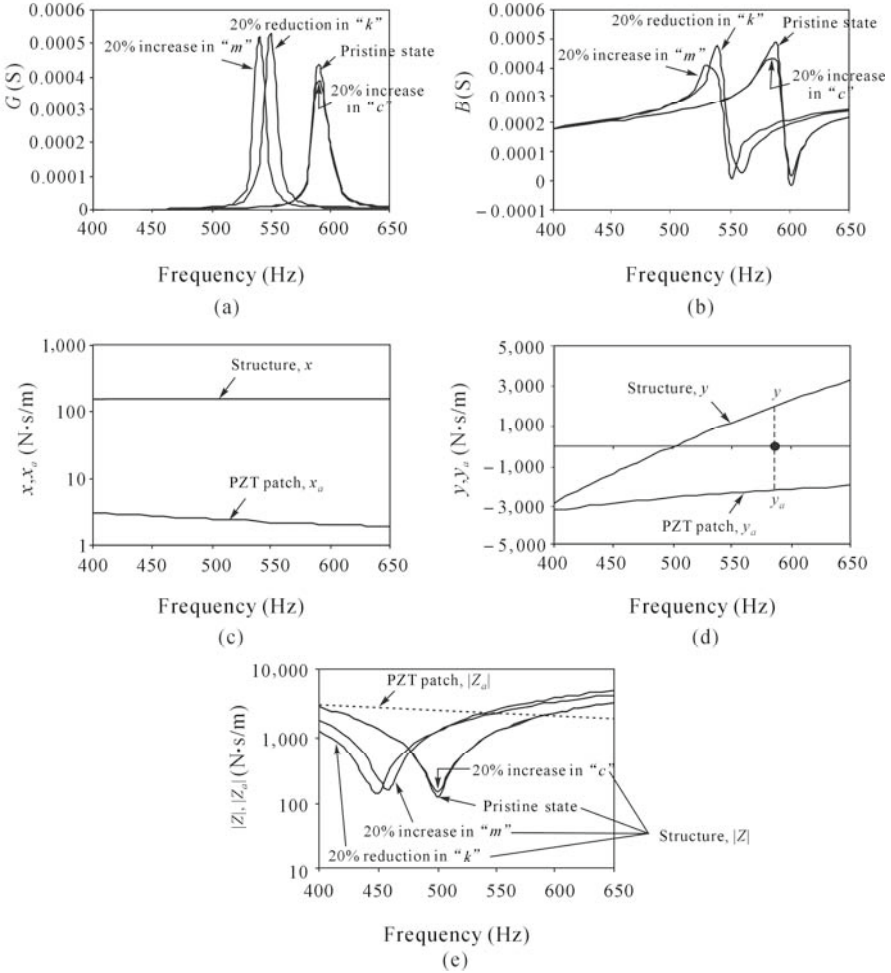


Fig. 2.10 Signatures for SDOF: $m=2.0$ kg, $k=1.974 \times 10^7$ N/m, $c=125.7$ N·s/m. (a) Conductance vs. frequency; (b) Susceptance vs. frequency; (c) Real impedance vs. frequency (pristine); (d) Imaginary impedance vs. frequency (pristine); (e) Absolute impedance vs. frequency

It should also be noted that the peak of the G -plot occurs at a frequency higher than the structural resonant frequency (500 Hz). This shifting of “system natural frequency” from 500 Hz to 593 Hz is due to the additional stiffness and mass contributed by the PZT transducer, since the dynamic stiffness of the PZT patch (or the mechanical impedance) is comparable to that of the structure.

Consider another SDOF system driven by the same PZT patch, with the following parameters: $m=200$ kg, $c=12,566.4$ N·s/m (damping ratio, $\xi_d=0.01$) and $k=1.974 \times 10^9$ N/m. This system also exhibits a resonant frequency of 500 Hz. The interaction plots for this case are shown in Fig. 2.11. Fig. 2.11(e) demonstrates that the magnitude of the structural impedance is much higher than that of the PZT

patch. However, Fig. 2.11(d) shows the condition $y = -y_a$ does occur at a frequency almost equal to 500 Hz. Since the magnitude of y exhibits a large fluctuation compared with y_a , the condition $y = -y_a$ occurs at a frequency only slightly higher than the resonant frequency of the system (500 Hz). It is at this frequency that the G -plot exhibits a sharp peak (Fig. 2.11(a)).

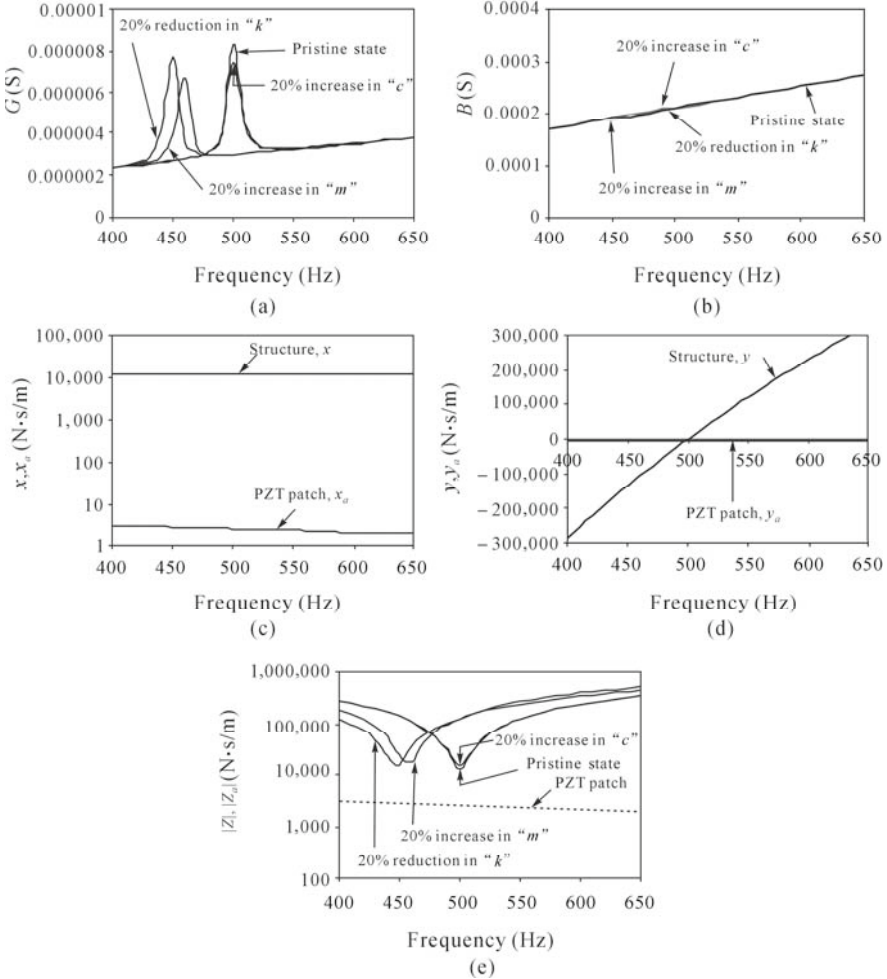


Fig. 2.11 Signatures for SDOF: $m=200$ kg, $k=1.974 \times 10^9$ N/m, $c=12,566.4$ N·s/m; (a) Conductance vs. frequency; (b) Susceptance vs. frequency; (c) Real impedance vs. frequency (pristine); (d) Imaginary impedance vs. frequency (pristine); (e) Absolute impedance vs. frequency

For all practical purposes, the system natural frequency is equal to that of the host structure because of the negligible additional stiffening effect caused by the PZT patch (note from Fig. 2.11(e) that $|Z| > |Z_a|$). This is highly desirable in real-world applications so that the peak of the G -plot can accurately signify the

resonant frequency of the structure.

The effect of variation in the structural parameters (due to damage) on the G -plot and B -plot is also shown in the figure. The variations in the G -plot caused by the damages (Fig. 2.11(a)), are of a similar nature to the first case study. Conversely, the imaginary part B (Fig. 2.11(b)), is largely insensitive to damages. This is because the excessive capacitive contribution of the PZT patch camouflages the structural impact on the signatures.

By rearranging the various terms, Eq. (2.31) can be rewritten as:

$$\bar{Y} = \underbrace{2\omega j \frac{wl}{h} \left[\overline{\epsilon_{33}^T} - d_{31}^2 \overline{Y^E} \right]}_{\text{Part I}} + \underbrace{2\omega j \frac{wl}{h} \frac{Z_a}{(Z + Z_a)} d_{31}^2 \overline{Y^E} \left(\frac{\tan kd}{kd} \right)}_{\text{Part II}} \quad (2.39)$$

From this equation, it can be observed that whereas the first part depends solely on the parameters of the PZT patch, the second part depends partly on the structural parameters and partly on the parameters of the PZT patch. Furthermore, Part II represents the EM coupling between the structure and the PZT patch (since both Z and Z_a appear in the expression of Part II). Hence, Eq. (2.39) can be written as:

$$\bar{Y} = \bar{Y}_p + \bar{Y}_A \quad (2.40)$$

where \bar{Y}_p denotes the PZT contribution and \bar{Y}_A represents the contribution arising from the PZT-structure interaction. \bar{Y}_A can be termed the ‘‘active’’ component since it represents the coupling between the structure and the patch. Also, it is sensitive (or responsive) to any damage to the structure (any change in Z) in the vicinity of the patch. On the contrary, \bar{Y}_p can be regarded as the ‘passive’ component since it is not affected by any damage in the vicinity of the patch. \bar{Y}_p can be decomposed into real and imaginary parts by expanding $\overline{\epsilon_{33}^T} = \epsilon_{33}^T(1 - \delta j)$ and $\overline{Y^E} = Y^E(1 + \eta j)$ and substituting in Part I of Eq. (2.39), which results in

$$\bar{Y}_p = \left[2\omega \frac{wl}{h} \left\{ \delta \epsilon_{33}^T + d_{31}^2 Y^E \eta \right\} \right] + j \left[2\omega \frac{wl}{h} \left\{ \epsilon_{33}^T - d_{31}^2 Y^E \right\} \right] \quad (2.41)$$

or

$$\bar{Y}_p = G_p + jB_p \quad (2.42)$$

where G_p and B_p are the real and the imaginary components of $\overline{Y_p}$. B_p has a large magnitude (comparable to B) whereas G_p has a small magnitude, due to the presence of δ and η , which are of very small order of magnitude (Table 2.1). In the measured susceptance signature, B_p camouflages the active component, which is why the raw-susceptance signature is traditionally not considered suitable for SHM.

Early investigations employed the raw conductance signatures directly for SHM/NDE. The susceptance signature has been deemed redundant, considering the high contribution arising out of the patch (Sun *et al.*, 1995). However, as the PZT parameters are known, the contribution can be filtered off. From Eq. (2.40),

$$\overline{Y_A} = \overline{Y} - \overline{Y_p} = (G + jB) - (G_p + jB_p) \quad (2.43)$$

or

$$Y_A = (G - G_p) + (B - B_p)j \quad (2.44)$$

Thus, the active conductance G_A and the active susceptance B_A can be determined as

$$G_A = G - G_p \quad (2.45)$$

and

$$B_A = B - B_p \quad (2.46)$$

Fig. 2.12 shows the plot of B_A for the SDOF system of Fig. 2.11. On comparison with Fig. 2.11(b), it can be observed that the plots have changed significantly after the removal of the PZT patch's passive contribution. Raw-susceptance (Fig. 2.11(b)), hardly reflects any information regarding the structure but after filtering the passive component (Fig. 2.12), it reflects the structural characteristics as prominently as the real component. Previously, the B -plot was unable to capture any damage; however the plot of B_A exhibits identifiable response to damages. Hence, the active components are more realistic representations of structural behavior. Also, signature decomposition can facilitate the utilization of the imaginary part. It is possible to derive useful information from the susceptance signature, which could be utilized for improved structural identification as well as SHM/NDE.

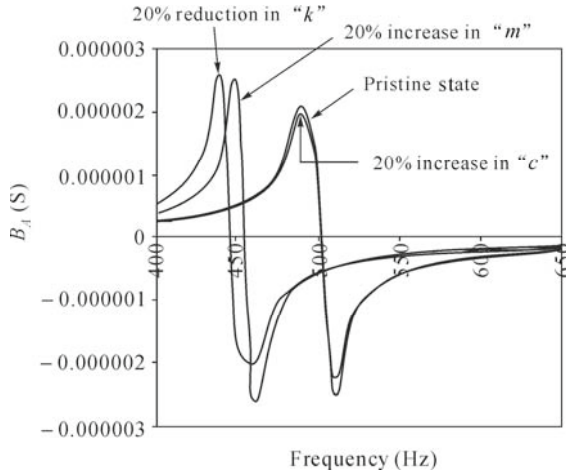


Fig. 2.12 Active-susceptance plot for SDOF system of Fig. 2.11

2.6 Practical Aspects of EMI Technique

In the EMI technique, the same PZT patch usually has to serve both actuating and sensing functions. It should therefore be sufficiently stiff in addition to being sensitive. Fig. 2.13 shows a typical, commercially available PZT patch suitable for this particular application (PI Ceramic, 2003). The characteristic feature of the patch is that the electrode from the bottom edge is wrapped around the thickness, so that both the electrodes are available on one side of the PZT patch, while the other side is bonded to the host structure. PZT patches of sizes ranging from 5 to 15 mm and thicknesses of 0.1 to 0.3 mm are best suited for most structural materials such as steel and reinforced concrete (RC). Such thin patches usually have a thickness resonance frequency in the order of a few MHz. Therefore, the frequency response signature in the kHz frequency range is characteristic of the structure only.

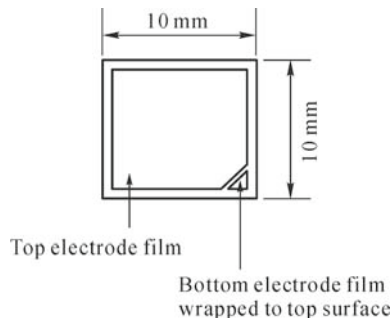


Fig. 2.13 A typical commercially available PZT patch

As far as the operating frequency range is concerned, it must be maintained in hundreds of kHz so that the wavelength of the resulting stress waves is smaller than the typical size of defects to be detected (Giurgiutiu and Rogers, 1997). Typically, for such high frequencies, the generated stress waves have a wavelength as small as a few mm. Contrary to the large wavelength stress waves generated in low frequency vibration techniques, these are substantially attenuated by the occurrence of any incipient damages (such as cracks) in the local vicinity of the PZT patch. Sun *et al.* (1995) recommended that a frequency band containing major vibrational modes of the structure (*i.e.*, a large number of peaks in the signature; Fig. 2.1b) serves as a suitable range. Larger number of peaks signifies greater dynamic interaction between the structure and the PZT patch. Park *et al.* (2003) recommended a frequency range from 30 to 400 kHz for PZT patches 5 to 15 mm in size. According to Park *et al.*, a higher frequency range (>200 kHz) is favorable in localizing the sensing range, while a lower frequency range (<70 kHz) covers a larger sensing area. Furthermore, frequency ranges higher than 500 kHz are found to be unfavorable since they render the sensing region of the PZT patch too small, with the result that the signature shows adverse sensitivity to patch's own bonding condition rather than to any damage to the monitored structure. It should also be noted that the piezo-impedance transducers do not behave well at frequencies less than 5 kHz. Below 1 kHz, the EMI technique is not recommended (Giurgiutiu and Zagari, 2002).

As impedance transducers, the PZT patches have a localized sensing zone of influence. This is because, vibrating at high frequencies, the patch excites ultrasonic modes of vibration of the structure which are essentially local in nature. In addition, damping is much more significant at high ultrasonic frequencies, leading to localization of the waves generated by the vibrating PZT patch. Esteban (1996) carried out extensive numerical modeling based on wave propagation theory, and conducted comprehensive parametric studies to identify the sensing zone of the piezo-impedance transducers. At such high frequencies, exact quantification of energy dissipation proved very difficult and the sensing zone could not be exactly identified. However, it was found that this zone depends on the material of the host structure, its geometry, excitation frequency and the presence of structural discontinuities. It was concluded that structural discontinuities acting as the sources of multiple reflections cause maximum attenuation to the propagating waves. Thereafter, based on experimental data from a large number of case studies, Park *et al.* (2000a) claimed that the sensing radius of a typical PZT patch might vary from 0.4m on composite reinforced structures to about 2m on simple metal beams. Naidu (2004) reported the sensing range to be greater than 1m in his experiments on thin aluminum beams. Therefore, for effective damage localization, in general, the structures must be instrumented with an array of PZT patches. Owing to a localized sensing region, the technique shares a rare ability to detect damages without being affected by the far field boundary conditions, external loading or normal operating conditions. However, this advantage comes at the cost

of a limited sensing area. More details on PZT sensing region are covered in Chapter 7.

The conductance signatures of piezo-impedance transducers have been found to be temperature sensitive. Therefore, in real situations, the effects of damage and temperature are bound to mix. This necessitates a method to decouple the two. Fortunately, over a small frequency band, the overall effect of temperature has been observed to be a superposition of uniform horizontal and vertical translations of the signature. This is entirely different from the signature deviation resulting from damage, which causes an abrupt local variation in the signature. It was observed by Pardo De Vera and Guemes (1997) that the horizontal shift is non-uniform and depends on frequency. However, if the frequency band is narrow, it can be assumed to be uniform.

Park *et al.* (1999) proposed a statistical cross-correlation-based method for temperature compensation. Bhalla (2001) studied temperature effects using finite element simulation. It was found that the major effects of temperature on the signatures are the horizontal shift due to change in the host material's Young's modulus, and the vertical shift due to variations in ϵ_{33} and d_{31} of the PZT patch resulting from temperature change. All the shifts were found to vary linearly with temperature over narrow frequency bands. Of these, the most prominent is the vertical shift due to change in ϵ_{33} . A simple temperature compensation method was proposed which required the acquisition of baseline signatures at two different temperatures. These facilitated determination of the average horizontal/ vertical shifts caused by unit temperature change. To apply the proposed approach in a real-life scenario, a two-step method was suggested:

(1) Transform the current signature to a temperature of the baseline signature (if the two are different), through vertical/ horizontal shifts.

(2) Compare the transformed current signature with that of the undamaged structure.

More details on temperature effect and other practical issues are presented in Chapter 7.

Most low-frequency vibration-based SHM/ NDE techniques for real structures are likely to encounter the presence of noise. The noise could be (a) mechanical noise caused by sources such as vehicle movement or wind; (b) electrical noise generated by variations in the power supply; or (c) electromagnetic noise caused by communication waves which affect the signal acquisition and transmission through cables and other susceptible circuitry (Samman and Biswas, 1994a). With this background, the greatest benefit of the high frequency EMI technique is that the signal (in a few hundred kHz frequency range) is not likely to be affected by mechanical noise, since this type of noise is dominant in the low-frequency ranges (typically less than 100 Hz). Park *et al.* (2000a) demonstrated that the EMI technique is indeed insensitive to distant boundary condition changes, distant mass loading and arbitrary ambient inputs to the structure. This is very important, especially for the monitoring of aircrafts or bridges, while in service. However, it should be noted that care must be exercised in applying the EMI technique on structures which are instrumented with ultrasonic transducers for purposes of NDE.

The high frequency excitations from these transducers could generate high frequency noise for the EMI technique: be sure to turn them off before applying the EMI technique.

Electrical noise is not crucial in the EMI technique either, since the power required by each PZT patch is in the low milli-watt range which does not call for the deployment of high-power generating sets. Rather, it makes possible the development of battery operated sensors (Park, 2000). The only possible noise could be electromagnetic noise, which can be minimized by using coaxial cables. Another source of error could be the parasitic electrical admittance of the connection wires. It can be accounted for by performing zero-correction in the impedance analyzer, prior to taking measurements. However, it could be problematic for large arrays where each PZT patch may have a different wire-length. It is recommended that the same set of connection wire be used for recording both the baseline signature as well as the signature at any future point of time, so that the residual admittance (if not properly accounted for in the zero correction) is the same in both cases. Thus, the change in signature, if any, will be due to structural damage alone. It should also be noted that extensive experimental study by Raju (1998) found that the technique can still work satisfactorily in spite of variable test wire-lengths.

Since the EMI technique is essentially acousto-ultrasonic in nature, the number of sensors needed depends upon the geometry and material of the component to be monitored. The number of sensors required for thin beams and plates is small because acoustic waves can easily travel long distances through such material medium. However, in complex structures with holes, notches, discontinuities and thickness variations, a large number of sensors may be required because of greater losses due to energy dissipation. Also, the same would be true for materials such as composites or concrete, which are characterized by high material damping. In such scenarios, it is important to have multi-sensor architecture with built-in redundancy for tolerating the failure of one or more sensors without rendering the entire system ineffective (Boller, 2002). Additionally, it is important to consider issues like sensor validation, data pre-processing, feature extraction and pattern recognition.

Suitable locations for bonding the patches can be easily determined from the geometry and loading conditions, by preliminary structural analysis, to which the structure is likely to be subjected during the course of its service. It is recommended to locate the patches at the points of maximum bending moments and shear, which can be ascertained by the theory of structures (Soh *et al.*, 2000). It should be mentioned here that, given an array of PZT patches, it can either be excited in self-impedance fashion (the EMI technique) or transfer impedance fashion (Esteban, 1996). In the transfer function method, one PZT patch acts as an actuator and emits acoustic signals into the structure. The signals are picked up by another patch acting as a sensor. The main advantage of the transfer impedance approach is that it provides a greater sensing range and therefore reduces the number of sensors required. Furthermore, it also enables determination of the mechanical properties of the monitored component. The impedance analyzer can be easily

utilized for the transfer impedance approach too. However, the “gain” levels attained in the transfer impedance approach are much smaller since the waves have to travel longer distances, as well as encounter higher noise (Park *et al.*, 2003). Increasing the excitation level could help overcome this problem, allowing the two techniques to supplement each other since the same sensor array can be utilized for both the techniques.

2.7 Signal Processing Techniques and Conventional Damage Quantification

The prominent effects of structural damages on the conductance signatures are the appearance of new peaks in the signatures and lateral and vertical shifting of the peaks, which are the main damage indicators. Samman and Biswas (1994a, b) reported several pattern recognition techniques to quantify the variations occurring in the structural signatures caused by damages, such as the waveform chain code (WCC) technique, signature assurance criteria (SAC), the equivalent level of degradation system (ELODS) and adaptive template matching (ATM). Similar statistical techniques were employed in early research studies on the EMI technique *e.g.*, the root mean square deviation (RMSD) (Giurgiutiu and Rogers, 1998), relative deviation (RD) (Sun *et al.*, 1995; Ayres *et al.*, 1998), the difference of transfer function between damaged and undamaged conditions (Pardo de Vera and Guemes, 1997) and the mean absolute percentage deviation (MAPD) (Naidu, 2004).

Giurgiutiu *et al.* (1999) defined the RMSD index as:

$$\text{RMSD (\%)} = \sqrt{\frac{\sum_{i=1}^N (G_i^1 - G_i^0)^2}{\sum_{i=1}^N (G_i^0)^2}} \quad (2.47)$$

where G_i^1 is the post-damage conductance at the i^{th} measurement point and G_i^0 is the corresponding pre-damage value. Similarly, RD is based on the sum of mean square algorithm, normalized with respect to an arbitrarily chosen maximum amount of damage, and is defined for the i^{th} patch (in an array) as (Sun *et al.*, 1995):

$$\text{RD}_i = \frac{\sum_{k=1}^N (G_{ik}^1 - G_{ik}^0)^2}{\sum_{k=1}^N (G_{1k}^1 - G_{1k}^0)^2} \quad (2.48)$$

where the numerator represents the mean square deviation at the i^{th} location and the denominator represents the deviation for the chosen reference maximum damage location “1”.

The MAPD index is defined by Naidu (2004) as:

$$\text{MAPD} = \frac{100}{N} \sum_{i=1}^N \left| \frac{G_i^1 - G_i^0}{G_i^0} \right| \quad (2.49)$$

The covariance (Cov) and correlation coefficient (CC) are respectively defined as:

$$\text{Cov}(G^0, G^1) = \frac{1}{N} \sum_{i=1}^N (G_i^0 - \overline{G^0})(G_i^1 - \overline{G^1}) \quad (2.50)$$

$$\text{CC} = \frac{\text{Cov}(G^0, G^1)}{\sigma_0 \sigma_1} \quad (2.51)$$

where σ_0 and σ_1 are, respectively, the standard deviations of the baseline signature and the signature after damage. $\overline{G^0}$ and $\overline{G^1}$ are, respectively, the mean values of the baseline signature and the signature after damage.

Of all the statistical indices, RMSD is the one most widely employed by researchers. Although the statistical methods are easy to implement, their main drawback is that they do not provide any clear picture of the associated damage mechanism or any change in the mechanical parameters of the structure under question. The indices defined above are typically the so-called non-parametric statistical damage indices. These do not have any relation with the absolute structural parameters as they merely measure the deviation from the baseline signature. It is assumed therefore that the greater the damage extent, the greater the resulting damage index. However, in many situations, incipient damage and high order damage may lead to an RMSD index of the same order of magnitude. As such, the particular “threshold value” demanding an alarm could vary from structure to structure (Soh *et al.*, 2000). In such situations, reliance on the slope of the RMSD curve rather than its absolute magnitude may be employed. However, this may also not work in all situations, as evident from the practical experience of the authors. The need for better indices was highlighted by Giurgiutiu *et al.* (2002), who remarked that further work was required to systematically investigate the most appropriate damage metric that can be used for processing frequency spectra successfully. In addition, all these statistical approaches only focused on the real part (conductance) of the admittance signature, ignoring the information carried by the imaginary part.

Chapter 4 of this book considers the work done by the authors towards rational parametric damage quantification, based on the mechanical impedance of the structure rather than the raw signatures.

2.8 Major Technological Developments During the Last One and a Half Decades

From its inception, several research groups across the world have been working in the field of the EMI technique, engaging in both theoretical and hardware issues. This section summarizes the major developments and contributions in this field.

The EMI technique resulted from the concerted efforts of Liang and co-workers at the Virginia Polytechnic Institute and State University during the early 1990s. Liang *et al.* (1994) proposed the first 1D analytical model for the coupled electro-mechanical phenomenon associated with the EMI technique. Later, Zhou *et al.* (1996) followed and extended the formulation to 2D case.

Application of the EMI technique for SHM on a lab-sized truss-structure was first reported by Sun *et al.* (1995). This study was then extended to a large-scale prototype truss-joint by Ayres *et al.* (1998).

Lopes *et al.* (1999) trained neural networks using statistical damage quantifiers (area under the conductance curve, root mean square (RMS) of the curve, RMSD between damaged and undamaged curves, and CC) based on experimental data from a bolted joint structure. The trained neural networks were found to be able to successfully locate and quantify the damages inflicted on the test-structure in different experiments.

Park *et al.* (2000a) reported proof-of-concept extension of the EMI technique on civil-structural components such as composite reinforced masonry walls, steel bridge joints and pipe joints. The technique was found to be very tolerant to mechanical noise and also to small temperature fluctuations. Park (2000) further extended the EMI technique to high temperature components (typically $>500^{\circ}\text{C}$), such as steam pipes and boilers in power plants. Additionally, he formulated a statistical cross-correlation-based method for temperature compensation.

Soh *et al.* (2000) established the damage detection and localization ability of piezo-impedance transducers on real-life RC structures. They did this by successfully monitoring a 5m span RC bridge during its destructive load testing (Fig. 2.14). This is the first ever reported demonstration of the EMI technique on a RC structure.

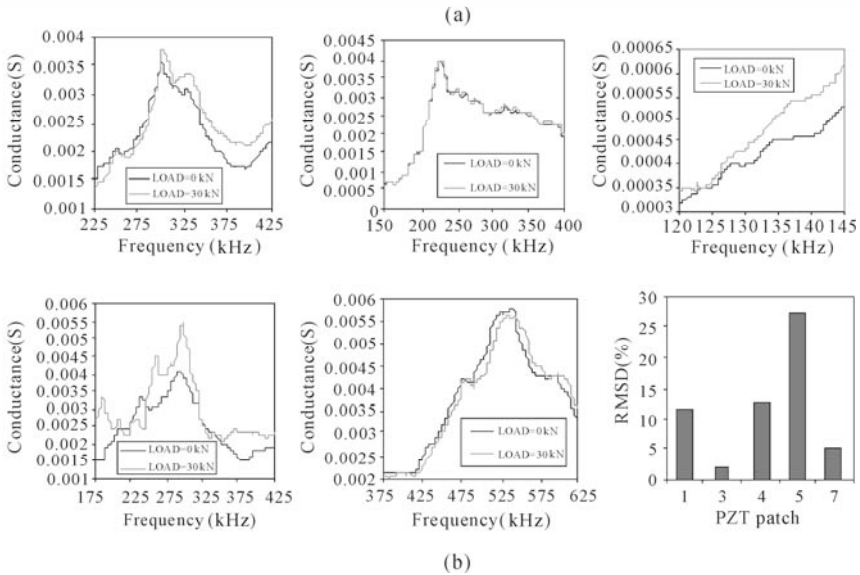
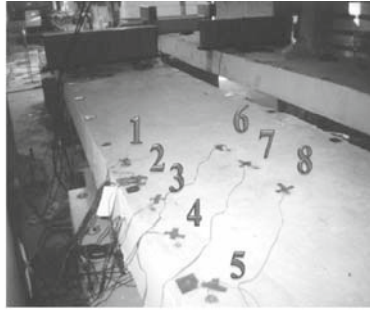


Fig. 2.14 Health monitoring of RC bridge using EMI technique (Soh *et al.*, 2000). (a) The instrumented 5 m RC bridge; (b) Shifts of conductance signatures of a few of the instrumented PZT patches

Park *et al.* (2000b) integrated the EMI technique with wave propagation modeling for thin beams (1D structures) under “free-free” boundary conditions, utilizing the axial modes. The conventional statistical indices of the EMI technique were used for locating the damages in the frequency range 70 – 90 kHz. The damage severity was determined by spectral finite element-based wave propagation approach, in the frequency range 10 – 40 kHz. However, this combination necessitated the use of some additional hardware and sensors, such as accelerometers, which are not accurate at ultrasonic frequencies.

Post-2000, numerous papers were published in leading journals demonstrating successful extension of the technique on sophisticated structural components such as re-strengthened concrete members (Saffi and Sayyah, 2001) and jet engine components under high temperature conditions (Winston *et al.*, 2001). Inman *et al.*

(2001) utilized the same PZT patch for health monitoring as well as vibration control. Until this time, the main focus of research was on investigating the potential of the EMI technique on a particular type of component, with few works devoted to the aspects of modeling or parametric damage quantification.

Abe *et al.* (2002) proposed a new stress monitoring technique for thin structural elements (such as strings, bars and plates) by applying wave propagation theory to the EMI measurement data in the moderate frequency range (1 – 10 kHz). They used the fact that a tension T increases the natural frequency of a thin bar from ω_0 to ω_1 , as given by

$$\omega_1 = \sqrt{\frac{\omega_0(T + \alpha\omega_0)}{\alpha}} \quad (2.52)$$

where $\alpha = \sqrt{EI/(\rho A)}$ (E is Young's modulus; I is moment of inertia; ρ is density; and A is cross-sectional area). Abe *et al.* (2002) demonstrated that lower frequencies increase under tension, from which the tension in the element could be estimated using Eq. (2.52). This made it possible for the application of the EMI technique on load monitoring as well as damage detection. Owing to localized wave propagation, the technique is insensitive to the boundary conditions and can make accurate stress identification. However, the suitable frequency band for this application is very narrow, and generally difficult to identify. In addition, the results reported were not accurate for 2D components.

Giurgiutiu *et al.* (2002) combined the EMI technique with a wave propagation approach for crack detection in aircraft components. While the EMI technique was employed for near-field damage detection, the guided ultrasonic wave propagation technique (pulse echo) was used for far-field damage detection.

Conventionally, the EMI technique employs an impedance analyzer (or LCR meter) which typically costs between \$20,000 to \$41,000, and is thus beyond the budget of small- and medium-sized companies. Peairs *et al.* (2004) proposed a low cost electrical admittance measurement technique based on an FFT analyzer (which typically costs about \$10,000) in place of the impedance analyzer. Fig. 2.15 shows the electrical circuit employed by Peairs *et al.* It essentially consists of a small resistance ($<200 \Omega$), connected in series with the PZT patch bonded to the structure to be monitored. Upon applying an input voltage \bar{V}_i across the combination through the FFT analyzer, the electric current \bar{I} flows through the circuit, as given by

$$\bar{I} = \frac{\bar{V}_o}{R} \quad (2.53)$$

where \bar{V}_o is the output voltage across the sensing resistor R , fed into the

measurement channel of the FFT analyzer. Taking into consideration that the electrical impedance of the PZT patch is very large as compared with the resistor R , the coupled EM admittance \bar{Y} of the bonded patch can be approximated as:

$$\bar{Y} \approx \frac{\bar{I}}{\bar{V}_i} = \frac{\bar{V}_o}{R\bar{V}_i} \quad (2.54)$$

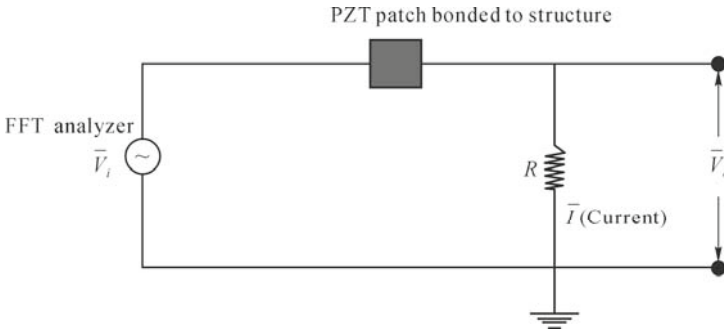


Fig. 2.15 Circuit employed by Peairs *et al.* (2004)

The measurement of the phase difference between \bar{V}_o and \bar{V}_i enables the determination of the real and imaginary components, G and B of \bar{Y} . This measurement approach is much more cost-effective than the conventional impedance analyzer-based approach. However, it involves fast Fourier transformation (FFT) of the time domain data, unlike the steady state measurements of an LCR meter/impedance analyzer. Therefore, it faces bandwidth restrictions and could not be relied upon for frequencies greater than 100 kHz.

Bhalla and Soh (2004a, b) introduced a new 2D PZT-structure electro-elastic interaction model based on the concept of “effective impedance”. The proposed model, is not only simpler than that of Zhou *et al.* (1996), but can be employed to extract the mechanical impedance of any unknown structure, enabling parametric damage quantification. The model was further extended to include shear lag effects introduced by the finitely thick adhesive bond layer (Bhalla and Soh, 2004c), strength and damage prediction of concrete (Soh and Bhalla, 2005), and damage assessment of rock (Yang *et al.* 2007). More details on this model are covered in Chapters 3 and 4 of this book.

Xu *et al.* (2004) focused on quantification of damage, *i.e.*, identification of damage location and intensity, by integrating the EMI technique with hybrid evolutionary programming. Low-frequency range (<30 kHz) was preferred since repeated structural analysis was required during the back calculation procedure in the evolutionary programming. Annamdas and Soh (2007) extended the 2D EMI model to 3D case, which is particularly useful for embedded PZT transducers. Hu and Yang (2007) developed a wave propagation model to determine the sensing

region of PZT transducers. Their theoretical and experimental works showed that the sensing region of the PZT transducers could be between 2.5 to 3.0 m in metallic materials and 0.4 m to 0.5 m in concrete material. More details on these works are covered in Chapters 3, 4 and 7.

Overly *et al.* (2008) made major hardware progress in the development of a miniaturized wireless sensor node using a low-cost integrated circuit chip that could measure and record the electrical impedance of the PZT patch, a microcontroller which could perform local computing, and a telemetry with wireless signal transmission, as illustrated in Fig. 2.16. However, their measurement from the sensor node differed several times in magnitude from the measurements of the impedance analyzer.

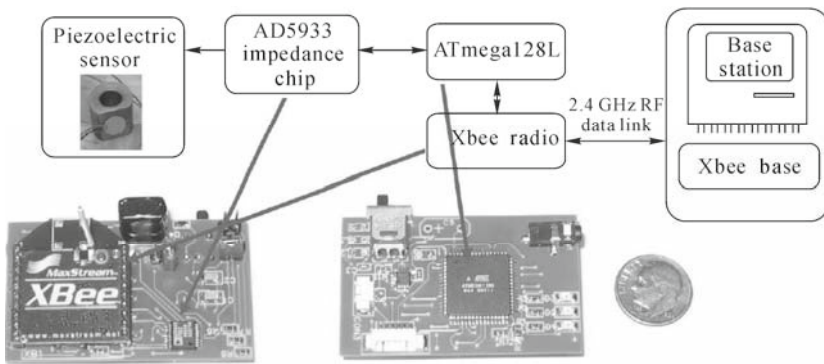


Fig. 2.16 Wireless impedance device developed by Overly *et al.* (2008); reproduced with permission from IOP and Dr. G. Park of LANL

Recently, Bhalla *et al.* (2009) proposed an ultra-low-cost adaptation of Peair's approach, using the set-up illustrated in Fig. 2.17. A combination of function generator and digital multimeter replaced the FFT analyzer. Together, the cost of the minimum hardware was reduced to about \$2,500 only.

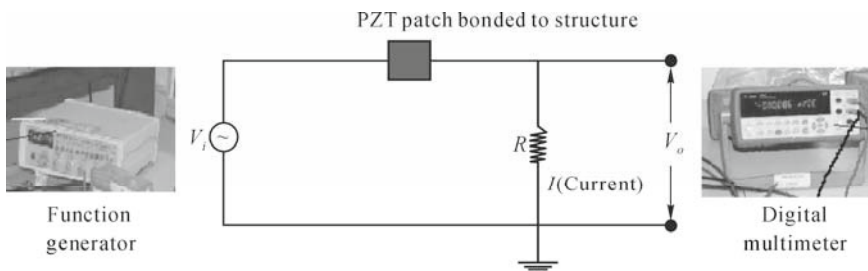


Fig. 2.17 Circuit for self impedance approach (Bhalla *et al.*, 2009)

2.9 Advantages of EMI Technique

The major advantages of the EMI technique over the prevalent global and local SHM techniques are summarized below:

(1) The EMI technique shows far greater damage sensitivity than the conventional global techniques. Typically, the sensitivity is of the order of the local ultrasonic techniques (Park *et al.*, 2003). Yet the technique is very straightforward to implement on large structures. It does not warrant expensive hardware like the ultrasonic techniques nor any probe to be physically moved from one location to another. The data acquisition is much more simplified as compared to the traditional accelerometer-shaker combination used in the global vibration techniques, since the measurement made is directly in the frequency domain. Thus, the EMI technique provides an appropriate interface between the global vibration based techniques and the local ultrasonic techniques.

(2) The PZT patches are bonded non-intrusively on the structure, and they possess negligible weight and demand low power consumption. Small and non-intrusive sensors can monitor the inaccessible locations of the structures and their components. Therefore, this could save time and effort involved in dismantling the machines and structural components for inspection purposes. Easy installation (no sub-surface installation) makes the piezo-impedance transducers equally suitable for existing as well as to-be-built structures.

(3) The use of the same transducer for actuating as well as sensing saves the number of transducers and associated wiring.

(4) The limited sensing area of the PZT patch helps in isolating changes due to far-field variations such as boundary conditions and normal operational vibrations. Also, multiple damages in different areas can be detected easily.

(5) The technique is virtually immune to mechanical, electrical and electromagnetic noise. This makes the technique suitable for implementation during operating conditions, such as in-flight aircrafts.

(6) The PZT patches are commercially available at very low costs, typically \$1 to \$10, in contrast to the conventional force balance accelerometers which may be as expensive as \$1,000 and at the same time bulky and narrow-banded.

(7) The technique is very favorable for autonomous and online implementation since the requirements for data processing are minimal.

(8) The technique can be implemented at any time in the life of a structure. For example, the PZT patches can be installed on structures after an earthquake to monitor growing cracks or loosening connections. Other SHM techniques might warrant installation of the sensors at the time of construction and hence are not suitable for existing structures. However, it should be noted that the PZT patches would only be able to detect any structural damages appearing in the post-installation period. Thus, they cannot detect “pre-existing” damages in the structures.

(9) Being non-model based, the technique can be easily applied to complex structures.

(10) The PZT patches are orders of magnitude lower in stiffness and mass as compared with the monitored structures. Therefore, the dynamics of the host-structure are not modified and accurate structural identification is possible.

(11) PZT sensors are non-resonant devices with wide-band capabilities and exhibit a large range of linearity, fast response, light weight, high-conversion efficiency and long-term stability

Clearly, therefore, the EMI technique has emerged as a universal SHM/ NDE method, applicable to almost all engineering materials and structures. If the damage location could be predicted in advance (*i.e.*, where to expect damage), the EMI technique would be the most powerful technique in such applications (Park *et al.*, 2003).

2.10 Limitations of EMI Technique

In spite of the many advantages over other techniques, the EMI technique has the below limitations:

(1) The PZT patch is only sensitive to structural damages over a relatively small sensing zone, depending on the material and geometrical configuration. Though sufficient for monitoring miniature components and mechanical/ aerospace systems, the small sensing zone warrants the deployment of several thousands of PZT patches for real-time monitoring of large infrastructures, such as bridges or high-rise buildings. Hence, critical locations must be judiciously decided based on the theory of structures.

(2) Since all civil and mechanical structures are statically indeterminate, cracking of a few joints may not necessarily affect the overall safety and stability of the monitored structure. Thus, a drawback of the EMI technique compared with global SHM techniques is its inability to assess overall structural stability. In this respect, global SHM techniques and the EMI techniques should complement each other, as will be illustrated in Chapter 6.

References

- Abe, M., Park, G. and Inman, D.J. (2002). "Impedance-Based Monitoring of Stress in Thin Structural Members", *Proceeding of 11th International Conference on Adaptive Structures and Technologies*, October 23-26, Nagoya, Japan, 285-292.
- Agilent Technologies (2009). <http://www.agilent.com>
- Annanddas, V.G.M. and Soh, C.K. (2007). "Three Dimensional Electromechanical Impedance Model I: Formulation of Directional Sum Impedance", *Journal of Aerospace Engineering*, 20(1): 53-62.

- Ayres, J.W., Lalande, F., Chaudhry, Z. and Rogers, C.A. (1998). "Qualitative Impedance-Based Health Monitoring of Civil Infrastructures", *Smart Materials and Structures*, 7(5): 599-605.
- Bhalla, S. (2001). "Smart System Based Automated Health Monitoring of Structures", *M.Eng. Thesis*, Nanyang Technological University, Singapore.
- Bhalla, S. and Soh, C.K. (2004a). "Structural Health Monitoring by Piezo-Impedance Transducers: Modeling", *Journal of Aerospace Engineering*, 17(4): 154-165.
- Bhalla, S. and Soh, C.K. (2004b). "Structural Health Monitoring by Piezo-Impedance Transducers: Applications", *Journal of Aerospace Engineering*, 17(4): 166-175.
- Bhalla, S. and Soh, C.K. (2004c). "Impedance Based Modeling for Adhesively Bonded Piezo-Transducers", *Journal of Intelligent Material Systems and Structures*, 15(12): 955-972.
- Bhalla, S., Gupta, A., Bansal, S. and Garg, T. (2009). "Ultra Low Cost Adaptations of Electro-mechanical Impedance Technique for Structural Health Monitoring", *Journal of Intelligent Material Systems and Structures*, 20(8): 991-999.
- Boller, C. (2002). "Structural Health Management of Ageing Aircraft and Other Infrastructure", *Monograph on Structural Health Monitoring*, Institute of Smart Structures and Systems (ISSS), 1-59.
- Dosch, J.J., Inman, D.J. and Garcia, E. (1992). "A Self Sensing Piezoelectric Actuator for Collocated Control", *Journal of Intelligent Material Systems and Structures*, 3: 166-185.
- Esteban, J. (1996). "Analysis of the Sensing Region of a PZT Actuator-Sensor", *Ph.D. Dissertation*, Virginia Polytechnic Institute and State University, Blacksburg, VA.
- Giurgiutiu, V. and Rogers, C.A. (1997). "Electromechanical (E/M) Impedance Method for Structural Health Monitoring and Non-Destructive Evaluation", *Proceedings of International Workshop on Structural Health Monitoring*, Stanford University, California, September 18-20, Technomic Publishing Co., 433-444.
- Giurgiutiu, V. and Rogers, C.A. (1998). "Recent Advancements in the Electro-Mechanical (E/M) Impedance Method for Structural Health Monitoring and NDE", *Proceedings of SPIE*, 3329: 536-547.
- Giurgiutiu, V., Reynolds, A. and Rogers, C.A. (1999). "Experimental Investigation of E/M Impedance Health Monitoring for Spot-Welded Structural Joints", *Journal of Intelligent Material Systems and Structures*, 10(10): 802-812.
- Giurgiutiu, V. and Zagari, A.N. (2002). "Embedded Self-Sensing Piezoelectric Active Sensors for On-Line Structural Identification", *Journal of Vibration and Acoustics*, 124: 116-125.
- Giurgiutiu, V., Zagari, A.N. and Bao, J.J. (2002). "Embedded Active Sensors for In-Situ Structural Health Monitoring of Thin-Wall Structures", *Journal of Pressure Vessel Technology*, 124: 293-302.
- Hewlett Packard (1996), "HP LF 4192A Impedance Analyzer", *Operation Manual*, Japan.

- Hu, Y.H. and Yang, Y.W. (2007). "Wave Propagation Modeling of PZT Sensing Region for Structural Health Monitoring", *Smart Materials and Structures*, 16(3): 706-716.
- Inman, D.J., Ahmadihan, M. and Claus, R.O. (2001). "Simultaneous Active Damping and Health Monitoring of Aircraft Panels", *Journal of Intelligent Material Systems and Structures*, 12(11): 775-783.
- Kawiecki, G. (2001). "Modal damping Measurement for Damage Detection", *Smart Materials and Structures*, 10: 466-472.
- Liang, C., Sun, F.P. and Rogers, C.A. (1994). "Coupled Electro-Mechanical Analysis of Adaptive Material Systems—Determination of the Actuator Power Consumption and System Energy Transfer", *Journal of Intelligent Material Systems and Structures*, 5: 12-20.
- Lopes, V., Park, G., Cudney, H.H. and Inman, D.J. (1999). "Smart Structures Health Monitoring Using Artificial Neural Network", *Proceedings of 2nd International Workshop on Structural Health Monitoring*, Stanford University, California, September 8-10, 976-985.
- Naidu, A.S.K. (2004). "Structural Damage Identification with Admittance Signatures of Smart PZT Transducers", *Ph.D. Thesis*, Nanyang Technological University, Singapore.
- Overly, T.G., Park, G., Farinholt, K.M. and Farrar, C.R. (2008). "Development of an Extremely Compact Impedance-based Wireless Sensing Device", *Smart Materials and Structures*, 17(6): 065011.
- Pardo De Vera, C. and Guemes, J.A. (1997). "Embedded Self-Sensing Piezoelectric for Damage Detection", *Proceedings of International Workshop on Structural Health Monitoring*, Stanford University, California, September 18-20, 445-455.
- Park, G., Kabeya, K., Cudney, H.H. and Inman, D.J. (1999). "Impedance-Based Structural Health Monitoring for Temperature Varying Applications", *JSME International Journal*, 42(2): 249-258.
- Park, G. (2000). "Assessing Structural Integrity Using Mechatronic Impedance Transducers with Applications in Extreme Environments", *Ph.D. Dissertation*, Virginia Polytechnic Institute and State University, Blacksburg, VA.
- Park, G., Cudney, H.H. and Inman, D.J. (2000a). "Impedance-Based Health Monitoring of Civil Structural Components", *Journal of Infrastructure Systems*, 6(4): 153-160.
- Park, G., Cudney, H.H. and Inman, D.J. (2000b). "An Integrated Health Monitoring Technique Using Structural Impedance Sensors", *Journal of Intelligent Material Systems and Structures*, 11: 448-455.
- Park, G., Sohn, H., Farrar, C.R. and Inman, D.J. (2003). "Overview of Piezoelectric Impedance-Based Health Monitoring and Path Forward", *The Shock and Vibration Digest*, 35(5): 451-463.
- Peairs, D.M., Park, G. and Inman, D.J. (2004). "Improving Accessibility of the Impedance-Based Structural Health Monitoring Method", *Journal of Intelligent Material Systems and Structures*, 15(2): 129-139.
- PI Ceramic (2003). *Product Information Catalogue*, Lindenstrabe, Germany,

- <http://www.piceramic.de>.
- Raju, V. (1998). "Implementing Impedance-Based Health Monitoring Technique", *Master's Dissertation*, Virginia Polytechnic Institute and State University, Blacksburg, VA.
- Saffi, M. and Sayyah, T. (2001). "Health Monitoring of Concrete Structures Strengthened with Advanced Composite Materials Using Piezoelectric Transducers", *Composites Part B: Engineering*, 32(4): 333-342.
- Samman, M.M. and Biswas, M. (1994a). "Vibration Testing for Non-Destructive Evaluation of Bridges. I: Theory", *Journal of Structural Engineering*, 120(1): 269-289.
- Samman, M.M. and Biswas, M. (1994b). "Vibration Testing for Non-Destructive Evaluation of Bridges. II: Results", *Journal of Structural Engineering*, 120(1): 290-306.
- Soh, C.K., Tseng, K.K.H., Bhalla, S. and Gupta, A. (2000). "Performance of Smart Piezoceramic Patches in Health Monitoring of a RC Bridge", *Smart Materials and Structures*, 9(4): 533-542.
- Soh, C.K. and Bhalla, S. (2005). "Calibration of Piezo-Impedance Transducers for Strength Prediction and Damage Assessment of Concrete", *Smart Materials and Structures*, 14(4): 671-684.
- Sun, F.P., Chaudhry, Z., Rogers, C.A., Majmundar, M. and Liang, C. (1995). "Automated Real-Time Structure Health Monitoring via Signature Pattern Recognition", *Proceedings of SPIE*, 2443: 236-247.
- Winston, H.A., Sun, F. and Annigeri, B.S. (2001). "Structural Health Monitoring with Piezoelectric Active Sensors", *Journal of Engineering for Gas Turbines and Power*, 123(2): 353-358.
- Xu, J.F., Yang, Y.W. and Soh, C.K. (2004). "Electromechanical Impedance-Based Structural Health Monitoring with Evolutionary Programming", *Journal of Aerospace Engineering*, 17(4): 182-193.
- Yang, Y.W., Bhalla, S., Wang, C., Soh, C.K. and Zhao, J. (2007). "Monitoring of Rocks Using Smart Sensors", *Tunnelling and Underground Space Technology*, 22(2): 206-222.
- Zhou, S.W., Liang, C. and Rogers, C.A. (1996). "An Impedance-Based System Modeling Approach for Induced Strain Actuator-Driven Structures", *Journal of Vibrations and Acoustics*, 118(3): 323-332.

Exercise 2.1

Fig. Ex 2.1 shows a 2D steel structure. The PZT patch is assumed to be 10 mm long and 0.2 mm thick, and extends along the width of the host structure. Assume the patch to possess the properties listed in Table 2.1. Model the structure using any commercial finite element solution package. Obtain the mechanical impedance by computing the drive point harmonic velocity corresponding to a

finite harmonic actuating force (e.g., 1 N), using the dynamic harmonic finite element method (FEM). Use the MATLAB program listed in Appendix A to obtain G and B in the frequency range of 100 to 200 kHz at an interval of 1 kHz. Consider the Rayleigh damping coefficients $\alpha = 0.001$ and $\beta = 2 \times 10^{-8}$. Draw figures similar to Figs. 2.10 and 2.11.

What are the new observations as compared with the SDOF system? What are the similarities or differences between the plots of x (real part of Z) and G , and y (imaginary part of Z) and B ?

NOTE: Take advantage of symmetry, and only model one half of the structure.

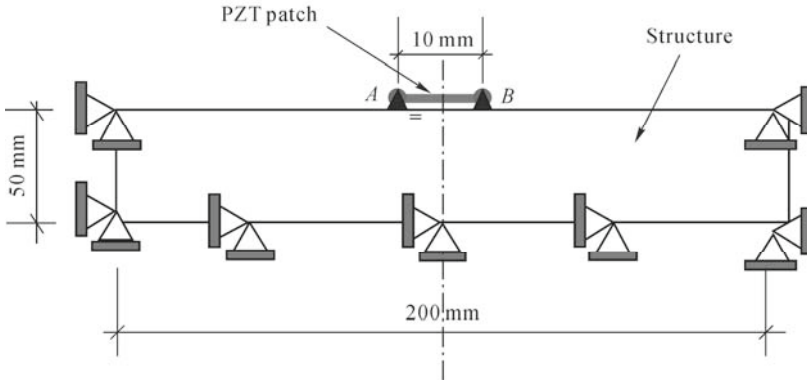


Fig. Ex 2.1

Impedance Models for Structural Health Monitoring Using Piezo-Impedance Transducers

S. Bhalla^{*}, Y. W. Yang, V. G. M. Annamdas, Y. Y. Lim, C. K. Soh

^{*}Department of Civil Engineering, Indian Institute of Technology Delhi,
Hauz Khas, New Delhi 110016, India
Tel: 91-11-2659-1040; Fax: 91-11-2658-1117
Email: sbhalla@civil.iitd.ac.in

3.1 Introduction

This chapter reviews the sequential evolution of PZT-structure interaction models starting from 1D models, followed by 2D and 3D PZT-structure electro-mechanical formulations. In all these models, impedance is defined as 1D, 2D and 3D equations depending on the nature of host structure to be monitored, size of PZT patch and adhesive layer. In addition, direct use of coupled field element in conjunction with finite element method (FEM) is covered.

3.2 Early PZT-Structure Interaction Models

PZT-structure interactions were first modeled using the static approach. This approach, proposed by Crawley and de Luis (1987), assumes the PZT transducer to exert a frequency-independent force on the host structure. The PZT patch is assumed to be a thin bar (length l , width w and thickness h), under static equilibrium with the structure, which is represented by its static stiffness K_s , as illustrated in Fig. 3.1. The actuation force can be determined from static equilibrium and strain compatibility between the transducer and the structure. In

this configuration, owing to the static condition, the imaginary component of the complex terms in the PZT constitutive relations (Eqs. (2.11) and (2.12)) can be dropped. Hence, the axial force in the PZT patch can be expressed as

$$F_P = whT_1 = wh(S_1 - d_{31}E_3)Y^E \quad (3.1)$$

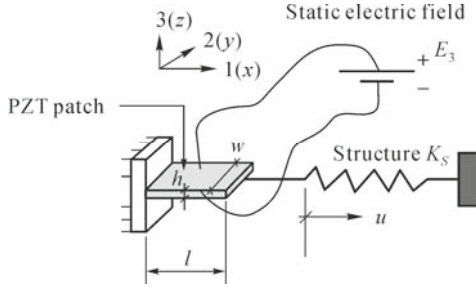


Fig. 3.1 Modeling of PZT-structure interaction by static approach

Similarly, the axial force in the structure can be determined as

$$F_S = -K_S u = -K_S l S_1 \quad (3.2)$$

The negative sign indicates that a positive displacement u causes a compressive force in the spring (the host structure). Force equilibrium in the system implies that F_P and F_S should be equal, which leads to the equilibrium strain, S_{eq} , given by

$$S_{eq} = \frac{d_{31}E_3}{\left(1 + \frac{K_S l}{Y^E wh}\right)} \quad (3.3)$$

Hence, from Eq. (3.2), the magnitude of the force in the PZT (or the structure) can be expressed as $F_{eq} = K_S l S_{eq}$. In order to determine the response of the system under an alternating electric field, the static approach simply recommends that a dynamic force with amplitude $F_{eq} = K_S l S_{eq}$ be applied to the host structure, irrespective of the frequency of actuation.

Since the static approach only employs the static PZT properties, the effects of damping and inertia, which significantly affect the PZT output characteristics, are completely ignored. Because of these reasons, the static approach leads to significant errors, especially near the resonant frequency of the structure or PZT patch (Liang *et al.*, 1993; Fairweather, 1998).

In order to alleviate this inaccuracy, the impedance approach was proposed by Liang *et al.* (1993), based on dynamic equilibrium rather than static equilibrium, which rigorously includes the dynamic PZT properties and structural stiffness. In

this approach, the host structure is represented by structural impedance Z , rather than a pure spring, as depicted in Fig. 2.4. The force-displacement relationship for the structure (Eq. (3.3)) is replaced by an impedance-based force-velocity relationship (Eq. (2.20)). Furthermore, instead of the actuator's static stiffness, the impedance approach considered actuator impedance Z_a , similar in principle to the structural impedance. The impedance model-based electro-mechanical formulation for 1D structures has already been presented in Chapter 2 (Eq. (2.31)). Although the formulation of Liang *et al.* is more accurate than the static approach, they ignored the 2D or higher order effects associated with PZT vibrations. Therefore, their formulation is valid for skeletal structures only; for other structures where 2D coupling is significant, Liang's model might introduce serious errors.

To address this problem, Zhou *et al.* (1995, 1996) extended Liang's 1D impedance approach to model the interactions of a generic PZT element coupled to a 2D host structure. The analytical model of Zhou *et al.* is schematically shown in Fig. 3.2. The structural impedance is represented by direct impedances Z_{xx} and Z_{yy} , and the cross impedances by Z_{xy} and Z_{yx} , which are related to the planar forces F_1 and F_2 (in directions 1 and 2 respectively) and the corresponding planar velocities \dot{u}_1 and \dot{u}_2 by

$$\begin{bmatrix} F_1 \\ F_2 \end{bmatrix} = - \begin{bmatrix} Z_{xx} & Z_{xy} \\ Z_{yx} & Z_{yy} \end{bmatrix} \begin{bmatrix} \dot{u}_1 \\ \dot{u}_2 \end{bmatrix} \quad (3.4)$$

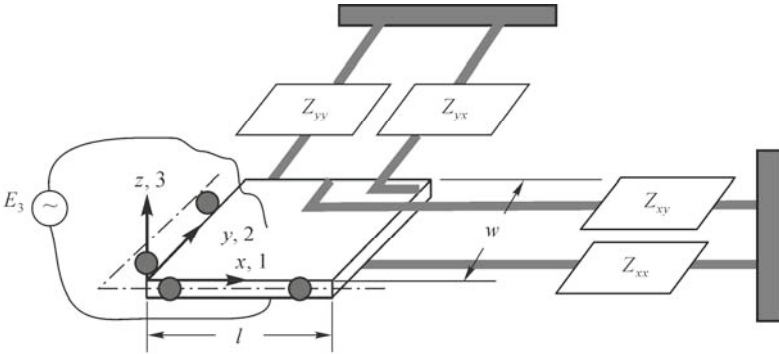


Fig. 3.2 Modeling PZT-structure 2D physical coupling by impedance approach (adapted from (Zhou *et al.*, 1995), with permission from SAGE Publications)

Applying D'Alembert's principle along the two principal axes and after imposing the boundary conditions, Zhou *et al.* (1995) derived the following expression for the electro-mechanical admittance across PZT terminals:

$$\bar{Y} = G + Bj = j\omega \frac{wl}{h} \left[\bar{\epsilon}_{33}^T - \frac{2d_{31}^2 \bar{Y}^E}{(1-\nu)} + \frac{d_{31}^2 \bar{Y}^E}{(1-\nu)} \left\{ \frac{\sin \kappa l}{l} \quad \frac{\sin \kappa w}{w} \right\} N^{-1} \begin{Bmatrix} 1 \\ 1 \end{Bmatrix} \right] \quad (3.5)$$

where κ , the 2D wave number, is given by

$$\kappa = \omega \sqrt{\frac{\rho(1-\nu^2)}{Y^E}} \quad (3.6)$$

and N is a 2×2 matrix, given by

$$N = \begin{bmatrix} \kappa \cos(\kappa l) \left\{ 1 - \nu \frac{w}{l} \frac{Z_{xy}}{Z_{axx}} + \frac{Z_{xx}}{Z_{axx}} \right\} & \kappa \cos(\kappa w) \left\{ \frac{l}{w} \frac{Z_{yx}}{Z_{ayy}} - \nu \frac{Z_{yy}}{Z_{ayy}} \right\} \\ \kappa \cos(\kappa l) \left\{ \frac{w}{l} \frac{Z_{xy}}{Z_{axx}} - \nu \frac{Z_{xx}}{Z_{axx}} \right\} & \kappa \cos(\kappa w) \left\{ 1 - \nu \frac{l}{w} \frac{Z_{yx}}{Z_{ayy}} + \frac{Z_{yy}}{Z_{ayy}} \right\} \end{bmatrix} \quad (3.7)$$

where Z_{axx} and Z_{ayy} are the two components of the mechanical impedance of the PZT patch in the two principal directions, derived using similar 1D impedance approach (Liang *et al.*, 1994) and expressed in Eq. (2.25).

Although the analytical derivations of Eqs. (3.4)–(3.7) are accurate by themselves, practical difficulties prohibit their direct application for extraction of a host structure’s mechanical impedance. For example, using the EMI technique, only two quantities— G (conductance) and B (susceptance) can be measured. For complete information about the structure, Eq. (3.5) needs to be solved for 4 complex unknowns— Z_{xx} , Z_{yy} , Z_{xy} , Z_{yx} (or 8 real unknowns). Thus, the system of equations is highly indeterminate (8 unknowns with only 2 equations). As such, the model could not be employed for experimental determination of drive point mechanical impedance.

To alleviate the shortcomings inherent in the existing models, Bhalla and Soh (2004a) introduced the concept of “effective impedance”. The next section provides the theory and step-by-step derivation of plane-stress-based electromechanical admittance across the PZT terminals. This formulation aimed to bridge the gap between the 1D model of Liang *et al.* (1993) and the 2D model of Zhou *et al.* (1995).

3.3 2D Effective Mechanical Impedance

Conventionally, the mechanical impedance at a point on the structure is defined as the ratio of the driving harmonic force (acting on the structure at the point in question) to the resulting harmonic velocity at that point. The existing impedance models are based on this definition where the points considered are the end points of the PZT patch. The corresponding impedance is called the “drive point mechanical impedance”. However, the mechanical interaction between the patch and the host structure is not restricted to the end points alone; rather, it extends

over two principal directions along the length and width of the PZT patch.

Bhalla and Soh (2004a) therefore introduced a new definition of mechanical impedance based on “effective velocity” rather than “drive point velocity”. In their derivations, it is assumed that the force transmission between the PZT patch and the host structure occurs along the entire boundary of the patch, and that plane-stress conditions exist within the patch. In addition, the patch is assumed to be square-shaped and infinitesimally small as compared with the host structure, so as to possess negligible mass and stiffness. Opposite edges of the patch therefore encounter equal dynamic stiffness from the structure, irrespective of the location of the patch on the host structure. Hence, the nodal lines invariably coincide with the two axes of symmetry of the PZT patch. At the same time, the effects of the patch’s vibrations in the thickness direction are ignored, assuming the frequency range of interest to be much lower than the dominant modes of thickness vibration.

In Fig. 3.3, a finite-sized square PZT patch, surface bonded to an unknown host structure is subjected to a spatially uniform electric field E_3 along axis 3 ($\frac{\partial E_3}{\partial x} = \frac{\partial E_3}{\partial y} = 0$), undergoing harmonic variations with time. The patch has half-length equals to “ l ”. Its interaction with the structure is represented in the form of boundary traction “ f ” per unit length, varying harmonically with time.

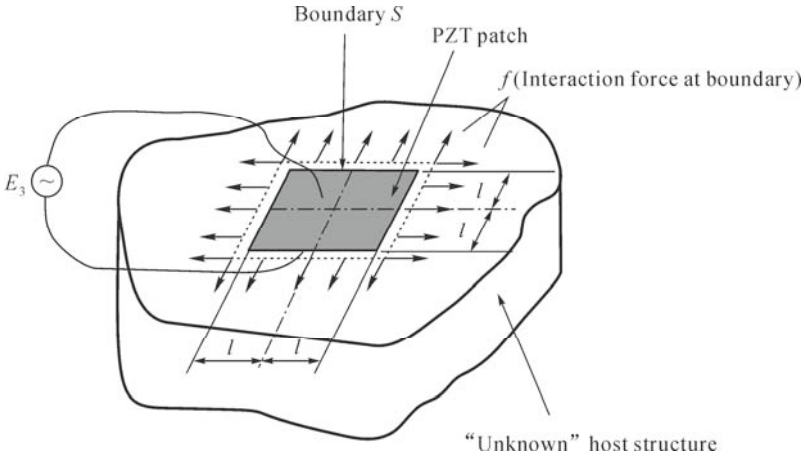


Fig. 3.3 A PZT patch bonded to an “unknown” host structure

This planar force causes planar deformations in the PZT patch, leading to variations in its overall area. The “effective mechanical impedance” of the patch is hereby defined as:

$$Z_{a,eff} = \frac{\oint_S \vec{f} \cdot \hat{n} ds}{\dot{u}_{eff}} = \frac{F}{\dot{u}_{eff}} \quad (3.8)$$

where \hat{n} is a unit vector normal to the boundary and “ F ” represents the overall planar force (or effective force) causing area deformation in the PZT patch. $u_{\text{eff}} = \delta A/p_o$ is defined as “effective displacement”, where δA is the change in surface area of the patch and p_o its perimeter in the undeformed condition. More precisely, p_o is equal to the summation of the lengths of “active boundaries”, *i.e.*, the boundaries undergoing mechanical interaction with the host structure. Differentiation with respect to time of effective displacement yields the effective velocity, \dot{u}_{eff} . It should be noted that in order to ensure overall force equilibrium,

$$\oint_S \vec{f} ds = 0 \tag{3.9}$$

The effective drive point (EDP) impedance of the host structure can also be defined along similar lines. However, for determining structural impedance, forces need to be applied on the surface of the host structure (without the patch) along the boundary of the proposed location of the PZT patch.

3.4 2D Formulation Based on Effective Impedance

In Fig 3.4, a square PZT patch is shown, under in-plane excitation by a spatially uniform electric field, which varies harmonically at an angular frequency ω . Since the nodal lines coincide with the axes of symmetry, it suffices to consider the interactions of one quarter of the patch with the corresponding one quarter of host structure, as it is only the ratio of the two mechanical impedances (Eq. (2.31)) that governs the electrical admittance across the terminals of the PZT patch.

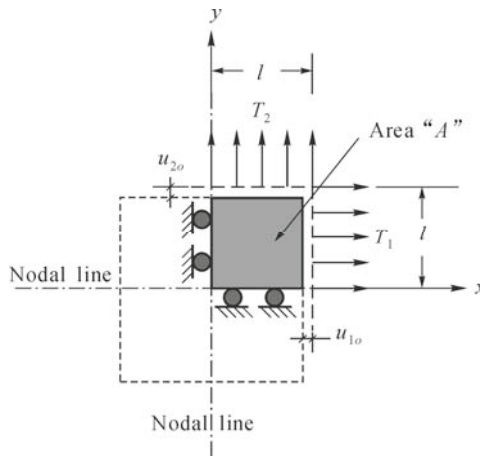


Fig. 3.4 A square PZT patch under 2D interaction with host structure

Let the PZT patch be mechanically and piezo-electrically isotropic in the xy plane. Hence, $\overline{Y}_{11}^E = \overline{Y}_{22}^E = \overline{Y}^E$ and $d_{31} = d_{32}$. Therefore, the PZT constitutive relations (Eqs. (1.1) and (1.2)) can be reduced to

$$D_3 = \overline{\varepsilon}_{33}^T E_3 + d_{31}(T_1 + T_2) \quad (3.10)$$

$$S_1 = \frac{T_1 - \nu T_2}{\overline{Y}^E} + d_{31} E_3 \quad (3.11)$$

$$S_2 = \frac{T_2 - \nu T_1}{\overline{Y}^E} + d_{31} E_3 \quad (3.12)$$

where ν is the Poisson's ratio of the PZT patch. By algebraic manipulation,

$$T_1 + T_2 = \frac{(S_1 + S_2 - 2d_{31}E_3)\overline{Y}^E}{1 - \nu} \quad (3.13)$$

If the PZT patch is in short-circuited condition (*i.e.* zero electric field), Eq. (3.13) can be reduced to

$$(T_1 + T_2)_{short-circuited} = \frac{(S_1 + S_2)\overline{Y}^E}{1 - \nu} \quad (3.14)$$

As derived by Zhou *et al.* (1996), the displacements of the PZT patch in the two principal directions are given by

$$u_1 = (A_1 \sin \kappa x) e^{j\omega t} \quad \text{and} \quad u_2 = (A_2 \sin \kappa y) e^{j\omega t} \quad (3.15)$$

where the wave number κ is given by Eq. (3.6), and A_1 and A_2 are constants to be determined from the boundary conditions. The corresponding velocities can be obtained by differentiating these equations with respect to time. Hence,

$$\dot{u}_1 = \frac{\partial u_1}{\partial t} = (A_1 j \omega \sin \kappa x) e^{j\omega t} \quad \text{and} \quad \dot{u}_2 = \frac{\partial u_2}{\partial t} = (A_2 j \omega \sin \kappa y) e^{j\omega t} \quad (3.16)$$

Similarly, corresponding strains can be obtained by differentiation with respect to x and y , that is,

$$S_1 = \frac{\partial u_1}{\partial x} = (A_1 \kappa \cos \kappa x) e^{j\omega t} \quad \text{and} \quad S_2 = \frac{\partial u_2}{\partial y} = (A_2 \kappa \cos \kappa y) e^{j\omega t} \quad (3.17)$$

From Fig. 3.4, the effective displacement of the PZT patch, considering

displacements at the active boundaries of one-quarter of the patch (the boundaries along the nodal axes are “inactive” boundaries), can be deduced as:

$$u_{eff} = \frac{\delta A}{p_o} = \frac{u_{1o}l + u_{2o}l + u_{1o}u_{2o}}{2l} \approx \frac{u_{1o} + u_{2o}}{2} \quad (3.18)$$

where u_{1o} and u_{2o} are the edge displacements (Fig. 3.4). Differentiating with respect to time, the effective velocity can be obtained as:

$$\dot{u}_{eff} = \frac{\dot{u}_{1o} + \dot{u}_{2o}}{2} = \frac{\dot{u}_{1(x=l)} + \dot{u}_{2(y=l)}}{2} \quad (3.19)$$

From Eqs. (3.8) and (3.19), we can obtain the short-circuited effective mechanical impedance of the quarter PZT patch as:

$$Z_{a,eff} = \frac{(T_{1(x=l)}lh + T_{2(y=l)}lh)_{short-circuited}}{\left(\frac{\dot{u}_{1(x=l)} + \dot{u}_{2(y=l)}}{2} \right)} \quad (3.20)$$

Making use of Eq. (3.14), we obtain

$$Z_{a,eff} = \frac{(S_{1(x=l)}lh + S_{2(y=l)}lh)Y^E}{(1-\nu) \left(\frac{\dot{u}_{1(x=l)} + \dot{u}_{2(x=l)}}{2} \right)} \quad (3.21)$$

Substituting the values of the velocities and strains (Eqs. (3.16) and (3.17) respectively) at the two active edges of the PZT patch, and upon solving, we obtain

$$Z_{a,eff} = \frac{2khY^E}{j\omega(\tan kl)(1-\nu)} \quad (3.22)$$

The overall planar force (or the effective force), F , is related to the EDP impedance of the host structure by

$$F = \oint_S \vec{f} \cdot \hat{n} ds = -Z_{s,eff} \dot{u}_{eff} \quad (3.23)$$

As in the 1D case, the negative sign signifies that a positive effective displacement causes compressive force on the patch (due to reaction from the host structure). Since a square patch is being considered here, Eq. (3.23) can be simplified as:

$$T_{1(x=l)}hl + T_{2(y=l)}hl = -Z_{s,eff} \left(\frac{\dot{u}_{1(x=l)} + \dot{u}_{2(y=l)}}{2} \right) \quad (3.24)$$

Making use of Eq. (3.13), we obtain

$$\frac{(S_{1(x=l)} + S_{2(y=l)} - 2d_{31}E_3)\overline{Y}^E hl}{(1-\nu)} = -Z_{s,eff} \left(\frac{\dot{u}_{1(x=l)} + \dot{u}_{2(y=l)}}{2} \right) \quad (3.25)$$

Substituting the expressions for $(\dot{u}_1 + \dot{u}_2)_{x=l}$ and $(S_1 + S_2)_{x=l}$ from Eqs. (3.16) and (3.17) respectively, and with $E_3 = (V_o/h)e^{j\alpha x}$, we can deduce

$$A_1 + A_2 = \frac{2d_{31}V_o Z_{a,eff}}{(\cos kl)kh(Z_{s,eff} + Z_{a,eff})} \quad (3.26)$$

The electric displacement (or the charge density) over the surface of the PZT patch can then be determined from Eq. (3.10). Substituting Eq. (3.13) into Eq. (3.10) and with $E_3 = (V_o/h)e^{j\alpha x}$, we get

$$D_3 = \overline{\epsilon}_{33}^T \frac{V_o}{h} e^{j\alpha x} + \frac{d_{31}\overline{Y}^E}{(1-\nu)} \left(S_1 + S_2 - 2d_{31} \frac{V_o}{h} e^{j\alpha x} \right) \quad (3.27)$$

The instantaneous electric current (the time rate of change of charge) can be derived as

$$\overline{I} = \iint_A \dot{D}_3 dx dy = j\omega \iint_A D_3 dx dy \quad (3.28)$$

Substituting D_3 from Eq. (3.27) and S_1 and S_2 from Eq. (3.17), and integrating from $-l$ to $+l$ with respect to both x and y , we obtain

$$\overline{I} = 4\overline{V}\omega j \frac{l^2}{h} \left[\frac{\overline{\epsilon}_{33}^T}{\epsilon_{33}^T} - \frac{2d_{31}^2 \overline{Y}^E}{(1-\nu)} + \frac{2d_{31}^2 \overline{Y}^E}{(1-\nu)} \left(\frac{Z_{a,eff}}{Z_{s,eff} + Z_{a,eff}} \right) \left(\frac{\tan \kappa l}{\kappa l} \right) \right] \quad (3.29)$$

where $\overline{V} = V_o e^{j\alpha x}$ is the instantaneous voltage across the PZT patch. Thus, the complex electro-mechanical admittance of the PZT patch is given by

$$\begin{aligned} \overline{Y} &= \frac{\overline{I}}{\overline{V}} = G + Bj \\ &= 4\omega j \frac{l^2}{h} \left[\frac{\overline{\epsilon}_{33}^T}{\epsilon_{33}^T} - \frac{2d_{31}^2 \overline{Y}^E}{(1-\nu)} + \frac{2d_{31}^2 \overline{Y}^E}{(1-\nu)} \left(\frac{Z_{a,eff}}{Z_{s,eff} + Z_{a,eff}} \right) \left(\frac{\tan \kappa l}{\kappa l} \right) \right] \end{aligned} \quad (3.30)$$

which is the desired coupling equation for a square PZT patch. It should be noted that a factor of four is introduced in the final expression since l represents half-

length of the patch. In the previous models (1D – Liang *et al.*, 1994 and 2D – Zhou *et al.*, 1996), only one half and one quarter of the PZT patch respectively (from the nodal point to the end of the patch) were considered as the generic elements (See Fig. 3.2). The governing equations in those models (such as Eq. (3.5)) correspond to one-half and one-quarter of the patch only.

The main advantage of the effective impedance approach introduced here is that a single complex term for $Z_{s,eff}$ accounts for the 2D interactions of the PZT patch with the host structure. This makes the equation simple enough to be utilized for extracting the mechanical impedance of the structure from \bar{Y} , which can be measured at any desired frequency using commercially available impedance analyzers/LCR meters. The related computational procedure is presented in the next chapter.

3.5 Experimental Verification

3.5.1 Details of Experimental Set-up

Fig. 3.5 shows the experimental test set-up used to verify the effective impedance-based electro-mechanical formulations. The test structure was an aluminum block, 48 mm×48 mm×10 mm in size, conforming to grade Al 6061-T6. Table 3.1 lists the major physical properties of Al 6061-T6. The test block was bonded to a much larger, stiffer base plate to simulate fixed-base support. The test block was instrumented with a PZT patch, 10 mm×10 mm×0.3 mm in size, conforming to grade PIC 151 (PI Ceramic, 2006). Table 3.2 lists the key properties of PIC 151. The patch was bonded to the host structure using RS 850 – 940 epoxy adhesive (RS Components, 2003), and was wired to a HP 4192A impedance analyzer (Hewlett Packard, 1996) via a 3499B multiplexer module (Agilent Technologies, 2003). In this manner, the electro-mechanical admittance signatures, consisting of the real part (G) and the imaginary part (B), were acquired in the frequency range 0 – 200 kHz.

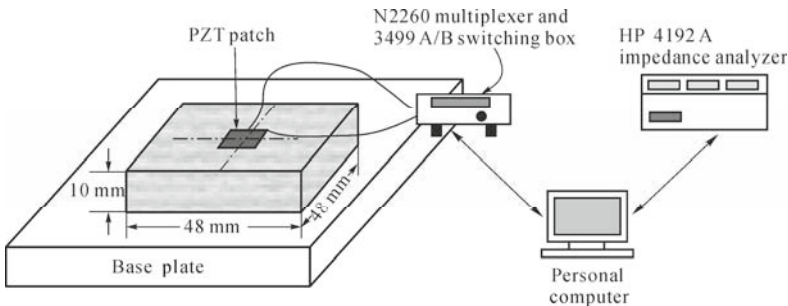


Fig. 3.5 Experimental set-up to verify effective impedance-based electro-mechanical formulations

Table 3.1 Physical Properties of Al 6061-T6

Physical parameter	Value
Density (kg/m^3)	2,715
Young's modulus, Y^E (N/m^2)	68.95×10^9
Poisson ratio	0.33

Table 3.2 Key properties of PZT patch (PI Ceramic, 2006)

Physical parameter	Value
Density (kg/m^3)	7,800
Electric permittivity, ϵ_{33}^T (Farad/m)	2.124×10^{-8}
Piezoelectric strain coefficient, d_{31} (m/V)	-2.10×10^{-10}
Young's modulus, Y^E (N/m^2)	6.667×10^{10}
Dielectric loss factor, δ	0.015

3.5.2 Determination of Structural EDP Impedance by FEM

Before using Eq. (3.30) to derive the theoretical signatures for comparison with the experimental signatures, we need to evaluate the effective mechanical impedance of the PZT patch ($Z_{a,eff}$) as well as the EDP impedance of the structure ($Z_{s,eff}$). Though a closed-form expression has been derived for $Z_{a,eff}$ (Eq. (3.22)), it is not possible to derive such a closed-form expression for $Z_{s,eff}$, especially for complex structural systems characterized by non-trivial 3D geometries. This holds true for most real-life structures and systems where NDE is of prime importance. Therefore, a numerical approach based on 3D dynamic finite-element analysis was used to determine the EDP impedance of the host structure. The main strength of the FEM lies in its ability to accurately model complex shapes and boundaries. It should be noted that FEM was solely employed for verifying the new impedance formulations derived above. In actual application of the formulations for SHM, no numerical analysis is required, as will be illustrated in the next chapter.

The excitation of this system by a harmonic electric field is a typical case of linear steady-state forced vibrations. Investigations by Makkonen *et al.* (2001) showed that reasonably accurate results can be obtained for dynamic harmonic problems by FEM, even for frequencies in the GHz range, if there is an appropriate degree of mesh refinement. In FEM, the physical domain (such as the aluminum block) is discretized into elementary volumes called elements. Fig. 3.6 shows the finitely discretized volume of the aluminum block. Owing to symmetry about the x and y axes, it suffices to perform computations using only one quadrant of the actual structure. Appropriate boundary conditions were imposed on the planes of symmetry, *i.e.*, the x and the y components of displacements were set to zero on the yz and the zx planes of symmetry respectively. In addition, the displacements at the bottom of the block were set to zero to simulate bonding with the base plate. The finite-element meshing was carried out using the preprocessor tool of ANSYS (ANSYS, 2004), with 1.0 mm sized linear 3D brick elements

(solid 45), possessing three degrees of freedom (DOFs) at each node. Since the stiffness and damping of the PZT patch were separately lumped in the term $Z_{a,eff}$ (Eqs. (3.22) and (3.30)), the PZT element need not be included in the finite element mesh.

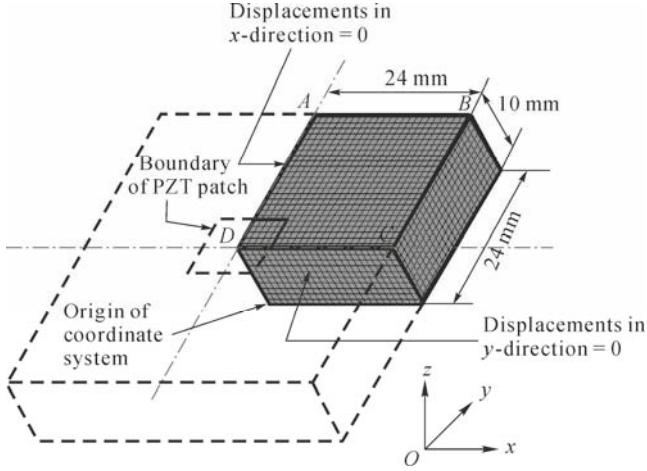


Fig. 3.6 Finite element model of one-quarter of test structure

In general, for a forced harmonic structural excitation, as in the present case, the Galerkin finite element discretization of the 3D domain leads to

$$[M][\ddot{\bar{u}}] + [C][\dot{\bar{u}}] + [K][\bar{u}] = [\bar{F}] \quad (3.31)$$

where $[K]$ is the stiffness matrix, $[M]$ the mass matrix, $[C]$ the damping matrix, $[\bar{F}]$ the force vector and $[\bar{u}]$ the displacement vector (the bar above a quantity indicates the quantity to be complex in nature).

The continuous field quantities, *i.e.*, the mechanical displacements, are approximated in each element through linear sums of the interpolation functions or shape functions (linear in the present case). The natural boundary conditions are included in the load vector, and the essential boundary conditions are imposed by adjusting the load vector and the stiffness matrix (Bathe, 1996). The simplest approach to determine the structural EDP impedance is to apply an arbitrary harmonic force (at the desired frequency) on the surface of the structure (along the boundary of the PZT patch), perform dynamic harmonic analysis by FEM, and obtain the complex displacement response at those points. The applied mechanical load can be expressed as

$$[\bar{F}] = [F_1 + F_2]e^{j\omega t} \quad (3.32)$$

The resulting displacements, which are also harmonic functions of time (at the

same frequency as the loads) can be similarly expressed as

$$[\bar{u}] = [u_1 + u_2 j] e^{j\omega t} \quad (3.33)$$

Substituting Eqs. (3.32) and (3.33) into Eq. (3.31), and noting that $[\bar{\ddot{u}}] = j\omega[\bar{u}]$ and $[\bar{\ddot{u}}] = -\omega^2[\bar{u}]$, we obtain

$$\{[K] + j\omega[C] - \omega^2[M]\} [u_1 + ju_2] = [F_1 + jF_2] \quad (3.34)$$

which can be written in a form similar to the static analysis as

$$[A^*][\bar{u}] = [\bar{F}] \quad (3.35)$$

The only difference from the static case is that all the terms are complex. Eq. (3.35) can be decomposed into two coupled equations involving real numbers only, and written as

$$\begin{bmatrix} -\omega^2[M] + [K] & -\omega[C] \\ \omega[C] & -\omega^2[M] + [K] \end{bmatrix} \begin{bmatrix} u_1 \\ u_2 \end{bmatrix} = \begin{bmatrix} F_1 \\ F_2 \end{bmatrix} \quad (3.36)$$

This set of equations can be solved to obtain the displacement components $[u_1]$ and $[u_2]$. This solution method is called the full solution method. The reduced solution method is another approach, but is not as accurate as the full solution method. It should be noted that computing the frequency response requires solution of the FEM equations at each desired frequency throughout the range of interest.

If the boundary of the PZT patch consists of N equal divisions on each adjacent edge ($N = 5$ in the present case, as shown in Fig. 3.6), the effective displacement can be obtained as

$$u_{eff} = \frac{\delta A}{p_o} \quad (3.37)$$

Substituting the expressions for δA and p_o , we get

$$\begin{aligned} \bar{u}_{eff} = & \frac{\left[\frac{1}{2}(u_{1x} + u_{2x}) \frac{l}{N} + \frac{1}{2}(u_{2x} + u_{3x}) \frac{l}{N} + \dots + \frac{1}{2}(u_{Nx} + u_{(N+1)x}) \frac{l}{N} \right]}{2l} \\ & + \frac{\left[\frac{1}{2}(u_{1y} + u_{2y}) \frac{l}{N} + \dots + \frac{1}{2}(u_{Ny} + u_{(N+1)y}) \frac{l}{N} \right]}{2l} \end{aligned} \quad (3.38)$$

Rewrite Eq. (3.38) as

$$\bar{u}_{eff} = \frac{1}{2}(\bar{u}_{eff,x} + \bar{u}_{eff,y}) \quad (3.39)$$

where

$$\bar{u}_{eff,x} = \frac{0.5(\bar{u}_{1x} + \bar{u}_{(N+1)x}) + (\bar{u}_{2x} + \bar{u}_{3x} + \dots + \bar{u}_{Nx})}{N} \quad (3.40)$$

and

$$\bar{u}_{eff,y} = \frac{0.5(\bar{u}_{1y} + \bar{u}_{(N+1)y}) + (\bar{u}_{2y} + \bar{u}_{3y} + \dots + \bar{u}_{Ny})}{N} \quad (3.41)$$

Furthermore, by splitting the real and the imaginary terms, we can alternatively write,

$$\bar{u}_{eff} = \frac{1}{2}(u_{eff,r} + u_{eff,i}j) \quad (3.42)$$

The structural EDP impedance can then be obtained from Eq. (3.8), noting that $\bar{u}_{eff} = j\omega\bar{u}_{eff}$. If a uniformly distributed planar force, with an effective magnitude $\bar{F} = F_r + F_i j$ is applied, from Eqs. (3.8) and (3.42), the structural EDP impedance can be derived as:

$$\begin{aligned} Z_{s,eff} &= \frac{2(F_r + F_i j)}{j\omega(u_{eff,r} + u_{eff,i}j)} \\ &= \left[\frac{2(F_i u_{eff,r} - F_r u_{eff,i})}{\omega(u_{eff,r}^2 + u_{eff,i}^2)} \right] - \left[\frac{2(F_r u_{eff,r} + F_i u_{eff,i})}{\omega(u_{eff,r}^2 + u_{eff,i}^2)} \right] j \end{aligned} \quad (3.43)$$

The computations can be simplified by applying a pure real force ($F_i = 0$), in which case, the effective impedance will be given by

$$Z_{s,eff} = - \left[\frac{2F_r u_{eff,i}}{\omega(u_{eff,r}^2 + u_{eff,i}^2)} \right] - \left[\frac{2F_r u_{eff,r}}{\omega(u_{eff,r}^2 + u_{eff,i}^2)} \right] j \quad (3.44)$$

This procedure enables the determination of structural EDP impedance using any commercial FEM software, without any adjustment or warranting the inclusion of electric degrees of freedom in the finite element model.

3.5.3 Modeling of Structural Damping

In most commercial FEM software, the damping matrix is determined from the stiffness and mass matrices as:

$$[C] = \alpha[M] + \beta[K] \quad (3.45)$$

where α is the mass-damping factor and β the stiffness-damping factor. This type of damping is called Rayleigh damping. Further simplification can be achieved by defining damping as a function of stiffness alone, that is

$$[C] = \left(\frac{\eta}{\omega} \right) [K] \quad (3.46)$$

Then, after substituting in Eq. (3.34), this simplification renders the stiffness matrix complex, as given by

$$[\bar{K}] = (1 + i\eta)[K] \quad (3.47)$$

where η is called the mechanical loss factor of the material. Its equivalent Rayleigh damping coefficients are $\alpha = 0$ and $\beta = \eta / \omega$. This type of damping is frequency independent. The present analysis considered $\alpha = 0$ and $\beta = 3 \times 10^{-9}$, resulting in $\eta \approx 0.002$ on an average for the frequency range considered (0 – 200 kHz).

3.5.4 Wavelength Analysis and Convergence Test

In dynamic harmonic problems, to obtain accurate results, a sufficient number of nodal points (3 to 5) per half wavelength should be present in the finite element mesh. In order to ensure this requirement, modal analysis was additionally performed on the model (Fig. 3.6). The frequency range 0 – 200 kHz was found to contain a total of 24 modes. The modal frequencies are listed in Table 3.3, computed for four different element sizes – 2 mm, 1.5 mm, 1 mm and 0.8 mm. The table shows that good convergence of the modal frequencies is achieved at an element size of 1 mm (the element size used in the present analysis). Thus, reasonably accurate results are expected from the present analysis using FEM. In addition, Figs. 3.7(a), 3.7(b) and 3.7(c) show the plots of the displacements u_x , u_y and u_z , respectively for the 24th mode (the highest excited mode), over the top surface of the block ($z = 10$ mm). Also, the displacements in the three principal directions are plotted for the edge AB (Fig. 3.6) to illustrate that there are sufficient numbers of nodes per half wavelength, to ensure accuracy of the analysis.

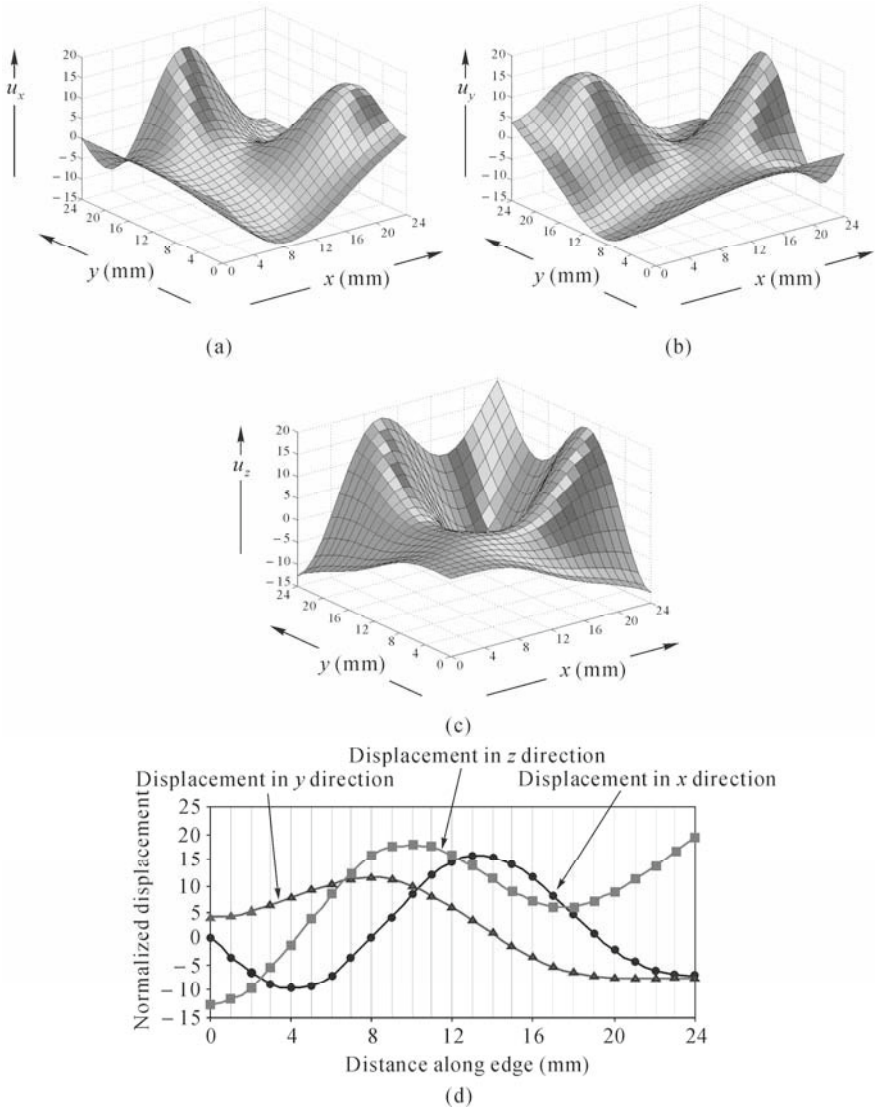


Fig. 3.7 Examination of mode 24 to check adequacy of mesh size of 1 mm. (a) Displacements in x direction on surface $z = 10$ mm; (b) Displacements in y direction on surface $z = 10$ mm; (c) Displacements in z direction on surface $z = 10$ mm; (d) Displacements in principal directions along the line defined by the intersection of surfaces $y = 24$ mm and $z = 10$ mm (see Fig. 3.6)

Table 3.3 Details of modes of vibration of test structure

Mode	Modal frequency (kHz)				Description of mode
	2 mm	1.5 mm	1 mm	0.8 mm	
1	81.710	81.480	81.320	81.256	Thickness shear (diagonal)
2	89.354	89.105	88.944	88.884	Face shear
3	90.991	90.765	90.610	90.547	Thickness shear (diagonal)
4	106.667	106.335	106.101	106.016	Face shear + flexure
5	123.847	123.125	124.623	124.464	Thickness flexure
6	139.579	138.916	138.521	138.367	Bending about diagonal
7	139.910	139.227	138.845	138.691	Bending about diagonal + rotation
8	142.425	141.406	140.745	140.525	Thickness flexure
9	146.653	143.852	143.420	143.249	Flexure
10	148.645	148.017	147.624	147.484	Flexure
11	150.387	149.511	149.000	148.801	Flexure
12	156.807	153.576	154.882	154.623	Flexure
13	157.744	156.706	156.119	153.905	Flexure + thickness extension
14	163.482	164.333	163.660	163.417	Flexure
15	168.217	166.960	166.207	163.941	Flexure
16	176.823	174.370	172.701	172.186	Thickness flexure
17	181.411	180.035	179.145	178.841	Flexure
18	183.001	181.943	181.222	180.984	Flexure
19	183.590	183.573	182.242	181.808	Flexure
20	191.910	189.760	188.364	187.902	Flexure
21	192.133	190.116	188.776	188.345	Flexure
22	193.335	193.208	191.869	191.424	Flexure
23	196.805	194.432	192.986	192.519	Flexure
24	200.887	199.026	197.845	197.457	Flexure

3.5.5 Comparison between Theoretical and Experimental Signatures

After computing the structural EDP impedance by FEM, the admittance functions were derived using Eq. (3.30). The values of ε_{33}^T and δ for the PZT patch were determined experimentally. The Poisson's ratio of the patch was assumed to be 0.3. The MATLAB program (The MathWorks Inc., 2009) listed in Appendix B was used to perform the computations. Fig. 3.8 shows a comparison between the experimental and theoretical signatures, based on the proposed approach as well as the model of Zhou *et al.* (1995). The predictions by the proposed method are very close to that of Zhou's as is evident from the highly complex nature of their governing equations (Eqs. (3.5) – (3.7)). Furthermore, the effective impedance model facilitates the solution of inverse problems (such as obtaining the structural mechanical impedance from the measured signatures, which will be shown in the next chapter).

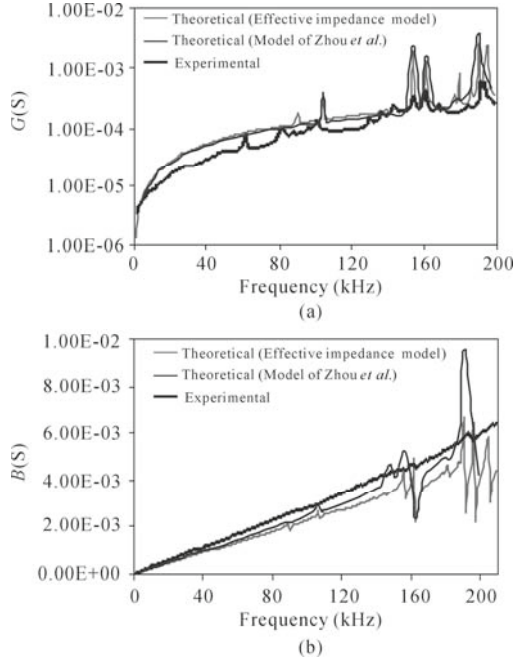


Fig. 3.8 Comparison between experimental and theoretical signatures. (a) Conductance plot; (b) Susceptance plot

A good agreement clearly exists between the experimental and the theoretical plots of the real part- conductance, predicted by the proposed model (Fig. 3.8(a)). Major peaks are reasonably well predicted, though the experimental spectrum contains a few unpredicted peaks (mainly due to edge roughness and the inability of FEM to accurately model solid-air interactions at the boundaries). However, in the susceptance-plots (Fig. 3.8(b)), a large discrepancy is clearly evident, especially the difference in slopes of the curves. This discrepancy is attributed to the deviation of PZT behavior from the ideal behavior predicted by Eq. (3.22). In addition, several parameters of the PZT patch could deviate from the values provided by the manufacturer. Fortunately, the admittance signatures of the PZT patch in “free-free” condition were recorded prior to bonding it on the structure. Hence, it was possible to investigate the behavior of the free PZT patch and use this information to obtain more accurate plots. The next section describes the investigations in detail.

3.6 Refining the 2D Impedance Model

The properties of piezoceramics are strongly dependent upon the process route, and they exhibit statistical fluctuations within a given batch (Giurgiutiu and Zagrai,

2000). The fluctuations are caused by inhomogeneous chemical composition, mechanical differences in the forming process, chemical modification during sintering and the polarization method (Sensor Technology Ltd., 1995). A variance of the order of 5% – 20% in properties is not uncommon. In the EMI technique, we solely depend upon the PZT patches to obtain the mechanical impedance spectra of the structures. Hence, it is very important to accurately model the behavior of PZT patches when using the formulations derived in the previous sections. For this purpose, it is recommended that the signatures of PZT patches be recorded in the “free-free” condition prior to their bonding to the host structure.

From Eq. (3.30), for a free (unbonded) PZT patch, the complex electro-mechanical admittance can be derived (by substituting $Z_{s,eff} = 0$ and simplifying) as:

$$\bar{Y}_{free} = 4\omega j \frac{l^2}{h} \left[\frac{\epsilon_{33}^T}{\epsilon_{33}^T} + \frac{2d_{31}^2 \bar{Y}^E}{(1-\nu)} \left(\frac{\tan \kappa l}{\kappa l} - 1 \right) \right] \quad (3.48)$$

Substituting $\bar{Y}^E = Y^E (1 + \eta j)$, $\bar{\epsilon}_{33}^T = \epsilon_{33}^T (1 - \delta j)$, $\frac{\tan \kappa l}{\kappa l} = r + tj$ and $\omega = 2\pi f$ (“ f ” being the frequency of vibrations in Hz), and simplifying, we get

$$\bar{Y}_{free} = G_f + B_f j \quad (3.49)$$

where

$$G_f = \frac{8\pi f l^2}{h} \left[\epsilon_{33}^T \delta - \frac{2d_{31}^2 Y^E}{(1-\nu)} \{ \eta(r-1) + t \} \right] \quad (3.50)$$

$$B_f = \frac{8\pi f l^2}{h} \left[\epsilon_{33}^T + \frac{2d_{31}^2 Y^E}{(1-\nu)} \{ (r-1) - \eta t \} \right] \quad (3.51)$$

Furthermore, under very low frequencies (typically < one-fifth of the first resonance frequency of the PZT patch), $\frac{\tan \kappa l}{\kappa l} \rightarrow 1$ (i.e. $r \rightarrow 1$, $t \rightarrow 0$) (Liang *et al.*, 1993), thereby leading to the quasi-static sensor approximations (Giurgiutiu and Zagari, 2002)

$$G_{f,qs} = \frac{8\pi f l^2 \epsilon_{33}^T \delta}{h} \quad (3.52)$$

$$B_{f,qs} = \frac{8\pi f l^2 \epsilon_{33}^T}{h} \quad (3.53)$$

Rearranging the various terms, Eqs. (3.52) and (3.53) can be rewritten as:

$$G_{f,qs}^* = \frac{G_{f,qs}h}{8\pi l^2 \epsilon_{33}^T} = \delta f \quad (3.54)$$

$$B_{f,qs}^* = \frac{B_{f,qs}h}{8\pi l^2} = \epsilon_{33}^T f \quad (3.55)$$

From Eqs. (3.54) and (3.55), the electrical constants ϵ_{33}^T and δ can be computed as the slopes of the frequency plots of $B_{f,qs}^*$ (unit S/m) and $G_{f,qs}^*$ (unit S/F) for sufficiently low frequencies (typically <10 kHz for 10 mm long PZT patches). Fig. 3.9 shows the typical plots of these functions in the frequency range 0 – 10 kHz for two PZT patches, labeled as *S2002-5* and *S2002-6*.

PZT patch *S2002-5* was used as the piezo-impedance transducer in the experiment described in the previous section. From these plots, ϵ_{33}^T is worked out to be 1.792×10^{-8} F/m and 1.733×10^{-8} F/m respectively for *S2002-5* and *S2002-6*, against a value of 2.124×10^{-8} F/m supplied by the manufacturer. Similarly, δ is worked out to be 0.0238 and 0.0225 respectively, against a value of 0.015 supplied by the manufacturer.

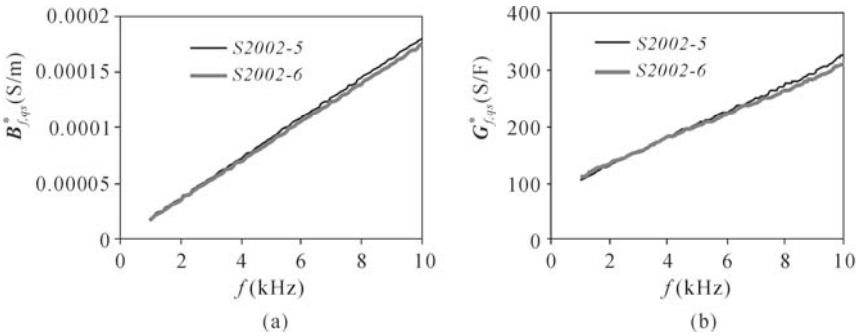


Fig. 3.9 Plots of quasi-static admittance functions of free PZT patches to obtain electric permittivity and dielectric loss factor. (a) $B_{f,qs}^*$ vs. frequency; (b) $G_{f,qs}^*$ vs. frequency

Using Eqs. (3.50) and (3.51) and the above PZT parametric values, respective conductance and susceptance signatures of PZT patches *S2002-5* and *S2002-6* are derived in the “free-free” condition in the frequency range 1 – 1,000 kHz. These are then compared with the experimental free PZT signatures in Fig. 3.10. Although the figures suggest reasonable agreement between the analytical and experimental signatures, there are some underlying discrepancies which need closer examination. A closer look at frequency range 0 – 300 kHz (Figs. 3.10(a) and 3.10(c)) shows an unpredicted mode at around 240 kHz. In the case of *S2002-5* (Fig. 3.10(a)), twin peaks can be observed in the experimental spectra around each

of the prominent resonance frequencies. A general observation is that the experimental resonance frequency is slightly higher than the theoretical frequency.

The twin peaks are due to deviation, during manufacturing, in the perfect square shape of the PZT patch. This leads to somewhat partly-independent resonance peaks corresponding to the two slightly unequal edge lengths. The unpredicted modes in the admittance spectra are due to edge roughness induced secondary vibrations. Higher experimental natural frequency suggests additional 2D stiffening, which is unaccounted for in the present model. A similar comparison was reported by Giurgiutiu and Zagari (2000), but considering 1D vibrations only. They assumed the patch to possess widely separated values for length, width and thickness so that the length, width and thickness vibrations are practically uncoupled. Their analytical predictions only matched the experimental results for aspect ratios higher than 2.0.

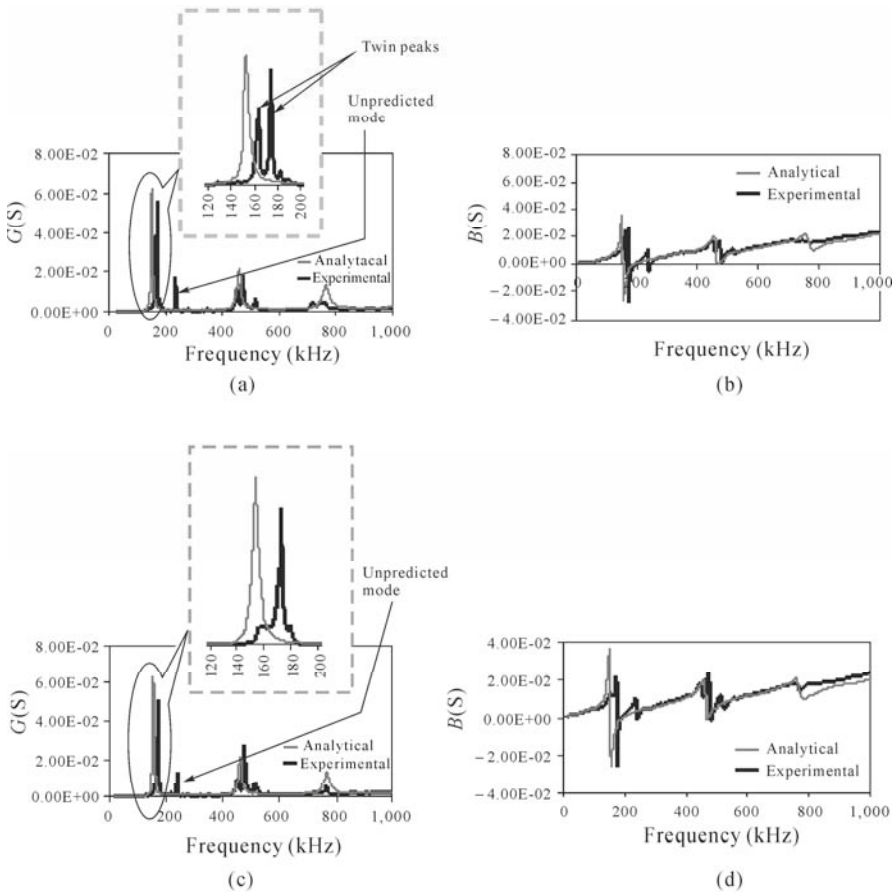


Fig. 3.10 Experimental and analytical plots of free PZT signatures. (a) *S2002-5*: Conductance (G) vs. frequency; (b) *S2002-5*: Susceptance (B) vs. frequency; (c) *S2002-6*: Conductance (G) vs. frequency; (d) *S2002-6*: Susceptance (B) vs. frequency

Here, the frequency range of interest is 0 – 200 kHz. The unpredicted modes do not come into play in this frequency range. In order to further “update” the model of the PZT patch, with respect to peaks, a correction factor is introduced in the term $\frac{\tan kl}{kl}$. In the case of PZT patch *S2002-5*, where twin peaks are observed, this term may be replaced by

$$\frac{1}{2} \left[\frac{\tan(C_1 kl)}{C_1 kl} + \frac{\tan(C_2 kl)}{C_2 kl} \right]$$

By trial and error, values of $C_1 = 0.94$ and $C_2 = 0.883$ are found to update the model of the PZT patch. Furthermore, the following values of the PZT parameters are determined from the experimental plots using the technique of curve fitting.

$$K = \frac{2d_{31}^2 Y^E}{(1-\nu)} = 5.16 \times 10^{-9} \text{ N/V}^2 \text{ and } \eta = 0.03$$

On the contrary, the value of K based on data supplied by the manufacturer worked out to be $8.4 \times 10^{-9} \text{ NV}^2$. Using these values and the correction factors C_1 and C_2 , the free PZT signatures were re-worked for the frequency range 0 – 200 kHz. Figs. 3.11(a) and 3.11(b) compare the updated signatures with the experimental signatures, which agree significantly with one another.

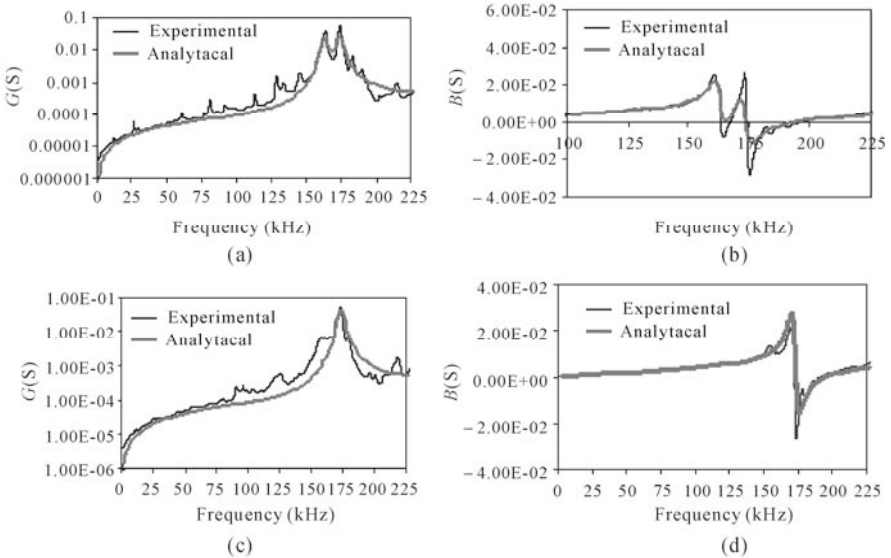


Fig. 3.11 Plots of free-PZT admittance signatures using the updated PZT model. (a) *S2002-5*: Conductance (G) vs. frequency; (b) *S2002-5*: Susceptance (B) vs. frequency; (c) *S2002-6*: Conductance (G) vs. frequency; (d) *S2002-6*: Susceptance (B) vs. frequency

Similarly, for PZT patch *S2002-6*, the value of the coefficient C is computed as 0.885, such that the term $\frac{\tan kl}{kl}$, when replaced by $\frac{\tan(Ckl)}{Ckl}$, yields good agreement between the experimental and analytical plots of free PZT signatures. Further, K is computed to be $4.63 \times 10^{-9} \text{ N/V}^2$ and η again worked out to be 0.03 by curve fitting. Figs. 3.11(c) and 3.11(d) compare the analytical and experimental plots. Again, the experimental signatures and the analytical signatures agree well using the updated PZT model.

Through these adjustments in the analytical model, aided by experimental measurements, the results have significantly improved in the frequency range 0-200 kHz. However, this approach is unable to yield any further improvement beyond 200 kHz. At the same time, unpredicted peaks, such as the one at around 220 kHz cannot be accounted for. The later parts of this chapter will demonstrate how numerical modeling, especially coupled field analysis, could be of further aid in predicting twin peaks as well as accounting for the peak around 220 kHz.

Considering the necessity of updating the model of the PZT patch, Eq. (3.30) is modified as

$$\bar{Y} = G + Bj = 4\omega j \frac{l^2}{h} \left[\frac{\bar{\epsilon}_{33}^T}{\epsilon_{33}^T} - \frac{2d_{31}^2 \bar{Y}^E}{(1-\nu)} + \frac{2d_{31}^2 \bar{Y}^E}{(1-\nu)} \left(\frac{Z_{a,eff}}{Z_{s,eff} + Z_{a,eff}} \right) \bar{T} \right] \quad (3.56)$$

where the term \bar{T} is the complex tangent ratio (ideally $\frac{\tan kl}{kl}$), which can be expressed as

$$\bar{T} = \frac{1}{2} \left(\frac{\tan C_1 k l}{C_1 k l} + \frac{\tan C_2 k l}{C_2 k l} \right) \quad (3.57)$$

($C_2 = 0$ in the case of single peak). Furthermore, the corrected actuator effective impedance (Eq. (3.22)) can be written as

$$Z_{a,eff} = \frac{2h \bar{Y}^E}{j\omega(1-\nu)\bar{T}} \quad (3.58)$$

As previously mentioned, PZT patch *S2002-5* is bonded to the host structure shown in Fig. 3.3. The theoretical signatures for this test structure were re-worked using the updated PZT model (Eqs. (3.56), (3.57) and (3.58)). The MATLAB program listed in Appendix C was used to perform the computations. Fig. 3.12 compares the theoretical signatures (obtained using the updated PZT model) with the experimental signatures. This time, a much better agreement is found between the two. A comparison of Figs. 3.8(b) and 3.12(b) reveals that improvement is especially significant in the case of the susceptance.

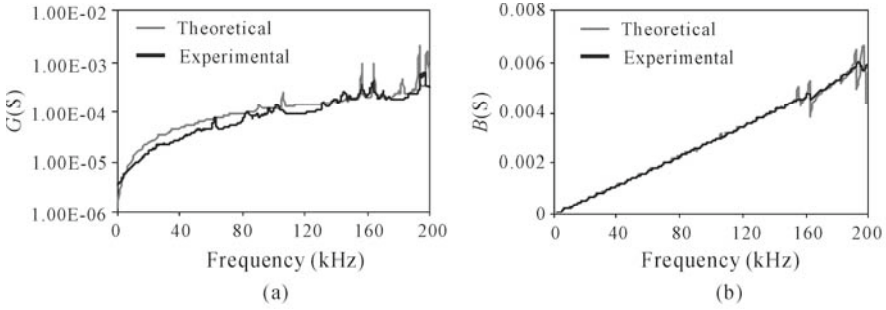


Fig. 3.12 Comparison between experimental and analytical signatures based on updated PZT model; (a) Conductance (G) vs. frequency; (b) Susceptance (B) vs. Frequency

Fig. 3.13(a) compares the idealized and the corrected effective impedance for PZT patch $S2002-5$. The influence of twin peaks is clearly reflected in the plot of the updated impedance. If the idealized model of PZT patch was solely employed to identify the structure, significant errors could have been introduced, as clearly observed in Fig. 3.13(b), which shows the plot of $|Z_{s,eff}|^{-1}$. Furthermore, Fig. 3.13(c) shows the plots of $|Z_{s,eff}|$ and $|Z_{a,eff}|$ obtained from the measured signatures (the computational procedure will be explained in detail in Chapter 4).

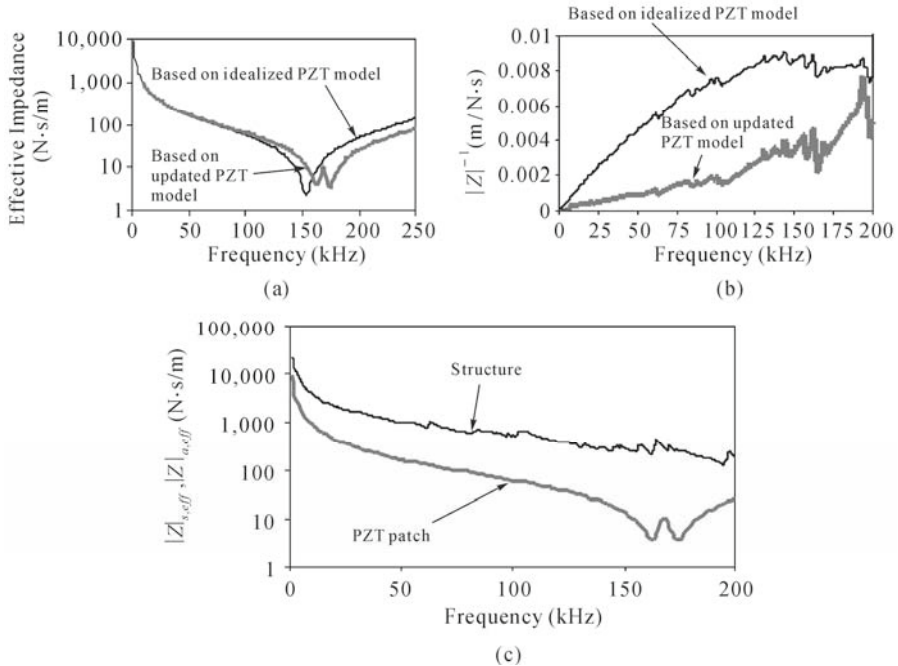


Fig. 3.13 (a) PZT effective impedance, based on idealized and updated models; (b) Error in extracted structural impedance in the absence of updated PZT model; (c) Relative magnitudes of structure and PZT impedances

It should be noted that Giurgiutiu and Zagrai (2002) also evaluated the electro-mechanical admittance across PZT terminals using analytical and numerical methods. However, they could only model simple structures, such as thin beams, under simple boundary conditions, *e.g.*, “free-free”. There were orders of magnitude of error between the experimental and analytical impedance spectra. Our formulations, on the other hand, are more general in nature and are valid for all types of structures. The agreement between the analytical and experimental results is also much better as compared to the previous models. Our approach is thus a semi-analytical approach since it first uses numerical models to compute $Z_{s,eff}$, and then an analytical formulation to obtain the complex electro-mechanical admittance. However, as already stated, numerical computation of $Z_{s,eff}$ will not be required, as shall be illustrated in the next chapter.

3.7 3D Interaction of PZT Transducer with Host Structure

3.7.1 Necessity of 3D Formulation

The 2D model described in Sections 3.4 to 3.6 assumes that the PZT patch vibrates along the length and width only (Fig. 3.4). This limits the application of the 2D plane model to surface-bonded thin PZT patches as it does not consider the thickness vibration of the PZT, which produces longitudinal actuation that is vital in the thick or confined/embedded PZT patches. Thus, the 2D model has limited applications for laminated and concrete structures, where critical zones to be monitored are usually within the structure. Moreover, issues like bonding layer and protection using adhesive layer are additional requirements for effective PZT-structure interaction models. Therefore, there is a need for a 3D impedance model.

3.7.2 Issues in 1D and 2D Impedance Models

Liang *et al.* (1993) developed the 1D PZT-structure impedance model utilizing only 1D actuation of PZT patch along the length direction. Zhou *et al.* (1996), Bhalla and Soh (2004a) and Yang *et al.* (2005) extended it to 2D plane stress models by considering the extensional actuations in the length and width directions of the patch. Annamdas and Soh (2006a) further extended it to a 2D plane-strain model by considering the extensional actuation along the length and the longitudinal actuation along the thickness direction of PZT patch. More recently, taking into consideration the limitations of existing 1D and 2D models such as restrictions on PZT shape, size and isotropy, Annamdas and Soh (2007) derived a 3D model utilizing 3D actuations of PZT transducers.

However, these 2D and 3D formulations do not consider the situation of multiple PZT patches bonded on the same host structure. In practical SHM problems, many PZT patches have to be used on the structure to be monitored. Moreover, the thin adhesive layer, which is employed to bond these PZT patches, does not adequately protect the patch from the environmental conditions. Thus, bonded PZT patches have to be further protected using protective covers or by wrapping adhesives. Additionally, the adhesive underneath the PZT patch plays a vital role in constraining the strain transfer from PZT patch to host structure and subsequently influences the EMI signatures. Hence, the practical applications of EMI technique warrant a 3D multiple PZT-structure interaction model with consideration of the wrapper or thick adhesive bond.

All these are considered by Madhav and Soh (2007a) in their 3D impedance model, which treats both the PZT patch and the bonding adhesive as integral parts of the host structure. Thus, it avoids any additional compensation factors to counter the problem of thick adhesive bonding. Furthermore, this 3D model is applicable for both embedded as well as surface bonded PZT-structure interaction.

3.7.3 Issues to Consider in 3D Impedance Model

- *Inclusion of Adhesive Layer*

The two main factors which influence the admittance signatures are (1) external factors like continuous loading, presence of acid or base, magnetic field, electric field, humidity, rain, heat, etc., and (2) internal factors like the electrical and mechanical properties of the PZT patches. There are two ways of arresting these influencing factors; either by compensation using correction factors or by protecting the PZT by wrapping. PZT material is very brittle and vulnerable to breaking especially when embedded; thus protection (such as wrapping) for the PZT becomes necessary (Fig. 3.14).

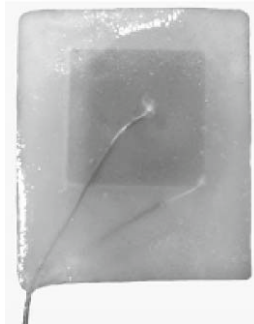


Fig. 3.14 Epoxy wrapped PZT patch

However, epoxy wrap has influence on the admittance signatures as illustrated in Fig. 3.15. The figure compares the conductance signatures of a free PZT patch (grade A PZT of size 10 mm×10 mm×2 mm) and a wrapped PZT patch (same PZT grade and size) under a free-free boundary condition. The properties of the PZT patches and the adhesive used in the study are listed in Table 3.4. It is apparent that the peaks are larger in magnitude for the free PZT patch than for the wrapped PZT patch. Moreover, the slope of the wrapped PZT patch is different from that of the free PZT patch due to mass effect of the wrapper on the PZT patch. It is essential therefore to better understand the 3D behavior of a wrapped PZT as the interaction is between the PZT patch and the bonding adhesive with the host structure instead of only between the PZT patch and the structure.

Table 3.4 Properties of PZT and epoxy adhesive

Physical property	PZT	Epoxy
Density (kg/m ³)	7,800	1,180
Young's modulus (N/m ²)	6.667×10 ¹⁰	2×10 ⁹
Poisson ratio	0.33	0.4
Electric permittivity, ϵ_{33} (Farad/m)	Grade A: 2.124×10 ⁻⁸	
	Grade B: 0.98×10 ⁻⁸	
	Grade C: 1.70×10 ⁻⁸	
Piezoelectric strain coefficient in direction X, Y : d_{31} or d_{32} (m/V)	-2.10×10 ⁻¹⁰	
	direction Z : d_{33} (m/V)	4.50×10 ⁻¹⁰
Dielectric loss factor, δ	0.015	
Mechanical loss factors η	0.023	

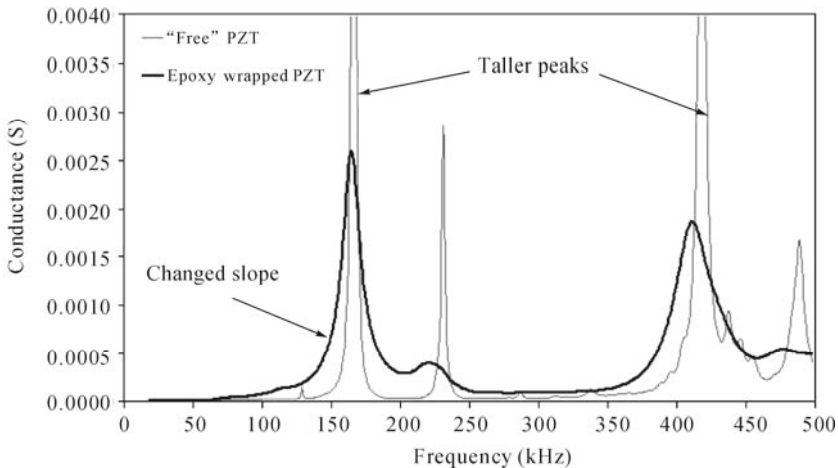


Fig. 3.15 Conductance signatures of “free” PZT and epoxy wrapped PZT

Bhalla and Soh (2004b) presented two types of PZT-adhesive-structure interactions for PZT patches bonded with thicker epoxy adhesive. One is based on

changing “mechanical impedance Z_S ” of the structure (see Section 3.4) by introducing compensation for the ‘shear lag’ caused by thicker epoxy adhesive. The other is based on reduced or equivalent surface dimensions of PZT ($L-dl$, $W-dw$) as shown in Fig. 3.16(a). The limitations are that Z_S can only be obtained for square and electrically-isotropic PZT patches, and that the thickness actuation is not included in the formulation; thus limiting its application to 2D plane stress.

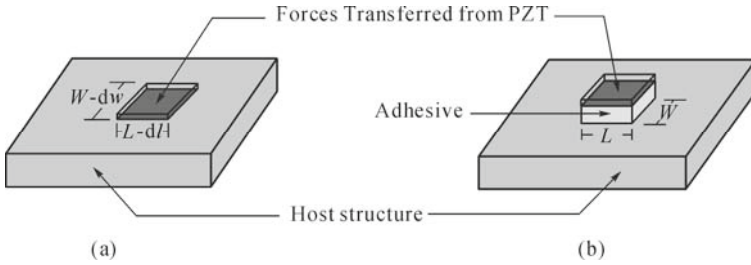


Fig. 3.16 PZT-structure interaction: (a) Equivalent dimensions of PZT patch; (b) Actual dimensions of PZT patch

- *Inclusion of Mass of PZT Patch*

The previous PZT-structure interaction models have ignored the mass and thickness of adhesive. Even if they were considered, the applications would be limited to 1D or 2D. Such non-inclusion can be tolerated if the mass of a PZT patch is small compared with the host structure. However, several practical SHM involve heavy or multiple PZT patches, where the influence of mass of PZT patch may become significant for light structures. Cheng and Lin (2005) developed a multiple PZT-structure model considering the “mass” of the patches; but the model is limited to 2D. Hence, there exists a need for the formulation of a 3D model which considers both the mass of PZT patch and the adhesive layer (beneath the PZT) for implementation in practical applications.

- *Actual Dimensions of PZT Patch and Adhesive*

This 3D model includes the actual dimensions of the PZT patch and the adhesive (L , W and $2H_E$) in its formulation, without any necessity for shear lag compensation; where L , W and $2H_E$ are the actual dimensions of the PZT patch and $2H_E$ is the thickness of the adhesive beneath the patch. Thus, this impedance model utilizes all 3D actuations of the PZT patch and includes the mass/ thickness of both PZT patch and adhesive. In addition, there is no restriction on the boundary conditions of the host structure, *i.e.*, the model is applicable for all boundary conditions of the host structure. Moreover, this 3D model does not

impose any restriction on the shape (square or rectangular), size (thin or thick) or electrical properties (isotropic or anisotropic) of the PZT transducer. The model was then experimentally verified for two case studies with different thicknesses of adhesive. Therefore, the model is expected to be applicable for the NDE of most engineering structures as the model is generic.

3.8 3D Model in Presence of Thick Adhesive Bonding

3.8.1 Impedance Formulation

Let E_1 , E_2 and E_3 represent the electric fields along directions X , Y and Z for the 3D PZT transducer shown in Fig. 3.17. The PZT patch in the presence of E_1 and E_2 produces shear actuations (d_{15} , d_{24}), and in the presence of E_3 produces extensional actuations (d_{31} , d_{32}) and longitudinal actuation (d_{33}) (Raja *et al.*, 2004). Note that d_{3j} is the strain displacement coefficient related to the normal strain in the presence of E_3 , and the subscript j denotes either the direction X , Y or Z . d_{15} and d_{24} are the strain displacement coefficients related to the shear strains in the XZ and YZ planes developed due to the fields E_1 and E_2 respectively. However for EMI models, only electric field E_3 is applied along the Z direction, thus the PZT patch produces extensional and longitudinal actuations but not shear actuation.

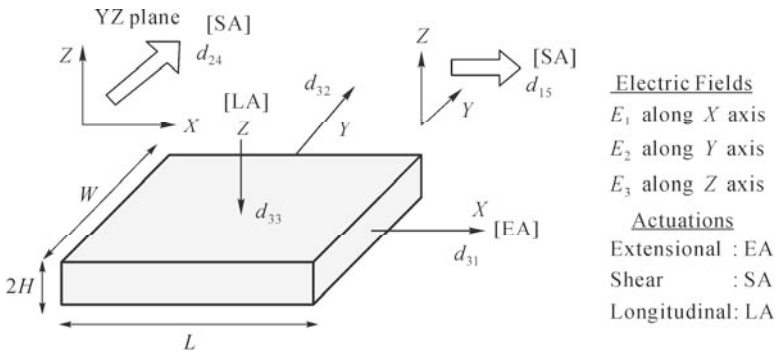


Fig. 3.17 Actuations of PZT patch

Fig. 3.18 depicts the multiple PZT-host structure interaction in the X , Y and Z directions, along the length, width and thickness of the PZT patch. Let L_s , W_s and $2H_s$ be the global dimensions of the host structure, and C_2 (0, 0, 0) be the global centre or reference point of the host structure. Let L_k , W_k and $2H_k$ be the local dimensions of the K^{th} PZT patch, and $2H_{KE}$ be the thickness of the adhesive beneath the K^{th} PZT patch.

The (distributed) forces are developed due to the extensional actuations along directions X and Y , and the longitudinal actuation along direction Z of the multiple PZT patches. At any instant of time, the forces developed due to the actuations correspond respectively to expansion in the X and Y directions, and shrinkage in the Z direction; and vice versa. The forces take into consideration the alternate signs of d_{31} (or d_{32}) and d_{33} , as listed in Table 3.4. Due to the opposite signs of d_{31} (or d_{32}) and d_{33} , expansion of the patch in the X and Y directions is accompanied by shrinkage in the Z direction; and vice versa. It should be noted that expansion and shrinkage of PZT patches generate vibrations in the adhesive layer first followed by the host structure.

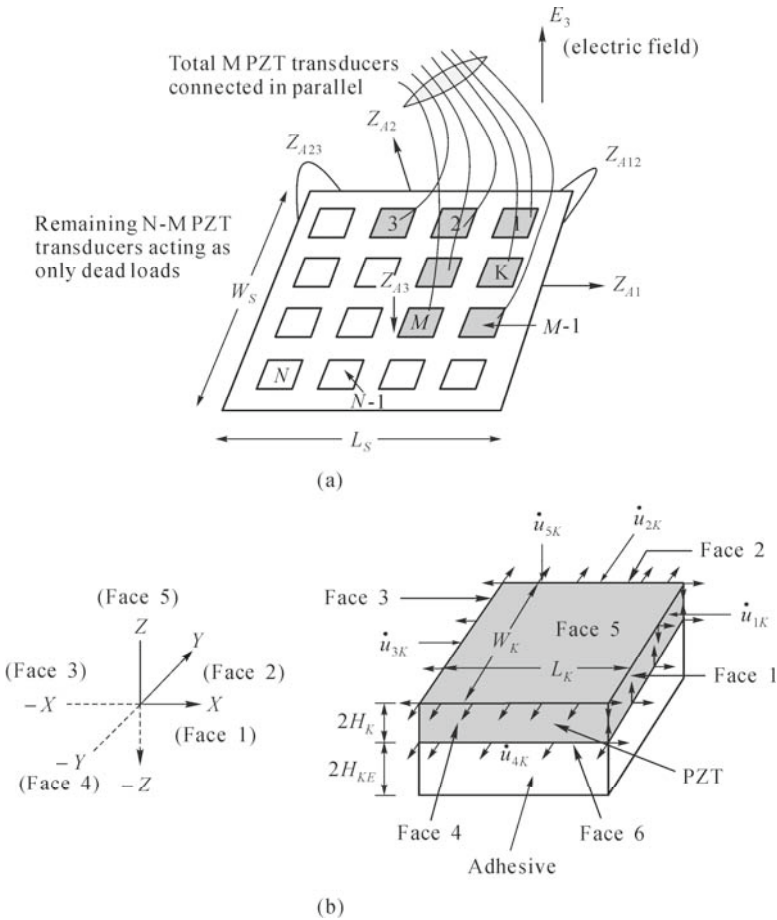


Fig. 3.18 PZT-adhesive-structure interaction model. (a) PZT-structure interaction; (b) K^{th} PZT forces

The impedance of multiple PZTs-structure is given by Annamdas and Soh (2006b) as the sum of the linear impedances along the X , Y and Z directions, and

the cross impedances in the XY , YZ and XZ planes of the multiple patches. However, it should be noted that, in the presence of thick epoxy adhesive layers between the structure and the PZT patches, the collective impedance response (Z_{AS}) of the structure and adhesive is used instead of the impedance of structure (Z_S) alone. This is obtained by adding all the impedances acting on all faces, as shown in Fig. 3.18, which resulted in the following equation.

$$-Z_{AS} = Z_{A1} + Z_{A2} - Z_{A3} + 2Z_{A12} - 2Z_{A23} - 2Z_{A13} \quad (3.59)$$

The negative sign indicates reaction to the applied forces. Positive and negative signs are in accordance with expansion along the X and Y directions and contraction along the Z direction, and vice versa.

If there are N patches surface-bonded to the host structure and if only M ($M \leq N$) are excited in parallel for a desired frequency range, (Fig. 3.18(a)), only the M functioning PZT patches are considered in the formulation. As the mass of the remaining $N-M$ patches contribute only towards the dead load at respective locations on the host structure, they are not considered in the formulation.

The linear collective impedances are given by

$$\begin{aligned} Z_{A1} &= \frac{F_1 - F_3}{\dot{u}_3 - \dot{u}_1} = \frac{F_1 - F_3}{\dot{u}}, Z_{A2} = \frac{F_2 - F_4}{\dot{u}_4 - \dot{u}_2} = \frac{F_2 - F_4}{\dot{v}} \\ Z_{A3} &= \frac{F_5 - F_6}{\dot{u}_6 - \dot{u}_5} = \frac{F_5 - F_6}{\dot{w}} \end{aligned} \quad (3.60a)$$

where the total force due to the M functioning PZT patches on Face I is $F_I = \sum_{K=1}^M F_{IK}$ and the total velocity is given by $\dot{u}_I = \sum_{K=1}^M \dot{u}_{IK}$. Subscript K represents the K^{th} PZT patch, and I represents the face number (4 sides + 1 top + 1 bottom = 6 faces) of the PZT patch (Fig. 3.18(b)). F_{IK} and \dot{u}_{IK} are the single patch force and single patch velocity of the K^{th} PZT patch on Face I . u , v and w are the total relative displacements of the patches along directions X , Y and Z axes. It should be noted that the PZT patches exert forces on the host structure through the adhesive layer.

Fig. 3.19 shows the normal stresses σ_X , σ_Y and σ_Z acting on the K^{th} PZT patch along directions X , Y and Z respectively; τ_{XY} , τ_{YZ} and τ_{ZX} are the shear stresses acting on planes XY , YZ and ZX respectively; and I_x , I_y and I_z are the inertial forces of the PZT patch along directions X , Y and Z respectively. The inertial forces of the adhesive are not considered as it is only a passive component fixed to the vibrating PZT patch. $C1$ is taken as $(0, 0, 0)$ in the local reference of the differential element.

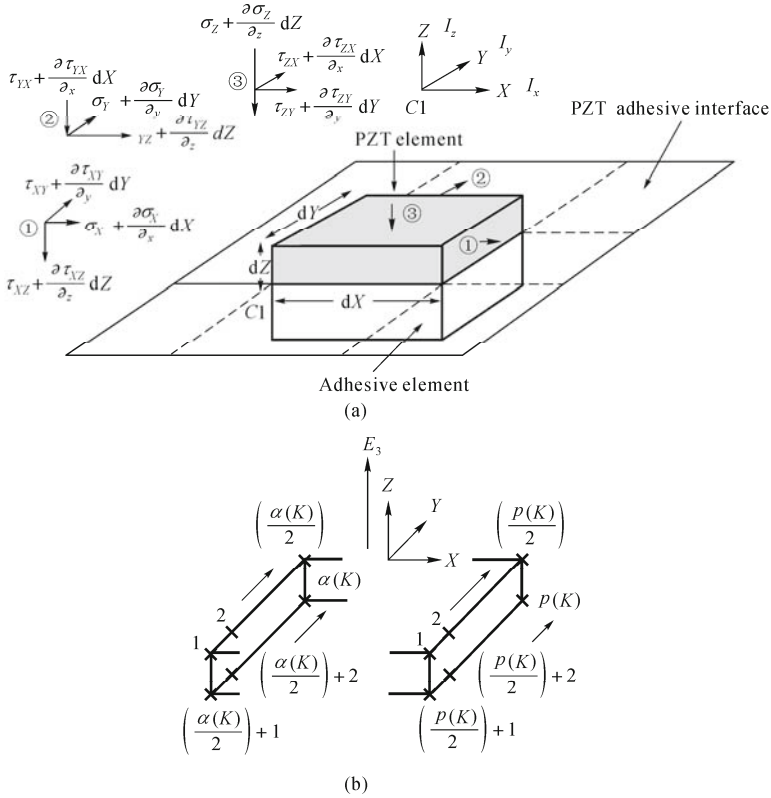


Fig. 3.19 Interaction stresses and forces. (a) Schematic representation of stresses acting on a differential element; (b) Force excitation points of PZT patch

The total patch forces acting on the faces are given as

$$\begin{aligned}
 F_1 = -F_3 = \sigma_X \left(\sum_{K=1}^M W_K 2H \right), \quad F_2 = -F_4 = \sigma_Y \left(\sum_{K=1}^M L_K 2H \right) \\
 F_5 = -F_6 = -\sigma_Z \left(\sum_{K=1}^M W_K L_K \right)
 \end{aligned}
 \tag{3.60b}$$

The collective cross impedances due to the shear forces (or stresses) acting on planes XY , YZ and ZX are empirically given by

$$\begin{aligned}
 Z_{A12} \approx -\frac{Z_{A1}Z_{A2}}{Z_{A1} + Z_{A2} - Z_{A3}}, \quad Z_{A23} \approx -\frac{Z_{A2}Z_{A3}}{Z_{A1} + Z_{A2} - Z_{A3}} \\
 \text{and } Z_{A13} \approx -\frac{Z_{A3}Z_{A1}}{Z_{A1} + Z_{A2} - Z_{A3}}
 \end{aligned}
 \tag{3.61}$$

Substituting Eqs. (3.60a) and (3.61) into Eq. (3.59), we obtain

$$-Z_{AS} = (Z_{A1}\lambda_{C1} + Z_{A2}\lambda_{C2} - Z_{A3}\lambda_{C3}) \quad (3.62)$$

where λ_{C1} , λ_{C2} and λ_{C3} are the collective response factors along directions X , Y and Z respectively of the functioning MPZT patches, and are given as

$$\lambda_{C1} = \left(\frac{Z_{A1}}{Z_{A1} + Z_{A2} - Z_{A3}} \right), \quad \lambda_{C2} = \left(\frac{Z_{A2}}{Z_{A1} + Z_{A2} - Z_{A3}} \right) \quad (3.63)$$

and $\lambda_{C3} = \left(\frac{Z_{A3}}{Z_{A1} + Z_{A2} - Z_{A3}} \right)$

Eq. (3.62) contains all the unknowns, and moreover, there is no close-form solution to determine the collective response factors (λ_{C1} , λ_{C2} and λ_{C3}) and collective impedances (Z_{A1} , Z_{A2} and Z_{A3}). Therefore, a numerical method is used, details of which are presented later.

Substituting Eq. (3.60) into Eq. (3.62), we get

$$Z_{AS} = \frac{F_1 - F_3}{\dot{u}_3 - \dot{u}_1} \lambda_{C1} + \frac{F_2 - F_4}{\dot{u}_4 - \dot{u}_2} \lambda_{C2} - \frac{F_5 - F_6}{\dot{u}_6 - \dot{u}_5} \lambda_{C3} \quad (3.64)$$

$$= 2 \left(\frac{\sigma_1 \sum W_K 2H_K}{\dot{u}} + \frac{\sigma_2 \sum L_K 2H_K}{\dot{v}} - \frac{\sigma_3 \sum L_K W_K}{\dot{w}} \right)$$

where σ_1 , σ_2 and σ_3 are the semi-analytical directional stresses (Annamdas and Soh, 2006b) given as:

$$\begin{bmatrix} \sigma_1 \\ \sigma_2 \\ \sigma_3 \end{bmatrix}_{Semi_analytical} = \begin{bmatrix} \lambda_{C1} & 0 & 0 \\ 0 & \lambda_{C2} & 0 \\ 0 & 0 & \lambda_{C3} \end{bmatrix}_{Numerical} \begin{bmatrix} \sigma_X \\ \sigma_Y \\ \sigma_Z \end{bmatrix}_{Analytical} \quad (3.65)$$

3.8.2 Stress-Strain Relationship of PZT Patch Subjected to 3D Loading

Consider the coordinate system shown in Fig. 3.19, the stress-strain relationship in terms of induced strains can be expressed as

$$\begin{bmatrix} \sigma_X \\ \sigma_Y \\ \sigma_Z \end{bmatrix} = Y_R \begin{bmatrix} 1 & R & R \\ R & 1 & R \\ R & R & 1 \end{bmatrix} \begin{bmatrix} \varepsilon_X \\ \varepsilon_Y \\ \varepsilon_Z \end{bmatrix} \quad \text{and} \quad \begin{bmatrix} \tau_{XY} \\ \tau_{YZ} \\ \tau_{ZX} \end{bmatrix} = Y_R \begin{bmatrix} r & 0 & 0 \\ 0 & r & 0 \\ 0 & 0 & r \end{bmatrix} \begin{bmatrix} \gamma_{XY} \\ \gamma_{YZ} \\ \gamma_{ZX} \end{bmatrix} \quad (3.66)$$

where Y_R , R and r are the simplification parameters given as

$$Y_R = \frac{\bar{Y}(1-\nu)}{(1+\nu)(1-2\nu)}, \quad \bar{Y} = Y(1+\eta j), \quad R = \frac{\nu}{1-\nu} \quad \text{and} \quad r = \frac{1-2\nu}{2(1-\nu)} \quad (3.67)$$

\bar{Y} is the complex Young's modulus of elasticity of the 3D PZT patch at zero electric field, Y is the static Young's modulus of elasticity of the PZT material, and η is the mechanical loss factor. ν is the Poisson's ratio of the PZT patch, and ε_X , ε_Y and ε_Z are the normal strains along the X , Y and Z directions. τ_{XY} , τ_{YZ} and τ_{ZX} are the shear stresses, and γ_{XY} , γ_{YZ} and γ_{ZX} are the shear strains.

The induced strains in terms of total relative displacements are given as

$$\begin{bmatrix} \varepsilon_X \\ \varepsilon_Y \\ \varepsilon_Z \end{bmatrix} = \begin{bmatrix} D_x u \\ D_y v \\ D_z w \end{bmatrix} \quad \text{and} \quad \begin{bmatrix} \gamma_{XY} \\ \gamma_{YZ} \\ \gamma_{ZX} \end{bmatrix} = \begin{bmatrix} D_x v + D_y u \\ D_y w + D_z v \\ D_z u + D_x w \end{bmatrix} \quad (3.68)$$

where $D_x = \frac{\partial}{\partial x}$, $D_y = \frac{\partial}{\partial y}$ and $D_z = \frac{\partial}{\partial z}$.

3.8.3 3D Differential Equations

Consider the differential element of the K^{th} PZT patch shown in Fig. 3.19. Let ρ be the mass density of the patch. The force equilibrium along directions X , Y and Z can be written as

$$\begin{aligned} & (\sigma_x + D_x \sigma_x dx) dydz + (\tau_{xy} + D_y \tau_{xy} dy) dx dz + (\tau_{xz} + D_z \tau_{xz} dz) dx dy \\ & - \sigma_x dydz - \tau_{xy} dx dz - \tau_{xz} dx dy - I_x = 0 \end{aligned} \quad (3.69a)$$

$$\begin{aligned} & (\sigma_y + D_y \sigma_y dy) dx dz + (\tau_{yx} + D_x \tau_{yx} dx) dy dz + (\tau_{yz} + D_z \tau_{yz} dz) dx dy \\ & - \sigma_y dx dz - \tau_{yx} dy dz - \tau_{yz} dx dy - I_y = 0 \end{aligned} \quad (3.69b)$$

$$\begin{aligned} & (\sigma_z + D_z \sigma_z dz) dx dy + (\tau_{zx} + D_x \tau_{zx} dx) dy dz + (\tau_{zy} + D_y \tau_{zy} dy) dx dz \\ & - \sigma_z dx dy - \tau_{zx} dy dz - \tau_{zy} dx dy - I_z = 0 \end{aligned} \quad (3.69c)$$

The inertial forces I_x , I_y and I_z are given by

$$I_x = \rho dx dy dz D_{tt} u, \quad I_y = \rho dx dy dz D_{tt} v \quad \text{and} \quad I_z = \rho dx dy dz D_{tt} w \quad (3.70)$$

Eq. (3.69) can be written as:

$$\begin{aligned} D_x \sigma_x + D_y \tau_{xy} + D_z \tau_{xz} &= \rho D_{tt} u, \\ D_y \sigma_y + D_x \tau_{xy} + D_z \tau_{yz} &= \rho D_{tt} v \\ D_z \sigma_z + D_x \tau_{zx} + D_y \tau_{yz} &= \rho D_{tt} w \end{aligned} \quad (3.71)$$

Substituting Eqs. (3.66) and (3.68) into Eq. (3.71), we get

$$\begin{aligned} &D_x \sigma_x + D_y \tau_{xy} + D_z \tau_{xz} \\ &= Y_R \left\{ \langle D_{xx} u \rangle + \langle R [D_{xy} v + D_{xz} w] + r [D_{yy} u + D_{zz} u + D_{xy} v + D_{xz} w] \rangle \right\} \\ &= \rho D_{tt} u \end{aligned} \quad (3.72)$$

$$Y_R \left\{ \langle D_{yy} v \rangle + R [D_{xy} u + D_{yz} w] + r [D_{xy} u + D_{xx} v + D_{zz} v + D_{yz} w] \right\} = \rho D_{tt} v \quad (3.73)$$

$$Y_R \left\{ \langle D_{zz} w \rangle + R [D_{xz} u + D_{yz} v] + r [D_{xz} u + D_{yz} v + D_{xx} w + D_{yy} w] \right\} = \rho D_{tt} w \quad (3.74)$$

where $D_{xx} = \frac{\partial^2}{\partial x^2}$, $D_{yy} = \frac{\partial^2}{\partial y^2}$, $D_{zz} = \frac{\partial^2}{\partial z^2}$, $D_{xy} = \frac{\partial^2}{\partial x \partial y}$, $D_{xz} = \frac{\partial^2}{\partial x \partial z}$, $D_{yz} = \frac{\partial^2}{\partial y \partial z}$

and $D_{tt} = \frac{\partial^2}{\partial t^2}$.

3.8.4 Solution to 3D Differential Equations

The exact solutions for Eqs. (3.72) to (3.74) are difficult to obtain. Hence, each differential equation is split into two equations relating the approximated relative displacements (u_A , v_A and w_A) of the patches instead of the total relative displacements (u , v and w), that is,

$$Y_R \{D_{xx} u_A\} = \rho D_{tt} u_A, \quad Y_R \{D_{yy} v_A\} = \rho D_{tt} v_A \quad \text{and} \quad Y_R \{D_{zz} w_A\} = \rho D_{tt} w_A \quad (3.75)$$

$$Y_R \{R(D_{xy} v_A + D_{xz} w_A) + r(D_{yy} u_A + D_{zz} u_A + D_{xy} v_A + D_{xz} w_A)\} = 0 \quad (3.76a)$$

$$Y_R \{R(D_{xy}u_A + D_{yz}w_A) + r(D_{xy}u_A + D_{xx}v_A + D_{zz}v_A + D_{yz}w_A)\} = 0 \quad (3.76b)$$

and $Y_R \{R(D_{xz}u_A + D_{yz}v_A) + r(D_{xz}u_A + D_{yz}v_A + D_{xx}w_A + D_{yy}w_A)\} = 0 \quad (3.76c)$

The solutions to Eq. (3.75) is in the form of a 3D wave acting along directions X , Y and Z , which are given as

$$\begin{aligned} u_A &= [A \sin kx + B \cos kx] e^{j\omega t} \\ v_A &= [C \sin ky + D \cos ky] e^{j\omega t} \\ w_A &= [E \sin kz + F \cos kz] e^{j\omega t} \end{aligned} \quad (3.77)$$

A , B , C , D , E and F are the coefficients to be determined, and k is the wave number given as:

$$k = \omega \sqrt{\frac{\rho(1+\nu)(1-2\nu)}{Y(1-\nu)}} \quad (3.78)$$

where ω is the angular frequency of excitation.

However, the exact total relative displacements, *i.e.*, solutions to Eqs. (3.72) to (3.74) can be assumed to be in the form of approximated solutions (Eq. 3.75) as

$$\begin{aligned} u &= u_A + f(x, y, z) + \phi_1(x, t) \\ v &= v_A + g(y, x, z) + \phi_2(y, t) \\ w &= w_A + h(z, x, y) + \phi_3(z, t) \end{aligned} \quad (3.79)$$

where f , g and h are the unknown wave functions in space, and ϕ_1 , ϕ_2 and ϕ_3 are the unknown wave functions in space and time. The unknown wave functions can be approximately obtained from the first derivative of the total relative displacements (Eq. 3.79) with respect to space and time.

The first derivatives of the total relative displacements with respect to space (x , y and z) are given as

$$\begin{aligned} D_x u &= \left\{ [Ak \cos kx] e^{j\omega t} \right\}_{Active} \\ &+ \left\{ (f(x, y, z) f') + (\phi_1(x, t) \phi_1' - e^{j\omega t} Bk \sin kx) \right\}_{Passive} \end{aligned} \quad (3.80a)$$

$$\begin{aligned} D_y v &= \left\{ [Ck \cos ky] e^{j\omega t} \right\}_{Active} \\ &+ \left\{ (g(y, x, z) g') + (\phi_2(y, t) \phi_2' - e^{j\omega t} Dk \sin ky) \right\}_{Passive} \end{aligned} \quad (3.80b)$$

$$D_z w = \left\{ [Ek \cos kz] e^{j\omega t} \right\}_{Active} + \left\{ (h(z, x, y)h'_1) + (\phi_3(z, t)\phi'_3 - e^{j\omega t} Fk \sin kz) \right\}_{Passive} \quad (3.80c)$$

The first derivatives of the total relative displacements with respect to time are given as:

$$\left. \begin{aligned} D_t u &= j\omega \left\{ \left[A \frac{Y_R}{k} \sin kx \right]_{Active} + \left(\left[\frac{\dot{\phi}_1}{e^{j\alpha t} j\omega} \phi_1(x, t) \right] - \left[A \left(\frac{Y_R}{k} - 1 \right) \sin kx - B \cos kx \right] \right) \right\}_{Passive} e^{j\alpha t} \\ D_t v &= j\omega \left\{ \left[C \frac{Y_R}{k} \sin ky \right]_{Active} + \left(\left[\frac{\dot{\phi}_2}{e^{j\alpha t} j\omega} \phi_2(y, t) \right] - C \left[\left(\frac{Y_R}{k} - 1 \right) \sin ky - D \cos ky \right] \right) \right\}_{Passive} e^{j\alpha t} \\ \text{and } D_t w &= j\omega \left\{ \left[E \frac{Y_R}{k} \sin kz \right]_{Active} + \left(\left[\frac{\dot{\phi}_3}{e^{j\alpha t} j\omega} \phi_3(z, t) \right] - E \left[\left(\frac{Y_R}{k} - 1 \right) \sin kz - F \cos kz \right] \right) \right\}_{Passive} e^{j\alpha t} \end{aligned} \right\} \quad (3.81)$$

3.8.5 Active Part of Solution

“Active” and “passive” are terms referring to “the part considered” and “the part not considered” in the formulation. They are formulated based on trial and error, and the closed-form solution is used in the present model (see later sections for verification of this model).

There could be many possible solutions to the 3D differential equations, Eqs. (3.72) to (3.74), of the total relative displacements; but in this study, only one solution is considered. All the possible solutions, using Eq. (3.79), assume that the coefficients $A \neq B \neq C \neq D \neq E \neq F \neq 0$ and the propagating waves generated by the applied sinusoidal electric field (along direction Z) are in the form of 3D sine wave patterns in space and time. It is also assumed that the solutions contain active and passive components, and are approximated to represent only the active part. Thus, the final unknown coefficients have only three coefficients A , C and E . After approximation, the first derivatives of the total relative displacements with respect to space (Eq. (3.80)) are modified as

$$\begin{aligned}
 D_x u &= u' = [Ak \cos kx] e^{j\alpha x} \\
 D_y v &= v' = [Ck \cos ky] e^{j\alpha x} \\
 D_z w &= w' = [Ek \cos kz] e^{j\alpha x}
 \end{aligned} \tag{3.82}$$

Similarly, Eq. (3.81) is modified as:

$$\begin{aligned}
 D_t u &= \dot{u} = j\omega \left[A \frac{Y_R}{k} \sin kx \right] e^{j\alpha x} \\
 D_t v &= \dot{v} = j\omega \left[C \frac{Y_R}{k} \sin ky \right] e^{j\alpha x} \\
 D_t w &= \dot{w} = j\omega \left[E \frac{Y_R}{k} \sin kz \right] e^{j\alpha x}
 \end{aligned} \tag{3.83}$$

Therefore, the unknown coefficients left to be solved are A , C and E .

3.8.6 Stress-Strain Relationships in Presence of Electric Fields

The stresses of the PZT patch in the presence of small electric fields along directions X , Y and Z are obtained by introducing electric fields and strain displacement coefficients into Eq. (3.66), as given by Sirohi and Chopra (2000):

$$\begin{aligned}
 \begin{bmatrix} \sigma_X \\ \sigma_Y \\ \sigma_Z \end{bmatrix}_e &= Y_R \begin{bmatrix} 1 & R & R \\ R & 1 & R \\ R & R & 1 \end{bmatrix} \begin{bmatrix} \varepsilon_X - E_3 d_{31} \\ \varepsilon_Y - E_3 d_{32} \\ \varepsilon_Z - E_3 d_{33} \end{bmatrix}, \\
 \begin{bmatrix} \tau_{XY} \\ \tau_{YZ} \\ \tau_{ZX} \end{bmatrix}_e &= Y_R \begin{bmatrix} r & 0 & 0 \\ 0 & r & 0 \\ 0 & 0 & r \end{bmatrix} \begin{bmatrix} \gamma_{XY} - 0 \\ \gamma_{YZ} - E_2 d_{24} \\ \gamma_{ZX} - E_1 d_{15} \end{bmatrix}
 \end{aligned} \tag{3.84}$$

The subscript e represents the presence of electric fields.

The normal and shear strains are obtained using Eqs. (3.68) and (3.82):

$$\begin{aligned}
 \begin{bmatrix} \varepsilon_X \\ \varepsilon_Y \\ \varepsilon_Z \end{bmatrix} &= \begin{bmatrix} D_x u \\ D_y v \\ D_z w \end{bmatrix} = e^{j\alpha x} \begin{bmatrix} Ak \cos kx \\ Ck \cos ky \\ Ek \cos kz \end{bmatrix}, \\
 \begin{bmatrix} \gamma_{XY} \\ \gamma_{YZ} \\ \gamma_{ZX} \end{bmatrix} &= \begin{bmatrix} D_x v + D_y u \\ D_y w + D_z v \\ D_z u + D_x w \end{bmatrix} = e^{j\alpha x} \begin{bmatrix} Ay \sin kx + Cx \sin ky \\ Cx \sin ky + Ex \sin kz \\ Ex \sin kz + Az \sin kx \end{bmatrix}
 \end{aligned} \tag{3.85}$$

However, in the present approach, the basic requirement is that all functioning

PZT patches are excited in parallel at a desired frequency range in the presence of electric field E_3 (along direction Z) only, (Fig. 3.17 and Fig. 3.18(a)). The excitations produce extensional actuations along the length and width, and longitudinal actuation along the thickness of the patch. These actuations in turn produce structural responses in the form of electro-mechanical admittance signatures, which are the basis for damage detection in SHM. The electric field E_3 along direction Z for patches 1, 2, ..., K and M are given in terms of applied voltage (V) and amplitude of voltage (V_0) as

$$(E_3)_K = \frac{V}{2H_K} \text{ and } V = V_0 e^{j\alpha t} \quad (3.86)$$

where the subscript K represents the K^{th} patch.

Substituting Eq. (3.84) into Eq. (3.65), the semi-analytical directional stresses in the presence of an electric field can be written as

$$\begin{bmatrix} \sigma_1 \\ \sigma_2 \\ \sigma_3 \end{bmatrix}_e = \begin{bmatrix} \lambda_{C1} & 0 & 0 \\ 0 & \lambda_{C2} & 0 \\ 0 & 0 & \lambda_{C3} \end{bmatrix} \left(Y_R \begin{bmatrix} 1 & R & R \\ R & 1 & R \\ R & R & 1 \end{bmatrix} \begin{Bmatrix} \varepsilon_X - E_3 d_{31} \\ \varepsilon_Y - E_3 d_{32} \\ \varepsilon_Z - E_3 d_{33} \end{Bmatrix} \right) \quad (3.87)$$

The unknowns A , C and E of Eqs. (3.82) and (3.83) and the unknowns Z_{A1} , Z_{A2} , Z_{A3} , λ_{C1} , λ_{C2} and λ_{C3} of Eq. (3.62) are dependent on the host structure, and are determined using numerical analysis.

3.8.7 Formulation of Structural Responses and Impedances

Summation of the M -functioning PZT patches is used in the formulation of response, which would need input from numerical analysis. Let

$$A = A_0 V_0 \sum_{K=1}^M \frac{L_K}{2H_K}, \quad C = C_0 V_0 \sum_{K=1}^M \frac{W_K}{2H_K} \text{ and } E = E_0 V_0 \sum_{K=1}^M \frac{1}{2H_K} \quad (3.88)$$

Substituting Eq. (3.88) into Eq. (3.83), the rates of change of the total relative displacements are given as

$$\left. \begin{aligned} \dot{u} &= j\omega \frac{Y_R}{k} A_0 \left\{ V_0 \sum_{K=1}^M \frac{L_K}{2H_K} \sin kL_K \right\} e^{j\alpha t}, \\ \dot{v} &= j\omega C_0 \frac{Y_R}{k} \left\{ V_0 \sum_{K=1}^M \frac{W_K}{2H_K} \sin kW_K \right\} e^{j\alpha t}, \\ \text{and } \dot{w} &= j\omega E_0 \frac{Y_R}{k} \left\{ V_0 \sum_{K=1}^M \frac{1}{2H_K} \sin 2kH_K \right\} e^{j\alpha t} \end{aligned} \right\} \quad (3.89)$$

Substituting Eqs. (3.60b), (3.64), and (3.85 to 3.88) into Eq. (3.60a), we obtain the collective linear impedances along directions X , Y and Z in the presence of an electric field

$$Z_{A1} = 2k \left[\frac{\sum_{K=1}^M (W_K \{ (A_0 k L_K \cos k L_K - d_{31}) + R(C_0 k W_K \cos k W_K - d_{32}) \})}{j \omega A_0 \sum_{K=1}^M \frac{L_K}{2H_K} \sin k L_K} \right] + 2k \left[\frac{\sum_{K=1}^M (W_K \{ R(E_0 k \cos 2k H_K - d_{33}) \})}{j \omega A_0 \sum_{K=1}^M \frac{L_K}{2H_K} \sin k L_K} \right] \quad (3.90a)$$

$$Z_{A2} = 2k \left[\frac{\sum_{K=1}^M (L_K \{ R(A_0 k L_K \cos k L_K - d_{31}) + (C_0 k W_K \cos k W_K - d_{32}) \})}{j \omega A_0 \sum_{K=1}^M \frac{W_K}{2H_K} \sin k W_K} \right] + 2k \left[\frac{\sum_{K=1}^M (L_K \{ R(E_0 k \cos 2k H_K - d_{33}) \})}{j \omega A_0 \sum_{K=1}^M \frac{W_K}{2H_K} \sin k W_K} \right] \quad (3.90b)$$

$$Z_{A3} = k \left[\frac{\sum_{K=1}^M \left(\frac{L_K W_K}{H_K} \{ R(A_0 k L_K \cos k L_K - d_{31}) + R(C_0 k W_K \cos k W_K - d_{32}) \} \right)}{j \omega A_0 \sum_{K=1}^M \frac{1}{2H_K} \sin k 2H_K} \right] + k \left[\frac{\sum_{K=1}^M \left(\frac{L_K W_K}{H_K} \{ (E_0 k \cos 2k H_K - d_{33}) \} \right)}{j \omega A_0 \sum_{K=1}^M \frac{1}{2H_K} \sin k 2H_K} \right] \quad (3.90c)$$

Rearranging Eq. (3.90a), one obtains

$$\begin{aligned}
 & A_0(2k^2 \sum_{K=1}^M W_K L_K \cos kL_K - Z_{A1} \sum_{K=1}^M \frac{L_K}{2H_K} j\omega \sin kL_K) \\
 & + C_0(2Rk^2 \sum_{K=1}^M W_K^2 \cos kW_K) + E_0(2Rk^2 \sum_{K=1}^M W_K \cos 2kH_K) \quad (3.91) \\
 & = R_1(d_{31} + R(d_{32} + d_{33}))
 \end{aligned}$$

Let a_1 , a_2 , a_3 and a_4 be substitution variables given by

$$\begin{aligned}
 a_1 &= (2k^2 \sum_{K=1}^M W_K L_K \cos kL_K - Z_{A1} \sum_{K=1}^M \frac{L_K}{2H_K} j\omega \sin kL_K) \\
 a_2 &= (2Rk^2 \sum_{K=1}^M W_K^2 \cos kW_K) \\
 a_3 &= (2Rk^2 \sum_{K=1}^M W_K \cos 2kH_K) \\
 \text{and } a_4 &= R_1(d_{31} + R(d_{32} + d_{33}))
 \end{aligned} \quad (3.92)$$

Substituting Eq. (3.92) into Eq. (3.91), one obtains

$$a_1 A_0 + a_2 C_0 + a_3 E_0 = a_4 \quad (3.93)$$

Similarly, the linear impedances (Z_{A2} and Z_{A3}) along directions Y and Z in the presence of an electric field are given as:

$$b_1 A_0 + b_2 C_0 + b_3 E_0 = b_4 \quad \text{and} \quad c_1 A_0 + c_2 C_0 + c_3 E_0 = c_4 \quad (3.94)$$

where

$$\begin{aligned}
 b_1 &= (2Rk^2 \sum_{K=1}^M L_K^2 \cos kL_K) \\
 b_2 &= (2k^2 \sum_{K=1}^M W_K L_K \cos kW_K - Z_{A2} \sum_{K=1}^M \frac{W_K}{2H_K} j\omega \sin kW_K) \\
 b_3 &= (2Rk^2 \sum_{K=1}^M L_K \cos 2kH_K) \\
 b_4 &= (R_1(d_{31} + R(d_{32} + d_{33}))) \\
 c_1 &= (Rk^2 \sum_{K=1}^M \frac{L_K^2 W_K}{H_K} \cos kL_K) \\
 c_2 &= (Rk^2 \sum_{K=1}^M \frac{L_K W_K^2}{H_K} \cos kW_K) \\
 c_3 &= \sum_{K=1}^M (k^2 \frac{W_K L_K}{H_K} \cos 2kH_K - Z_{A3} \frac{1}{2H_K} j\omega \sin k2H_K) \\
 \text{and } c_4 &= R_1(d_{31} + R(d_{32} + d_{33}))
 \end{aligned} \tag{3.95}$$

Z_{A1} is determined using ANSYS 8.0 software, as a ratio of the sum of distributed load to the sum of velocities produced at the points/nodes of consideration (see later sections). From Eq. (3.60), $F_1 = -F_3$; therefore, the collective linear impedance along direction X can be expressed as

$$Z_{A1} = \frac{F_1 - F_3}{\dot{u}_3 - \dot{u}_1} = \frac{2 \left[\sum_{k=1}^M F_{1k} \right]}{\left[\sum_{k=1}^M \dot{u}_{3k} \right] - \left[\sum_{k=1}^M \dot{u}_{1k} \right]} = \frac{2F_1}{\dot{u}} \tag{3.96}$$

Further to this, Eq. (3.96) can be deduced to

$$Z_{A1} = \frac{2 \left(\sum_{D=1}^{P(1)} F_{1D} + \dots + \sum_{D=1}^{P(K)} F_{KD} + \dots + \sum_{D=1}^{P(M)} F_{MD} \right)}{\left(\sum_{D=1}^{\alpha(1)} \dot{y}_{1D} + \dots + \sum_{D=1}^{\alpha(K)} \dot{y}_{KD} + \dots + \sum_{D=1}^{\alpha(M)} \dot{y}_{MD} \right) - \left(\sum_{D=1}^{P(1)} \dot{x}_{1D} + \dots + \sum_{D=1}^{P(K)} \dot{x}_{KD} + \dots + \sum_{D=1}^{P(M)} \dot{x}_{MD} \right)} \tag{3.97}$$

where $F_{1D} = \dots = F_{KD} = \dots = F_{MD} = 1 + 0j$ are the unit forces applied on all the distributed points on Face 1 of each of the M -functioning PZT patches (Fig. 3.19(b)). $P(K)$ and $\alpha(K)$ represent the distributed points of the K^{th} PZT patch on Faces 1 and 3 respectively (Figs. 3.18(b) and 3.19(b)). The total number of distributed points on Face 1 of M -functioning PZT patches is the same as on Face

3, *i.e.* $P(1) = \alpha(1), P(2) = \alpha(2), \dots, P(K) = \alpha(K) \dots P(M) = \alpha(M)$. \dot{x}_{KD} and \dot{y}_{KD} are the obtained velocities of the K^{th} PZT patch at the D^{th} distributed point of Face 1 and Face 3 respectively. Similarly $\sum_{D=1}^{P(K)} \dot{x}_{KD}$ and $\sum_{D=1}^{\alpha(K)} \dot{y}_{KD}$ are the single patch velocities of the K^{th} PZT which are respectively equal to \dot{u}_{1k} and \dot{u}_{3k} .

Finally, Eq. (3.97) is reduced to

$$Z_{A1} = 2 \frac{F_{11} + \dots + F_{1K} + \dots + F_{1M}}{(\dot{u}_{31} + \dots + \dot{u}_{3K} + \dots + \dot{u}_{3M}) - (\dot{u}_{11} + \dots + \dot{u}_{1K} + \dots + \dot{u}_{1M})} \quad (3.98)$$

where $\dot{u}_{11}, \dots, \dot{u}_{1K}$, and \dot{u}_{1M} are the sum of velocities on Face 1 of PZT 1, ..., K , and M . Similarly $\dot{u}_{31}, \dots, \dot{u}_{3K}$, and \dot{u}_{3M} are the sum of velocities on Face 3 of PZT 1, ..., K , and M . F_{1K} is the total unit force applied (equal to single patch force) on Face 1 of the K^{th} PZT. Similarly, the linear impedances along direction Y (*i.e.*, Z_{A2} using Faces 2 and 4) and direction Z (*i.e.*, Z_{A3} using Faces 5 and 6) are determined using ANSYS

$$Z_{A2} = 2 \frac{F_{21} + \dots + F_{2K} + \dots + F_{2M}}{(\dot{u}_{41} + \dots + \dot{u}_{4K} + \dots + \dot{u}_{4M}) - (\dot{u}_{21} + \dots + \dot{u}_{2K} + \dots + \dot{u}_{2M})} \quad (3.99)$$

and

$$Z_{A3} = -2 \frac{F_{51} + \dots + F_{5K} + \dots + F_{5M}}{(\dot{u}_{61} + \dots + \dot{u}_{6K} + \dots + \dot{u}_{6M}) - (\dot{u}_{51} + \dots + \dot{u}_{5K} + \dots + \dot{u}_{5M})} \quad (3.100)$$

where $\dot{u}_{21}, \dots, \dot{u}_{2K}$, and \dot{u}_{2M} are the sum of velocities on Face 2 of PZT 1, 2, ..., K , ..., and M . Similarly $\dot{u}_{41}, \dots, \dot{u}_{4K}$, and \dot{u}_{4M} are the sum of velocities on Face 4 of PZT 1, ..., K , and M . $\dot{u}_{51}, \dots, \dot{u}_{5K}$, and \dot{u}_{5M} are the sum of velocities on Face 5 of PZT 1, ..., K , and M . $\dot{u}_{61}, \dots, \dot{u}_{6K}$, and \dot{u}_{6M} are the sum of velocities on Face 6 of PZT 1, ..., K , and M . F_{2K} and F_{5K} are the total unit forces applied on Faces 2 and 5 of the K^{th} PZT.

Substituting Eq. (3.98) into Eq. (3.92), Eqs. (3.99) and (3.100) into Eq. (3.95), and using Eqs. (3.93) and (3.94) for A_0, C_0 and E_0 one obtains

$$\begin{aligned} E_0 &= \frac{(a_4 b_1 - a_1 b_4)(b_2 c_1 - b_1 c_2) - (a_2 b_1 - a_1 b_2)(b_4 c_1 - b_1 c_4)}{(a_3 b_1 - a_1 b_3)(b_2 c_1 - b_1 c_2) - (a_2 b_1 - a_1 b_2)(b_3 c_1 - b_1 c_3)} \\ C_0 &= \frac{(b_4 c_1 - b_1 c_4) - (b_3 c_1 - b_1 c_3) E_0}{(b_2 c_1 - b_1 c_2)} \quad \text{and} \quad A_0 = \frac{a_4 - a_2 c_0 - a_3 E_0}{a_1} \end{aligned} \quad (3.101)$$

The unknowns A , C and E can be obtained by substituting Eq. (3.101) into Eq. (3.87). λ_{C1} , λ_{C2} and λ_{C3} can be obtained using Z_{A1} (Eq. (3.98)), Z_{A2} (Eq. (3.99)) and Z_{A3} (Eq. (3.100)) in Eq. (3.63). Therefore, all the unknowns which cannot be determined using the analytical equations can be determined using numerical analysis.

3.8.8 EM Admittance Formulation for M-Functioning PZT Patches

The “total” electric displacements (or “total” charge density), D_3 , (where the subscript 3 refers to the electric field in direction Z) over the top or bottom surface of the functioning PZT patches (Fig. (3.18)) can be written as

$$D_3 = \sum_{K=1}^M (D_3)_K = \overline{\epsilon_{33}} E_3 + d_{31} \sigma_1 + d_{32} \sigma_2 + d_{33} \sigma_3 \quad (3.102)$$

where $\overline{\epsilon_{33}} = \epsilon_{33}(1 - \delta)$ is the complex electric permittivity of the PZT at zero stress, δ is the dielectric loss factor, ϵ_{33} is the static electric permittivity of the PZT patch, and $(D_3)_K$ is the charge density of the K^{th} PZT patch.

Eq. (3.102) is referred to as the “sensor” equation by Sirohi and Chopra (2000), and it serves as the basis for obtaining the admittance equation.

Substituting Eq. (3.86) into Eq. (3.102), we obtain the charge density of the K^{th} PZT patch as

$$(D_3)_K = \overline{\epsilon_{33}} (E_3)_K + Y_R (d_{31} \lambda_{C1} \{st_1 + R(st_2 + st_3)\} + d_{32} \lambda_{C2} \{R(st_1 + st_3) + st_2\} + Y_R (d_{33} \lambda_{C3} \{R(st_1 + st_2) + st_3\}) \quad (3.103a)$$

where $st_1 = [\epsilon_x - (E_3)_K d_{31}]$, $st_2 = [\epsilon_y - (E_3)_K d_{32}]$ and $st_3 = [\epsilon_z - (E_3)_K d_{33}]$.

Substituting Eqs. (3.84) and (3.85) into Eq. (3.103a), one obtains

$$\begin{aligned} (D_3)_K &= \overline{\epsilon_{33}} (E_3)_K + Y_R (d_{31} \lambda_{C1} \{ [Ak(\cos kx)e^{j\alpha} - (E_3)_K d_{31}] \\ &\quad + R[Ck(\cos ky)e^{j\alpha} - (E_3)_K d_{32}] + R[Ek(\cos kz)e^{j\alpha} - (E_3)_K d_{33}] \} \\ &\quad + d_{32} \lambda_{C2} \{ R[Ak(\cos kx)e^{j\alpha} - (E_3)_K d_{31}] + [Ck(\cos ky)e^{j\alpha} - (E_3)_K d_{32}] \\ &\quad + R[Ek(\cos kz)e^{j\alpha} - (E_3)_K d_{33}] \} + d_{33} \lambda_{C3} \{ R[Ak(\cos kx)e^{j\alpha} - (E_3)_K d_{31}] \\ &\quad + R[Ck(\cos ky)e^{j\alpha} - (E_3)_K d_{32}] + [Ek(\cos kz)e^{j\alpha} - (E_3)_K d_{33}] \} \end{aligned} \quad (3.103b)$$

Electric current I is the rate of change of the total electric charge over the surface area SA ($= \sum_{K=1}^M A_K = \sum_{K=1}^M L_K W_K$) of the M-functioning PZT patches (Fig. 3.18). Mathematically, it can be represented as

$$I = \sum_{K=1}^M I_K = \iint_{SA} \sum_{K=1}^{K=M} (\dot{D}_3)_K dA = j\omega \sum_{K=1}^{K=M} \left[\iint_{A_K} (D_3)_K dx dy \right] \quad (3.104)$$

where \dot{D}_3 is the time rate of change of charge and I_K is the electric charge over the surface area A_K of the K^{th} PZT patch. Substituting Eq. (3.103b) into Eq. (3.104), one obtains the electric charge of the K^{th} PZT patch as

$$I_K = j\omega [L_K W_K \overline{\varepsilon_{33}}(E_3)_K + Y_R (d_{31} \lambda_{C1} \{s_A + R(s_C + s_E)\} + d_{32} \lambda_{C2} \{R(s_A + s_E) + s_C\} + d_{33} \lambda_{C3} \{R(s_A + s_C) + s_E\})] \quad (3.105)$$

where

$$s_A = [W_K A \sin kx \cdot e^{j\omega t} - L_K W_K (E_3)_K d_{31}], \quad s_C = [L_K C \sin ky \cdot e^{j\omega t} - L_K W_K E_3 d_{32}]$$

$$s_E = [L_K W_K E k \cos kz \cdot e^{j\omega t} - L_K W_K E_3 d_{33}]$$

Electrical admittance (\bar{Y}^A) is the ratio of the electric current (I) to the applied instantaneous voltage across the functioning PZT patches (V), which is, $\bar{Y}^A = \frac{I}{V} = \frac{1}{V} \sum_{K=1}^M I_K = \sum_{K=1}^M \bar{Y}_K^A$. \bar{Y}_K^A is for the K^{th} PZT patch, and is obtained using Eqs. (3.86), (3.88) and (3.105).

$$\begin{aligned} \bar{Y}^A &= G + Bj \\ &= \sum_{K=1}^M \bar{Y}_K^A = \sum_{K=1}^M \frac{j\omega L_K W_K}{2H_K} [\overline{\varepsilon_{33}} + Y_R (d_{31} \lambda_{C1} \{A_0 \sin kL_K - d_{31}\} \\ &\quad + R[C_0 \sin kW_K - d_{32}] + R[E_0 k \cos k2H_K - d_{33}]) \\ &\quad + d_{32} \lambda_{C2} \{R[A_0 \sin kL_K - d_{31}] + [C_0 \sin kW_K - d_{32}] \\ &\quad + R[E_0 k \cos k2H_K - d_{33}]\} + d_{33} \lambda_{C3} \{R[A_0 \sin kL_K - d_{31}] \\ &\quad + R[C_0 \sin kW_K - d_{32}] + [E_0 k \cos k2H_K - d_{33}]\})] \end{aligned} \quad (3.106)$$

where G and B are, respectively, the cumulative conductance and susceptance signatures of M-functioning PZT patches.

Eq. (3.106) can be simplified, depending on the dimensions of the functioning PZT patches. If all the functioning PZT patches are of equal dimensions, *i.e.*, lengths of all patches are L , widths are W and heights are H , the final admittance can be written as

$$\begin{aligned} \bar{Y}^A = M^2 \frac{j\omega LW}{2H} & \left[\overline{\varepsilon}_{33} + Y_R(d_{31}\lambda_{C1}\{[MA_0 \sin kL - d_{31}] \right. \\ & + R[MC_0 \sin kW - d_{32}] + R[E_0k \cos k2H - d_{33}] \} \\ & + d_{32}\lambda_{C2}\{R[MA_0 \sin kL - d_{31}] + [MC_0 \sin kW - d_{32}] \quad (3.107) \\ & + R[E_0k \cos k2H - d_{33}] \} + d_{33}\lambda_{C3}\{R[MA_0 \sin kL - d_{31}] \\ & \left. + R[MC_0 \sin kW - d_{32}] + [E_0k \cos k2H - d_{33}] \} \right] \end{aligned}$$

Eq. (3.107) can be further reduced for square PZT patches, *i.e.*, where the lengths and widths of the patches are both equal to L , by changing W to L in the equation. Eq. (3.106) serves as the basis for predicting EM admittance, which is generic and can be used for an unlimited number of functioning PZT patches. If all the bonded patches are functioning, simply replace M by N (the total number of PZT patches).

By changing the value of M , *i.e.* between 1 to N , different admittance signatures can be obtained for the same structure, which leads to the situation of multiple (m) admittance signatures. These m_p -admittance signatures of before and after damage states can help to locate the damage faster than the existing single PZT-structure interaction models. Thus, the developed interaction model of any functioning PZT-adhesive-host structure for predicting admittance signatures is generic and can be used for different boundary conditions and types of host structure. There is no restriction on the thickness of adhesive and number of PZT, *i.e.*, the model is applicable for cases where the PZT and adhesive are either of negligible or considerable mass. Furthermore, it is applicable for one-quarter or one-half of the PZT patch; this interesting aspect of using the model for one-quarter of a PZT is presented in one of the case studies (see below).

The formulations can be modified depending on the type of problems and their requirements, as adopted in the following case studies.

3.8.9 Modifications of Linear Impedance Formulations for Case Studies

Two cases were used to verify the model: I) Multiple PZT patches bonded to a host structure (one specimen) with thin epoxy layers, and II) PZT patches bonded one each to three different host structures (three specimens) with different epoxy layers, (Figs. 3.20 and 3.21). Table 3.5 lists the details of the specimens used in the model.

- *General Description*

In Case I, an aluminum plate of grade A1 6061-T6 (Table 3.1) was surface bonded with 4 PZT patches of grade B at locations 1 to 4 using epoxy adhesive (Table 3.4). Three of the patches (at locations 2 to 4) were considered functioning, and the other (at location 1) non-functioning, *i.e.*, acting as a dead load (Fig. 3.20(a)). Thus, in this case, $M=3$ and $N=4$ for one-quarter of the aluminum plate. All dimensions are given in Table 3.5.

Table 3.5 Dimensions of epoxy, aluminum and PZT

Cases	Specimen	Epoxy (mm)	Aluminum (mm)	PZT (mm)
I	M	Negligible	525×75×2	
	S-1	Negligible		10×10×0.3
II	S-2	10×10×0.5	100×100×2	
	S-3	10×10×1.0		

The whole specimen “M” was modeled with the boundary conditions shown in Fig. 3.21(a), *i.e.*, the x and y components of displacements were set to zero at the YZ and the ZX planes respectively. In addition, at the bottom of the plate, which is at C2 (Figs. 3.20 and 3.21), the z component of displacement was set to zero. The finite-element meshing was carried out using discretized 3D brick elements (solid 45) which possess 3 DOFs at each node with suitable meshing size for aluminum (1 mm×1 mm×1 mm) and PZT (1 mm×1 mm×0.3 mm). The adhesive was not included in the model as it was assumed to be negligible in thickness. The linear impedances and response factors were obtained as explained previously. The admittance signatures were predicted using Eq. (3.107); but the experimental verification for this case (specimen m) was not simple since the modeled boundary conditions could not be achieved. Hence, the verification was carried out using a 4-times larger symmetric host structure bonded with 16 PZT patches, and for a “free-free” boundary condition (Fig. 3.20(a)). In the experiment, 12 PZT patches were actuated in parallel and 4 PZT patches acted as dead loads. The obtained experimental signatures were divided by 4 to obtain the actual experimental signatures for the considered specimen.

In Case II, PZT patch of grade C (Table 3.4) was employed. The main difference between this case and the previous case lies in number of PZT patches and the specimen size. In this case only one PZT patch is considered so its mass effect in the formulations is ignored. However, the adhesive beneath the PZT patch is relatively heavier and hence adhesive mass is considered in the formulations. However, as explained before, depending on the number of PZT patches and their mass, the boundary conditions and symmetric conditions of the host structure, modifications were needed for the impedance and force equations to reduce simulation time. In this case, three identical PZT patches bonded with three different thicknesses of adhesive on three identical aluminum plate specimens were considered, *i.e.*, one PZT on each host structure. The PZT patch was placed centrally on top of the adhesive at the centre of the host aluminum plate as shown in Fig. 3.20(b).

In the cases studied, the PZT patch mass was neglected, and the actuating forces of the PZT patch were transferred on to the top surface of the adhesive (Fig. 3.20). At any instant of time, the forces developed due to the actuations correspond respectively to expansion in the X and Y directions, and shrinkage in the Z direction, and vice versa.

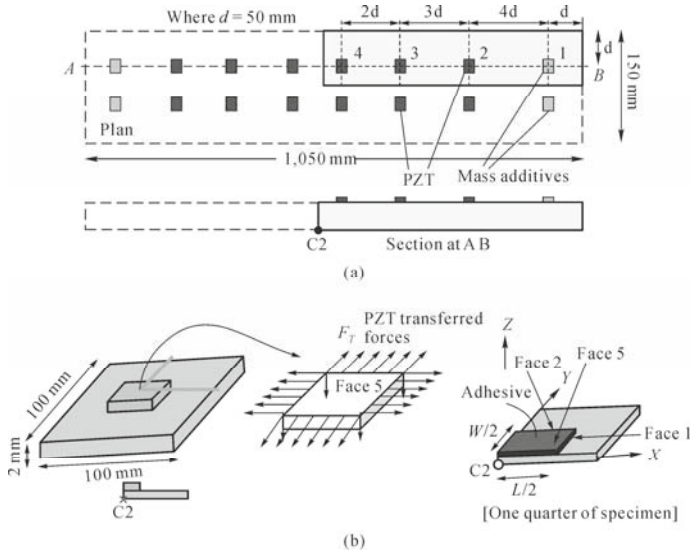


Fig. 3.20 Specimens used in case studies. (a) Case I; (b) Case II

• *Modifications of Linear Impedances and PZT Forces*

Case I:

(a) **Necessary Modifications:** The impedance (Z_{AS}) of the host structure bonded with adhesives at various locations is defined as the sum of the linear impedances and the cross impedances of the functioning patches (Eq. (3.60a)). However, in this case study, only forces acting on 5 of the 6 faces were considered (Fig. 3.20).

It should be noted that the 6th face along direction $-Z$ was not considered because the PZT patches were assumed to be thinner and lighter than both the epoxy adhesive and the host structure. Therefore, the modified linear impedances (Eq. (3.60a)) are:

$$Z_{A1} = \frac{F_1^T - F_3^T}{\dot{u}_3 - \dot{u}_1} = \frac{F_1^T - F_3^T}{\dot{u}}, \quad Z_{A2} = \frac{F_2^T - F_4^T}{\dot{u}_4 - \dot{u}_2} = \frac{F_2^T - F_4^T}{\dot{v}}, \quad (3.108)$$

and $Z_{A3} = \frac{F_5^T}{-\dot{u}_5} = \frac{F_5^T}{\dot{w}}$

where the total force transferred on Face I , $F_I^T = \sum_{K=1}^M F_{IK}^T$, and the superscript T represents forces transferred from the PZT patches. The total transferred velocity (produced as a result of transferred force) is $\dot{u}_I^T = \sum_{K=1}^M \dot{u}_{IK}^T$. M represents the total number of PZT patches, and subscript I represents the face number (4 sides + 1 top = 5 faces) of the PZT patch (Fig. 3.20). F_{IK}^T and \dot{u}_{IK}^T are the single PZT transferred force and single PZT transferred velocity of the K^{th} PZT patch on Face I . u , v and w are the total relative displacements obtained as a result of transferred forces along directions X , Y and Z of the PZT patches.

The total transferred forces acting on the faces are:

$$\begin{aligned} F_1^T = -F_3^T = \sigma_X \left(\sum_{K=1}^M W_K 2H \right), \quad F_2^T = -F_4^T = \sigma_Y \left(\sum_{K=1}^M L_K 2H \right) \\ F_5^T = -\sigma_Z \left(\sum_{K=1}^M W_K L_K \right) \end{aligned} \quad (3.109)$$

The modifications (Eq. (3.108) and Eq. (3.109)) are valid for M-functioning PZT patches of negligible mass but with considerable adhesive mass. The rest of the formulation remains the same. Therefore, Eq. (3.107) can be used for this case.

(b) **Numerical Analysis:** The numerical analysis was performed using ANSYS 8.0 software to obtain the linear impedances and response factors (A_o , B_o and C_o), for use as input to the analytical Eqs. (3.96) to (3.101)), to predict the admittance signatures. The unit-distributed loads were applied along the three principal directions of the PZT patches in accordance with the extensional and longitudinal actuations of the patches (Figs. 3.21 (b)–(c)). The structure was then subjected to harmonic analysis in the frequency range of interest, which resulted in displacements (u , v and w) at the locations of applied unit-distributed loads. The displacements were used to determine the velocities $j\omega u$ which were used in calculating the impedances (Eqs. (3.96)–(3.101)) and finally predicting the admittance using Eqs. (3.106) and (3.107). Note that accuracy of the model largely depends on the adopted suitable mesh size and boundary conditions.

Case II:

(a) **Specimens:** The specimens S-1, S-2 and S-3, with dimensions given in Table 3.5, were assumed to rest freely on foam, and therefore the boundary condition of “free-free” was assumed to prevail.

As each specimen has only one PZT, *i.e.*, $M = N = 1$, the modifications below were needed.

(b) **Necessary Modifications for Impedances:** The three specimens were symmetric about directions X and Y , and free-free boundary conditions were

assumed. Because of symmetry, only one quadrant of each specimen, adhesive and patch was considered in the formulation (Fig. 3.20). Hence, the total transferred force acting on each face of the quadrant is given as

$$F_1^T = \sigma_X([0.5W_K]2H), F_2^T = \sigma_Y([0.5L_K]2H) \quad (3.110)$$

and $F_5^T = -\sigma_Z(0.25W_K L_K)$

Forces on Faces 3 and 4 were not considered in the formulation because of the symmetry of the specimen. Similarly, the linear impedances (Eq. (3.108)) are modified as below

$$Z_{A1} = \frac{F_1^T}{-\dot{u}_1} = \frac{F_1^T}{\dot{u}}, Z_{A2} = \frac{F_2^T}{-\dot{u}_2} = \frac{F_2^T}{\dot{v}} \quad \text{and} \quad Z_{A3} = \frac{F_5^T}{-\dot{u}_5} = \frac{F_5^T}{\dot{w}} \quad (3.111)$$

The rest of the formulation, except admittance, remains the same.

(c) **Modification of Admittance Signature:** Eq. (3.107) is modified as

$$\begin{aligned} \bar{Y}^A = & \frac{j\omega L W}{2H} [\overline{\varepsilon}_{33} + Y_R(d_{31}\lambda_{C1}\{[MA_0 \sin kL - d_{31}] \\ & + R[MC_0 \sin kW - d_{32}] + R[E_0 k \cos k2H - d_{33}]\}] \\ & + d_{32}\lambda_{C2}\{R[MA_0 \sin kL - d_{31}] + [MC_0 \sin kW - d_{32}] \quad (3.112) \\ & + R[E_0 k \cos k2H - d_{33}]\} + d_{33}\lambda_{C3}\{R[MA_0 \sin kL - d_{31}] \\ & + R[MC_0 \sin kW - d_{32}] + [E_0 k \cos k2H - d_{33}]\}] \end{aligned}$$

Moreover, only “one-quarter of the specimen” was modeled. Thus, Eq. (3.112) is further modified for 1/4th of the PZT patch as

$$\bar{Y}_Q^A = 0.25\bar{Y}^A \quad (3.113)$$

where \bar{Y}_Q^A is the one-quarter admittance of the considered one-quarter specimen.

The unknowns (coefficients A_0 , C_0 and E_0 and the response factors) obtained from the numerical analysis were substituted in Eq. (3.112) to obtain \bar{Y}_Q^A from Eq. (3.113). However, to obtain the complete admittance signature of the complete structure, \bar{Y}_Q^A needs to be multiplied by 4.

Additionally, for S-1, one quarter of the aluminum plate with one quarter of the PZT patch surface bonded (Fig. 3.20) with negligible thickness of adhesive was modeled (Fig. 3.21(b)). For S-2, one quarter of the plate with one quarter of PZT patch surface bonded with 0.5 mm thick epoxy adhesive was modeled (Fig. 3.21(c)). Similarly for S-3, one quarter of the plate with one quarter of PZT patch surface bonded with 1 mm thick adhesive was modeled.

(d) **Numerical Analysis:** In the numerical analysis, the host structure and the adhesive layer were discretized into finite elements (Figs. 3.21(b) and 3.21(c)). The unit-distributed patch forces were then applied on the host structure (Fig.

3.21(b)) and on the adhesive layer (Fig. 3.21(c)) along the three principal directions in accordance with the extensional and longitudinal actuations of the patches. The specimens were discretized into 3D brick elements (solid 45, possessing 3 DOFs at each node) with differential element mesh size (*i.e.*, different sizes for different layers, viz., aluminum and epoxy layer). The details of the mesh sizes are given in Table 3.6. Fig. 3.21 shows the FE model of S-1 and S-2. The model for S-3 is the same as for S-2. Appropriate boundary conditions were imposed on the planes of symmetry for all the 3 specimens, *i.e.*, the x and y components of displacement were set to zero on the YZ and ZX planes of symmetry, respectively. In addition, at the centre of the plate, C2 (Figs. 3.20 and 3.21), the z component of displacement was set to zero. If the structure is non-symmetrical, the complete structure should be modeled by considering appropriate boundary conditions. In order to determine the impedance at a particular frequency, an arbitrary harmonic force was applied on the edges (Figs. 3.21(a) and 3.21(b)). Using ANSYS 8.0, the dynamic harmonic analysis was performed and the complex displacement responses at the points of force application were obtained for the frequency range of 50 kHz. The results obtained were then used as input to the newly formulated 3D EMI model to determine the structural responses. Fig. 3.21(b) – (c) shows the FE mesh of host structure for specimens S-1 and S-2. The admittance signatures were obtained using Eqs. (3.110) and (3.111), and then multiplied by “4”, as the numerical model is a quarter of the experimental specimens.

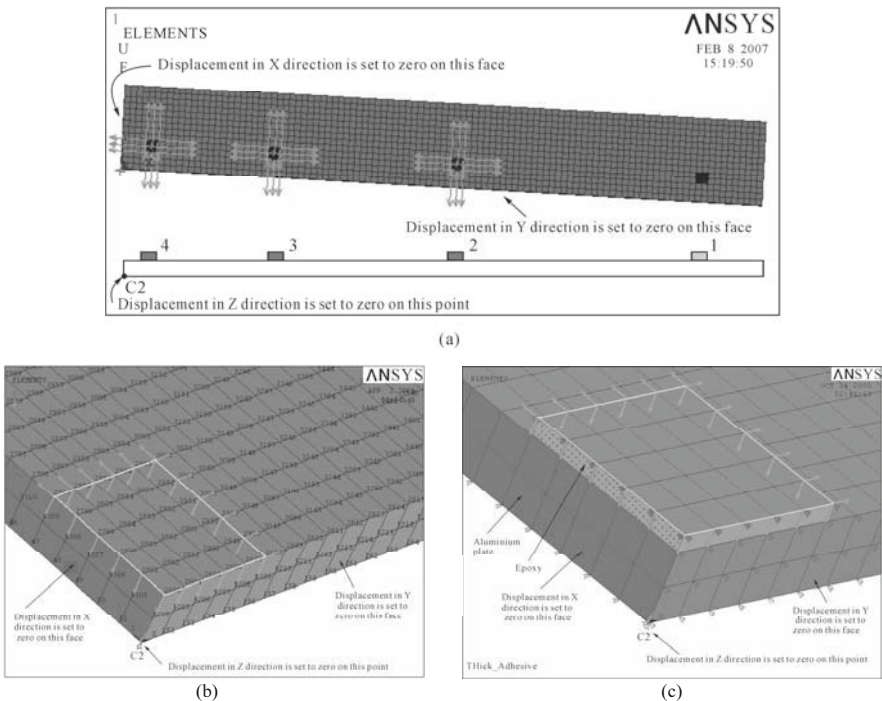


Fig. 3.21 Numerical models for (a) Case I, (b) Case II: S-1 and (c) Case II: S-2

Table 3.6 Mesh sizes for case II

Specimen	Mesh size (mm ³)	
	Epoxy	Al
S-1	–	
S-2	1×1×0.5	1×1×1
S-3	1×1×1.0	

3.8.10 Results and Discussions

The predicted and experimentally obtained signatures are compared in Fig. 3.22, and the closeness of signatures is satisfied in the range considered.

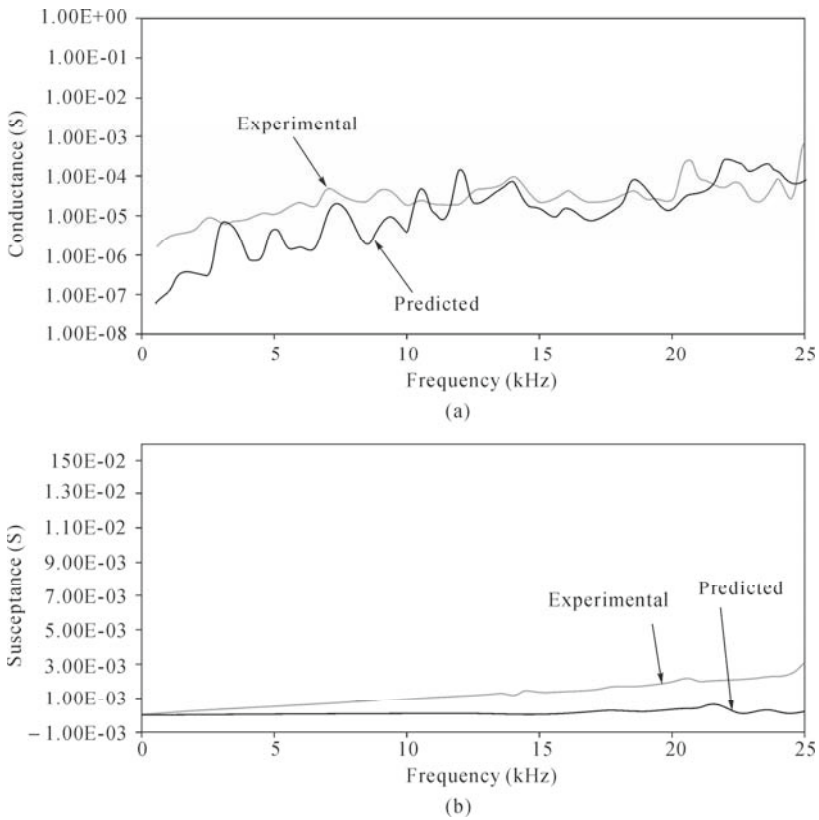


Fig. 3.22 Admittance signatures for Case I. (a) Conductance; (b) Susceptance

In Case II, the mass of the adhesive was considered as the epoxy adhesive was modeled for S-2 and S-3. For S-1, the epoxy adhesive was ignored in the model and the PZT patch forces were directly transferred to the host structure. S-2 and

S-3 reflected more realistic applications since, in-order to protect the PZT from external factors, it is important to wrap the PZT with epoxy or another adhesive which may be heavier than the PZT. So, in practice, the mass of the protective cover will be heavier than the PZT. Thus, in our model, this feature of mass consideration was successfully implemented. Comparisons between the predicted and experimental signatures for the considered frequency range (0 – 50 kHz) are shown in Figs. 3.23 and 3.24. It can be seen that there are around 12 peaks in the experimental conductance signatures (Fig. 3.23) which were successfully predicted by the model. Similar trends and occurrence of peaks at the same locations in the predicted conductance signatures prove the successful formulation of the 3D impedance model. Moreover, the susceptance signatures also matched satisfactorily. However it should be noted that unlike the 2D models, the satisfactory matching is not the identical replication of experimental and predicted signatures but predicting similar signatures to the closest possible extent. The dimension of the host structure in this model is much larger compared with those of the 2D model; therefore, exact predictions of experimental signature is difficult. However, there exists satisfactory agreement between the experimental and the predicted signatures.

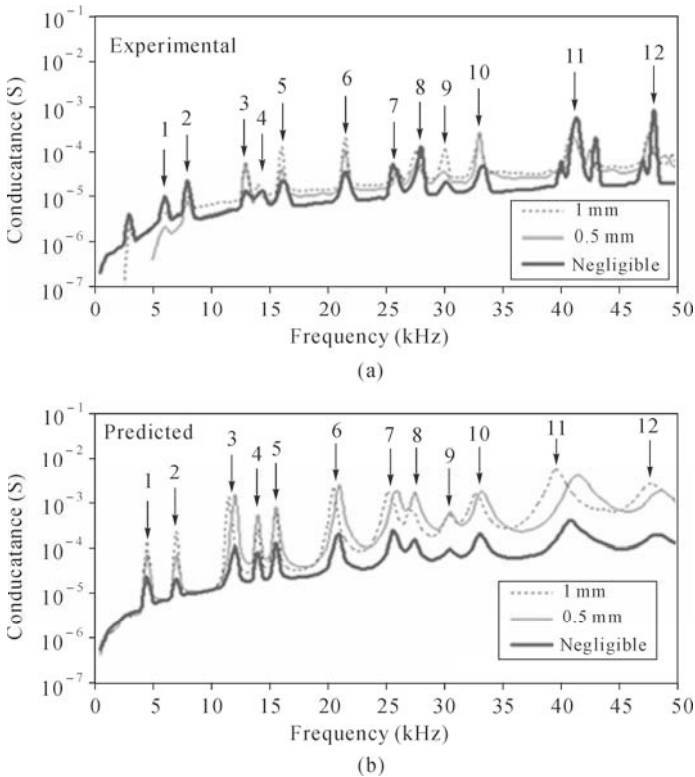


Fig. 3.23 Case II conductance signatures. (a) Experimental; (b) Predicted

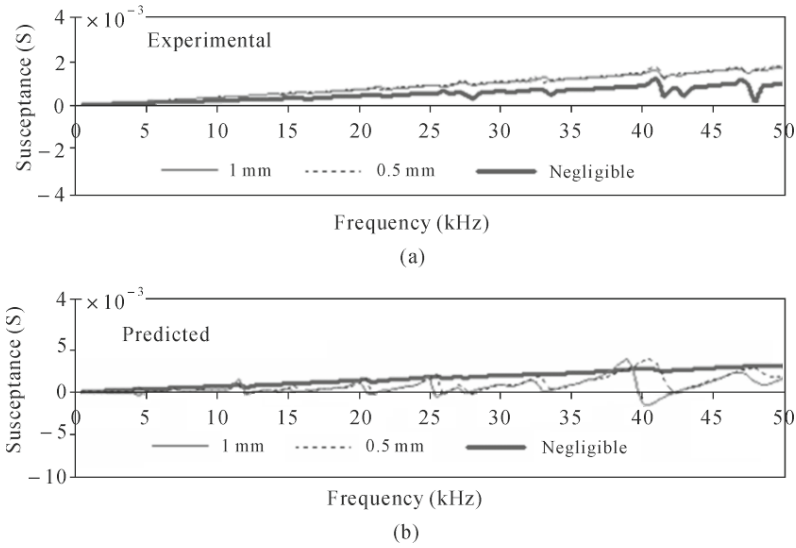


Fig. 3.24 Case II susceptance signatures. (a) Experimental; (b) Predicted

In specimens S-1 to S-3, the PZT patches were the same but the mass of the epoxy varied. Therefore, the changes in signatures of S-1 to S-3 show that the adhesive has to be considered.

Consequently, in a structure, if there are N bonded PZT patches and only M ($\leq N$) are functioning, by varying M , (*i.e.*, $M=1, 2, 3, \dots$) one can obtain different admittance for the same structure. This will lead to multiple admittance signatures which, when obtained before and after the damage states, can help to locate the damage faster than the existing single PZT-structure interaction models. In addition, the 3D impedance model of any functioning PZT-adhesive-structure for predicting admittance signatures is generic and can be used for different boundary conditions and types of host structure. There are no restrictions on the mass of PZT and adhesive, *i.e.*, the model is applicable for both negligible and considerable mass of both PZT and adhesive. Furthermore, there is no limitation on the number of PZT patches. The satisfactory matching of both conductance and susceptance signatures of the experimental with the predicted signatures shows the reliability of the model, which is potentially useful in the NDE of most engineering structures.

3.9 FE Modeling of EMI Technique Using Coupled Field Element

3.9.1 Review on FE Modeling of PZT-Structure Interaction

Lalande (1995) provided an insightful review of the FE modeling approaches for

the simulation of PZT-structure interactions. They could be broadly classified into 3 categories, namely direct formulation of elements for specific application, utilization of a thermoelastic analogy, and the use of commercially available FE analysis (FEA) codes incorporated with piezoelectric element formulation. Lalande attempted the dynamic FEA of ring and shell structures using the commercially available software ANSYS 5.6. Good agreement was found between the FE results and results from impedance-based model.

Fairweather (1998) developed an FEA-based impedance model for the prediction of structural response to induced-strain actuation. The model utilizes FEM to determine the host structure's impedance. In his model, he computed the frequency response of a structure based on eigenvalues and mass-normalized eigenvectors. This operation could be performed by most commercial FE solvers. The simplicity of this model is reflected in the fact that modeling of the actuator (PZT patch) is not required as it is represented by a force or moment. The driving point mechanical impedance could be derived by evaluating the ratio of force to velocity.

Initial applications of the above-mentioned models were mainly focused on relatively low frequency of excitation, typically lower than 1 kHz. The FEA-based impedance models were later applied to the EMI technique, which involved much higher frequency of excitation, in the order of tens to hundreds of kHz. Several of the impedance models have been discussed in the previous sections.

Bhalla (2001) simulated a concrete FE model with damages incorporating 1D FEA-based impedance model. Lim (2004) showed reasonably good comparison of mechanical impedance between experiment and 1D FEA-based impedance model for aluminum beam, truss and concrete cube. Bhalla (2004) improved the model by incorporating 2D effective impedance. Furthermore, the FEA-based impedance model is a semi-analytical model incorporating the impedance-based analytical model into the FE model. This model makes use of the robustness of the FEM in modeling a complex system while retaining the simplicity of an impedance-based analytical model to obtain the admittance signatures from the mechanical impedance.

At a low frequency of excitation, simplification of the PZT patch into a force or moment is normally acceptable. However, at a high frequency of excitation such as in the application of the EMI technique, such simplification could lead to considerable loss of accuracy (which will be discussed later). Liu and Giugiurtiu (2007) compared the real part of impedance from both the FEA-based impedance model (non-coupled) and coupled field FE model of a 1D narrow beam structure with that of the experiment. The coupled field FE model exhibited closer agreement with the experimental results. Madhav and Soh (2007b) presented a semi-analytical 3D PZT-structure interaction model incorporating the adhesive. In their model, the effect of the bonding layer is incorporated collectively in the impedance of the structure by adding additional impedance terms for the bonding layer.

Makkonen *et al.* (2001) showed that fairly accurate results could be obtained for dynamic harmonic problems by FEM, up to GHz frequency range. Therefore,

the ability of FEM to predict the behavior of the PZT-structure interaction system in the EMI technique should not be questioned, provided that the simulation is appropriately performed.

3.9.2 Inclusion of Induced Strain Actuator in FE Model

There are several commercially available software packages offering piezoelectric analysis which allow modeling of the PZT-structure interaction to include the induced strain actuator (PZT patch). An example is ANSYS version 8.1, which the authors found to be very useful.

In ANSYS version 8.1, piezoelectric analysis comes under the category of coupled field analysis which considers the interaction or coupling between two or more disciplines of engineering (ANSYS, 2004). The piezoelectric analysis caters for the interaction between structural and electric fields, and static, modal, harmonic and transient analyses could be performed. Other coupled field analyses include thermal-stress, fluid-structure, magnetic-thermal, magneto-structural and MEMS.

Coupled field analysis derives solutions to problems not possible with the usual FEM, by simplifying the modeling of coupled-field problems. However, this leads to other problems such as increased wavefront, inefficient matrix reformulation and large storage requirements.

Piezoelectric analysis makes use of the direct coupling method, which involves just one analysis with the use of one coupled-field element containing all necessary DOFs. The FE formulation used for developing the matrix equations is the strong coupling method (ANSYS, 2004):

$$\begin{bmatrix} K_{11} & K_{12} \\ K_{21} & K_{22} \end{bmatrix} \begin{Bmatrix} X_1 \\ X_2 \end{Bmatrix} = \begin{Bmatrix} F_1 \\ F_2 \end{Bmatrix} \quad (3.114)$$

where X_1 and X_2 are two different types of DOF. The coupled effect is taken into account by the off-diagonal sub-matrices $[K_{12}]$ and $[K_{21}]$. Using this method, coupled response could be obtained after one iteration.

With the linear electromechanical constitutive equations incorporated into the general equation of motion for a forced structural system, the FE discretization can be performed by establishing nodal solution variables and element shape functions over an element domain, in which the solution could be approximated. With the application of variational principle and FE discretization, the coupled FE matrix for one element model can be expressed as:

$$\begin{bmatrix} [M] & [0] \\ [0] & [0] \end{bmatrix} \begin{Bmatrix} \{\ddot{u}\} \\ \{\dot{V}\} \end{Bmatrix} + \begin{bmatrix} [C] & [0] \\ [0] & [0] \end{bmatrix} \begin{Bmatrix} \{\dot{u}\} \\ \{V\} \end{Bmatrix} + \begin{bmatrix} [K] & [K^z] \\ [K^z]^T & [K^d] \end{bmatrix} \begin{Bmatrix} \{u\} \\ \{V\} \end{Bmatrix} = \begin{Bmatrix} \{F\} \\ \{L\} \end{Bmatrix} \quad (3.115)$$

in which $\{\dot{V}\}$ is the vector of nodal electric potential where the dot above variables denotes time derivative, $\{L\}$ is the vector of nodal, surface and body charges, $[K^z]$ is the piezoelectric coupling matrix and $[K^d]$ is the dielectric conductivity.

This formulation is convenient for evaluating admittance signatures as it is measured by the impedance analyzer in the EMI technique. The complex admittance signature, which is the ratio of electric current to voltage, can be expressed as:

$$\bar{Y} = \frac{\bar{I}}{\bar{V}} \quad (3.116)$$

where \bar{V} is the voltage applied by impedance analyzer and \bar{I} is the modulated current, with the bars above variables indicating complex terms.

The complete modeling technique which includes the PZT patch and preferably, the bonding layer, should yield a more accurate result, especially at high frequency of excitation. Moreover, the outcome acquired, which is the electric current, can be directly compared with the admittance signature from the EMI technique. This obviates the difficulty of converting the mechanical impedance into electrical admittance through the impedance-based electromechanical coupling equation as required in the FEA-based impedance model.

3.9.3 Comparison of FE Model with Existing Impedance-Based Analytical Model and Experimental Tests

- *FE Modeling of Freely Suspended PZT Patch*

In order to better understand piezoelectric analysis, modeling of a freely suspended PZT patch was first performed without the presence of the host structure. In our study, 3D modeling was performed using both Solid 5 and Solid 226 elements available in ANSYS 8.1. Solid 5 element is a coupled field solid with eight nodes and up to six DOFs at each node. Solid 226, on the other hand, has 20 nodes with up to four DOFs per node.

A freely suspended PZT patch with size 10 mm×10 mm×0.3 mm was modeled as depicted schematically in Fig. 3.25. The material properties used are tabulated in Table 3.7. An alternating (sinusoidal) voltage of 1 volt was applied across the patch for excitation along the Z direction. Owing to symmetry of both the geometrical shapes and loadings, only one-quarter of the patch was modeled. The interfacial nodes along the YZ plane were restrained in the X direction and those along the ZX plane were restrained in the Y direction (Fig. 3.25).

Table 3.7 Piezoelectric properties of PIC 151 (PI Ceramics, 2006).

Parameters	Symbols	Values	Unit
Density	ρ	7800	kg/m ³
Dielectric loss factor	$\tan\delta$	0.02	—
Compliance	s_{11}	15.0	10 ⁻¹² m ² /N
	$s_{22} = s_{33}$	19.0	
	$s_{12} = s_{21}$	-4.50	
	$s_{13} = s_{31}$	-5.70	
	$s_{23} = s_{32}$	-5.70	
	$s_{44} = s_{55}$	39.0	
Electric permittivity	ϵ_{11}^T	1.75	10 ⁻⁸ F/m
	ϵ_{22}^T	1.75	
	ϵ_{33}^T	2.12	
Piezoelectric strain coefficients	d_{31}	-2.10	10 ⁻¹⁰ m/V or 10 ⁻¹⁰ C/N
	d_{32}	-2.10	
	d_{33}	5.00	
	d_{24}	5.80	
	d_{15}	5.80	

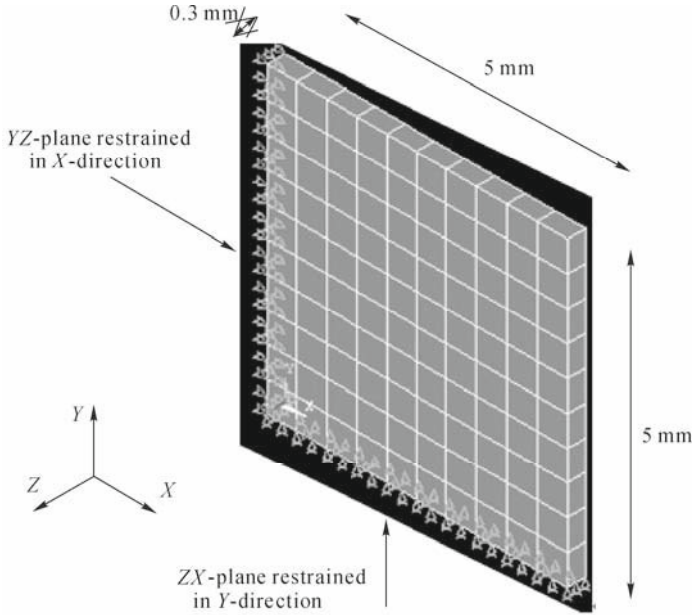


Fig. 3.25 Isometric view of one-quarter of PZT patch modeled in ANSYS 8.1 workspace

Convergence of the solutions was tested in two ways. First, as recommended by Makkonen *et al.* (2001) to ensure sufficient accuracy, the size of the element should typically lie between three to five nodal points (*i.e.*, two or three elements) per half wavelength for harmonic analysis. In this case, with a mesh size of 0.2 mm as the smallest element size achievable within the available computing facility, the maximum frequency allowable was estimated to be approximately 610 kHz. In addition, convergence was also tested by performing several analyses with reduced element sizes for each analysis.

Convergence was reached at Solid 5 element size 0.2 mm and Solid 226 element size 0.5 mm, even at very high frequency (such as resonance peak near to 800 kHz), (Fig. 3.26). Thus, it was deduced that element size of 0.5 mm using Solid 5 element would be sufficiently fine for the modeling of PZT-structure interaction in the EMI technique, which normally would not exceed 200 kHz.

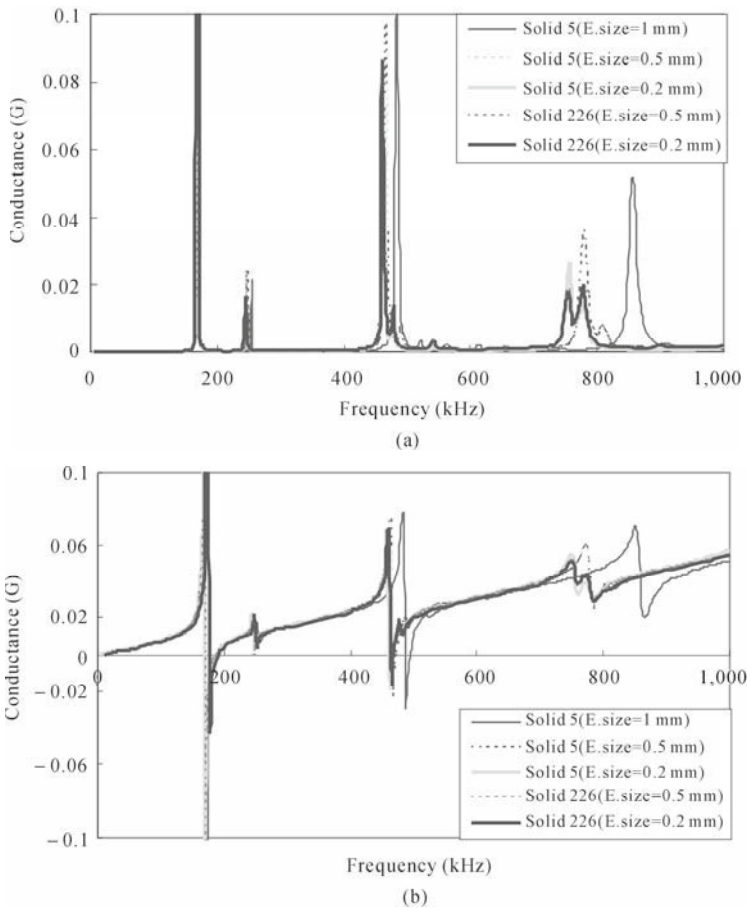


Fig. 3.26 Admittance signatures vs. frequency plot for numerically simulated PZT patch with different element sizes. (a) Conductance signatures; (b) Susceptance signatures

• 1D and 2D Analytical Model for Free-Ended PZT Patch

An analytical model of the free-ended PZT patch can be conveniently obtained by setting the mechanical impedance of the host structure to zero in the impedance-based electromechanical coupling equations. For the 1D free PZT patch model, the impedance-based electromechanical coupling equation (Liang *et al.*, 1994) can be reduced (when $Z = 0$) to:

$$\bar{Y} = 2\omega j \frac{wl}{h} \left[\frac{\overline{\epsilon}_{33}^T}{\epsilon_{33}^T + d_{31}^2 \overline{Y}^E} \left(\left(\frac{\tan \kappa l}{\kappa l} \right) - 1 \right) \right] \quad (3.117)$$

where ω is the angular frequency of the driving voltage, j is the imaginary number, and w , l and h are the width, half length and thickness of the PZT patch respectively, $\overline{\epsilon}_{33}^T$ is the complex dielectric permittivity, d_{31} is the piezoelectric strain coefficients, \overline{Y}^E is the complex Young's modulus and κ is the wave number.

Rearranging the terms, and expressing them as real and imaginary parts:

$$\bar{Y} = \left\{ -4\pi f \frac{wl}{h} \left[d_{31}^2 Y^E (t + \eta(r-1) - \delta \epsilon_{33}^T) \right] \right\} + j \left\{ 4\pi f \frac{wl}{h} \left[\epsilon_{33}^T + d_{31}^2 Y^E (r - \eta t - 1) \right] \right\} \quad (3.118)$$

where f is the frequency, $r + tj = \frac{\tan \kappa l}{\kappa l}$, $\overline{Y}^E = Y^E (1 + \eta j)$, $\overline{\epsilon}_{33}^T = \epsilon_{33}^T (1 - \delta j)$ with δ and η indicating the electrical loss factor and mechanical loss factor respectively.

In the case of a 2D model based on cross impedance using the equation proposed by Zhou *et al.* (1995), free PZT vibration can be modeled by setting all 4 terms related to the structural mechanical impedance to zero. The equation can thus be reduced to:

$$\bar{Y} = 4j\omega \frac{wl}{h} \left[\frac{\overline{\epsilon}_{33}^T}{\epsilon_{33}^T} - \frac{2d_{31}^2 \overline{Y}^E}{(1-\nu)} + \frac{d_{31}^2 \overline{Y}^E}{(1-\nu)} \left\{ \frac{\sin \kappa l}{l} \quad \frac{\sin \kappa w}{w} \right\} \left[\begin{array}{cc} \kappa \cos \kappa l & 0 \\ 0 & \kappa \cos \kappa w \end{array} \right]^{-1} \right] \quad (3.119)$$

where ν is the Poisson ratio.

Again, rearranging and expressing in complex notations:

$$\bar{Y} = 8\pi f \frac{wl}{h} \left\{ \left[\frac{\overline{\epsilon}_{33}^T}{\epsilon_{33}^T} \delta - \frac{d_{31}^2 Y^E}{(1-\nu)} (t+T+\eta(r+R-2)) \right] + j \left[\frac{\overline{\epsilon}_{33}^T}{\epsilon_{33}^T} + \frac{d_{31}^2 Y^E}{(1-\nu)} [r+R-\eta(t+T)-2] \right] \right\} \quad (3.120)$$

where $R + Tj = \frac{\tan \kappa w}{\kappa w}$.

Similarly, setting the effective structural impedance to zero in the 2D effective impedance modeling equation (Bhalla, 2004) yields

$$\bar{Y} = 4\omega j \frac{l^2}{h} \left[\frac{\epsilon_{33}^T}{\epsilon_{33}^T} + \frac{2d_{31}^2 \bar{Y}^E}{(1-\nu)} \left(\frac{\tan \kappa l}{\kappa l} - 1 \right) \right] \quad (3.121)$$

Further rearranging and expressing in complex notations:

$$\bar{Y} = 8\pi f \frac{l^2}{h} \left\{ \left[\delta \epsilon_{33}^T - N(t + \eta r - \eta) \right] + j \left[\epsilon_{33}^T + N(r - \eta t - 1) \right] \right\} \quad (3.122)$$

where $N = \frac{2d_{31}^2 Y^E}{(1-\nu)}$.

• Experimental Results, Comparisons and Discussions

The admittance signatures of two freely-suspended PZT patches (size 10 mm × 10 mm × 0.3 mm), as shown in Fig. 3.27, were acquired using an impedance analyzer. As both patches possessed almost identical admittance signature plots, only one of the signatures was used for comparison.

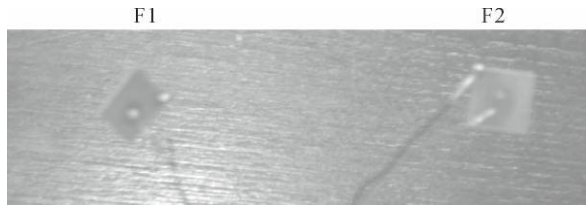


Fig. 3.27 Freely suspended PZT patches

The admittance signatures obtained analytically, numerically and experimentally from a free-ended PZT patch are compared in Fig. 3.28. The numerical results were obtained using Solid 226 elements, with mesh size of 0.5 mm and stiffness damping multiplier (of Rayleigh damping) of $\beta = 3 \times 10^{-9}$. As the analytical outcome of the 2D models based on cross impedance and effective impedance yielded exactly the same results, only one is plotted to represent both.

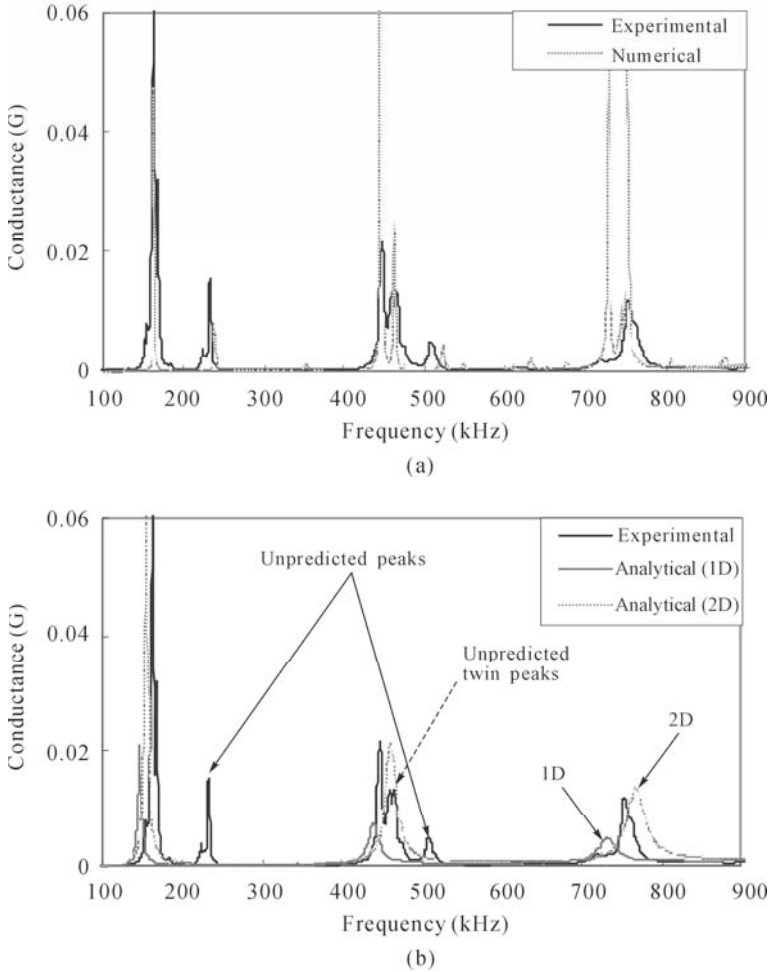


Fig. 3.28 Conductance signatures vs. frequency plot for free ended PZT patch. (a) Experimental vs. numerical (100 – 900 kHz); (b) Experimental vs. analytical (100 – 900 kHz)

It is apparent from Fig. 3.28 that both the numerical and analytical methods provided reasonably good predictions on the actual (experimental) vibrational behavior of the PZT patch as the major resonance peaks were well predicted. However, in the frequency range 100 – 600 kHz, the analytical models were unable to predict two resonance peaks and a twin peak as indicated in Fig. 3.28(b). On the other hand, the twin peaks and two smaller resonance peaks were successfully predicted by the numerical model as shown in Fig. 3.28(a).

The reason is that for the 1D and 2D analytical models, the PZT patch is either simplified as a 1D (1 point interaction) or 2D (4 points or perimeter interaction) structure. This simplification causes some minor modes of resonance not to be excited. However, the 3D coupled field model used in this study is a

comprehensive model which is able to account for all the vibration modes.

This outcome indicated the robustness and capability of FEM through ANSYS 8.1 in simulating the dynamic motion of PZT patch under high frequency of excitation, up to hundreds of kHz.

With adjusted stiffness, another numerical model was constructed based on PZT patch of size 15 mm×15 mm×0.5 mm under similar free-ended condition. Comparing with the signatures obtained from the experiment (Fig. 3.29), a very good match was achieved even for the minor peaks. Both cases showed that the adjusted stiffness is applicable in the frequency range less than 600 kHz; above this, accuracy decreases.

Despite the higher accuracy in predicting the resonance peaks, one limitation of the numerical method is reflected in Figs. 3.28(a) and 3.29, where the magnitudes of the predicted peaks differ significantly from the experimental peaks. Adjustment of peak height was difficult as it depends largely on trial and error of different parameters such as damping ratio. Damping ratio, on the other hand, varies for the different frequency ranges.

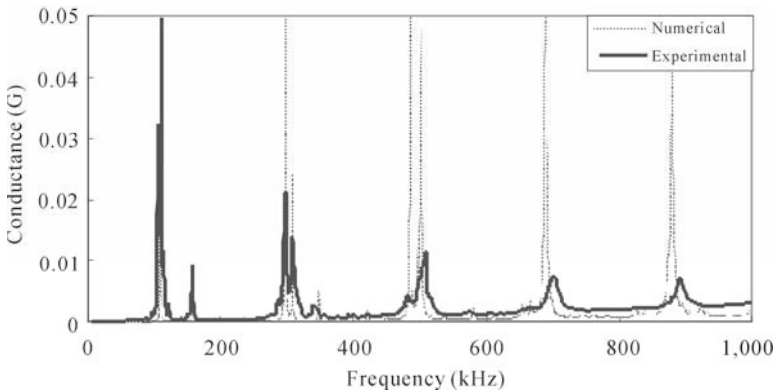


Fig. 3.29 Conductance signatures vs. frequency plot for experimental test and numerical model of PZT patch

3.9.4 FE Modeling of PZT-Structure Interaction

With the successful FE modeling of freely suspended PZT patches under harmonic excitation of up to 1,000 kHz, the FE model was extended to simulate the PZT-structure interaction, inclusive of the interfacial adhesive layer. The outcome of simulation is compared with the experimental test of an identical lab-size structure.

In the subsequent sections, all the PZT patches were modeled with Solid 5 elements instead of Solid 226 since the Solid 5 element possesses fewer nodes,

which are more convenient for modeling multiple structural interactions.

- *Simple Beam*

A simple rectangular aluminium beam of dimensions 231 mm×21 mm×2 mm was used as the test specimen in this study. A 10 mm×10 mm×0.2 mm PZT patch was bonded at the middle of the beam. The test specimen was modeled in ANSYS 8.1 workspace (Fig. 3.30). To be more realistic, the bonding layer (measuring 0.03 mm) was also simulated.

The Young's modulus and Poisson ratio of the bonding layer were taken as $5.1 \times 10^9 \text{ N/m}^2$ and 0.4 respectively, as recommended by Ong (2003). The material properties of the aluminium beam and adhesive are listed in Table 3.8.

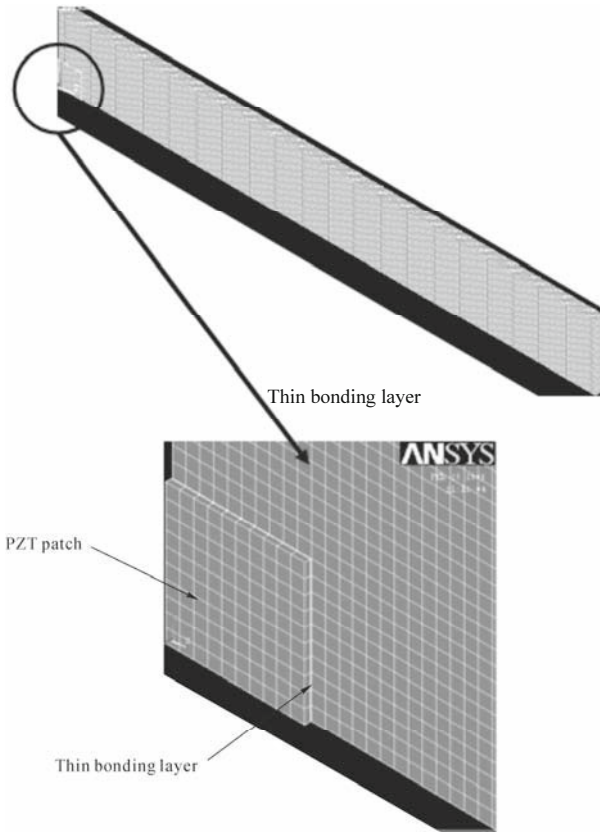


Fig. 3.30 Isometric view of one-quarter of aluminium beam bonded with PZT patch

Table 3.8 Material properties for aluminum beam and adhesive

Parameters	Symbols	Materials	Values	Unit
Density	ρ	Aluminium	2,715	kg/m^3
		Epoxy	1,000	
Poisson ratio	ν	Aluminium	0.3	—
		Epoxy	0.4	
Young's modulus (Isotropic)	E	Aluminium	68.95	10^9 N/m^2
		Epoxy	5.1	
Constant stiffness multiplier	B	Aluminium	1×10^{-9}	—
		Epoxy	6×10^{-9}	

Solid 45 element of size 0.5 mm was used to model both the bonding layer and aluminium beam. This element, with eight nodes and three DOFs per node, is suitable for modeling solid structures. Solid 5 element of size 0.5 mm was used to simulate the PZT patch.

The numerical outcome was compared with the experimental results in Fig. 3.31 for two different frequency ranges. From the figure, it can be concluded that the simulation was successful as apparent from the close matching of the slope of the curve, modal frequencies and the peaks' magnitudes, even up to a frequency as high as 100 kHz.

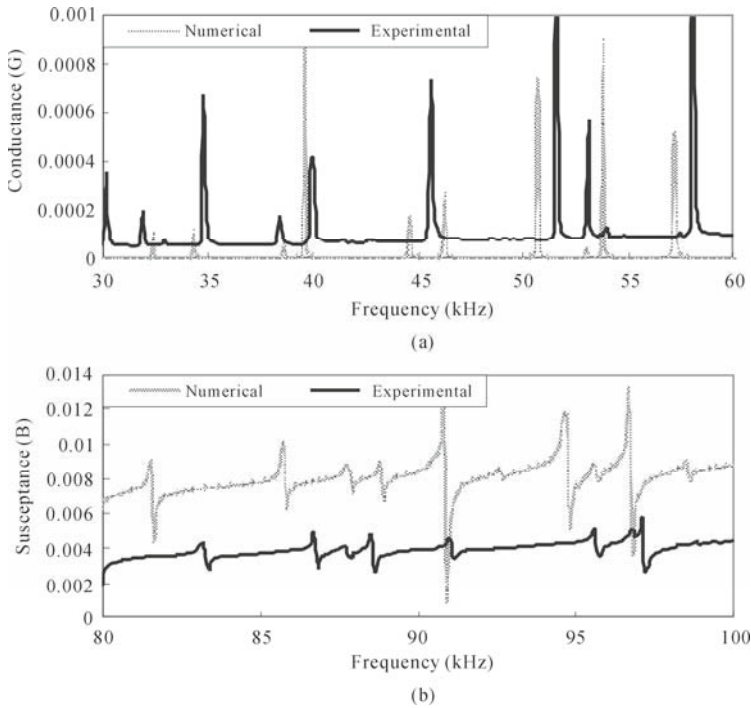


Fig. 3.31 Admittance signatures vs. frequency plot for experimental test and numerical model of aluminium beam specimen. (a) Conductance signatures (30 – 60 kHz); (b) Susceptance signatures (80 – 100 kHz)

Comparing the other models used in the EMI technique, this numerical model exhibited exceptional robustness. For instance, most of the models studied by other researchers, either purely analytical through impedance-based modeling or semi-analytical through FEA-based impedance modeling, were often either unable to model the minor peaks (Zagrai and Giurgiutiu, 2001), exhibited large variation in magnitudes (Bhalla 2001; Lim 2004; Giurgiutiu and Zagrai, 2000) or showed low accuracy when the frequency range exceeded 60 kHz (Ong *et al.*, 2002).

These shortcomings are attributed to a number of reasons. Firstly, it should be noted that the actual interaction between the PZT patch and host structure through the bonding layer involves the entire finite area of the patch. At high frequency of excitation, the mode shapes of the excited structure are numerous and complex. Simplification of the finite area interaction into point forces or moments would render some vibrational modes unexcited as well as giving inaccurate predictions of certain modal frequencies. Modeling the PZT patch as a coupled field element, on the other hand, overcame the above-mentioned limitation by allowing more points of interactions throughout the entire area. The accuracy of the results also increases with finer mesh.

Secondly, the basic assumption which neglected the effect of bonding (ideal bonding) in other researchers' models is not realistic at high frequency on account of highly localized actuation. The effect of shear lag is usually not negligible unless the bonding film is sufficiently thin. Some researchers (Ong *et al.*, 2002; Xu and Liu, 2003; Bhalla, 2004) introduced modification to the impedance-based electromechanical coupling equation (Liang *et al.*, 1994; Bhalla, 2004) by incorporating the effect of bonding. However, simplification of the point interaction remains.

This numerical model is similar to the semi-analytical model proposed by Madhav and Soh (2007b). The main difference is that this model is fully numerical with the coupled field element used to represent the PZT patch, whereas the semi-analytical model uses unit-distributed loads to represent the patch. The advantage of this numerical model is that the electrical admittance signatures can be obtained directly from the FEA output as if measured experimentally from an impedance analyzer, without the need to convert the mechanical impedance which is necessary for all the analytical or semi-analytical models.

- *Modeling of Bonding Film*

One of the inherent advantages exhibited by FE modeling of PZT-structure interaction is the ability to physically model the bonding film, which is essential for strain transfer. This section presents a numerical study on the effect of bonding thickness on the admittance signatures acquired from surface bonded PZT patches.

A lab-size rectangular aluminium beam (50 mm×2 mm×2 mm) with properties similar to the previous test specimen was bonded with a PZT patch (10 mm×10 mm×0.3 mm) at the middle of the beam. In this study, a smaller beam was purposely selected to reduce the computational time as the frequency involved

was relatively wider, ranging from 0 to 1,000 kHz.

The actual bonding thickness was measured to be 0.03 mm. The numerical model, incorporating this bonding thickness was generated and analyzed using ANSYS 8.1. Mesh size of 0.5mm was adopted globally. The numerical and experimental results are shown in Fig. 3.32.

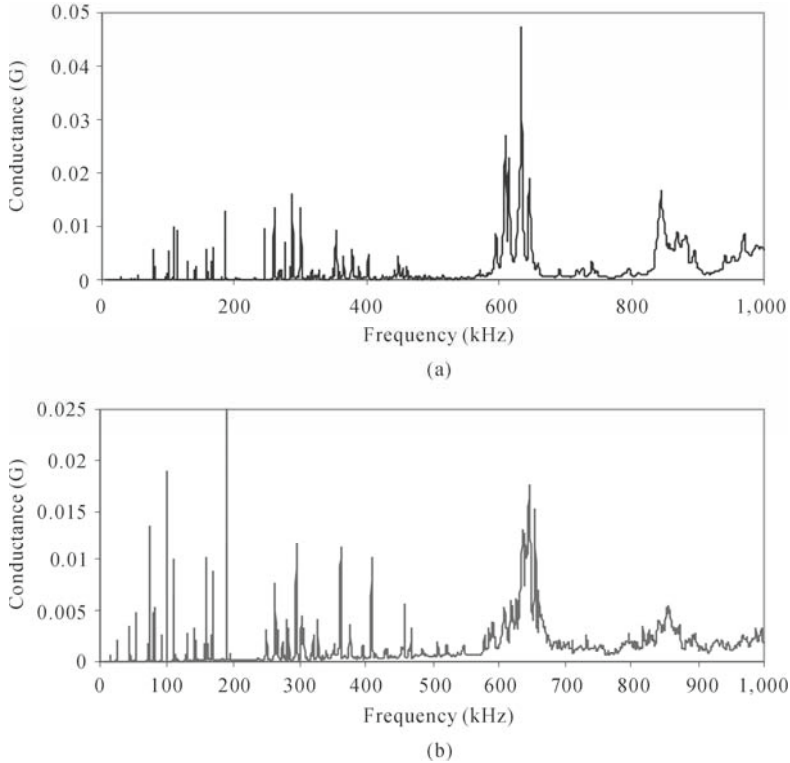


Fig. 3.32 Conductance signatures vs. frequency plot for experimental test and numerical model of aluminium beam specimen. (a) Numerical; (b) Experimental

The admittance signature plots indicate that those structural peaks below 500 kHz and the two PZT peaks occurring at 600 kHz and 850 kHz were satisfactorily simulated by the numerical model. This outcome again shows that the overall vibrational behavior of the test specimen was satisfactorily simulated through FEM for a frequency of up to 1,000 kHz.

Subsequently, models with different bonding thicknesses were further simulated and analyzed. The admittance signatures were plotted against frequency (Fig. 3.33), and the relative phase differences of the first PZT resonances are summarized in Table 3.9. From Fig. 3.33(a), the progressive leftward shift of PZT peaks with increasing bonding thickness indicates the increasingly dominating PZT patch's resonances. However, at moderate frequency of excitation (less than 200 kHz), increase in bonding thickness did not affect the modal frequency of the host

structural resonance (Fig. 3.33b).

This is a general observation for various peaks at frequency lower than 200 kHz. It could be inferred that at moderate frequency range (less than 200 kHz), the structural modal frequencies (reflecting the host structure) are not significantly affected by the bonding thickness. However, the adverse effect of bonding on overall magnitudes of signatures caused by leftward shifts of PZT peaks was inevitable when bonding thickness is 0.2 mm (larger than one-third of the PZT patch's thickness). Above 200 kHz, the domination of PZT peaks rendered the structural peaks more susceptible to contamination, for example, due to temperature variation. Therefore, at moderate frequency of excitation, the assumption of neglecting the effect of bonding is acceptable if the peaks' magnitudes are not the major concern but the modal frequencies, which are applicable in the EMI technique. The numerical results showed satisfactory agreement with the experimental observations presented by Yang *et al.* (2008).

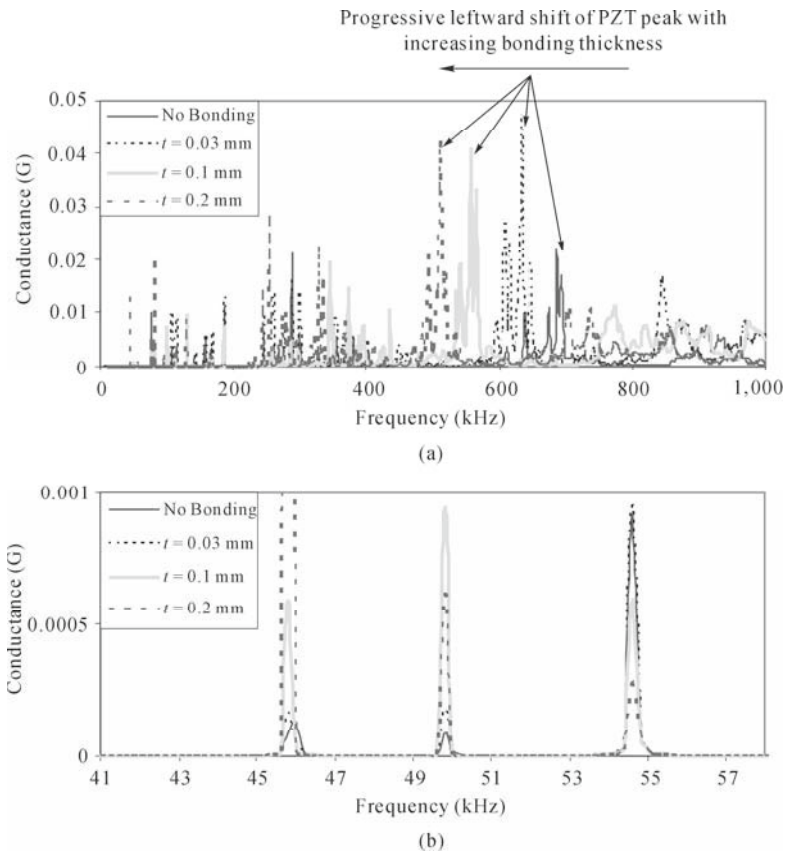


Fig. 3.33 Conductance signatures vs. frequency plot for numerically simulated surface-bonded PZT patch with varying bonding thickness on aluminium beam specimen. (a) 0 – 1000 kHz; (b) 40 – 60 kHz

Table 3.9 Summary of phases' information of first PZT resonance

Numerically simulated surface-bonded PZT patch with varying bonding thickness (Fig. 3.33a)		
	First PZT resonance occurrence (kHz)	Phase reduction w.r.t. "No bonding" (kHz)
No bonding	688	0
$t = 0.03$ mm	634	54
$t = 0.1$ mm	558	130
$t = 0.2$ mm	512	176

Numerically simulated PZT patch B4 with temperature varying from 30 °C – 60 °C (Fig. 3.36a)		
	First PZT resonance occurrence (kHz)	Phase reduction w.r.t. "30 °C" (kHz)
30°C	280	0
40°C	263	17
50°C	250	30
60°C	215	65

Experimental PZT patch B4 with temperature varying from 30 °C – 60 °C (Fig. 3.36b)		
	First PZT resonance occurrence (kHz)	Phase reduction w.r.t. "30 °C" (kHz)
30°C	273	0
40°C	256	17
50°C	231	42
60°C	204	69

- *Modeling of More Complex Structures*

In addition to the ability to realistically simulate the bonding film, FE simulation possesses another inherent advantage over the analytical model, namely, the ability to simulate irregular shapes with complicated boundary conditions normally impossible to have a closed-form solution. This section reports the feasibility of simulating an L-shaped aluminium beam ($l = 200$ mm, $w = 20$ mm, $t = 1$ mm) of identical properties as the previous test specimens and with a PZT patch (10 mm × 10 mm × 0.3 mm) surface bonded at its inner center, as represented schematically in Fig. 3.34. The numerically predicted admittance signatures are compared with the experimentally acquired signatures in Fig. 3.35.

In this case, reasonable accuracy between the two was achieved as most of the resonance peaks were predicted. However, the matching of resonance peaks was not as accurate as in the previous case for the simple beam. One of the reasons could be due to some distortion in the L-shaped beam, from its ideal shape, caused by imperfect hand cutting during preparation of the specimen. Another reason could be the nature of the specimen having a more complex shape resulting in more complex mode shapes during vibration. The presence of numerous local peaks could not be fully simulated by FEM unless a highly accurate model is simulated or a more perfect specimen is used.

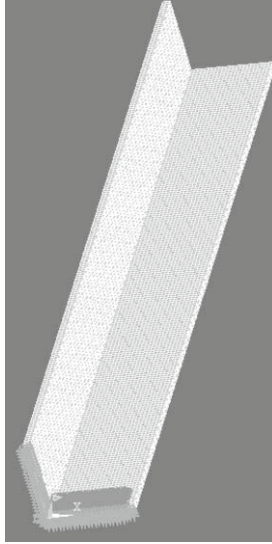


Fig. 3.34 Isometric view of one-half of free-ended L-shaped aluminium angle bonded with PZT patch

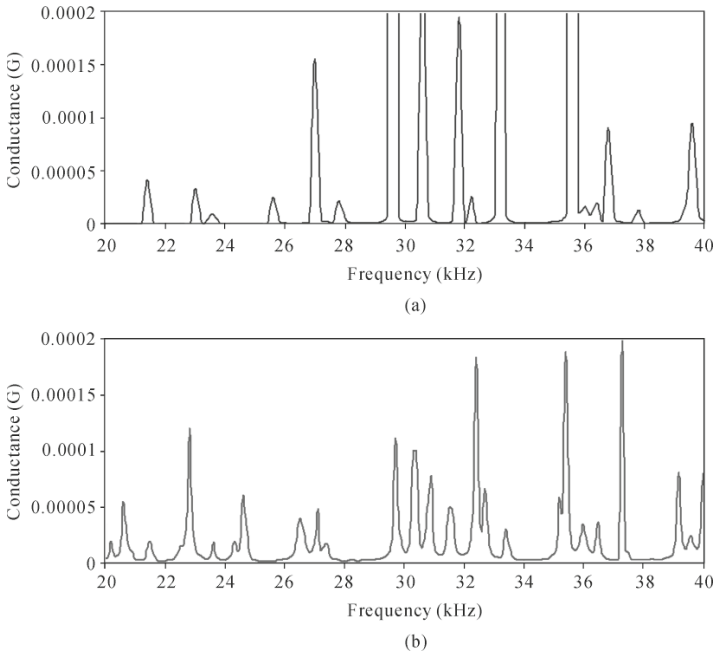


Fig. 3.35 Conductance signatures vs. frequency plot for numerical and experimental results of a PZT patch surface-bonded on an L-shaped aluminium beam specimen. (a) Numerical; (b) Experimental

- *Effect of Temperature*

In this section, the FEM simulation is brought a step further to include the effect of temperature. It is known that change in temperature would affect certain properties of the host structure, the bonding layer and the PZT patch (Yang *et al.*, 2008). However, at frequencies higher than 200 kHz, the horizontal shifts of PZT's resonances are dominated by the stiffness of the bonding layer.

A lab-sized structural beam (331 mm×31 mm×6 mm) was used for both experimental and numerical study on the effect of temperature (Yang *et al.*, 2008). The properties of PZT patch and aluminium beam susceptible to temperature variations were simulated according to recommendations from the manufacturer (PI Ceramic, 2006) and other relevant sources. The stiffness (Young's modulus) of the bonding layer was obtained through trial and error for each temperature of interest as the relevant data were not available from the manufacturer.

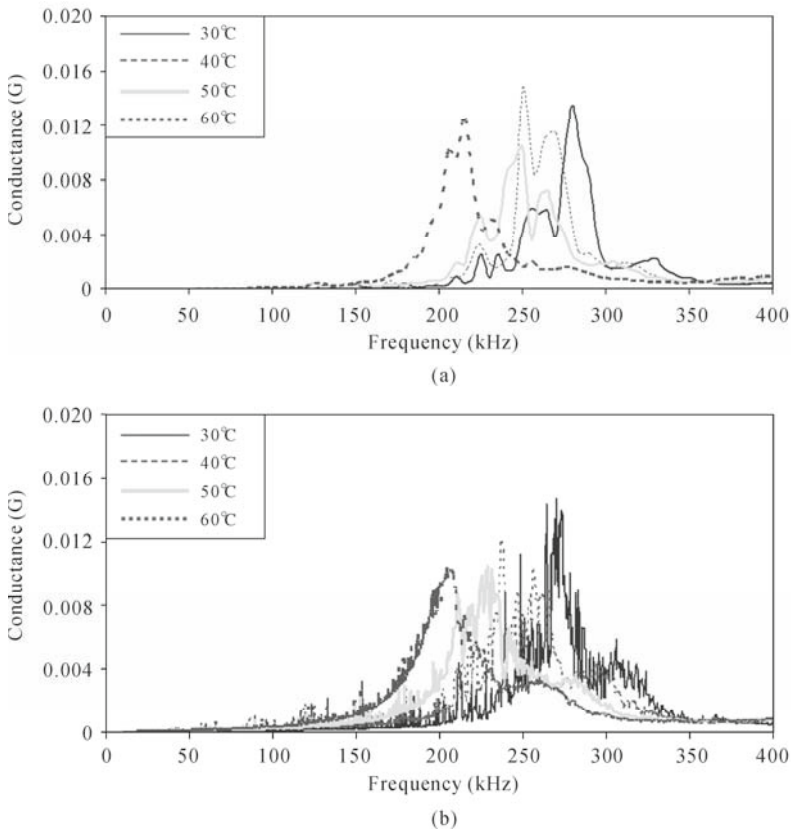


Fig. 3.36 Conductance signatures vs. frequency plot for experimental test and numerical simulation of aluminium beam bonded with PZT patch at varying temperature. (a) Numerical; (b) Experimental

Fig. 3.36 compares the numerically predicted and experimentally acquired admittance signatures at different temperatures. There is a high degree of consistency between the numerical and experimental results for the first PZT resonance over the frequency range of 0 – 400 kHz. The frequency of occurrence of the first PZT resonance and the relative phase shift at different temperatures are tabulated in Table 3.9. The gradual shift of the first resonance of the PZT patch to the left against the progressive elevating temperature was satisfactorily simulated. It was found that this phenomenon was mainly caused by a reduction of stiffness of the bonding layer against rising temperature. It should be noted that the alteration in stiffness of the host structure (aluminium beam) against elevated temperature plays a minor role in this case because it mainly affects the structural peaks.

It is also worth mentioning that the dense structural peaks were absent in the numerical plot because the frequency steps used for numerical simulation (5 kHz) were significantly larger than the experimental counterparts (0.1 kHz), and were thus unable to reflect the closely-spaced structural peaks. A wide frequency step was chosen for the simulation to reduce the computational time as the structural peaks are not the focus of this study.

This promising outcome once again verified the robustness and versatility of FEM in simulating PZT-structure interaction in the application of EMI technique inclusive of the effects of bonding layer and temperature change, which is unattainable in the conventional analytical model.

References

- Agilent Technologies (2003). *Test and Measurement Catalogue*, USA.
- Annanddas, V.G.M. and Soh, C.K. (2006a). “Embedded Piezoelectric Ceramic Transducers in Sandwiched Beams”, *Smart Materials and Structures*, 15(2): 538-549.
- Annanddas, V.G.M. and Soh, C.K. (2006b). “Multiple PZT-Host Structure Interaction Model”, *Proceedings of SPIE*, 6174, 61743G (paper No. 6174-124)
- Annanddas, V.G.M. and Soh, C.K. (2007). “Three Dimensional Electromechanical Impedance Model I: Formulation of Directional Sum Impedance”, *Journal of Aerospace Engineering*, 20(1): 53-62.
- ANSYS Inc. (2004). *ANSYS Reference Manual Release 8.1*, Canonsburg, PA, USA.
- Bathe, K.J. (1996). *Finite Element Procedures*, New Jersey: Prentice Hall, USA
- Bhalla, S. (2001). “Smart System Based Automated Health Monitoring of Structures”, *M. Eng. Thesis*, Nanyang Technological University, Singapore.
- Bhalla, S. (2004). “Mechanical Impedance Approach for Structural Identification, Health Monitoring and Non-destructive Evaluation Using Piezo-impedance Transducers”, *Ph.D. Thesis*, Nanyang Technological University, Singapore.

- Bhalla, S. and Soh, C.K. (2004a). "Structural Health Monitoring by Piezo-impedance transducers: Modeling", *Journal of Aerospace Engineering*, 17(4): 154-165.
- Bhalla, S. and Soh, C.K. (2004b). "Electromechanical Impedance Modeling for Adhesively Bonded Piezo-transducers", *Journal of Intelligent Material Systems and Structures*, 15(12): 955-972.
- Cheng, C.C. and Lin, C.C. (2005). "An impedance approach for vibration response synthesis using multiple PZT actuators", *Sensors and Actuators A*, 118: 116-126.
- Crawley, E.F. and de Luis, J. (1987). "Use of Piezoelectric Actuators as Elements of Intelligent Structures", *AIAA Journal*, 25(10): 1373-1385.
- Fairweather, J.A. (1998). "Designing with Active Materials: An Impedance Based Approach", *Ph.D. Thesis*, Rensselaer Polytechnic Institute, New York.
- Giurgiutiu, V. and Zagrai, A.N. (2000). "Characterization of Piezoelectric Wafer Active Sensors", *Journal of Intelligent Material Systems and Structures*, 11: 959-976.
- Giurgiutiu, V. and Zagrai, A.N. (2002). "Embedded Self-Sensing Piezoelectric Active Sensors for On-Line Structural Identification", *Journal of Vibration and Acoustics*, 124: 116-125.
- Hewlett Packard (1996). *HP LF 4192A Impedance Analyzer, Operation Manual*, Japan.
- Lalande, F. (1995). "Modelling of the Induced Strain Actuation of Shell Structures", *Ph.D. Dissertation*, Virginia Polytechnic Institute and State University, Blacksburg, V.A.
- Liang, C., Sun, F.P. and Rogers, C.A. (1993). "An Impedance Method for Dynamic Analysis of Active Material Systems", *Proceedings of AIAA/ASME/ASCE/Material Systems*, La-Jolla, California, 3587-3599.
- Liang, C., Sun, F.P. and Rogers, C.A. (1994). "Coupled Electro-Mechanical Analysis of Adaptive Material Systems—Determination of the Actuator Power Consumption and System Energy Transfer", *Journal of Intelligent Material Systems and Structures*, 5(1): 12-20.
- Lim, Y.Y. (2004). "Structural Identification by Smart Materials", *Final year report*, Nanyang Technological University, Singapore.
- Liu, W. and Giurgiutiu, V. (2007). "Finite Element Simulation of Piezoelectric Wafer Active Sensors for Structural Health Monitoring with Coupled-Field Elements", *Proceedings of SPIE*, 6529: 6529-25.
- Madhav, A.V.G. and Soh, C.K. (2007a). "Uniplexing and Multiplexing of PZT Transducer for Structural Health Monitoring", *Journal of Intelligent Material Systems and Structures*, 19(4): 457-467.
- Madhav, A.V.G. and Soh, C.K. (2007b). "An Electromechanical Impedance Model of a Piezoceramic Transducer-Structure in the Presence of Thick Adhesive Bonding", *Smart Materials and Structures*, 16: 673-686.
- Makkonen, T., Holappa, A., Ella, J. and Salomaa, M.M. (2001). "Finite Element Simulations of Thin-Film Composite BAW Resonators", *IEEE Transactions on Ultrasonics, Ferroelectrics and Frequency Control*, 48(5): 1241-1258.

- Ong, C.W. (2003). "Dynamic Identification and Health Monitoring of Structural Systems with the Electromechanical Impedance Method", *M. Eng. Thesis*, Nanyang Technological University, Singapore.
- Ong, C.W., Yang, Y., Wong, Y.T., Bhalla, S., Lu, Y. and Soh, C.K. (2002). "The Effects of Adhesive on the Electromechanical Response of a Piezoceramic Transducer Coupled Smart System", *Proceedings of SPIE*, 5062, 241-247.
- PI Ceramic (2006). *Product Information Catalogue*, Lindenstrabe, Germany, <http://www.piceramic.de>.
- Raja, S., Sreedeeep, R. and Prathap, G. (2004). "Bending behavior of Hybrid-Piezoelectric Sandwich Beams", *Journal of Intelligent Material Systems and Structures*, 15(4): 611-619.
- RS Components (2003). Northants, UK, <http://www.rs-components.com>.
- Sensor Technology Limited (1995). *Product Catalogue*, Collingwood.
- Sirohi, J. and Chopra, I. (2000). "Fundamental Understanding of Piezoelectric Strain Sensors", *Journal of Intelligent Material Systems and Structures*, 11(4): 246-257.
- The MathWorks, Inc. (2009). <http://www.mathworks.com>
- Xu, Y.G. and Liu, G.R. (2003). "A Modified Electro-mechanical Impedance Model of Piezoelectric Actuator-Sensors for Debonding Detection of Composite Patches", *Journal of Intelligent Material Systems and Structures*, 13(6): 389-396.
- Yang, Y.W., Xu, J.F. and Soh, C.K. (2005). "Generic Impedance-Based Model for Structure-Piezoceramic Interacting System", *Journal of Aerospace Engineering*, 18(2): 93-101.
- Yang, Y.W., Lim, Y.Y. and Soh, C.K. (2008). "Practical Issues Related to the Application of the Electromechanical Impedance Technique in the Structural Health Monitoring of Civil Structures: I. Experiment", *Smart Materials and Structures*, 17(3): 035008.
- Zagrai, A.N. and Giurgiutiu, V. (2001). "Electro-Mechanical Impedance Method for Crack Detection in Thin Plates", *Journal of Intelligent Material Systems and Structures*, 12(12): 709-718.
- Zhou, S.W., Liang, C. and Rogers, C.A. (1995). "Integration and Design of Piezoceramic Elements in Intelligent Structures", *Journal of Intelligent Material Systems and Structures*, 6(6): 733-743.
- Zhou, S.W., Liang, C. and Rogers, C.A. (1996). "An Impedance-Based System Modeling Approach for Induced Strain Actuator-Driven Structures", *Journal of Vibrations and Acoustics*, 118(3): 323-331.

Exercise 3.1

Consider an aluminium structure bonded with a PZT transducer, as shown in Fig. Ex 3.1. The PZT patch is 10 mm square by 0.3 mm thick, with properties listed in

Table 3.2. Model the structure using any commercial FEM software to obtain the effective mechanical impedance using dynamic harmonic finite-element approach. (Consider a 2D plane stress model).

(a) Use the program listed in Appendix B to obtain the conductance, G and susceptance, B signatures in the frequency range 0 – 200 kHz at an interval of 1 kHz (consider Rayleigh damping coefficients $\alpha = 0$, $\beta = 2 \times 10^{-9}$). Plot the obtained G and B signatures as shown in Fig. 3.8.

(b) Repeat the computations using the program listed in Appendix C. Comment on the differences between the plots of (a) and (b).

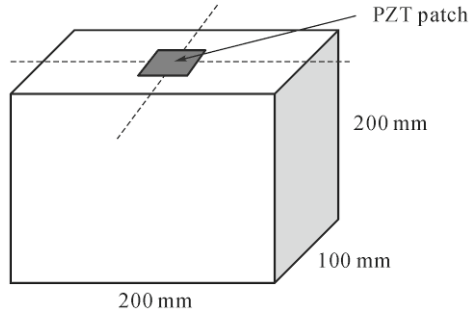


Fig. Ex 3.1

Exercise 3.2

Consider the same aluminium structure shown in Fig. Ex 3.1. The PZT patch of grade C is 10 mm square by 0.25 mm thick, and possesses the properties listed in Table 3.4. Assume a 1.0 mm thick bonding adhesive beneath the patch. Model one quarter of the structure using any commercial FEM software.

(a) Obtain the G and B signatures using the program given in Appendix D for a frequency range of 0 – 100 kHz at an interval of 0.5 kHz (Rayleigh damping coefficients: for aluminium $\alpha = 0$, $\beta_M = 1.5923 \times 10^{-7}$, and for epoxy $\alpha = 0$, $\beta_M = 1.5923 \times 10^{-9}$). Plot the obtained G and B signatures as shown in Fig. 3.31. Compare these signatures with the signatures of Ex. 3.1 (2D stress model).

(b) Modify the program in Appendix D so that it can be used to model one quarter of the structure with a rectangular PZT patch of dimensions $12 \text{ mm} \times 10 \text{ mm} \times 0.25 \text{ mm}$. (Consider modifying UX or UY or UZ).

(c) Plot the G and B signatures for the PZT patch with thicknesses of 0.3 mm, 0.4 mm and 0.5 mm.

(d) Plot the G and B signatures for the adhesive with thicknesses of 0.25 mm, 0.5 mm and 0.75 mm.

Exercise 3.3

(a) Analyze a freely suspended PZT patch using coupled field element in any commercial FEM software, and compare it with the experimental results. Try PZT patches of different sizes and shapes. Start with a coarser mesh and gradually refine to seek for convergence. Discuss these results with experimental results as well as any limitations.

(b) Analyze a lab-size simple beam, inclusive of the PZT patch and adhesive layer, using any commercial FEM software. Study the PZT-structure interaction and compare it with the experimental results. Try different beam materials such as concrete and aluminium. Compare the accuracy of the results.

Damage Quantification Using EMI Technique

S. Bhalla^{*}, Y. W. Yang, J. F. Xu, C. K. Soh

^{*}Department of Civil Engineering, Indian Institute of Technology Delhi,
Hauz Khas, New Delhi 110016, India
Tel: 91-11-2659-1040; Fax: 91-11-2658-1117
Email: sbhalla@civil.iitd.ac.in

4.1 Extraction of Structural Mechanical Impedance from Admittance Signatures

This section outlines a computational procedure to extract the mechanical impedance of the host structure from the EM admittance signatures of the surface-bonded PZT patches. As in the case of the 1D impedance model (see Chapter 2), the EM admittance given by Eq. (3.30) can be separated into active and passive components as

$$\bar{Y} = \underbrace{4\omega j \frac{l^2}{h} \left[\frac{\bar{\epsilon}_{33}^T}{\epsilon_{33}^T} - \frac{2d_{31}^2 \bar{Y}^E}{(1-\nu)} \right]}_{\text{Passive}} + \underbrace{\frac{8\omega d_{31}^2 \bar{Y}^E l^2}{h(1-\nu)} \left(\frac{Z_{a,eff}}{Z_{s,eff} + Z_{a,eff}} \right)}_{\text{Active}} \bar{T} j \quad (4.1)$$

or

$$\bar{Y} = \bar{Y}_P + \bar{Y}_A \quad (4.2)$$

where \bar{Y}_A is the “active” component and \bar{Y}_P the “passive” component. \bar{Y}_P can be

broken down into real and imaginary parts by expanding $\overline{\varepsilon_{33}^T} = \varepsilon_{33}^T(1 - \delta)$ and $\overline{Y^E} = Y^E(1 + \eta j)$, and expressed as

$$\overline{Y_p} = G_p + B_p j \quad (4.3)$$

where

$$G_p = \frac{4\omega l^2}{h} \{ \delta \varepsilon_{33}^T + K \eta \} \quad (4.4)$$

$$B_p = \frac{4\omega l^2}{h} \{ \varepsilon_{33}^T - K \} \quad (4.5)$$

with

$$K = \frac{2d_{31}^2 Y^E}{(1 - \nu)} \quad (4.6)$$

G_p and B_p can be predicted with reasonable accuracy if the conductance and susceptance signatures of the PZT patch are recorded in “free-free” condition prior to its bonding to the host structure (as illustrated in Chapter 3). Hence, the PZT contribution can be filtered off from the raw signatures, and the active component deduced as

$$\overline{Y}_A = \overline{Y} - \overline{Y}_p \quad (4.7)$$

or

$$\overline{Y}_A = (G + B j) - (G_p + B_p j) \quad (4.8)$$

Thus, the active components (G_A and B_A) can be derived from the measured raw admittance signatures (G and B) as

$$G_A = G - G_p \quad (4.9)$$

and

$$B_A = B - B_p \quad (4.10)$$

In the complex form, the active component can be expressed as

$$\overline{Y}_A = G_A + B_A j = \frac{8\omega l_{31}^2 \overline{Y}^E l^2}{h(1-\nu)} \left(\frac{Z_{a,eff}}{Z_{s,eff} + Z_{a,eff}} \right) \overline{T} j \quad (4.11)$$

It has been demonstrated in Chapter 2, using 1D interaction models, that elimination of the passive component renders the admittance signatures more sensitive to structural damages. The same holds true for the 2D PZT-structure interaction considered in this chapter. This section outlines a computational procedure for the more general class of structures, based on the new EM admittance formulations.

Substituting $\overline{Y}^E = Y^E(1 + \eta j)$ and $\overline{T} = r + tj$ into Eq. (4.11), and rearranging the various terms, the following can be obtained

$$M + Nj = \left(\frac{Z_{a,eff}}{Z_{s,eff} + Z_{a,eff}} \right) (R + Sj) \quad (4.12)$$

where

$$M = \frac{B_A h}{4\omega Kl^2} \quad \text{and} \quad N = -\frac{G_A h}{4\omega Kl^2} \quad (4.13)$$

$$R = r - \eta t \quad \text{and} \quad S = t + \eta r \quad (4.14)$$

Further expanding $Z_{S,eff} = x + yj$ and $Z_{a,eff} = x_a + y_a j$, and upon solving, the real and imaginary components of the EDP structural impedance can be obtained as

$$x = \frac{M(x_a R - y_a S) + N(x_a S + y_a R)}{M^2 + N^2} - x_a \quad (4.15)$$

$$y = \frac{M(x_a S + y_a R) - N(x_a R - y_a S)}{M^2 + N^2} - y_a \quad (4.16)$$

In all these computations, the term \overline{T} (which plays a significant role) depends on $\frac{\tan \kappa l}{\kappa l}$ as given by

$$\overline{T} = \frac{1}{2} \left[\frac{\tan(C_1 \kappa l)}{C_1 \kappa l} + \frac{\tan(C_2 \kappa l)}{C_2 \kappa l} \right] \quad (4.17)$$

where κl is a complex number. It is essential to determine this quantity precisely.

Furthermore, it is desirable that $|x| > |x_a|$ and $|y| > |y_a|$ in order to ensure smooth computations and accurate identification of the structural resonance frequencies.

The simple computational procedure outlined above, results in the determination of the drive-point mechanical impedance of the structure, $Z_{s,eff} = x + yj$, at a particular frequency ω , from the active admittance signatures. Following this procedure, “x” and “y” can be determined for the entire frequency range of interest. This procedure is employed to extract the structural EDP impedance of the aluminium block used for validating the new impedance model described in Chapter 3. The MATLAB program listed in Appendix D is used to perform the computations. Fig. 4.1 shows a plot of $|Z_{eff}^{-1}|$, derived by this procedure, comparing it with the plot determined using FEM (as discussed in Chapter 3). Reasonable agreement can be observed between the two. The main reason for plotting $|Z_{s,eff}^{-1}|$ (instead of $Z_{s,eff}$) is that the resonant frequencies can be easily identified as peaks of the plot.

As will be demonstrated in the forthcoming sections, this procedure enables us to “identify” any unknown structure without needing any *a priori* information governing the phenomenological nature of the structure. The only requirement is an “updated” model of the PZT patch, which can be derived from the preliminary specifications of the PZT patch, and by recording its admittance signatures in the “free-free” condition, prior to bonding it to the host structure. The next section will present a simple procedure to derive equivalent system parameters from the structural EDP impedance.

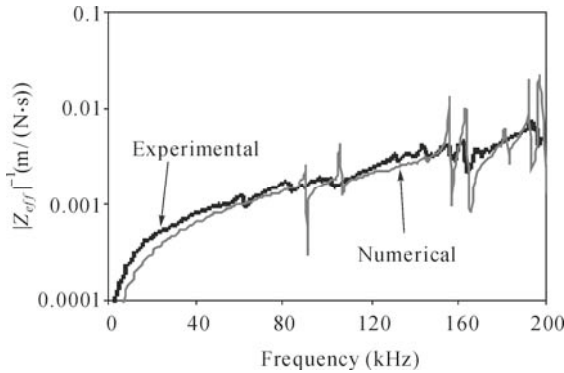


Fig. 4.1 Comparison between $|Z_{eff}^{-1}|$ obtained experimentally and numerically

4.2 System Parameter Identification from Extracted Impedance Spectra

The structural EDP impedance, extracted by means of the procedure outlined earlier, carries information about the dynamic characteristics of the host structure.

This section presents a general approach to “identify” the equivalent structural system. Before considering any real-life structural system for this purpose, it would be worthwhile to observe the impedance pattern of a few simple systems. Fig. 4.2 shows plots of the real and imaginary components of the mechanical impedance of basic structural elements—the mass, the spring and the damper (refer to Eqs. (2.4) to (2.7)). These basic elements can be combined in a number of different ways (series, parallel or a mixture) to evolve complex mechanical systems. Table 4.1 shows the impedance plots (real part, x , and imaginary part, y , vs. frequency) for some possible combinations of the basic elements. The expressions for x and y can be derived using Eqs. (2.8) and (2.9) (Hixon, 1988).

In general, for any real-life structure, the x and y components of the extracted EDP impedance may not display ideal behavior (e.g., a pure mass or pure stiffness or pure damper). The real and imaginary terms may vary with frequency similar to a combination of the basic elements. From the nature of the plots of x and y (and taking note of the systems listed in Table 4.1), the “unknown” structure can thus be identified as an “equivalent” structure (series or parallel combination of basic elements), and the equivalent system parameters can thereby be determined.

To demonstrate this approach, let us consider an aluminium block (grade Al 6061-T6), 50 mm×48 mm×10 mm in size, representing an unknown structural system. The PZT patch *S2002-6* (10 mm×10 mm×0.3 mm in size), whose updated model was derived in the preceding chapter, was bonded to the surface of this specimen. An HP 4192A impedance analyzer was used to acquire the raw admittance signatures (conductance and susceptance) of this PZT patch. The passive components were filtered off from the raw signatures, and the structural EDP impedance extracted using the MATLAB program listed in Appendix E (considering the parameters of patch *S2002-6* to be derived experimentally). A close examination of the extracted impedance components in the frequency range 25 – 40 kHz suggested that the system behavior is similar to a parallel spring-damper ($k-c$) combination (System 1 in Table 4.1), which represents the widely known *Kelvin-Voigt* model. For this system,

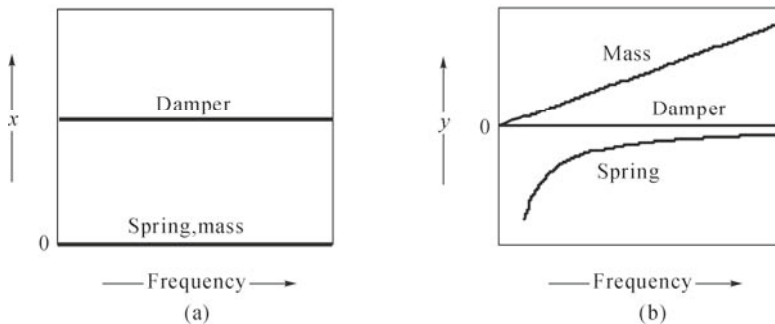

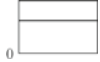

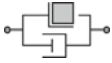
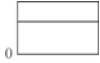

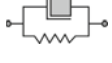
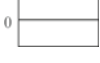
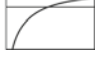

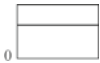
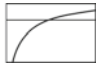

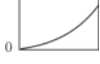
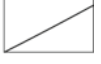
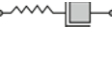




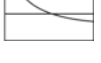






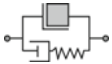
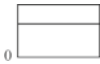




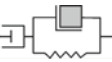

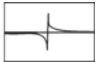





Fig. 4.2 Impedance plots of basic structural elements—spring, damper and mass: (a) Real part, x , vs. frequency; (b) Imaginary part, y , vs. frequency

Table 4.1 Mechanical impedance of combinations of spring, mass and damper (based on Hixon, 1988, from Shock and Vibration Handbook, edited by C. M. Harris, © The McGraw-Hill Companies, 1988)

No.	Combination	x	y	x vs. Freq.	y vs. Freq.
1		c	$-\frac{k}{\omega}$		
2		c	$m\omega$		
3		0	$m\omega - \frac{k}{\omega}$		
4		c	$m\omega - \frac{k}{\omega}$		
5		$\frac{c^{-1}}{c^{-2} + (\omega m)^{-2}}$	$\frac{(\omega m)^{-1}}{c^{-2} + (\omega m)^{-2}}$		
6		0	$\frac{-1}{(\omega/k) - (\omega m)^{-1}}$		
7		$\frac{c^{-1}}{c^{-2} + (\omega/k - 1/(\omega m))^2}$	$\frac{-(\omega/k - 1/(\omega m))}{c^{-2} + (\omega/k - 1/(\omega m))^2}$		
8		c	$\frac{\omega m k}{k - \omega^2 m}$		
9		$\frac{c^{-1}}{c^{-2} + (\omega m)^{-2}}$	$\frac{m^{-1} - k(c^{-2} + \omega^2 m^{-2})}{\omega[c^{-2} + (\omega m)^{-2}]}$		
10		$\frac{c^{-1}}{c^{-2} + (\omega/k)^2}$	$\frac{\omega[m(c^{-2} + \omega^2 k^{-2}) - k^{-1}]}{c^{-2} + (\omega/k)^2}$		
11		$\frac{cm^2\omega^2}{c^2 + (\omega m - k/\omega)^2}$	$\frac{m\omega\left[c^2 - \frac{k}{\omega}(\omega m - k/\omega)\right]}{c^2 + (\omega m - k/\omega)^2}$		
12		$\frac{c^{-1}}{c^{-2} + [\omega/(k - m\omega^2)]^2}$	$\frac{-\omega/(k - m\omega^2)}{c^{-2} + [\omega/(k - m\omega^2)]^2}$		
13		$\frac{ck^2/\omega^2}{c^2 + (\omega m - k/\omega)^2}$	$\frac{-km\left[(\omega m - k/\omega) + \frac{c^2 k}{\omega m}\right]}{c^2 + (\omega m - k/\omega)^2}$		

$$x = c \text{ and } y = -\frac{k}{\omega} \quad (4.18)$$

Using Eq. (4.18) and the actual impedance plots, the average “equivalent” system parameters are worked out as $c = 36.54 \text{ N}\cdot\text{s}/\text{m}$ and $k = 4.18 \times 10^7 \text{ N}/\text{m}$. The analytical plots of “ x ” and “ y ” obtained by these equivalent parameters match well with their experimental counterparts (Fig. 4.3).

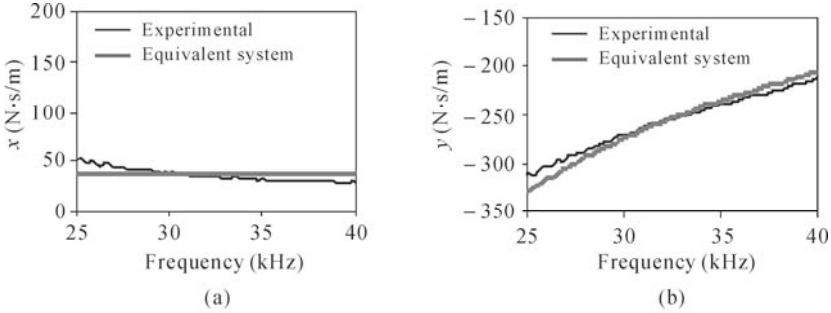


Fig. 4.3 Mechanical impedance of equivalent system (System 1 in Table 4.1): (a) Real part, x , vs. frequency; (b) Imaginary part, y , vs. frequency

Similarly, in the frequency range 180 – 200 kHz, the system behavior is found to be similar to a parallel spring-damper (k - c) combination, in series, with mass m (System 11 in Table 4.1). For this combination,

$$x = \frac{cm^2\omega^2}{c^2 + \left(m\omega - \frac{k}{\omega}\right)^2} \text{ and } y = \frac{m\omega \left[c^2 - \frac{k}{\omega} \left(m\omega - \frac{k}{\omega} \right) \right]}{c^2 + \left(m\omega - \frac{k}{\omega} \right)^2} \quad (4.19)$$

and the peak frequency of the x -plot is given by

$$\omega_o = \sqrt{\frac{k}{m - \frac{c^2}{k}}} \quad (4.20)$$

If the peak magnitude $x = x_o$ occurs at frequency $\omega = \omega_o$ and a value $x = x_1$ (somewhat less than the peak magnitude) at frequency $\omega = \omega_1 (< \omega_o)$, using Eqs. (4.19) and (4.20), the system parameters, namely m , c and k can be determined as

$$m = \left[\frac{-B \pm \sqrt{B^2 - 2AC}}{2A} \right]^{1/2} \quad (4.21)$$

$$c = \frac{m^2 \omega_o^2 x_o}{x_o^2 + m^2 \omega_o^2} \tag{4.22}$$

$$k = \frac{x_o c}{m} \tag{4.23}$$

where

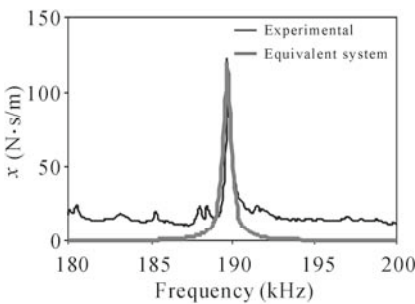
$$A = \omega_o^4 \omega_1^4 (x_1 - x_o) \tag{4.24}$$

$$B = 2x_1 \omega_o^2 \omega_1^2 x_o^2 (\omega_1^2 - \omega_o^2) + \omega_o^4 \omega_1^2 x_o^2 x_1 - \omega_o^2 \omega_1^4 x_o^3 \tag{4.25}$$

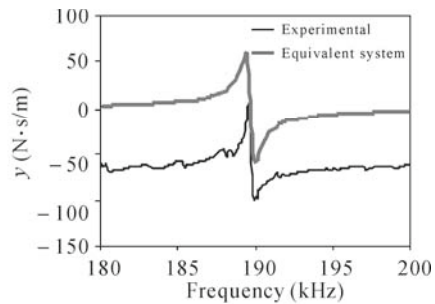
$$C = (\omega_1^2 - \omega_o^2)^2 x_o^4 x_1 \tag{4.26}$$

From the above equations, the system parameters are computed as $c=1.1 \times 10^{-3}$ N·s/m, $k=4.33 \times 10^5$ N/m and $m=3.05 \times 10^{-7}$ kg. These values produced an impedance pattern similar to the experimental plot (Fig. 4.4). Further refinement is achieved by adding a spring $K^*=7.45 \times 10^7$ N/m and a damper $C^*=12.4$ N·s/m in parallel, to make the equivalent system appear as shown in Fig. 4.5. Hence, Eq. (4.19) can be refined as:

$$x = C^* + \frac{cm^2 \omega^2}{c^2 + \left(m\omega - \frac{k}{\omega}\right)^2} \text{ and } y = \frac{m\omega \left[c^2 - \frac{k}{\omega} \left(m\omega - \frac{k}{\omega}\right) \right]}{c^2 + \left(m\omega - \frac{k}{\omega}\right)^2} - \frac{K^*}{\omega} \tag{4.27}$$



(a)



(b)

Fig. 4.4 Mechanical impedance of equivalent system (System 11 of Table 4.1). (a) Real part; (b) Imaginary part

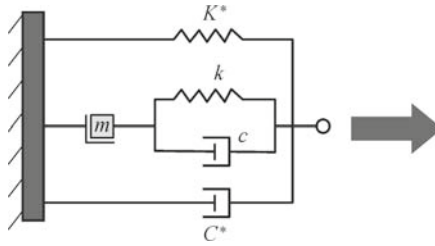


Fig. 4.5 Refinement of equivalent system by introduction of additional spring K^* and additional damper C^*

Fig. 4.6 compares the experimental plots with the analytical plots for this equivalent system. A much better agreement can be observed between the plots obtained experimentally and those pertaining to the equivalent system. Hence, the structural system is identified with reasonably good accuracy. The next section explains how this method can be used to quantify damages in aerospace and mechanical structures.

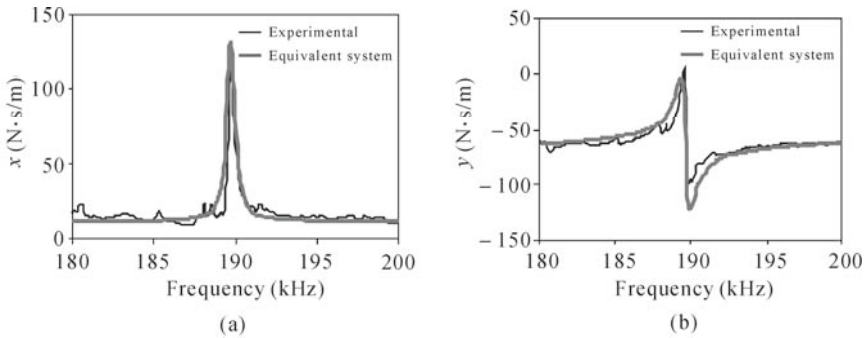


Fig. 4.6 Mechanical impedance of refined equivalent system (shown in Fig. 4.5). (a) Real part; (b) Imaginary part

4.3 Damage Diagnosis in Aerospace and Mechanical Systems

This section describes a damage diagnosis study, carried out on the same aluminium block specimen as described in the previous section. This is a typical small-sized rigid structure, characterized by high natural frequencies in the kHz range. Several critical aircraft components, such as turbo engine blades, are small and rigid, and are characterized by typically high natural frequencies in the kHz range (Giurgiutiu and Zagrai, 2002), thereby exhibiting similar dynamic behavior.

Damage was induced in the test structure by drilling holes, 5 mm in diameter, through the thickness of the specimen. Three levels of damage were induced—

incipient, moderate and severe (Figs. 4.7(b), (c) and (d) respectively). The number of holes was increased from two to eight in three stages, so as to simulate a gradual growth of damage from the incipient to the severe level. After each damage, the admittance signatures of the PZT patch were recorded and the equivalent structural parameters were worked out in the 25 – 40 kHz and 180 – 200 kHz ranges.

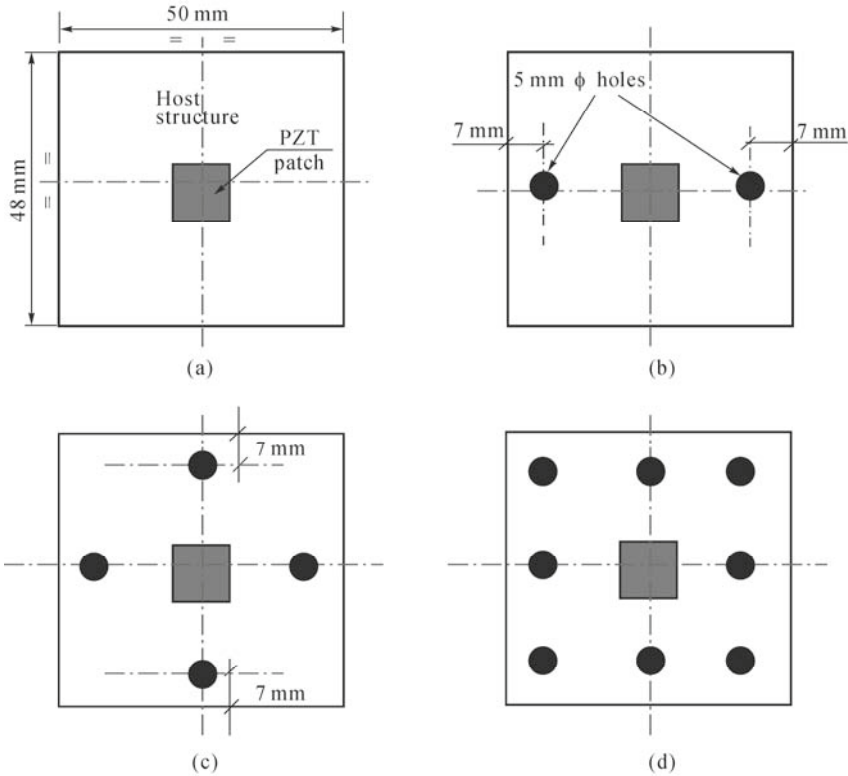


Fig. 4.7 Levels of damage induced on test specimen: (a) Pristine state; (b) Incipient damage; (c) Moderate damage; (d) Severe damage

Fig. 4.8 shows the effect of these damages on the real and imaginary components of the extracted mechanical impedance in the frequency range 25 – 40 kHz. Fig. 4.9 shows the effect of the damages on the identified structural parameters. As expected, with damage progression, the stiffness can be observed to reduce and the damping to increase. The stiffness was found to reduce by about 12% and the damping to increase by about 7% after the incipient damage. Thereafter, with further damage propagation, very small reductions/increases were observed in these parameters. However, it should be noted that the incipient damage was captured reasonably well.

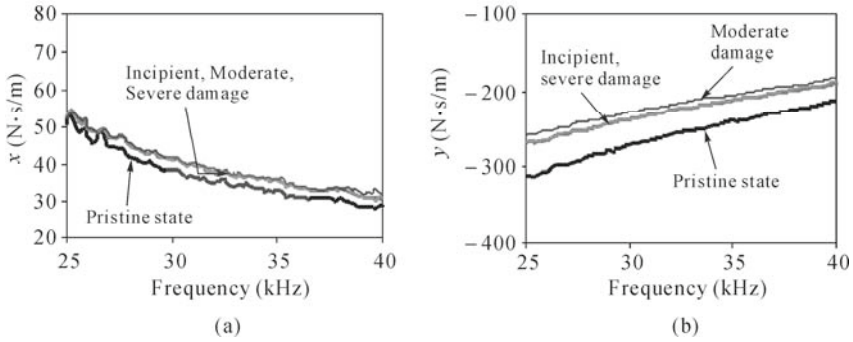


Fig. 4.8 Effect of damage on extracted mechanical impedance in 25 – 40 kHz range. (a) Real part, x , vs. frequency; (b) Imaginary part, y , vs. frequency

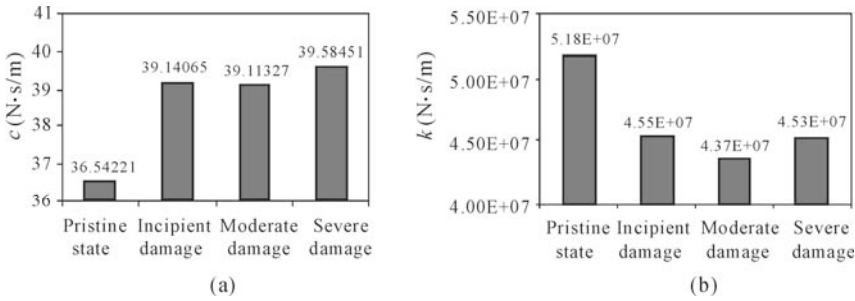


Fig. 4.9 Effect of damage on equivalent system parameters in 25 – 40 kHz range. (a) Equivalent damping constant; (b) Equivalent spring constant

Fig. 4.10 shows the effect of these damages on the impedance spectra in the frequency range of 180 – 200 kHz. Equivalent lumped system parameters were determined for each damage state using the procedure outlined in the preceding section.

Fig. 4.11 compares the experimental impedance plots with the plots based on the equivalent system parameters for each damage state. A high degree of agreement between the two demonstrates reasonably accurate structural identification for the damaged structure also.

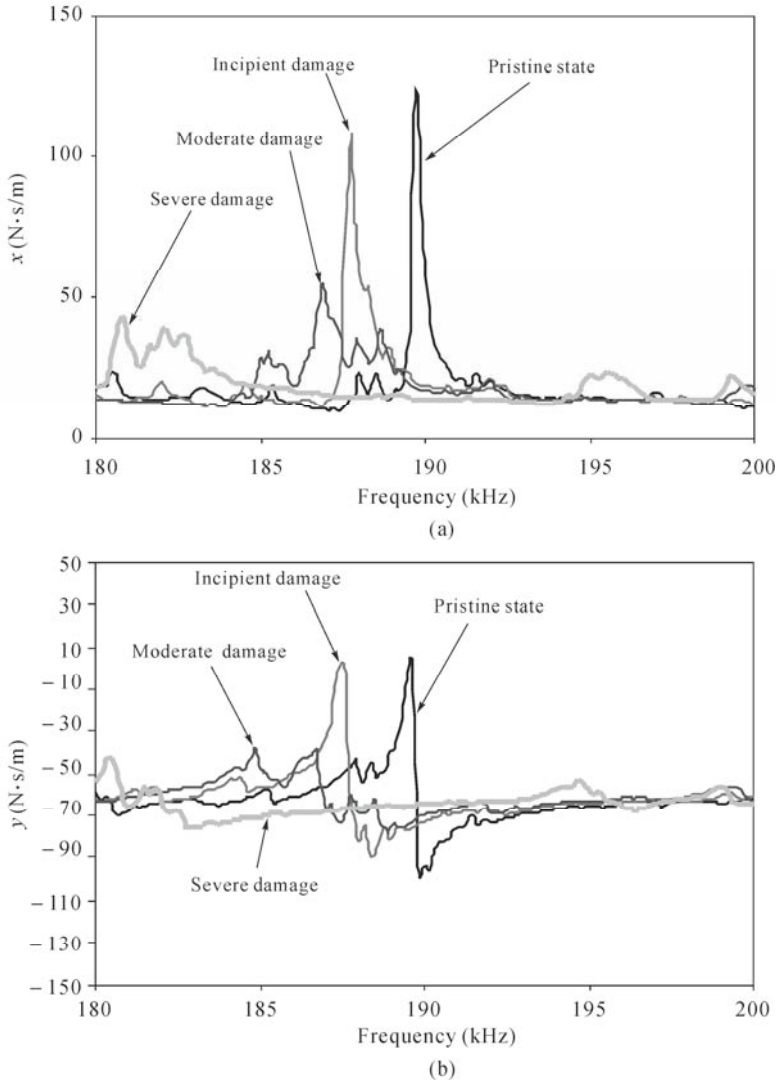


Fig. 4.10 Effect of damage on extracted mechanical impedance in 180 – 200 kHz range. (a) Real part, x , vs. frequency; (b) Imaginary part, y , vs. frequency

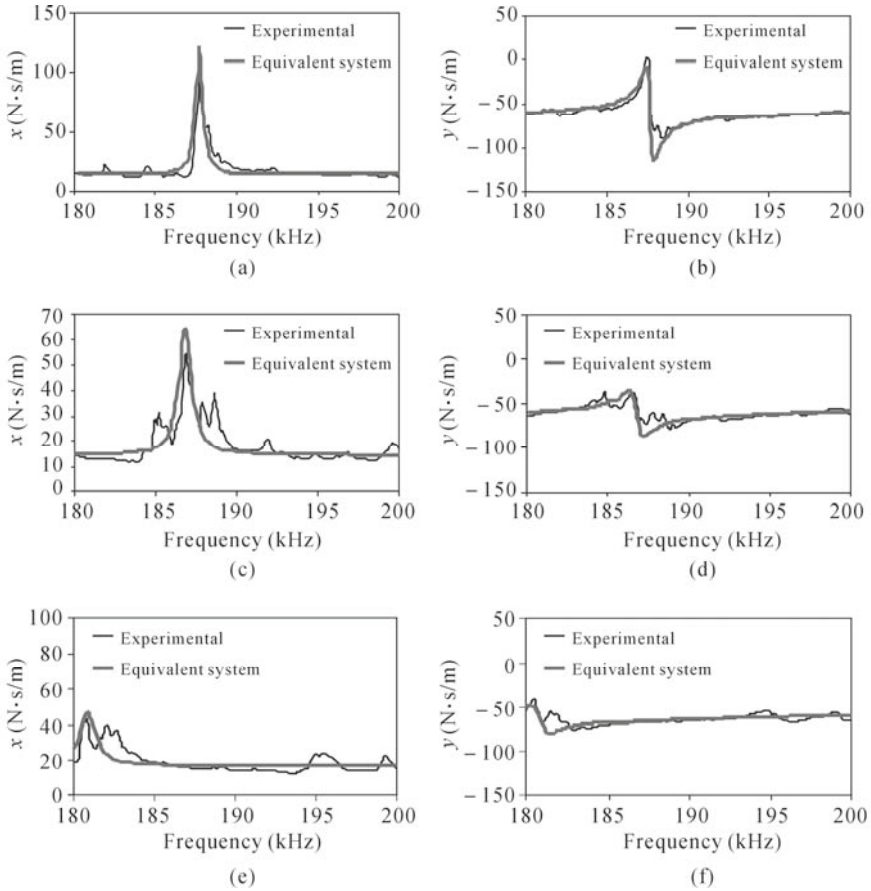


Fig. 4.11 Plot of mechanical impedance in 180 – 200 kHz range for various damage states: (a) Incipient damage: Real part; (b) Incipient damage: Imaginary part; (c) Moderate damage: Real part; (d) Moderate damage: Imaginary part; (e) Severe damage: Real part; (f) Severe damage: Imaginary part

The effect of damages on the equivalent parameters for 180 – 200 kHz range is shown in Fig. 4.12. Again, the trend is highly consistent with expected behavior and much more prominent than for the frequency range 25 – 40 kHz. With damage progression, the mass and stiffness can be seen to reduce and the damping to increase. The stiffness reduced gradually: 17% for incipient damage, 31% for moderate damage and 47% for severe damage. Similarly, the mass was also found to reduce with damage severity: 16% for incipient damage, 28% for moderate damage and 42% for severe damage. The damping values (c and C^*) were found to increase with damage (Figs. 4.12(c) and (e)), though “ c ” displayed a slight decrease after the incipient damage. The only exception is found in the parallel stiffness K^* , which remains largely insensitive to all the levels of damage.

Contrary to the 25 – 40 kHz range, the 180 – 200 kHz range was found to

diagnose the damages much better, as demonstrated by the significant variation in the parameters for the moderate and severe damages, in addition to the incipient damages.

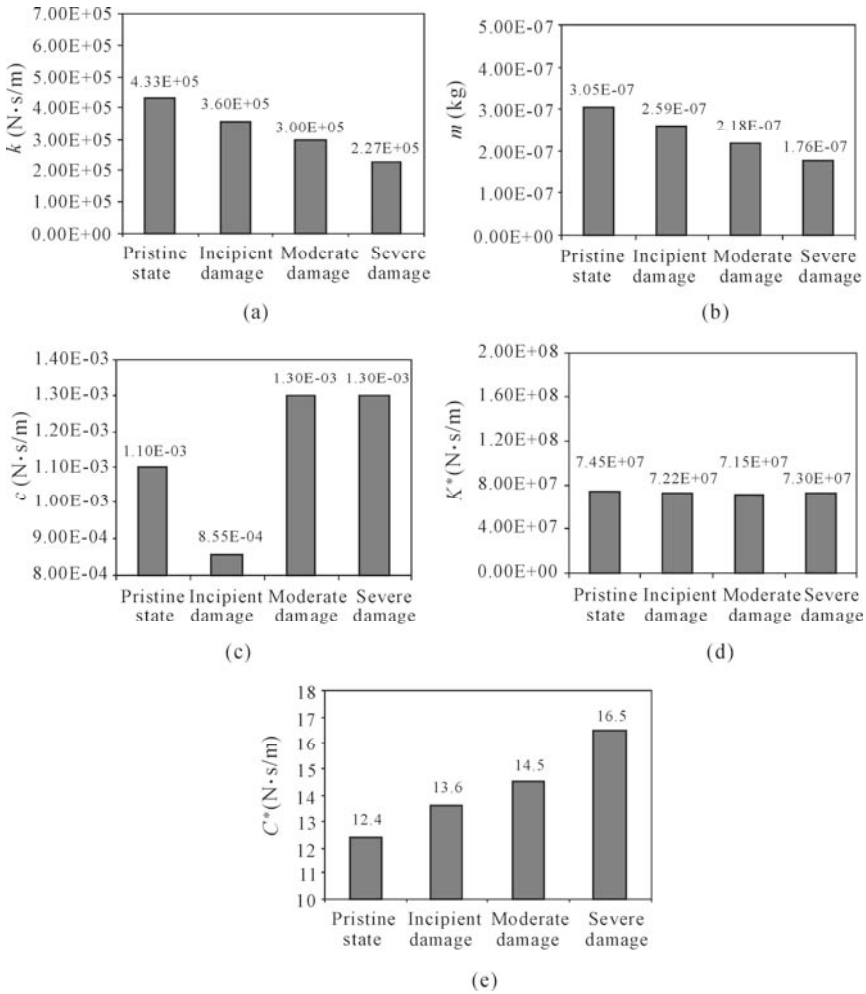


Fig. 4.12 Effect of damage on equivalent system parameters in 180 – 200 kHz range. (a) Equivalent spring constant; (b) Equivalent mass; (c) Equivalent damping constant; (d) Equivalent additional spring constant; (e) Equivalent additional damping constant

Fig. 4.13 shows a plot between the area of the specimen, “ A ” (a measure of the residual capacity of the specimen) and the equivalent spring stiffness “ k ” identified by the PZT patch. Using regression analysis, the following empirical relation was found between the two

$$A = 1874.2 + 0.0021k - 2.02 \times 10^{-9} k^2 \quad (4.28)$$

This demonstrates that it is possible to calibrate the damage-sensitive-system parameters with damage, and to employ them for damage diagnosis in real situations.

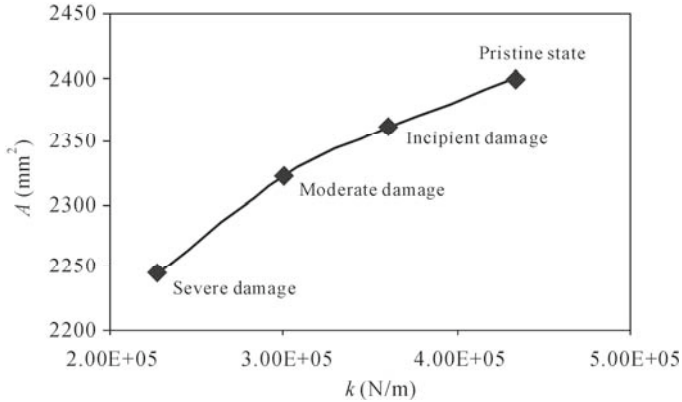


Fig. 4.13 Plot of residual specimen area versus equivalent spring constant

The higher sensitivity of damage detection in the frequency range 180 – 200 kHz (as compared with 25 – 40 kHz range) is due to the fact that, with increase in frequency, the wavelength of the induced stress wave becomes smaller and is therefore more sensitive to any defects and damages. This is also due to the presence of a damage-sensitive anti-resonance mode in the frequency range 180 – 200 kHz (Fig. 4.10) and the absence of any major resonance/ anti-resonance mode in the 25 – 40 kHz range (Fig. 4.8). This agrees with the recommendation of Sun *et al.* (1995) that the frequency range must contain prominent vibration modes to ensure high sensitivity to damages. However, it should be noted that in spite of the absence of any major resonance mode in the frequency range 25 – 40 kHz, the damage was still effectively captured at the incipient stage, although severe damages were not well differentiated from the incipient damage.

This study demonstrates that the proposed method can evaluate and quantify structural damages in aerospace components reasonably well. Besides miniature aerospace gadgets, the method is also ideal for identifying damages in precision machinery components, turbo machine parts and computer parts such as hard disks. These components are quite rigid and exhibit a dynamic behavior similar to the test structure studied in this section. The piezo-impedance transducers, because of their miniature characteristics, are unlikely to alter the dynamic characteristics of these miniature systems. Thus, they are preferred over the other sensor systems and techniques (Giurgiutiu and Zagari, 2002).

In Fig. 4.12(b), it is clear that by using this method, it is possible to detect “mass loss” in critical space shuttle components (*e.g.*, reinforced carbon-carbon panels), which is commonly encountered. This type of damage is presently difficult to identify using other prevalent NDE techniques, and was the main

reason for the collapse of the space shuttle Columbia during its re-entry into the earth's atmosphere on 1 February 2003 (CAIB, 2003).

4.4 Extension to Damage Diagnosis in Civil-Structural Systems

In order to demonstrate the feasibility of the proposed methodology for monitoring large civil-structures, the data recorded during the destructive load test on a prototype reinforced concrete (RC) bridge was utilized. The test bridge consisted of two spans of about 5m, instrumented with several PZT patches of size 10 mm×10 mm × 0.2 mm and grade PIC 151 (PI Ceramic, 2003). The bridge was subjected to three load cycles in order to induce damages of increasing severity. Details of the instrumentation as well as loading can be found in Bhalla (2001) and Soh *et al.* (2000). RMSD index was used to evaluate the damages. This section uses the approach based on extracted impedances to carry out damage assessment.

Fig. 4.14 shows a view of the top surface of the bridge deck after subjecting it to a maximum load of 40 kN during the first cycle. The PZT patches detected the presence of surface cracks much earlier than the global condition indicators, such as the load-deflection curve (Soh *et al.*, 2000). Patch 4 (Fig. 4.14) was selected as a representative PZT in the present analysis. Fig. 4.15 shows the impedance spectra of the pristine structure as identified by Patch 4 in the frequency range 120 – 145 kHz. This figure shows that the PZT patch has “identified” the structure as a parallel spring-damper combination (*Kelvin-Voigt* system); the average identified parameters being $k=9.76\times 10^7$ N/m and $c=26.1823$ N·s/m. The equivalent parameters were also determined for the damaged bridge after one more cycle, subjecting the bridge to a load of 64 kN.

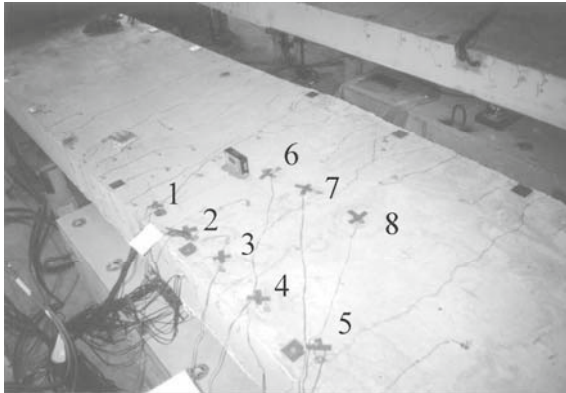


Fig. 4.14 Damage diagnosis of a prototype RC bridge using proposed methodology

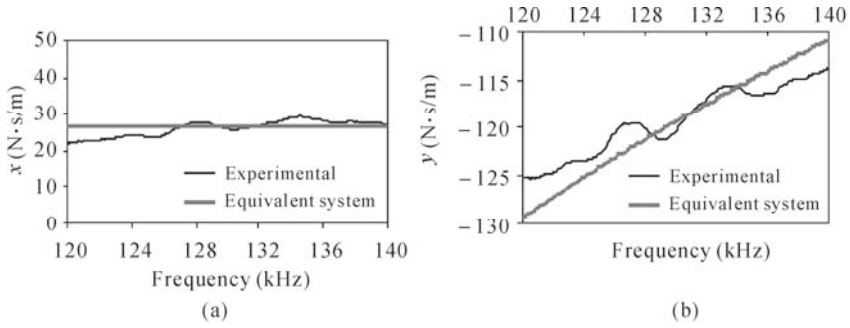


Fig. 4.15 Mechanical impedance of RC bridge in 120 – 140 kHz frequency range. (a) Real part, x , vs. frequency; (b) Imaginary part, y , vs. frequency

The associated damage mechanism can be observed from Fig. 4.16: k tends to reduce and c to increase with damage progression. Reduction in the stiffness and increase in the damping are well known phenomena associated with crack development in concrete. Damping increased by about 20% after cycle I and about 33% after cycle II. This correlated well with the appearance of cracks in the vicinity of this patch after cycles I and II. After cycle II, stiffness was found to reduce marginally by about 3%, indicating the higher sensitivity of damping to damage compared with stiffness.

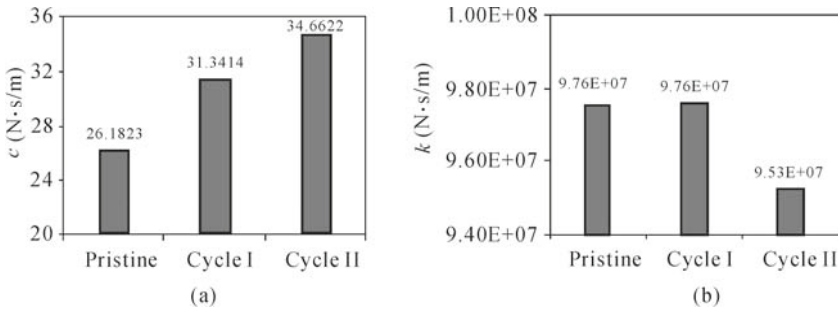


Fig. 4.16 Effect of damage on equivalent system parameters of RC bridge. (a) Equivalent damping constant; (b) Equivalent spring constant

Thus, the proposed methodology can be easily extended to large civil-structures as well. However, it should be noted that owing to the large size of typical civil-structures, the patch can only “identify” a localized region of the structure, frequently representative of the zone of influence of the patch. For large structures, complete monitoring warrants an array of PZT patches. The patches can be monitored on a one-to-one basis and can effectively localize as well as evaluate the extent of damages. The next chapter will present how the identified system parameters can be calibrated with extent of damage for concrete.

This section has presented a diagnostic approach for the identification and NDE of structures based on the equivalent system “identified” by means of the

EMI technique. It makes use of the real as well as the imaginary components of the admittance signature for determining damage sensitive equivalent structural parameters. In order to make full use of the proposed methodology, it is necessary to calibrate the identified system parameters with damage progression. This could serve as an empirical phenomenological model for the component concerned. The piezo-impedance transducers can be installed on inaccessible parts of crucial machine components, an aircraft's main landing-gear fitting or turbo-engine blades, reinforced carbon-carbon panels of space shuttles and civil structures to perform continuous real-time SHM. The equivalent system (the structural model) is identified from the experimental data alone. No analytical/numerical model is required as a prerequisite. The approach is not only simple to apply but also provides an essence of the associated damage mechanism. In addition to NDE, the proposed model can be employed in numerous other applications, such as predicting a system's response, energy conversion efficiency and system power consumption.

4.5 Identification of Higher Modal Frequencies from Conductance Signatures

In this part of the chapter, the changes in natural frequencies for higher modes (identified from conductance signatures) and the corresponding mode shapes of the undamaged structure are used to locate damage. This method, proposed by Naidu and Soh (2004a, 2004b), only requires the information of natural frequency changes of the damaged structure and the mode shapes of the undamaged structure. Natural frequency shifts for higher modes can be found experimentally from the peak frequency changes in the conductance signatures of PZT transducers bonded on to the host structure. To experimentally estimate the higher mode shapes would require a large number of sensors, which is often not practical. Therefore, this method circumvents this difficulty using only the undamaged state mode shapes of the structure, from a "well-refined" finite element (FE) model.

Let the natural frequencies (in Hz) and mode shape vectors of the host structure be

$$\{f\} = \{f_1, f_2, f_3, \dots, f_j, \dots, f_n\} \quad (4.29)$$

$$[\Phi] = [\{\phi_1\}, \{\phi_2\}, \{\phi_3\}, \dots, \{\phi_j\}, \dots, \{\phi_n\}] \quad (4.30)$$

Let damage be introduced in one of the elements, resulting in frequency shifts as given by

$$\{\Delta f\} = \{\Delta f_1, \Delta f_2, \Delta f_3, \dots, \Delta f_j, \dots, \Delta f_n\} \quad (4.31)$$

Additionally, a function, $\text{Max} [\{\Delta f\}, m]$ is defined such that from the set $\{\Delta f\}$, it chooses a subset of highest m natural frequency changes, in descending order, that is

$$\{\Delta f\}^m = \text{Max} [\{\Delta f\}, m] = \{\Delta f^1, \Delta f^2, \Delta f^3, \dots, \Delta f^i, \dots, \Delta f^m\} \quad (4.32)$$

The superscript, i ($i = 1$ to m) is the i^{th} entity of the set and does not denote power of the quantity. It should also be noted that

$$|\Delta f^1| > |\Delta f^2| > |\Delta f^3| > \dots > |\Delta f^i| > \dots > |\Delta f^m| \quad (4.33)$$

In general, $\Delta f^i > 0$ for all $i = 1$ to m . Also, the values of Δf^i are usually larger for the higher modes compared with the lower modes. For example, the frequency shifts of modes between 21 and 25 will most likely be larger than the frequency shifts of modes 1 – 5. However, when comparing consecutive modes, *e.g.*, the 21st – 25th, depending on the location of the damage, a lower mode, *e.g.*, the 22nd, may have a larger frequency shift value than a higher mode, *e.g.*, the 25th. Corresponding to the frequencies in Eq. (4.33), the mode shapes for the undamaged structure are chosen from Eq. (4.30) and are similarly ordered as

$$[\Phi]^m = [\{\phi\}^1, \{\phi\}^2, \{\phi\}^3, \dots, \{\phi\}^i, \dots, \{\phi\}^m]. \quad (4.34)$$

The mode shape vectors can be split into their individual translation and rotational components, in the way most FE packages provide, as:

$$[\Phi_x]^m = [\{\phi_x\}^1, \{\phi_x\}^2, \{\phi_x\}^3, \dots, \{\phi_x\}^i, \dots, \{\phi_x\}^m] \quad (4.35a)$$

$$[\Phi_y]^m = [\{\phi_y\}^1, \{\phi_y\}^2, \{\phi_y\}^3, \dots, \{\phi_y\}^i, \dots, \{\phi_y\}^m] \quad (4.35b)$$

$$[\Phi_r]^m = [\{\phi_r\}^1, \{\phi_r\}^2, \{\phi_r\}^3, \dots, \{\phi_r\}^i, \dots, \{\phi_r\}^m] \quad (4.35c)$$

where the subscripts x , y and r represent the x component, the y component and the rotational component, respectively.

Next, the element deformation parameter, $\{\Delta E\}$, for each element is determined from the above mode shape vectors as

$$\{\Delta E_x\}^i = \{\Delta E_{1x} \ \Delta E_{2x} \ \dots \ \Delta E_{px} \ \dots \ \Delta E_{n_e x}\} \quad (4.36a)$$

$$\{\Delta E_y\}^i = \{\Delta E_{1y} \ \Delta E_{2y} \ \dots \ \Delta E_{py} \ \dots \ \Delta E_{n_e y}\} \quad (4.36b)$$

$$\{\Delta E_r\}^i = \{\Delta E_{1r} \ \Delta E_{2r} \ \dots \ \Delta E_{pr} \ \dots \ \Delta E_{n_e r}\} \quad (4.36c)$$

where the subscript, p , is the element number ranging from 1 to n_e (n_e is the total

number of elements in the FE model). $\{\Delta E_x\}^i$ refers to the longitudinal deformations of the elements in the longitudinal vibration mode. Similarly, $\{\Delta E_y\}^i$ and $\{\Delta E_r\}^i$ respectively refer to the average curvatures and effective rotation of the elements in the bending vibration mode. The superscript, i , is the indicator of the mode number. For example, consider beam element number 3, which has two nodes numbered 3 and 4: the element deformation parameters are evaluated as

$\{\Delta E_{3x}\}^i =$ longitudinal displacement of node 4 for mode i – longitudinal displacement of node 3 for mode i .

$\{\Delta E_{3y}\}^i = \frac{1}{2} \times$ {curvature value of node 3 for mode i + curvature value of node 4 for mode i }.

$\{\Delta E_{3r}\}^i =$ rotation of node 4 for mode i – rotation of node 3 for mode i .

The values of the longitudinal displacements, curvature and rotation for the nodes are obtained from the mode shape vectors, $\{\phi_x\}^i$, $\{\phi_y\}^i$ and $\{\phi_r\}^i$ from Eq. (4.35). For the longitudinal mode, the greater the elongation of the element, the larger the frequency shift for that particular mode. Similarly, for bending modes, the greater the curvature of the element, the larger the frequency shift for that mode. Curvature of the beam element is the second derivative of the elastic curve or displacement profile. Thus, by twice differentiating the mode shape vector, $\{\phi_y\}^i$, the mode shape curvature vector can be obtained. This differentiation can be performed numerically using the central difference approximation (Salawu and Williams, 1994). The damage indicator or damage metric, DI , for each element is defined as:

$$DI_p^x = \frac{\sum_{i=1}^m |\Delta E_{px}^i| \Delta f^i}{\sum_{i=1}^m \Delta f^i} \times 100 \tag{4.37a}$$

$$DI_p^y = \frac{\sum_{i=1}^m |\Delta E_{py}^i| \Delta f^i}{\sum_{i=1}^m \Delta f^i} \times 100 \tag{4.37b}$$

$$DI_p^r = \frac{\sum_{i=1}^m |\Delta E_{pr}^i| \Delta f^i}{\sum_{i=1}^m \Delta f^i} \times 100 \tag{4.37c}$$

where the index p is the element number and i is one of the chosen mode shapes. The damage indicator for an element is the weighted average of the element

deformation parameters, ΔE , over the chosen m modes, which have the largest frequency changes. The damaged element is identified as that which has the maximum value of the damage metric DI .

An associated question with this approach is that if the mode shapes change after damage, how can the undamaged state mode shapes be used for identifying the damage location? To answer this question the following is considered. For any particular longitudinal or bending mode shape, there are elements with almost zero deformation or zero average curvature values. If one such element is damaged, the corresponding mode shape of the damaged beam will not change much compared with the undamaged beam (Farrar and Jauregui, 1998). On the other hand, if the damaged element has a non-zero deformation or average curvature for that particular mode, the damaged state mode shape only changes near the location of the damage (Salawu and Williams, 1994). It is readily deducible that such an element will necessarily have significant deformation (in longitudinal mode) or average curvature value (in bending mode) even in the mode shape of the undamaged state; otherwise, frequency reductions for that mode would not be observed. The proposed damage identification method automatically considers such an element as one of the probable damaged elements. Thus, the information about changes of the mode shapes is not considered necessary. As for accuracy, it may also be noted that since the mode shape changes are very small after damage (Farrar and Jauregui, 1998), the undamaged state mode shapes from the FE model will be accurate for identification of incipient damages. Mode shapes of the damaged structure will significantly change only in the cases when the damage is severe enough, for example, if one or more of the following conditions occur:

(a) Stiffness of the whole structure is altered, which means that the crack or the damage has propagated throughout the structure.

(b) Boundary conditions are altered, such as some support constraints being released.

(c) The region around the damage zone crosses the yield limit and plastic collapse mechanism begins to occur.

In such cases, using undamaged mode shapes for damage location identification will certainly be erroneous. However, since the main interest of health monitoring systems using smart sensors is to detect and locate damages at its incipient stage so as to take preventive measures against future catastrophe, the use of undamaged mode shapes will suffice. The most important requirement for accuracy is that the FE model should correctly represent the structure's dynamic characteristics. This can be ensured by comparing the natural frequencies of the FE model with the natural frequencies of the test structure from the conductance signatures. In real-life situations, if the frequencies from the model and the actual structure do not match, the FE model can be updated to match the actual structure using the well known model updating techniques (Doebbling *et al.*, 1998; Xia, 2002).

In general, in order to derive accurate mode shapes using the FEM, there should be at least five nodes (or four elements) per half wavelength. For mesh densities of two to four elements per half wavelength, somewhat distorted mode

shapes will be obtained. Below the density of two elements per half wavelength, the distortions in mode shapes are severe. Thus, if the mode shape of mode n is to be predicted accurately by the FE model, the minimum number of elements should be $4n$. This was proven by Naidu and Soh (2004a) using numerical examples.

4.6 Numerical Example

Consider a 60 element FE model of an aluminium beam of length 300 mm, width 20 mm and depth 2 mm, as shown in Fig. 4.17. The support conditions are assumed to be pin-pin at both ends. The material properties considered are: Young's modulus 6.9×10^{10} N/m², density 2,600 kg/m³ and Poisson's ratio 0.33. Since the pin-ended beam is symmetric in geometry about its centre, all the mode shapes are either symmetric or anti-symmetric. Hence, the element deformations and average curvature values are equal in magnitude for the elements located symmetrically about the centre of the beam. As such, equal damage metric values are expected for the elements located symmetrically. Therefore, in all the results to follow, only half of the elements of the beam are shown.

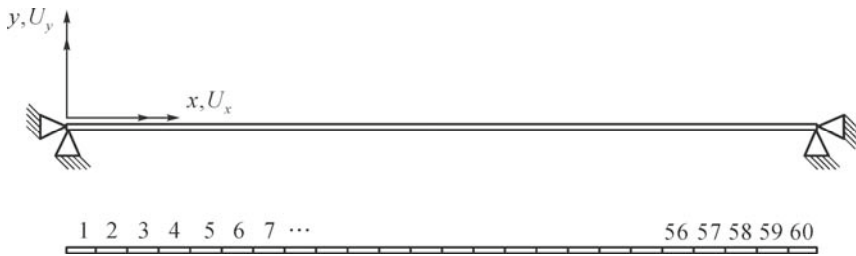


Fig. 4.17 Numerical model of pin-pin supported beam for illustration of damage detection algorithm of Naidu and Soh (2004a)

In the damage identification method, only the maximal deformations and average curvatures are considered for the few chosen “sensitive modes”, *i.e.*, the modes that have large frequency shifts. As such, all the elements will necessarily have non-zero damage metric values. From the mode shapes that are unity normalized, it is estimated that for the first mode shape, at least two-thirds of the length has displacement values greater than 0.5. In fact, most of the elements are likely to display damage metric values of about 66.67%, when several sensitive modes are considered. Therefore, for an element to be considered as the probable damaged element, a minimum damage metric value of 70% is chosen as the threshold value. In all the results to follow, the damage metric values are illustrated from 70% to 100%. It should be noted that the determination of damage location is based on the largest damage metric. A non-zero damage metric value for an element does not necessarily mean it is damaged.

Figs. 4.18 and 4.19 present the damage metric values for the 60 element beam, evaluated using the bending modes and the longitudinal modes, respectively, for various damage locations. Damage was simulated by reducing the Young's modulus of elasticity by 20% in one element at a time. Figs. 4.18(a), (b) and (c) correspond to damage in Elements 31, 44 and 50 respectively. In all the cases, the frequency shifts are only considered up to the first ten modes, and of these, four sensitive modes are chosen. In all three damage cases, the elements near the end supports show the largest damage metric values. If these are ignored, the elements at the correct damage locations (*i.e.*, Elements 31, 44 and 50) will have the highest damage metrics, and hence be correctly identified.

The reason for this error at the edges is investigated as follows. In all of the modes, it is observed that at least one of the nodes of Element 58 has a high or even maximum value of curvature. This is unlike the elements in the mid-span. For example, if we consider the mid-span node, for every anti-symmetric mode, the displacement is zero in the mode shape, which means it is a vibration nodal point. Furthermore, the curvature value is zero at that point. When average curvature is computed for the elements on either side of this mid-span node, it is again very small. Thus, every anti-symmetric mode will yield somewhat low average curvature values around the mid-span. But in the case of Element 58, for almost every mode, the average curvature value is high. Since the damage metrics are based on average curvature, when bending modes are considered, invariably one such element near the edge will have a high damage metric value, whether the element is damaged or not.

The longitudinal modes are now considered. In the longitudinal mode shapes, the same magnitudes of nodal displacements are present in the longitudinal direction (U_x) as in the lateral direction for the bending mode shapes. It is observed that the node next to the end support always has significant displacement. It will never be zero, like the nodes in the middle span of the beam for some modes. So, it can be concluded that the end element in the longitudinal mode shapes will definitely have non-zero or even the highest value for deformation (relative displacement of nodes). Since the damage metrics are based on deformation values for longitudinal modes, invariably the element next to the edge will have large damage metric values, whether or not the element is damaged.

This limitation of obtaining erroneous damage predictions at the edges is because we did not use the change in mode shapes as a damage indicator; rather, we used the undamaged mode shapes as they were. Even for refined meshes, this difficulty cannot be overcome since there would be some elements close to the boundary displaying the same phenomenon. Hence, a corrective reduction factor is introduced at the edges to circumvent this inherent error at the boundaries. The probability that the elements near the edges have deformation and average curvature parameters greater than the threshold value of 0.7 is evaluated using the chosen mode shape vectors shown in Eq. (4.34). The probability is found to be about 90% – 100%, which means for the elements near the edges, 9 or 10 out of every 10 mode shapes have deformation and curvature values greater than the

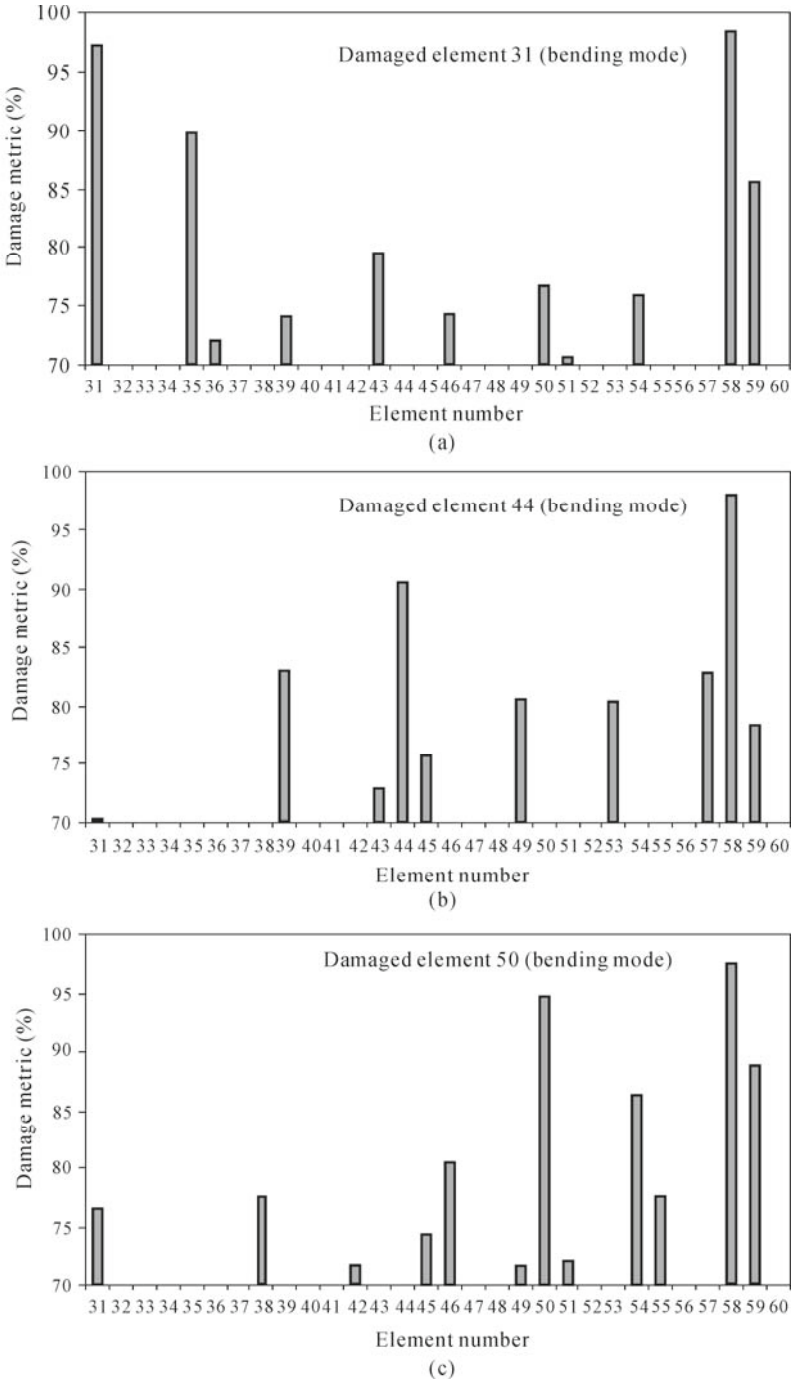


Fig. 4.18 Damage metric values for elements of the 60-element beam using bending modes—for 20% stiffness reduction introduced in: (a) Element 31; (b) Element 44; (c) Element 50

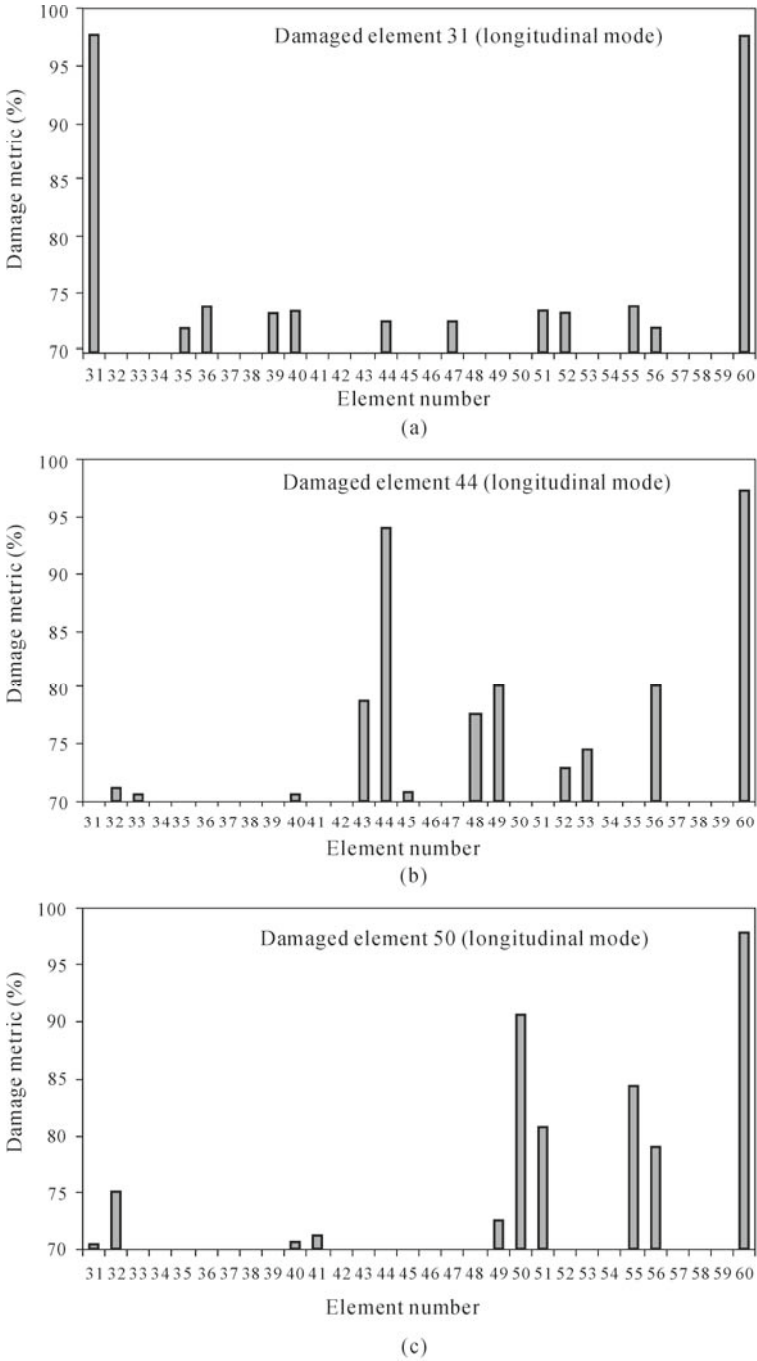


Fig. 4.19 Damage metric values for elements of the 60-element beam using longitudinal modes—for 20% stiffness reduction introduced in: (a) Element 31; (b) Element 44; (c) Element 50

threshold. For the elements in the rest of the span, these probabilities are between 40% to 60%. Thus, the probabilities of elements at the edges are corrected to be on a par with the other elements. Therefore, in all the results that followed, this correction factor at the edges is included.

In order to study the case of damage in two adjacent elements, 20% stiffness is simultaneously reduced in Elements 49 and 50. The damage metric values are evaluated using the bending and longitudinal mode shapes, and are presented in Fig. 4.20. The damage locations are correctly identified, as the damage metric values of Elements 49 and 50 have the largest magnitudes. Thus, if the size of the damage is greater than the element size, the location can still be accurately detected. However, it is also found that the location can only be accurately detected up to three or four consecutive damaged elements. It was found that when more than 4 consecutive elements are simultaneously damaged, the locations cannot be accurately identified.

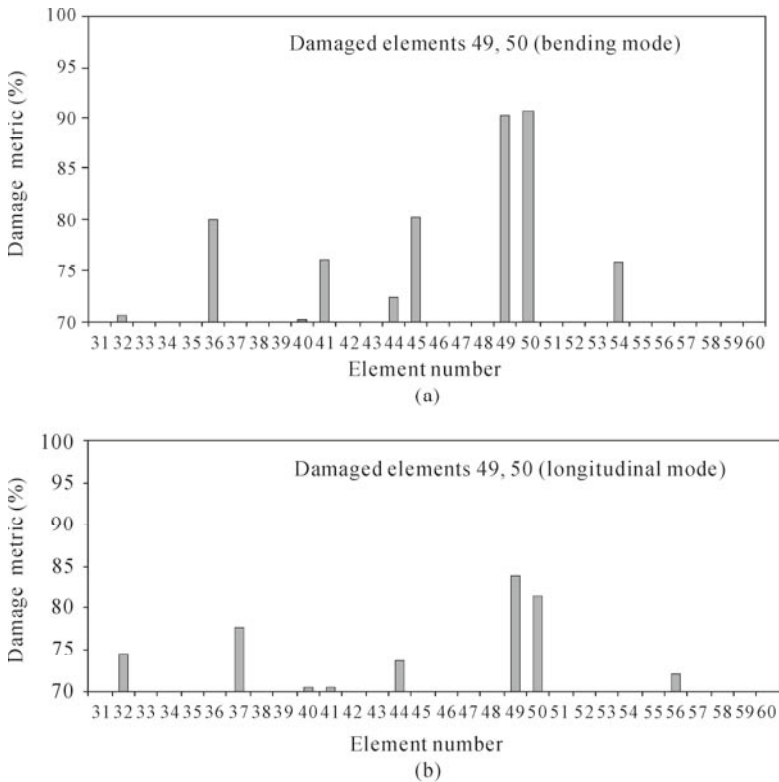


Fig 4.20 Damage metric values for damage in Elements 49 and 50 using: (a) bending modes; (b) longitudinal modes

4.7 Experimental Verification

This section presents the experimental verification of the damage detection algorithm introduced in the preceding sections. The setup for the data acquisition system, consisting of an impedance analyzer, a multiplexer and a personal computer, is shown in Fig. 4.21. For the experimental verification, the aluminium beams were chosen to have the same geometric and material properties as the FE model of Fig. 4.17. In the test, the beams were excited in pure bending by out-of-phase excitation of two PZT transducers bonded to the top and bottom surfaces of the specimen. Three aluminium beams of the same dimensions were tested. Two PZT transducers were bonded on each beam as follows (Fig. 4.22):

- (1) **Specimen-1:** At the mid-span of the beam; damage was induced by drilling a 5 mm diameter hole at 50 mm distance from the edge.
- (2) **Specimen-2:** At 90 mm distance from one edge of beam; a 5 mm diameter hole was drilled at 50 mm distance from the other edge.
- (3) **Specimen-3:** At 90 mm distance from one edge of beam; a 5 mm diameter hole was drilled at 80 mm from the other edge.

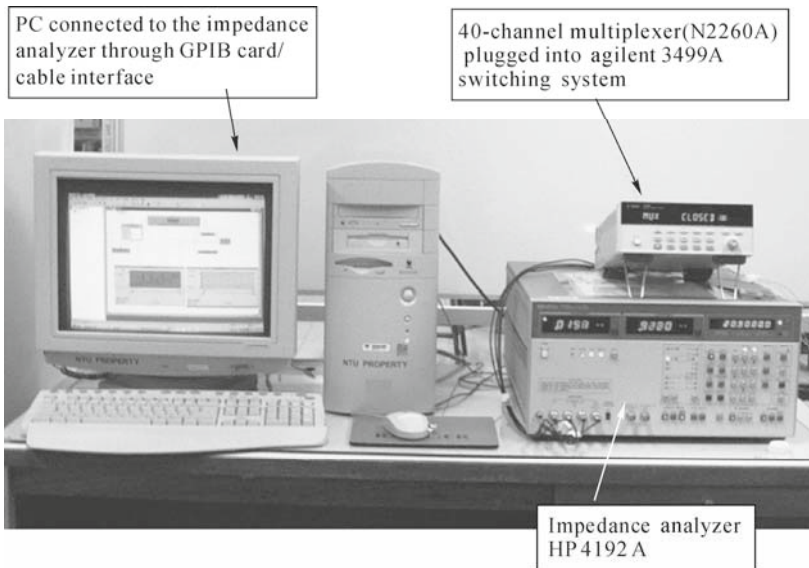


Fig. 4.21 Set-up of the impedance data acquisition system

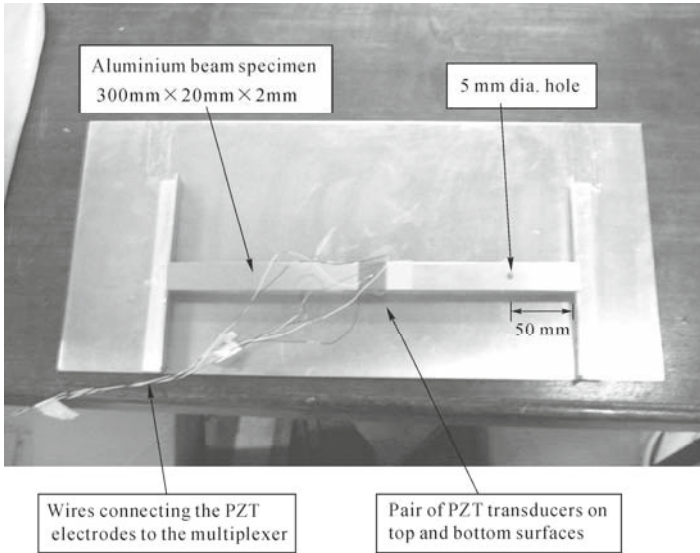


Fig. 4.22 Simply-supported aluminium beam specimen bonded with PZT transducers

For Specimen-1 and Specimen-2, the hole 50 mm from the edge corresponded to Element 50 in the 60-element beam mesh. For Specimen-3, the hole 80 mm from the edge corresponded to Element 44. For each specimen, before and after drilling the hole, the PZT transducers were excited in the bending mode and the admittance signatures were acquired. The frequency shifts in the peaks of the damaged state signatures were noted, and the corresponding modes in the FE model were identified. Using the mode shapes from the FE modal analysis and the natural frequency shifts obtained experimentally, the damage location was determined using the proposed method.

The pin-ended boundary conditions were ensured by supporting the ends of the beam on thin metallic edges. A pin-ended support has both horizontal and vertical movements constrained at the edges of the beam, and the rotation unconstrained. To achieve these conditions, the edges were lightly bonded to the supports using cello tape, running from the top surface of the beam to the supporting metallic edge. The horizontal or longitudinal movements were not fully restrained by this arrangement, which is confirmed by a few unidentified or erroneous peaks in the admittance signatures of the transducers for longitudinal modes. But, for pure bending excitation of the beam, since the amplitude of the longitudinal motion was very small, lack of proper constraints at the boundary did not significantly affect the bending modes. However, the vertical movements were effectively restrained and free rotation was also allowed, which was evident by obtaining the natural frequencies with reasonable accuracy (Table 4.2).

The chosen frequency range for acquiring the signatures was 1 – 60 kHz. Beginning from mode number 5, approximately 30 bending modes were expected in this range. The first 20 natural frequencies obtained experimentally for the

undamaged beam specimens in bending mode are presented in Table 4.2. For Specimen-1, the PZT transducers were bonded at the midpoint of the beam, where, for every alternative mode, there was a vibration nodal point. Therefore, only alternate resonant peaks were observed in the conductance signature. For the other two specimens, the PZT patches were placed 90 mm from one of the edges. As such, most of the natural frequencies of the beam, correspondingly, had peaks in the conductance signatures. There was some discrepancy in mode 17, where one specimen showed no peak, while the other showed a resonant peak. Other than this, the modes were clearly identifiable and were fairly accurate. Fig. 4.23 shows the conductance signatures for Specimen-1 in the bending mode, which can be correlated with Table 4.2. The shifts in the resonant frequencies after damage are also clearly shown.

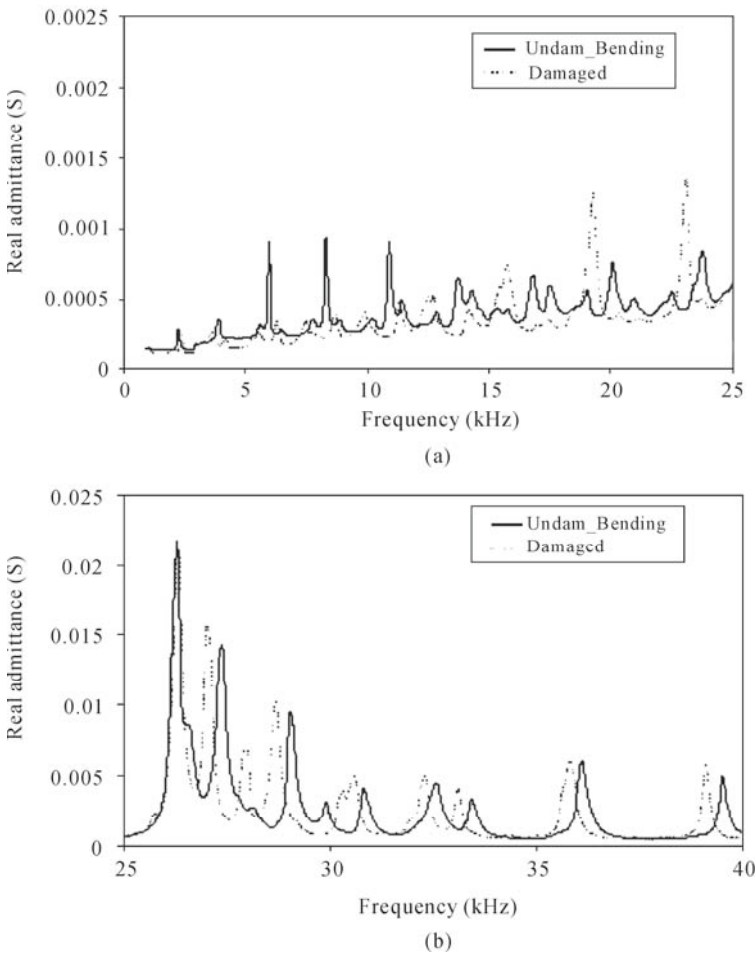


Fig. 4.23 Conductance signatures for Specimen 1: (a) bending mode, 1 – 20 kHz; (b) bending mode, 20 – 40 kHz

Table 4.2 Natural frequencies obtained experimentally for the undamaged beam specimens (bending mode)

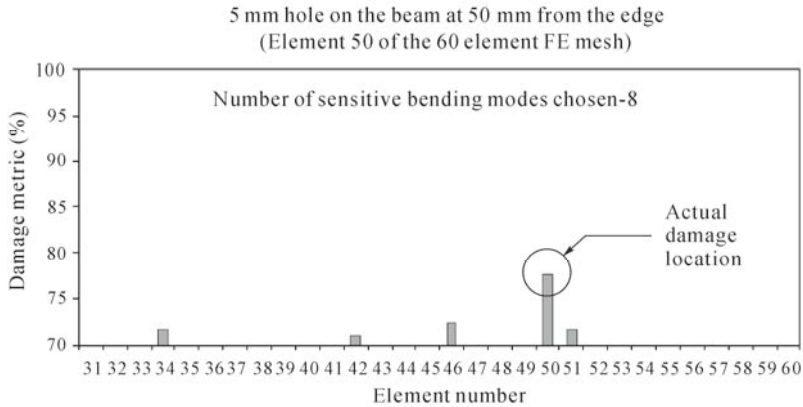
Bending mode no.	Natural frequency			
	Analytical (kHz)	Experiment		
		Specimen 1 (kHz)	Specimen 2 (kHz)	Specimen 3 (kHz)
1	0.052	—	—	—
2	0.207	—	—	—
3	0.467	—	—	—
4	0.830	—	—	—
5	1.297	1.240	1.400	1.355
6	1.867	***	2.000	1.955
7	2.542	2.420	***	***
8	3.320	***	3.400	3.310
9	4.202	4.050	4.300	4.220
10	5.187	***	5.290	5.175
11	6.277	6.030	6.300	6.225
12	7.470	***	7.520	7.435
13	8.767	8.430	8.800	8.545
14	10.167	***	10.100	10.690
15	11.671	11.000	11.600	11.350
16	13.279	***	13.200	13.510
17	14.991	13.950	***	14.400
18	16.807	***	16.600	16.685
19	18.726	16.900	18.400	18.420
20	20.749	***	20.300	19.120

Note: “—” and “***” Both essentially mean that “No experimental data”.

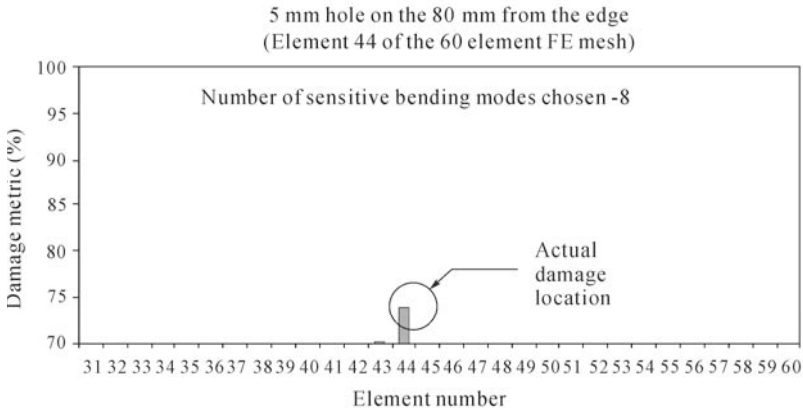
4.7.1 Damage Location Identification

The natural frequency shifts obtained experimentally and the corresponding mode shapes obtained numerically were then input into the proposed damage identification method. As only a few natural frequency shifts were obtained for Specimen-1 because of alternatively missing peaks in the conductance signature, the damage was not successfully located. It was also observed from this test that accuracy of the method is dependent on where the PZT transducers are bonded on the beam. Ideally, the transducers should be bonded where most of the frequency peaks can be captured.

Figs. 4.24(a) and (b) show the results for Specimens 2 and 3, respectively, obtained using the 60-element beam mesh. From the range of modes 5 to 15 (*i.e.*, between 1 – 12 kHz), 8 sensitive modes (*i.e.*, modes with largest frequency shifts) were selected. The damages in both specimens were located accurately.



(a)



(b)

Fig. 4.24 Damage metric values using bending modes of 60-element beam: (a) Specimen-2; (b) Specimen-3

4.7.2 Effect of Number of Sensitive Modes

For Specimen-3, using the 60-element mesh, the number of sensitive modes chosen was varied from 4 to 7. Fig. 4.25 shows the plots of the damage metric values for the elements. It should also be noted that the preceding Fig. 4.24(b) shows the result for the same specimen with 8 sensitive modes. It can thus be seen that when fewer sensitive modes are chosen, the damage metric values are higher. However, other than the actual location (Element 44), a number of other non-damaged elements also have large damage metric values above the threshold. With increase in the sensitive modes, the damage metric values decrease; but, the actual damage location becomes more distinguishable as the values for the other

non-damaged locations reduce considerably. The decrease in damage metric values is due to the weighted average of the element average-curvature value from a large number of modes. When a large number of modes is included, in several mode shapes, the element curvature value will be small, which contributes to the decrease in the weighted average. Finally, with 8 sensitive modes, this phenomenon can be clearly observed in Fig. 4.24(b). Thus, with the increase in the number of sensitive modes the damage location identification becomes clearer.

4.7.3 Effect of Frequency Range

Using the same 60-element mesh, 8 sensitive modes were chosen; the frequency range for these 8 sensitive modes was then varied. Specimen-2 was considered, with the damage located at Element 50. Figs. 4.26(a), (b) and (c) show the results for frequency ranges 1 – 12 kHz (5 – 15 modes), 1 – 35 kHz (5 – 25 modes) and 1– 50 kHz (5 – 30 modes), respectively. It was earlier noted that to obtain “ n ” accurate mode shapes using an FE mesh, the minimum number of elements required is $4n$. If the elements chosen are between $2n$ and $4n$, the distortion of mode shapes is not severe; but, if the number of elements is less than $2n$, the distortion in the mode shapes can be severe.

Thus, while choosing a 60-element mesh, the first 15 mode shapes would be accurate; between 15 to 30 modes, the distortion in the mode shapes (compared with the analytical solution) exists but is not severe. However, the mode shapes near and beyond the 30th mode would be severely distorted. Therefore, the choice of frequency range from which the resonant frequency shifts are evaluated will affect the results, and this is illustrated in Fig. 4.26, which also shows that when only the first 15 modes were used (which are correctly predicted by the FE model), the damage location is clearly distinguishable. In Fig. 4.26(b), the correct damage location was identified, but there are many other elements having almost equal damage metric values. This is because the modes between 16 and 25 were used, which were not quite accurately predicted by the FE model. However, when the frequency range was such that most of the modes were not accurately predicted by the 60-element mesh, the damage location was not identifiable (Fig.4.26(c)). This implies that the FE model needs to be accurate at least within the chosen frequency range. Conversely, for a chosen FE mesh, the frequency range for extracting the impedance signatures has to be within the accuracy of the FE model, to achieve satisfactory damage identification.

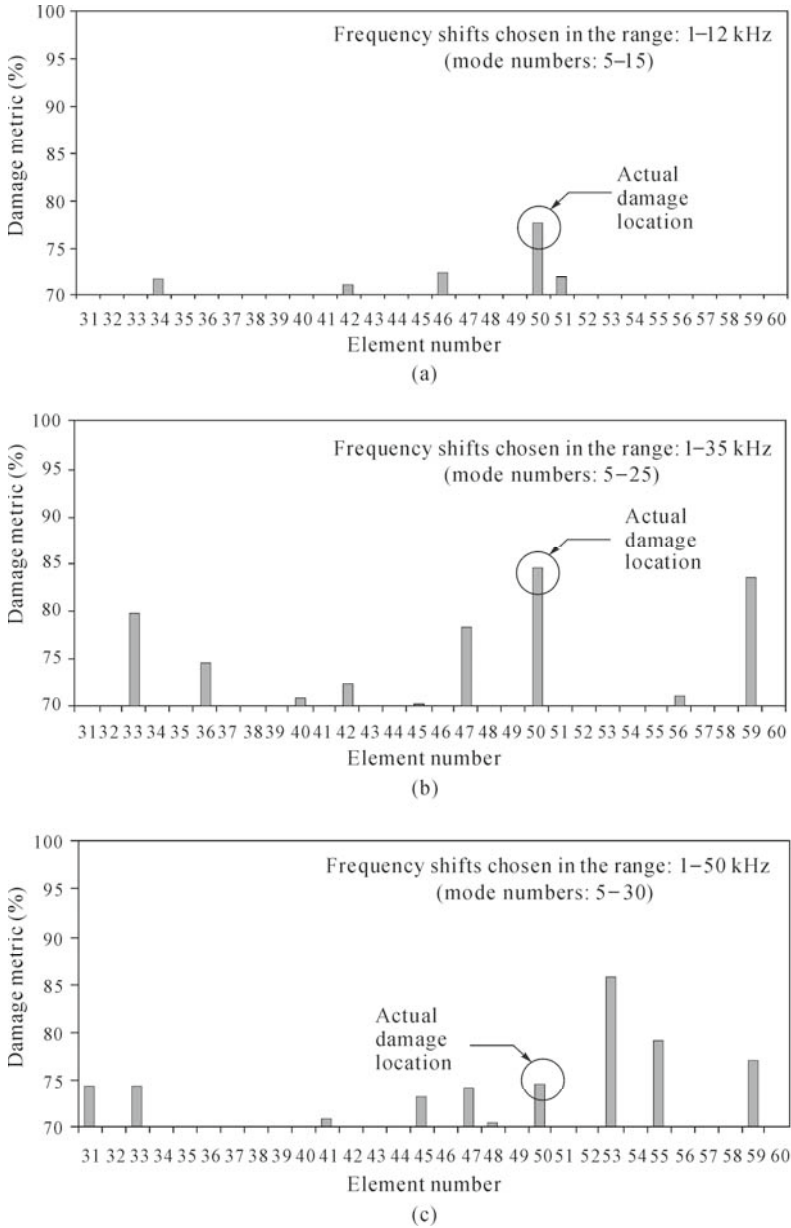


Fig. 4.26 Damage metric values using the 60-element mesh for Specimen-2: (a) for modes 5 – 15; (b) for modes 5 – 25; (c) for modes 5 – 30

4.8 Advantages of Modal Approach

The modal damage location identification method has the following advantages:

(1) A single PZT transducer or a transducer pair is sufficient to locate the damages in small structures, or structural members, with homogenous materials. This method can be exploited for economical health monitoring of structures such as trusses and can be further developed for monitoring aircraft wings and railway tracks.

(2) The knowledge of mode shape changes for the damaged structure is not required. This significantly reduces the experimental complexity involved in extracting mode shapes using the conventional methods.

(3) PZT transducers, being light-weight and non-intrusive to the structures, do not significantly affect the natural frequencies of the system, as was observed from the experimental results.

(4) The mesh refinement requirements for the successful working of the damage detection technique are not stringent. Without requiring highly refined meshes, accurate solutions can be obtained for even reasonably small-sized FE meshes.

(5) Clearly, the sensitivity of the method to incipient damages is high on account of its operation in the higher frequency range. This method can be used where the conventional vibration-based methods fail.

4.9 Limitations and Concerns of Modal Approach

Despite its advantages, for more effective damage identification with the proposed method, the following limitations and concerns need to be considered:

(1) For symmetric structures, the damage location identification is not unique. This is because only frequency changes are considered, which are not spatially specific. Nonetheless, this problem is not likely to occur in non-symmetric structures.

(2) The limitation of using only the undamaged state mode shapes is that, for most of the modes, the element deformations (in longitudinal mode) and average-curvature (in bending mode) at the edges have large values. For refined FE meshes, this gives an erroneous damage prediction at the edges, even when there is no damage. If the damage identification were to be based on changes in mode shapes, this problem would not occur. But to determine the mode shape changes for such high frequencies is not practically feasible using conventional sensors. A sophisticated instrument like the Scanning Doppler Laser Vibrometer (SDLV) can accurately measure mode shapes at high frequencies (Winston *et al.*, 2001). Therefore, in the proposed method, correction factors need to be assigned to the elements at the edges in order to make their damage probability on a par with the other elements. This correction of modal error at the edges can also be effectively

tackled by a knowledge-based reasoning network (Naidu *et al.*, 2006)

(3) Accurate FE models can easily be obtained for structures with homogeneous material properties and regular geometries. However, for complex structures and those with non-homogeneous materials like concrete, where accurate FE models are difficult to derive, application of the method can be difficult. Meaningful application of the method is restricted to structures which have accurate FE models.

4.10 Damage Identification Using EMI and Evolutionary Programming

The previous study mainly focused on high frequency (typically higher than 30 kHz) to ensure high sensitivity to incipient damage. However, at such a high frequency, system identification techniques are difficult, if not impossible, to apply because of the necessity of repeated structural analysis, which is time consuming. Thus, the damage was previously assessed by a damage index, which is statistically calculated by comparing the amplitudes of the two spectra (damaged vs. pristine). RMSD, mean absolute percentage deviation, covariance change and correlation coefficient deviation have been used as damage indices (as outlined in Chapter 2). However, it is not enough to use these overall-statistics damage indices for damage assessment, *i.e.*, it is not possible to locate and quantify the damage simultaneously, since a severe damage far from the measured point and a minor damage close to the point could have the same damage index. Moreover, values of various criteria may need to be determined to predict the failure for different structures.

This section applies the EMI-based SHM technique at relatively lower frequency so that precise structural analysis is possible. In addition, the system identification techniques can be more conveniently employed to simultaneously locate and quantify the damage. The EMI spectra were predicted using the generic model presented by Yang *et al.* (2005), and the vibration of the damaged structure was analyzed using the Ritz method. Acceptable matches with minor differences between the predictions and measurements were obtained. The differences were caused by the inaccuracy in representing the real structure using the Ritz method-based numerical model. Owing to the sensitivity of the back-calculated results to the input data, such minor differences will affect the final results. A special fitness function was therefore designed to further reduce the effect of these differences, which are unavoidable no matter what analytical or numerical model is used.

Another difficulty of using system identification techniques is that there are many local optima existing in the search space. The traditional optimization techniques may not be able to find the global optimum effectively. Thus, a hybrid evolutionary programming was employed in our method as a global search technique to identify the damage.

4.11 EMI of PZT Transducers

Yang *et al.* (2005) analyzed the in-plane vibration of 1D and 2D PZT patches (Figs. 4.27 and 4.28). All the boundaries of the PZT patches are assumed to be bonded to the host structure. By representing the effect of the structure with mechanical impedance at the corresponding points, the EMI of the PZT patches was calculated. The predicted results coincide well with the experimental measurements. The results are summarized as follows.

For the 1D model, the EM admittance Y is

$$Y = \frac{j\omega w}{h} \left\{ d_{31} \tilde{Y}_p^E \left[2\alpha' \tan \frac{k_p l}{2} - d_{31} l \right] + \tilde{\epsilon}_{33}^T l \right\} \quad (4.38)$$

where j symbolizes the imaginary part and ω the input angular frequency. The subscript p denotes the variables corresponding to the PZT transducer; l , w and h are the length, width and thickness, respectively; d_{31} is the strain coefficient; $\tilde{\epsilon}_{33}^T = \epsilon_{33}^T (1 - i\delta)$ is the complex dielectric permittivity at constant stress, with ϵ_{33}^T being the real dielectric permittivity and δ the dielectric loss factor. $\tilde{Y}_p^E = Y_p^E (1 + i\eta)$ is the complex Young's modulus at zero elastic field, with Y_p^E being the real Young's modulus and η being the mechanical loss factor. $k_p = \omega \sqrt{\rho_p / \tilde{Y}_p^E}$ is the wave number; ρ_p is the mass density; and the coefficient α' is calculated by

$$\alpha' = \frac{1}{k_p + \frac{Z_{str} j \omega \tan(k_p l / 2)}{\tilde{Y}_p^E w h}} d_{31} \quad (4.39)$$

where Z_{str} is the mechanical impedance of the structure (Fig. 4.27).

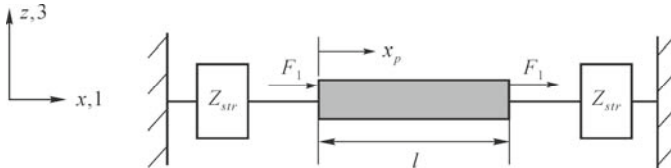


Fig. 4.27 Generic 1D structure-PZT interacting system

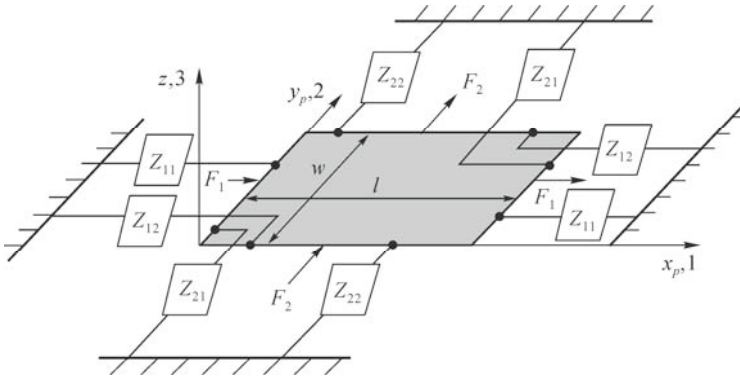


Fig. 4.28 Generic 2D structure-PZT interacting system

The force output of the PZT transducer is a pair of forces with the same amplitude but in opposite directions:

$$F_1 = \bar{F}_1 [\delta(x - x_1) - \delta(x - x_2)] \tag{4.40}$$

where x is the coordinate system established for the structure, and x_1 and x_2 are the coordinates of the PZT transducer (Fig. 4.29).

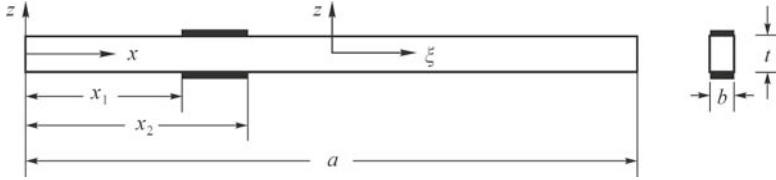


Fig. 4.29 Beam actuated by a pair of PZT patches

For the 2D model, the admittance is calculated as:

$$Y = \frac{j\omega}{h} \left\{ \frac{\tilde{Y}_p^E}{1 - \nu_p^2} \left[(d_{31} + \nu_p d_{32}) \left(2A'w \tan \frac{K_p l}{2} - d_{31} l w \right) + (\nu_p d_{31} + d_{32}) \left(2C'l \tan \frac{K_p w}{2} - d_{32} l w \right) \right] + \tilde{\epsilon}_{33}^T l w \right\} \tag{4.41}$$

where ν_p is the Poisson's ratio; d_{31} and d_{32} are the strain coefficients;

$K_p = \omega \sqrt{\frac{\rho_p (1 - \nu_p^2)}{\tilde{Y}_p^E}}$ is the spatial frequency of the oscillations; and the

coefficients A' and C' are calculated by:

$$\begin{Bmatrix} A' \\ C' \end{Bmatrix} = \mathbf{N}^{-1} \begin{Bmatrix} d_{31} \\ d_{32} \end{Bmatrix} \quad (4.42)$$

where

$$\mathbf{N} = \mathbf{I} - \frac{j\omega}{\tilde{Y}_p^E K_p h} \begin{bmatrix} \frac{Z_{11}}{w} - \nu_p \frac{Z_{21}}{l} & \frac{Z_{12}}{w} - \nu_p \frac{Z_{22}}{l} \\ -\nu_p \frac{Z_{11}}{w} + \frac{Z_{21}}{l} & -\nu_p \frac{Z_{12}}{w} + \frac{Z_{22}}{l} \end{bmatrix} \begin{bmatrix} -\tan\left(\frac{K_p l}{2}\right) & 0 \\ 0 & -\tan\left(\frac{K_p w}{2}\right) \end{bmatrix} \quad (4.43)$$

with Z_{11} and Z_{22} being the direct mechanical impedances, and Z_{12} and Z_{21} being the cross impedances of the structure (Fig. 4.28).

The output forces of the 2D PZT transducer can be described as:

$$\begin{aligned} F_1 &= \bar{F}_1 [\delta(x - x_1) - \delta(x - x_2)] \\ F_2 &= \bar{F}_2 [\delta(y - y_1) - \delta(y - y_2)] \end{aligned} \quad (4.44)$$

where x - y is the coordinate system established for the structure; and x_1, x_2, y_1 and y_2 are the coordinates of the PZT transducer (Fig. 4.30).

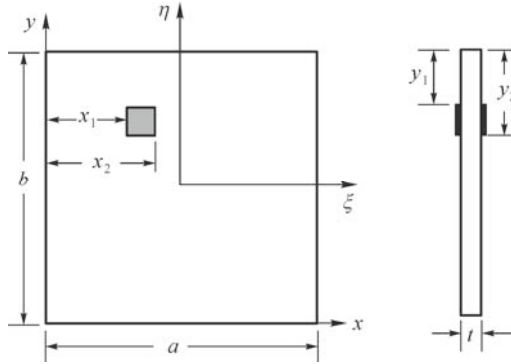


Fig. 4.30 Plate actuated by a pair of PZT patches

4.12 Mechanical Impedance of Damaged Structure

Eqs. (4.38) and (4.41) indicate that the EMI depends on both the properties of the

PZT transducer and the mechanical impedance of the structure. They are general expressions to predict the EMI for 1D and 2D cases since no restriction has been imposed on the host structure so far. In this section, for simplicity, beam and plate are selected to simulate 1D and 2D structures, respectively. The length, width and thickness of the structure are denoted as a , b and t , respectively.

Assume that two PZT patches are bonded to the beam and the plate, at the same location but on the opposite sides of the structure (Figs. 4.29 and 4.30), so that only bending vibration is actuated. The transverse displacement of the structure is denoted as w_s , and the rotation angles are described as

$$\beta_1 = -\frac{\partial w_s}{\partial x} \text{ and } \left\{ \begin{matrix} \beta_1 \\ \beta_2 \end{matrix} \right\} = \left\{ \begin{matrix} -\frac{\partial w_s}{\partial x} \\ -\frac{\partial w_s}{\partial y} \end{matrix} \right\} \quad (4.45)$$

for the beam and the plate, respectively. From Eqs. (4.40) and (4.44), the applied moment on the structure can be described as

$$M_1 = \bar{M}_1 [\delta(x-x_1) - \delta(x-x_2)] \text{ and } \left\{ \begin{matrix} M_1 = \bar{M}_1 [\delta(x-x_1) - \delta(x-x_2)] \\ M_2 = \bar{M}_2 [\delta(y-y_1) - \delta(y-y_2)] \end{matrix} \right\} \quad (4.46)$$

for the beam and the plate, respectively.

Yang *et al.* (2005) calculated the mechanical impedances of an undamaged beam and an undamaged plate using the p-version Ritz method. The p-version Ritz method is able to analyze plates with general shapes and boundary conditions. Moreover, using polynomial as the shape functions enables precise differentiation and integration processes, and enhances computational accuracy (Liew *et al.*, 1998). Thus, in this section, the p-version Ritz method is employed to analyze the vibration of both the beam and the plate with damages.

The damage can be simulated by the change of Young's modulus in the damaged area. The change of mass density caused by the damage is neglected. The potential and kinetic energy for the beam and the plate with damage can be expressed as

$$U^b = \frac{1}{24} Ebt^3 \int_0^a \left(\frac{\partial^2 w_s}{\partial x^2} \right)^2 dx - \frac{1}{24} (E - E_d) bt^3 \int_{L_d} \left(\frac{\partial^2 w_s}{\partial x^2} \right)^2 dx \quad (4.47a)$$

$$T^b = \frac{1}{2} \rho bt \int_0^a \dot{w}_s^2 dx \quad (4.47b)$$

$$U^p = \frac{Et^3}{24(1-\nu^2)} \int_{A_d} \left\{ \left(\frac{\partial^2 w_s}{\partial x^2} + \frac{\partial^2 w_s}{\partial y^2} \right)^2 - 2(1-\nu) \left[\frac{\partial^2 w_s}{\partial x^2} \frac{\partial^2 w_s}{\partial y^2} - \left(\frac{\partial^2 w_s}{\partial x \partial y} \right)^2 \right] \right\} dA \quad (4.48a)$$

$$- \frac{(E-E_d)t^3}{24(1-\nu^2)} \int_{A_d} \left\{ \left(\frac{\partial^2 w_s}{\partial x^2} + \frac{\partial^2 w_s}{\partial y^2} \right)^2 - 2(1-\nu) \left[\frac{\partial^2 w_s}{\partial x^2} \frac{\partial^2 w_s}{\partial y^2} - \left(\frac{\partial^2 w_s}{\partial x \partial y} \right)^2 \right] \right\} dA$$

$$T^p = \frac{1}{2} \rho t \int_A \dot{w}_s^2 dA \quad (4.48b)$$

where the superscripts b and p denote beam and plate, respectively; E is the Young's modulus; the subscript d represents damage; ν is the Poisson's ratio; L_d is the length of the damaged element in the beam; and A_d is the damaged area in the plate.

For small damage, the following approximation is adopted

$$\int_{L_d} f(x) dx = f(x_c) \times L_d \quad (4.49a)$$

$$\int_{A_d} f(x, y) dA = f(x_c, y_c) \times A_d \quad (4.49b)$$

where $f(x)$ and $f(x, y)$ are the integrands in Eqs. (4.47a) and (4.48a), respectively; and x_c and y_c are the coordinates of the center of the damage.

Without loss of generality, the following non-dimensionalized relationships are introduced

$$\xi = \frac{2x}{a} - 1 \quad (4.50a)$$

$$\eta = \frac{2y}{b} - 1 \quad (4.50b)$$

such that $-1 \leq \xi \leq 1$ and $-1 \leq \eta \leq 1$.

Thus, Eqs. (4.47) and (4.48) can be rewritten as

$$U^b = \frac{1}{3} \frac{Ebt^3}{a^3} \int_{-1}^1 \left(\frac{\partial^2 w_s}{\partial \xi^2} \right)^2 d\xi - \frac{1}{3} \frac{(E-E_d)bt^3}{a^3} \cdot \left(\frac{\partial^2 w_s}{\partial \xi^2} \right)^2 \Bigg|_{\xi=\xi_c} \cdot \frac{2}{a} L_d \quad (4.51a)$$

$$T^b = \frac{1}{4} \rho a b t \int_{-1}^1 \dot{w}_s^2 d\xi \quad (4.51b)$$

$$\begin{aligned}
 U^P &= \frac{Et^3}{24(1-\nu^2)} \frac{ab}{4} \int_{-1}^1 \int_{-1}^1 \left\{ \left(\frac{4}{a^2} \frac{\partial^2 w_s}{\partial \xi^2} + \frac{4}{b^2} \frac{\partial^2 w_s}{\partial \eta^2} \right)^2 \right. \\
 &\quad \left. - 2(1-\nu) \frac{16}{a^2 b^2} \left[\frac{\partial^2 w_s}{\partial \xi^2} \frac{\partial^2 w_s}{\partial \eta^2} - \left(\frac{\partial^2 w_s}{\partial \xi \partial \eta} \right)^2 \right] \right\} d\xi d\eta \\
 &\quad - \frac{(E-E_d)t^3}{24(1-\nu^2)} \left\{ \left(\frac{4}{a^2} \frac{\partial^2 w_s}{\partial \xi^2} + \frac{4}{b^2} \frac{\partial^2 w_s}{\partial \eta^2} \right)^2 \right. \\
 &\quad \left. - 2(1-\nu) \frac{16}{a^2 b^2} \left[\frac{\partial^2 w_s}{\partial \xi^2} \frac{\partial^2 w_s}{\partial \eta^2} - \left(\frac{\partial^2 w_s}{\partial \xi \partial \eta} \right)^2 \right] \right\} \Bigg|_{\substack{\xi=\xi_c \\ \eta=\eta_c}} \cdot A_d \quad (4.52a)
 \end{aligned}$$

$$T^P = \frac{1}{2} \rho t \frac{ab}{4} \int_{-1}^1 \int_{-1}^1 \dot{w}_s^2 d\xi d\eta \quad (4.52b)$$

In the p-version Ritz method, the transverse displacement is approximated as

$$w_s = \sum_{i=0}^N c_i \phi_i e^{j\omega t} = \mathbf{C} \boldsymbol{\phi} e^{j\omega t} \quad \text{and} \quad w_s = \sum_{q=0}^N \sum_{i=0}^q c_m \phi_m e^{j\omega t} = \mathbf{C} \boldsymbol{\phi} e^{j\omega t} \quad (4.53)$$

for the beam and the plate, respectively; where N is the degree set of polynomial space; \mathbf{C} is the coefficient vector; $\boldsymbol{\phi}$ is the shape function vector; $e^{j\omega t}$ stands for harmonic vibration; and m is set as $\frac{(q+1)(q+2)}{2} - i$ for the plate.

Following Liew *et al.* (1998), the shape function is designed as $\phi_i = \xi^i \phi_0, i=1,2,\dots,N$ and $\phi_i = \xi^i \eta^{q-i} \phi_0, i=1,2,\dots, \frac{(N+1)(N+2)}{2}$ for the beam and the plate, respectively, where $\phi_0 = \prod_n \psi_n^{r_n}$, and ψ_n is the function of the boundary, *i.e.*, $\xi \pm 1$ for the beam and $\xi \pm 1, \eta \pm 1$ for the rectangular plate. The shape function must satisfy the geometric boundary conditions; so, r_n is dependent on the constraints on the corresponding boundary, *e.g.*, $r_n = 0$ for a free boundary.

Thus, the stiffness and mass matrices can be calculated as

$$K_{ik}^b = \frac{\partial^2 U^b}{\partial c_i \partial c_k} = \frac{2}{3} \frac{Ebt^3}{a^3} \int_{-1}^1 \phi_{ik}^b d\xi - \frac{4}{3} \frac{(E - E_d)bt^3}{a^4} \phi_{ik}^b \Big|_{\xi=\xi_c} \cdot L_d \quad (4.54a)$$

$$M_{ik}^b = \frac{1}{\omega^2} \frac{\partial^2 T^b}{\partial c_i \partial c_k} = \frac{1}{2} \rho abt \int_{-1}^1 \phi_i \phi_k d\xi \quad (4.54b)$$

$$K_{ik}^p = \frac{\partial^2 U^p}{\partial c_i \partial c_k} = \frac{Eabt^3}{3(1-\nu^2)} \int_{-1}^1 \int_{-1}^1 \phi_{ik}^p d\xi d\eta - \frac{4(E - E_d)t^3}{3(1-\nu^2)} \phi_{ik}^p \Big|_{\substack{\xi=\xi_c \\ \eta=\eta_c}} A_d \quad (4.55a)$$

$$M_{ik}^p = \frac{1}{\omega^2} \frac{\partial^2 T^p}{\partial c_i \partial c_k} = \frac{ab}{4} \rho t \int_{-1}^1 \int_{-1}^1 \phi_i \phi_k d\xi d\eta \quad (4.55b)$$

where

$$\phi_{ik}^b = \frac{\partial^2 \phi_i}{\partial \xi^2} \frac{\partial^2 \phi_k}{\partial \xi^2} \quad (4.56a)$$

$$\begin{aligned} \phi_{ik}^p = & \left(\frac{1}{a^2} \frac{\partial^2 \phi_i}{\partial \xi^2} + \frac{1}{b^2} \frac{\partial^2 \phi_i}{\partial \eta^2} \right) \left(\frac{1}{a^2} \frac{\partial^2 \phi_k}{\partial \xi^2} + \frac{1}{b^2} \frac{\partial^2 \phi_k}{\partial \eta^2} \right) \\ & - (1-\nu) \frac{1}{a^2 b^2} \left[\frac{\partial^2 \phi_i}{\partial \xi^2} \frac{\partial^2 \phi_k}{\partial \eta^2} + \frac{\partial^2 \phi_i}{\partial \eta^2} \frac{\partial^2 \phi_k}{\partial \xi^2} - 2 \frac{\partial^2 \phi_i}{\partial \xi \partial \eta} \frac{\partial^2 \phi_k}{\partial \xi \partial \eta} \right] \end{aligned} \quad (4.56b)$$

$i, k = 0, 1, \dots, N$ for the beam; and $i, k = 0, 1, \dots, \frac{(N+1)(N+2)}{2}$ for the plate.

By solving the equation $(\mathbf{K} - \mathbf{M}\lambda)\mathbf{C} = 0$, the natural frequencies and mode shapes can be calculated as

$$\omega_m = \sqrt{\lambda_m} \quad \text{and} \quad \Phi_m = \sum_n c_{mn} \phi_n = \mathbf{C}_m^T \boldsymbol{\phi}$$

where \mathbf{C}_m is the eigenvector corresponding to the m^{th} eigenvalue; and the superscript T denotes transpose.

Assuming that the actuated vibration is a superposition of different vibration

modes,

$$w_s = \sum_m \gamma_m \Phi_m e^{j\alpha x}$$

and considering the orthogonality of the mode shapes, the modal participation factor can be calculated as

$$\gamma_m = \frac{G_m}{\omega_m^2 - \omega^2} \quad (4.57)$$

where $G_m = \frac{\int_0^a \mathbf{C}_m^T \boldsymbol{\varphi} \frac{\partial M_x}{\partial x} dx}{\mathbf{C}_m^T \mathbf{M} \mathbf{C}_m}$ and $G_m = \frac{\int_0^a \int_0^b \mathbf{C}_m^T \boldsymbol{\varphi} \left(\frac{\partial M_x}{\partial x} + \frac{\partial M_y}{\partial y} \right) dx dy}{\mathbf{C}_m^T \mathbf{M} \mathbf{C}_m}$ for the beam and the plate, respectively.

The relative rotation angle at the opposite boundaries of the PZT transducer can be calculated as:

$$\left\{ \beta_1 \Big|_{x=x_1} - \beta_1 \Big|_{x=x_2} \right\} = Q_{11} M_1 = \mathbf{Q}_{1 \times 1} \{ M_1 \} \quad \text{for 1D vibration}$$

$$\left\{ \begin{array}{l} \beta_1 \Big|_{x=x_1} - \beta_1 \Big|_{x=x_2} \\ \beta_2 \Big|_{y=y_1} - \beta_2 \Big|_{y=y_2} \end{array} \right\} = \begin{bmatrix} Q_{11} & Q_{12} \\ Q_{21} & Q_{22} \end{bmatrix} \left\{ \begin{array}{l} M_1 \\ M_2 \end{array} \right\} = \mathbf{Q}_{2 \times 2} \left\{ \begin{array}{l} M_1 \\ M_2 \end{array} \right\} \quad \text{for 2D vibration}$$

where Q_{pq} is the relative angle under a unit moment pair with the first and second subscripts representing the directions of the displacement and the moment pair, respectively.

The mechanical impedance of the beam can be calculated as

$$Z_{str} = 2 \frac{F}{\dot{u} \Big|_{x=x_1} - \dot{u} \Big|_{x=x_2}} \quad \text{or} \quad \mathbf{Z}_{1 \times 1} = \frac{4}{j\omega (t+h)^2} \mathbf{Q}_{1 \times 1}^{-1} \quad (4.58)$$

Similarly, the mechanical impedance of the plate can be expressed as:

$$\mathbf{Z}_{2 \times 2} = \frac{4}{j\omega (t+h)^2} \mathbf{Q}_{2 \times 2}^{-1} \quad (4.59)$$

The admittance of the PZT patch bonded on the beam or the plate can be obtained from Eq. (4.38) or (4.41) after the mechanical impedance of the structure is calculated from Eq. (4.58) or (4.59).

4.13 Damage Identification Method

If the frequency of the applied electrical voltage is near to the natural frequencies of the structure, because of resonance, the mechanical impedance of the structure will be minor. From Eqs. (4.38), (4.39), (4.41), (4.42) and (4.43), peak values of the admittance will appear at the natural frequencies. Change of mechanical properties in the structure affects the natural frequencies, and thus leads to shifts in the admittance peaks. Different damages cause different shifts. Therefore, the damage identification problem can be mathematically stated as

$$\text{Find } \mathbf{D} \subset \mathbf{S}, \text{ such that } f(\mathbf{D}) \rightarrow \text{minimum} \quad (4.60)$$

where \mathbf{D} is a trial solution of the damage; \mathbf{S} is the feasible domain which contains all possible damages; and $f(\mathbf{D})$ is the fitness function to assess the correctness of the trial solution. From the above formulation, the damage identification problem is essentially an optimization problem.

It is noted that the formulation (Eq. 4.60) may have a number of local minima in the region \mathbf{S} , which would cause difficulty for the traditional local optimization strategies to find the global optimum. In the past decades, evolutionary programming (EP) has been developed for global optimization (Fogel, 1962). The robustness of EP in finding the global optimum has been convincingly proven (McDonnell *et al.*, 1995; Fogel *et al.*, 1996; Angeline *et al.*, 1997). EP has also been employed to solve inverse problems in civil engineering (Minster *et al.*, 1995; Soh and Dong, 2001). In our study, a hybrid EP proposed by Yang *et al.* (2006) was selected to find the damage in structures.

4.13.1 EP Algorithm

By simulating natural evolution, EP has been developed into a powerful global search and optimization technique. The basic EP method has four steps:

- (1) A pool of trial solutions (called chromosomes) is randomly selected from the feasible region;
- (2) Each chromosome (parent) generates an offspring by mutation;
- (3) All chromosomes are assessed by computing their fitness; and
- (4) Typically, a stochastic tournament selection is performed to select a half of the parent and offspring chromosomes to be retained for the next population.

Steps 2, 3 and 4 are repeated until a threshold for iteration is exceeded or an adequate solution is obtained.

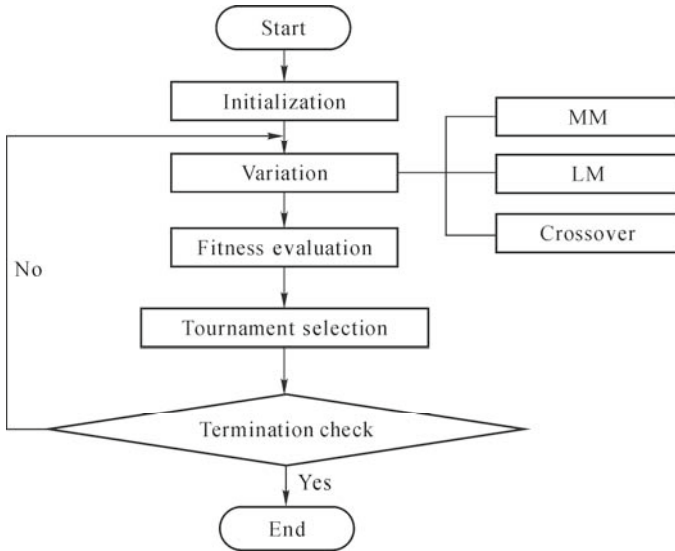


Fig. 4.31 Flowchart of hybrid EP algorithm

When applying an EP algorithm for damage identification, iterative structural analysis has to be performed in Step 3, which is time consuming. Two specially designed mutation operators, namely, macro mutation (MM) operator and local mutation (LM) operator, plus a crossover operator, were implemented in the hybrid EP algorithm (Yang *et al.*, 2006) to improve the search efficiency. The MM operator was designed to explore the whole search space by enabling the mutated chromosome to reach any point in the feasible region, while the LM operator was designed to exploit the neighborhood of the parental chromosomes to find better offspring. The LM operator can find the optima in a small region rapidly, and the MM operator and the crossover operator can prevent the evolution from being trapped in local optima. The process of the hybrid EP algorithm is illustrated in Fig. 4.31. The following parameters are adopted in this section for the hybrid EP algorithm: *population size*=50, *maximum generation number*=100, *tournament size*=10, and probabilities of the MM, LM and crossover are 0.6, 0.2 and 0.2, respectively.

4.13.2 Fitness Function

The traditional non-destructive evaluation techniques directly compare the differences between the predicted and measured data to assess the trial solution

$$f(\mathbf{D}) = \sum_i \left| P_i^n(\mathbf{D}) - P_i^m \right| \quad (4.61)$$

where P represents the peaks of the admittance, and the superscripts n and m represent the numerical predictions and measurements, respectively.

In real applications, no matter how careful the structural analysis models are designed, they can never exactly represent the real structures. Thus, differences always exist between the predicted and measured data. For SHM, the final results are usually sensitive to the input data. These differences may lead to dramatically different results from the correct solution. In order to reduce the effect of such differences, a special fitness function is designed in our study:

$$f(\mathbf{D}) = \sum_i \left| (P_i^{nu}(\mathbf{D}) - P_i^{nd}(\mathbf{D})) - (P_i^{mu} - P_i^{md}) \right| \quad (4.62)$$

where the superscripts u and d represent the variables of the undamaged structure and the damaged structure, respectively.

With this fitness function, the measured data for the damaged structure are compared with the recording of the undamaged structure, and the predicted data based on the structural model with presumed damage are compared with the predicted data based on the undamaged structural model. Consequently, only changes caused by the damage are counted in the fitness function. Thus, any inaccuracy in the numerical simulation of the real structure is reduced.

4.14 Experimental Set-up

The experimental setup included the test specimens, an electrical impedance analyzer, a multiplex terminal, electrical wire connections, and a personal computer (PC) equipped with data acquisition software and a PC-analyzer interface cable, as shown in Fig. 4.32. A beam and a plate were selected to simulate 1D and 2D structures, respectively.

Standard installation procedure was employed to bond a pair of PZT transducers to the specimens at the same location but on opposite sides (Figs. 4.29 and 4.30). RS159-3957 high-strength epoxy adhesive was used in the bonding. Free boundary conditions were simulated by resting the specimens on soft paper for the plate specimen (Fig. 4.32). The properties of the specimens and the PZT transducers are listed in Table 4.3.

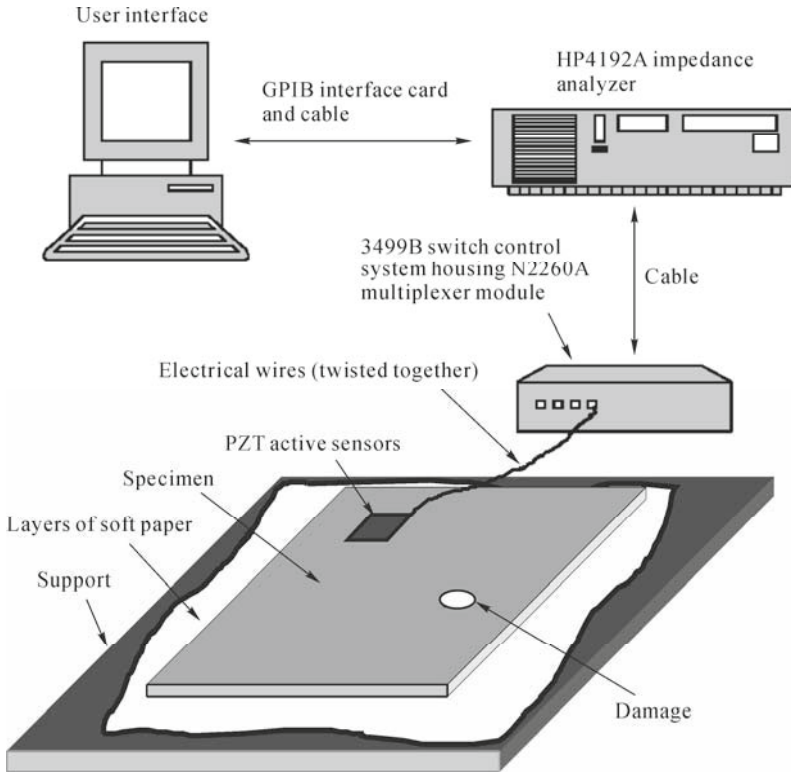


Fig. 4.32 Schematic sketch of experimental setup

Table 4.3 Properties of specimens and PZT patches

		Specimen	Beam	Plate
Host structure	Length (mm)		300	101
	Width (mm)		20	101
	Height (mm)		2	2
	Young's modulus (N/m ²)		6.65E+10	6.65E+10
	Mass density (kg/m ³)		2600	2800
	Damping ratio		0.01	0.005
	Poisson's ratio		N/A	0.33
	Damage	Radius (mm)		2.8
	Location (mm)		$X_c=227.3$	$x_c=80.4, y_c=21.0$
	Dimension ($l \times w \times h$) (mm ³)		$20 \times 20 \times 0.2$	$10 \times 10 \times 0.2$
	Location (mm)		$x_1=80,$ $x_2=100$	$x_1=30, x_2=40,$ $y_1=70.5, y_2=80.5$
PZT	Young's modulus (N/m ²)		6.67E+10	6.67E+10
	Loss factor		0.03	0.005
	Mass density (kg/m ³)		7800	7800
	Strain constant d (m/V)		$d_{11}=-2.10E-10$	$d_{31}=d_{32}=-2.10E-10$
	Permittivity (Farad/m)		2.14E-08	1.93E-08
	Dielectric loss factor		1.85E-02	1.50E-02

Through the multiplex terminal, an electrical field was applied on the PZT transducer with opposite directions so that pure bending vibration was actuated on the specimens. The actuating frequencies of the electrical field range were 1 – 10 kHz and 5 – 30 kHz for the beam and the plate, respectively. Considering that the damage will cause very minor change in the EMI, the intervals of the actuating frequencies were selected to be as small as 1 Hz. The EMI spectra were recorded by an HP4192A impedance analyzer. The control and acquisition of the experimental data were achieved through the multiplex terminal and the GPIB interface card installed in the computer (Fig. 4.32). Damages were simulated by drilled holes in the specimens. The position and radius of the holes are also listed in Table 4.3.

4.15 Experimental Results and Numerical Predictions

In the numerical prediction, the hole in the beam was simulated by an element with the same width and height as the beam but with different elastic constant. The length of the damaged element was defined as $L_d = 6r_d$ based on Saint Venan's principle, and the Young's modulus in this area was approximated by:

$$E_d \frac{bt^3}{12} \cdot L_d = \int_{L_d} E \frac{bt^3}{12} dx = E \frac{bt^3}{12} (L_d - 2r_d) + E \frac{t^3}{12} (2br_d - \pi r_d^2) \quad (4.63)$$

The damage in the plate was simply considered as $A_d = \pi r_d^2$ and $E_d = 0$.

The measured and predicted admittances are illustrated in Figs. 4.33 and 4.34 for the beam and plate specimens, respectively. Good matches between them confirm the validity of the impedance model. However, some predicted peaks cannot be measured because of damping, and there are some measured minor peaks which were not predicted by the impedance model. These peaks were probably caused by machine noise or accidental disturbance of the specimens. Even for those peaks that appear in both the prediction and the measurement, there are still some small differences between them, as shown in Table 4.4 and Table 4.5 for the beam and plate specimens, respectively. These differences are unavoidable because of the inaccuracy in numerical simulation of the real structure, *e.g.*, the specimens were not strictly homogeneous and isotropic, and the boundary conditions were not completely free.

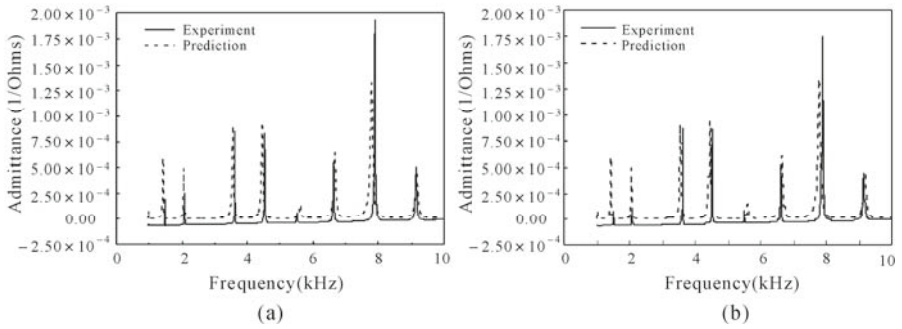


Fig. 4.33 Comparison between experiment and prediction of beam specimen. (a) Undamaged; (b) Damaged

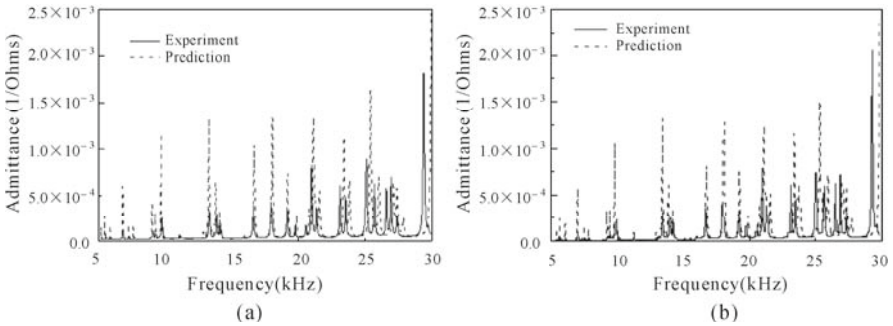


Fig. 4.34 Comparison between experiment and prediction of plate specimen. (a) Undamaged; (b) Damaged

Table 4.4 Measured and predicted peaks for beam specimen (in kHz)

Experimental measurement			Numerical prediction		
Undamaged	Damaged	Shift	Undamaged	Damaged	Shift
1.508	1.507	0.001	1.447	1.447	0
2.102	2.095	0.007	2.079	2.073	0.006
3.614	3.61	0.004	3.557	3.552	0.005
4.523	4.519	0.004	4.443	4.443	0
5.507	5.495	0.012	5.599	5.583	0.016
6.615	6.59	0.025	6.656	6.633	0.023
7.867	7.854	0.013	7.766	7.751	0.015
9.116	9.106	0.010	9.131	9.13	0.001

Table 4.5 Measured and predicted peaks for plate specimen (in kHz)

Experimental measurement			Numerical prediction		
Undamaged	Damaged	Shift	Undamaged	Damaged	Shift
5.465	5.452	0.013	5.401	5.389	0.012
5.762	5.735	0.027	5.672	5.647	0.025
6.126	6.102	0.024	6.068	6.041	0.027
7.029	7.018	0.011	6.996	6.987	0.009
7.460	7.458	0.002	7.427	7.426	0.001
7.862	7.864	-0.002	7.784	7.78	0.004
9.257	9.254	0.003	9.165	9.164	0.001
9.459	9.443	0.016	9.403	9.388	0.015
9.902	9.891	0.011	9.844	9.818	0.026
11.263	11.263	0.000	11.23	11.227	0.003
11.8	—	—	—	—	—
12.937	12.915	0.022	12.97	12.925	0.045
13.404	13.397	0.007	13.388	13.384	0.004
—	—	—	13.583	13.58	0.003
13.969	13.962	0.007	13.89	13.889	0.001
14.239	14.208	0.031	14.178	14.158	0.02
—	—	—	15.565	15.565	0
15.9	—	—	15.987	15.972	0.015
16.672	16.655	0.017	16.741	16.701	0.04
17.988	17.958	0.030	18.082	18.057	0.025
19.189	19.182	0.007	19.214	19.206	0.008
19.777	19.749	0.028	19.889	19.886	0.003
20.564	20.548	0.016	20.806	20.727	0.079
20.982	20.969	0.013	21.123	21.115	0.008
21.356	21.326	0.030	21.577	21.541	0.036
23.110	23.105	0.005	23.389	23.387	0.002
23.530	23.49	0.040	23.808	23.774	0.034
25.087	25.01	0.077	25.364	25.343	0.021
25.667	25.656	0.011	25.983	25.946	0.037
26.536	26.488	0.048	27.045	27.038	0.007
26.896	26.897	-0.001	27.329	27.329	0
27.340	27.332	0.008	27.792	27.772	0.02
29.305	29.296	0.009	29.883	29.878	0.005
29.648	29.618	0.030	30.491	30.45	0.041

It is also observed that the appearance of damages in both structures has caused shifts in the admittance peaks, as expected. A typical shift is shown in Figs. 4.35 and 4.36 for the beam and the plate specimens, respectively. Although inaccuracy exists in representing the beam or the plate specimen with an Euler beam or a Kirchhoff plate, the shifts in the admittance peaks caused by the same damage are similar for both measurements and predictions.

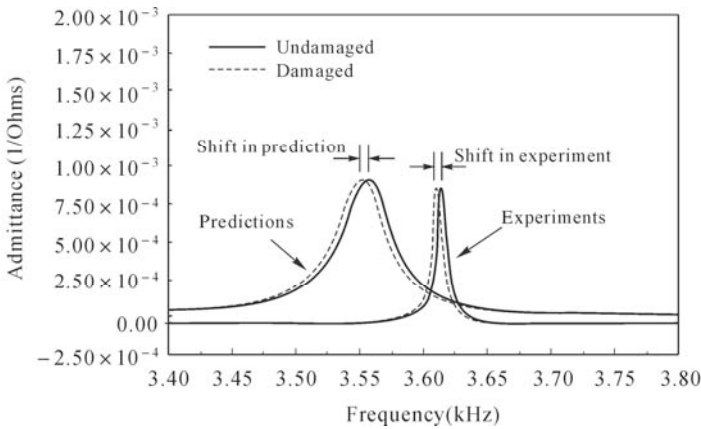


Fig. 4.35 Typical peak shift for beam specimen

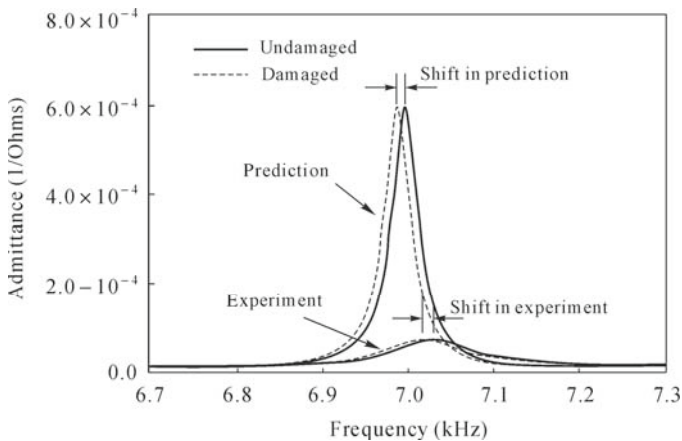


Fig. 4.36 Typical peak shift for plate specimen

Figs. 4.37 and 4.38 illustrate the changes in admittance peaks for the beam and the plate, respectively, with only those peaks which can be both detected in experiment and predicted in numerical simulation under consideration. Since the proposed fitness function counts only the shifts in the admittance peaks caused by the damage, the above similarity indicates that it is possible to identify damages with the system identification technique and the proposed fitness function.

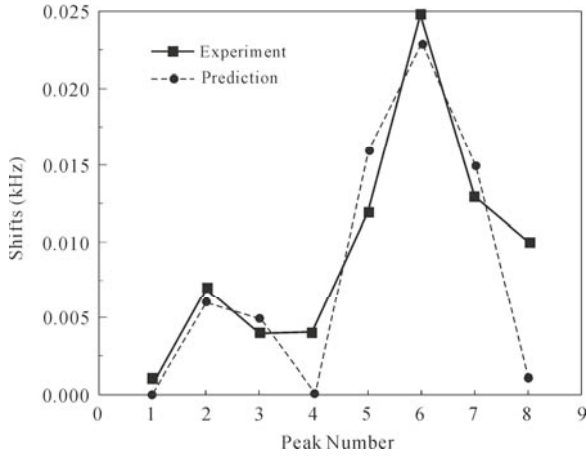


Fig. 4.37 Shifts of EMI peaks for beam specimen

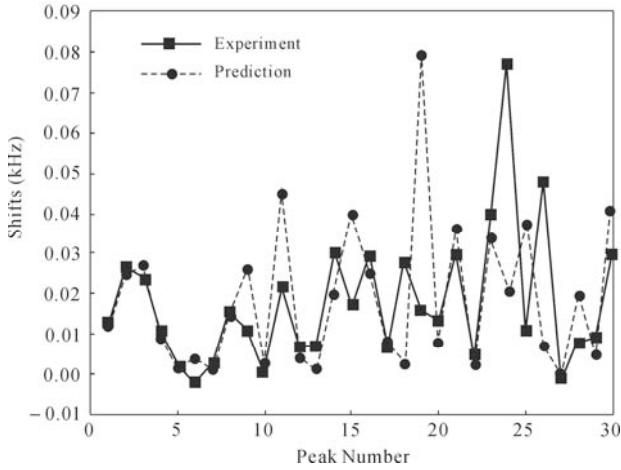


Fig. 4.38 Shifts of EMI peaks for plate specimen

4.15.1 Damage Identification Results

The damages in the structure were detected using the hybrid EP algorithm. For the beam, the damage was defined by three variables: E_d , x_c and L_d . Since the level of E_d is much larger than the other variables, it will force the search to converge to a solution that can only produce a good estimate of E_d . To overcome this

problem, the variables were non-dimensionalized as $\frac{E_d}{E}$, $\frac{x_c}{a}$ and $\frac{L_d}{a}$, so that the search space was constrained in $0 < \frac{E_d}{E} < 1$, $0 < \frac{x_c}{a} < 1$ and $0 < \frac{L_d}{a} < 0.1$. The upper bound of the third variable was set at 0.1 because in this research the damage was considered minor. The admittance peaks, ranging from 1 to 10 kHz, were used as input information for optimization. The optimization process is illustrated in Fig. 4.39. After 100 generations, the center of the damage was found at $\frac{x_c}{a} = 0.75828$ ($x_c = 227.48$ mm). The distance from the predicted damage center to the exact position ($x_c = 227.3$ mm) was less than 0.2mm. The other two variables were obtained as $\frac{E_d}{E} = 0.86247$ and $\frac{L_d}{a} = 0.02579$. By substituting these solutions into Eq. (4.63), the radius of the hole was calculated to be $r_d = 2.6$ mm, which is only 0.2 mm less than the exact solution ($r_d = 2.8$ mm), *i.e.*, a difference of only 7%.

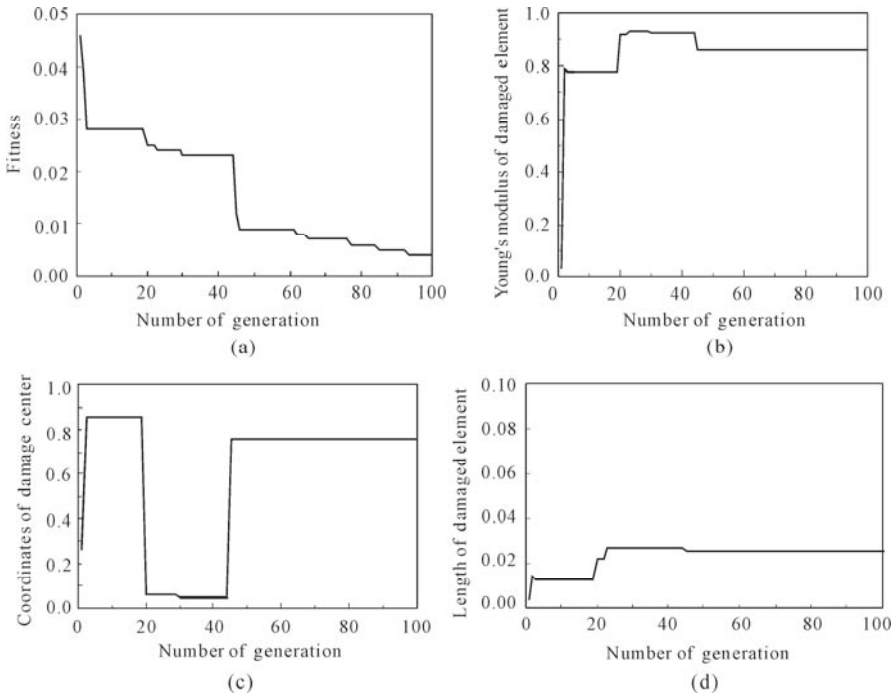


Fig. 4.39 Evolutionary process of damage detection for beam specimen: (a) Fitness; (b) Young's modulus; (c) Damage location; (d) Damage length

For the plate, the damage was defined by three variables, x_c , y_c and r_d , which satisfied $0 < \frac{x_c}{a} < 1$, $0 < \frac{y_c}{a} < 1$, and $0 < \frac{r_d}{a} < 0.1$. The admittance peaks range from 5 to 30 kHz. The evolutionary process for damage identification is shown in Fig. 4.40. After 100 generations, the center of the hole was identified to be at $\frac{x_c}{a} = 0.85008$ and $\frac{y_c}{a} = 0.20642$ (i.e., $x_c = 85.86$ mm, $y_c = 20.85$ mm), which is 5.46 mm from the exact position ($x_c = 80.4$ mm, $y_c = 21.0$ mm). The radius of the hole was obtained as $\frac{r_d}{a} = 0.02544$ (i.e., $r_d = 2.57$ mm). The difference with the exact radius $r_d = 2.8$ mm is only 0.23 mm or about 8%. From the comparison, it can be concluded that the damage has been successfully identified using the hybrid EP algorithm.

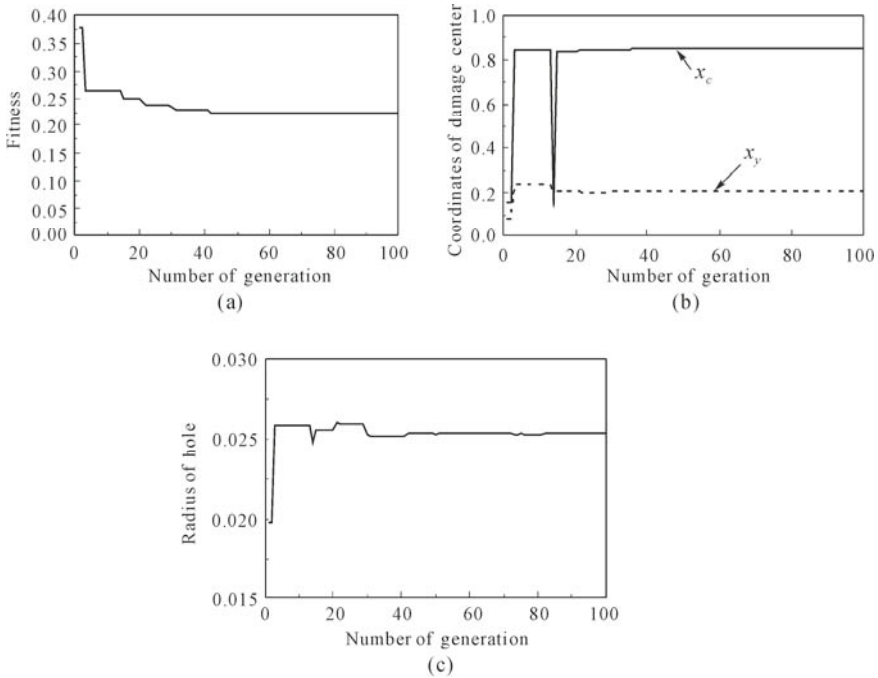


Fig. 4.40 Evolutionary process of damage detection for plate specimen: (a) Fitness; (b) Damage location; (c) Damage radius

4.15.2 Summary

Damages in beam and plate have been successfully identified from the changes in the admittance spectra using a hybrid EP algorithm. The EMI-EP combined technique is based on relatively lower frequencies so that accurate structural analysis is possible. The hybrid EP method was employed as a global search technique to back-calculate the damage. A special fitness function was designed to effectively reduce the inaccuracy in representing the real structure with analytical or numerical models. Experiments performed on a beam and a plate have demonstrated the effectiveness and reliability of the proposed SHM technique. Compared with the previous application of the EMI method for damage identification, this proposed technique can obtain more detailed information of the damage, *i.e.*, both its location and extent.

References

- Angeline, P.J., Reynolds, R.G., McDonnell, J.R. and Eberhart, R.C. (1997). *Proceedings of the 6th Annual Conference on Evolutionary Programming*, Indianapolis, Indiana, USA.
- Bhalla, S. (2001). "Smart System Based Automated Health Monitoring of Structures", *M.Eng. Thesis*, Nanyang Technological University, Singapore.
- CAIB (Columbia Accident Investigation Board) (2003), <http://www.caib.us> (date of access: 9 September, 2003).
- Doebbling, S.W., Farrar, C.R. and Prime, M.B. (1998). "A Summary Review of Vibration-Based Damage Identification Methods", *The Shock and Vibration Digest*, 30(2): 91-105.
- Farrar, C.R. and Jauregui, D.A. (1998). "Comparative Study of Damage Identification Algorithms Applied to a Bridge: I. Experiment", *Smart Materials and Structures*, 7: 704-719.
- Fogel, L.J. (1962). "Toward inductive inference automata", *Proceedings of the International Federation for Information Processing Congress*, Munich, Germany, 395-399.
- Fogel, L.J., Angeline, P.J. and Bäck, T. (1996). *Proceedings of the 5th Annual Conference on Evolutionary Programming*, Cambridge: MIT Press, Mass, USA.
- Giurgiutiu, V. and Zagrai, A.N. (2002). "Embedded Self-Sensing Piezoelectric Active Sensors for On-Line Structural Identification", *Journal of Vibration and Acoustics*, 124: 116-125.
- Hixon, E.L. (1988). "Mechanical Impedance", *Shock and Vibration Handbook*, edited by C. M. Harris, 3rd ed., New York: Mc Graw Hill Book Co., 10.1-10.46.
- Liew, K.M., Wang, C.M., Xiang, Y. and Kitipornchai, S. (1998). *Vibration of*

- Mindlin Plates*, Elsevier Science Ltd.
- McDonnell, J.R., Reynolds, R.G. and Fogel, D.B. (1995). *Proceedings of the 4th Annual Conference on Evolutionary Programming*, Cambridge: MIT Press, Mass, USA.
- Minster, J.B.H., Williams, N.P., Masters, T.G., Gilbert, J.F. and Haase, J.S. (1995). "Application of evolutionary programming to earthquake hypocenter determination", *Proceedings of the 4th Annual Conference on Evolutionary Programming*, Cambridge: MIT Press, Mass., USA, 1-17.
- Naidu, A.S.K. and Soh, C.K. (2004a). "Damage Severity and Propagation Characterization with Admittance Signatures of Piezo-transducers", *Smart Materials and Structures*, 15: 627-642.
- Naidu, A.S.K. and Soh, C.K. (2004b). "Identifying Damage Location with Admittance Signatures of Smart Piezo-Transducers", *Journal of Intelligent Material Systems and Structures*, 13: 393-403.
- Naidu, A.S.K., Soh, C.K. and Pagalthivarthi, K.V. (2006). "Bayesian Network for E/M Impedance-Based Damage Identification", *Journal of Computing in Civil Engineering*, 20(4): 227-236.
- PI Ceramic (2003), *Product Information Catalogue*, Lindenstrabe, Germany, <http://www.piceramic.de>.
- Salawu, O.S. and Williams, C. (1994). "Damage Location using Vibration Mode Shapes", *Proceedings of the 12th International Modal Analysis Conference*, Honolulu, Hawaii, USA, 933-939.
- Soh, C.K. and Dong, Y.X. (2001). "Evolutionary Programming for Inverse Problems in Civil Engineering", *Journal of Computing in Civil Engineering*, 15(2): 144-150.
- Soh, C.K., Tseng, K.K.H., Bhalla, S. and Gupta, A. (2000). "Performance of Smart Piezoceramic Patches in Health Monitoring of a RC Bridge", *Smart Materials and Structures*, 9(4): 533-542.
- Sun, F.P., Chaudhry, Z., Rogers, C.A., Majmundar, M. and Liang, C. (1995). "Automated Real-Time Structure Health Monitoring via Signature Pattern Recognition", *Proceedings of SPIE*, 2443: 236-247.
- Winston, H.A., Sun, F. and Annigeri, B.S. (2001). "Structural Health Monitoring with Piezoelectric Active Sensors", *Journal of Engineering for Gas Turbines and Power*, 123(2): 353-358.
- Xia, Y. (2002). "Condition Assessment of Structures using Dynamic Data", *Ph.D. Thesis*, Nanyang Technological University, Singapore.
- Yang, Y.W., Xu, J.F. and Soh, C.K. (2005). "Generic Impedance-Based Model for Structure-Piezoceramic Interacting System", *Journal of Aerospace Engineering*, 18(2): 93-101.
- Yang, Y.W., Xu, J.F. and Soh, C.K. (2006). "An Evolutionary Programming Algorithm for Continuous Global Optimization", *European J of Operational Research*, 168(2): 354-369.

Exercise 4.1

(a) Consider the 3D aluminium structure shown in Fig. Ex 3.1. Using 3D FEM, obtain a plot of x and y in the frequency range 100 – 300 kHz at an interval of 1 kHz. Idealize the structure as a suitable combination of the basic elements k , c and m which produce matching plots of x and y .

(b) Obtain the plots of G and B using the MATLAB program listed in Appendix C. What is common between the plots of G and x and those of B and y ?

(c) Induce damage in the structure by reducing the Young's modulus of elasticity by 20% for the four top corners of size 20 mm×20 mm×20 mm each. Repeat Step 1 and determine the values of k , c and m after this simulated damage. What difference can be observed?

Exercise 4.2

Repeat the exercise of Section 4.6 on a beam with both the ends fixed. All the other geometric as well as material properties may be considered to be the same. What are the similarities and differences compared with the results of Section 4.6?

Strength and Damage Assessment of Concrete

S. Bhalla^{*}, V. G. M. Annamdas, C. K. Soh

^{*}Department of Civil Engineering, Indian Institute of Technology Delhi, Hauz Khas, New Delhi 110016, India
Tel: 91-11-2659-1040; Fax: 91-11-2658-1117
Email: sbhalla@civil.iitd.ac.in

5.1 Introduction

A method is presented in Chapter 4 to “identify” system parameters and to predict system behavior using the EM admittance signatures of surface bonded piezo-impedance transducers. However, it is equally important to relate the identified impedance parameters with physical parameters such as strength and stiffness, and to calibrate changes in these parameters with damage progression in the host structure. This is the main objective of this chapter, which covers both surface-bonded and embedded PZT patches.

5.2 Conventional NDE Techniques for Concrete

In general, when considering NDE, concrete technologists are interested in (i) concrete strength determination, and (ii) concrete damage detection. Special importance is attached to strength determination of concrete because its elastic behavior and, to some extent, service behavior can be easily predicted from its strength characteristics. Although direct strength tests, which are destructive in nature, are excellent for quality control during construction, their main limitation is that the tested specimens may not truly represent the concrete in the constructed structure. The destructive tests reflect more the quality of the supplied materials

rather than the constructed structures. Delays in obtaining results, lack of reproducibility and high costs are some of the other drawbacks. NDE techniques, on the other hand, aim to measure the strength of concrete in constructed structures. However, these cannot be expected to yield absolute values of strength. They measure some properties of concrete from which an estimation of its strength, durability and elastic parameters can be obtained. Below are very brief descriptions of some of the common techniques for concrete strength estimation.

- *Surface Hardness Techniques*

These techniques are based on the principle that strength of concrete is proportional to its surface hardness. Surface hardness is measured using the indentation test, which involves impacting the specimen surface with a standard mass, activated by a given energy, and measuring the size of the resulting indentation. Although there is little theoretical relationship between indentation size and strength, several empirical correlations have been established, which give a reasonable estimation of strength within a 20%–30% error. Most common indentation devices are *William's testing pistol*, the *Frank spring hammer* and the *Einbeck pendulum hammer*. The main limitation of these tests is that the devices need frequent calibration; the results are also highly dependent on the type of cement, aggregates, age and moisture content of the specimen, and are not very reproducible.

- *Rebound Hammer*

The rebound hammer technique predicts concrete strength based on the rebound of a hardened steel hammer dropped on the specimen surface. The rebound hammer, also known as the *Schmidt rebound hammer*, was invented by Ernst Schmidt in 1948. Empirical correlations have since been established between rebound number and concrete strength. In spite of a quick and inexpensive estimation of strength, the results are influenced by surface roughness, type of specimen (shape and size), age, moisture content, type of cement and aggregates.

- *Penetration Techniques*

These techniques are based on measuring the depth of penetration of a standard probe, impacted on the surface of a concrete specimen, with a standard energy. The penetration is performed mechanically in the case of the *Simbi hammer* and by gunpowder blast in the case of the *Spit pin hammer* and *Windsor probe*. The main drawback of penetration techniques is that they leave a minor damage on a small area of concrete (for example, the *Windsor Probe* leaves an impression of about 8 mm diameter). Furthermore, the calibration is strongly dependent on the

source and type of aggregates used, and large variations in strength prediction are observed.

- *Pullout Test*

This test measures the force required to pull out a specially shaped steel rod from the concrete where the rod has an enlarged end cast into the concrete. A high degree of correlation exists between the pullout force and the compressive strength. The pullout tests are, in general, reproducible with a high degree of accuracy. The major drawback, however, is that the test will cause a small amount of damage to the concrete surface, which must be repaired. Another drawback is that, since the pullout assemblies need to be incorporated into the form work before concreting, the tests have to be planned in advance.

- *Resonant Frequency Technique*

This technique is based on the principle that the velocity of sound traveling through a structure is proportional to the natural frequency of the structure, which in turn is proportional to the Young's modulus of elasticity (and hence strength) of the medium. This technique has been standardized by the American Society for Testing and Materials (ASTM). The velocity of sound in concrete is obtained by determining the fundamental resonant frequency of vibration of a standard specimen, which is usually a cylinder (150 mm diameter by 300 mm high) or a prism (75 mm×75 mm×300 mm). An electronic audio oscillator generates the required electrical audio frequency voltages, which are converted into mechanical pulses by the transmitter. As the waves travel through the concrete, they are picked up by a piezo-electric crystal acting as receiver at the other end of the specimen. The frequency of the oscillator is tuned until maximum deflection is displayed in the meter, which indicates resonance. From the measured frequency, the dynamic Young's modulus is determined, which in turn is correlated empirically with concrete strength. The main disadvantage of this technique is that it can only be carried out on small laboratory-sized specimens rather than structural members in the field. The test demands the availability of two opposite free surfaces on the specimen.

- *Ultrasonic Pulse Velocity Technique*

This technique is based on a principle similar to the resonant frequency technique. The difference is that the velocity of sound is determined by measuring the time of travel of electronically-generated longitudinal waves (15 – 50 kHz) through concrete, using a digital meter or a cathode ray oscilloscope. The pulse generation and reception are carried out using piezo-crystals. This test has also been standardized

by ASTM. Commercially available test equipment includes *soniscope*, *ultrasonic concrete tester* and *portable ultrasonic non-destructive digital indicating tester* (PUNDIT). The pulse velocity measurements are correlated with strength, and the error is typically less than 20%. As the velocity of the pulses is independent of the geometry of the component (depending on its elastic properties alone), the technique is suitable in both laboratory and field environments. It is typically used to test the quality of concrete in bridge piers, road pavements and concrete hydraulic structures up to 15 m in thickness (Malhotra, 1976). However, the main limitation of the technique is that the transducers must always be placed on the opposite faces of the structure for accurate results. Often, this is not possible, thereby limiting the technique's application. Also, the correlation between strength and velocity is highly dependent on the type of cement and aggregates.

5.3 Concrete Strength Evaluation Using EMI Technique

In Chapter 3, Eq. (3.56) was derived to calculate the electrical admittance across the terminals of a square PZT patch, surface-bonded to a structure possessing an effective mechanical impedance $Z_{s,eff}$. From this relationship, admittance spectra can be obtained for a “free” and a “clamped” PZT patch, by substituting $Z_{s,eff}$ equals 0 and ∞ respectively. Fig. 5.1 displays the admittance spectra (0 – 1,000 kHz) corresponding to these boundary conditions for a grade PIC 151 PZT patch of size 10 mm×10 mm×0.3 mm (PI Ceramic, 2003). It is apparent from this figure that the three resonance peaks, corresponding to “free-free” planar PZT vibrations, vanish on clamping the patch. The act of bonding a PZT patch to the surface of a structure also tends to similarly restrain the PZT patch. However, in real situations, the level of clamping is expected to be intermediate between these two extreme situations and therefore the admittance curves are likely to lie in-between the curves corresponding to these extreme situations, depending on the stiffness (or strength) of the component.

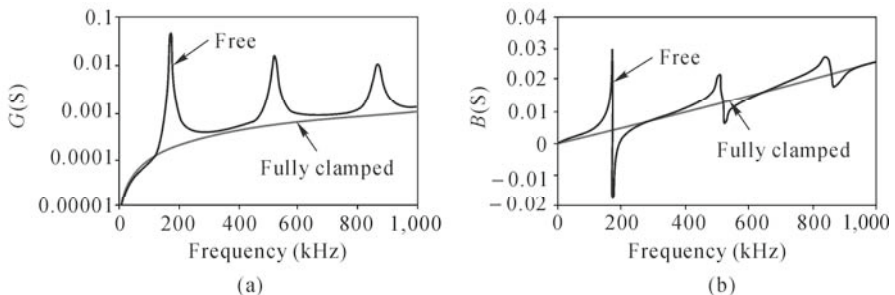


Fig. 5.1 Admittance spectra for free and fully clamped PZT patches. (a) Conductance vs. frequency; (b) Susceptance vs. frequency

In order to test the feasibility of predicting concrete strength using this principle, Soh and Bhalla (2005) bonded identical PZT patches of size $10\text{ mm} \times 10\text{ mm} \times 0.3\text{ mm}$ and grade PIC 151 onto the surface of 150 mm concrete cubes. At the time of casting, the proportions of various constituents were adjusted such that different characteristic strengths could be achieved. After casting, a minimum curing period of 28 days was observed for all the specimens, except two, which were kept one week only so as to achieve a lower strength at the time of the testing. In order to achieve identical bonding conditions, the same thickness of RS 850-940 epoxy adhesive layer (RS Components, 2006) was applied between the PZT patches and the concrete surfaces. To ensure this, two optical fiber pieces, 0.125 mm in diameter, were first laid parallel to each other on the concrete surface (Fig. 5.2(a)). A layer of epoxy was then applied onto the concrete surface and the PZT patch placed on top. A light pressure was maintained over the assembly using a small weight. The set-up was left undisturbed under these conditions at room temperature for 24 h to enable full curing of the adhesive. The optical fiber pieces were left permanently in the adhesive layer. This procedure ensured a uniform bonding layer thickness of 0.125 mm in all the specimens.

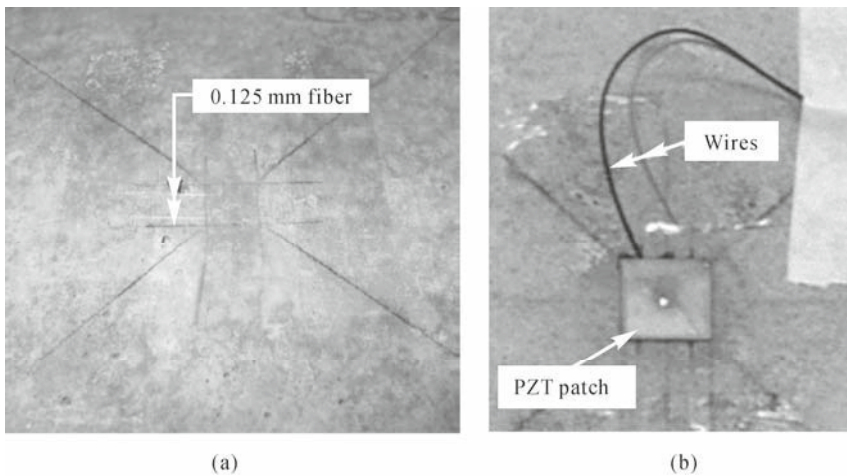


Fig. 5.2 (a) Optical fiber pieces laid on concrete surface before applying adhesive; (b) Bonded PZT patch

Fig. 5.3 shows the conductance and susceptance plots of the PZT patches bonded to concrete cubes of five different strengths. The strengths indicated on the figure were determined experimentally by subjecting the cubes to cyclic loading on a universal testing machine (the test procedure will be covered in the next section). The figure also shows the analytical curves for the PZT patches in free as well as clamped conditions.

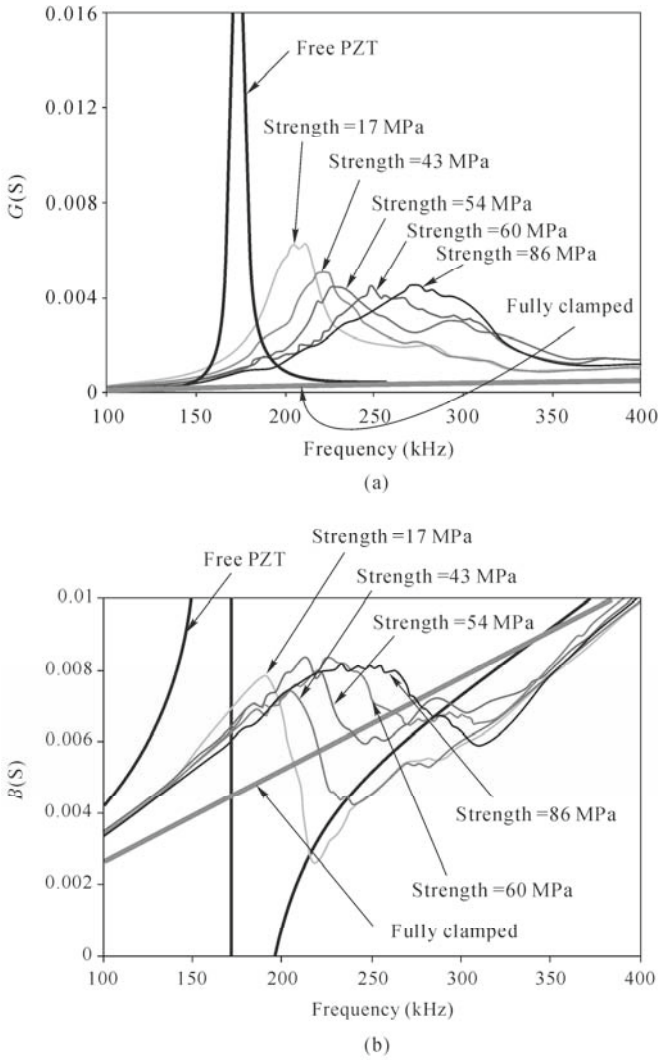


Fig. 5.3 Effect of concrete strength on first resonant frequency of PZT patch. (a) Conductance vs. frequency; (b) Susceptance vs. frequency

The figures show that the first peak frequency (Fig. 5.3(a)) gradually shifts in the right direction as the strength of concrete increases. This shifting is caused by the additional stiffening action due to bonding with concrete (the level of stiffening being related to the concrete strength). Fig. 5.4 shows a plot between the observed first resonant frequency and the measured concrete strength for data pertaining to a total of 17 PZT patches. The free PZT curve was used to obtain the data point corresponding to zero strength.

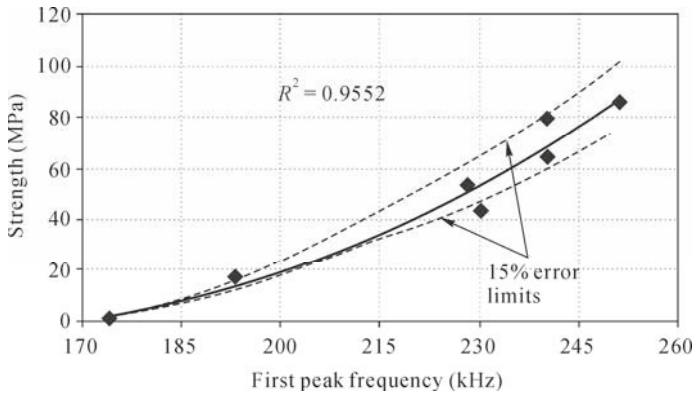


Fig. 5.4 Correlation between concrete strength and first resonant frequency

From regression analysis, the following empirical relationship is found between concrete strength (S) and the observed first resonant frequency

$$S \text{ (MPa)} = 0.0089f^2 - 2.6657f + 196.94 \quad (5.1)$$

where the resonant frequency, f , is measured in kHz. This empirical relationship can be used to evaluate concrete strength, non-destructively, for low-to-high strength concrete ($10 \text{ MPa} < S < 100 \text{ MPa}$).

It should be mentioned that a good correlation is not found between concrete strength and the second and third peaks (Fig. 5.1). The most probable reason is that at frequencies higher than 500 kHz, the PZT patches become sensitive to their own conditions rather than the conditions of the structure they were bonded to, as pointed out by Park *et al.* (2003).

Although the tests reported in this study were carried out on 150 mm cubes, the empirical relationship represented by Eq. (5.1) can be conveniently used for real structures since, in concrete, the zone of influence of PZT patches is usually very small. However, it should be noted that the strength considered in our study was obtained by cyclic compression tests, which was expected to be lower than that obtained by the standard testing procedure. Also, the relationship will depend on the type of aggregates and the type of cement used, and on the type and size of the PZT patches and type and thickness of the bonding layer. Hence, Eq. (5.1) cannot be considered as a universal relationship. It is therefore recommended that similar calibration should be established first in the laboratory for the particular concrete under investigation before using the method in the field.

The main advantage of the EMI-based approach is that there is no requirement of the availability of two opposite surfaces, unlike the resonant frequency method and the ultrasonic pulse velocity method. Also, no expensive transducers or equipment are required.

5.4 Extraction of Damage-Sensitive Concrete Parameters from Admittance Signatures

The test specimens were 150 mm concrete cubes instrumented with square PZT patches of size 10 mm×10 mm×0.3 mm and grade PIC 151 (Fig. 5.5). Using the procedure outlined in Chapter 3, updated “models” were obtained for five representative PZT patches of the test set. Table 5.1 lists the key averaged PZT parameters obtained experimentally for the patches.

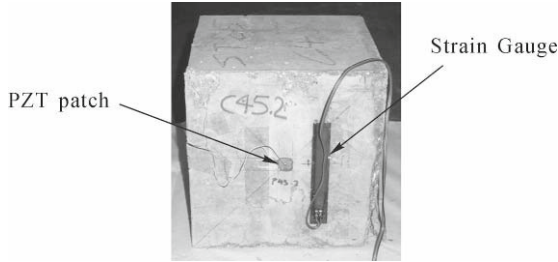


Fig. 5.5 Concrete cube to be “identified” by piezo-impedance transducer

Table 5.1 Averaged parameters of PZT patches

Physical Parameter	Value
Electric Permittivity, ϵ_{33}^T (Farad/m)	1.7785×10^{-8}
Peak correction factor, C_f	0.898
$K = \frac{2d_{31}^2 Y^E}{(1-\nu)}$ (N/V ²)	5.35×10^{-9}
Mechanical loss factor, η	0.0325
Dielectric loss factor, δ	0.0224

Using the computational procedure outlined in Chapter 4, the impedance parameters of the concrete cubes were extracted from the admittance signatures of the bonded PZT patches in the frequency range 60 – 100 kHz. The MATLAB program listed in Appendix E, incorporating the parameters listed in Table 5.1, was employed to perform the computations. The real and imaginary components of the extracted mechanical impedance were found to exhibit a response similar to that of a parallel spring-damper combination (*Kelvin Voigt* model), as shown in Fig. 5.6. Typically, for a concrete cube with a strength of 43 MPa (designated as C43), the system parameters were identified to be $k = 5.269 \times 10^7$ N/m and $c = 12.64$ N·s/m. Fig. 5.7 compares the experimental impedance spectra with the corresponding parallel spring-damper combination, with $k = 5.269 \times 10^7$ N/m and $c = 12.64$ N·s/m. A good agreement can be observed between the two.

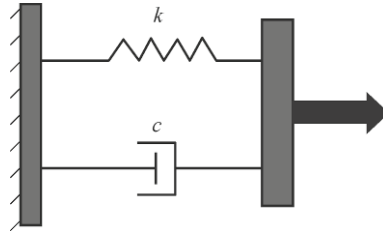


Fig. 5.6 Equivalent system “identified” by PZT patch

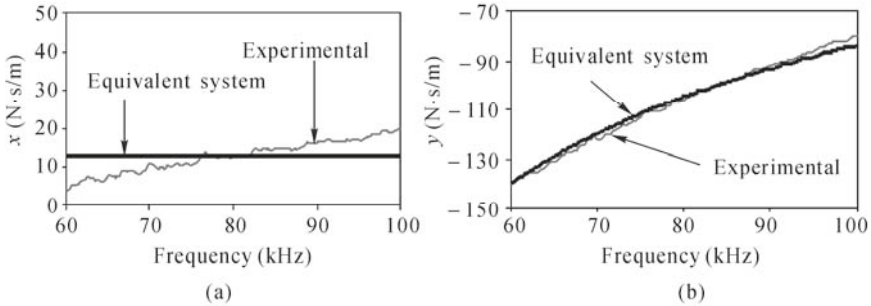


Fig. 5.7 Impedance plots for concrete cube C43. (a) Real component of mechanical impedance, x , vs. frequency; (b) Imaginary component of mechanical impedance, y , vs. frequency

The cubes were then subjected to cyclic loading in an experimental set-up (Fig. 5.8). The PZT patches instrumented on the cubes were wired to an impedance analyzer; which was controlled using the personal computer (PC) labeled as PC1 in the figure. The strain gauge was wired to a strain-recording data logger, which was in turn connected to another PC, marked PC2, which also controlled the operation of the universal testing machine (UTM). The cube was then loaded in compression at a rate of 330 kN/min until it reached the first predetermined load. It was then unloaded and the conductance and susceptance signatures were acquired. In the next cycle, the cube was loaded to the next higher level of load and the signatures were again acquired after unloading.

This loading, unloading and signature acquisition process was repeated until failure. Thus, the damage was induced in a cyclical fashion. Typical load histories for four cubes designated as C17 (Strength = 17 MPa), C43 (Strength = 43 MPa), C52 (Strength = 52 MPa) and C86 (Strength = 86 MPa) are shown in Fig. 5.9.

It can be observed from Fig. 5.9 that the secant modulus of elasticity progressively diminishes as the number of load cycles gradually increases. The loss in secant modulus was worked out after each load cycle. At the same time, the extracted equivalent spring stiffness, worked out from the recorded PZT signatures, was found to diminish proportionally.

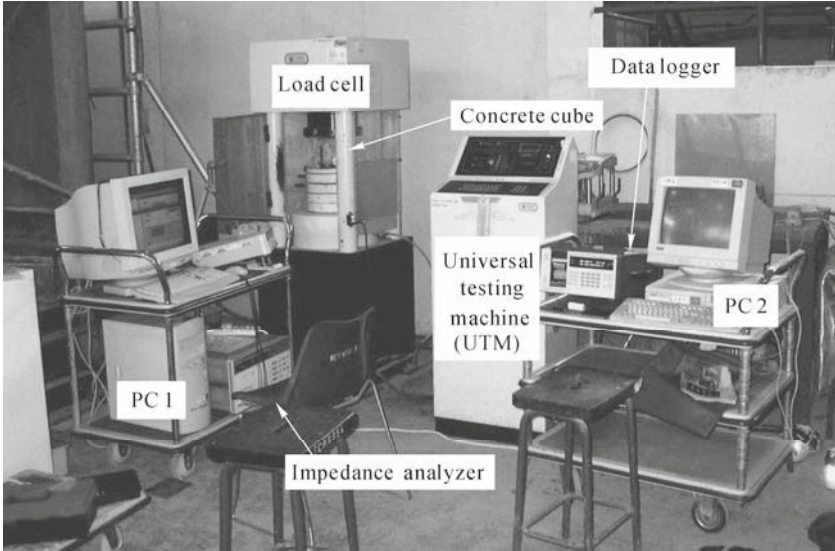


Fig. 5.8 Experimental set-up for inducing damage on concrete cubes

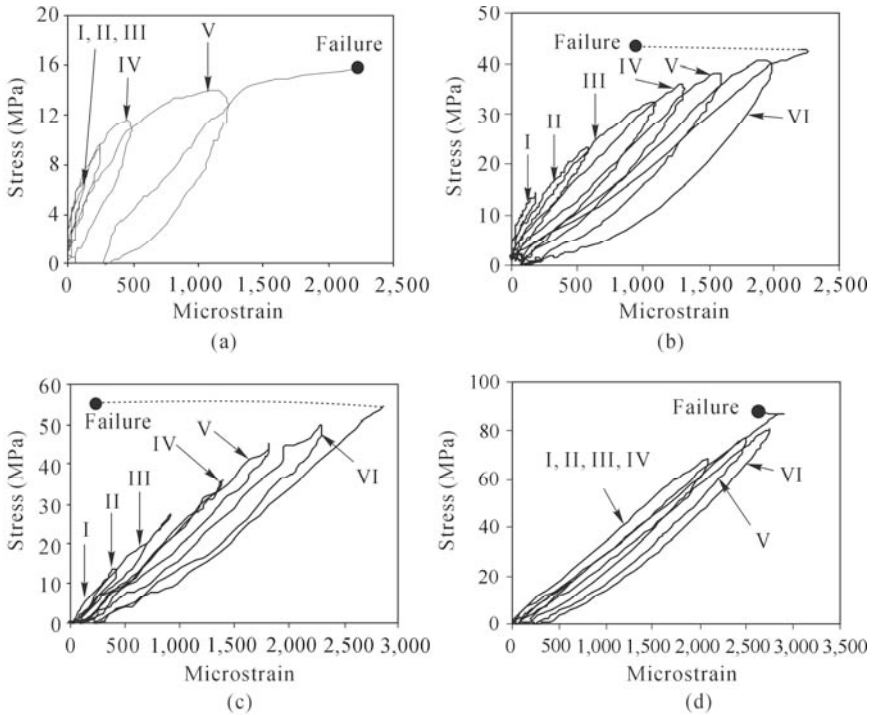


Fig. 5.9 Load histories of four concrete cubes. (a) C17; (b) C43; (c) C52; (d) C86

Fig. 5.10 plots the loss of secant modulus against the loss of equivalent spring stiffness for four typical cubes C17, C43, C52 and C86. A good correlation can be observed between the loss in secant modulus and the loss in equivalent stiffness as identified by the PZT transducers. From these results, it is evident that equivalent spring stiffness can be regarded as a damage sensitive parameter and can be utilized for quantitatively predicting the extent of damage in concrete (it should be noted that the equivalent spring stiffness was obtained solely from the signatures of the PZT transducers. No information about concrete specimen is warranted *a priori*).

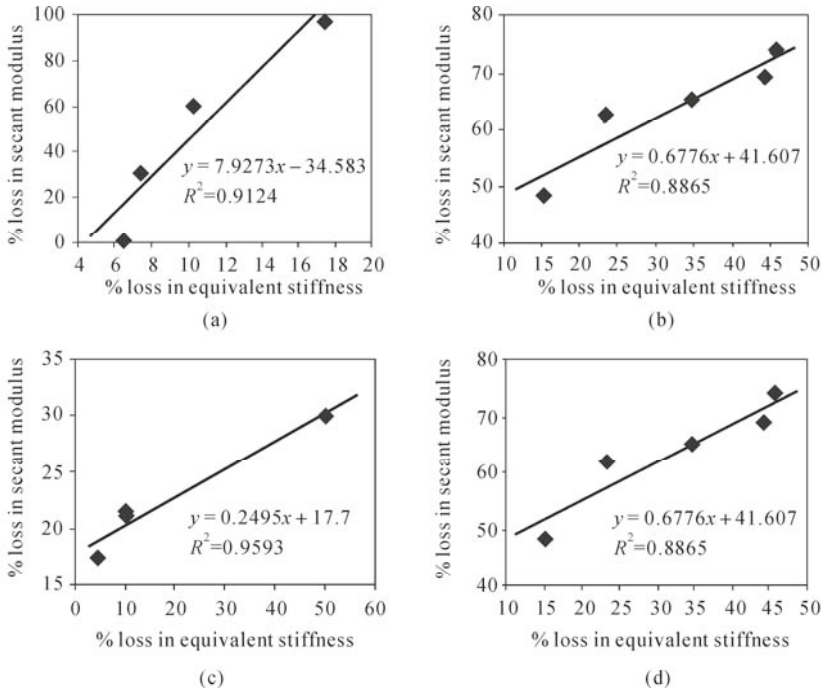


Fig. 5.10 Correlation between loss of secant modulus and loss of equivalent spring stiffness with damage progression: (a) C17; (b) C43; (c) C52; (d) C86

It should also be mentioned that the extracted equivalent damping was found to increase with damage. This was as expected, since damping is known to increase with the development of cracks in concrete. Fig. 5.11 shows the typical plot for the increase in equivalent damping with damage progression for cube C43. Also shown is the progressive loss in the equivalent stiffness with load ratio. However, in most other cubes, no consistent pattern was found with respect to damping. Only an exceedingly large increase near failure was observed. For this reason, the equivalent stiffness was selected as the damage sensitive parameter because of its progressive decrease with damage progression and consistent performance.

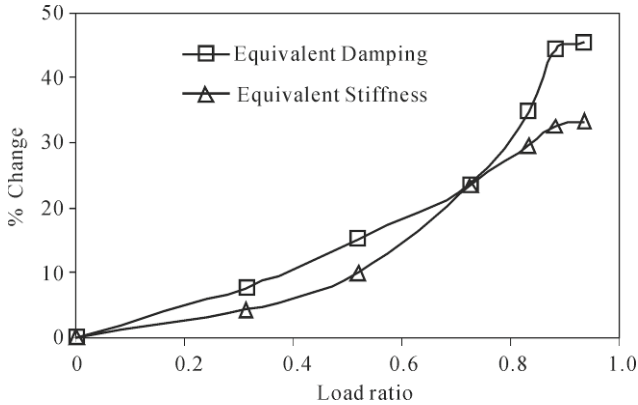


Fig. 5.11 Changes in equivalent damping and equivalent stiffness for cube C43

Section 5.6 covers the development of an empirical damage model based on the equivalent spring stiffness.

5.5 Monitoring Concrete Curing Using Extracted Impedance Parameters

In order to evaluate the feasibility of the “identified” spring stiffness in monitoring concrete curing, a PZT patch of size 10 mm×10 mm×0.3 mm and grade PIC 151 was instrumented on a 150 mm concrete cube (Fig. 5.12). Again, a bond layer thickness of 0.125 mm was achieved with the aid of optical fiber pieces. The instrumentation was implemented three days after casting the cube. The PZT patch was periodically interrogated for the acquisition of electrical admittance signatures, and this continued for a period of one year.

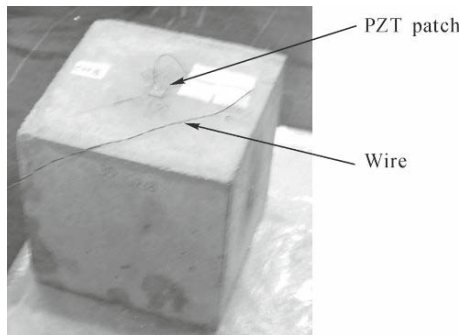


Fig. 5.12 Monitoring concrete curing using EMI technique

Figs. 5.13 and 5.14, respectively, show the short-term and long-term effects of ageing on the conductance signatures in the frequency range 100 – 150 kHz. It can be observed that with ageing, the peak shifts towards the right and, at the same time, becomes sharper. This trend is opposite to the trend for compression tests, where the peaks usually shift towards the left. The shifting of resonance peak towards the right, in the present case, indicates that the stiffness (and hence the strength) increased with curing time. The phenomenon of peaks becoming sharper with time suggests that the material damping was reducing (concrete was initially “soft”). Damping in concrete is known to occur mainly in the matrix, some in the interfacial boundaries and a small fraction in the aggregates. Moisture in the matrix is the major contributor to damping (Malhotra, 1976). Hence, with curing, as moisture content drops, the damping in concrete tends to reduce.

It should be noted that the particular peak in this figure is the resonance peak of the host structure. It should not be confused with the resonance peak of the PZT patch, such as that shown in Fig. 5.3. As concrete strength increases, the resonance peak of the PZT patch subsides owing to the predominance of structural interaction (Fig. 5.3). However, the structural resonance peak (Figs. 5.13 and 5.14) tends to become sharper. In other words, increasing structural stiffness tends to “dampen” PZT resonance and “sharpen” the host structure’s resonance peak.

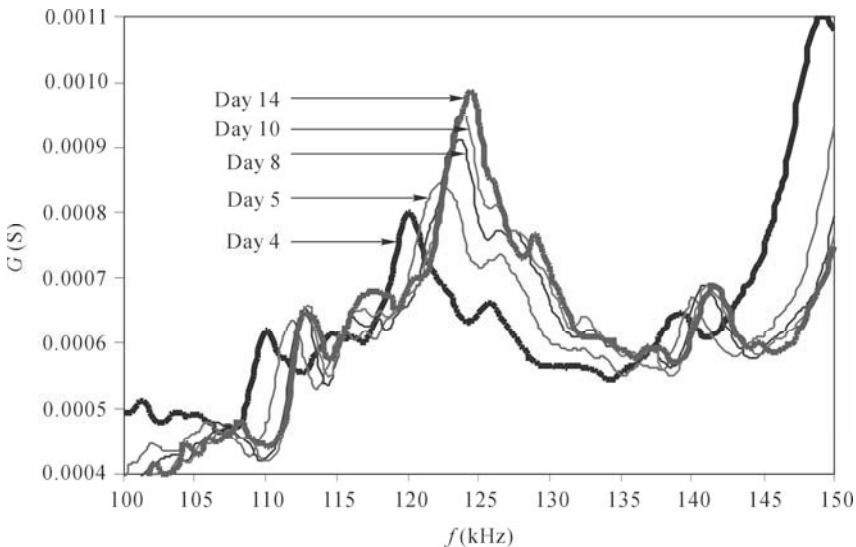


Fig. 5.13 Short-term effect of concrete curing on conductance signatures

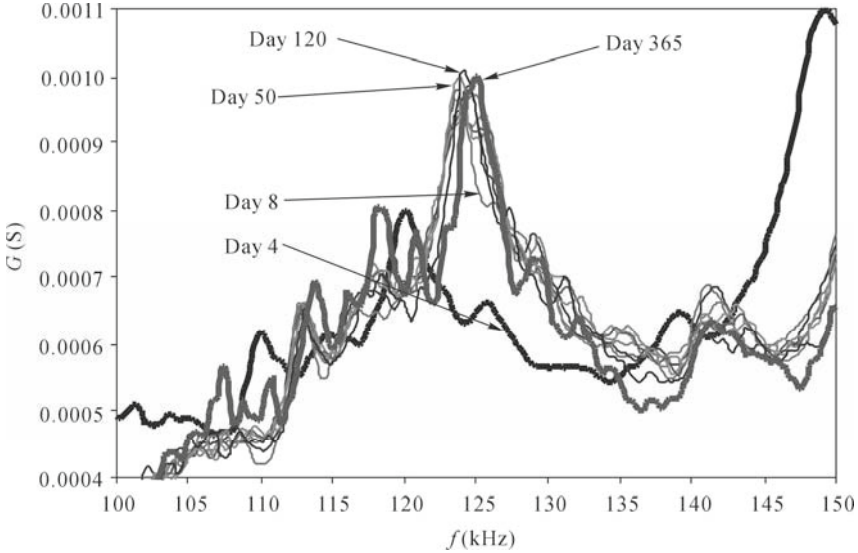


Fig. 5.14 Long-term effect of concrete curing on conductance signatures

In order to quantitatively describe the phenomenon, the equivalent spring constant of the cube was worked out in the frequency range 60 – 100 kHz using the signatures of the bonded PZT patch. The results are presented in Fig. 5.15, which shows that as the curing progresses, the equivalent spring stiffness increases, reaching an asymptotic value of about 115% higher than the first recorded value (four days after casting). After 28 days, the increase in the equivalent spring stiffness is about 80%. Comparing with similar monitoring, using the ultrasonic pulse velocity technique, our approach is seen to be much better in monitoring concrete curing. For example, Malhotra (1976) reported an increase of only 7% in the ultrasonic pulse velocity between days 4 and 10 (after casting). On the other hand, in our experiment, a much higher increase of 60% was observed between days 4 and 10. This establishes the superior performance of the EMI-based approach for monitoring concrete curing. This technique can be applied in the construction industry to decide the time of removal of the form work. It can also be employed to determine the time of commencement of pre-stressing operations in the construction of pre-stressed structures. Numerous other industrial processes which involve curing of materials (other than concrete) can also benefit from this technique.

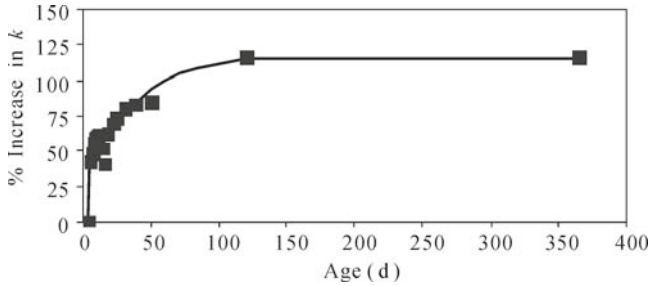


Fig. 5.15 Effect of concrete curing on equivalent spring stiffness

5.6 Establishment of Impedance-Based Damage Model for Concrete

5.6.1 Definition of Damage Variable

It has been shown that, in the frequency range 60 – 100 kHz, concrete essentially behaves as a parallel spring damper (*Kelvin Voigt*) system. The equivalent stiffness k has been established as a damage sensitive system parameter since it was found to exhibit a reasonable sensitivity to any changes taking place in the system on account of damages. This section deals with calibrating k against damage using the data from compression tests on concrete cubes of strengths ranging from moderate to high values.

In general, any damage to concrete causes reduction in the equivalent spring stiffness as identified by the piezo-impedance transducer surface-bonded to it. At the i^{th} frequency, the associated damage variable, D_i , can be defined as

$$D_i = 1 - \frac{k_{di}}{k_{oi}} \quad (5.2)$$

where K_{oi} is the equivalent spring stiffness at the i^{th} measurement point in the pristine state, and K_{di} the corresponding value after damage (note: $0 < D_i < 1$; thus, D_i measures the extent of “softening” of the identified equivalent stiffness due to damage). D_i is expected to increase in magnitude with damage severity, and the host structure is deemed to fail if it exceeds a critical value D_c . However, from comprehensive tests on concrete cubes, it was found that it is not possible to define a unique value of D_c . This is due to unavoidable uncertainties related to concrete, its constituents and the PZT patches. On this account, Soh and Bhalla (2005) proposed to define the critical value of the damage variable using the theory of fuzzy sets.

Mathematical statistics is mainly concerned with *random variables*, that is, variables which can assume different values due to unpredictable factors. For example, the damage variable D_i defined earlier is a random variable. Within a given excitation frequency range (60 – 100 kHz in the present case), it usually carries random values. In general, a random variable can be either *discrete* or *continuous*. The mean value of a sample consisting of N values ($x_1, x_2, x_3, \dots, x_n$) of a random variable “ x ” is defined by

$$\mu = \frac{1}{N} \sum_{j=1}^N x_j \quad (5.3)$$

and the variance, s^2 , is defined by

$$s^2 = \frac{1}{(N-1)} \sum_{j=1}^N (x_j - \mu)^2 \quad (5.4)$$

The square root of s^2 is the *standard deviation* and is denoted by σ . Most random experiments (involving a random variable) exhibit statistical regularity or “stability”. If D is a random event, there exists a number $p(D)$ ($0 \leq p(D) \leq 1$) called the *probability* of D , such that if the experiment is performed repeatedly, it is almost certain that the relative frequency of occurrences of D is approximately equal to $p(D)$.

For a continuous random variable “ x ”, the *probability density function*, $p(x)$, is a function which defines the probability of the variable over the possible range of values the variable can attain, satisfying the following condition

$$\int_{x=-\infty}^{x=\infty} p(x) dx = 1 \quad (5.5)$$

The *distribution function* or *cumulative distribution function*, $F(x)$, of such a continuous variable is defined as

$$F(x) = \int_{v=-\infty}^{v=x} p(v) dv \quad (5.6)$$

where the integrand is continuous, except possibly at multiple finite values of v . Differentiating Eq. (5.6) with respect to x , one obtains

$$F'(x) = p(x) \quad (5.7)$$

The mean of a continuous distribution is defined by

$$\mu = \int_{x=-\infty}^{x=\infty} xp(x)dx \tag{5.8}$$

Eqs. (5.5) to (5.8) can be easily modified to suit a discrete random variable by replacing the integration by summation (Kreyszig, 1993).

Given a data set $x_1, x_2, x_3, \dots, x_N$ of independent observations, the empirical cumulative distribution function can be obtained by

$$\hat{F}(x) = \frac{1}{N} \sum_{x_i \leq x} n_i \tag{5.9}$$

where n_i is the frequency of x_i in the data set. This provides an empirical estimate of $F(x)$.

The distribution of a random variable encountered in real situations may conform to any of the standard distributions, such as the normal, the Binomial, the hypergeometric or the Poisson distribution. Table 5.2 lists the probability distribution function for these distributions. Details of other standard distributions are covered by Kreyszig (1993). Whether a given random variable has a distribution, conforming to a standard distribution, can be ascertained by means of the *Kolmogorov-Smirnov* “goodness-of-fit” test. For this purpose, the empirical distribution, $\hat{F}_n(x)$, needs to be worked out using Eq. (5.9). The unknown distribution $F(x)$ is said to fit the specified distribution $F_o(x)$ with a confidence level of $(1-\alpha)$ (where $0 \leq \alpha \leq 1$, typically 10 to 15%) if

$$\max|\hat{F}_n(x) - F_o(x)| \leq \alpha \tag{5.10}$$

Table 5.2 Common probability distributions

Distribution	Probability density function $f(x)$
Normal	$\frac{1}{\sigma\sqrt{2\pi}} e^{-\frac{(x-\mu)^2}{2\sigma^2}}$
Poisson	$\frac{\mu^x e^{-\mu}}{x!}$
Binomial	$C_x^n \left(\frac{\mu}{n}\right)^x \left(1 - \frac{\mu}{n}\right)^{n-x}$

Note: C_x^n = Number of possible combinations of x objects out of n

5.6.2 *Damage Variable Based on the Theory of Fuzzy Sets*

Scientists and engineers describe complex physical systems by simple mathematical models, often making considerable idealization in the process. A practical approach to simplify a complex system is to tolerate a reasonable amount of imprecision, vagueness and uncertainty during the modeling phase. It was this logic which Zadeh (1965) employed when he introduced the notion of *fuzzy sets*. This principle of scientifically accepting a certain loss of information has turned out to be satisfactory in many knowledge-based systems. Fuzzy systems are widely used to model information that is afflicted with imprecision, vagueness and uncertainty.

A fuzzy set is defined as a class of objects with continuum grades of membership. Such a set is characterized by a *membership* (or *characteristic*) *function*, which assigns to each object a grade of membership ranging from 0 to 1. Let X be a space of objects with the generic element of X denoted by “ x ”. When A is a set in space X in the ordinary sense of terms, its membership function can take only two values 1 and 0, according to whether “ x ” does or does not belong to X . On the other hand, a fuzzy set (or class) A_f in X is characterized by a membership function $f_m(x)$, which associates with each object in “ x ” a real number in the interval $[0,1]$ representing the “grade of membership of x ” in A . The nearer the value of $f_m(x)$ to unity, the higher the grade of membership of “ x ” in A . For example, let X be the real line R and let A_f be a fuzzy set of numbers which are “much” greater than “1”. A precise, albeit subjective, value of characterization of A by specifying $f_m(x)$, can then be given. The representative values of such a function might be $f_m(0) = 0$, $f_m(10) = 0.1$ and $f_m(100) = 1.0$, and so on. In general, fuzzy sets have merely an intuitive basis as a formal description of vague data and are generally specified directly by experts intuitively.

Fuzzy sets were first used in civil engineering in the late 1970s (*e.g.* Brown, 1979), and Chameau *et al.* (1983) suggested several potential applications for them in civil engineering. Typically in structural analysis, a number of basic variables are involved such as geometry and dimensions, material parameters, boundary conditions, loads and the methods of modeling and analysis. Some of these variables show randomness, some show fuzziness and some are characterized by both. The element of randomness is due to the uncertainty of the loads, modeling uncertainties and statistical uncertainties (due, in turn, to the use of limited information). The fuzziness-related uncertainty is due to the definition of internal parameters such as structural performance. Many innovative applications of fuzzy logic and fuzzy sets in civil engineering can be found in the literature, such as Dhingra *et al.* (1992), Valliappan and Pham (1993), Soh and Yang (1996), Wu *et al.* (1999) and Yang and Soh (2000).

The membership functions represent the subjective degree of preference of a decision maker, as well as the most controversial part of applying the theory of fuzzy sets for solving engineering problems. In engineering applications, the most commonly used shapes are linear, half concave, exponential, triangular, trapezoidal,

parabolic, sinusoidal and the extended π -shape (Valliappan and Pham, 1993; Wu *et al.*, 2001), several of which are shown in Fig. 5.16. The choice of a particular shape depends on the opinion of the expert, since there is no hard and fast rule to ascertain which shape is the most realistic.

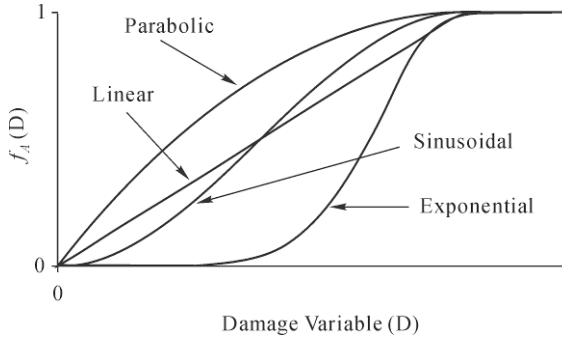


Fig. 5.16 Different types of membership functions for fuzzy sets

If $p(D)$ is the probability density function for describing a structural failure event D , the failure probability may be expressed as

$$P_f = \int_S p(D) dD \quad (5.11)$$

where S is the space of the structural failure event. However, by the use of fuzzy set theory, a failure event can be treated as a “fuzzy failure event”. If the failure space is a fuzzy set with a membership function $f_m(D)$, Wu *et al.* (1999) defined the fuzzy failure probability as

$$P_f = \int_S f_m(D) p(D) dD \quad (5.12)$$

This principle has been used in evaluating concrete damage.

Returning to damage diagnosis in concrete, Fig. 5.17 shows the equivalent spring stiffness worked out at various load ratios (applied load divided by failure load) for five cubes labeled C17, C43, C52, C60 and C86. Damage variables were computed at each frequency in the interval 60 – 100 kHz, corresponding to each load ratio, for all the five cubes.

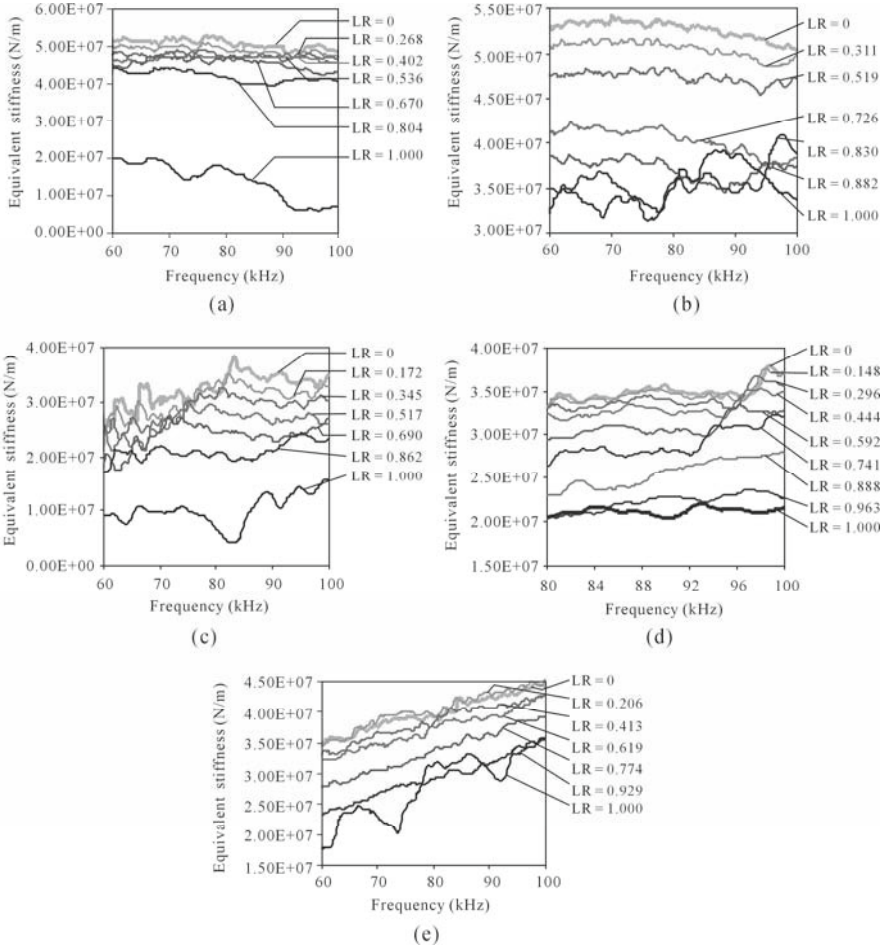


Fig. 5.17 Effect of damage on equivalent spring stiffness (LR: Load Ratio): (a) C17; (b) C43; (c) C52; (d) C60; (e) C86

The mean and standard deviation of damage variables were then evaluated at each damage ratio. Statistical examination of the data pertaining to the damage variables indicated that it followed a normal probability distribution (Table 5.2). To verify this, Fig. 5.18 shows the empirical cumulative probability distribution of D_i and also the theoretical normal probability distribution for all the cubes at or near failure. It was found that the damage variables statistically fitted very well into the normal distribution. The adequacy of the normal distribution was quantitatively tested by the *Kolmogorov-Smirnov* “goodness-of-fit” test technique and the normal distribution was found to be acceptable under an 85% confidence limit for all the cubes. Similarly, damage variables for all the other damage states were also found to follow the normal probability distribution reasonably well.

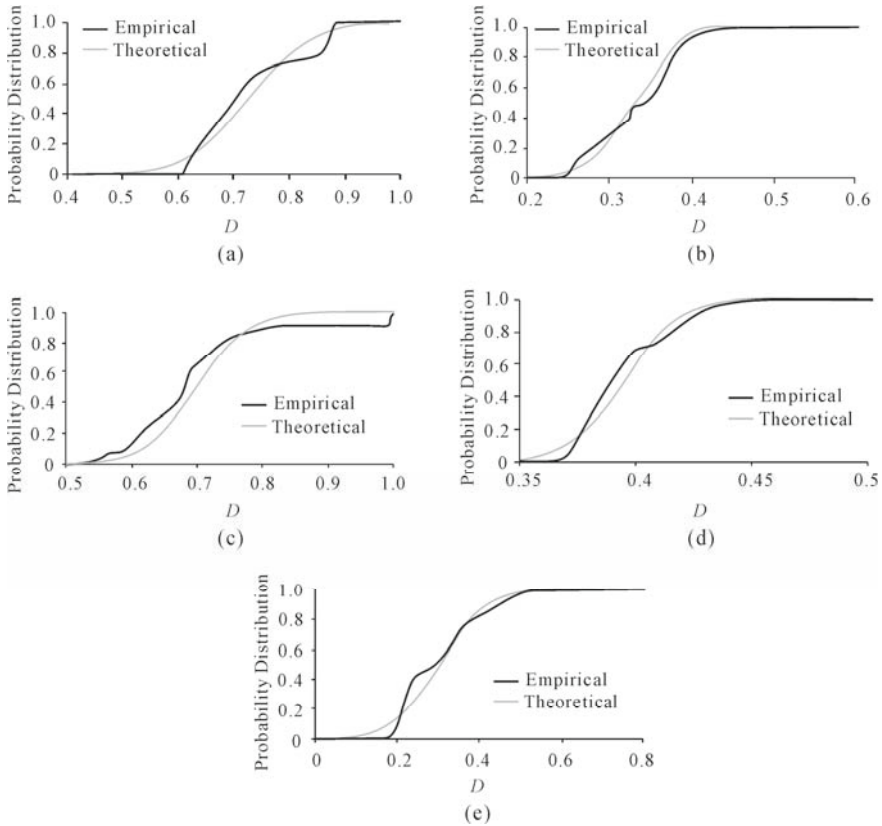


Fig. 5.18 Theoretical and empirical probability density functions near failure: (a) C17; (b) C43; (c) C52; (d) C60; (e) C86

5.6.3 Fuzzy Probabilistic Damage Calibration of Piezo-Impedance Transducers

From the theory of continuum damage mechanics, an element can be deemed to fail if $D > D_c$. As mentioned earlier, rather than defining a unique value of the critical damage variable D_c , we employed a fuzzy definition to account for uncertainties. Using the fuzzy set theory, a fuzzy region can be defined in the interval (D_L, D_U) where D_L and D_U , respectively, represent the lower and upper limits of the fuzzy region. $D > D_U$ represents a failure region with 100% failure possibility and $D < D_L$ represents a safe region with 0% failure possibility. Within the fuzzy, or transition region, that is $D_L < D < D_U$, the failure possibility can vary between 0% and 100%. A characteristic, or membership function, f_m , can be defined ($0 < f_m(D) < 1$) to express the grade of failure possibility within the region (D_L, D_U) . The fuzzy failure probability can then be determined from Eq. (5.10), as

$$P_f = P(D \geq D_C) = \int_{D=0}^{D=1} f_m(D)p(D)dD \quad (5.13)$$

where $p(D)$ is the probability density function of the damage variable D , which in the present case complies with normal distribution. Based on observations during concrete cube compression tests, D_L and D_U are chosen as 0.0 and 0.40 respectively. Further, sinusoidal membership function given by the following equation is adopted

$$f_m = 0.5 + 0.5 \sin \left[\frac{\pi}{(D_U - D_L)} (D - 0.5D_U - 0.5D_L) \right] \quad (5.14)$$

This function is chosen since it reflects the observed trend in transducer response (in terms of damage variable based on “identified” equivalent stiffness) with damage growth. It has been observed that the damage variable typically follows the trend of an S-curve, *i.e.* initially rising steeply with damage progression before attaining saturation. This is represented very well by the sinusoidal membership function. Making use of this membership function, the fuzzy failure probability (FFP) was worked out for the five concrete cubes at each load ratio. It should be mentioned that Wu *et al.* (1999) used similar principles to carry out fuzzy probabilistic damage prediction of rock masses subjected to explosive loads.

A load ratio of 0.4 can be regarded as incipient damage since concrete is expected to be under “working loads”. All concrete cubes were found to exhibit a fuzzy failure probability of less than 30% at this load ratio. Similarly, after a load ratio of 0.8, the concrete cubes can be expected to be under “ultimate loads”. For this case, all the cubes exhibited a fuzzy failure probability of greater than 80% irrespective of their strength (Fig. 5.19). Fig. 5.20 shows the FFP of the cubes at intermediate stages during the tests. Based on minute observations during these tests, the following classification of damage is recommended based on FFP:

- | | |
|---------------------|---|
| (1) FFP < 30% | Incipient Damage (Micro-cracks) |
| (2) 30% < FFP < 60% | Moderate damage (Cracks start opening up) |
| (3) 60% < FFP < 80% | Severe damage (Large visible cracks) |
| (4) FFP > 80% | Failure imminent. |

Thus, the fuzzy probabilistic approach quantifies the extent of damage on a uniform 0 – 100% scale. This can be employed to evaluate damage in real-life concrete structures.

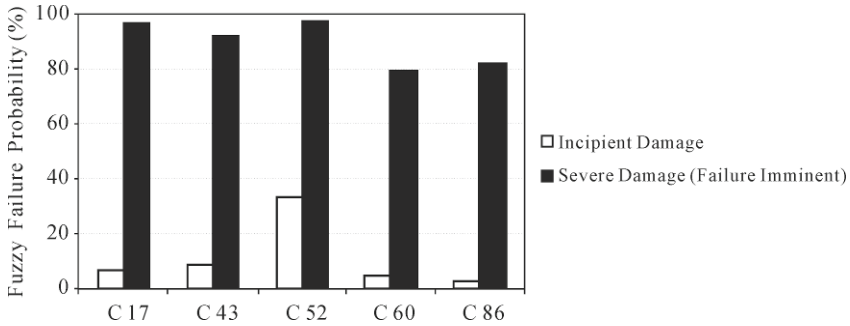


Fig. 5.19 Fuzzy failure probabilities of concrete cubes at incipient damage level and at failure stage

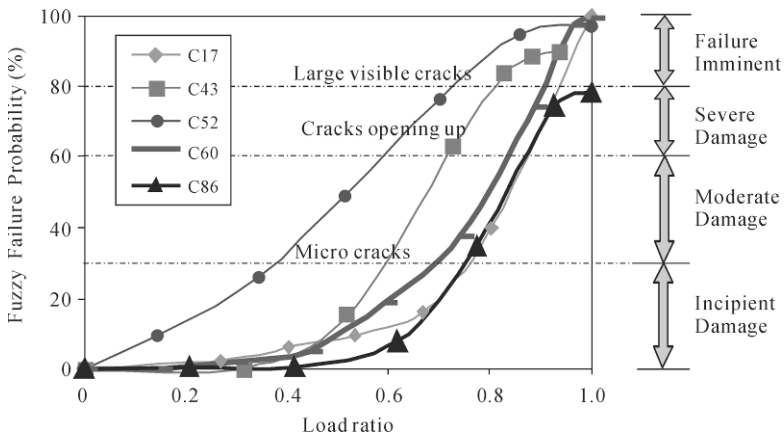


Fig. 5.20 Fuzzy failure probabilities of concrete cubes at various load levels

All the PZT patches exhibited more or less uniform behavior with damage progression in concrete, although the strength of concrete cubes varied from as low as 17 MPa to as high as 86 MPa. Hence, the PZT patches were subjected to a wide range of mechanical stresses and strains during the tests. At a load ratio of 1.0, almost the same order of FFP was observed, irrespective of the absolute load or stress level (for example 17 MPa for C17 and 86 MPa for C86). In general, the PZT material showed very high compressive strength, typically over 500 MPa and it essentially exhibited a linear stress-strain relationship up to strains as high as 0.006 (Cheng and Reece, 2001). In the experiments conducted on concrete cubes, the strain level never exceeded 0.003 (50% of the linear limit).

It was also observed that in all the cubes tested, the damage typically initiated near the edges of the cube and migrated to regions near the PZT patch with increasing load ratios. After failure of the cubes, all the PZT patches were found intact. Fig. 5.21 shows close-up views of the cubes after the tests. The results showed that the sensor response reflected the damage to the surrounding concrete more than damage to the patches themselves.

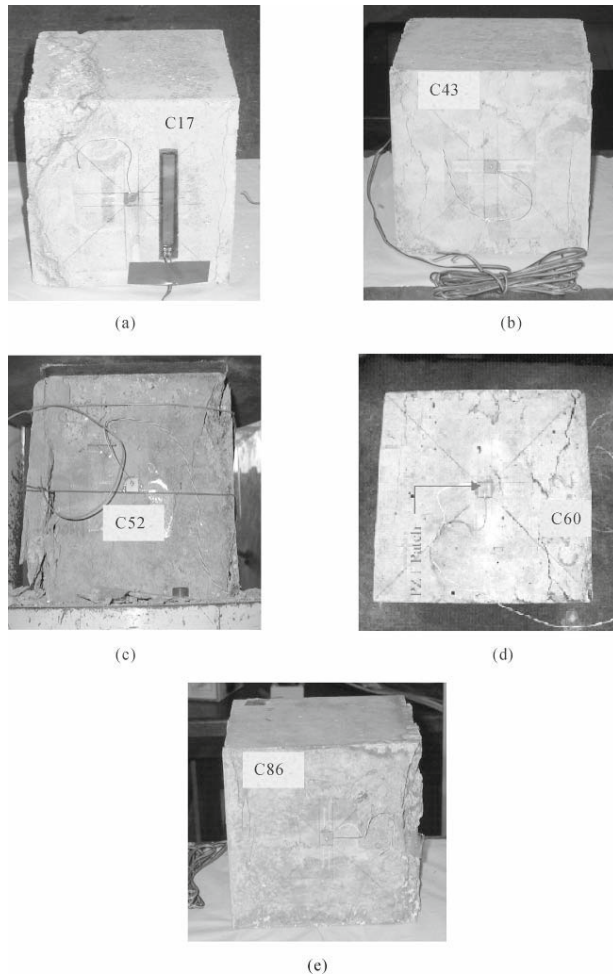


Fig. 5.21 Cubes after the test: (a) C17; (b) C43; (c) C52; (d) C60; (e) C86

In general, we can expect such good performance in materials like concrete, characterized by low strength, compared with the PZT patches. Thus, damage to concrete is likely to occur first, rather than to the PZT patch. Furthermore, though the cubes were tested in compression, the same fuzzy probabilistic damage model can be expected to hold good for tension too.

5.7 Embedded PZT Patches and Issues Involved

Typically, surface-bonded PZT patches are more effective when they are stiffer than the host structure, and embedded PZT patches are more efficient when they

are less stiff than the host structure. It is much simpler to bond PZT patches onto the host structure though embedment is advantageous as it offers durability and protection from surface finish, vandalism and environmental attack (Annamdas and Soh, 2007). Additionally, embedded PZT patches can be more effective in monitoring the crucial areas inside the structure, whilst not interfering with the aesthetic appearance of the structure.

However, embedment of PZT patches in the structure is not as simple as surface bonding. Primarily, the host structure must be made of materials which allow PZT patches to be embedded, such as concrete, laminates or polymers. Next, the embedded PZT patches must be non-reactive with the host structure's materials. Hence, the embedded PZT patches must be properly isolated using inert materials to make them chemically stable, yet properly bonded to the host structure. It should not increase the stiffness or strength of the host structure, *i.e.* not influence the original design of the host structure. It should be reliable during electrical and mechanical loading, and should withstand the combined mechanical and electrical cyclical loading (Mall, 2002). The interface between the PZT patch and the host structure needs to have reliable electrical conduction and bonding, and therefore needs sound inter-connectors (Hagood *et al.*, 1988, Paget *et al.*, 2002). Additionally, if the host structure is made of concrete (as in the present case), the embedded patch must withstand the vibration induced in the casting process. Moreover, it must withstand the curing pressures and temperatures of the host material (Annamdas, 2007).

5.8 Experimental Set-up

The experimental set-up required for embedded PZT patch-based EMI technique is the same as that for the surface-bonded PZT patch described in Section 4.7. The concrete specimen, through the embedded PZT patch, is connected to the HP Impedance analyzer (Hewlett Packard, 1996) through the Agilent Multiplexer (Agilent Technologies, 2007).

5.8.1 Methods to Fabricate Embeddable PZT

Several configurations of embedded PZT patches are described in the literature. The basic design constitutes a PZT transducer, inter connectors (wires), bonding adhesive and bonding fibers/layers assembled into an embeddable PZT patch. Researchers such as Paget *et al.* (2002), Chen *et al.*, (2004), Annamdas (2007) and Wen *et al.*, (2007) used embedded PZT patches where the PZT transducers were sandwiched inside layers of rubber or cardboard. However, all these embeddable PZT patches, assembled by different fabrication methods, are not general purpose

and are mostly application-based, *e.g.*, an embeddable patch prepared for axial load monitoring is neither useful nor appropriate for transverse load monitoring.

Researchers such as Elspass *et al.* (1995) and Paget *et al.* (2002) chose design constituents such as glass-fiber-reinforced thermoplastics (GFRP-plyes) or carbon-fiber-reinforced thermoplastic (CFRP) composite plies, inter connectors and PZT transducers. The assembly was achieved by cutting the composite plies and fitting the PZT transducer into the laminated composites. The materials for the inter connectors were the same as that of the composite. The two inter connectors were placed on each side of the PZT transducer. Cut-outs in the GFRP or CFRP were made to allow electrical contact between the terminals and the embedded PZT transducer. Elspass *et al.* (1995) achieved electrical insulation from the upper and lower inter connectors by two CFRP. Hagood *et al.* (1988) used a cut-out window of approximately the same dimension as the PZT transducer, and slits were cut in the plies directly above and below the PZT transducer to allow the inter connectors to be drawn in or out. Hence, the design and fabrication of such lay-ups are complex. Chen *et al.* (2004) sandwiched their PZT transducer between two circular rubber layers. The PZT transducer had the same dimension as the rubber layers, where the upper/lower inter connectors were sandwiched between the PZT surfaces and the upper/lower rubber layers. Fig. 5.22 shows our design where the PZT transducer was completely encapsulated to ensure better protection, unlike the design of Chen *et al.* (2004). However, the PZT transducer was not circular but square, and a part of the inter connectors was inside the rubber composite.

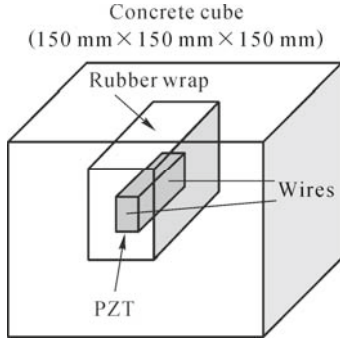


Fig. 5.22 Embeddable PZT patch using encapsulation of silicon rubber

In general, the fabrication method of embeddable PZT patches is case-specific, and depends on the type of composite or materials into which the PZT patches need to be embedded (Paget, 2001) which limits their application. Furthermore, embedded PZT patches can fail if they are not properly assembled, *e.g.*, two out of three PZT patches, from our design, failed to function after a few days of their embedment in three similar concrete cubes (150 mm×150 mm×150 mm). A more robust method of PZT embedment was thus later presented by Annamdas *et al.* (2009). The new method assembled the embeddable PZT patch in four steps, and at every step the admittance signatures were recorded to observe the changes and

check whether the PZT patch was functioning normally without incurring any damage during the fabrication process. The method is presented below to show the ease in assembling a robust embeddable PZT patch for damage monitoring.

5.8.2 Fabrication of Robust Embeddable PZT Patch

Step 1: “Free” PZT Patch

Two PZT transducers of size 10 mm×10 mm×2.0 mm and grade PIC 151 are selected for assembly into two embeddable PZT patches. Two 1 m length electrical wires are soldered to the electrodes of each PZT transducer. The soldered wires are then connected to the impedance analyzer via the switch box for recording the admittance signatures for the desired frequency ranges. Admittance signatures for the two free (un-bonded and un-embedded) PZT patches are recorded.

Step 2: PZT Patch Wrapped with Epoxy

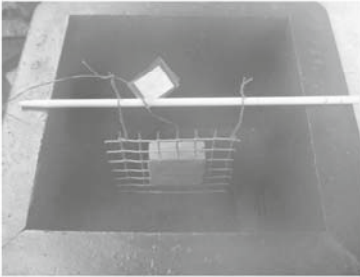
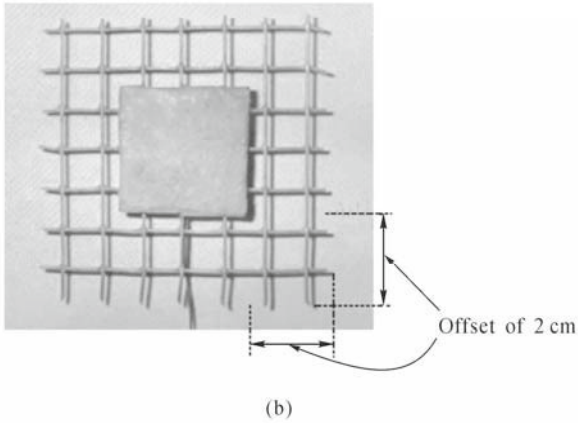
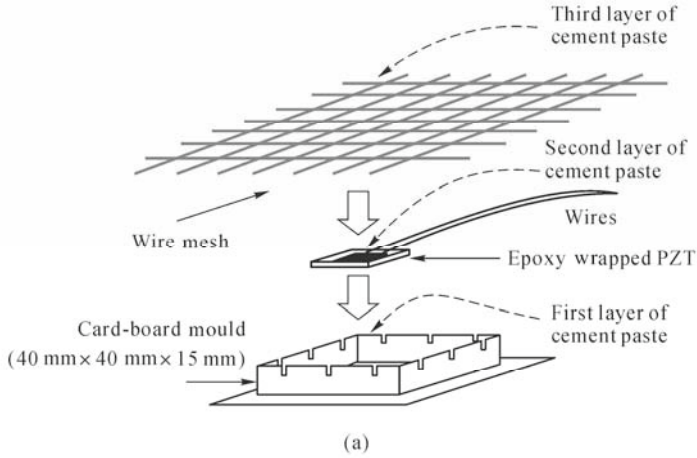
A two-part RS 850-940 epoxy adhesive consisting of equal proportions of hardener and resin is thoroughly mixed, and a thin layer of the epoxy adhesive mix is wrapped around the PZT patch (Fig. 3.14). A nominal pressure is applied over the wrapped PZT patch to ensure a thin uniform thickness of epoxy layer around the PZT patch. This epoxy wrap will seal the PZT patch from all the chemical, mechanical and electrical effects. The wrapped PZT patch is then allowed to cure at room temperature for 24 h. The irregular shape of the epoxy wrap is later trimmed. The admittance signatures are again recorded to check for any damage (*e.g.*, cracks or breaks in the PZT patch) incurred during the wrapping process.

Fig. 3.15 shows the representative admittance signatures of a “free” and an epoxy-wrapped PZT patch. The free PZT signatures are found to be slightly inconsistent and the variations (<10%) could be due to the heterogeneous chemical composition and mechanical differences during the formation and polarization process. If there is any abnormality in the signature of the epoxy wrapped PZT patch (because of the epoxy wrap), it would be regarded as a failure, occurring during Step 2, and so a new PZT transducer would need to be used, repeating Steps 1 and 2. The major peaks observed, compared with the “free” PZT signature (Step 1), are quite similar but with different magnitudes and slight leftward shifts due to the changes in its mass, stiffness and dampness. It should be noted that admittance signatures are generally sensitive to shear lag effect of the bonding epoxy wrap, causing some vertical and horizontal shifts of signatures (Ong *et al.*, 2002). Therefore, if the epoxy wrap is consistent and homogenous throughout, the differences in variation of the signatures could be minimized.

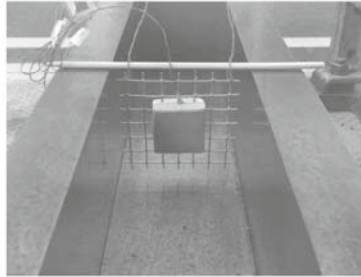
Step 3: Robust Embeddable PZT Patch

A cardboard mould (40 mm×40 mm×15 mm) is prepared, and a Portland cement paste of 1:2 cement-to-sand ratio is then poured into the cardboard mould in three layers. The epoxy-wrapped PZT patch is positioned after the first layer, followed

by wire mesh positioned after the second layer. This arrangement is to reinforce the vicinity of the patch to provide strong bonding between the patch and host structure. Finally, the third layer is poured, as shown in Fig. 5.23(a). The function



(c)



(d)

Fig. 5.23 Robust embeddable PZT patch - preparation and alignments. (a) Layering sequence; (b) Embeddable PZT patch; (c) Mould for cube; (d) Mould for beam

of the wire mesh is to ensure effective bonding upon inclusion of the embedding PZT patch in the concrete specimen. Hence, a wire mesh with an off-set of 2 cm on all sides of the embeddable PZT patch is provided (Fig. 5.23(b)). The embedded PZT patch is then left to cure for 24 h at room temperature. The admittance signatures are again recorded to identify any damage incurred during this step. If there is any abnormality in the signatures, other than appearances of new modes (because of surrounding material), they would be regarded as a failure incurred during this step and a new PZT transducer would have to be used, repeating steps 1, 2 and 3.

All the embeddable robust PZT patches are fabricated using the same dimension cardboard moulds. After completion of step 3, the embeddable patch can be used for embedment in concrete specimens. Figs. 5.23(c)–(d) show the ready-to-use embeddable PZT patches located at a central position inside the concrete moulds of dimension 150 mm×150 mm×150 mm for cube and dimension 500 mm×100 mm×100 mm for beam.

Fig. 5.24 shows the representative conductance signatures for steps 2 and 3. The magnitudes of the major peaks are reduced, with rightward shifts. More peaks can be observed which are due to the cement casing and the wire mesh (mass, stiffness and damping of the casing and mesh).

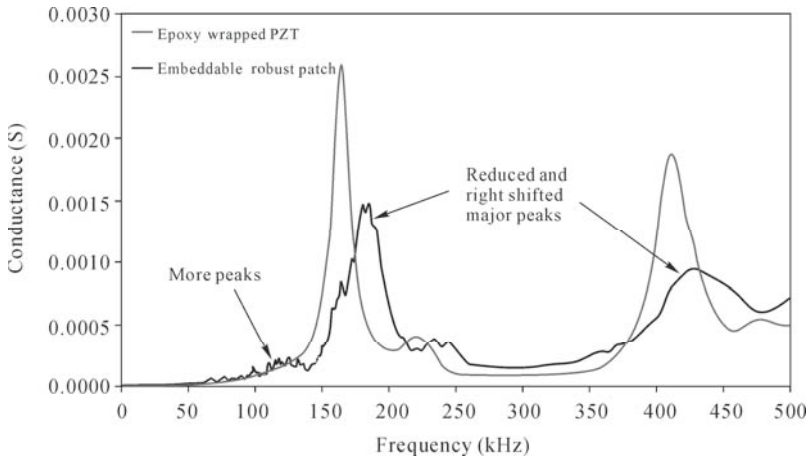


Fig. 5.24 Conductance signatures of epoxy-wrapped and robust PZT patches

Step 4: Application of Embeddable Patches in Concrete Specimens

After the robust embeddable PZT patches are placed in the centre of the concrete moulds, the moulds are filled with concrete. The concrete mix is in accordance to the “Design of normal concrete mixes”, British Standard 8110 (1985). The specimens are then allowed to cure for 24 hours at room temperature, after which time the admittance signatures are recorded to check the functionality of the embedded PZT patch, and to obtain the required pristine state (undamaged) signatures of the concrete specimens. C25 grade concrete is used to prepare the concrete cubes and beams. Fig. 5.25 compares the conductance for an “embeddable

PZT patch” inside a concrete cube. Major peaks occurred within the same frequency range; however, the magnitude of the peaks (at frequency <150 kHz) is reduced on account of the high damping effect of concrete.

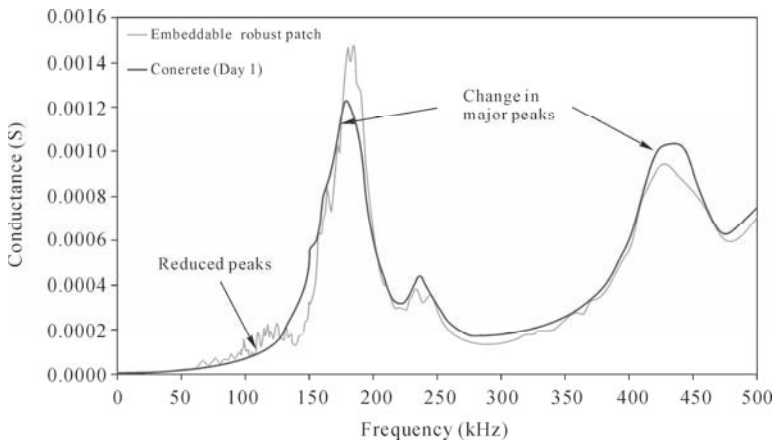


Fig. 5.25 Effect of robust PZT patch in C25 grade cube

5.9 Efficiency of Embedded PZT

The experimental study was extended to include a comparison test and monitoring test in order to determine the efficiency of an embedded PZT patch, with respect to a surface-bonded PZT patch.

5.9.1 Comparison Test

A PZT patch of size 10 mm×10 mm×2.0 mm and grade PIC 151 was surface-bonded on a concrete cube using a thin epoxy adhesive (Fig. 5.12). An admittance signature of the unprotected, surface-bonded PZT patch was first recorded. The PZT patch was then sealed using a silicon coating as protection, and again the admittance signature recorded. Signatures of the unprotected, the protected and the embedded PZT patch are compared in Fig. 5.26. All three admittance signatures are similar up to a frequency of 300 kHz; differences are then noticed up to 500 kHz. There is large variation after 500 kHz which is probably caused by the extremely localized sensing area. The figure shows that the embedded patch has slightly shorter peaks than the surface-bonded patch because of the greater damping effect inside the concrete. Taller and sharper peaks imply greater dynamic interaction over that frequency range. However, the embedded patch is still highly sensitive to minor cracks on the surfaces for frequencies less than 500 kHz.

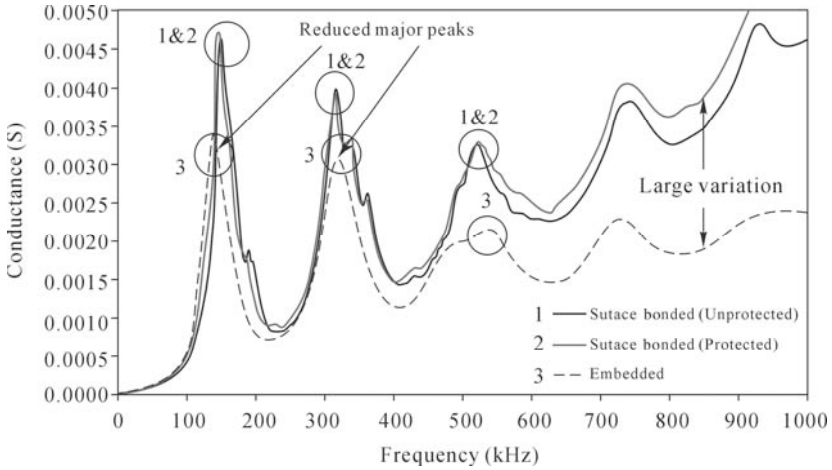


Fig. 5.26 Conductance signatures of surface-bonded and embedded PZT patches

5.9.2 Monitoring Test

Fig.5.27 shows the conductance signatures of concrete during curing, monitored using an embedded PZT patch. The peak shifted rightwards and became progressively sharper with time. The shifting of the peaks suggests that the stiffness increased with the gain in concrete strength. The signatures for the embedded PZT patch can be correlated with those for the surface-bonded PZT patch (Fig 5.13) as there is a similar shift in peaks with an increase in curing period. This demonstrates the possibility of monitoring concrete curing using both embedded and surface-bonded PZT patches.

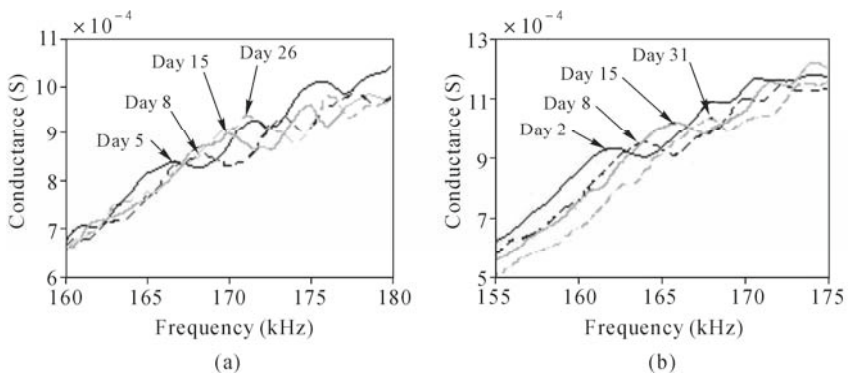


Fig. 5.27 Conductance signatures of C25 grade concrete specimens with embedded PZT patch. (a) Cube; (b) Beam

5.10 Damage Analysis Using Statistical Method

Two types of damages, D1 and D2, were induced on the concrete specimens to study the changes in admittance signatures. In the first type, four edges of the concrete cube specimen were chipped off one after another using a hammer to create loss of mass (disturbance to structure integrity) (Fig. 5.28(a)). The second type of damage was created by inducing four cuts (line damages) 5 mm deep with a spacing of 50 mm on the upper surface of the concrete beam specimen (Fig. 5.28(b)). Each crack-line represented a new damaged state. The locations of 1, 2, 3 and 4 crack-lines were 200 mm, 150 mm, 100 mm and 50 mm respectively from the embedded transducer at the centre of the beam.

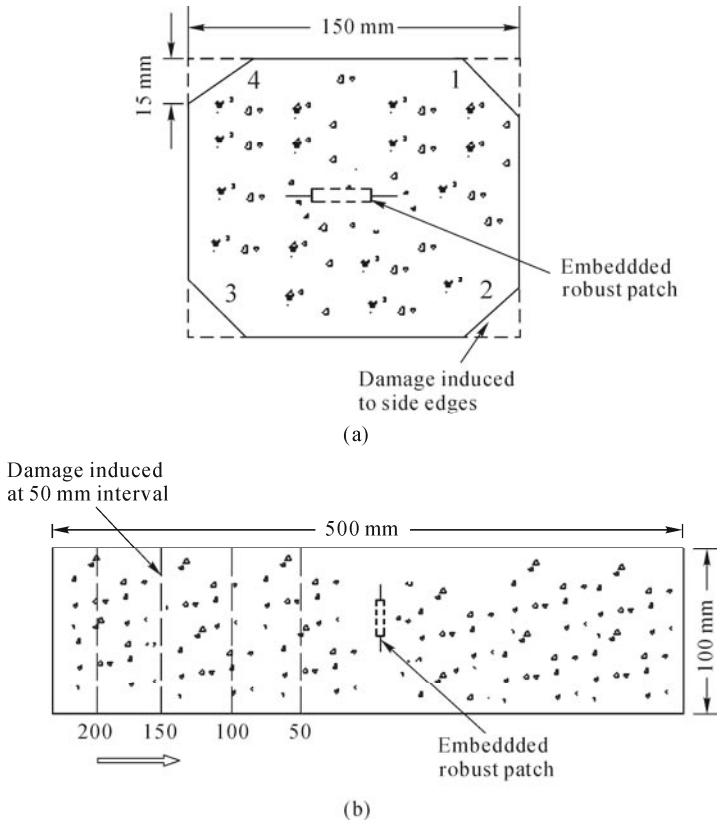


Fig. 5.28 Plan view of two damage types. (a) D1 in cube; (b) D2 in beam

As explained in Section 2.7, in EMI-based SHM, the key indicator of damage is the change in the admittance signature with respect to the damage-free condition, and there are several statistical measures to quantify it.

RMSD index was used to evaluate the deviations in admittance signatures

during the damaged states. The signature of each damaged state was compared with the signature of the undamaged state (baseline). Fig. 5.29 shows the RMSD variations for D1 and D2 types of damages respectively. As the number of damaged states (intensity of damage) increases, the RMSD value increases gradually, which is indicated by the linear regression (trend) line. The selection of frequency range for determining the damage index was achieved by extensive observation of the signatures over a wide range of frequency.

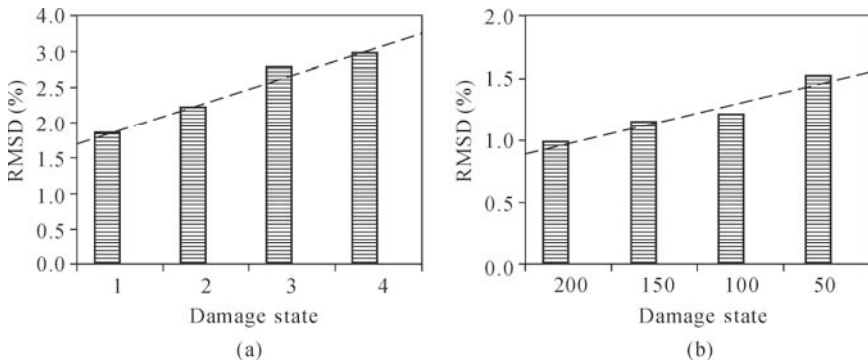


Fig. 5.29 RMSD variations. (a) Concrete cube; (b) Concrete beam

Fig. 5.29(a) depicts the RMSD values for the damaged state signatures in different concrete grades obtained in a frequency range of 80 – 100 kHz. The lowest RMSD value is 1.7% for the first damage, and the largest RMSD value is 3.5% for the fourth damage; for the same excitation, the lowest RMSD value is 1.0% for the first crack-line (200 mm away from the PZT patch) and the largest RMSD value is 1.5% for the fourth crack-line (50 mm away from the PZT patch). The trend has an upward (positive) slope, and a linear relationship between the RMSD value and the damage. The damage progression leads to an increase in the RMSD value. The upward trend in RMSD was because of the increase in overall damage, and also because the damaged states were approaching the PZT patch (Fig. 5.29(b)).

Analysis of both types of damages demonstrates the feasibility of using robust embeddable PZT patches in concrete structures. The embedded PZT patch was able to detect damage as far away as 200 mm, which is similar to that of surface-bonded PZT patches (see Sections 5.3 – 5.6). Smaller-sized PZT patches have better representation for progressive damage in both the cube and beam specimens (Annamdas *et al.*, 2009). The maximum RMSD value of the cube and beam specimens were about 7.4% and 7.0% respectively in the frequency range of 80 – 100 kHz, as observed by Annamdas *et al.* (2009).

References

- Agilent Technologies (2007). *Test and Measurement Catalog*, USA, 496.
- Annamdas, V.G.M. (2007). "Characterization of Smart PZT Transducer and Admittance Signatures using PZT-Structure Interaction Models for Structural Health Monitoring", *Ph.D. Thesis*, Nanyang Technological University, Singapore.
- Annamdas, V.G.M. and Soh, C.K. (2007). "Three Dimensional Electromechanical Impedance Model II: Damage analysis and PZT characterization", *Journal of Aerospace Engineering*, 20(1): 63-71.
- Annamdas, V.G.M., Radhika, M.A. and Soh, C.K. (2009). "Health monitoring of concrete structures using embedded piezoceramic transducers based electromechanical impedance model", *Proceedings of SPIE*, 7292: 729225.
- British Standard-8110 (1985). *Structural Use of Concrete, Part 1, Code of Practice for Design and Construction*.
- Brown, C.B. (1979). "A Fuzzy Safety Measure", *Journal of Engineering Mechanics*, 105: 855-872.
- Chameau, J.L.A., Alteschaeffl, A., Michael, H.L. and Yao, J.P.T. (1983). "Potential Applications of Fuzzy Sets in Civil Engineering", *International Journal of Man-Machine Studies*, 19: 9-18.
- Chen, Y., Wen, Y. and Li, P. (2004). "Characterizations of Dissipation Factors in Piezoelectric Ceramic Discs under Stress and Temperature", *J. Info. Acqu.*, 1(4): 213-219.
- Cheng, B.L. and Reece, M.J. (2001). "Stress Relaxation and Estimation of Activation Volume in a Commercial Hard PZT Piezoelectric Ceramic", *Bulletin of Material Science*, Indian Academy of Sciences, 24(2): 165-167.
- Dhingra, A.K., Rao, S.S. and Kumar, V. (1992). "Non-linear Membership Functions in Multi-Objective Fuzzy Optimization of Mechanical and Structural Systems", *AIAA Journal*, 30(1): 251-260.
- Elspass, W.J., Kunzmann, J., Flemming, M. and Baumann, D. (1995). "Design, Manufacturing and Verification of Piezoceramics Embedded in Fiber-Reinforced Thermoplastics", *Proceedings of SPIE*, 2443: 327-333.
- Hagood, N.W., Crawley, E.F., de Luis, J. and Anderson, E.H. (1988). "Development of Integrated Components for Control of Intelligent Structures Smart Materials", *Structures and Mathematical Issues*, U.S. Army Research Office Workshop, Blacksburg, VA, USA, 80-104.
- Hewlett Packard (1996). *LF 4192 Impedance Analyzer Operation Manual*, Japan.
- Kreyszig, E. (1993). *Advanced Engineering Mathematics*, 7th Ed., New York: Wiley.
- Malhotra, V.M. (1976). *Testing Hardened Concrete: Nondestructive Methods*, American Concrete Institute (ACI) Monograph No. 9.
- Mall, S. (2002), "Integrity of Graphite/Epoxy Laminate Embedded with Piezoelectric Sensor/Actuator under Monotonic and Fatigue Loads", *Smart Materials and Structures*, 11: 527-533.

- Ong, C.W., Yang, Y., Wong, Y.T., Bhalla, S., Lu, Y. and Soh, C.K. (2002). "The Effects of Adhesive on the Electro-mechanical Response of a Piezo-ceramic Transducer Coupled", *Proceedings of ISSS-SPIE International Conference on Smart Materials Structures and Systems*, India, December 12-14, 191-197.
- Paget, C.A. (2001). "Active Health Monitoring of Aerospace Composite Structures by Embedded Piezoceramic Transducers", *Ph.D. Thesis 0117*, Royal Institute of Technology, Valenciennes University.
- Paget, C.A., Levin, K. and Delebarre, C. (2002). "Actuation Performance of Embedded Piezoceramic Transducer in Mechanically Loaded Composites", *Smart Materials and Structures*, 11: 886-891.
- Park, G., Sohn, H., Farrar, C.R. and Inman, D.J. (2003). "Overview of Piezoelectric Impedance-Based Health Monitoring and Path Forward", *The Shock and Vibration Digest*, 35(5): 451-463.
- PI Ceramic (2003). *Product Information Catalogue*, Lindenstrabe, Germany, <http://www.piceramic.de>.
- RS Components (2006). *Product Information Catalogue*, Northants, UK, <http://www.rs-components.com>.
- Soh, C.K. and Bhalla, S. (2005). "Calibration of Piezo-Impedance Transducers for Strength Prediction and Damage Assessment of Concrete", *Smart Materials and Structures*, 14(4): 671-684.
- Soh, C.K. and Yang, J.P. (1996). "Fuzzy Controlled Genetic Algorithm Search for Shape Optimization", *Journal of Computing in Civil Engineering*, 10(2): 143-150.
- Valliappan, S. and Pham, T.D. (1993). "Fuzzy Finite Element Analysis of a Foundation on an Elastic Soil Medium", *International Journal for Numerical and Analytical Methods on Geomechanics*, 17: 771-789.
- Wen, Y., Chen, Y., Li, P., Jiang, D. and Guo, H. (2007). "Smart Concrete with Embedded Piezoelectric Devices: Implementation and Characterization", *Journal of intelligent materials and systems*, 18(3): 265-274.
- Wu, C.Q., Hao, H. and Zhou, Y.X. (1999). "Fuzzy-Random Probabilistic Analysis of Rock Mass Responses to Explosive Loads", *Computers and Geotechnics*, 25(4): 205-225.
- Wu, C.Q., Hao, H., Zhao, J. and Zhou, Y.X. (2001). "Statistical Analysis of Anisotropic Damage of the Bukit Timah Granite", *Rock Mechanics and Rock Engineering*, 34(1): 23-38.
- Yang, Y.W. and Soh, C.K. (2000). "Fuzzy Logic Integrated Genetic Programming for Optimization and Design", *Journal of Computing in Civil Engineering*, 14(4): 249-254.
- Zadeh, L.A. (1965). "Fuzzy Sets", *Information Control*, 8: 338-353.

Integration of EMI Technique with Global Vibration Techniques

S. Bhalla^{*}, R. Shanker, A. Gupta

^{*}Department of Civil Engineering, Indian Institute of Technology Delhi,
Hauz Khas, New Delhi 110016, India
Tel: 91-11-2659-1040; Fax: 91-11-2658-1117
Email: sbhalla@civil.iitd.ac.in

6.1 Introduction

The global vibration techniques, which rely on changes in the first few natural frequencies and the corresponding mode shapes of the structure for damage detection and severity assessment, have been experimented on several real-life structures across the world. Their limitations have been well acknowledged (Catbas *et al.*, 2007). In general, it is not practical to use the global techniques, which are tedious due to long interrogation and computation times, for checkups over short periods. This shortcoming can be easily alleviated by using the EMI technique alongside the global vibration techniques, as will be demonstrated in this chapter.

As pointed out in Chapter 2, in principle, the EMI technique is essentially similar to the global vibration techniques. Whereas the global vibration techniques are considered good for overall condition assessment of the structures, the EMI technique is capable of interrogating the remote regions and can capture damage at microscopic level. This chapter presents the integration of the EMI technique with global vibration techniques, using the same set of PZT transducers. In the integrated approach, the presence and location of incipient damage are ascertained by the EMI technique, and for moderate to severe damages the global vibration techniques are used. With no additional sensors required and with minimum hardware, the benefits of the two techniques, so far applied independently, are harnessed more efficiently.

6.2 Piezoelectric Materials as Dynamic Strain Sensors

If a PZT patch surface bonded on a structure is designated to be used as a sensor only (with no external electric field applied across its terminals), its governing equation (Eq. (2.11)) can be reduced to

$$D_3 = d_{31} \overline{Y^E} S_1 \quad (6.1)$$

where $\overline{Y^E} S_1$ substituted T_1 , based on the Hooke's law. From the theory of parallel plate capacitors, the charge density can be expressed as

$$D_3 = \frac{\overline{\epsilon_{33}^T} V}{h} \quad (6.2)$$

where V is the potential difference across the terminals of the PZT patch of thickness h . Therefore, from Eqs. (6.1) and (6.2), the voltage measured across the terminals of the PZT patch can be expressed in terms of the strain in the patch (and hence on the surface of the structure) as

$$V = \left(\frac{d_{31} h \overline{Y^E}}{\overline{\epsilon_{33}^T}} \right) S_1 = K_p S_1 \quad (6.3)$$

The output voltage can be easily measured by an oscilloscope aided by conditioning circuit or directly using modern digital multimeters.

Strictly speaking, Eq. (6.3) is valid only for skeletal structures (such as beams) where the PZT-structure interaction is essentially 1D in nature. For a PZT patch bonded to a 2D-structure (such as plates), the behavior will be governed by Eqs. (3.10) to (3.13), with the charge density (for use as sensor only) expressed as

$$D_3 = \frac{d_{31} \overline{Y^E} (S_1 + S_2)}{(1-\nu)} \quad (6.4)$$

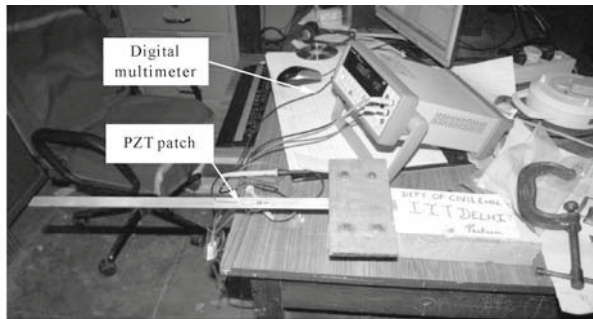
where S_1 and S_2 are the strains along the two principal directions, respectively, and ν is the Poisson's ratio. Similar to the 1D case, following relation can be derived for the voltage output across a PZT patch bonded to a 2D-structure

$$V = \frac{d_{31} \overline{Y^E} h (S_1 + S_2)}{\overline{\epsilon_{33}^T} (1-\nu)} = K'_p \times (S_1 + S_2) \quad (6.5)$$

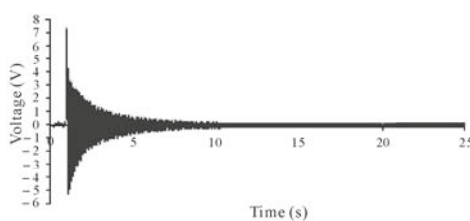
Hence, for the 2D case, the voltage measured across the PZT sensor is proportional to the sum of the two principal strains. Fig. 6.1 shows the typical voltage signal generated across a PZT patch bonded to an aluminium beam of size 300 mm×22 mm×3 mm, which was excited to free vibrations. The response was measured using an Agilent 34411A digital multimeter (Agilent Technologies, 2009) at a sampling interval of 1 ms, with the set up shown in Fig. 6.1(a). Fig. 6.1(b) shows the time response whereas Fig. 6.1(c) the frequency response. From the plots, it may be noted that the signal to noise ratio is excellent, facilitating easy capturing of the natural frequencies. Detailed experimental studies by Bhalla *et al.* (2009) have demonstrated that the performance of the surface-bonded patches is as good as the expensive accelerometers.

It should be noted that, as strain sensors, PZT patches are suitable for measuring dynamic strains and not static strains. This is because the charges developed on account of static forces tend to dissipate quickly in the dissipative elements of the measurement circuit. Through experimental studies, it has been found that frequencies as low as 1 Hz can be captured by PZT patches employed as dynamic strain sensors (Khokker, 2009).

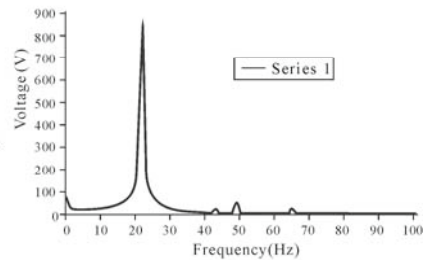
The next sections describe the integration of global dynamic response technique with EMI technique as originally proposed by the authors and covered in detail in related publication (Shanker *et al.*, 2011).



(a)



(b)



(c)

Fig. 6.1 Response from PZT sensor as a dynamic strain sensor. (a) Experimental set-up; (b) Time domain response; (c) Frequency domain response

6.3 Determination of Strain Mode Shapes Using Surface-Bonded PZT Patches

The general equation of motion for a dynamic system is

$$[M]\{\ddot{u}\} + [C]\{\dot{u}\} + [K]\{u\} = \{F(t)\} \quad (6.6)$$

where $[M]$ is the mass matrix, $[C]$ the damping matrix, $[K]$ the stiffness matrix, $\{\ddot{u}\}$, $\{\dot{u}\}$ and $\{u\}$ the acceleration, the velocity and the displacement vectors, respectively, and $\{F(t)\}$ the force vector. For free vibration, $\{F(t)\}$ is zero, then

$$[M]\{\ddot{u}\} + [C]\{\dot{u}\} + [K]\{u\} = 0 \quad (6.7)$$

The roots ω_n^2 of Eq. (6.7) are known as the eigen values. For every natural frequency ω_i , there corresponds a mode shape vector Φ_i satisfying Eq. (6.7). Corresponding to the i^{th} natural frequency ω_i , there are N independent displacements which make up the mode shape Φ_i , which is the displacement profile of the structure (at the N points) vibrating at the frequency ω_i . In general, for a vibrating structure, the displacement at any point can be expressed as the summation of the displacement due to all modes. If the displacement is measured, the relative contribution of each mode can be separated by fast Fourier Transform (FFT).

In this chapter, an experimental approach is outlined to obtain the curvature or the strain mode shapes directly using the surface bonded PZT patches. For a linear structure, by Betti's theorem, the response at point "a" due to a unit load acting at point "b" equals the response at point "b" due to a unit load acting at point "a". This theorem facilitates measuring responses along the entire structure using a few (even a single) sensors. By varying the point of application of that fixed load, the response of the sensor (fixed at a particular point) is equivalent to the response at the point of application of the force (to a force applied at the point of the sensor). Plotting the ordinates of the FFT curve corresponding to that frequency for all measurement points represents the mode shape of the structure corresponding to a particular frequency.

Fig. 6.2 shows the experimental setup. The test structure was a 4 m long simply supported steel beam (ISBM 150 as per Indian Standards). It was instrumented with a PZT patch at a distance of 120.4 cm from the right support. The beam was divided into 12 parts (that is 11 inner nodes), at each of which a standard excitation was made by dropping a steel ball of 0.2 kg from a fixed height of 1.5 m. The voltage response of the PZT sensor patch was recorded for a period of 2 s using the Agilent 34411A digital multimeter at a sampling interval of 200 μs , automatically through programs running in VEE PRO (Agilent Technologies, 2009). The recorded time-domain data were transformed into frequency domain by carrying out FFT in MATLAB (The Mathworks, 2009) environment. Fig. 6.3 shows a typical FFT response from the PZT patch. From this plot, the first three

experimental bending frequencies of the steel beam can be identified as 45 Hz, 190 Hz and 410 Hz. Applying this procedure, frequency plots were determined by making impact at each of the 13 nodes which, by Betti's theorem, amounted to response at these nodes for an impact at the location of the PZT patch. The ordinates of the FFT curves were noted corresponding to the first three bending frequencies for all the nodes, through which the first three bending mode shapes were plotted, as shown in Fig. 6.4.

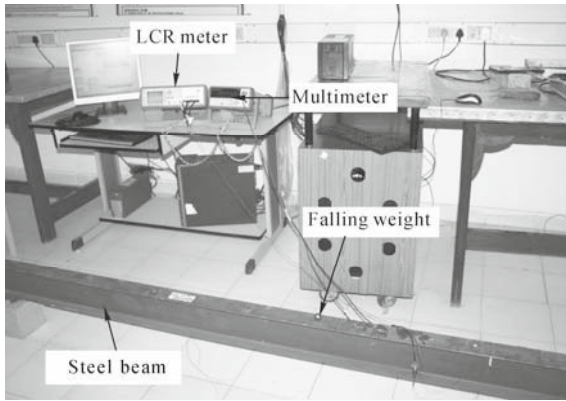


Fig. 6.2 Experimental setup for strain mode shapes

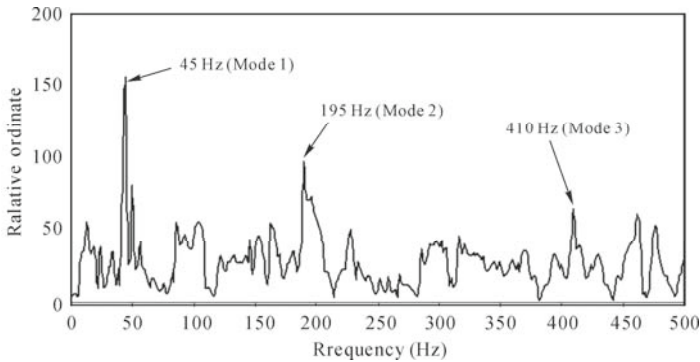


Fig. 6.3 Typical FFT of response from PZT patch attached to steel beam

Keeping in mind Eq. (6.3), it will be noted that the voltage output from the PZT patch is a function of the strain at the point of measurement. Hence, the mode shapes so derived are strain or curvature mode shapes since curvature y'' (the second derivative of displacement) is related to strain by

$$y'' = \frac{\varepsilon}{d} \quad (6.8)$$

where d is the distance of the PZT patch from the neutral axis.

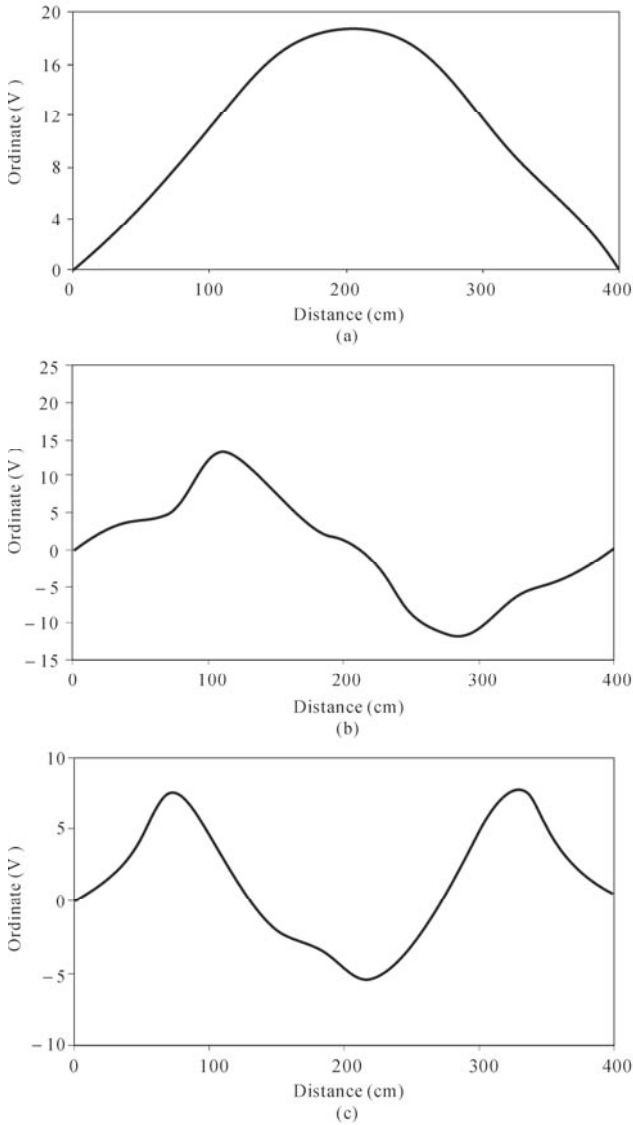


Fig. 6.4 Experimental curvature mode shapes of beam. (a) Mode 1; (b) Mode 2; (c) Mode 3

Similarly, Fig. 6.5 shows the strain mode shapes of a mild steel plate of dimensions 1260 mm×630 mm×6.5 mm, simply supported on the four edges, obtained using a PZT sensor patch located at a distance of 378 mm along the *X* axis and 252 mm along the *Y* axis from the top right corner, as shown in Fig. 6.5(a). The plate was divided into a 5×10 grid (size 126 mm in both directions), resulting in interior 36 (4×9) nodes, as shown in Fig. 6.5(b). The PZT patch was also located at one of the resulting nodes. In order to excite the plate, a weight of

1 kg was dropped at each node from 1.5 m height. Figs. 6.5(c), (d) and (e) show the first three strain mode shapes of the plate obtained using the same procedure as for the beam. The first three natural frequencies of the plate were measured as 20 Hz, 230 Hz and 490 Hz.

Through this measurement approach, the number of mode shapes extracted will depend on the minimum sampling interval of measurement. In general, the first few (2 – 3) mode shapes, if accurately determined, will be sufficient from SHM considerations. Accuracy of the mode shape depends on how many nodes the structure is divided into. The more number of measurement points, the higher is the accuracy.

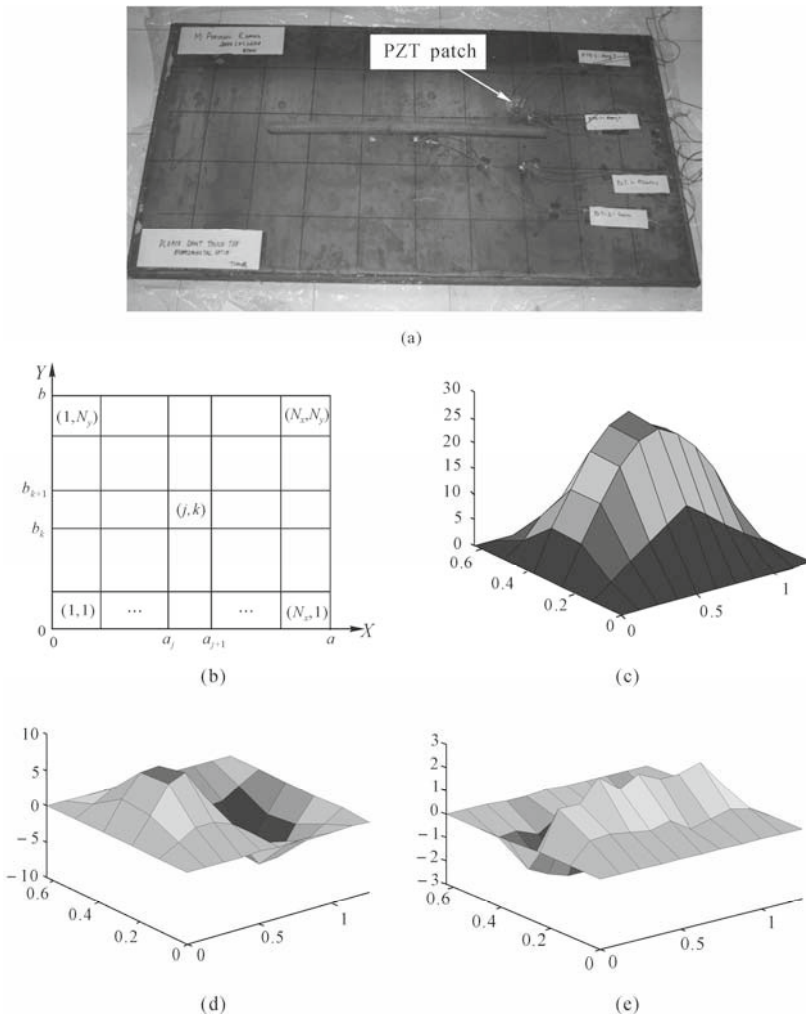


Fig. 6.5 Extraction of strain mode shapes for steel plate. (a) Top view of plate; (b) Grid showing points of excitation; (c) Mode 1; (d) Mode 2; (e) Mode 3

6.4 Identification and Localization of Incipient Damage

As pointed out earlier, the major drawback of the global vibration techniques is that they cannot detect any incipient damage, leave alone ascertaining its location. The incipient level damage, if gone unnoticed, could be detrimental for structures such as precision machine parts and aerospace components. This section describes the utilization of the EMI technique for identification and localization of incipient level damages. This is illustrated using the 4 m long steel beam shown in Fig. 6.2. The beam was instrumented with a total of 11 equally spaced PZT patches on the top face, as shown in Fig. 6.6. Artificial damages were induced in the beam at a section situated 800 mm from the left support in seven stages of gradually increasing severity, as detailed in Fig. 6.7.

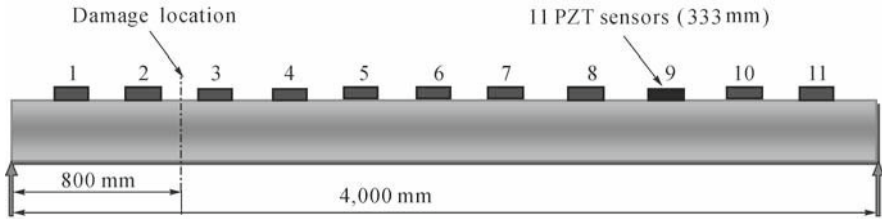


Fig. 6.6 Experimental set up for damage detection using PZT patches

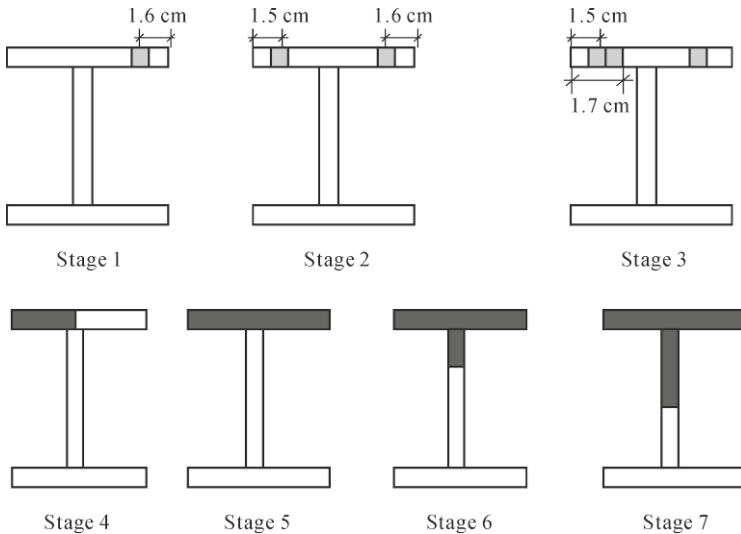


Fig. 6.7 Various stages of damage severity in steel beam

The first three damages shown in Fig. 6.7 were introduced by drilling holes of 6 mm diameter. In the fourth stage, a cut of 6.5 cm length was made through the

entire thickness of the flange, starting from the left corner and extending to the middle of the flange. To induce the fifth stage damage, the cut was extended across the entire width of the flange. In the sixth stage, the severity of the damage was enhanced by extending the cut to one fourth depth of the web. In the seventh and the final stage, the cut was extended till the middle of the web.

After each damage, the modal frequencies as well as the corresponding mode shapes, the parameters associated with the global vibration techniques, were derived for the beam as described in the previous section. Table 6.1 lists the first three frequencies for all the seven damage stages. From this table, the first two damage stages could be treated as incipient since the frequencies changed negligibly (less than 0.5%), which cannot be taken as a definite indication of damage. As far as the EMI technique is concerned, the admittance signatures of all the 11 PZT patches were acquired for each damage scenario using the Agilent 4980 LCR meter (Agilent Technologies, 2009) in the frequency range 100 – 160 kHz. The PZT patches were found to identify the structure as a *Kelvin-Voigt* (parallel spring-damper, see Table 4.1) system. Equivalent stiffness and damping were then worked out using the computational approach described in Chapter 4 (also refer to Appendix E).

Table 6.1 First three natural frequencies of steel beam after each damage stage

S.No.	Damage stage	First natural frequency (% change)	Second natural frequency (% change)	Third natural frequency (% change)
1	Undamaged	45 (–)	190 (–)	410 (–)
2	Stage-1	45 (0.0%)	189 (0.52%)	410 (0.00%)
3	Stage-2	45 (0.0%)	189 (0.52%)	408 (0.49%)
4	Stage-3	41 (8.9%)	185 (0.97%)	402 (1.95%)
5	Stage-4	39 (13.3%)	182 (4.21%)	399 (2.68%)
6	Stage-5	37 (17.8%)	179 (5.79%)	392 (4.39%)
7	Stage-6	36 (20.0%)	174 (8.42%)	387 (5.61%)
8	Stage-7	34 (24.4%)	170 (10.52%)	380 (7.32%)

Fig. 6.8 shows the typical plot of conductance (G) for PZT patch 6 (see Fig. 6.6) in the frequency range 100 – 120 kHz for the pristine beam and the first three damage stages. It is observed that, contrary to the first three natural frequencies, the conductance signatures changed significantly at the first damage stage itself. The shifting of the major frequency peak clearly indicates the presence of damage. Table 6.2 lists the equivalent stiffness k identified by the PZT patches for the first three damage stages. It can be observed from the table that the value of k increased with damage severity. At such high frequencies, a local damage may soften a few modes but at the same time stiffen a few others, and not much can be predicted theoretically. This phenomenon leads to lateral shifting of the peaks in the conductance signature. The point to note here is that, unlike the first three natural frequencies identified by the global vibration techniques, the indication provided by the identified k was very concrete in nature, with the changes observed being as

high as 11% (PZT patch 3) even after the first damage stage, which was a small hole of 6 mm diameter only.

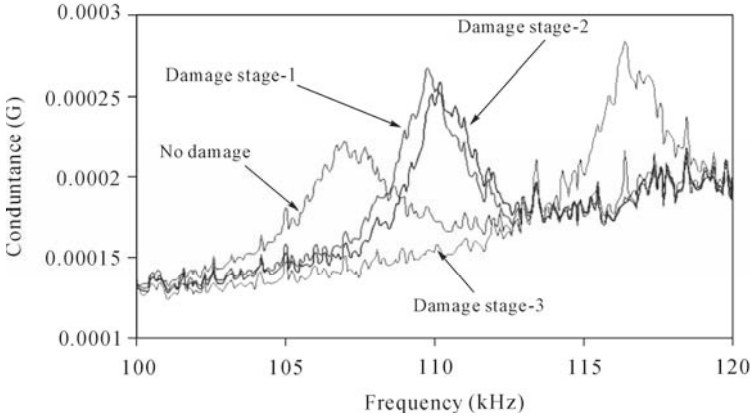


Fig. 6.8 Conductance signatures of PZT patch 6 for first three damage stages

Table 6.2 Percentage variation of equivalent stiffness *k* identified by PZT patches

PZT No.	Undamaged <i>k</i> (10 ⁶ N/m)	Damage Stage 1		Damage Stage 2		Damage Stage 3	
		<i>k</i> (10 ⁶ N/m)	Change (%)	<i>k</i> (10 ⁶ N/m)	Change (%)	<i>k</i> (10 ⁶ N/m)	Change (%)
PZT 1	6.56	6.86	4.7	6.97	6.3	7.44	13.5
PZT 2	8.67	9.47	9.2	9.73	12.3	10.54	21.6
PZT 3	7.65	8.51	11.2	8.83	15.5	9.53	24.6
PZT 4	5.97	6.41	7.4	6.67	11.6	7.20	20.7
PZT 5	8.45	8.92	5.6	9.26	9.7	10.03	17.5
PZT 6	6.78	7.04	3.9	7.28	7.4	7.70	13.6
PZT 7	8.56	9.44	3.3	9.09	6.2	9.37	9.5
PZT 8	6.53	6.73	2.9	6.83	5.4	6.83	7.2
PZT 9	8.56	8.65	1.1	8.66	1.2	8.66	1.2
PZT 10	6.63	6.68	0.8	6.69	0.9	6.69	0.9
PZT 11	7.89	7.92	0.4	7.92	0.4	7.92	0.4

It can further be observed from Table 6.2 that, in relative terms, there was very small change in *k* identified by PZT patches 9, 10 and 11, which were located very far from the damage location (see Fig. 6.6). In general, the data of Table 6.2 suggest that the percentage change of *k* increased with damage severity and decreased with distance of the PZT patch from the damage location. This fact can be better appreciated from Fig. 6.9, which shows the plot of the change of *k* of various sensors for three damage stages. To locate the damage, the PZT patches corresponding to the first two largest variation of *k* were identified, which, shown in Fig. 6.9, boil down to patches 2 and 3 after damage stage 1. The same trend was observed for damage stages 2 and 3. Hence, it can be concluded that the damage location was between sensors 2 and 3, which is correct (see Fig. 6.6).

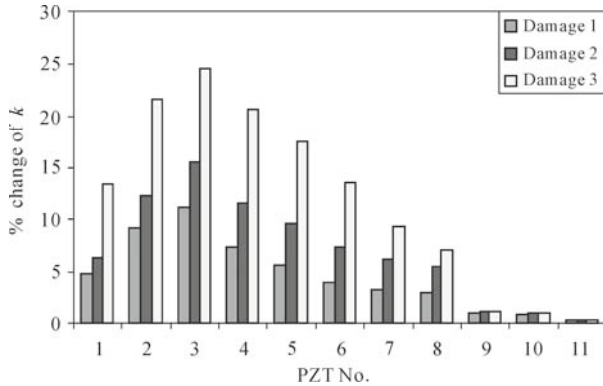


Fig. 6.9 Variation of k for all PZT sensors bonded to steel beam

Once the damage was traced to be between two sensors, its more precise location can then be predicted through statistical interpolation. Let the damage be traced to be between the i^{th} and $(i+1)^{\text{th}}$ PZT sensors located at a distance x from each other. If the observed percentage change in k for the two sensors is Δk_1 and Δk_2 , respectively, the approximate location of damage from the i^{th} sensor is given by

$$d = \left(\frac{\Delta k_2}{\Delta k_1 + \Delta k_2} \right) x \quad (6.9)$$

Using Eq. (6.9), the location of damage was determined as 18.28 cm from PZT patch 2 after stage 1, which compares well with the actual value of 13.34 cm. In the same way, the damage location after the second and the third damage stages was determined as 18.58 cm and 17.73 cm, respectively. Hence, using the EMI technique, the incipient damage can be detected, and at the same time reasonably located. The greater the density of the sensor network, the greater will be the accuracy of damage localization.

Although the EMI technique performed well in identifying and locating the incipient level damage, it was not able to distinguish very well the moderate and the severe damage stages. This fact, which has been pointed out by several researchers (e.g., Naidu, 2004), can be well appreciated in light of Table 6.3, which lists the values of k for PZT patch 8 for all seven damage stages. Apparently, after damage stage 4, any further change of the identified parameters became negligible. This may be compared with changes in the first three frequencies (obtained from global vibration technique) listed in Table 6.1. As the severity of damage increased (especially from damage stage 4 onwards), the distinguish ability provided by the global technique increased, as evidenced by much higher percent changes in the first three natural frequencies. Hence, when the EMI technique failed to provide any new information, global technique began to act more efficiently. Thus, the two techniques complemented each other. The incipient damage can be detected at the very initial stage using the EMI technique, and the moderate to severe damages using the global technique. Another

advantage of the integrated approach is that the same PZT patches are used as sensors in both techniques.

The next section outlines an approach for locating and quantifying moderate to severe damages using the global vibration techniques.

Table 6.3 Equivalent k and c identified by PZT patch 8 for each damage.

S. No.	Damage stage	Equivalent stiffness (k) (N/m)	Equivalent damping (c) (N·s/m)	% change	
				k	c
1	Undamaged	6.53×10^6	8.94	0	0
2	Stage-1	6.73×10^6	8.50	2.9	4.9
3	Stage-2	6.83×10^6	8.45	5.4	5.5
4	Stage-3	7.04×10^6	8.39	7.2	6.2
5	Stage-4	7.05×10^6	8.35	7.4	6.6
6	Stage-5	7.06×10^6	8.32	7.5	6.9
7	Stage-6	7.09×10^6	8.30	7.8	7.2
8	Stage-7	7.09×10^6	8.30	7.8	7.2

6.5 Localization of Moderate and Severe Damages Using Global Vibration Techniques

6.5.1 For 1D Structures (Beams)

The previous section demonstrates how the EMI technique can detect an incipient level damage in structures. Corrective action can be taken at that stage itself if the structure type demands so. However, in most structures, incipient level damage does not pose any serious risk. In such scenarios, it would be more cost-effective to closely monitor the damage growth and wait till the damage grows to moderate or severe nature. This section explains how moderate to severe damage types can be monitored using the global vibration techniques. The global vibration techniques may also provide a back up to capture any damages that were missed being detected during the incipient stage due to any unavoidable reasons.

Fortunately, the experimental strain (or curvature) mode shapes of the structure obtained using the PZT patches, as explained in Section 6.3, can be directly utilized. If an element undergoes damage, its flexural stiffness, namely EI (product of Young's modulus and moment of inertia) reduces, thereby increasing its curvature. In the case of 1D structures such as a beam, the damage index for each element can be defined as

$$D.I. = \sum_{n=1}^N (C_{damaged} - C_{undamaged}) \quad (6.10)$$

where $C_{undamaged}$ is the curvature before damage, $C_{damaged}$ is the curvature after damage and N is the number of modes considered.

After the section of the experimental steel beam (considered in the previous sections) underwent damage in seven stages, the first three strain mode shapes of the beam were determined using the experimental procedure described earlier for all the seven damage stages. These are shown in Fig. 6.10. Compared to the undamaged structure, the mode shapes appear to change significantly. In fact, a closer inspection of the first mode clearly point towards the damage location.

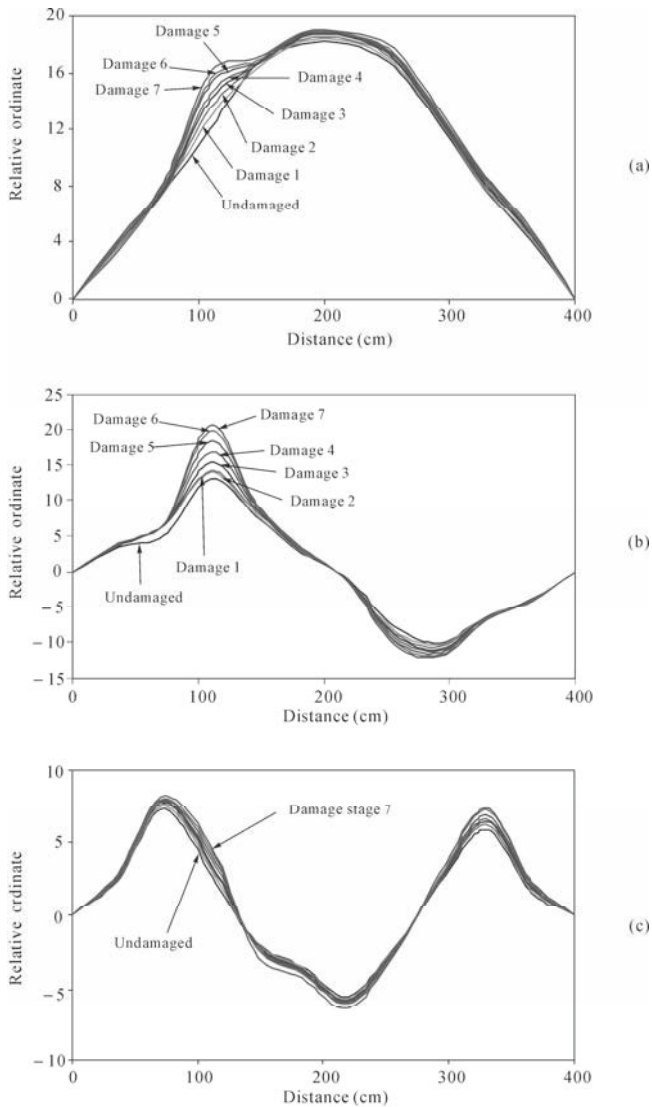


Fig. 6.10 First three bending mode shapes of steel beam for various damage stages. (a) Mode 1; (b) Mode 2 (c) Mode 3

It should be highlighted that the mode shapes were determined directly using a single PZT patch. Other sensors, such as accelerometers, are not only expensive but also require much larger computational effort in the numerical integration and differentiation to derive the data which can be used in SHM.

Next, the damage index was determined using Eq. (6.10) for all the damage stages. A plot of the damage index versus the element number is shown in Fig. 6.11. It can be observed from the figure that, at all damage stages, the damage index was highest at the damaged element as compared to the other elements. The index increased numerically as the damage severity increased. Thus, the damage was correctly identified. It should also be noted that the damage index of the adjacent elements is comparable to that of the damaged element. Hence, at the location of the damage, it appears like an umbrella-shaped structure.

For a single damage scenario, the greatest value of the damage index will indicate the location of damage. Since it represents value for the whole element, if greater accuracy is desired, the distance between the nodes can be further subdivided into suitable number of elements, which can be treated as new nodes and the process be repeated until damage is located with the desired accuracy. There is no requirement to determine the damage index for the other elements which exhibited lesser damage index in the previous cycle of measurements.

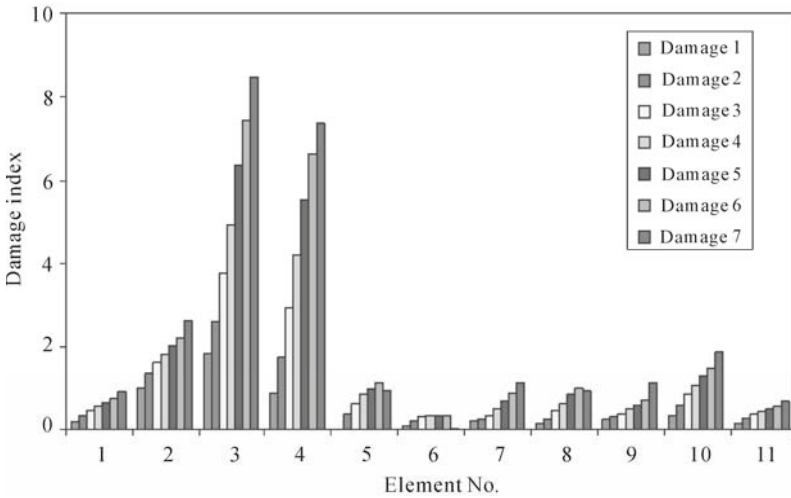


Fig. 6.11 Plot of damage index for beam structure

6.5.2 For 2D Structures (Plates)

The damage index for 2D structures, such as plates, can be similarly defined. The plate can be divided into suitable number of elements using a grid, such as the one

shown in Fig. 6.5(b). Considering a typical plate of N_x, N_y elements along the X and Y directions, the following terms can be defined

$$[x]_{j,k}^i = i^{\text{th}} \text{ Normalized strain mode shape ordinate before damage at } (j,k) \quad (6.11)$$

$$[X]_{j,k}^i = i^{\text{th}} \text{ Normalized strain mode shape ordinate after damage at } (j,k) \quad (6.12)$$

The average curvatures for an element along the X and Y directions for the undamaged and the damaged cases are respectively given as

$$P_{j,k}^{x,i} = (x_{j,k}^i + x_{j+1,k}^i) / 2 \quad (6.13)$$

and

$$P_{j,k}^{X,i} = (X_{j,k}^i + X_{j+1,k}^i) / 2 \quad (6.14)$$

where

$P_{j,k}^{x,i}$ = average curvature of i^{th} strain mode shape along X axis before damage,

$P_{j,k}^{X,i}$ = average curvature of i^{th} strain mode shape along X axis after damage.

Similarly, the average curvatures before and after damage along the Y axis respectively can be defined as

$$P_{j,k}^{y,i} = (x_{j,k}^i + x_{j,k+1}^i) / 2 \quad (6.15)$$

and

$$P_{j,k}^{Y,i} = (X_{j,k}^i + X_{j,k+1}^i) / 2 \quad (6.16)$$

Now, a damage index can be defined for the nodes for change in curvature along the X and Y directions as

$$B_{j,k}^x = \sum_{i=1}^m \frac{P_{j,k}^{x,i}}{P_{j,k}^{X,i}} \quad (6.17)$$

$$B_{j,k}^y = \sum_{i=1}^m \frac{P_{j,k}^{y,i}}{P_{j,k}^{Y,i}} \quad (6.18)$$

and

$$B_{j,k} = (B_{i,j,k}^x + B_{i,j,k}^y) / 2 \quad (6.19)$$

where

$B_{j,k}^x$ = Damage index for node (j, k) using change in curvature along X axis,

$B_{j,k}^y$ = Damage index for node (j, k) using change in curvature along Y axis,

$B_{j,k}$ = Damage index for node (j, k) using combined change in curvature.

Finally, the damage index for the element can be defined by summing up the nodal damage indices of the four nodes, *i.e.*,

$$D_{j,k}^x = (B_{j,k}^x + B_{j,k+1}^x + B_{j+1,k}^x + B_{j+1,k+1}^x) \quad (6.20)$$

$$D_{j,k}^y = (B_{j,k}^y + B_{j,k+1}^y + B_{j+1,k}^y + B_{j+1,k+1}^y) \quad (6.21)$$

$$D_{j,k} = D_{j,k}^x + D_{j,k}^y \quad (6.22)$$

where

$D_{j,k}^x$ = Damage index for element (j, k) using change in curvature along X axis,

$D_{j,k}^y$ = Damage index for element (j, k) using change in curvature along Y axis,

$D_{j,k}$ = Damage index for element (j, k) using combined change in curvature in curvature along both X and Y axis.

Damage location is identified as the location with the maximum value of D .

In order to demonstrate the approach, an artificial damage was induced in the plate of Fig. 6.5(a) by drilling a hole of diameter 55 mm in the plate at a distance of 300 mm along the X axis and 200 mm along the Y axis from the bottom left corner, as shown in Fig. 6.12. This represents the first stage of damage. Thereafter, another artificial damage was induced by drilling a hole of diameter 55 mm in the plate at a distance of 200 mm along the X axis and 300 mm along the Y axis from the right corner, marking the second stage damage. Finally, diameter of the second hole was increased to 100 mm to enhance the severity of damage to the third stage. The first three mode shapes were obtained similar to those of the beam. The damage indices of all the elements were determined using Eq. (6.22), and plotted in Fig. 6.13. From the figure, it is obvious that the damage location, which is the element corresponding to the maximum damage index, is correctly identified. Furthermore, it is clear from Figs. 6.13(b) and (c) that multiple damage scenarios can also be tackled very well by the proposed approach.

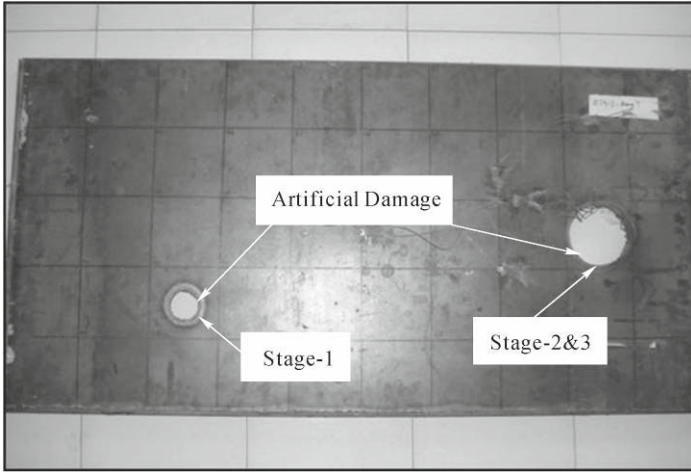


Fig. 6.12 Damage induction in experimental steel plate

6.6 Severity of Damage

In Eq. (6.7), let the amplitude of motion be denoted by the generalized coordinate $Z(t)$. Hence, the displacement at any point can be expressed as

$$y(x,t) = \phi(x)Z(t) \quad (6.23)$$

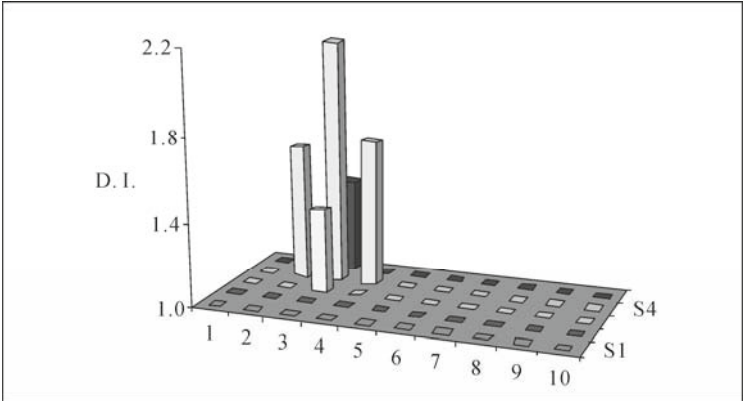
where $\phi(x)$ is the shape function. This effectively reduces the structure to a single degree of freedom (DOF) system, if we consider the continuous system as one with infinite DOF. Thus, the harmonic variation of the generalized coordinate in free vibration can be expressed as

$$y(x,t) = \phi(x)Z_0 \sin \omega t \quad (6.24)$$

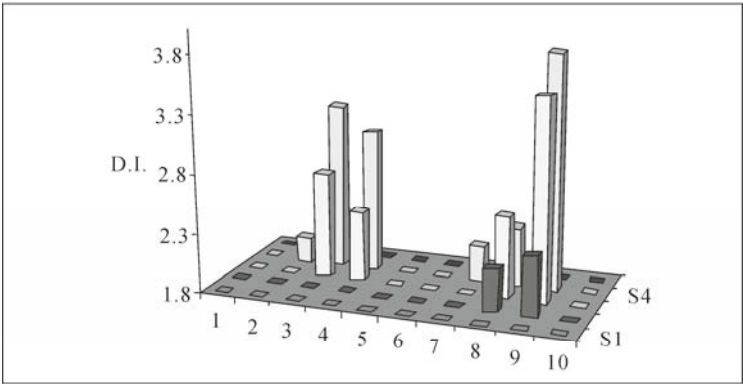
This equation expresses the assumption that the shape of the vibrating beam does not change with time, but only the amplitude of motion varies; that is, it varies harmonically in a free-vibration condition. At the point of maximum displacement,

$$y(x,t) = Z_0 \sin \omega t \quad (6.25)$$

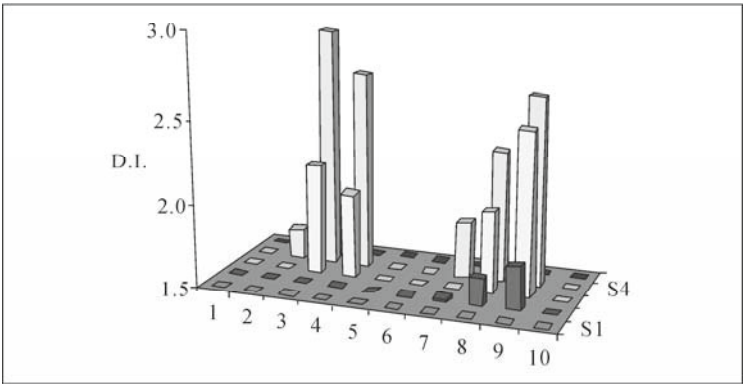
The strain energy of this flexural system is given by



(a)



(b)



(c)

Fig. 6.13 Plot of damage indices for plate. (a) Damage stage 1; (b) Damage stage 2; (c) Damage stage 3

$$V = \frac{1}{2} \int_0^L EI(x) \left(\frac{\partial^2 y}{\partial x^2} \right)^2 dx \quad (6.26)$$

where L is the length of the beam, E the Young's modulus of the material of the structure and I the moment of inertia. Thus, substituting the assumed shape function and letting the displacement amplitude take its maximum value lead to

$$V_{\max} = \frac{1}{2} Z_0^2 \int_0^L EI(x) (\phi''(x))^2 dx \quad (6.27)$$

In general, the total energy of the system will be distributed into various mode shapes. However, 80% – 90% of the energy is normally distributed among the first few (3 to 5) mode shapes alone. If the structure is damaged, it is assumed that there is no significant change in the distribution of the energy in various modes if the excitation force and the boundary conditions remain unchanged. This is true in the context of the experiments reported in this chapter. The total strain energy is the same in both the damaged and undamaged cases due to the fact that the height of free fall of the mass used for excitation during the test was constant. If there occurs any damage/crack in the structure at any location, the Young's modulus of elasticity will reduce more at that location than at any other parts. This change reflects the severity of damage. In the present approach, only the average value of “ EP ” of the whole structure has been determined.

If any element of the structure is damaged, the tendency of that element is to undergo greater displacement than in the undamaged case. However, due to the inertia and the adhesive forces, the neighboring elements, which are less damaged, will oppose and also undergo somewhat greater displacement to balance the equilibrium. Hence, this affects the entire mode shape of the structure, which reflects the presence of damage. As the severity of damage increases, the strain at the damaged section increases further. Due to increase of deflection at the damage point, it will also increase the value of Z_0 . By conservation of energy for any mode,

$$(V_{\max})_{undamaged} = (V_{\max})_{damaged} \quad (6.28)$$

Solving Eq. (6.27), we can derive

$$\frac{(EI(x))_{damaged}}{(EI(x))_{undamaged}} = \eta = \frac{(Z_0^2)_{undamaged} \left(\int_0^L \phi''^2(x) dx \right)_{undamaged}}{(Z_0^2)_{damaged} \left(\int_0^L \phi''^2(x) dx \right)_{damaged}} \quad (6.29)$$

where η represents the ratio of the current stiffness of structure to the undamaged

stiffness and $\phi''(x)$ denotes the second derivative of the mode shape (*i.e.* mode shape curvature). In the case of PZT sensors and the measurement approach described herein, $\phi''(x)$ is obtained directly from measurement. Clearly, this circumvents the necessity of numerical differentiation, which would otherwise have to be performed if the other sensor types, say accelerometers, were employed.

Using the first three experimental damaged and undamaged mode shapes of the steel beam and plate, at different damage stages, the average percentage change of stiffness was determined using the above formula. From Eq. (6.29), integration of $[\phi''(x)]^2$ with respect to x gives the area of square of the mode shape. Hence, the damage severity can be determined in terms of the original stiffness after drawing the experimental mode shape of structure and the computed area of square of the mode shape and the maximum relative amplitude Z_0 .

This approach was applied to the steel beam as well as to the steel plate. The severity of damage increased in all seven damage stages in the steel beam, and only three damage stages in the steel plate, as explained earlier. The severity of all damage stages of the steel beam is listed in Table 6.4. In the same way, the severity of damage for the mild steel plate is listed in Table 6.5. It is observed that, as the damage severity increases, η decreases and this is clearly visible from the two tables. The main advantage is that the severity is determined in terms of the ratio of the residual stiffness with the original stiffness, which provides the most direct estimate of the overall damage severity of the structure.

Table 6.4 Variation of stiffness ratio with damage for steel beam

S. No.	Damage stage	η = ratio of current stiffness with undamaged stiffness
1	State-1	0.97
2	State-2	0.94
3	State-3	0.92
4	State-4	0.88
5	State-5	0.85
6	State-6	0.83
7	State-7	0.81

Table 6.5 Variation of stiffness ratio with damage for steel plate

S. No.	Damage stage	η = ratio of current stiffness with undamaged stiffness
1	Stage-1	0.98
2	Stage-2	0.93
3	Stage-3	0.83

Thus, from the experimental demonstrations described in this chapter, it is established that the EMI technique can be suitably integrated with the global vibration techniques for improved SHM, without warranting any additional sensors.

References

- Agilent Technologies (2009), <http://www.agilent.com>.
- Bhalla, S., Gupta, A., Shanker, R., Sethi, A., Jain, S. and Medury, A. (2009). "Performance and conditional monitoring of civil structures from discrete strain measurements", *International Journal of COMADEM*, 12 (1): 2-12.
- Catbas, F.N., Ciloglu, S.K., Hasancebi, O., Grimmelsman, K. and Aktans, A.E. (2007). "Limitations in structural identification of large constructed structures", *Journal of Structural Engineering*, 133(8): 1051-1066.
- Khokker, S. (2009). "Improvements in Structural Health Monitoring Based on Piezo-Transducers", *M. Tech. Thesis*, Department of Civil Engineering, Indian Institute of Technology Delhi, India.
- Naidu, A.S.K. (2004). "Structural Damage Identification with Admittance Signatures of Smart PZT Transducers", *Ph.D. Thesis*, Nanyang Technological University, Singapore.
- Shanker, R., Bhalla, S. Gupta, A. and Kumar, M.P. (2011). "Dual use of PZT patches as sensors in global dynamic and local EMI techniques for structural health monitoring", *Journal of Intelligent Material Systems and Structures*, in press.
- The Mathworks (2009). <http://www.mathworks.com>.

Sensing Region, Load Monitoring and Practical Issues

Y. W. Yang*, Y. Y. Lim, V. G. M. Annamdas, Y. H. Hu, C. K. Soh

School of Civil and Environmental Engineering, Nanyang Technological University,
50 Nanyang Avenue, Singapore 639798.

Tel: (65)-6790-4057, Fax: (65)-6791-0676

Email: cywyang@ntu.edu.sg

7.1 Sensing Region of PZT Patches

7.1.1 Introduction

Despite various successful applications of EMI technique for SHM, the fundamental research work on determining the PZT patch's sensing region has not received much attention, partially due to the difficulty in modeling PZT-generated wave propagation in different materials.

The waves generated by PZT actuators carry the information of the host structure, and thus can be used to identify the existence and nature of the damage. The application of wave propagation method has been used for damage detection in various engineering structures (Wang and Huang, 2001; Giurgiutiu *et al.*, 2004; Yang and Qiao, 2005). In order to ensure high sensitivity to incipient structural damage, the elastic waves should be generated by actuators at high frequencies, typically hundreds of kHz, so that the wavelength of the resulting stress waves is smaller than the typical size of the defects to be detected (Giurgiutiu and Rogers, 1997). The high frequency excitation provided by PZT actuators ensures the detection of minor changes in the monitored structure, but it also limits the sensing area to a region close to the PZT source. This is because the PZT patch vibrating at high frequencies excites ultrasonic modes of vibration of the structure, which

are essentially local in nature. Besides, damping is much more significant at high frequencies, leading to wave localization. Based on wave propagation approach, Esteban (1996) made an effort to identify various factors that affect PZT sensing region. A number of experiments have been conducted on several engineering structures to determine the PZT patch's sensing region (Park *et al.*, 2000). However, neither theoretical nor numerical model has been established to identify the sensing region of PZT transducers. Before a broad use of PZT transducers for SHM using EMI technique, fundamental research work on determining PZT transducers' sensing region is necessary.

Vibration of elastic structures, such as strings, beams and plates, can be described in terms of wave propagation and attenuation in waveguides (Rose, 1999). A waveguide directs the wave energy along its length, and is reflected and transmitted when the incident waves encounter discontinuities such as boundaries, general point supports, externally applied forces and moments, and damages. The wave propagation method provides a concise and systematic approach to the analysis of built-up structures. The practical application of such an approach relies on the knowledge of detailed propagation, reflection and transmission characteristics of waves. The reflection and transmission matrices of waves in Euler-Bernoulli beams and Timoshenko beams corresponding to various discontinuities were derived by Mace (1984) and Mei and Mace (2005), respectively. However, in their analysis, the effects of material damping and energy dissipation were not taken into account, which will be considered in this section.

The localization of PZT patch's sensing region is primarily due to energy dissipation mechanisms, among which material damping in the structure is of significant influence. Since the excitation is at high frequency, the effect of damping is prodigious. For convenience in structural analysis, damping is usually assumed to be viscous in nature, which is the cause of dissipative force. Many viscoelasticity problems can be reduced to mathematically equivalent elasticity problems by using the correspondence principle. This procedure has been used to solve several structural damping problems effectively (Kalyanasundaram *et al.*, 1987; Kinra and Yapura, 1992). Therefore, it is used in this section to solve the wave propagation problem in a Timoshenko beam.

7.1.2 Theoretical Modeling

- *Wave Propagation Modeling*

Due to the high frequency range employed, Timoshenko beam theory including the effect of rotary inertia and transverse shear deformation is used to model the beam structure. The equations of motion of Timoshenko beam are expressed in terms of the transverse displacement y and the angle of rotation ψ as

$$GA\kappa \frac{\partial}{\partial x} \left[\psi - \frac{\partial y}{\partial x} \right] + \rho A \frac{\partial^2 y}{\partial t^2} = q(x,t) \quad (7.1a)$$

$$EI \frac{\partial^2 \psi}{\partial x^2} + GA\kappa \left[\frac{\partial y}{\partial x} - \psi \right] - \rho I \frac{\partial^2 \psi}{\partial t^2} = 0 \quad (7.1b)$$

where $\kappa = \pi^2/12$ denotes the shear correction factor; ρ the mass density; A the cross sectional area; I the moment of inertia; E the Young's modulus; G the shear modulus; and $q(x,t)$ the distributed load on the beam. In Eq. (7.1), there are two modes of deformation and the coupled governing equations represent the physical coupling that occurs between them. One mode of deformation is simply the transverse deflection of the beam as measured by $y(x,t)$. The other mode is the transverse shearing deformation as measured by the difference $\frac{\partial y}{\partial x} - \psi$.

The shear force $V(x,t)$ and bending moment $M(x,t)$ at any section of the beam are related to the transverse deflection $y(x,t)$ and the slope $\psi(x,t)$ by

$$M = -EI \frac{\partial \psi}{\partial x} \quad (7.2a)$$

$$V = GA\kappa \left[\frac{\partial y}{\partial x} - \psi \right] \quad (7.2b)$$

Considering the free vibration problem where no external force is applied, the differential equation of motion can be obtained by eliminating $\psi(x,t)$ from Eq. (7.1) as

$$EI \frac{\partial^4 y}{\partial x^4} + \rho A \frac{\partial^2 y}{\partial t^2} - \rho I \left(1 + \frac{E}{G\kappa} \right) \frac{\partial^4 y}{\partial x^2 \partial t^2} + \frac{\rho^2 I}{G\kappa} \frac{\partial^4 y}{\partial t^4} = 0 \quad (7.3)$$

Using fast Fourier transformation, the spectral solution for primary displacement can be expressed as

$$y(x,t) = \sum_{n=1}^N \hat{y}(x) e^{j\omega_n t} \quad (7.4)$$

where ω_n is the frequency. Substituting Eq. (7.4) into Eq. (7.3) and suppressing the time dependence term $e^{j\omega_n t}$, we obtain

$$EI \frac{\partial^4 \hat{y}}{\partial x^4} - \rho A \omega_n^2 \hat{y} + \rho I \left(1 + \frac{E}{G\kappa} \right) \omega_n^2 \frac{\partial^2 \hat{y}}{\partial x^2} + \frac{\rho^2 I}{G\kappa} \omega_n^4 \hat{y} = 0 \quad (7.5)$$

Assuming the solution of the form

$$\hat{y} = Y e^{-jkx} \quad (7.6)$$

and substituting Eq. (7.6) into Eq. (7.5), the dispersion equation can be expressed as

$$EI k^4 - \rho A \omega_n^2 - \rho I \left(1 + \frac{E}{G \kappa}\right) \omega_n^2 k^2 + \frac{\rho^2 I}{G \kappa} \omega_n^4 = 0 \quad (7.7)$$

The solution to the dispersion equation gives a set of wave numbers that are functions of frequency ω_n and properties of the structure, namely,

$$k^2 = \frac{1}{2} \left[\left(\frac{1}{C_s} \right)^2 + \left(\frac{C_r}{C_b} \right)^2 \right] \omega_n^2 \pm \sqrt{\frac{\omega_n^2}{C_b^2} + \frac{1}{4} \left[\left(\frac{1}{C_s} \right)^2 - \left(\frac{C_r}{C_b} \right)^2 \right]^2} \omega_n^4 \quad (7.8)$$

where the coefficients are related to the bending stiffness, shear stiffness and rotational effects as

$$C_b = \sqrt{\frac{EI}{\rho A}}, \quad C_s = \sqrt{\frac{GA \kappa}{A \rho}}, \quad C_r = \sqrt{\frac{\rho I}{\rho A}} \quad (7.9)$$

According to Eq. (7.8), there are four values for k . Therefore, the solution can be expressed as

$$y(x, t) = \sum_{n=1}^N \hat{y}(x, k) e^{j\omega_n t} = \sum_{n=1}^N \left(\sum_{j=1}^4 Y_j e^{jk_j x} \right) e^{j\omega_n t} \quad (7.10)$$

For convenience of expression, Eq. (7.8) is separated as

$$k_1 = \left| \frac{1}{2} \left[\left(\frac{1}{C_s} \right)^2 + \left(\frac{C_r}{C_b} \right)^2 \right] \omega_n^2 + \omega_n \sqrt{\frac{1}{C_b^2} + \frac{1}{4} \left[\left(\frac{1}{C_s} \right)^2 - \left(\frac{C_r}{C_b} \right)^2 \right]^2} \right|^{1/2} \quad (7.11a)$$

$$k_2 = \left| \frac{1}{2} \left[\left(\frac{1}{C_s} \right)^2 + \left(\frac{C_r}{C_b} \right)^2 \right] \omega_n^2 - \omega_n \sqrt{\frac{1}{C_b^2} + \frac{1}{4} \left[\left(\frac{1}{C_s} \right)^2 - \left(\frac{C_r}{C_b} \right)^2 \right]^2} \right|^{1/2} \quad (7.11b)$$

Depending on the frequency, there are either two propagating waves (one positive-going and one negative-going) plus two evanescent (near-field) waves or four propagating waves (two positive-going and two negative-going). The cut-off frequency for the second flexural mode, obtained by setting $k_2 = 0$, is

$$\omega_c = \frac{C_s}{C_r}. \quad (7.12)$$

When $\omega_n < \omega_c$, the resulting expression for \hat{y} is

$$\hat{y}(x) = Y_1^+ e^{-jk_1 x} + Y_2^+ e^{-k_2 x} + Y_1^- e^{jk_1 x} + Y_2^- e^{k_2 x} \quad (7.13a)$$

A similar solution would hold for $\hat{\psi}$ with arbitrary coefficients that are not independent but related. Thus, the solution for $\hat{\psi}$ can be expressed as

$$\hat{\psi}(x) = \Psi_1^+ e^{-jk_1 x} + \Psi_2^+ e^{-k_2 x} + \Psi_1^- e^{jk_1 x} + \Psi_2^- e^{k_2 x} \quad (7.13b)$$

The wave amplitudes Y of $\hat{y}(x)$ and Ψ of $\hat{\psi}(x)$ are related to each other through Eq. (7.1). For example, the amplitude of a positive-going propagating transverse deflection wave component Y_1^+ is related to that of a positive-going propagating bending slope wave component Ψ_1^+ as

$$\begin{bmatrix} k_1^2 GA\kappa - \rho A \omega^2 & -jk_1 GA\kappa \\ -jk_1 GA\kappa & -k_1^2 EI - GA\kappa + \rho I \omega^2 \end{bmatrix} \begin{bmatrix} Y_1^+ \\ \Psi_1^+ \end{bmatrix} = \begin{bmatrix} 0 \\ 0 \end{bmatrix} \quad (7.14)$$

From Eq. (7.14) we have

$$\frac{\Psi_1^+}{Y_1^+} = j \frac{\rho A \omega^2 - k_1^2 GA\kappa}{k_1 GA\kappa} = j \frac{\omega^2 - k_1^2 C_s^2}{k_1 C_s^2} \quad (7.15)$$

The relations between the coefficients of wave components of $\hat{y}(x)$ and those of $\hat{\psi}(x)$ are listed as

$$\frac{\Psi_1^+}{Y_1^+} = -jP, \quad \frac{\Psi_1^-}{Y_1^-} = jP, \quad \frac{\Psi_2^+}{Y_2^+} = -Q, \quad \frac{\Psi_2^-}{Y_2^-} = Q \quad (7.16)$$

Therefore

$$\hat{\psi}(x) = -jPY_1^+ e^{-jk_1x} - QY_2^+ e^{-k_2x} + jPY_1^- e^{jk_1x} + QY_2^- e^{k_2x} \quad (7.17)$$

where

$$P = k_1 \left(1 - \frac{\omega_n^2}{k_1^2 C_s^2} \right) \quad (7.18a)$$

$$Q = k_2 \left(1 + \frac{\omega_n^2}{k_2^2 C_s^2} \right) \quad (7.18b)$$

The boundary conditions of the beam can be used to determine any four independent coefficients in Eq. (7.13) and the rest can be calculated using Eq. (7.16).

• *Wave Reflection and Transmission*

The wave approach provides a concise and systematic vibration analysis of a build-up structure. The amplitudes of waves can be expressed in terms of a series of matrices. When the propagation, reflection, transmission and excitation matrices are known, the structural vibration solutions involving a series of matrix operations can be derived. For the beam structure shown in Fig. 7.1, the discontinuities which lead to wave reflection and transmission involve a free boundary at point A and the bending moments at points B and C generated by a pair of PZT actuators. It is worth mentioning that the purpose of the double-sided application of PZT actuators is to ease the modeling work. However, the conclusions drawn are applicable for both double-sided and single-sided applications.

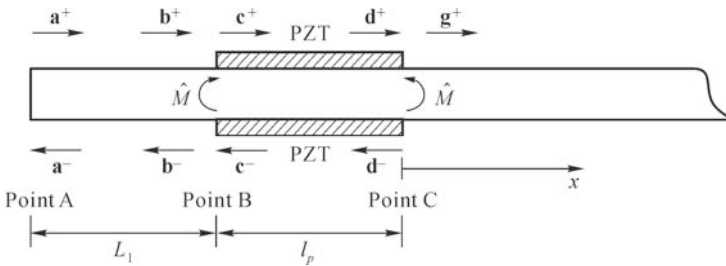


Fig. 7.1 A semi-infinite beam model

The positive-going and negative-going wave vectors at points A, B and C are denoted as \mathbf{a}^+ , \mathbf{b}^+ , \mathbf{c}^+ , \mathbf{d}^+ , \mathbf{g}^+ and \mathbf{a}^- , \mathbf{b}^- , \mathbf{c}^- , \mathbf{d}^- , respectively. The beam is assumed to be infinitely long at the right hand side. At point C, the amplitudes of the waves propagating along the positive and negative directions before and after this point can be related as

$$\mathbf{g}^+ = \mathbf{d}^+ + \mathbf{m} \quad (7.19)$$

$$\mathbf{d}^- = \mathbf{m} \quad (7.20)$$

After propagating a distance of length l_p , the amplitudes of the waves become

$$\mathbf{d}^+ = \mathbf{f}(l_p)\mathbf{c}^+ \quad (7.21)$$

$$\mathbf{c}^- = \mathbf{f}(l_p)\mathbf{d}^-, \quad (7.22)$$

where the propagation matrix is

$$\mathbf{f}(l_p) = \begin{bmatrix} e^{-jk_1 l_p} & 0 \\ 0 & e^{-jk_2 l_p} \end{bmatrix} \quad (7.23)$$

At point B, the beam structure is subjected to another point moment with the same amplitude but in the opposite direction as that at point C. The relationship of the waves before and after point B can be expressed as

$$\mathbf{c}^+ = \mathbf{b}^+ - \mathbf{m} \quad (7.24)$$

$$\mathbf{b}^- = \mathbf{c}^- + \mathbf{m} \quad (7.25)$$

The positive-going and the negative-going waves between points A and B can be related as

$$\mathbf{b}^+ = \mathbf{f}(L_1)\mathbf{a}^+ \quad (7.26)$$

$$\mathbf{a}^- = \mathbf{f}(L_1)\mathbf{b}^- \quad (7.27)$$

For the free boundary at point A, the amplitudes of the incipient waves and the reflected waves are related via the following relationship

$$\mathbf{a}^+ = \mathbf{R}_{\text{free}}\mathbf{a}^- \quad (7.28)$$

where the reflection matrix \mathbf{R}_{free} has been described by Mei and Mace (2005) as

$$\mathbf{R}_{\text{free}} = \begin{bmatrix} \frac{-Pk_1(-Q+k_2)+jk_2Q(k_1-P)}{Pk_1(-Q+k_2)+jk_2Q(k_1-P)} & \frac{2Qk_2(-Q+k_2)}{Pk_1(-Q+k_2)+jk_2Q(k_1-P)} \\ \frac{2jPk_1(-P+k_1)}{Pk_1(-Q+k_2)+jk_2Q(k_1-P)} & \frac{Pk_1(-Q+k_2)-jk_2Q(k_1-P)}{Pk_1(-Q+k_2)+jk_2Q(k_1-P)} \end{bmatrix} \quad (7.29)$$

After a series of substitutions and calculations, the amplitudes of the waves propagating in the beam at the right hand side of point C can be expressed in the form of external moments as:

$$\mathbf{g}^+ = (\mathbf{f}(l_p)\mathbf{f}(L_1)\mathbf{R}_{\text{free}}\mathbf{f}(L_1)\mathbf{f}(l_p) + \mathbf{f}(l_p)\mathbf{f}(L_1)\mathbf{R}_{\text{free}}\mathbf{f}(L_1) - \mathbf{f}(l_p) + \mathbf{\Lambda}) \cdot \mathbf{m} \quad (7.30)$$

where

$$\mathbf{\Lambda} = \begin{bmatrix} 1 & 0 \\ 0 & 1 \end{bmatrix} \quad (7.31)$$

and \mathbf{m} can be expressed as

$$\mathbf{m} = \begin{Bmatrix} -1 \\ 1 \end{Bmatrix} \frac{\hat{M}}{2EI(k_1P+k_2Q)} = \mathbf{n}\hat{M} \quad (7.32)$$

with \hat{M} being the amplitude of the external moment.

Substituting Eqs. (7.31) and (7.32) into Eq. (7.30), we can express Eq. (7.30) in terms of the external moment as

$$\begin{Bmatrix} \mathbf{g}_1^+ \\ \mathbf{g}_2^+ \end{Bmatrix} = \begin{Bmatrix} N_1 \\ N_2 \end{Bmatrix} \hat{M} = \mathbf{N}\hat{M} \quad (7.33)$$

where

$$\mathbf{N} = (\mathbf{f}(l_p)\mathbf{f}(L_1)\mathbf{R}_{\text{free}}\mathbf{f}(L_1)\mathbf{f}(l_p) + \mathbf{f}(l_p)\mathbf{f}(L_1)\mathbf{R}_{\text{free}}\mathbf{f}(L_1) - \mathbf{f}(l_p) + \mathbf{\Lambda}) \cdot \mathbf{n} \quad (7.34)$$

The transverse displacement and the bending slope of the beam at the right hand side of point C can be denoted as

$$\hat{y}(x) = g_1^+ e^{-jk_1x} + g_2^+ e^{-k_2x} \quad (7.35a)$$

$$\hat{\psi}(x) = -jPg_1^+ e^{-jk_1x} - Qg_2^+ e^{-k_2x} \quad (7.35b)$$

• *PZT-Structure Coupling Effect*

The coupling relationship between PZT actuator and structure has been investigated by Sirohi and Chopra (2000). The force exerted at point C is given by

$$\hat{F} = K_A l (\varepsilon_{mech} - \varepsilon_0) \quad (7.36)$$

where $K_A = \frac{Y_p^E w h}{l}$ is the static stiffness of PZT; $\varepsilon_0 = \frac{d_{31} \hat{V}}{h}$ is the free strain; ε_{mech} is the mechanical strain of the structure at the actuator's location; \hat{V} is the amplitude of electric voltage applied to the PZT; l , w and h are the length, width and thickness of the PZT patch, respectively; and d_{31} and Y_p^E are the constants of the PZT material.

As shown in Fig. 7.2, when two PZT patches bonded to the beam at the same location but on the opposite sides are simultaneously subjected to opposite voltages, pure bending moment is excited on the beam.

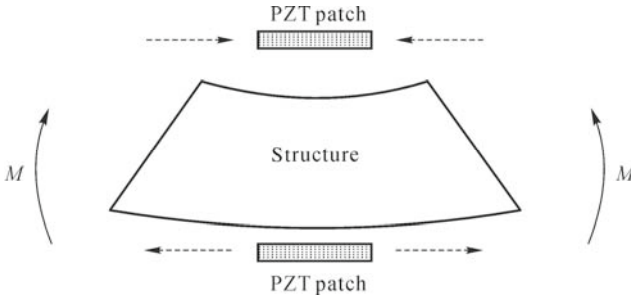


Fig. 7.2 Pure bending excitation generated by a pair of PZT patches

The bending moment generated by these two PZT patches and the force exerted by one of them have the following relation

$$\hat{M} = (h + h_b) \hat{F} \quad (7.37)$$

where h_b is the thickness of the beam. The mechanical strain ε_{mech} at the PZT location can be calculated from the following relationship

$$\varepsilon_{mech} = \frac{h_b}{2} \frac{\partial \psi}{\partial x} \quad (7.38)$$

Substituting Eq. (7.35b) into Eq. (7.38), we obtain the mechanical strain at point C in the form of \hat{M} as

$$\varepsilon_{mech} = \frac{h_b}{2}(-k_1PN_1 + k_2QN_2)\hat{M} \quad (7.39)$$

From Eqs. (7.36), (7.37) and (7.39), the amplitude of the moment generated by the two PZT patches is obtained as

$$\hat{M} = \frac{d_{31}\hat{V}}{\frac{hh_b}{2}(-k_1PN_1 + k_2QN_2) - \frac{1}{Y_p^E w(h+h_b)}} \quad (7.40)$$

The transverse displacement and the bending slope at any location along the beam can be calculated by solving the spectral coefficients. For example, the transverse displacement and the bending slope of the beam at the right hand side of point C are

$$\hat{y}(x) = N_1\hat{M}e^{-jk_1x} + N_2\hat{M}e^{-k_2x} \quad (7.41a)$$

$$\hat{\psi}(x) = -jPN_1\hat{M}e^{-jk_1x} - QN_2\hat{M}e^{-k_2x} \quad (7.41b)$$

Only $\hat{y}(x)$ and $\hat{\psi}(x)$ at the right hand side of point C are of interest, because sensors will be placed at the right hand side of point C to determine the PZT sensing region.

• Viscoelastic Solutions

Generally, damping is the primary reason for energy dissipation in vibrating systems. Several damping constants are defined in relation to the method used to measure them (Graesser and Wong, 1992). The specific damping capacity used here is

$$\varphi = \frac{\Delta W}{W} \quad (7.42)$$

where ΔW is the mechanical energy dissipated during one cycle of strain and W is the maximum stored elastic strain energy during the cycle. The specific damping capacity can also be written as

$$\varphi = 2\pi \tan \phi \quad (7.43)$$

where ϕ is the so-called loss-tangent, *i.e.* the phase by which the strain lags the

stress.

The elastic response of an isotropic material is governed by two independent elastic constants, namely, the Young's modulus E and the shear modulus G . The correspondence principle can be used to convert elastic solutions to viscoelastic solutions. The two corresponding complex moduli, E^* and G^* , governing the response of a viscoelastic material can be expressed as

$$E^* = |E^*| e^{j \tan \phi_E} = E' + jE'' \quad (7.44a)$$

$$G^* = |G^*| e^{j \tan \phi_G} = G' + jG'' \quad (7.44b)$$

Using the correspondence principle of linear viscoelasticity, the elastic solution can be readily extended to the corresponding viscoelastic solution simply by replacing E by E^* , and G by G^* .

For a Timoshenko beam, the dispersive relation as described before is

$$k(\omega) = \pm \left[\frac{1}{2} \left[\left(\frac{1}{C_s} \right)^2 + \left(\frac{C_r}{C_b} \right)^2 \right] \omega^2 \pm \sqrt{\frac{\omega^2}{C_b^2} + \frac{1}{4} \left[\left(\frac{1}{C_s} \right)^2 - \left(\frac{C_r}{C_b} \right)^2 \right]^2} \omega^4 \right]^{\frac{1}{2}} = \pm [K]^{\frac{1}{2}} \quad (7.45)$$

where K is defined as the dynamic elastic stiffness of the structure. Based on this equation, we can observe that the wave number k is proportional to the square root of the dynamic elastic stiffness K of the structure, and the phase lags between them have the following relationship

$$k \exp(j\phi_k) = \sqrt{K \exp(j\phi_K)} \quad (7.46)$$

Therefore,

$$\phi_K = 2\phi_k \quad (7.47)$$

Substituting Eq. (7.47) into the expression of damping capacity, Eq. (7.43), and assuming a small phase lag, we have

$$\varphi = 2\pi \tan \phi_K = 2\pi \tan \phi_k = 4\pi \frac{k''}{k'} \quad (7.48)$$

where k' and k'' are the real and imaginary parts of k , respectively.

The next task is to derive the imaginary part of k . In the first step, we calculate k' by using the implicit expression of the perfectly elastic beam, Eq. (7.7), given by

$$f(k, E, G) = G\kappa EI k^4 - G\kappa\rho A\omega^2 - \rho I(G\kappa + E)\omega^2 k^2 + \rho^2 I\omega^4 = 0 \quad (7.49)$$

Next, if all the moduli are viscoelastic, the dispersion relation becomes

$$f(k^*, E^*, G^*) = G^* \kappa E^* I k^{*4} - G^* \kappa \rho A \omega^2 - \rho I (G^* \kappa + E^*) \omega^2 k^{*2} + \rho^2 I \omega^4 = 0 \quad (7.50)$$

where,

$$k^* = k' + k''_j \quad (7.51)$$

By carrying out a Taylor expansion on Eq. (7.50), we obtain

$$f(k^*, E^*, G^*) = f(k, E, G) + E''_j \frac{\partial f}{\partial E} + G''_j \frac{\partial f}{\partial G} + k''_j \frac{\partial f}{\partial k} \quad (7.52)$$

Therefore

$$k''_1 \approx - \left. \frac{E'' \frac{\partial f}{\partial E} + G'' \frac{\partial f}{\partial G}}{\frac{\partial f}{\partial k}} \right|_{k=k_1} \quad (7.53a)$$

$$k''_2 \approx - \left. \frac{E'' \frac{\partial f}{\partial E} + G'' \frac{\partial f}{\partial G}}{\frac{\partial f}{\partial k}} \right|_{k=k_2} \quad (7.53b)$$

The viscoelastic solutions can then be directly derived from the elastic solutions as

$$\hat{y}(x) = t_1 \hat{M} e^{-jk_1^* x} + t_2 \hat{M} e^{-k_2^* x} \quad (7.54a)$$

$$\hat{\psi}(x) = -jPt_1 \hat{M} e^{-jk_1^* x} - Qt_2 \hat{M} e^{-k_2^* x} \quad (7.54b)$$

where

$$k_1^* = k_1' + k_1''j \quad \text{and} \quad k_2^* = k_2' + k_2''j \quad (7.55)$$

• *PZT Sensing Voltage*

For the viscoelastic solutions, the mechanical strain at the PZT sensor location can be calculated from Eqs. (7.38) and (7.54b) as

$$\hat{\epsilon}_{mech}^* = \frac{h_b}{2} \left(-k_1^* P N_1 e^{jk_1^* x} + k_2^* Q N_2 e^{-k_2^* x} \right) \hat{M} \quad (7.56)$$

According to the constitutive equations of piezoelectric materials, the electric displacement of PZT sensor is given by

$$D_3 = d_{31} Y_p^E \hat{\epsilon}_{mech}^* \quad (7.57)$$

The charge on the sensor is

$$q = D_3 l w \quad (7.58)$$

The output voltage V_{out} across the sensor electrodes is related to the capacitance C_p of the sensor as

$$V_{out} = \frac{q}{C_p} \quad (7.59)$$

Therefore, the sensor voltage versus the actuation voltage can be expressed as

$$\frac{V_{sensor}}{V_{actuator}} = \frac{V_{out}}{\hat{V}} = \frac{l w d_{31}^2 Y_p^E h_b}{C_p h h_b (-k_1^* P N_1 + k_2^* Q N_2) - \frac{2 C_p}{Y_p^E w (h + h_b)}} \times (-k_1^* P N_1 e^{jk_1^* x} + k_2^* Q N_2 e^{-k_2^* x}) \quad (7.60)$$

It can be observed from the above equality that $V_{sensor}/V_{actuator}$ is a function of the material properties, the thicknesses of PZT and structure, the frequency of actuation, and the distance between the actuator and sensor.

It is worth mentioning that the same PZT patch can be used as both actuator

and sensor in the EMI technique. However, for the purpose of determining PZT sensing region, we need to use different PZT patches as actuators and sensors, where the sensors are placed in certain distances away from the actuators.

7.1.3 Experimental Verification

In order to verify the developed theoretical model, an experiment was carried out on an aluminum beam bonded with a number of PZT patches, two of which served as actuators and the rest as sensors. The specimen used in this experiment is shown in Fig. 7.3 and the equipments used are the same as shown in Fig. 4.21.

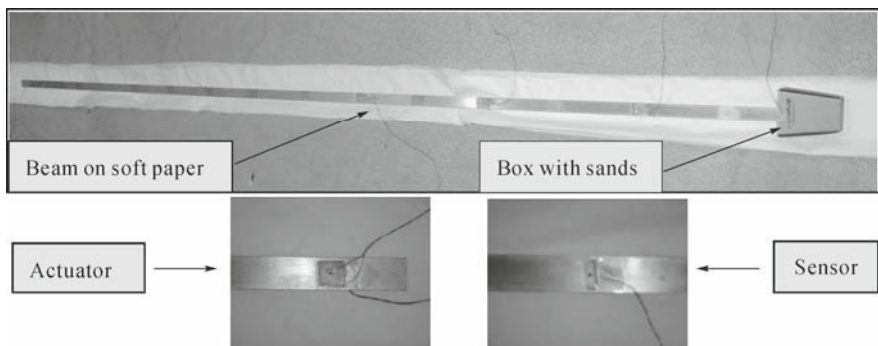


Fig. 7.3 Configuration of beam specimen

The HP4192A analyzer was used to excite the PZT actuators and simultaneously record the signatures received by the PZT sensors. The switch box was used to make multiple connections between the analyzer and the sensors. The right end of the beam specimen was inserted into a box filled with sands to achieve negligible wave reflection at the boundary, simulating a semi-infinite beam condition. In order to facilitate automation of testing, the program VEE Pro v.6.01 was used to control the analyzer via a GPIB interface card installed in the PC. Fig. 7.4 schematically shows the overall experimental setup.

Two PZT patches were bonded to one end of the beam specimen, at the same location but on the opposite sides. These two PZT patches were counter connected to the input slot of the analyzer to work as actuators. A sinusoidal sweep voltage with an amplitude of 1 Volt was applied to these actuators to excite pure bending vibration in the beam over various frequency ranges. Another five PZT patches were bonded to the beam specimen at different distances from the actuators. These five PZT patches worked as sensors which were connected to different channels of the switch box. The switch box was then connected to the output slot of the HP 4192A analyzer to record the signals received by the PZT sensors. The properties and locations of the PZT patches are listed in Tables 7.1 and 7.2, respectively. The properties of the beam specimen are listed in Table 7.3.

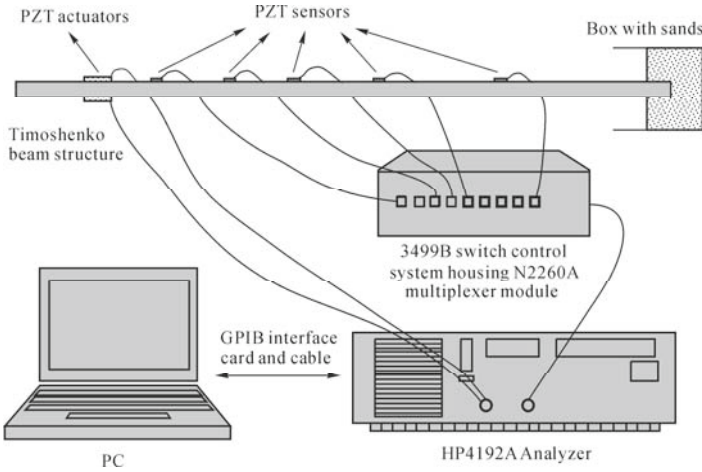


Fig. 7.4 Experiment setup

Table 7.1 Material property of PZT patches

Young's modulus Y (GPa)	Loss factor η	Mass density ρ (kg/m ³)	Strain constant d_{13} (m/V)	Permittivity ϵ_{33}^T (F/m)	Dielectric loss factor δ
66.7	0.005	7,800	-2.10E-10	1.93E-08	1.50E-02

Table 7.2 Dimensions and locations of PZT patches

	Actuators	Sensors
Dimensions (mm)	$l = w = 20, h = 0.2$	$l = 5, w = 20, h = 0.15$
Locations (mm)	50 mm from the left end	$x_1 = 200, x_2 = 500, x_3 = 1,500, x_4 = 2,100, x_5 = 2,900$ (measured from the left end of the beam)

Table 7.3 Property of Timoshenko beam specimen

Length (mm)	Width (mm)	Thickness (mm)	Young's modulus (GPa)	Poisson's ratio	Mass density (kg/m ³)	Damping ratio
3,000	250	45	66.5	0.33	2,800	0.049

7.1.4 Results and Discussions

According to the theoretical model, the sensing voltage of each sensor along the beam structure can be calculated, which simulates the signal detected by the sensor. Five sensors were employed in this study, which were located at 0.2 m, 0.5 m, 1.5 m, 2.1 m and 2.9 m away from the actuators, respectively. The theoretical results of sensor output voltage versus excitation frequency are illustrated in Fig. 7.5. It can be observed that, as the distance between the sensor and the actuator increases, the sensor output voltage decreases. This indicates that the waves

generated by the actuators attenuated while propagating through the beam; and this effect is especially obvious at higher excitation frequencies. It can also be observed that peaks appear when the excitation frequencies approach the beam's natural frequencies due to resonance. However, not all the peak values coincide well with the basic observation that the output voltage decreases as the distance between the sensor and the actuator increases. This is attributed to the fact that the sensor may be situated at the anti-nodes of certain vibration modes. If this happens, the sensor output voltage will be very small.

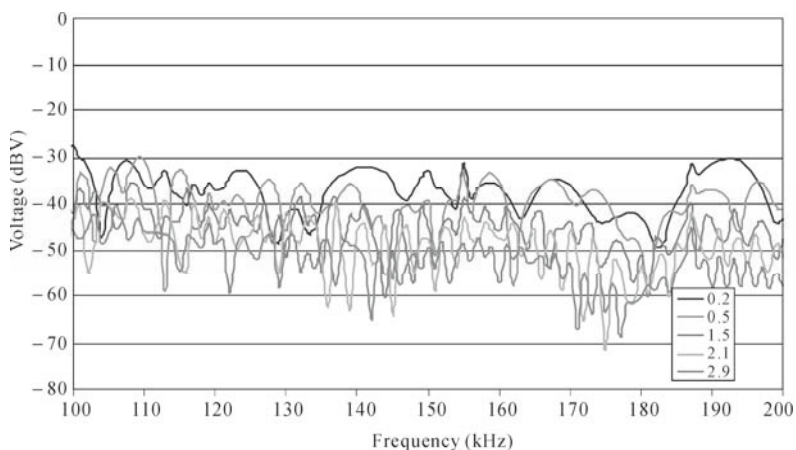


Fig. 7.5 Signatures of predicted output voltages of PZT sensors

For clarity, several peaks were selected and presented in Fig. 7.6, where the peak values of each sensor at certain frequencies, namely, 119 kHz, 155 kHz and 187 kHz, are marked. At these three frequencies, the theoretical peak values for the five sensors are listed in the first rows of Tables 7.4–7.6, respectively. It is obvious that the larger the distance, the smaller the peak values. Therefore, the phenomenon of wave attenuation along the beam length is clear. In this analytical model, attenuation of the waves is mainly caused by the material and structural damping.

Fig. 7.7 shows the experimental output voltages of the five PZT sensors sequentially bonded to the beam specimen. Again, as expected, the phenomenon of wave attenuation is apparent. The peak values under certain excitation frequencies, illustrated and marked in Fig. 7.8, generally match well with those illustrated in Fig. 7.6. For easy comparison, the experimental peak values at three different frequencies are listed in the second rows of Tables 7.4–7.6. Good agreement between the theoretical predictions and experimental results is observed. The differences between them can be ascribed to several model assumptions as well as experimental errors. For example, in the theoretical model, effect of the adhesive layer between the PZT and the beam was not considered and the dissipation mechanism was assumed to be due to damping only. On the other hand, in the experimental test, the two PZT actuators were difficult to be pasted exactly at the same location, so the pure bending excitation was only an approximation.

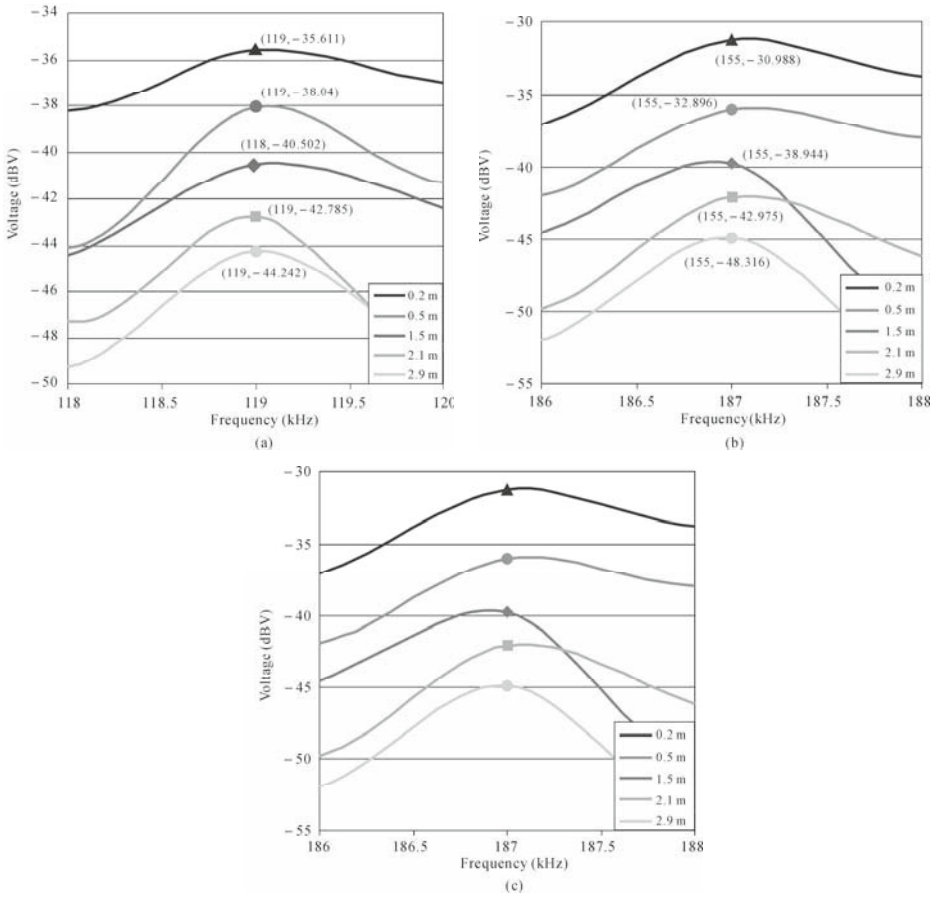


Fig. 7.6 Signatures of predicted output voltages of sensors at selected frequencies. (a) Excitation frequency of 119 kHz; (b) Excitation frequency of 155 kHz; (c) Excitation frequency of 187 kHz

Table 7.4 Theoretical and experimental peak values at 119 kHz

	0.2 m	0.5 m	1.5 m	2.1 m	2.9 m
Theoretical predictions (dBV)	-35.611	-38.04	-40.502	-42.785	-44.242
Experimental results (dBV)	-29.08	-31.08	-36.63	-41.3	-43.36

Table 7.5 Theoretical and experimental peak values at 155 kHz

	0.2 m	0.5 m	1.5 m	2.1 m	2.9 m
Theoretical predictions (dBV)	-30.988	-32.896	-38.994	-42.975	-48.316
Experimental results (dBV)	-30.25	-32.86	-38.02	-42.45	-44.56

Table 7.6 Theoretical and experimental peak values at 187 kHz

	0.2 m	0.5 m	1.5 m	2.1 m	2.9 m
Theoretical predictions (dBV)	-31.18	-35.984	-39.772	-42.059	-44.927
Experimental results (dBV)	-31.09	-35.06	-38.85	-41.95	-44.29

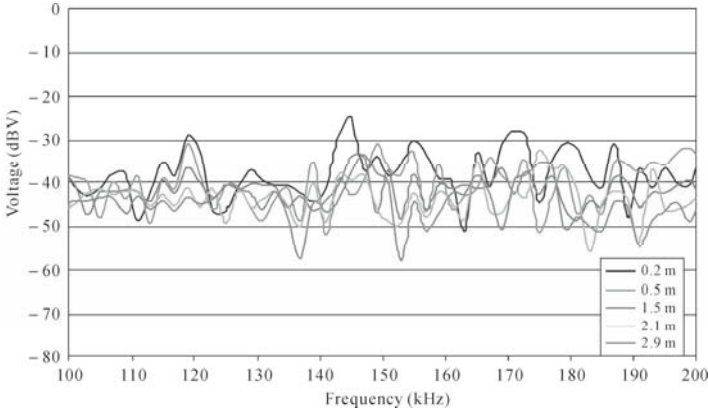


Fig. 7.7 Signatures of experimental output voltages of PZT sensors

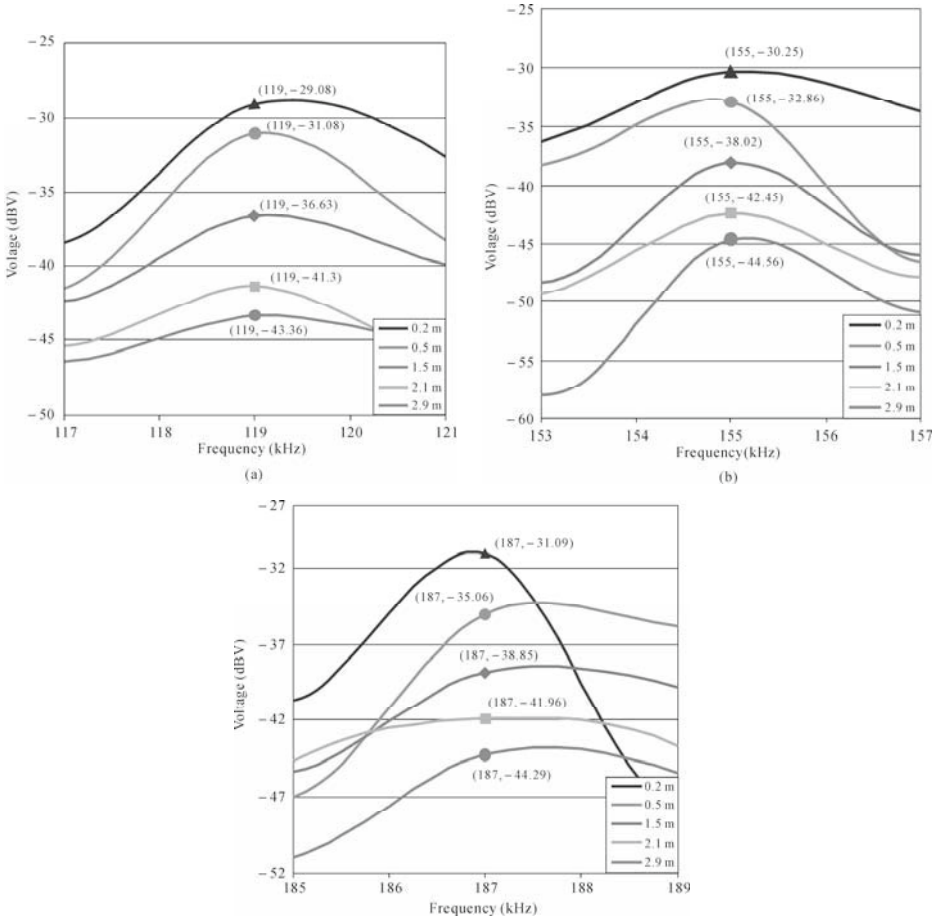


Fig. 7.8 Signatures of experimental output voltages of sensors at selected frequencies: (a) Excitation frequency of 119 kHz; (b) Excitation frequency of 155 kHz; (c) Excitation frequency of 187 kHz

In order to demonstrate the attenuation tendency of the wave propagating along the beam, the relationship between the output voltage and the distance of the sensor from the actuator at different excitation frequencies, namely 119 kHz, 155 kHz and 187 kHz, was derived using the developed theoretical model. The results are compared with the experimental data in Fig. 7.9. As the distance increases, the amplitude of waves presents a clear decay tendency; and the decay tendencies in the theoretical predictions and in the experimental results coincide well especially at longer distances. For instance, at distance farther than 1.2 m, differences between the theoretically predicted voltages and the experimentally detected ones are less than 0.005 V.

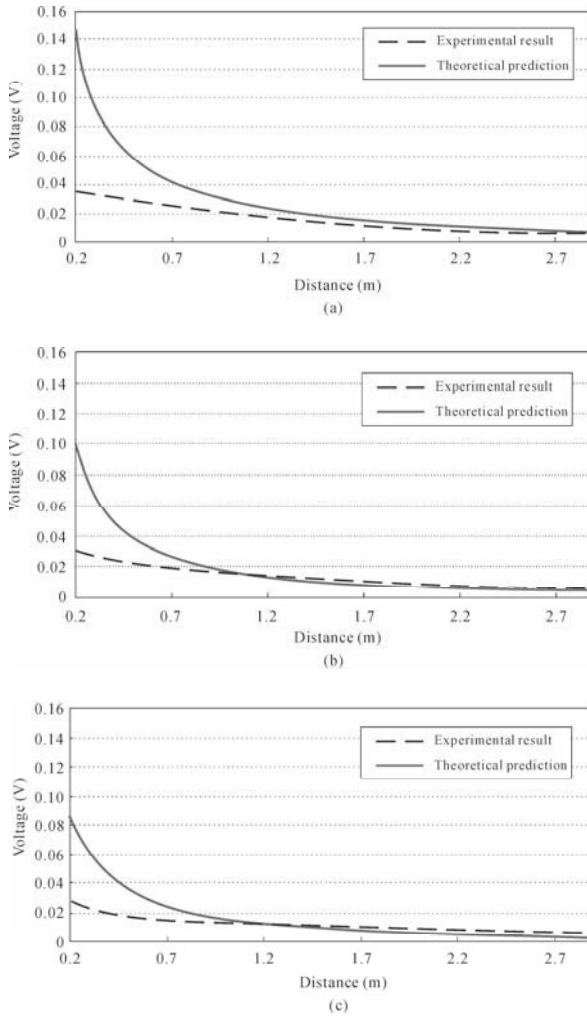


Fig. 7.9 Comparison of theoretical and experimental output voltages of PZT sensors. (a) Excitation frequency of 119 kHz; (b) Excitation frequency of 155 kHz; (c) Excitation frequency of 187 kHz

Due to the material and structural damping, waves generated by the PZT actuator are attenuated while propagating through the structure. With increase of distance between the PZT actuator and sensor, the output voltage of sensor decreases. When the output voltage becomes too small to be detected, the PZT reaches its sensing limit. For the beam structure studied, the sensing region is defined as the maximum distance between the actuator and sensor where the sensor output voltage is measurable. For 2D structures such as plates, the PZT sensing region is defined as the circular area with a radius of that maximum distance.

The minimal voltage that can be captured by the HP 4192A analyzer used in this study was 0.005 V. In order to ensure the reliability of engineering applications, it is reasonable to set the PZT sensing limit as 0.01 V, *i.e.*, one percent of the original excitation voltage. The PZT sensing region is closely related to the excitation frequency. If the frequency is too high, the sensing region may become so small that the PZT sensors exhibit sensitivity only to their bonding conditions or the PZT itself rather than the behavior of the structure monitored. According to the above sensing limit, *i.e.*, 0.01 V, and the typical excitation frequency range of 100 – 200 kHz for the EMI technique, the valid sensing region of PZT sensors is about 2 to 2.5 m from the results shown in Fig. 7.9. Beyond this range of 2 to 2.5 m, the output voltage received by the PZT sensors is less than 0.01 V and is difficult for the analyzer to steadily record this small voltage. In this situation, the signatures captured by the analyzer may lose some information of the host structure and in turn the EMI technique will lose its sensitivity to structural damages. Therefore, it is concluded that the PZT sensing region for EMI-based SHM is within 2 to 2.5 m in aluminum. This conclusion coincides with the experimental experience for metal specimens by Park *et al.* (2000), where a stable 2 m sensing region was observed using a similar impedance analyzer. It is worth noting that the HP 4192A analyzer used in the experimental test has only a resolution of 5 mV. If a more powerful analyzer with higher precision of measurement is used, the PZT sensing region could be larger than 2 to 2.5 m.

7.1.5 Summary

Based on the wave propagation theory, this section presents a method to determine the sensing region of PZT sensors for their applications in SHM. The Timoshenko beam theory is adopted to study the waves generated by PZT actuators at high frequencies to ensure the high sensitivity to damages of the EMI technique. The developed wave propagation modeling involves only a number of matrix operations related to the reflection and transmission matrices at the discontinuities. After the elasticity solution is obtained, the viscoelasticity solution is derived directly from the elasticity solution according to the correspondence principle.

The theoretical predictions and the experimental results coincide well, which demonstrates the applicability of the developed model. The results also show that the PZT sensing region is dependent on the excitation frequency. At high frequencies,

typically hundreds of kilohertz, the sensing region is small due to the significant effect of material and structural damping. The sensing region also depends on the experimental conditions as well as the precision of the measurement equipments. Under the experimental condition of this study, a reliable PZT sensing region in an aluminum beam is concluded to be within 2 to 2.5 m.

To extend the study to a more general situation, the PZT sensing region for other materials, *e.g.*, rock and concrete, definitely deserves further investigation. Moreover, for other practical structures such as ribs, tapers and joints, the developed wave propagation model should be modified and enhanced. For instance, for a joint connecting two beams, the PZT sensors can be installed on both beams and the wave propagation should be modeled separately for the two beams, taking into account the joint as one type of discontinuity.

7.2 PZT Patches for Load Monitoring

7.2.1 Introduction

Civil and aerospace structural components such as slabs, beams, columns or wings are constantly subjected to some forms of external loadings which may or may not lead to any damage. Admittance signatures obtained for such constantly loaded structures are different from those obtained when damages are present in the structures. This section presents the experimental and statistical investigations carried out by Annamdas *et al.* (2007) to show the influence of loading on admittance signatures. In the investigation, it was also observed that susceptance signatures are better indicator than conductance signatures for detecting in-situ stresses (especially transverse loading) in the host structure. This observation was verified by statistical analysis.

7.2.2 Effect of Stress in Structure

Since the early development of the EMI technique, it has evolved as a technique for monitoring damage/crack. However, a few other developments have shown that this technique is equally capable of predicting or monitoring in-situ stresses associated with such damage/crack. Abé *et al.* (2000) first proposed the use of the EMI technique to identify in-situ stresses in thin structural members. Experiments were carried out and in-situ tensile stress was successfully identified. Ong *et al.* (2002) investigated the effects of in-situ stresses on the frequency response functions of beam and plate structures. In their study, the case of pure bending actuation which was achieved by a pair of symmetrically surface bonded PZT

transducers was considered. The structures were axially loaded and the electrical response of the PZT transducer was simulated using 1D and 2D EMI models for the beam and plate specimens, respectively. Moreover, it was shown from the simulated results that in the presence of in-situ stresses, shifts in the natural frequencies of the structures took place and these shifts were reflected in the admittance, which could be directly measured.

7.2.3 Influence of Applied Load on EM Admittance Signatures

From Euler-Bernoulli’s beam theory, the maximum bending stress in a beam is

$$\sigma_s = -My / I_s \tag{7.61}$$

where M is the maximum bending moment, y is the distance from the neutral axis of the beam to the extreme surface and I_s is the moment of inertia. In our investigations, $y = \frac{1}{2}H_S$ and $I_s = \frac{W_S H_S^3}{12}$ as the beam specimens used were homogeneous and symmetrical. For the simply supported and centrally loaded beam specimens, the maximum bending moment occurs at the centre of the specimen, where the PZT transducers were located. In general, PZT transducers will function as long as they are stressed within the operational design limit (Mall, 2002). Fig. 7.10 shows the schematic diagram of stress distribution for a beam with a PZT bonded at the centre. Table 7.7 lists the maximum stresses experienced by each of the specimen under different loadings.

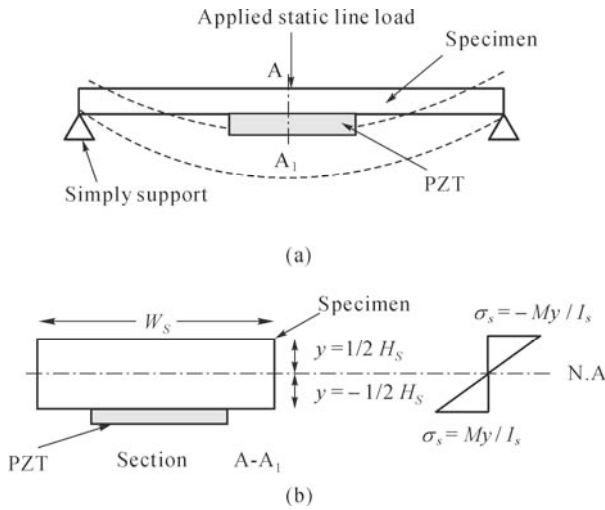


Fig. 7.10 Stress distribution in a typical beam specimen. (a) Elevation; (b) Section A-A₁

Table 7.7 Maximum stress values in specimens

Specimen	$I_x (\text{m}^4) \times 10^{-9}$	Maximum stress (MPa)			
		Load = 50 N	Load = 100 N	Load = 150 N	Load = 200 N
1	0.11	46.9	93.8	140.6	187.5
2	0.54	20.8	41.7	62.5	83.3
3	4.17	3.0	6.0	9.0	12.0

7.2.4 Experimental Investigations and Discussions

The experiments were conducted in such a way that they replicated a common real-life beam under a simplified loading and support conditions (Fig. 7.11). The PZT transducers were bonded on the bottom surface at the centre of the beam specimen. The three lab-sized aluminum beams and nine PZT patches used are listed in Tables 7.8 and 7.9, respectively.

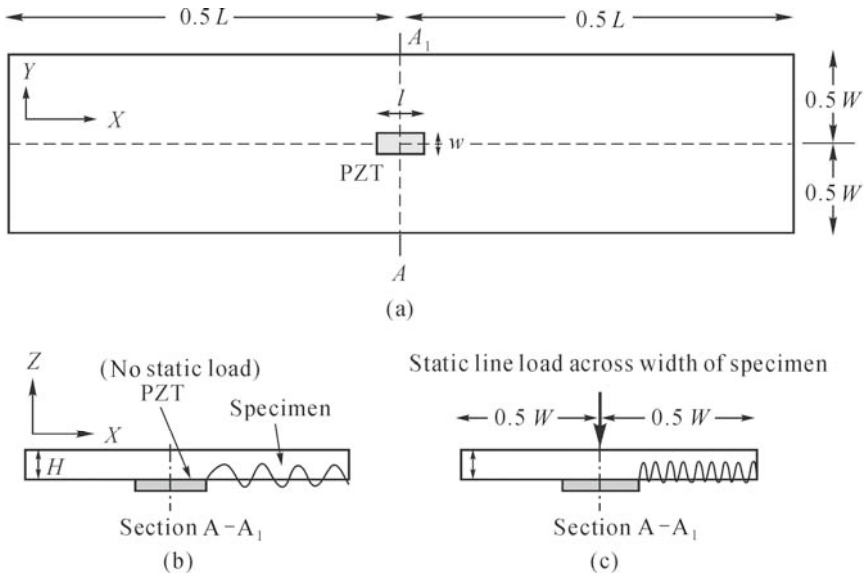


Fig. 7.11 Experimental specimens. (a) Plan view; (b) Section A-A₁ in absence of load; (c) Section A-A₁ in presence of applied load

Table 7.8 Dimensions and mechanical properties of aluminum beam specimens

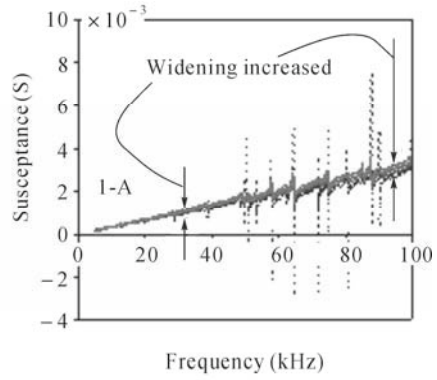
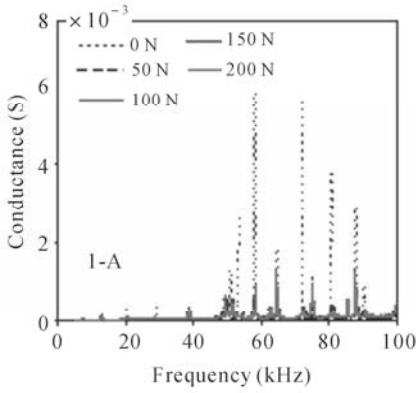
Aluminum beam	1	2	3
Dimensions L (m) $\times W$ (m) $\times H$ (m)	0.2 \times 0.02 \times 0.004	0.3 \times 0.03 \times 0.006	0.2 \times 0.05 \times 0.01
Density (kg/m ³)	2,715	2,715	2,715
Mass, m (kg)	0.043	0.147	0.272
Young's modulus, E_s (GPa)	68.95	68.95	68.95
Poisson's ratio	0.33	0.33	0.33
Stiffness, $E_s I_s/L$ (N·m)	37.92	124.11	1,437.61

Table 7.9 Dimensions and properties of PZT patches

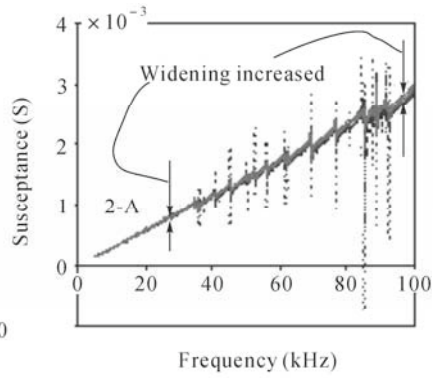
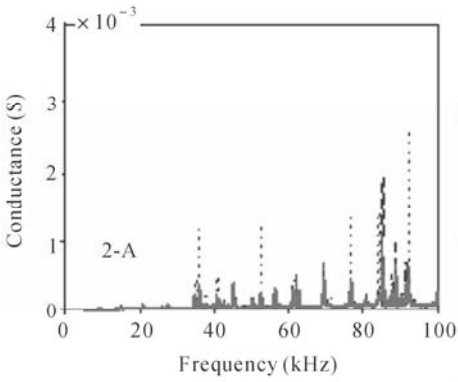
PZT	A/B	C
Dimensions, l (mm) $\times w$ (mm) $\times h$ (mm)	10 \times 10 \times 0.3/15 \times 15 \times 0.75	20 \times 10 \times 0.5
Density (kg/m ³)	7,800	7,800
Young's modulus, E_u (GPa)	65	66.67
Poisson's ratio	0.33	0.33
Mechanical loss factor	0.023	0.023
Piezoelectric strain coefficients, d_{31} , d_{32} (10^{-10} m/V)	-1.9	-2.1
Piezoelectric strain coefficient, d_{33} (10^{-10} m/V)	4.18	4.5
Dielectric loss factor	0.015	0.015
Electric permittivity (F/m)	0.98	1.75

First, three PZT patches were separately bonded on the three beams at the center, and the experimental tests were conducted with the admittance signatures recorded. After the tests, these PZT patches were removed and another three patches were bonded to replace the first three. The experimental tests were repeated with the admittance signatures recorded. The procedure was again repeated for another set of three PZT patches. The loads applied were proportional to the specimen sizes so as to limit the stresses within the elastic range for both the aluminum beams and the PZT patches. Therefore, static line loads of 0 N (no load, base-line) to 200 N at increments of 25 N were used. As the investigation concentrated on the influence of signatures due to applied external loadings only, the mass of the PZT transducers was assumed to be negligible.

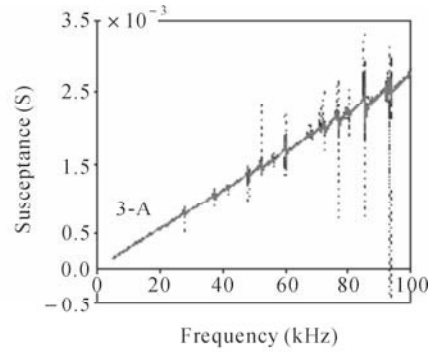
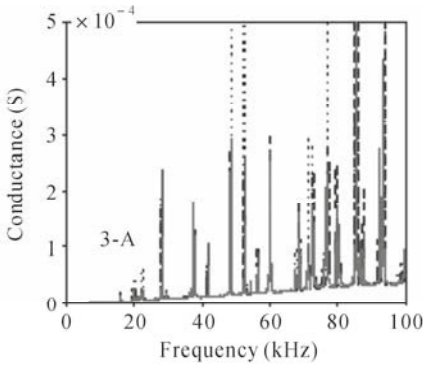
A total of nine different admittance signatures were plotted for nine combinations of the three beam specimens bonded with three different PZT patches, *i.e.*, 1-A, 1-B, 1-C, 2-A, 2-B, 2-C, 3-A, 3-B and 3-C. The trends of admittance signatures of transducers A, B and C bonded to specimen 1 (*i.e.*, 1-A, 1-B and 1-C) were the same. Similarly, the trends of admittance signatures of transducers A, B and C bonded to specimen 2 (*i.e.*, 2-A, 2-B and 2C) and specimen 3 (*i.e.*, 3-A, 3-B and 3-C) were the same. Thus, only three representative signatures for specimens 1 (1-A), 2 (2-A) and 3 (3-A) are shown in Fig. 7.12; and some typical details of the conductance and susceptance signatures for specimen 1 (1-A) are presented in Figs. 7.13 and 7.14.



(a)



(b)



(c)

Fig. 7.12 Conductance and susceptance signatures of PZT A for specimens: (a) 1; (b) 2; (c) 3

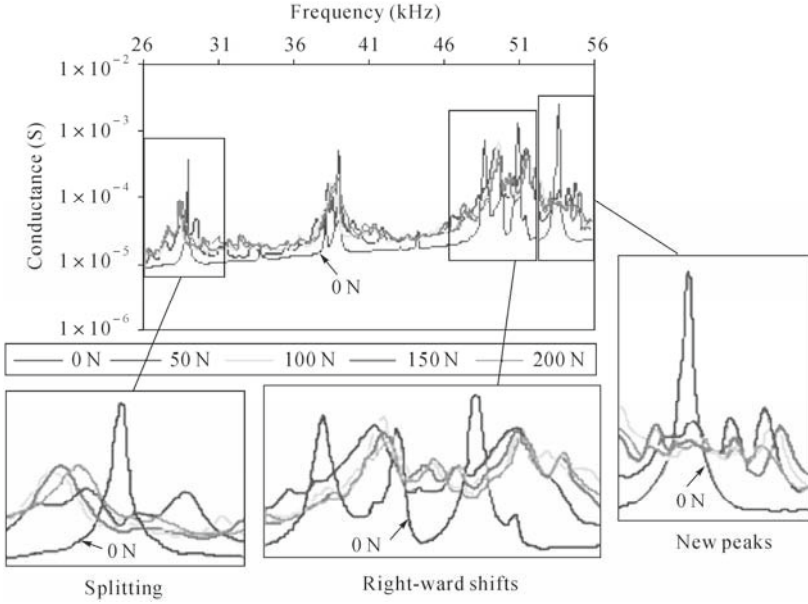


Fig. 7.13 Close-up view of conductance signatures of 1-A

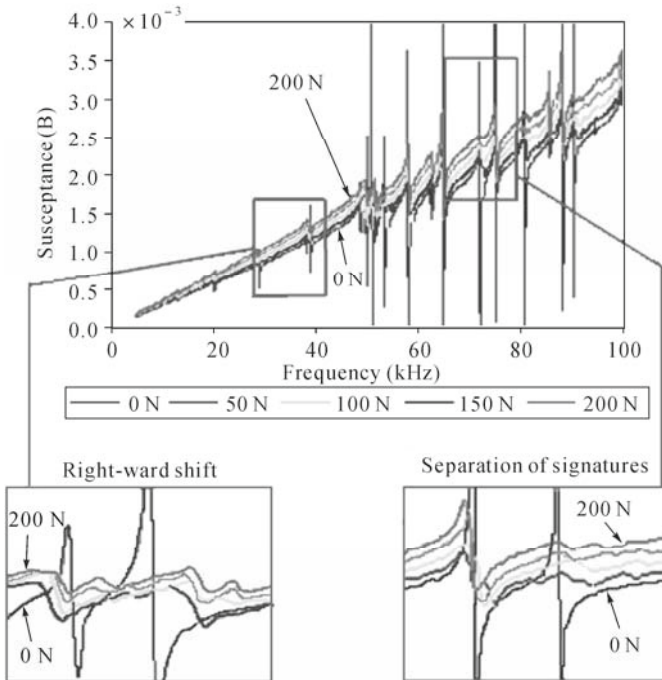


Fig. 7.14 Close-up view of susceptance signatures of 1-A

In all the nine conductance signatures (see representative Fig. 7.13), it was observed that the signatures of the loaded specimens seem to shift upwards from the base-line signature (0 N). The magnitude of the upward shifts has some correlation with the magnitude of the load applied. It was also observed that the upward shift of the signatures increases with increase in the magnitude of applied load as well as increase in the frequency range (Fig. 7.12). This indicates that there was actually a rotation of conductance signature in the anti-clockwise direction about the origin. The above variations in the signatures could be attributed to the fact that the interaction between the PZT transducer and the host structure has been altered. The PZT patch, when actuated, induced waves which propagate through the host structure and the applied loads can be viewed as an external force interfering with the wave propagation (Figs. 7.11(b)–(c)). Table 7.10 lists the values of susceptance signatures of the three specimens, about the origin, for various load cases bonded with PZT A.

Table 7.10 Value of susceptance (S) for various load cases @ 25 kHz

Specimen	Value of susceptance (S)				
	Load = 0 N	Load = 50 N	Load = 100 N	Load = 150 N	Load = 200 N
1	7.40	7.60	8.00	8.38	8.80
2	7.04	7.12	7.21	7.34	7.45
3	6.92	6.92	6.93	6.93	6.94

7.2.5 Efficiency of EM Admittance Signatures Using Statistical Index

Most of the statistical indices were obtained based on signatures (peaks/valleys) of the EM admittance. However, at low frequency range of less than 15 kHz, the external loading has negligible influence on the conductance signatures. Thus, a statistical index which considers both the conductance and susceptance signatures (peaks/valleys) and the frequencies of excitation is needed to account for changes in the admittance. In this investigation, the PZT efficiency factor (PEF) was employed to study the effects of variations in PZT properties on EM admittance, and the effects of variations in load magnitudes on EM admittance (Annamdas and Soh, 2007).

The PEF for chosen ranges of frequency is given as:

$$\text{PEF} = \frac{\frac{C_1 + C_2 + \dots + C_k + \dots + C_n}{n} \sqrt{R_1^2 + R_2^2 + \dots + R_k^2 + \dots + R_n^2}}{R_1 C_1 + R_2 C_2 + \dots + R_k C_k + \dots + R_n C_n} \quad (7.62)$$

where $C_1, C_2, \dots, C_k, \dots, C_n$ are the means of the frequency ranges (*i.e.*, mean of sum of the upper and lower frequencies), and subscripts 1, 2, ..., k and n are the number of considered frequency ranges as shown in Fig. 7.15. In Fig. 7.15, $f_1, f_3, \dots, f_{2k-1}, \dots, f_{2n-1}$ are the pre-peak frequencies and $f_2, f_4, \dots, f_{2k}, \dots, f_{2n}$ are the post-peak frequencies. The mean frequencies were calculated as the average of the pre- and post-peak frequencies [$C_n = (f_{2n-1} + f_{2n})/2$].

In all the nine conductances and susceptances recorded in the experimental tests, there were around 17 peaks observed for the different frequencies in the overall frequency range of 0 – 100 kHz. Details of these frequencies and frequency means are given in Table 7.11.

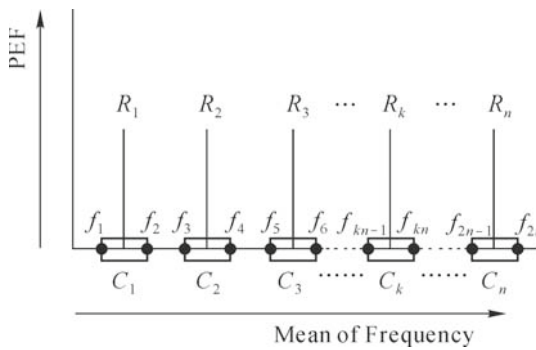


Fig. 7.15 PEF versus mean frequencies

In Eq. (7.62), R_1, R_2, R_3 and R_4 are the root mean square deviation (R) values for the considered frequency ranges. For $N = 1$, PEF becomes a ratio of R to R , that is, $PEF = 1$, and thus cannot be used for comparison. Therefore, $N > 1$ is the necessary condition for the application of PEF. R is given as

$$R (\%) = \sqrt{\frac{\sum_{i=1}^N (y_i - x_i)^2}{\sum_{i=1}^N x_i^2}} \times 100 \tag{7.63}$$

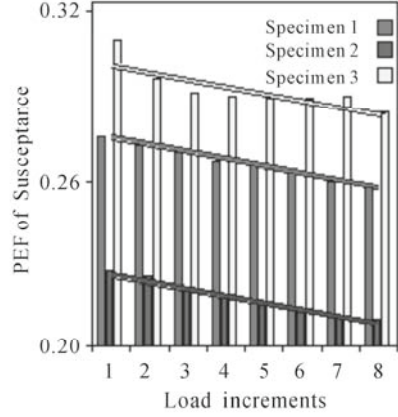
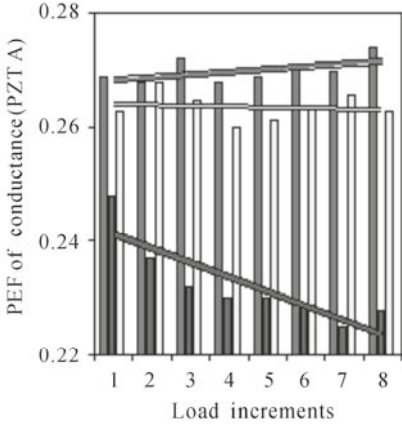
where x_i and y_i ($i = 1, 2, 3, \dots, N$) are the signatures obtained from the PZT transducer bonded to the structure for the initial and later stages of monitoring, respectively.

Table 7.11 PEF values for specimens 1, 2 and 3

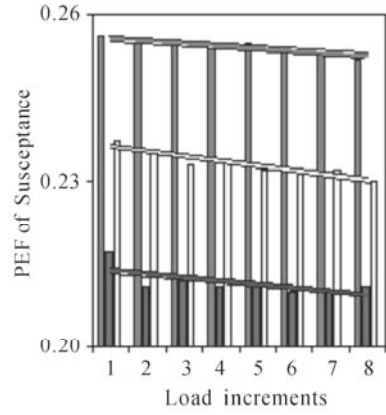
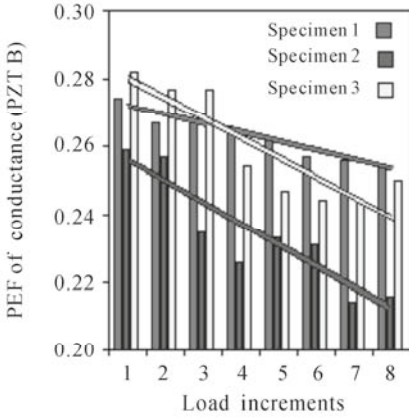
Conductance/ Susceptance		Load (N)	PEF (Specimen 1)			PEF (Specimen 2)			PEF (Specimen 3)			
Frequency range (kHz)	Mean of frequency (kHz)		A	B	C	A	B	C	A	B	C	
15.5 – 16.8	16.1	Conductance (S)	0	0.269	0.274	0.299	0.248	0.259	0.206	0.263	0.282	0.243
18.9 – 21.0	20		25	0.268	0.267	0.309	0.237	0.257	0.226	0.268	0.277	0.242
21.7 – 23.1	22.4		50	0.272	0.267	0.296	0.232	0.235	0.223	0.265	0.277	0.247
27.2 – 28.4	27.8		100	0.268	0.265	0.288	0.23	0.226	0.245	0.26	0.254	0.253
37.0 – 38.0	37		125	0.269	0.272	0.296	0.23	0.233	0.264	0.261	0.247	0.271
47.0 – 49.0	48		150	0.271	0.257	0.265	0.229	0.231	0.256	0.264	0.244	0.305
52.0 – 53.0	52.5		175	0.27	0.256	0.293	0.225	0.214	0.224	0.266	0.244	0.337
55.7 – 56.7	56.2		200	0.274	0.255	0.29	0.228	0.216	0.221	0.263	0.25	0.345
59.3 – 60.3	59.8											
67.0 – 68.0	67.5	Susceptance (S)	0	0.276	0.256	0.292	0.227	0.217	0.219	0.311	0.237	0.261
68.1 – 69.1	68.6		25	0.273	0.255	0.285	0.225	0.211	0.217	0.297	0.235	0.257
70.6 – 71.7	71.2		50	0.271	0.255	0.282	0.22	0.212	0.217	0.292	0.233	0.257
71.8 – 73.6	72.7		100	0.267	0.254	0.284	0.218	0.211	0.215	0.291	0.234	0.257
79.0 – 81.0	80		125	0.266	0.255	0.286	0.215	0.211	0.214	0.29	0.232	0.255
94.4 – 85.7	85		150	0.263	0.254	0.284	0.213	0.21	0.211	0.29	0.232	0.253
91.8 – 92.5	92.1		175	0.26	0.253	0.283	0.211	0.21	0.209	0.291	0.232	0.253
92.6 – 94.2	93.4		200	0.258	0.252	0.282	0.21	0.211	0.208	0.285	0.23	0.253

Fig. 7.16 plots the PEFs of the nine conductance and susceptance signatures tabulated in Table 7.11. It is apparent that, for all the specimens, there is a decrease in trend of the susceptance PEFs as the magnitude of load increases, unlike there is no obvious trend for the conductance PEFs. For example, in the conductance plot, PEFs of PZT C bonded to specimens 1, 2 and 3 can either increase or decrease with the increase in magnitude of loading. On the other hand, in the susceptance plot, PEFs of PZT A bonded to specimens 1, 2 and 3 constantly decrease with the increase in load magnitude. The point to note is that there exists an inverse relationship between the load magnitude and the susceptance PEF.

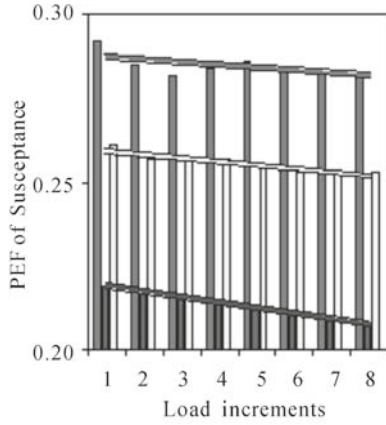
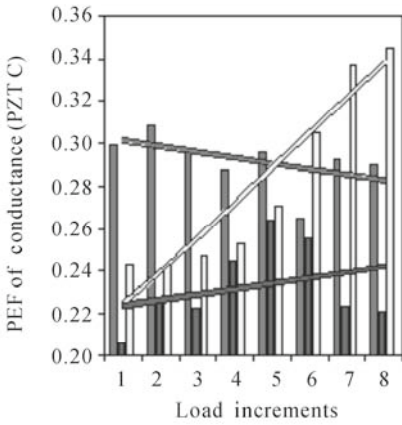
The above statistical results show that in-situ stress has larger influence on the susceptance signatures than on the conductance signature, indicating that susceptance could be a more efficient indicator than conductance for detecting in-situ stress in the structure. Since stress levels in the structure are related to the structural stiffness, which depends on the mechanical properties, it can be deduced that the mechanical properties of the structure have a larger influence on the imaginary part of the admittance signature than the real part when the structure is loaded.



(a)



(b)



(c)

Fig. 7.16 PEF of signatures for specimens 1, 2, 3. (a) PZT A; (b) PZT B; (c) PZT C

7.2.6 Summary

The effects of external loading on admittance signatures were investigated. Experimental tests were conducted on different sizes of PZT and host structures for various magnitudes of loading. It was observed that the influence of stress levels is more noticeable in the susceptance signature making it better than conductance in stress monitoring. This observation has more relevance in practical applications, especially for SHM of compressed or stretched structural members that are more likely to undergo simultaneous variations in stress level and occurrence of damage. The observation was verified using statistics based PEF of the conductance and susceptance signatures. Therefore, it is concluded that the parametric indices, *e.g.*, RMSD and PEF, which have been widely applied to conductance signatures by many researchers, can be extended to susceptance signatures to acquire more meaningful and comprehensive conclusions.

7.3 Practical Issues Related to Application of EMI Technique in SHM

7.3.1 Introduction

The EMI technique possesses distinct advantages such as the ability to detect incipient damage, use of non-intrusive transducers and potentially low-cost applications. However, most of the researches conducted so far are laboratory-based, under well-controlled environment, and most of the idealized assumptions may not be practical in real-life applications (Lim *et al.*, 2006). Hence, there exist practical application issues such as durability of both the transducers and bonding layers to ensure consistency in monitoring signatures and their resistances towards harsh environmental effects such as rain and sunlight as well as fluctuating temperature. In addition, their ability to sustain continuous and long term monitoring is also essential. Therefore, various problems related to real-life applications (Yang *et al.*, 2008) including workability, reliability, durability and applicability of the EMI technique ought to be circumvented before actual field applications.

Giurgiutiu (2008) investigated the effect of cyclic temperature change (oven test), climatic factors (outdoor tests) and operational fluids (immersion tests) on the durability of EMI technique. No significant changes were reported on the impedance spectrum. Park *et al.* (1999) investigated the effect of temperature on the signatures acquired and proposed a statistics-based compensation method.

This section presents our investigations into the long term repeatability of the

admittance signatures acquired from PZT patches under various environmental conditions. Protection of the PZT patches from wear and tear and environmental attack were also studied. Reliability of the EMI technique, in terms of long term consistency of the measured electrical admittance signatures under various foreseeable environmental conditions, was experimentally investigated with different level of protections applied on the piezo-impedance transducers. Effects of bonding layer on the EMI technique, especially under varying temperature, were investigated experimentally.

7.3.2 Consistency of Admittance Signatures Acquired from PZT Patch

The electrical admittance signatures are directly affected by the PZT patch, the bonding layer and the host structure. Under normal working condition, the consistency of piezoelectric properties is relatively high. Aging rate of the key piezoceramic properties is generally lower than 5% per decade (PI Ceramic, 2006). Endurance test conducted on piezoceramics showed that the material performed consistently even after several billion of cycles. Therefore, deterioration of the PZT patch itself is not a major concern under normal use. However, this may not be true when the patch is surface-bonded on civil structures which may be constantly exposed to harsh environment. The following section elucidates a series of experimental studies conducted to investigate the consistency of signatures acquired under different environmental conditions.

• *Experimental Investigation*

Three lab-size aluminum beam specimens of grade Al 6061-T6 were surface-bonded with PZT patches of grade PIC-151, as shown in Fig. 7.17, for the experimental study. The bonding adhesive used was two-part high strength epoxy, RS 159-3957. Dimensions of the specimens, the PZT patches and relevant exposed environmental conditions are tabulated in Table 7.12. The admittance signatures of the PZT patches were monitored at selected time intervals up to a period of one and a half years.

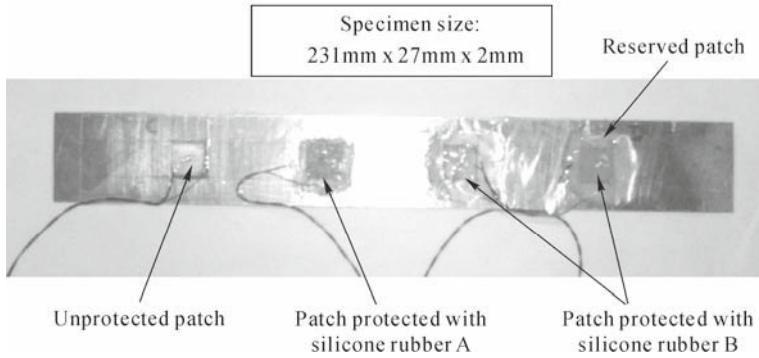


Fig. 7.17 Aluminum beam bonded with PZT patches (Identical configurations for all specimens: B1, B2 & B3)

Only three of the patches are discussed as the extra patches served as reserves. All three specimens, B1, B2 and B3, were identical. Both specimens B1 and B2 were placed outdoor. Specimen B1 was exposed to air while specimen B2 was buried under clayey soil (placed inside a bucket). These two samples were however prevented from direct exposure to sunlight and rain. They were in contact with water only during heavy rain. This was an attempt to simulate the situation of nominal construction site or in-service civil structures. Situation of extreme harsh environment was not considered in this study. Specimen B3 was placed inside the laboratory (room condition).

Table 7.12 Details of aluminum beam specimens for consistency test

Specimen labels	Patch labels	Patch sizes (mm ³)	Protections	Environmental conditions
B1	1	10×10×0.2	Silicone rubber A	Outdoor
	2	10×10×0.2	Silicone rubber B	
	A	10×10×0.5	Unprotected	
B2	3	10×10×0.2	Silicone rubber A	Outdoor (Buried under dry soil)
	4	10×10×0.2	Silicone rubber B	
	C	10×10×0.5	Unprotected	
B3	5	10×10×0.2	Silicone rubber A	Indoor
	6	10×10×0.2	Silicone rubber B	
	E	10×10×0.5	Unprotected	

In this study, a layer of silicone rubber was applied across the selected patches, covering a small portion of the host structure surrounding the patch as a mean of protection. Two types of commercially available silicone rubber, herein indicated as silicone rubber A (Hi-Bond, 2006) and silicone rubber B (Dow Corning Corporation, 2006), were used. Silicone rubber A, normally used as glass sealant, was much cheaper than silicone rubber B and of better quality.

An HP 4192A impedance analyzer was used for sensing and actuation of the

PZT patches. All specimens were returned to the laboratory a few hours before acquiring the signatures in order to eliminate the effects of temperature and humidity. This was to ensure the signatures were acquired under consistent environment (effects of temperature will be separately considered in later section). Thus, any deviations in the signatures were inferred to be attributed to degradation in the PZT patch or the bonding layer. The host structure was assumed to be sufficiently robust and remained intact throughout the experimental study.

Only the conductance signatures were compared in this study as conductance signatures are more sensitive to damage detection (Sun *et al.*, 1995).

• Results and Discussions

Figs. 7.18 and 7.19 plot the admittance signatures against frequencies, ranging from 10 to 100 kHz, for the different PZT patches. A summary of the RMSD statistical quantifier calculated for each PZT patch relative to the baseline signature is tabulated in Table 7.13.

Specimen B1—outdoor condition

It is obvious from Fig. 7.18 that, in spite of the different levels of protection, the conductance signatures remained virtually unchanged throughout the monitoring period for all three patches. Comparing their RMSD at different monitoring periods (Table 7.13), all values for the protected patches (Patches 1 and 2) were well within 5%, while the values for the unprotected patch (Patch A) were slightly higher. The RMSD values fluctuated faintly throughout the period of monitoring but showed no increasing trend against time. Minor fluctuation in RMSD values may be attributed to slight variation in humidity and temperature as well as possible minor inconsistency during calibration of the impedance analyzer. Higher fluctuation in the unprotected patch could be due to some degradation in the bonding layer. The absence of variation in modal frequency (no horizontal shift in resonance peaks) indicated no sign of structural deterioration.

However, an initially unforeseen problem arose in the unprotected patch (Patch A) as one of the wires soldered onto its terminal was jerked off due to wear and tear after six months. Alternatively, it can be viewed as the silicone rubber provided good protection to the soldered wires from being disconnected easily. Monitoring of this sample was forced to be terminated on the eighth month when it was spoiled by some mischievous passerby who plucked out all the wires and caused damages on the patch terminals. This happened to all other samples placed outdoor. However, the specimens placed in the lab remained intact and functional till the end of the experimental study.

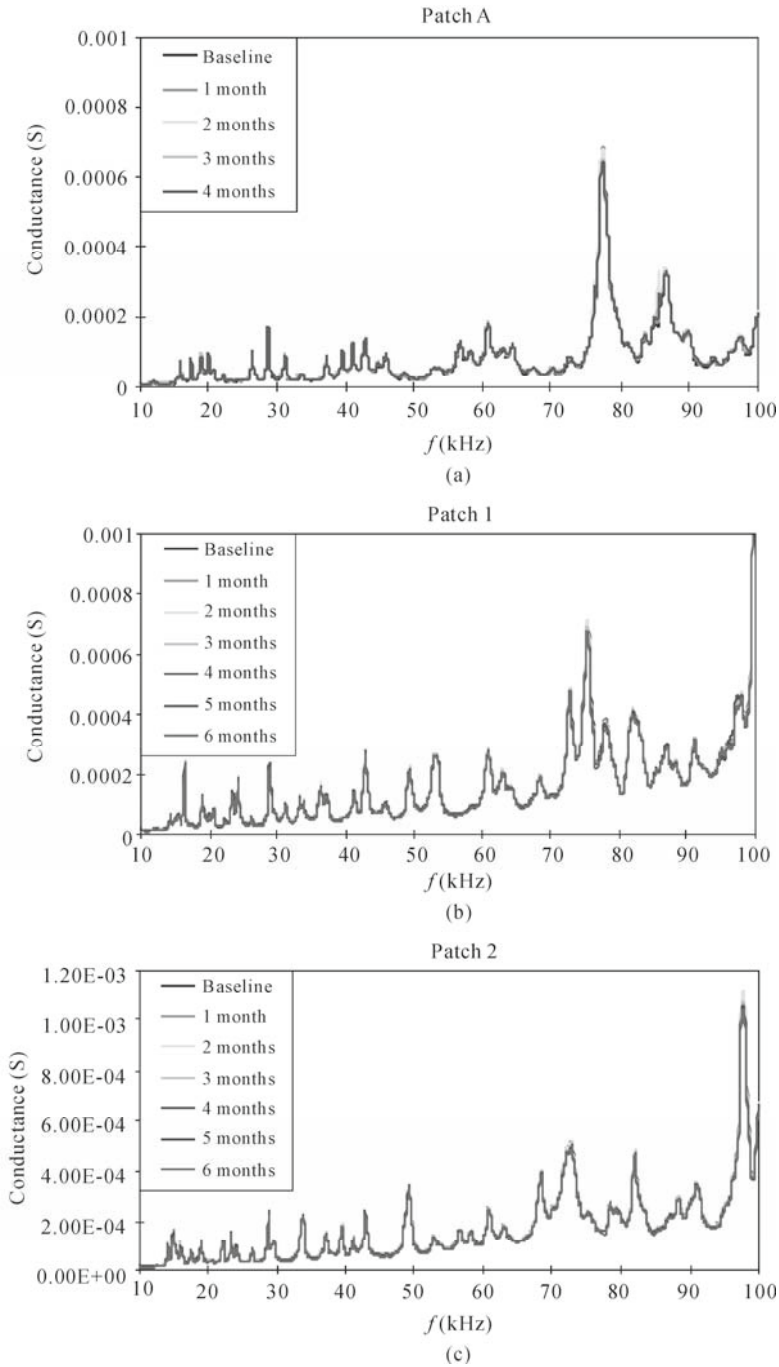


Fig. 7.18 Conductance signatures for Specimen B1 (10 – 100 kHz): (a) Patch A (unprotected); (b) Patch 1 (protected with silicone rubber A); (c) Patch 2 (protected with silicone rubber B)

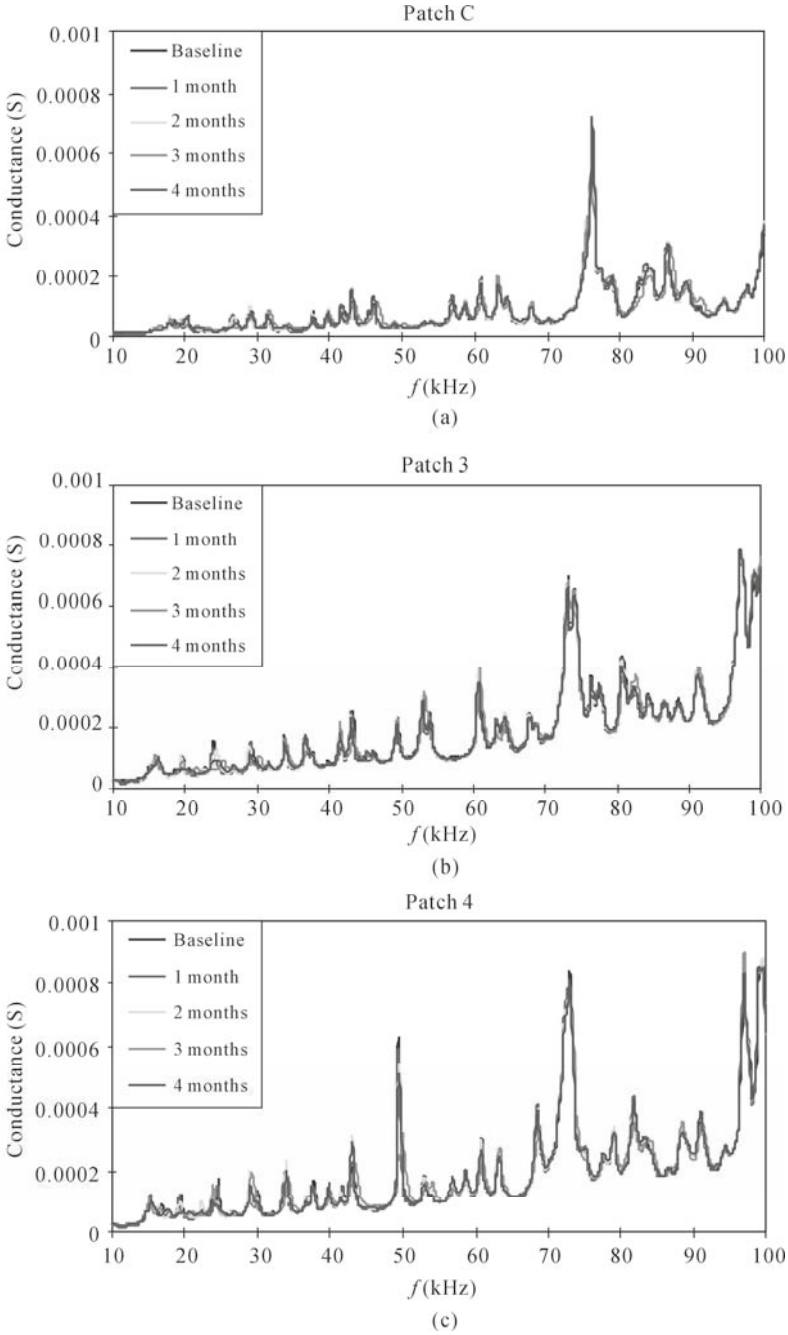


Fig. 7.19 Conductance signatures for Specimen B2 (10 – 100 kHz): (a) Patch C (unprotected); (b) Patch 3 (protected with silicone rubber A); (c) Patch 4 (protected with silicone rubber B)

Table 7.13 RMSD values (%) calculated from admittance signatures (10 – 100 kHz) at different stages in comparison to baseline signatures

Stage (month)	Specimen B1 (Outdoor)			Specimen B2 (Soil)			Specimen B3 (Indoor)		
	Patch 1	Patch 2	Patch A	Patch 3	Patch 4	Patch C	Patch 5	Patch 6	Patch E
1	3.41	1.93	3.03	7.45	8.15	16.91	2.19	2.05	3.28
2	3.29	2.99	6.30	7.93	8.97	17.94	2.06	2.05	3.75
3	3.33	3.25	4.39	11.20	13.52	23.62	3.65	3.04	5.65
4	3.84	3.12	3.82	7.03	8.01	18.69	1.38	1.46	2.12
6	4.54	3.55	8.94				2.32	2.13	2.81
8							3.71	2.88	4.20
11							3.06	4.29	4.32
15							3.30	2.81	4.86
Avg.	3.68	2.97	5.30	8.40	9.66	19.29	2.71	2.59	3.88

Specimen B2—buried under dry soil

For the specimen buried under soil, visible fluctuations in admittance signatures throughout the monitoring period can be observed in Fig. 7.19. Visually, signatures from all three patches suffered similar amount of disturbance. The average RMSD values throughout the four months computed for the patch protected with silicone rubber B, silicone rubber A and the unprotected patch were 8.40%, 9.66% and 19.29%, respectively. This proved that the silicone layers, especially silicone rubber B which was more expensive than A, provided better protection to the patches.

The reason of variations was attributed to the gradual loss of humidity in the soil especially during the first two months (the specimen was buried in soil contained in a bucket which originally contained some moisture). The monitoring was again terminated prematurely when the sample was removed and the soil thrown away by unknown vandal.

The experiment also exposed an implicit weakness of the RMSD approach. The RMSD approach calculates the relative vertical difference between two signatures at all frequencies. However, damage on host structure is mainly reflected through the horizontal shift of resonance peaks. Therefore, in the case where there were substantial vertical shifts caused by environmental factors, the change in RMSD values would give a false impression of damage.

Specimen B3—indoor condition

The signatures acquired from the patches placed under room condition showed even higher consistency (with an average RMSD value = 2.72%) than those under outdoor conditions (specimen B1, average RMSD = 3.98%). No sign of degradation was seen on the specimen placed in the room after one and a half years of monitoring.

PZT Patches

All the unprotected PZT patches bonded on the various specimens performed excellently throughout the period of monitoring, despite showing slightly higher fluctuations than the protected patches. The unprotected patch buried in dry soil remained workable without significant degradation. Constant fluctuating humidity and even in contact with rain water did not degrade the patches nor affected their signatures acquired as long as they were dried before the signature acquisition. This demonstrated the robustness of the EMI technique against the outdoor environment. Hence, with further protection using either silicone A or B, the PZT patches should function well in the normal construction sites.

7.3.3 Effects of Bonding Layer and Temperature

If a PZT patch is surface bonded onto a structure, the bonding adhesive will form the only interface for strain transfer between them. Generally, the bonding layer is much softer than the patch and the structure. The stiffness could be further reduced at elevated temperature. Temperature changes could lead to changes in the mechanical and electrical properties of all components, including the PZT patch, the bonding layer and the host structure. However, previous researches have mainly focused on the effects of temperature on the PZT patch and the structure (Sun *et al.*, 1995, Park *et al.*, 1999), but often omitted the bonding layer.

This section first reviews some relevant previous works and summarizes the necessity and focus of further study. Detailed experimental investigation on the effect of bonding layer variation on the admittance signatures acquired, with special attention paid to the influences of varying temperature, is then presented.

- *Review of Relevant Studies*

Bonding layer

Crawley and de Luis (1987) proposed a static-based model, and Ha *et al.* (1992) proposed a dynamic FE model for the PZT-structure interaction. Both methods ignored the excitation frequency. This is highly impractical for the EMI technique, which utilizes high frequency of excitation. Xu and Liu (2003) incorporated the effect of bonding into the 1D impedance-based EM model (Liang *et al.*, 1994) by simplifying the bonding layer into a single spring-mass-damper system. However, no investigations were carried out on its application using the EMI technique.

Nguyen *et al.* (2004) studied the actuation efficiency of PZT patches under varying ambient temperature and adhesive thickness. It was found that increase in bonding thickness would cause more losses in terms of actuation power than increase in temperature. They unveiled that reduction of adhesive hardness due to higher temperature or increase in bonding thickness would reduce the local stiffening effect of the actuators on the host structure and the overall stiffness of the system. However, their study was based on low frequency of actuation (<4 kHz) which may not be representative for the case of the EMI technique.

Bhalla and Soh (2004) proposed a 2D effective impedance-based model inclusive of the bonding layer, and concluded that the effect of bonding could be omitted for engineering models with thin bonding layer and under stable ambient temperature.

Temperature

Sun *et al.* (1995) discovered that the variations in electrical impedance caused by thermal drift and damage differ significantly. Effect of rise in temperature could be viewed as an effect of softening which reduces the overall stiffness of the host structure. Krishnamurthy *et al.* (1996) investigated the temperature effect on free PZT patch. Schulz *et al.* (2003) reported that piezoelectric properties decreased with increasing temperature but recovered each time the sensor was cooled.

Park *et al.* (1999) illustrated that temperature change imposed major effect on the dielectric constant and piezoelectric coupling constant of the PZT patch. They also discovered that the real part of signatures acquired from free PZT patch changed negligibly with temperature. Therefore, the real part of signatures was preferred over the imaginary part in the EMI technique.

Overall, in depth investigations into the effect of bonding layer especially under varying temperature on the admittance signatures have so far been omitted. However, this is essential in the practical applications of the EMI technique.

● *Experimental Study*

As shown in Fig. 7.20, an aluminum beam, an aluminum plate and two freely suspended PZT patches were prepared in a similar manner as previously described. The details of each specimen including size of the structure and the bonding thicknesses are summarized in Table 7.14. The dimensions of all PZT patches used in this study were 10 mm×10 mm×0.3 mm.

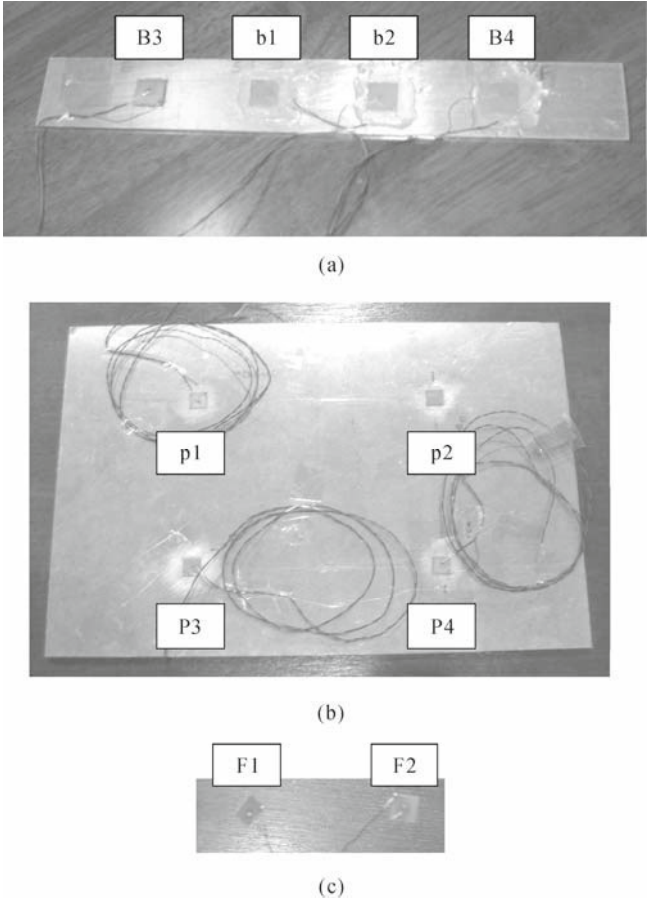


Fig. 7.20 Lab-sized specimens surface-bonded with PZT patches. (a) Aluminum beam; (b) Aluminum plate; (c) Freely suspended PZT patches

The patches bonded on both the aluminum beam and plate were carefully arranged in a symmetrical manner. This enabled the comparison of admittance signatures for different bonding thicknesses but with identical PZT-structure interactions.

According to recommendation by Bhalla (2004), when the thickness of bonding is smaller than one third of the thickness of PZT patch, the effect of bonding is negligible. In this case, one third of the PZT’s thickness was 0.1 mm. Therefore, from Table 7.14, patches b1, b2, p1 and p2 fell under the category of “less than one third” (hereafter denoted as “thin”) whereas patches B3, B4, P3 and P4 were within the category of “more than one third” (hereafter denoted as “thick”).

Table 7.14 Details of PZT patches and specimens

Host structures	Size of structures	Patch labels	Measured bonding thicknesses (mm)	Descriptions
Aluminum beam	331 mm×31 mm×6 mm	b1	0.04	Thin bonding
		b2	0.03	Placed symmetrically (inside)
		B3	0.14	Thick bonding
		B4	0.22	Placed symmetrically (ends)
Aluminum plate	302 mm×201 mm×4 mm	p1	0.05	Thin bonding
		p2	0.06	Placed symmetrically
		P3	0.13	Thick bonding
		P4	0.21	Placed symmetrically

● Results and discussions

Bonding Layer

As depicted in Fig. 7.21(a), high repeatability of the conductance signatures can be observed for patches bonded on symmetrical locations on the plate specimen but with different bonding thicknesses. In other words, they possessed identical PZT-structure interactions even with different bonding thicknesses. All resonance peaks can be accurately matched indicating that the PZT patches were consistent in the process of actuating and sensing, despite minor variations in magnitude caused by different bonding thicknesses. This further confirmed the consistency and reliability of the EMI technique.

However, slight variations were expected especially in the higher frequency range as some of the local peaks were not repeatable. At high frequency range, the sensitivity of admittance signatures to local changes was very high. Slight difference in bonding thickness or PZT location would change the admittance signature. When the frequency exceeded 100 kHz, the situation became worse as shown in Fig. 7.21(b). The repeatability of the resonance peaks was less obvious. Moreover, it was observed that the overall signature for patch P3 (thicker bond) shifted significantly upwards with increase in frequency. This effect has also been observed by Bhalla (2004) and Ong *et al.* (2002).

The reason for this phenomenon can be readily explained by Fig. 7.22 where the frequency spectrums of patches with different bonding thicknesses are plotted for a larger bandwidth (0 – 1,000 kHz). Observing the frequency plot for the free PZT patch (no bonding) in Fig. 7.22(c), there are a number of strong PZT resonance peaks within the range of plot. When compared to those bonded on the structure (Figs. 7.22(a) and 7.22(b)), resonance peaks of the free PZT patch are much smoother (no structural peaks) and occurred at significantly lower frequencies. This is attributed to the fact that when the PZT patch was bonded on the structure, it was significantly stiffened by the structure. Therefore, the peaks of

the bonded PZT patches were shifted to the right, indicating the effect of stiffening. Table 7.15 summarizes the frequency at which the first PZT resonance occurred for all 3 cases as well as the relative phase difference.

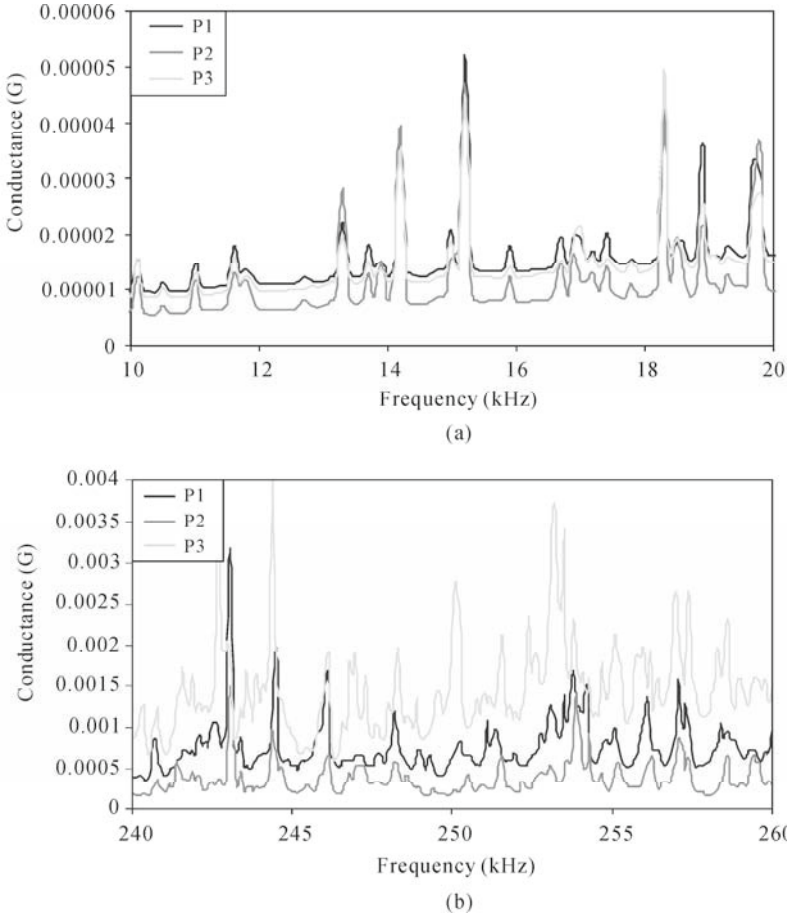


Fig. 7.21 Conductance signatures for PZT patches bonded on plate specimen with different bonding thicknesses. (a) 10 – 20 kHz; (b) 240 – 260 kHz

On the other hand, comparing Figs. 7.22(a) and 7.22(b), the PZT resonances of P3 occurred earlier (*i.e.*, at lower frequencies) than p2. This phenomenon can be explained by the decrease in strain transfer efficiency (due to more significant shear lag effect) with thicker bonding thickness, thus “isolating” the PZT patch from the structure. Furthermore, comparing the thin bonding with the thick bonding in Figs. 7.22(a) and 7.22(b), the thick bonding caused leftward shift of the PZT resonances and forced the structural resonance peaks in between 100 – 300 kHz vertically upwards.

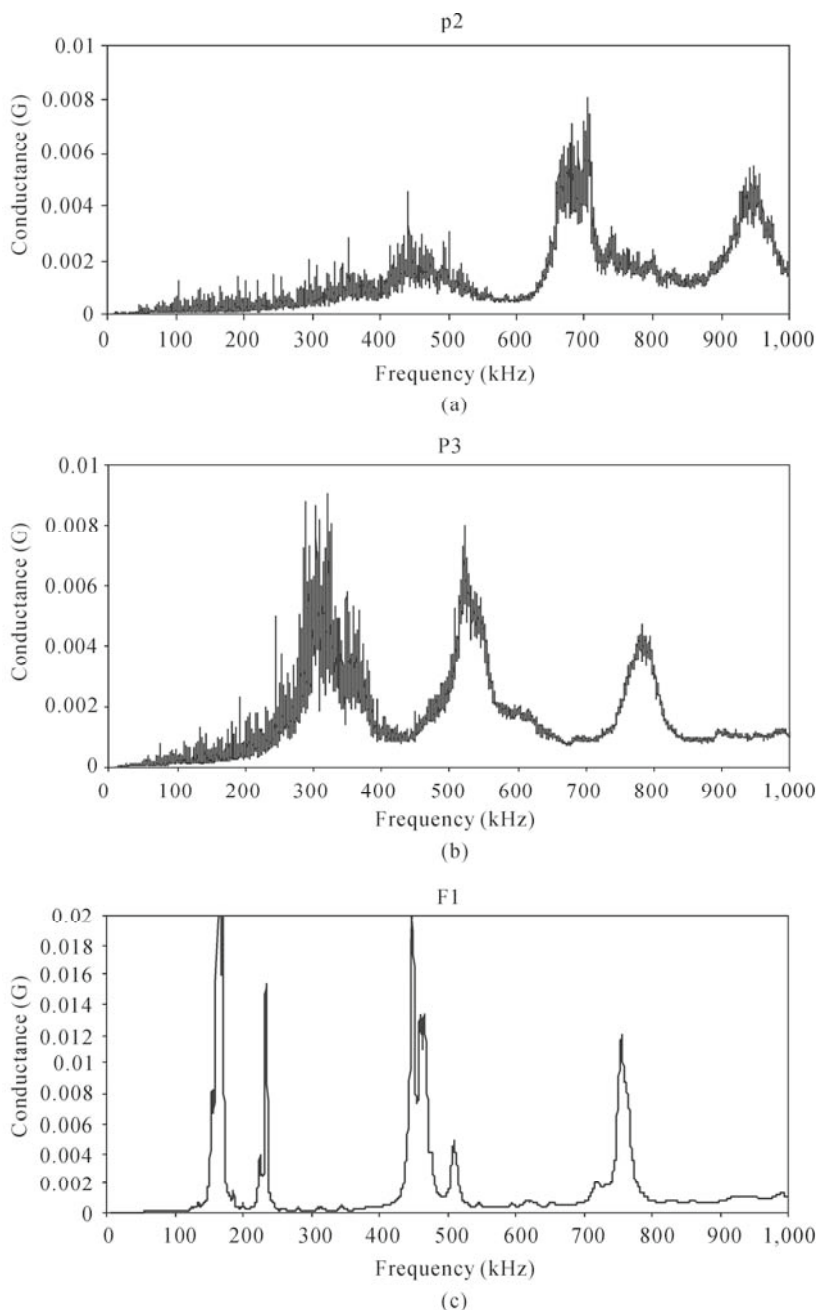


Fig. 7.22 Conductance signatures for PZT with different bonding thicknesses (0 – 1,000 kHz). (a) Patch p2 (bonding thickness = 0.06 mm); (b) Patch P3 (bonding thickness = 0.13 mm); (c) Patch F1 (no bonding, freely suspended patch)

Table 7.15 Summary of phases' information of first PZT resonance

PZT patches with different bonding thicknesses (Fig. 7.22)		
	First PZT resonance occurrence (kHz)	Phase reduction w.r.t. "p2" (kHz)
Patch p2 (Bonding thickness = 0.06 mm)	450	0
Patch P3 (Bonding thickness = 0.13 mm)	310	140
Patch F1 (Freely suspended)	160	290

PZT patch b2 with temperature varying from 30 °C – 80 °C (Fig. 7.24a)		
	First PZT resonance occurrence (kHz)	Phase reduction w.r.t. "30 °C" (kHz)
30 °C	406	0
40 °C	404	2
50 °C	403	3
60 °C	401	5
80 °C	392	14

PZT patch B4 with temperature varying from 30 °C – 80 °C (Fig.7.24(b) and 7.25(a))		
	First PZT resonance occurrence (kHz)	Phase reduction w.r.t. "30 °C" (kHz)
30 °C	270	0
40 °C	250	20
50 °C	230	40
60 °C	205	65
80 °C	175	95

PZT patch B4 of healthy and damage states at 30 °C (Fig. 7.25(b))		
	First PZT resonance occurrence (kHz)	Phase reduction w.r.t. "30 °C" (kHz)
Healthy	278	0
Damaged	272	6

The above observations were similarly obtained for the beam specimen; thus not presented here. Hence, the recommendation by Bhalla (2004) stating that the bonding thickness shall not exceed one-third of the PZT patch's thickness was further verified. In this case, thick bonding should be avoided to reduce contamination of the structural resonance peaks by the PZT resonances.

On the other hand, it can be concluded that the frequency range used in the EMI technique (for surface bonded patches) should preferably be lower than 200 kHz, unless a sufficiently thin bonding could be assured. The requirement would be more stringent at elevated temperature as the abovementioned adverse effect would be significantly amplified, which will be discussed in the later sections.

There is another phenomenon noted in Fig. 7.22. At very high frequency range, for thick bonding, significantly localized actuation of the PZT patch caused a PZT peak to occur between 700 – 800 kHz (Fig. 7.22(b)), which is at the same location as its counterpart of the free PZT (Fig. 7.22(c)). This indicates that the PZT actuation on the host structure at this frequency range was highly inefficient. The patch was almost vibrating independently.

Temperature

All the specimens described in the previous section (Fig. 7.20 and Table 7.14) were reused for investigation on the effects of temperature. The admittance signatures of the PZT patches were acquired at various predetermined ambient temperatures. Starting from room temperature, 30 °C (baseline), temperature in the chamber was gradually increased to 40 °C, 50 °C, 60 °C and 80 °C in an attempt to simulate the foreseeable temperature range normally experienced by civil structures in the tropical region.

Fig. 7.23 shows that, at high temperature, the admittance signatures acquired from patches of thicker bonding layer exhibited more severe deviation than those with thinner bond. With similar PZT-structure interaction, signature acquired from Patch B4 with bonding thickness of 0.22 mm (Fig. 7.23(b)) undergone significant upward shift when compared to the one from Patch B3 with bonding thickness of 0.14 mm (Fig. 7.23(a)). This phenomenon was again caused by the leftward shift of the first PZT resonance peak, similar to the case of increase in bonding thickness.

The leftward shift in the first PZT resonance peak (Fig. 7.23(c)) forced up the signatures representing the host structural vibration near its left end. With thick bonding ($>1/3$ of PZT patch thickness), the effect was significant and undesirable.

Plotting on the same scale in Fig. 7.24, the momentous adverse effect of temperature on admittance signatures became obvious, especially for the thick bonding layer (Fig. 7.24(b)). However, the deviation was not that significant for the thin bonding layer (Fig. 7.24(a)). A temperature difference as large as 50 °C (between 30 °C and 80 °C) caused only minor distortion of up to 150 kHz. In comparison with Fig. 7.24(b), significant deviation occurred even with a mere difference of 10 °C. The frequency of occurrence and relative phase shift of the first PZT resonance is summarized in Table 7.15. The amount of phase shift for thick bonding was almost ten times that of the thin bonding at various temperatures.

Similar to the previous case on increase in bonding thickness, the leftward shift of the resonance peak can be inferred to have been controlled by the bonding layer. In this case, the softening of bonding layer with increase in temperature reduced the stiffness of bonding, thus amplifying the shear lag effect. This, in turn, diminished the stiffening effect caused by the host structure and isolated the PZT patch, thus inducing the leftward shift of the PZT resonance peak. From previous study by Park *et al.* (1999), it is known that the real part of electrical impedance from a freely suspended PZT patch is negligibly affected (in terms of phase difference) by moderate changes in temperature. Thus, in this case, the PZT patch did not contribute to the shifting. On the other hand, the temperature effect on host structure affected mainly the dense structural peaks rather than the PZT peaks. Therefore, it is sensible to conclude that the leftward shift of the first PZT resonance was caused mainly by the softening of bonding layer.

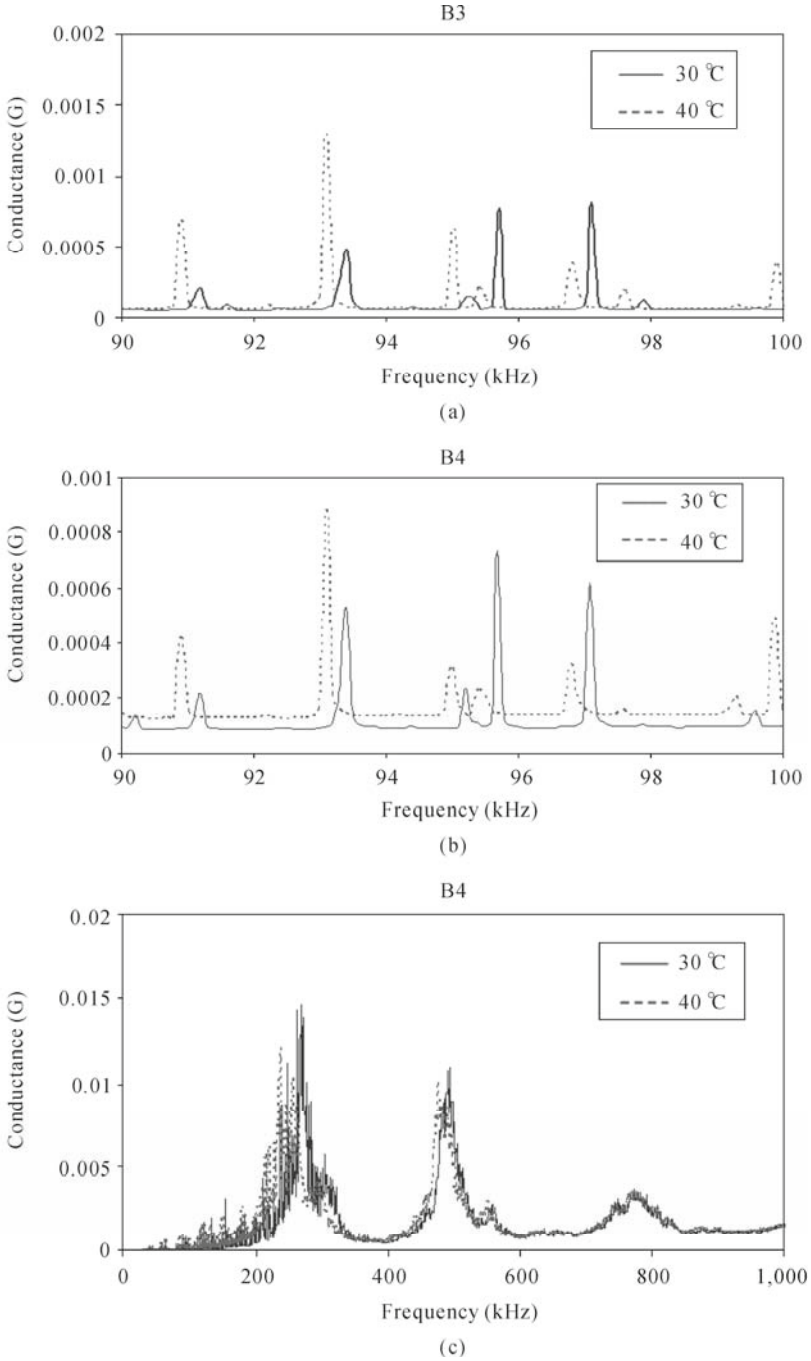


Fig. 7.23 Conductance signatures of PZT bonded on beam specimen with ambient temperature. (a) Patch B3 (90 – 100 kHz); (b) Patch B4 (90 – 100 kHz); (c) Patch B4 (0 – 1,000 kHz)

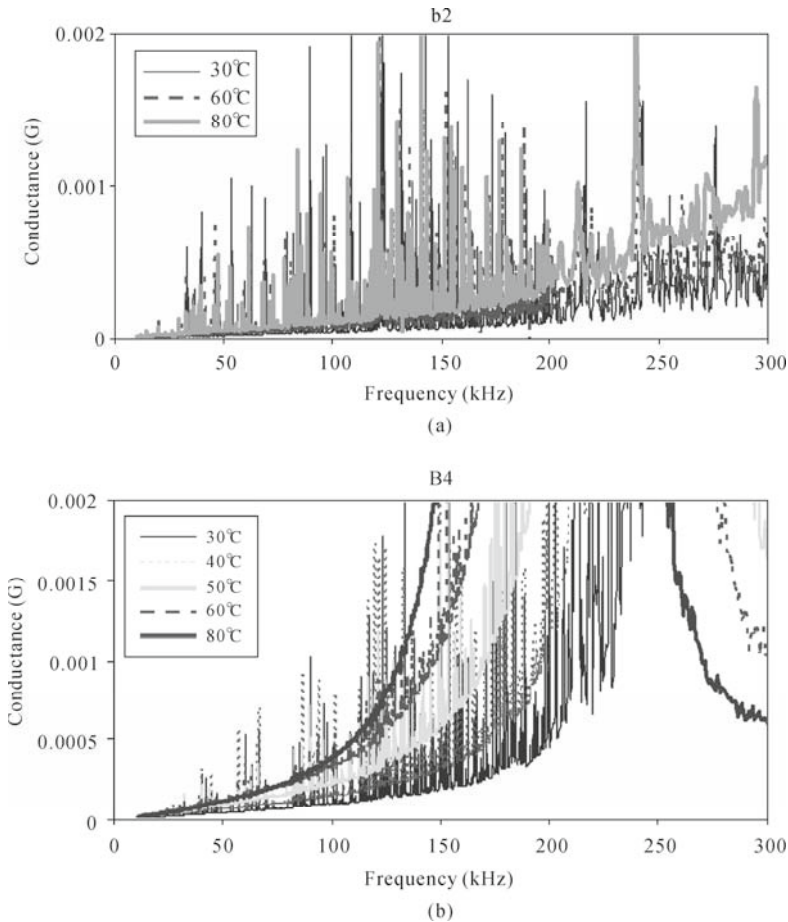


Fig. 7.24 Conductance signatures for PZT bonded on beam specimen with ambient temperature. (a) Patch b2; (b) Patch B4

Hence, in practical applications of the EMI technique, the use of normal adhesive such as the two-part epoxy with thick bonding is highly undesirable. Also, the frequency range used for the EMI technique is preferably lower than 100 kHz for a more reliable and efficient application. The problem may be alleviated with the use of temperature insensitive adhesive but the adverse effect is expected to be similar.

7.3.4 Differentiating Temperature-Induced and Damage-Induced Signature Deviations

In this study, an interesting observation was made, which can potentially be used

as a method to differentiate between temperature-induced and damage-induced signature deviations. This was achieved by observing the admittance signatures at high frequency range (200 – 1,000 kHz), as exemplified in Fig. 7.25.

Temperature-induced deviation triggered the shift of PZT resonance peaks at higher frequency range (Fig. 7.25(a)), but was negligible in the case of damage-induced deviation. Fig. 7.25(b) shows that the high frequency range was virtually unaffected by damages caused by drilling three holes with diameter of 5 mm and cutting a notch on the host structure. The frequency spectrum at the higher end remained unaffected in spite of serious damage inflicted on the host structure. The relative phase shift of the first resonance frequency for both cases is tabulated in Table 7.15. Hence, such observation could serve as a quick guide to differentiate actual damage from temperature effect by a mere glance at the admittance signature plots for the high frequency range.

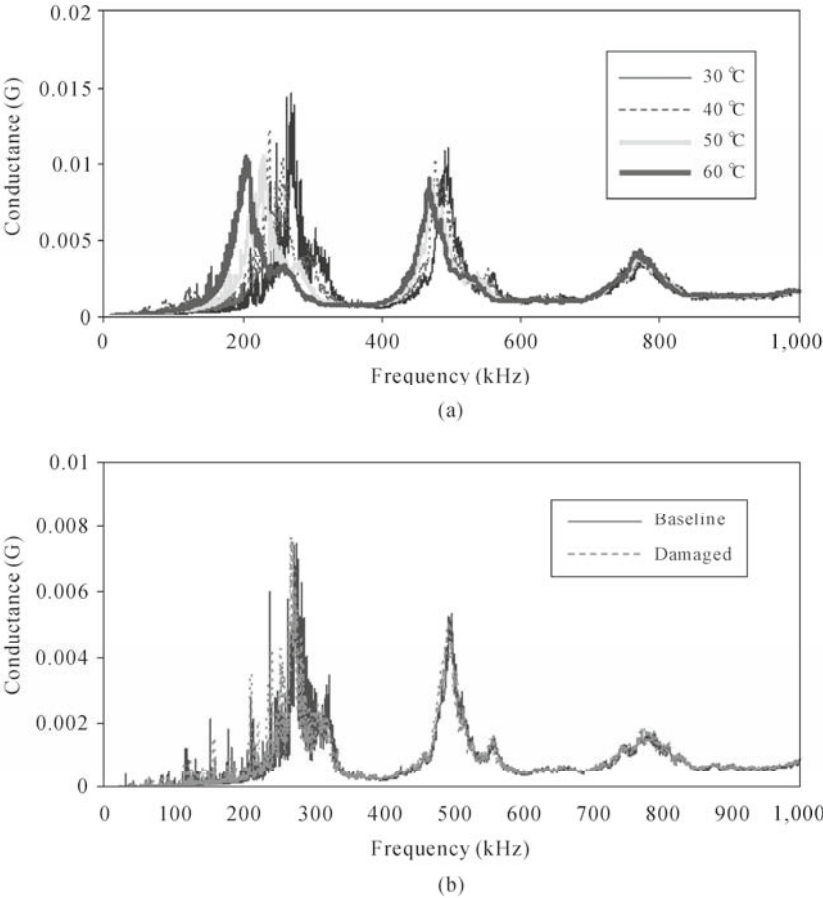


Fig. 7.25 Conductance signatures for PZT patch B4 bonded on aluminum beam specimen. (a) Temperature varying from 30 °C to 60 °C; (b) Damages induced at 30 °C

7.3.5 Differentiating Damage in Host Structure and in PZT Patch

Fig. 7.26 plots the admittance signatures against frequency for PZT patch inflicted with different levels of damage by cutting the patch using a pen knife. Level S1 indicated a cut from the center of the PZT to one of the corners, whereas level S2 was inflicted with a more severe cut from the center to the other two corners leaving only the corner with electrode intact. Visually, the PZT patch appeared to be severely spoiled after damage level S2 as some fragments of the patch has fallen off. However, both wires remained connected to the electrodes.

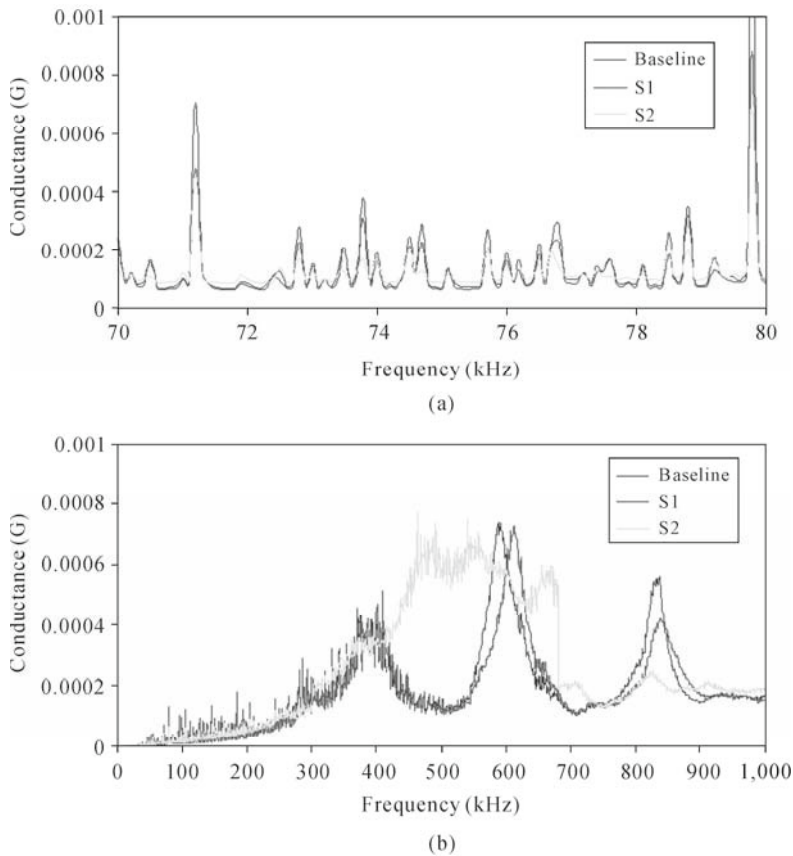


Fig. 7.26 Conductance signatures for PZT patch b1 bonded on aluminum beam specimen with different level of damages (S1 and S2) induced in PZT patch. (a) Frequency range 70 – 80 kHz; (b) Frequency range 0 – 1,000 kHz

It was found that the admittance signatures remained practically the same within the lower frequency range (<150 kHz), which is usually used for damage detection, despite the second level of damage (S2) being inflicted on the PZT

patch (Fig. 7.26(a)). However, the damage on the patch could be differentiated from Fig. 7.26(b) in the higher frequency range (>200 kHz) as significant deviation in the PZT's resonance peaks indicated that serious damage has been inflicted on the patch.

Therefore, as long as the location of the PZT patch and its actuation capability remained the same, the structural modes excited below 200 kHz would be the same. However, the structural resonance peak heights were reduced by damage in the PZT patch (Fig. 7.26(a)) due to reduction in the actuation energy caused by reduction in the patch's surface area.

7.3.6 Summary

This section addresses the practical issues faced by real-life applications of the EMI technique, especially in the health monitoring of civil structures. Various issues related to the actual applications including consistency of signatures for long term monitoring, environmental effect, temperature effect and bonding effect were investigated. The studies conducted on these topics are mainly based on experiments and are qualitative in nature.

Through the experimental study, it is found that the repeatability of admittance signatures, in terms of modal frequency and magnitudes of resonance peaks, from the PZT patches surface bonded on lab-sized aluminum structures under various environmental conditions is excellent for a monitoring period of up to one and a half years. This is true even for patches without any protection.

Various experimental case studies conducted on PZT patch sized $10\text{ mm} \times 10\text{ mm} \times 0.3\text{ mm}$ showed that the effect of bonding could be neglected even for thickness up to $2/3$ of the PZT patch's thickness, provided the excitation frequency does not exceed 100 kHz. Above this frequency, the adverse effect of thick (larger than $1/3$ of PZT thickness) bonding is obvious. With thick bonding and at high frequency of excitation, the PZT resonance will dominate the structural resonance as a result of localized actuation and sensing, rendering contamination to the admittance signatures and reduction in the damage detection capability. The effect of increase in temperature on the admittance signatures is found to be similar to the increase in bonding thickness.

An observation was made, which could potentially be developed as a quick guide to differentiate the effect of temperature from actual damage. This is to compare the admittance at high frequency range (200 – 1,000 kHz) as temperature change triggers the shift of PZT resonance peaks but not in the case of damage.

In addition, damage inflicted on PZT patch can also be distinguished from structural damage by observing the admittance signatures at high frequency range (200 – 1,000 kHz). Damage inflicted on PZT patch (as long as the patch is still functional) will not affect the modal frequency of the structural resonances (below 200 kHz) though it may affect its peak height.

References

- Abé, M., Park, G. and Inman, D.J. (2000). "Impedance-Based Monitoring of Stress in Thin Structural Members", *Proceedings of Adaptive Structures and Technologies*, Nagoya, Japan, Oct., 285-292.
- Annamdas, V.G.M. and Soh, C.K. (2007). "Three Dimensional Electromechanical Impedance Model II: Damage analysis and PZT characterization", *Journal of Aerospace Engineering*, 20(1): 63-71.
- Annamdas, V.G.M., Yang, Y.W. and Soh, C.K. (2007). "Influence of Loading on Electromechanical Admittance of Piezoceramic Transducers", *Smart Materials and Structures*, 16(5): 1888-1897.
- Bhalla, S. (2004). "A Mechanical Impedance Approach for Structural Identification, Health Monitoring and Non-Destructive Evaluation Using Piezo-Impedance Transducer", *Ph.D. Thesis*, Nanyang Technological University, Singapore.
- Bhalla, S. and Soh, C.K. (2004). "Electro-Mechanical Impedance Modeling for Adhesively Bonded Piezo-Transducers", *Journal of Intelligent Material Systems and Structures*, 15(12): 955-972.
- Crawley, E.F. and de Luis, J. (1987). "Use of piezoelectric actuators as elements of intelligent structures", *AIAA Journal*, 25: 1373-1385.
- Dow Corning Corporation (2006). <http://www.dowcorning.com>.
- Esteban, J. (1996). "Analysis of the Sensing Region of a PZT Actuator-Sensor", *Ph.D. Dissertation*, Virginia Polytechnic Institute and State University, Blacksburg, VA.
- Giurgiutiu, V. and Rogers, C.A. (1997). "Electromechanical Impedance Method for Structural Health Monitoring and Non-Destructive Evaluation", *Proceedings of SPIE*, 3329: 536-547.
- Giurgiutiu, V., Zagrai, A. and Bao, J. (2004). "Damage Identification in Aging Aircraft Structures with Piezoelectric Wafer Active Sensors", *Journal of Intelligent Material Systems and Structures*, 15: 673-687.
- Giurgiutiu, V. (2008). *Structural Health Monitoring with Piezoelectric Wafer Active Sensors*. Academic Press, USA, 300-305.
- Graesser, E.J. and Wong, C.R. (1992). "The Relationship of Traditional Damping Measures for Materials with High Damping Capacity: A Review", *M3D: Mechanics and Mechanisms of Material Damping*, ASTM STP, 1169: 316-343.
- Ha, S.K., Keilers, C. and Chang, F.K. (1992). "Finite Element Analysis of Composite Structures Containing Distributed Piezoceramic Sensors and Actuators", *AIAA Journal*, 30: 772-780.
- Hi-Bond (2006). www.hi-bond.co.uk.
- Kalyanasundaram, S., Allen, D.H. and Schapery, R.A. (1987). *Dynamic Response of a Viscoelastic Timoshenko Beam*. Mechanics and Materials Center, Texas A&M University, College Station, TX.
- Kinra, V.K. and Yapura, C.L. (1992). "A Fundamental Connection between Intrinsic Material Damping and Structural Damping", *M3D: Mechanics and*

- Mechanisms of Material Damping*, ASTM STP, 1169: 396-420.
- Krishnamurthy, K., Lalande, F. and Rogers, C.A. (1996). "Temperature Effects on Piezoelectric Elements Used as Collocated Actuator/Sensors", *Proceedings of SPIE*, 2717: 302-310.
- Liang, C., Sun, F.P. and Rogers, C.A. (1994). "Coupled Electro-Mechanical Analysis of Adaptive Material Systems- Determination of Actuator Power Consumption and System Energy Transfer", *Journal of Intelligent Material Systems and Structures*, 5: 12-20.
- Lim, Y.Y., Bhalla, S. and Soh, C.K. (2006). "Structural Identification and Damage Diagnosis Using Self-Sensing Piezo-Impedance Transducers", *Smart Materials and Structures*, 15: 987-995.
- Mace, B.R. (1984). "Wave Reflection and Transmission in Beams", *Journal of Sound and Vibration*, 97: 237-246.
- Mall, S. (2002). "Integrity of Graphite/Epoxy Laminate Embedded with Piezoelectric Sensor/Actuator under Monotonic and Fatigue Loads", *Smart Materials and Structures*, 11: 527-533.
- Mei, C. and Mace, B.R. (2005). "Wave Reflection and Transmission in Timoshenko Beams and Wave Analysis of Timoshenko Beam Structures", *Journal of Vibration and Acoustics*, 127: 382-394.
- Nguyen, C., Pietrzko, S. and Buetikofer, R. (2004). "The Influence of Temperature and Bonding Thickness on the Actuation of a Cantilever Beam by PZT Patches", *Smart Materials and Structures*, 13: 851-60.
- Ong, C.W., Yang, Y.W., Wong, Y.T., Bhalla, S., Lu, Y. and Soh, C.K. (2002). "The Effects of Adhesive on the Electro-mechanical Response of a Piezo-ceramic Transducer Coupled Smart System", *Proceedings of SPIE*, 5062: 241-247
- Park, G., Kabeya, K., Cudney, H.H. and Inman, D.J. (1999). "Impedance-based Structural Health Monitoring for Temperature Varying Applications", *JSME International Journal*, 42: 249-258.
- Park, G., Cudney, H.H. and Inman, D.J. (2000). "Impedance-based Health Monitoring of Civil Structural Components", *Journal of Infrastructure Systems*, 6 (4): 153-160.
- PI Ceramic (2006). *Product information catalogue*. Lindenstrabe, Germany <http://www.piceramic.de>.
- Rose, J.L. (1999). *Ultrasonic Waves in Solid Media*. New York: Cambridge University Press.
- Schulz, M.J., Sundaresan, M.J., McMichael, J., Clayton, D., Sadler, R. and Nagel, B. (2003). "Piezoelectric Materials at Elevated Temperature", *Journal of Intelligent Material Systems and Structures*, 14: 693-704.
- Sirohi, J. and Chopra, I. (2000). "Fundamental Behaviour of Piezoceramic Sheet Actuators", *Journal of Intelligent Material Systems and Structures*, 11 (1): 47-61.
- Sun, F.P., Chaundhry, Z., Rogers, C.A., Majmunder, M. and Liang, C. (1995). "Automated Real-time Structural Health monitoring via Signature Pattern Recognition", *Proceedings of SPIE*, 2443: 236-247.

- Wang, X.D. and Huang, G.L. (2001). "Wave Propagation in Electromechanical Structures: Induced by Surface-bonded Piezoelectric Actuators", *Journal of Intelligent Material Systems and Structures*, 12: 105-115.
- Xu, Y.G. and Liu, G.R. (2003). "A Modified Electro-mechanical Impedance Model of Piezoelectric Actuator-sensors for Debonding Detection of Composite Patches", *Journal of Intelligent Material Systems and Structures*, 13: 389-396.
- Yang, M.J. and Qiao, P.Z. (2005). "Modeling and Experimental Detection of Damage in Various Materials Using the Pulse-echo Method and Piezoelectric Sensors/Actuators", *Smart Materials and Structures*, 14: 1083-1100.
- Yang, Y.W., Lim, Y.Y. and Soh, C.K. (2008). "Practical Issues Related to the Application of the Electromechanical Impedance Technique in the Structural Health Monitoring of Civil Structures: I. Experiment", *Smart Materials and Structures*, 17(3): 035008.

Smart Beams: A Semi-Analytical Method

Y. W. Yang*, C. K. Ju, C. K. Soh

School of Civil and Environmental Engineering, Nanyang Technological University,
50 Nanyang Avenue, Singapore 639798.

Tel: (65)-6790-4057, Fax: (65)-6791-0676

Email: cywyang@ntu.edu.sg

8.1 Introduction

One of the key challenges in structural engineering is to find better ways to control structural vibrations so as to better protect the structures from vibration-induced damages. Structural control methods can be classified into two main groups: passive control and active control. The basic role of passive control is to absorb or consume a portion of the input energy, thereby reducing the energy dissipation demand on the primary structural members and minimizing possible structural damage. On the other hand, in active control, the motion of a structure is controlled or modified by means of the action of a control system, which usually consists of sensors, actuators and controller, through certain external energy supply.

Comparing with passive control, research and development of active structural control technology has a more recent origin. In active control, the effects of undesirable forces are counteracted by an auxiliary mechanism either embedded in or bonded to the structures. The mechanism typically uses electromechanical or electromagnetic actuators, such as piezoelectric actuators. Due to the converse piezoelectric effects, a polarized piezoelectric device, when activated by applying a voltage along its polarization direction, develops compressive or extensional strains, depending upon the orientation of the applied voltage; whereas due to the direct piezoelectric effect, it generates a voltage if mechanically deformed (Ikeda, 1990). The converse and direct piezoelectric effects enable the piezoelectric materials to serve as both actuator and sensor.

Owing to its enhanced control effectiveness and significant advantages in

comparison with passive control, active vibration control of structures has attracted much attention in recent years. In particular, with the rapid development of piezoelectric materials in the past two decades, there has been extensive research on the application of piezoelectric materials as actuators and/ or sensors to actively control structural vibrations. These works include solving problems in the fields of civil, mechanical and aerospace engineering, especially for structural elements like beams, plates and shells.

In 1985, Bailey and Hubbard introduced a novel technique which allowed all modes of a cantilever beam to be controlled using a spatially, uniformly distributed PVDF actuator. A linear constant-gain controller, a nonlinear constant-amplitude controller and a Lyapunov controller were designed in their study, and the first two were implemented experimentally (Bailey and Hubbard, 1985). Gaudenzi *et al.* (1997) demonstrated the feasibility of vibration suppression in aluminum and composite cantilever beams by a simple single-input single-output control system that utilized PZT patches as actuator and sensor. Librescu and Na (1998a; 1998b) dealt with the problem of controlling bending oscillations of a cantilever beam modeled as closed cross-section thin-walled beam and incorporating a number of non-classical effects, such as transverse shear, secondary warping, and heterogeneity, through a combined feedback control method.

Shih (2000) presented a mathematical model to study the effectiveness of active vibration control of a simply supported piezoelectric laminated curved beam. The model included the mass and stiffness of sensor/actuator for a more accurate representation of the actual system. Sun and Huang (2001) derived an analytical formulation for modeling the behavior of laminated composite beams with integrated piezoelectric sensor and actuator. Their model was based on the first-order shear deformation theory (Mindlin plate theory) and included the coupling between mechanical and electrical deformations.

Gardonio and Elliott (2005) theoretically studied the flexural vibration of a beam with a control system which implemented direct velocity feedback using either an ideal collocated force actuator or a closely located piezoelectric patch actuator. They found that, as the control gain increased, the vibration of the beam initially reduced at resonance frequencies because of the active damping effect. However, when the control gain passed an optimal value, the vibration of the beam rearranged into a new set of lightly damped resonance frequencies since the control system imposed new boundary conditions at the control position on the beam. Vasques and Rodrigues (2005) developed a fully coupled electromechanical FE formulation of a three-layered smart beam with two piezoelectric layers acting as sensors or actuators. A partial layer-wise theory was considered for the approximation of the displacement field of the core and piezoelectric layers, and an electrical model for different electric boundary conditions was adopted.

Lin and Liu (2006) designed a novel resonant fuzzy logic controller (FLC) to minimize structural vibration using collocated piezoelectric actuator/sensor pairs. The fuzzy controller increased the damping of the structures to minimize certain resonant responses. The vibration absorber was experimentally examined using a cantilever beam for impulse and near-resonant excitation cases. Karami-Mohammadi

and Sadri (2009) also studied the active vibration control of a smart cantilever beam using a fuzzy control method. Their elastic beam consisted two piezoelectric layers bonded on its upper and lower surfaces, and was excited by base motion. Kayacik *et al.* (2008) included the viscous and Kelvin-Voigt (strain rate) damping to the Euler-Bernoulli beam model of transverse vibrations to study active vibration control under damping. More research on active control of beams can be found in literatures like Lin *et al.* (1999), Wang and Quek (2000), Manning *et al.* (2000), Yang *et al.* (2003), Hong *et al.* (2006) and Nbenjjo (2009).

A recent application of active vibration control using piezoelectric materials as actuators and/or sensors is flutter suppression in aerospace engineering. Han *et al.* (2006) presented numerical and experimental investigations on active flutter suppression of a sweptback cantilevered lifting surface using piezoelectric actuation. A FE method, a panel aerodynamic method, and the minimum state-space realization were involved in the development of the equation of motion in state-space. Piezoelectric actuators, bonded symmetrically on the plate, were optimally grouped into two equivalent actuator sets using genetic algorithms (GAs) to enhance controllability. Fazelzadeh and Jafari (2008) developed an active optimal integral/feed-forward control for a supersonic panel under gust disturbance effects with piezoelectric actuators. The optimal control problem was set up to minimize panel deflection using a linear quadratic regulator (LQR). Simulation results showed that the controller model was effective for flutter suppression and gust alleviation for various piezo-configurations. More applications of piezoelectric material for flutter suppression can be found in Sadri *et al.* (2002), Moon and Kim (2003), and Sebastijanovic *et al.* (2007).

Of the abovementioned studies, many are on the active vibration control of beams and beam-like structures. However, the case of applying an axial force on the beam has seldom been studied; in particular, closed-form solutions for the dynamic response of actively controlled columns have not been reached. In addition, the influence of axial force on the control effectiveness of piezoelectric actuators and the effect of axial force on the transverse vibration control have not yet been systematically studied.

In recent years, several researchers reported some results on the active control of columns; for example, Kamada *et al.* (1998) experimentally investigated the effectiveness of bending moment control and axial force control of columns using a building model for a four-storey frame structure. Rao and Singh (2001) proposed a new method to increase the buckling load of columns by using the follower forces, which can be applied by employing piezoelectric actuators. Chen *et al.* (2002) considered the dynamic stability of a laminated composite beam with piezoelectric layers subjected to axial periodic compressive loads. Sloss *et al.* (2003) studied the effect of axial force in the vibration control of beams by means of an integral equation formulation, which facilitated the numerical solution of the problem of finding the eigen-frequencies and eigen-functions of a freely vibrating beam controlled by piezo patch sensors and actuators. Mukherjee and Chaudhuri (2005) investigated the effect of tip masses on the vibration control of piezo-laminated columns that have adhesively bonded piezoelectric skins on

substrates. Their experiments demonstrated the efficacy of the piezoelectric materials in vibration control of column structures. The increased tip mass increased the natural periods of the structure; however, the damping coefficient only increased marginally with an increase in tip mass.

One of the cases for which a beam is subjected to axial loads is that the beam rotates about an axis perpendicular to the beam axis, for example, the rotorcraft blades. Fung and Yau (2004) investigated the vibration behavior and control of a clamped-free rotating flexible cantilever arm with fully covered active constrained layer damping (ACLD) treatment, which is typically a three-layer composite consisting of a passive visco-elastic material (VEM) layer sandwiched between an active piezoelectric actuator layer and a piezoelectric sensor layer. Their model took into account the effects of centrifugal stiffening due to the rotation of the beam and the potential energies of the VEM due to extension and bending. The vibration frequencies and damping factors of the closed-loop beam/ACLD system were obtained numerically, after solving the characteristic complex eigen-value problem. Chandiramani *et al.* (2004) designed an optimal vibration control of a rotating composite beam with distributed piezoelectric sensing and actuation. They studied the effect of the location and weight of piezo patches on the controlled response of the rotating beam. Liu *et al.* (2007) studied the dynamic characteristics and vibration control of a rotating cantilever plate with fully covered ACLD treatments. The effects of different rotating angular velocities on modal characteristics of regular, passive constrained layer damping (PCLD) and ACLD treated-plate systems were investigated. Their numerical simulation results showed that ACLD is an effective means for suppressing the vibration of rotating cantilever plates.

This chapter describes the application of piezoelectric materials as actuators for the active vibration control of a cantilevered column. Two feedback control strategies, displacement feedback control and velocity feedback control, are adopted to derive the analytical and semi-analytical formulae for the dynamic response of the column. The closed-form formulae obtained are verified using numerical examples. The control effectiveness of the piezoelectric actuator is investigated by comparing the dynamic responses of the column under various control gains. The influence of axial force on the control effectiveness is studied by comparing the dynamic responses of the cantilevered column subjected to different axial forces with those of a cantilevered beam without any axial force.

8.2 Analysis of a Column Coupled with Distributed Piezoelectric Actuator

In the analysis, treatment of the flexure behavior of the column is based on the Euler-Bernoulli theory, which takes into account the inertia force due to transverse translation, but neglects the effect of shear deflection and rotary inertia. In the

Euler-Bernoulli theory, any cross-section of the column is assumed to remain as a plane during flexure.

The influence of time-invariant axial load is considered in the analysis. In general, the presence of an axial load will lead to coupling between the flexural and axial vibrations. The motion equations in such a case are coupled and their solutions are quite complex (Humar, 1990). In this study, the motion equations for the transverse vibration of cantilevered column are derived with consideration of an axial force; however, the axial deformation is assumed to be negligible. This is reasonable provided the axial rigidity is large as compared to the flexural rigidity, so that the axial deformations are comparatively small.

The effect of damping resistance on the structural response is included in the analysis. This damping is represented by a distributed viscous damping mechanism, with a damping coefficient $c(x)$ per unit length. The damping forces are proportional to the magnitude of the velocity, and opposite to the direction of motion. The piezoelectric-bonded column is considered as an under-damped system in the analysis.

8.2.1 Motion Equations

The uniform column of length L , width b and height h shown in Fig. 8.1(a) is studied. It is bonded with a piezoelectric actuator layer of thickness h_p on its top surface. The piezoelectric layer is assumed to be perfectly bonded to the column, and its thickness is assumed to be much smaller than that of the column. Physical properties of the bonding material and mechanical properties of the piezoelectric layer are neglected because their contributions to the dynamic response are small compared with those of the elastic column. A time-invariant axial force $N(x)$ is applied along the longitudinal axis of the column. The axial force is assumed to remain in its direction during vibration, but may arbitrarily vary along the length L . The axial force $N(x)$ is positive if the load is compressive, while negative if the load is tensile.

Fig. 8.1(b) depicts a differential element of the column, of length dx , with the acting forces indicated. \bar{m} is the mass per unit length of the column, and $p(x,t)$ and $w(x,t)$ are the transverse loading and the transverse displacement of the column, respectively. The motion equations of the column are established by considering the equilibrium of the differential element. First, the force equilibrium in the vertical direction yields

$$\frac{\partial V(x,t)}{\partial x} + \bar{m} \frac{\partial^2 w(x,t)}{\partial t^2} + c(x) \frac{\partial w(x,t)}{\partial t} = p(x,t) \quad (8.1)$$

Then, the moment equilibrium of the differential element gives

$$V(x,t) = \frac{\partial M(x,t)}{\partial x} + N(x) \frac{\partial w(x,t)}{\partial x} \quad (8.2)$$

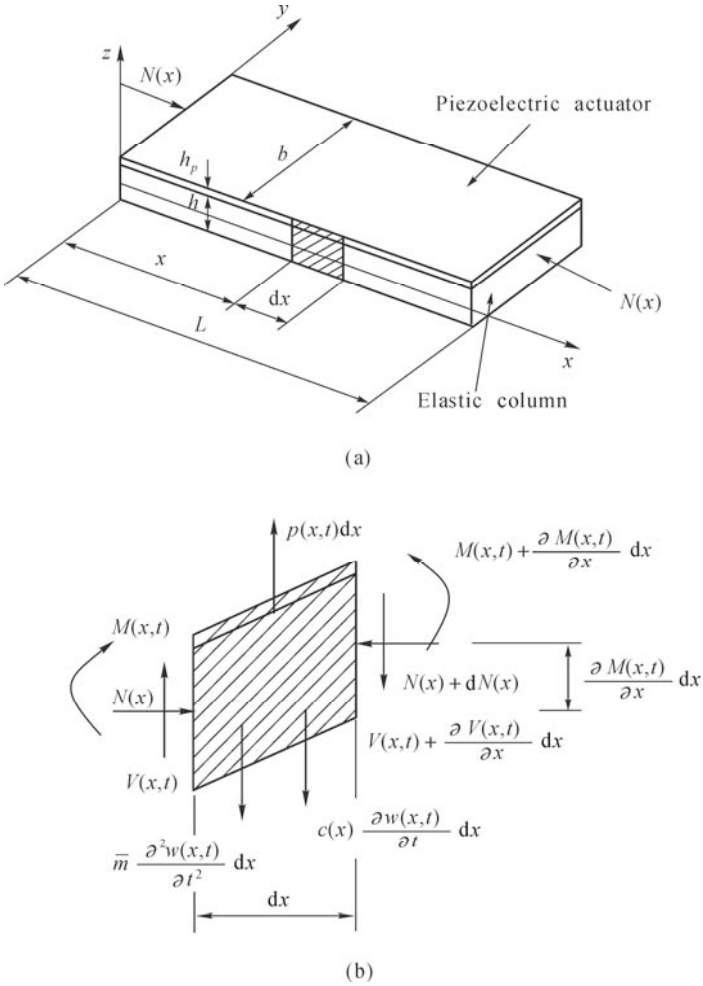


Fig. 8.1 Column bonded with distributed piezoelectric actuator. (a) Column model; (b) Forces acting on a differential element

The vertical force $V(x,t)$ has two components: a shear force, $\frac{\partial M(x,t)}{\partial x}$, and a component arising from the presence of the axial load, $N(x)\frac{\partial w(x,t)}{\partial x}$. Thus, the following motion equation of the column is obtained by differentiating Eq. (8.2) with respect to x and substituting the result into Eq. (8.1)

$$\frac{\partial^2 M(x,t)}{\partial x^2} + \frac{\partial}{\partial x} \left[N(x) \frac{\partial w(x,t)}{\partial x} \right] + \bar{m} \frac{\partial^2 w(x,t)}{\partial t^2} + c(x) \frac{\partial w(x,t)}{\partial t} = p(x,t) \quad (8.3)$$

It should be noted that, in Eq. (8.3), the term of moment $M(x,t)$ includes the contribution of the distributed piezoelectric actuator, *i.e.*,

$$M(x,t) = YI \frac{\partial^2 w(x,t)}{\partial x^2} - M_p \quad (8.4)$$

where Y is the Young's modulus of the column; I is the moment of inertia of the cross-sectional area with respect to the neutral axis; and M_p is the contribution of the distributed piezoelectric actuator.

According to the converse piezoelectric effect, the strain in the piezoelectric layer is

$$\varepsilon_{11} = -d \frac{U}{h_p} \quad (8.5)$$

where U is the voltage applied to the piezoelectric actuator and d is the piezoelectric constant. The stress in the piezoelectric layer is then obtained from Hooke's law:

$$\sigma_{11} = -Y_p d \frac{U}{h_p} \quad (8.6)$$

where Y_p is the Young's modulus of piezoelectric material. From this, contribution of the distributed piezoelectric actuator to the moment can be obtained as (Preumont, 1997)

$$M_p = -Y_p d U b \frac{h + h_p}{2} \quad (8.7)$$

Introducing Eq. (8.4) into Eq. (8.3), Eq. (8.3) is reduced to

$$YI \frac{\partial^4 w(x,t)}{\partial x^4} + \frac{\partial}{\partial x} \left[N(x) \frac{\partial w(x,t)}{\partial x} \right] + \frac{m}{m} \frac{\partial^2 w(x,t)}{\partial t^2} + c(x) \frac{\partial w(x,t)}{\partial t} - \frac{\partial^2 M_p}{\partial x^2} = p(x,t) \quad (8.8)$$

Eq. (8.8) is the generic motion equation of a uniform column, including the effects of the piezoelectric actuator, the axial force and the damping force. When focusing on the free vibration of the cantilevered piezoelectric column, the externally applied transverse loading vanishes, *i.e.*, $p(x,t)=0$. It is assumed that the axial force remains constant during the vibration, and the viscous damping coefficient is uniformly distributed along the length of the column. These

assumptions, when introduced into Eq. (8.8), lead to

$$YI \frac{\partial^4 w(x,t)}{\partial x^4} + N \frac{\partial^2 w(x,t)}{\partial x^2} + \bar{m} \frac{\partial^2 w(x,t)}{\partial t^2} + c \frac{\partial w(x,t)}{\partial t} - \frac{\partial^2 M_p}{\partial x^2} = 0 \quad (8.9)$$

which is the motion equation for the free vibration of a uniform column.

In the following sections, the designed displacement feedback and velocity feedback controls are presented. The analytical and semi-analytical solutions for Eq. (8.9) are obtained under these two control strategies, respectively. Details of the derivation can be found in Yang *et al.* (2003).

8.2.2 Analytical Solutions for Displacement Feedback Control

In the displacement feedback control strategy, the tip displacement of the column $w(L,t)$ is amplified by a control gain, g_d , as the feedback voltage U is applied to the piezoelectric actuator. Hence

$$U = g_d w(L,t) \quad (8.10)$$

The induced control moment M_p is then obtained from Eq. (8.7) as

$$M_p = -Y_p db \frac{h+h_p}{2} g_d w(L,t) \quad (8.11)$$

Resulting from the uniformly distributed feedback voltage applied to the piezoelectric actuator layer, the control moment M_p is uniform along the length of the column. Thus, Eq. (8.9) can be reduced to

$$YI \frac{\partial^4 w(x,t)}{\partial x^4} + N \frac{\partial^2 w(x,t)}{\partial x^2} + \bar{m} \frac{\partial^2 w(x,t)}{\partial t^2} + c \frac{\partial w(x,t)}{\partial t} = 0 \quad (8.12)$$

The solution of Eq. (8.12) is found by the method of separation of variables. It is assumed that the solution may be expressed as a product of the function of position $\Phi(x)$ and function of time $f(t)$, that is,

$$w(x,t) = \Phi(x)f(t) \quad (8.13)$$

Substituting Eq. (8.13) into Eq. (8.12) gives the following two differential equations:

$$\frac{d^4 \Phi(x)}{dx^4} + \beta^2 \frac{d^2 \Phi(x)}{dx^2} - a^4 \Phi(x) = 0 \quad (8.14)$$

and

$$\frac{d^2 f(t)}{dt^2} + \frac{c}{\bar{m}} \frac{df(t)}{dt} + \omega^2 f(t) = 0 \quad (8.15)$$

where $\beta^2 = \frac{N}{EI}$, $a^4 = \frac{\bar{m}\omega^2}{EI}$ and ω^2 is a constant.

Solution for the Shape Function $\Phi(x)$

By introducing a solution of the form $\Phi(x) = Ge^{sx}$ into Eq. (8.14), we can obtain the characteristic equation of Eq. (8.14)

$$s^4 + \beta^2 s^2 - a^4 = 0 \quad (8.16)$$

with roots of

$$s_1 = p_1, \quad s_2 = -p_1, \quad s_3 = jp_2, \quad s_4 = -jp_2 \quad (8.17)$$

where $p_{1,2} = \sqrt{\mp \frac{\beta^2}{2} + \sqrt{\left(\frac{\beta^2}{2}\right)^2 + a^4}}$ and $j = \sqrt{-1}$.

Thus, the solution of Eq. (8.14) is found to be

$$\Phi(x) = A \sin p_2 x + B \cos p_2 x + C \sinh p_1 x + D \cosh p_1 x \quad (8.18)$$

where A , B , C and D are integration constants that can be evaluated by the boundary conditions of the column.

For a cantilevered column that is fixed at $x = 0$ and free at $x = L$, the boundary conditions are zero displacement and slope at the fixed end, and zero bending moment and vertical force at the free end. Therefore, at the fixed end ($x = 0$),

$$w(0, t) = 0 \quad (8.19)$$

and

$$\frac{\partial w(0,t)}{\partial x} = 0. \quad (8.20)$$

At the free end ($x=L$), from Eq. (8.4),

$$YI \frac{\partial^2 w(L,t)}{\partial x^2} - M_p = 0 \quad (8.21)$$

and

$$YI \frac{\partial^3 w(L,t)}{\partial x^3} + N \frac{\partial w(L,t)}{\partial x} = 0 \quad (8.22)$$

These boundary conditions, Eqs. (8.19) to (8.22), imply the following conditions on the shape function after Eqs. (8.11) and (8.13) are used,

$$\Phi(0) = 0 \quad (8.23)$$

$$\frac{d\Phi(0)}{dx} = 0 \quad (8.24)$$

$$\frac{d^2\Phi(L)}{dx^2} = C_d \Phi(L) \quad (8.25)$$

and

$$\frac{d^3\Phi(L)}{dx^3} + \beta^2 \frac{d\Phi(L)}{dx} = 0 \quad (8.26)$$

where $C_d = -Y_p db \frac{h+h_p}{2YI} g_d$.

Substituting Eq. (8.18) into the boundary conditions of Eqs. (8.23) to (8.26), we obtain

$$Q[A \ B \ C \ D]^T = \{0\} \quad (8.27)$$

where

$$Q = \begin{bmatrix} 0 & 1 & 0 & 1 \\ p_2 & 0 & p_1 & 0 \\ (-p_2^2 - C_d) \sin p_2 L & (-p_2^2 - C_d) \cos p_2 L & (p_1^2 - C_d) \sinh p_1 L & (p_1^2 - C_d) \cosh p_1 L \\ (-p_2^3 + \beta^2 p_2) \cos p_2 L & (p_2^3 - \beta^2 p_2) \sin p_2 L & (p_1^3 + \beta^2 p_1) \cosh p_1 L & (p_1^3 + \beta^2 p_1) \sinh p_1 L \end{bmatrix}$$

To obtain a nontrivial solution of Eq. (8.27), it is required that the determinant of the square matrix Q is equal to zero, thus giving the frequency equation of the cantilevered piezoelectric column as

$$\begin{aligned} & (1 + \cos p_2 L \cosh p_1 L) - \frac{C_d \beta^2}{2a^4} (1 - \cos p_2 L \cosh p_1 L) \\ &= -\frac{\beta^2}{2a^2} \left(\frac{\beta^2}{a^2} \cos p_2 L \cosh p_1 L - \sin p_2 L \sinh p_1 L \right) + \frac{C_d}{a^2} \sin p_2 L \sinh p_1 L \end{aligned} \quad (8.28)$$

For given C_d , β^2 and L , the solution of Eq. (8.28) can be obtained by a numerical method which will lead to an infinite number of values for a and hence the frequency ω , where

$$\omega_n = a_n^2 \sqrt{\frac{YI}{m}} \quad (8.29)$$

Corresponding to each value of a , a solution can be obtained for the shape function $\Phi(x)$ by substituting a into Eq. (8.27) and solving for the coefficients A , B , C and D , and then substituting the resultant values into Eq. (8.18).

However, in this procedure, not all four coefficients A , B , C and D can be uniquely determined; and any three of them may be expressed in terms of the fourth. For example, when express A , C and D in terms of B from Eq. (8.27) and substituting them into Eq. (8.18), the solution for the shape function is

$$\Phi_n(x) = B_n \left((\cos p_2 x - \cosh p_1 x) + \sigma_n \left(\sin p_2 x - \frac{p_2}{p_1} \sinh p_1 x \right) \right) \quad (8.30a)$$

where

$$\sigma_n = \frac{(p_2^2 - \beta^2) \sin p_2 L - \frac{p_1}{p_2} (p_1^2 + \beta^2) \sinh p_1 L}{(p_2^2 - \beta^2) \cos p_2 L + (p_1^2 + \beta^2) \cosh p_1 L} \quad (8.30b)$$

In Eq. (8.30a), the fourth constant B_n cannot be directly evaluated in a free-vibration analysis because it represents an arbitrary amplitude of the shape function $\Phi(x)$. If a numerical value is given to B_n , say $B_n = -1$, then

$$\Phi_n(x) = -(\cos p_2 x - \cosh p_1 x) - \sigma_n \left(\sin p_2 x - \frac{p_2}{p_1} \sinh p_1 x \right) \quad (8.31)$$

In fact, it will be found later that the constant B_n is absorbed by the other constants in the time-dependent function $f(t)$.

In Eq. (8.28), if set $C_d = 0$, which means $g_d = 0$, and let $U=0$ and $M_p=0$, we get

$$1 + \cos p_2 L \cosh p_1 L = -\frac{\beta^2}{2a^2} \left(\frac{\beta^2}{a^2} \cos p_2 L \cosh p_1 L - \sin p_2 L \sinh p_1 L \right) \quad (8.32)$$

This is actually the frequency equation of a conventional cantilevered beam subjected to axial forces. It has the same form as the results given by Bokaian (1988; 1990) and Maurizi and Belles (1991). Eq. (8.32) integrates the influences of both compressive and tensile axial forces into one formula. If further assumed that $N=0$ in Eq. (8.32), which implies $\beta^2=0$ and $p_1=p_2=a$, the well-known frequency equation for a conventional cantilevered beam can be obtained,

$$1 + \cos aL \cosh aL = 0 \quad (8.33)$$

Solution for the Time-Dependent Function $f(t)$

By substituting $f(t) = He^{rt}$ into Eq. (8.15), the general solution of the time-dependent function $f(t)$ is given by the superposition of two possible solutions, namely,

$$f(t) = H_1 e^{r_1 t} + H_2 e^{r_2 t} \quad (8.34)$$

where H_1 and H_2 are integration constants to be determined. Considering the piezoelectric-bonded column as an under-damped system, we get $r_{1,2} = -\xi\omega \pm j\omega_D$

with $\xi = \frac{c}{2\bar{m}\omega}$ as the damping ratio of the system and $\omega_D = \omega\sqrt{1-\xi^2}$.

Expressing the exponential functions in Eq. (8.34) in terms of trigonometric functions, we can obtain

$$f(t) = e^{-\xi\omega t} (\bar{E} \cos \omega_D t + \bar{F} \sin \omega_D t) \quad (8.35)$$

where \bar{E} and \bar{F} are integration constants to be determined from the initial conditions.

Solution for the Dynamic Response

Upon substituting Eq. (8.35) into Eq. (8.13), a normal mode of vibration is given by

$$w_n(x,t) = \Phi_n(x)e^{-\xi\omega t} (E_n \cos \omega_{nD}t + F_n \sin \omega_{nD}t) \quad (8.36)$$

Here, it is assumed that E_n and F_n absorbed the undetermined coefficient B_n in Eq. (8.30) by considering $E_n = B_n \bar{E}_n$ and $F_n = B_n \bar{F}_n$. Then, the general solution of the motion equation, Eq. (8.12), is the sum of all the normal modes of vibration, Eq. (8.36), that is,

$$w(x,t) = \sum_{n=1}^{\infty} \left[\Phi_n(x)e^{-\xi\omega t} (E_n \cos \omega_{nD}t + F_n \sin \omega_{nD}t) \right] \quad (8.37)$$

The initial conditions together with the orthogonality property of the normal modes can be used to determine the unknown coefficients E_n and F_n .

The initial conditions are assumed to be given by the initial displacement and initial velocity, and are expressed as

$$w(x,0) = u(x) \quad (8.38)$$

for the initial displacement, and

$$\frac{dw(x,0)}{dt} = v(x) \quad (8.39)$$

for the initial velocity.

Substituting these initial conditions into the general solution of the motion equation, Eq. (8.37), multiplying both sides of the equation by $\Phi_m(x)$, integrating from 0 to L , and introducing the orthogonality property of the normal modes,

$$\int_0^L \Phi_r(x) \bar{m} \Phi_s(x) dx = 0 \quad (r \neq s) \quad (8.40)$$

The coefficients E_n and F_n can be obtained:

$$E_n = \frac{\int_0^L \Phi_n(x) u(x) dx}{\int_0^L \Phi_n^2(x) dx} \quad (8.41)$$

and

$$F_n = \frac{\int_0^L \Phi_n(x) v(x) dx}{\omega_{nD} \int_0^L \Phi_n^2(x) dx} + \frac{\xi_n}{\sqrt{1-\xi_n^2}} E_n \quad (8.42)$$

Finally, the solution for the dynamic response of the cantilevered piezoelectric column subjected to a displacement control strategy can be obtained by substituting Eqs. (8.31), (8.41) and (8.42) into Eq. (8.37). The derivative of Eq. (8.37) with respect to time t gives the vibration velocity of the cantilevered column.

8.2.3 Semi-Analytical Solutions for Velocity Feedback Control

In the velocity feedback control strategy, the tip velocity, *i.e.*, the first derivative of the tip displacement with respect to time, $\frac{\partial w(L,t)}{\partial t}$, of the column is amplified by a control gain, g_v , as the feedback voltage U is applied to the piezoelectric actuator. Hence

$$U = g_v \frac{\partial w(L,t)}{\partial t} \quad (8.43)$$

The induced control moment M_p can be obtained from Eq. (8.7),

$$M_p = -Y_p db \frac{h+h_p}{2} g_v \frac{\partial w(L,t)}{\partial t} \quad (8.44)$$

The control moment M_p is also uniform along the length of the column. Thus, Eq. (8.9) can be reduced to

$$YI \frac{\partial^4 w(x,t)}{\partial x^4} + N \frac{\partial^2 w(x,t)}{\partial x^2} + \bar{m} \frac{\partial^2 w(x,t)}{\partial t^2} + c \frac{\partial w(x,t)}{\partial t} = 0 \quad (8.45)$$

Note that Eq. (8.45) is the same as the motion equation of the column under displacement feedback control, *i.e.*, Eq. (8.12). Furthermore, for the four boundary conditions, three of them are the same as the conditions in the displacement feedback control. Only the one involving the feedback control moment is different. For clarification of derivation, all the boundary conditions are rewritten here

$$w(0,t) = 0 \quad (8.46)$$

$$\frac{\partial w(0,t)}{\partial x} = 0 \quad (8.47)$$

$$YI \frac{\partial^2 w(L,t)}{\partial x^2} - M_p = 0 \quad (8.48)$$

and

$$YI \frac{\partial^3 w(L,t)}{\partial x^3} + N \frac{\partial w(L,t)}{\partial x} = 0 \quad (8.49)$$

After substituting Eq. (8.44) into Eq. (8.48), we obtain

$$\frac{\partial^2 w(L,t)}{\partial x^2} - C_v \frac{\partial w(L,t)}{\partial t} = 0 \quad (8.50)$$

where $C_v = -Y_p db \frac{h+h_p}{2YI} g_v$

• Discretization of the Motion Equation

In the velocity feedback control, the boundary condition, Eq. (8.50), is time-dependent. As it is difficult to obtain full-analytical solutions for problems with time-dependent boundary condition, a semi-analytical solution is deduced for this velocity feedback control case by adopting the central difference formulae to approximate the partial derivatives with respect to the spatial variable x in the motion equation. Then the partial differential equation, Eq. (8.45), is reduced into a series of ordinary differential equations with derivatives, with respect to the time variable t .

A mesh along the length of the column, with mesh points $x_i=i\Delta$ ($i=1,2,\dots,n$), is introduced; where, $\Delta = \frac{L}{n}$ is the mesh size and n is the number of mesh points.

Using Taylor series expansions, we obtain

$$\begin{aligned} w(x_i \pm \Delta, t) = & w(x_i, t) \pm \frac{dw(x_i, t)}{dx} \Delta + \frac{d^2 w(x_i, t)}{dx^2} \frac{\Delta^2}{2} \\ & \pm \frac{d^3 w(x_i, t)}{dx^3} \frac{\Delta^3}{6} + \frac{d^4 w(x_i, t)}{dx^4} \frac{\Delta^4}{24} \pm \dots \end{aligned} \quad (8.51, 8.52)$$

Subtracting Eq. (8.52) from Eq. (8.51) and neglecting the terms of order higher than 2,

$$\frac{dw(x_i, t)}{dx} = \frac{w(x_i + \Delta, t) - w(x_i - \Delta, t)}{2\Delta} \quad (8.53)$$

Adding Eqs. (8.51) and (8.52), and dropping the terms of order higher than 3:

$$\frac{d^2 w(x_i, t)}{dx^2} = \frac{w(x_i + \Delta, t) - 2w(x_i, t) + w(x_i - \Delta, t)}{\Delta^2} \quad (8.54)$$

Using Eqs. (8.53) and (8.54), we derive

$$\frac{d^3 w(x_i, t)}{dx^3} = \frac{w(x_i + 2\Delta, t) - 2w(x_i + \Delta, t) + 2w(x_i - \Delta, t) - w(x_i - 2\Delta, t)}{2\Delta^3} \quad (8.55)$$

and

$$\frac{d^4 w(x_i, t)}{dx^4} = \frac{w(x_i + 2\Delta, t) - 4w(x_i + \Delta, t) + 6w(x_i, t) - 4w(x_i - \Delta, t) + w(x_i - 2\Delta, t)}{\Delta^4} \quad (8.56)$$

Substituting Eqs. (8.54) and (8.56) into Eq. (8.45), and denoting $w(x_i + 2\Delta, t)$, $w(x_i + \Delta, t)$, $w(x_i, t)$, $w(x_i - \Delta, t)$ and $w(x_i - 2\Delta, t)$ by $w_{i+2}(t)$, $w_{i+1}(t)$, $w_i(t)$, $w_{i-1}(t)$ and $w_{i-2}(t)$, respectively, result in

$$\begin{aligned} \bar{m}\ddot{w}_i(t) + c\dot{w}_i(t) + \bar{a}w_{i-2}(t) + (-4\bar{a} + \bar{b})w_{i-1}(t) + (6\bar{a} - 2\bar{b})w_i(t) \\ + (-4\bar{a} + \bar{b})w_{i+1}(t) + \bar{a}w_{i+2}(t) = 0 \quad (i = 1, 2, \dots, n) \end{aligned} \quad (8.57)$$

where $\bar{a} = \frac{YI}{\Delta^4}$, $\bar{b} = \frac{N}{\Delta^2}$ and the overdots indicate derivatives with respect to time.

Using the above derived difference formulae, the boundary conditions become

$$w_0(t) = 0 \quad (8.58)$$

$$w_{-1}(t) = w_1(t) \quad (8.59)$$

$$w_{n+1}(t) = \Delta^2 C_v \dot{w}_n(t) + 2w_n(t) - w_{n-1}(t) \quad (8.60)$$

and

and $[M]^{-1}$ is the inverse of $[M]$.

The solution of this state equation can be written in the form

$$\{r\} = \{\gamma\}e^{st} \quad (8.64)$$

where $\{\gamma\}$ is a constant vector and s a complex number. Substituting Eq. (8.64) into Eq. (8.63), gives

$$([H] - sI_{2n})\{\gamma\} = \{0\} \quad (8.65)$$

where I_{2n} is the $2n \times 2n$ identity matrix.

Eq. (8.65) has nontrivial solutions for $\{\gamma\}$ if and only if

$$\det([H] - sI_{2n}) = 0 \quad (8.66)$$

Eq. (8.66) represents a characteristic equation, which is a real polynomial of order $2n$ in s . It has $2n$ solutions for the characteristic value s , and $2n$ corresponding vectors for $\{\gamma\}$. The general solution to Eq. (8.63) is the superposition of the $2n$ solutions obtained by substituting s and $\{\gamma\}$ into Eq. (8.64):

$$\{r\} = \sum_{k=1}^{2n} \eta_k \{\gamma^{(k)}\} e^{s_k t} \quad (8.67)$$

where η_k are constants determined by the initial conditions that are also given by Eqs. (8.38) and (8.39). However, in this case, the initial conditions should be substituted in a discrete form

$$w_i(0) = u(x_i) \quad (i = 1, 2, \dots, n) \quad (8.68)$$

and

$$\dot{w}_i(0) = v(x_i) \quad (i = 1, 2, \dots, n) \quad (8.69)$$

Actually, the values of s_k must be either real or in complex conjugate pairs since the coefficient matrix in Eq. (8.66) is real. For an under-damped structural system, all the characteristic values must be in complex conjugate pairs with a negative real part; then the solutions of Eq. (8.64) represent an oscillating exponential convergence. s_k can be expressed as

$$s_k = -n_k \pm j\omega_{kD} \quad (8.70)$$

The k^{th} natural frequency of the column is given by

damping ratio $\xi = 0.0015$, which is a reasonable value for this steel column (Bailey and Hubbard, 1985). The vibration characteristics, such as natural frequencies, mode shapes and dynamic responses of the column are calculated for different values of axial forces and control gains. In the following discussion,

$P_{cr} = \frac{\pi^2 YI}{4L^2}$ is the buckling load of the cantilevered column.

Table 8.1 Properties of the steel column

Young's modulus Y	$210 \times 10^9 \text{ N/m}^2$
Length L	0.146 m
Thickness h	0.381 mm
Width b	1.27 cm
Density ρ	$7,800 \text{ kg/m}^3$

Table 8.2 Properties of the PVDF layer

Young's modulus Y_p	$2.0 \times 10^9 \text{ N/m}^2$
Length L	0.146 m
Thickness h_p	$28 \times 10^{-3} \text{ mm}$
Width b	1.27 cm
Piezoelectric Constant d	$22 \times 10^{-12} \text{ m/V}$

8.3.1 Numerical Results for Displacement Feedback Control

Fig. 8.2 shows the variation of natural frequencies with the displacement feedback control gains g_d for the first three vibration modes. For each mode, different values of axial force N are considered. It is apparent from Fig. 8.2 that all the natural frequencies have the tendency to increase with an increase in the control gain g_d ; however, this tendency is not significant, especially for the higher modes. This indicates that the lower vibration modes are more affected by the piezoelectric actuator than the higher modes. It can also be observed from Fig. 8.2 that the natural frequencies increase with the change of axial force from compressive to tensile. This agrees with Bokaian's work (Bokaian, 1988; 1990) for the conventional beam. Another observation is that the variations of curves for the highly tensioned column are less than the others, which implies that it is much harder to change the natural frequencies of a highly tensioned column through displacement feedback control.

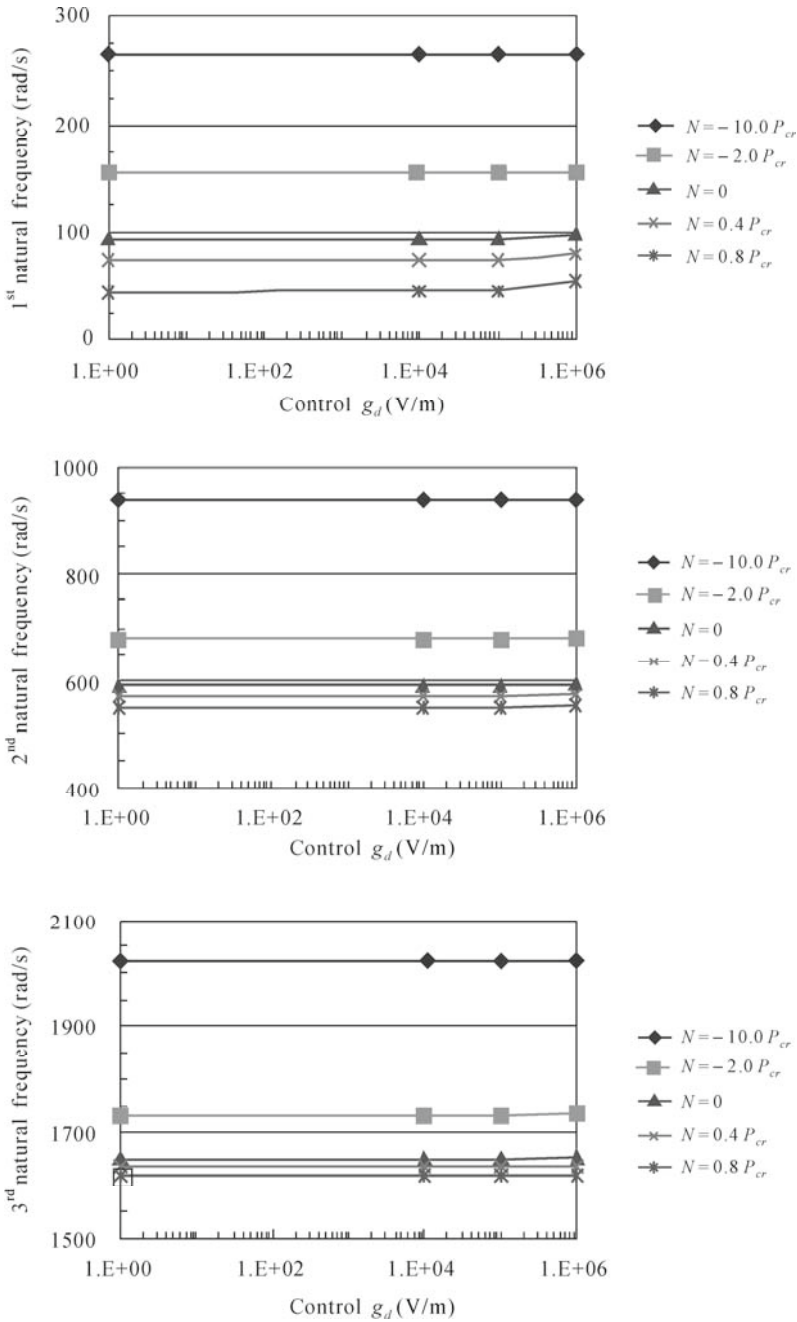


Fig. 8.2 Variation of natural frequency with control gain g_d

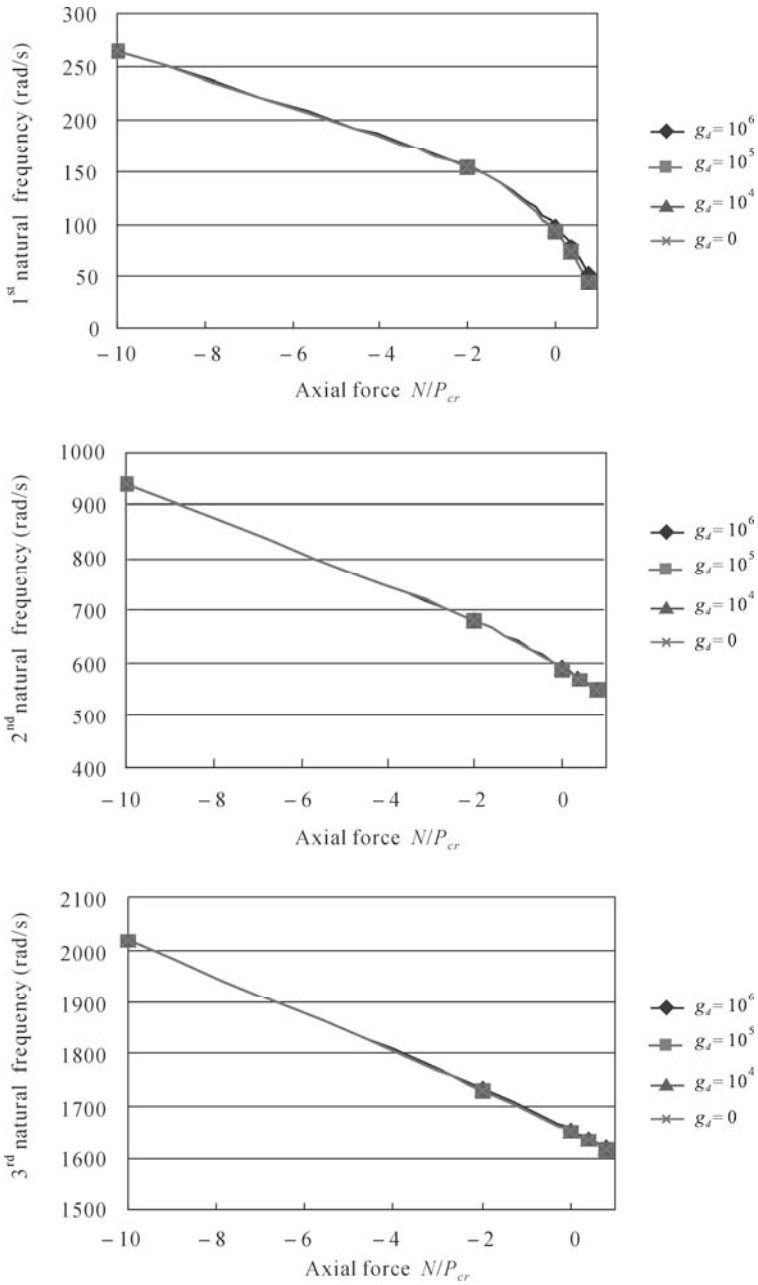


Fig. 8.3 Variation of natural frequency with axial force N

The variations of natural frequencies with the axial forces are shown in Fig. 8.3. As expected, the compressive axial force has the effect of decreasing the natural frequencies while the tensile force has the converse effect. For example, the first natural frequency of the structure decreased from 265 to 154, 94, 74, and 44 rad/s with the change of axial force from $-10.0P_{cr}$ to $-2.0P_{cr}$, 0, $0.4P_{cr}$, and $0.8P_{cr}$, respectively. It is also observed from Fig. 8.3 that the displacement feedback control cannot effectively change the natural frequencies of the column because all the curves with different control gains almost completely overlapped with each other. This indicates that, although the effect of displacement feedback control is to change the stiffness of the structure, the variation of stiffness caused by piezoelectric actuator is very minor for the steel column studied herein.

The influences of axial force and displacement control gain on the vibration mode shapes are studied by plotting the first three mode shapes of the column for different axial forces ($N = 0.8P_{cr}$, $0.4P_{cr}$, 0, $-2.0P_{cr}$, and $-10.0P_{cr}$) and different displacement control gains ($g_d = 0, 10^4, 10^5$, and 10^6 V/m). Figs. 8.4 and 8.5 show the typical variations of the normalized amplitude against the column length. Fig. 8.4 indicates that the effect of piezoelectric actuator on the mode shapes is minor even though a very high feedback voltage is applied (e.g. $g_d = 10^6$ V/m). In Fig. 8.5, the effect of axial force on the mode shapes is also minor for the second and third modes, unless a large tensile force (e.g. $N \leq -10.0P_{cr}$) is applied. In fact, the influence of axial force on the mode shapes higher than the third mode is more negligible. However, this effect on the first mode shape is more significant than on the other mode shapes. Note that the initial conditions do not arise in the above procedure for computing the natural frequencies and mode shapes.

Using the obtained closed-form expression for the dynamic responses of the piezoelectric column, the displacement and velocity of the column are computed. Table 8.3 lists some of the tip displacements of the column at $t = 10$ s for different control gains g_d and axial forces. It is found that the control effectiveness of the displacement feedback control is very weak. Actually, when control gain $g_d = 10^5$ V/m, the feedback voltage is very high, even higher than the breakdown voltage of the piezoelectric material. Hence, the displacement feedback control method is not applicable in practice, but it provides a way to theoretically study the influence of piezoelectric materials on the natural frequencies and mode shapes.

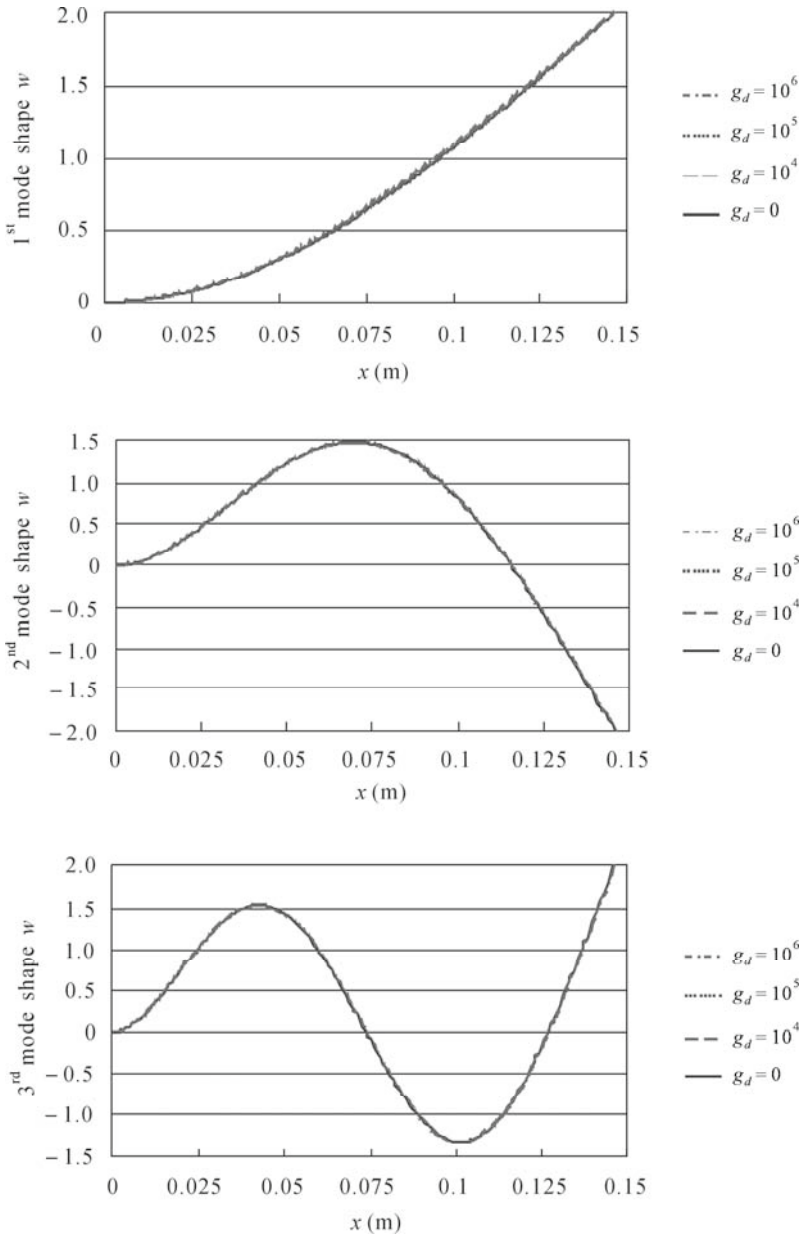


Fig. 8.4 Variation of mode shape with control gain g_d (for $N = 0.8P_{cr}$)

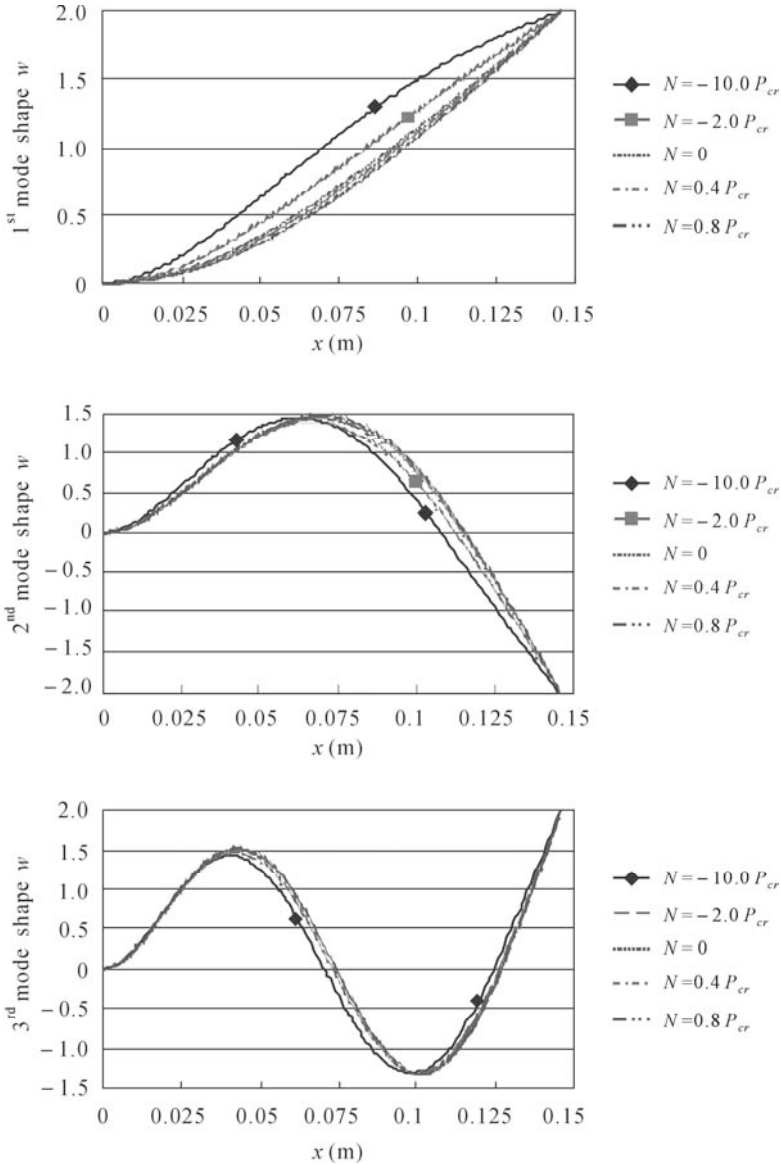


Fig. 8.5 Variation of mode shape with axial force N (for $g_d = 10^5$ V/m)

Table 8.3 Tip displacements (mm) for different control gains g_d and axial forces N (at $t = 10$ s)

g_d (V/m)	$N = 0.8P_{cr}$	$N = 0.4P_{cr}$	$N = 0$	$N = -2.0P_{cr}$	$N = -10.0P_{cr}$
$g_d = 10^0$	5.12	4.92	4.89	4.65	4.43
$g_d = 10^5$	5.19	4.98	4.88	4.64	4.34
$g_d = 10^4$	5.23	5.02	4.94	4.69	4.35
$g_d = 0$	5.18	4.97	4.94	4.67	4.36

8.3.2 Numerical Results for Velocity Feedback Control

The numerical simulations for the velocity feedback control focused on the dynamic responses of the structure for various sets of axial force ($N = 0.8P_{cr}$, $0.4P_{cr}$, 0 , $-2.0P_{cr}$, and $-10.0P_{cr}$) and velocity feedback control gain ($g_v = 0, 10, 20, 30$, and $40 \text{ V}\cdot\text{s/m}$). In the simulations, 1,000 mesh points were used to calculate the natural frequencies of the column, and the first 10 vibration modes were superposed to obtain the dynamic responses. A convergence study showed that accuracy of the numerical results increases with the increase in mesh points, and that the cut-off number of mesh points depends on how many vibration modes are used for the superposition of the dynamic responses. In this example, the cut-off number of mesh points is about 100 when the first 10 vibration modes are considered; hence 1,000 mesh points are adequate for the required accuracy of results.

Figs. 8.6 to 8.9 depict the typical dynamic responses of the tip displacement and velocity of the column under velocity feedback control with axial forces $N = 0.8P_{cr}$ and $-2.0P_{cr}$, respectively. It is apparent that the piezoelectric actuator effectively damped the vibration of the structure in the velocity feedback control. For instance, for the case with a compressive axial force $N = 0.8P_{cr}$, the tip displacements of the column at $t = 10 \text{ s}$ are 5.16 mm for $g_v = 0$ and 4.26 mm for $g_v = 40 \text{ V}\cdot\text{s/m}$ in Figs. 8.6 and 8.7, respectively. It means that the velocity feedback control caused 17.4% reduction in the vibration amplitude. The corresponding maximum tip velocities in these two figures are 0.33 and 0.24 m/s, respectively. This indicates that the vibration slowed down by 27.3% due to the feedback control. The value of the feedback voltage is obtained from the tip velocity of the column; which fell in an acceptable range, for example, for the case of $N = -2.0P_{cr}$ and $g_v = 40 \text{ V}\cdot\text{s/m}$, the maximum feedback voltage U is about 150 V.

Table 8.4 lists the tip displacements of the column for different velocity feedback control gains g_v and different axial forces N , where the percentages in the brackets are the decrements of the tip displacement as compared with the result for $g_v = 0$, under the same axial force. Fig. 8.10 is the graphical illustration of Table 8.4. From Fig. 8.10(a), it can be observed that, at a certain time ($t = 10 \text{ s}$ in this example), the tip displacement of the tensioned column is smaller than that of the compressed column under the same feedback control gain g_v , and that the value of the tip displacement decreases with increase in the tensile axial force, but increases with increase in the compressive axial force. This indicates that a tensile axial force can depress the vibration of the column, while a compressive axial force has a converse effect. Furthermore, from Fig. 8.10(a), the relation between the tip displacement and control gain g_v can be treated as a linear function for certain axial force. However, the absolute value of the slope of the line for compressive axial force is larger than that for the tensile axial force. It implies that the vibration characteristics of a tensioned column are harder to be affected by the piezoelectric actuator than those of a compressed column. From Fig. 8.10(b), it can be seen that the larger the control gain g_v , the smaller the variation of the tip displacement curves. This means that it is difficult for the axial force to affect the vibration of the column applied with a large control force.

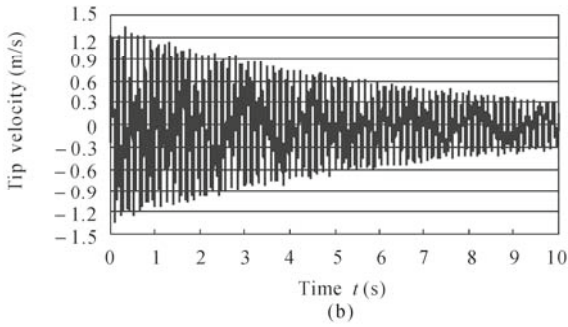
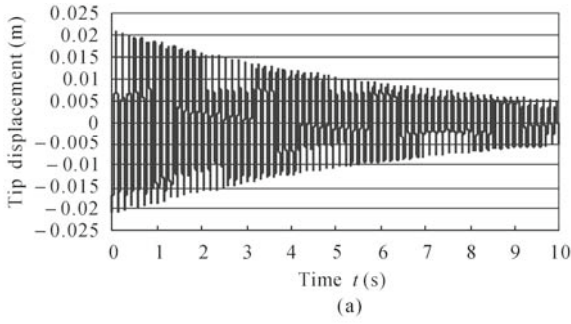


Fig. 8.6 Dynamic responses for $N = 0.8P_{cr}$ and $g_v = 0$

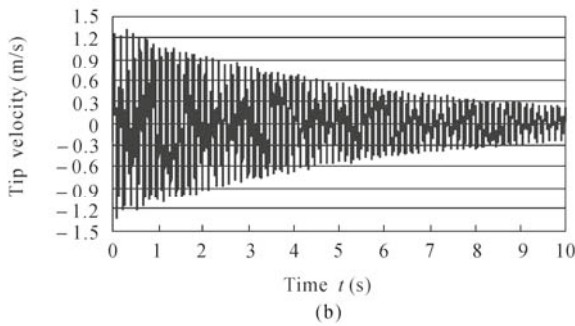
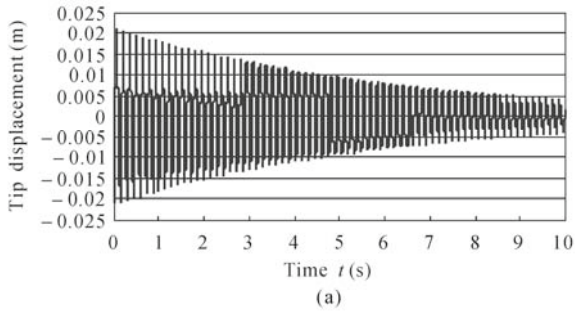


Fig. 8.7 Dynamic responses for $N = 0.8P_{cr}$ and $g_v = 40 \text{ V}\cdot\text{s}/\text{m}$

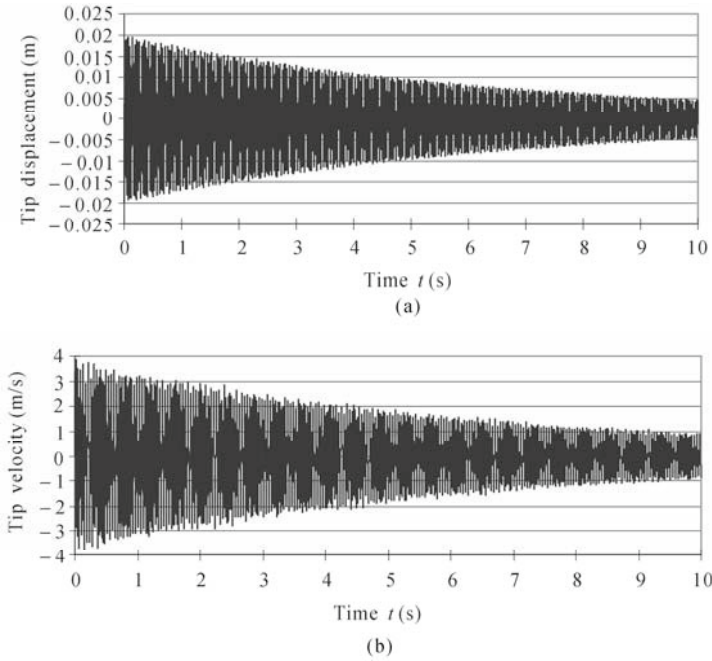


Fig. 8.8 Dynamic responses for $N = -2.0P_{cr}$ and $g_v = 0$

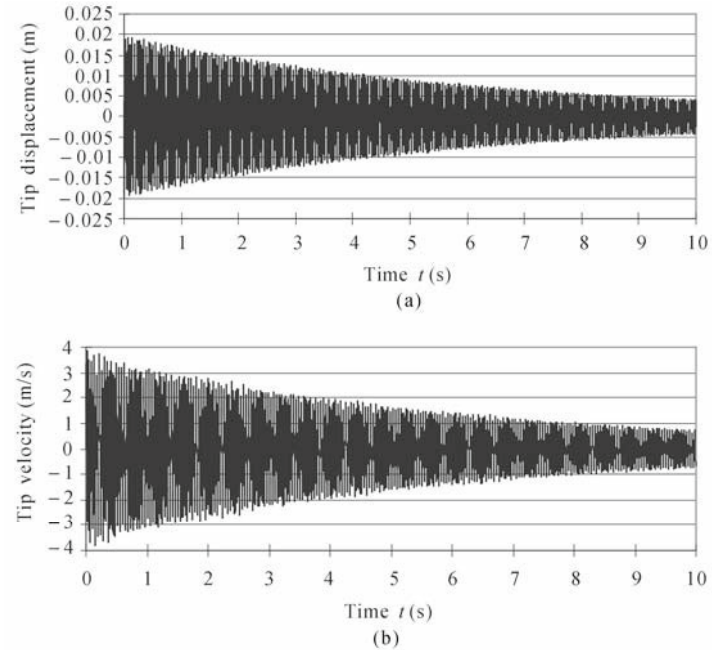


Fig. 8.9 Dynamic responses for $N = -2.0P_{cr}$ and $g_v = 40 \text{ V}\cdot\text{s}/\text{m}$

Table 8.4 Tip displacements (mm) for different control gains g_v and axial forces N (at $t = 10$ s)

g_v (V·s/m)	$N = 0.8P_{cr}$	$N = 0.4P_{cr}$	$N = 0$	$N = -2.0P_{cr}$	$N = -10.0P_{cr}$
$g_v = 0$	5.16	4.99	4.86	4.61	4.36
$g_v = 10$	4.93 (4.46%)	4.8 (3.81%)	4.68 (3.70%)	4.52 (1.95%)	4.25 (2.52%)
$g_v = 20$	4.73 (8.33%)	4.55 (8.82%)	4.51 (7.20%)	4.38 (4.99%)	4.1 (5.96%)
$g_v = 30$	4.48 (13.18%)	4.37 (12.42%)	4.33 (10.91%)	4.26 (7.59%)	4.05 (7.11%)
$g_v = 40$	4.26 (17.44%)	4.18 (16.23%)	4.17 (14.20%)	4.12 (10.63%)	3.97 (8.94%)

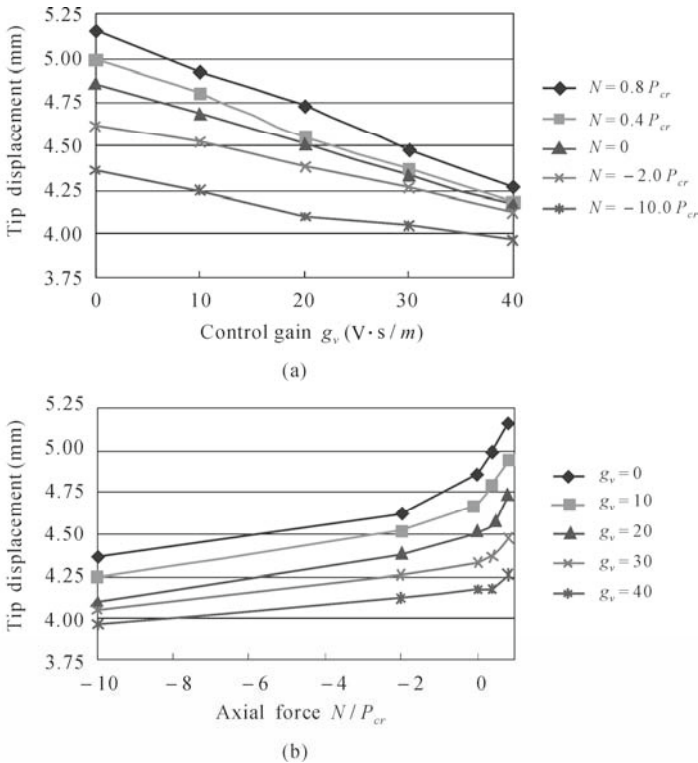


Fig. 8.10 Tip displacements for different control gains and axial forces (at $t = 10$ s). (a) Tip displacements for different velocity control gains g_v ; (b) Tip displacements for different axial forces N

8.4 Conclusions and Recommendations

8.4.1 Conclusions

In this chapter, a cantilevered piezoelectric column is investigated. First, the differential equations governing the transverse deflection of the column, with the presence of external axial loads, are derived. Second, two control strategies, namely, displacement feedback and velocity feedback control, are designed to control the vibration of the column. The analytical and semi-analytical solutions for the governing equations are obtained under these two control methods, respectively. Finally, the solutions are applied to a steel column bonded with a PVDF layer.

The numerical results show that the displacement feedback control method did not perform well on the vibration control of the structure; however, it provided a way to theoretically study the influence of piezoelectric materials on the natural frequencies and mode shapes. The study indicated that the compressive axial force has the effect of decreasing the natural frequencies while the tensile force has the converse effect, and that the natural frequency has a tendency to increase with the increase of the displacement feedback control gain g_d although this tendency is not significant. As for the mode shape, it is observed that the effect of piezoelectric actuator on the mode shapes is minor, and that the effect of axial force on the mode shapes is also minor, unless a large tensile force (e.g., $N \leq -10.0P_{cr}$) is applied.

On the other hand, the velocity feedback control is able to provide a satisfactory control effect on the vibration; *i.e.*, it successfully damped the vibration of the column under an acceptable feedback voltage range. It is also shown that a tensile axial force can depress the vibration of the column, while a compressive axial force has a converse effect, and that the vibration characteristics of a tensioned column are harder to be affected by the piezoelectric actuator than those of a compressed column.

8.4.2 Recommendations

The work presented in this chapter primarily focuses on the analytical study of vibration control of a cantilevered column bonded with piezoelectric actuator. Hence, the recommendations are mainly given in the following directions.

(1) All the presented solutions and discussions center around columns with clamped-free boundary conditions as the other boundary conditions have not been studied. However, the developed method can be extended to columns with the other boundary conditions, such as clamped-pinned, pinned-pinned, sliding-pinned,

sliding-free, and so on.

(2) The influences of piezoelectric materials and axial loads on the vibration control of structures are theoretically studied. Some experimental studies should be carried out to verify the analytical solutions, although it would be difficult to fulfill all the conditions adopted in the analytical study. Especially, the axial load would be difficult to be applied along the longitudinal axis of the column while it is vibrating.

(3) All the derivations are for free vibration. Transverse load should also be included in the model so that the solutions will have a wider application in practice. The introduction of transverse load will make the computation much more complicated. For the displacement feedback control, analytical or semi-analytical solutions may be obtained if certain mathematical techniques, such as modal analysis, are adopted. However, for the velocity feedback control, only numerical solution may be obtained due to the time-dependent boundary conditions

References

- Bailey, T. and Hubbard, J.E. (1985). "Distributed Piezoelectric-Polymer Active Vibration Control of a Cantilever Beam", *Journal of Guidance, Control and Dynamics*, 8(5): 605-611.
- Bokaian, A. (1988). "Natural Frequencies of Beams under Compressive Axial Loads", *Journal of Sound and Vibration*, 126(1): 49-65.
- Bokaian, A. (1990). "Natural Frequencies of Beams under Tensile Axial Loads", *Journal of Sound and Vibration*, 142(3): 481-498.
- Chandiramani, N.K., Librescu, L.I., Saxena, V. and Kumar, A. (2004). "Optimal Vibration Control of a Rotating Composite Beam with Distributed Piezoelectric sensing and Actuation", *Smart Materials and Structures*, 13: 433-442.
- Chen, L.W., Lin, C.Y. and Wang, C.C. (2002). "Dynamic Stability Analysis and Control of a Composite Beam with Piezoelectric Layers", *Composite Structures*, 56: 97-109.
- Fazelzadeh, S.A. and Jafari, S.M. (2008). "Active Control Law Design for Flutter Suppression and Gust Alleviation of a panel with Piezoelectric Actuators", *Smart Materials and Structures*, 17: 035013.
- Fung, E.H.K. and Yau, D.T.W. (2004). "Vibration Characteristics of a Rotating Flexible Arm with ACLD Treatment", *Journal of Sound and Vibration*, 269: 165-182.
- Gardonio, P. and Elliott, S. (2005). "Modal Response of a Beam with Sensor-Actuator Pair for the Implementation of Velocity Feedback Control", *Journal of Sound and Vibration*, 284: 1-22.
- Gaudenzi, P., Carbonaro, R. and Barboni, R. (1997). "Vibration Control of an

- Active Laminated Beam”, *Composite Structures*, 38(1-4): 413-420.
- Han, J.H., Tani, J. and Qiu, J. (2006). “Active Flutter Suppression of a Lifting Surface Using Piezoelectric Actuation and Modern Control Theory”, *Journal of Sound and Vibration*, 291: 706-722.
- Hong, S., Park, C.H. and Park, H.C. (2006), “Vibration Control of Beams using multiobjective State-Feedback Control”, *Smart Materials and Structures*, 15: 157-163.
- Humar, J.L. (1990). *Dynamics of Structures*. Englewood Cliffs, New Jersey: Prentice-Hall.
- Ikeda, T. (1990). *Fundamentals of Piezoelectricity*. Oxford; New York: Oxford University Press.
- Kamada, T., Fujita, T., Hatayama, T., Arikabe, T., Murai, N., Aizawa, S. and Tohyama, K. (1998). “Active Vibration Control of Flexural-Shear Type Frame Structures with Smart Structures Using Piezoelectric Actuators”, *Smart Materials and Structures*, 7: 479-488.
- Karami-Mohammadi, A. and Sadri, A. (2009). “An Active Vibration Control of Beam by Piezoelectric with Fuzzy Approach”, *International Journal of Signal System Control and Engineering Application*, 2: 1-7.
- Kayacik, O., Bruch, J.C., Sloss, J.M., Adali, S. and Sadek, I.S. (2008). “Integral Equation Approach for Piezo Patch Vibration Control of Beams with Various types of Damping”, *Computers and Structures*, 86: 357-366.
- Librescu, L. and Na, S. (1998a). “Boundary Control of Free and Forced Oscillation of Shearable Thin-Walled Beam Cantilevers”, *European Journal of Mechanics – A/Solids*, 17(4): 687-700.
- Librescu, L. and Na, S. (1998b). “Bending Vibration Control of Cantilevers via Boundary Moment and Combined Feedback Control Laws”, *Journal of Vibration and Control*, 17(4): 733-746.
- Lin, J. and Liu, W.Z. (2006). “Experimental Evaluation of a Piezoelectric Vibration Absorber Using a Simplified Fuzzy Controller in a Cantilever Beam”, *Journal of Sound and Vibration*, 296: 567-582.
- Lin, Y.J., Lee, T., Choi, B. and Saravanos, D. (1999). “An Application of Smart-Structure Technology to Rotor Blade Tip Vibration Control”, *Journal of Vibration and Control*, 5: 639-658.
- Liu, L., Zhang, Z. and Hua, H. (2007). “Dynamic Characteristics of Rotating Cantilever Plates with Active Constrained Layer Damping Treatments”, *Smart Materials and Structures*, 16: 1849-1856.
- Manning, W.J., Plummer, A.R. and Levesley, M.C. (2000). “Vibration Control of a Flexible Beam with Integrated Actuators and Sensors”, *Smart Materials and Structures*, 9: 932-939.
- Maurizi, M.J. and Belles, P.M. (1991). “General Equation of Frequencies for Vibrating Uniform One-Span Beams under Compressive Axial Loads”, *Journal of Sound and Vibration*, 145(2): 345-347.
- Moon, S.H. and Kim, S.J. (2003). “Suppression of Nonlinear Composite Panel Flutter with Active/Passive Hybrid Piezoelectric Networks Using Finite Element Method”, *Composite Structures*, 59: 525-533.

- Mukherjee, A. and Chaudhuri, A.S. (2005). "Active Control of Piezolaminated Columns - Exact Solutions and Experimental Validation", *Smart Materials and Structures*, 14: 475-482.
- Nbendjo, B.R.N. (2009). "Amplitude Control on Hinged-Hinged Beam Using Piezoelectric Absorber: Analytical and Numerical Explanation", *International Journal of Non-Linear Mechanics*, 44: 704-708.
- Preumont, A. (1997). *Vibration Control of Active Structures*. Dordrecht, Kluwer Academic.
- Rao, G.V. and Singh, G. (2001). "A Smart Structures Concept for the Buckling Load Enhancement of Columns", *Smart Materials and Structures*, 10: 843-845.
- Sadri, A.M., Wright, J.R. and Wynne, R.J. (2002). "LQG Control Design for Panel Flutter Suppression Using Piezoelectric Actuators", *Smart Materials and Structures*, 11: 834-839.
- Sebastijanovic, N., Ma, T. and Yang, H.T.Y. (2007). "Panel Flutter Detection and Control Using the Eigenvector Orientation Method and Piezoelectric Layers", *AIAA Journal*, 45, 118-127.
- Shih, H.R. (2000). "Distributed Vibration Sensing and Control of a Piezoelectric Laminated Curved Beam", *Smart Materials and Structures*, 9: 761-766.
- Sloss, J.M., Bruch, J.C., Sadek, I.S. and Adali, S. (2003). "Piezo Patch Sensor/Actuator Control of the Vibrations of a Cantilever under Axial Load", *Composite Structures*, 62: 423-428.
- Sun, B. and Huang, D. (2001). "Vibration Suppression of Laminated Composite Beams with a Piezo-Electric Damping Layer", *Composite Structures*, 53: 437-447.
- Vasques, C.M.A. and Rodrigues, J.D. (2005). "Coupled Three-Layered Analysis of Smart Piezoelectric Beams with Different Electric Boundary Conditions", *International Journal for Numerical Methods in Engineering*, 62: 1488-1518.
- Wang, Q. and Quek, S.T. (2000). "Flexural Vibration Analysis of Sandwich Beam Coupled with Piezoelectric Actuator", *Smart Materials and Structures*, 9: 103-109.
- Yang, Y.W., Ju, C.K. and Soh, C.K. (2003). "Analytical and semi-analytical solutions for vibration control of a cantilevered column using a piezoelectric actuator", *Smart Materials and Structures*, 12: 193-203.

Smart Plates and Shells

Y. W. Yang*, L. Zhang, Z. L. Jin, C. K. Soh

School of Civil and Environmental Engineering, Nanyang Technological University,
50 Nanyang Avenue, Singapore 639798.

Tel: (65)-6790-4057; Fax: (65)-6791-0676

Email: cywyang@ntu.edu.sg

9.1 Optimal Vibration Control using Genetic Algorithms

9.1.1 Introduction

Smart structures for vibration control of flexible space structures have attracted considerable amount of research in recent years. The development of smart structures with piezoelectric sensor/actuators (S/As) offers great potential for use in advanced aerospace, nuclear and automotive structural applications. The smart structure, which contains the main structure and the distributed piezoelectric S/As, can sense the excitations induced by its environment and can also generate control forces to either eliminate the undesirable effects or to enhance the desirable effects. Application of smart structures to vibration control may be traced to Bailey and Hubbard (1985), who used polyvinylidene fluoride (PVDF) as a distributed actuator on a cantilever beam to control its vibration. Subsequently, the modeling, basic equations, control laws, FE analysis methods, and experiments for smart structures have been investigated by several other researchers such as Wang and Rogers (1991), Chandrashekhara and Agarwal (1993) and Song *et al.* (2002).

Smart shell structures with integrated piezoelectric S/A laminae have been widely investigated in the past decades. Cylindrical shells are extensively used in engineering structures, such as oil tanks and bodies of aircraft and space shuttles. Vibration control of cylindrical shells was first initiated to solve the cabin noise

problem, and has been an area of active research. The research has mainly been focused on modeling, FE formulation and vibration control of the smart shells (Qiu and Tani, 1995; Chee *et al.*, 1998; Henry and Clark, 1999).

To utilize the advantages of piezoelectric transducers, it is necessary to select appropriate positions for the transducers and to select the sensor signals to be fed back to the actuators. The problems of finding the optimal placement and sizing of the S/As as well as the feedback gains are very challenging. Crawley and de Luis (1987) were the first to address the criterion for finding the optimal location of a piezoelectric actuator for a cantilever beam. Since then, several other researchers like Baz and Poh (1988), Devasia *et al.* (1993), Aldraihem *et al.* (2000), Qiu *et al.* (2007), and Kumar and Narayanan (2007) have done a great deal of study on the optimal control of beam and plate structures. However, investigation of the optimal vibration control of shell structures has seldom been carried out. Furthermore, most attention has been paid to the geometric optimization of S/As such as their placement, size and thickness. The integrated control system optimization considering the geometric distribution of the piezoelectric patches and the feedback control gains of the control system has rarely been investigated. Sun and Tong (2001) have carried out modal control of a smart cylindrical shell by optimizing the discretely distributed piezoelectric transducers, but the integrated optimization of control system and the effect of the number of piezoelectric patches have never been investigated.

In this section, integrated optimization of the control system for the cylindrical shell structures is formulated and implemented, in which the geometric distribution of the piezoelectric S/As and the feedback gains are considered as design variables. The energy dissipation method (Lee and Chen, 1994), which is essentially a negative velocity feedback control method, is employed as the criterion for optimizing the control system based on maximization of the dissipated energy due to the control action.

Genetic algorithms (GAs), as an optimization technique different from the conventional methods, have been applied to the vibration control of smart structures (Han and Lee, 1999; Zhang *et al.*, 2000). In this section, a modified real-encoded GA dealing with various constraints is employed for the integrated optimization of the control system. First, the state-space equation is formulated for smart cylindrical shells. Then, formulation of the integrated optimization of the control system is obtained based on the criterion of maximization of energy dissipation. Numerical examples of a simply supported plate, a simply supported cylindrical shell and a clamped-simply supported plate are presented to demonstrate the feasibility of this method and the effectiveness of vibration suppression. The results illustrate that vibration suppression could be significantly enhanced with the appropriate distribution of piezoelectric S/As and selection of feedback control gains. Furthermore, for specific controlled vibration modes, optimal distribution of the piezoelectric S/As should be located at the areas separated by the nodal lines to achieve optimal control effect.

9.1.2 Sensing and Actuating Equations

Fig. 9.1 shows a generic shell continuum defined in a tri-orthogonal curvilinear coordinate system, with α_1 and α_2 defining the shell neutral surface and α_3 the normal direction. The shell continuum has a constant thickness h which is relatively thin with respect to its radii of curvatures R_1 and R_2 . Generic deflections, U_1 , U_2 and U_3 , in the three principal directions, α_1 , α_2 and α_3 , are assumed to be sufficiently small with respect to the first power so as to allow the second and higher powers to be neglected. Furthermore, the transverse normal stresses are small compared with the other normal stresses in the shell and hence can be neglected. In addition, a line, originally normal to the shell reference surface, will remain normal to the deformed reference surface and will remain unstrained or unstretched. This is referred to as the Kirchhoff's hypothesis.

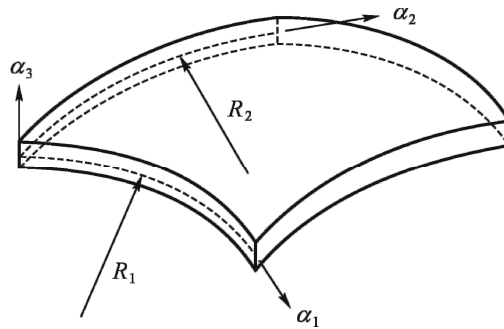


Fig. 9.1 A generic shell continuum

Consider a thin cylindrical elastic shell with N_p pairs of collocated piezoelectric patches bonded on its surfaces as discretely distributed S/As (Fig. 9.2), where R , h , L and β^* are the radius, thickness, length and curvature angle of the cylindrical shell, respectively. The patches on the upper surface are the actuators and those on the lower surface (not shown) are the sensors. The tri-orthogonal curvilinear coordinate system with axes x , β , and α_3 , in which x defines the longitudinal direction (length), β the circumferential direction, and α_3 the transverse direction, is also schematically shown in Fig. 9.2. Assume that the piezoelectric patches are much thinner than the host shell, and are perfectly bonded to the shell surfaces. The effects of the bonding material on the properties of the whole structure are neglected.

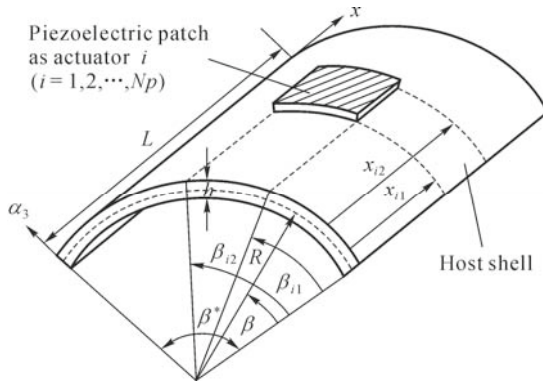


Fig. 9.2 A cylindrical shell with distributed piezoelectric patches

9.1.2.1 Sensing Equations

For the general thin shell configuration, only the transverse electric field E_3 is considered so that the strains and dielectric displacement D_3 are independent of α_3 . The voltage across the electrodes can be obtained by integrating the electric field over the thickness of the piezoelectric sensor, *i.e.*,

$$\phi = - \int_0^{h^s} E_3 d\alpha_3 \tag{9.1}$$

where h^s denotes the piezoelectric sensor thickness. Based on the governing equations for piezoelectric effects, we get

$$\phi = h^s (h_{31}\epsilon_1^s + h_{32}\epsilon_2^s - \beta_{33}D_3) \tag{9.2}$$

where ϵ_1^s and ϵ_2^s are the normal strains in the α_1 and α_2 directions, respectively; and h_{31} and h_{32} are piezo-constants. The superscript “s” denotes the distributed sensor.

Rearranging Eq. (9.2), we can write the electric displacement D_3 as:

$$D_3 = \frac{1}{\beta_{33}} (h_{31}\epsilon_1^s + h_{32}\epsilon_2^s - \frac{\phi}{h^s}) \tag{9.3}$$

Since D_3 is defined as the charge per unit area, we can integrate Eq. (9.3) over the electrode surface S_e to estimate the total surface charge. An open-circuit voltage ϕ^s condition can be obtained by setting the charge zero, *i.e.*,

$$\phi^s = \frac{h^s}{S^e} \int_{S^e} (h_{31}\varepsilon_1^s + h_{32}\varepsilon_2^s) A_1 A_2 d\alpha_1 d\alpha_2 \quad (9.4)$$

Substituting the strains of the sensor into Eq. (9.4) yields the distributed sensor output in terms of displacements and other system parameters.

$$\begin{aligned} \phi^s = & \frac{h^s}{S^e} \iint_{S^e} \left\{ h_{31} \left[\left(A_2 \frac{\partial u_1}{\partial \alpha_1} + u_2 \frac{\partial A_1}{\partial \alpha_2} + A_1 A_2 \frac{u_3}{R_1} \right) \right. \right. \\ & + r^s \left[A_2 \frac{\partial}{\partial \alpha_1} \left(\frac{u_1}{R_1} - \frac{1}{A_1} \frac{\partial u_3}{\partial \alpha_1} \right) + \left(\frac{u_2}{R_2} - \frac{1}{A_2} \frac{\partial u_3}{\partial \alpha_2} \right) \frac{\partial A_1}{\partial \alpha_2} \right] \left. \right\} \\ & + h_{32} \left\{ \left[A_1 \frac{\partial u_2}{\partial \alpha_2} + u_1 \frac{\partial A_2}{\partial \alpha_1} + A_1 A_2 \frac{u_3}{R_2} \right] + r^s \left[A_1 \frac{\partial}{\partial \alpha_2} \left(\frac{u_2}{R_2} - \frac{1}{A_2} \frac{\partial u_3}{\partial \alpha_2} \right) \right. \right. \\ & \left. \left. + \left(\frac{u_1}{R_1} - \frac{1}{A_1} \frac{\partial u_3}{\partial \alpha_1} \right) \frac{\partial A_2}{\partial \alpha_1} \right] \right\} d\alpha_1 d\alpha_2 \end{aligned} \quad (9.5)$$

where u_1, u_2 and u_3 are the displacements of the neutral surface of the shell in the three principal directions; r^s denotes the distance measured from the neutral surface of the shell to the mid-plane of the sensor; and A_1 and A_2 are the Lamé parameters.

As $h_{31} = h_{32} = e_{31} / \varepsilon_{33}$, where ε_{33} is the permittivity constant and e_{31} is the piezoelectric stress constant, substituting them into Eq. (9.5), we get similar expression of the sensor output as Tzou and Bao (1996):

$$\begin{aligned} \phi^s = & \frac{h^s e_{31}}{S^e \varepsilon_{33}} \iint_{S^e} \left\{ \left[\left(A_2 \frac{\partial u_1}{\partial \alpha_1} + u_2 \frac{\partial A_1}{\partial \alpha_2} + A_1 A_2 \frac{u_3}{R_1} \right) + \left(A_1 \frac{\partial u_2}{\partial \alpha_2} + u_1 \frac{\partial A_2}{\partial \alpha_1} + A_1 A_2 \frac{u_3}{R_2} \right) \right] \right. \\ & + r^s \left[A_2 \frac{\partial}{\partial \alpha_1} \left(\frac{u_1}{R_1} - \frac{1}{A_1} \frac{\partial u_3}{\partial \alpha_1} \right) + \left(\frac{u_2}{R_2} - \frac{1}{A_2} \frac{\partial u_3}{\partial \alpha_2} \right) \frac{\partial A_1}{\partial \alpha_2} \right. \\ & \left. \left. + A_1 \frac{\partial}{\partial \alpha_2} \left(\frac{u_2}{R_2} - \frac{1}{A_2} \frac{\partial u_3}{\partial \alpha_2} \right) + \left(\frac{u_1}{R_1} - \frac{1}{A_1} \frac{\partial u_3}{\partial \alpha_1} \right) \frac{\partial A_2}{\partial \alpha_1} \right] \right\} d\alpha_1 d\alpha_2 \end{aligned} \quad (9.6)$$

Eq. (9.6) can be simplified for the cylindrical shell shown in Fig. 9.2, for $A_1=1$, $A_2=R$, $R_1=\infty$ and $R_2=R$. Considering that the transverse component is much more prominent than the other two in-plane displacement components, we can simplify the sensor signal equation into the following form:

$$\phi^s = \frac{h^s e_{31}}{S^e \epsilon_{33}} \iint_{S^e} \left[\frac{u_3}{R} - r^s \left(\frac{\partial^2 u_3}{\partial x^2} + \frac{\partial^2 u_3}{R^2 \partial \beta^2} \right) \right] R dx d\beta \quad (9.7)$$

Using the modal decomposition method, the transverse response $u_3(t)$ of the shell can be expressed as the summation of all vibration modes

$$u_3(t) = \sum_{m=1}^{\infty} \sum_{n=1}^{\infty} \eta_{mn}(t) U_{mn}(x, \beta) \quad (9.8)$$

where $U_{mn}(x, \beta)$ is the mode shape function and $\eta_{mn}(t)$ is the modal participation factor.

The output voltage of the i^{th} sensor, ranging from x_{i1} to x_{i2} in the x -direction, and from β_{i1} to β_{i2} in the β -direction, can thus be written as

$$\phi_i^s = \frac{h^s e_{31}}{S_i^e \epsilon_{33}} \sum_{m=1}^{\infty} \sum_{n=1}^{\infty} \eta_{mn}(t) \int_{\beta_{i1}}^{\beta_{i2}} \int_{x_{i1}}^{x_{i2}} \left[\frac{U_{mn}}{R} - r^s \left(\frac{\partial^2 U_{mn}}{\partial x^2} + \frac{\partial^2 U_{mn}}{R^2 \partial \beta^2} \right) \right] R dx d\beta \quad (9.9)$$

• *Actuating Equations*

For the actuators bonded on the shell surface, the induced strains due to imposed control voltages, *i.e.*, the converse piezoelectric effect, are used to counteract the shell oscillation. The induced strains and the resultant effect are illustrated in Fig. 9.3. Note that these strains are generated in the distributed actuator which is located a distance away from the shell neutral surface. Thus, these strains introduce counteracting control moments to the shell structure. The sign of the feedback voltage should be carefully controlled so that the induced moments will counteract the shell oscillation.

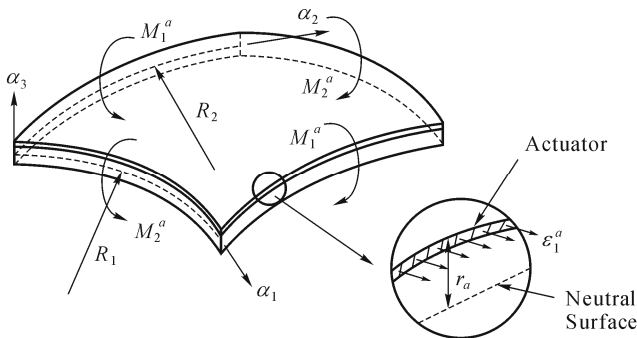


Fig. 9.3 Distributed control by a distributed piezoelectric actuator

When external charges are exerted on the piezoelectric actuators, the differential equations of motion for the cylindrical shell can be expressed as

$$\frac{\partial^2 u_x}{\partial x^2} + \frac{1-\mu}{2R^2} \frac{\partial^2 u_x}{\partial \beta^2} + \frac{1+\mu}{2R} \frac{\partial^2 u_\beta}{\partial x \partial \beta} + \frac{\mu}{R} \frac{\partial u_3}{\partial x} + \frac{1-\mu^2}{Eh} \sum_{i=1}^{N_p} F_{1i}^a = \frac{1-\mu^2}{E} \rho \ddot{u}_x \quad (9.10a)$$

$$\begin{aligned} & \frac{1+\mu}{2} \frac{\partial^2 u_x}{\partial x \partial \beta} + \left[R \frac{1-\mu}{2} + \frac{h^2(1-\mu)}{24R} \right] \frac{\partial^2 u_\beta}{\partial x^2} + \left(\frac{1}{R} + \frac{h^2}{12R^3} \right) \frac{\partial^2 u_\beta}{\partial \beta^2} + \frac{1}{R} \frac{\partial u_3}{\partial \beta} \\ & - \frac{h^2}{12R} \frac{\partial^3 u_3}{\partial x^2 \partial \beta} - \frac{h^2}{12R^3} \frac{\partial^3 u_3}{\partial \beta^3} + \frac{(1-\mu^2)R}{Eh} \sum_{i=1}^{N_p} F_{2i}^a = \frac{(1-\mu^2)R}{E} \rho \ddot{u}_\beta \end{aligned} \quad (9.10b)$$

$$\begin{aligned} & \mu \frac{\partial u_x}{\partial x} + \frac{1}{R} \frac{\partial u_\beta}{\partial \beta} + \frac{u_3}{R} + \frac{h^2 R}{12} \left(\frac{\partial^4 u_3}{\partial x^4} + \frac{2}{R^2} \frac{\partial^4 u_3}{\partial x^2 \partial \beta^2} + \frac{1}{R^4} \frac{\partial^4 u_3}{\partial \beta^4} \right) - \frac{h^2}{12R} \frac{\partial^3 u_\beta}{\partial x^2 \partial \beta} \\ & - \frac{h^2}{12R^3} \frac{\partial^3 u_\beta}{\partial \beta^3} - \frac{(1-\mu^2)R}{Eh} \sum_{i=1}^{N_p} F_{3i}^a = - \frac{(1-\mu^2)R}{E} \rho \ddot{u}_3 \end{aligned} \quad (9.10c)$$

where E , ρ and μ are the Young's modulus, mass density and Poisson's ratio of the shell, respectively; and F_{1i}^a , F_{2i}^a and F_{3i}^a are the forces induced by actuator i , which can be written as

$$\begin{aligned} F_{1i}^a &= -d_{31} E_p \frac{\partial V_i^a}{\partial x} \\ F_{2i}^a &= - \left(1 + \frac{r_a}{R} \right) \frac{d_{31} E_p}{R} \frac{\partial V_i^a}{\partial \beta} \\ F_{3i}^a &= -r_a d_{31} E_p \frac{\partial^2 V_i^a}{\partial x^2} - \frac{r_a}{R^2} d_{31} E_p \frac{\partial^2 V_i^a}{\partial \beta^2} + \frac{d_{31} E_p V_i^a}{R} \end{aligned} \quad (9.11)$$

where d_{31} and E_p are the piezoelectric strain constant and the Young's modulus of the actuators, respectively; V_i^a is the voltage applied to actuator i ; and r_a denotes the distance measured from the neutral surface of the cylindrical shell to the mid-plane of the actuator.

The voltage distribution of actuator i can be expressed as

$$V_i^a(x, \beta, t) = V_i^a(t) [H(x - x_{i1}) - H(x - x_{i2})] [H(\beta - \beta_{i1}) - H(\beta - \beta_{i2})] \quad (9.12)$$

in which $H(\cdot)$ is the Heaviside function.

Using the modal expansion technique and the modal orthogonality, and substituting Eqs. (9.8), (9.11) and (9.12) into Eq. (9.10c), we can derive the transverse modal vibration equations with distributed actuators as:

$$\begin{aligned}
 \ddot{\eta}_{mn}(t) + 2\zeta_{mn}\omega_{mn}\dot{\eta}_{mn}(t) + \omega_{mn}^2\eta_{mn}(t) &= \frac{1}{\rho h N_{mn}} \sum_{i=1}^{N_p} \int_0^{\beta^*} \int_0^L F_{3i}^a U_{mn} R dx d\beta \\
 &= \frac{1}{\rho h N_{mn}} \sum_{i=1}^{N_p} \int_0^{\beta^*} \int_0^L -r_a d_{31} E_p \left(\frac{\partial^2 V_i^a}{\partial x^2} + \frac{1}{R^2} \frac{\partial^2 V_i^a}{\partial \beta^2} - \frac{V_i^a}{r_a R} \right) U_{mn} R dx d\beta \cdot V_i^a(t) \\
 &= \frac{-e_{31}}{\rho h N_{mn}} \sum_{i=1}^{N_p} \int_{\beta_{i1}}^{\beta_{i2}} \int_{x_{i1}}^{x_{i2}} \left[r_a \left(\frac{\partial^2 U_{mn}}{\partial x^2} + \frac{1}{R^2} \frac{\partial^2 U_{mn}}{\partial \beta^2} \right) - \frac{U_{mn}}{R} \right] R dx d\beta \cdot V_i^a(t)
 \end{aligned} \tag{9.13}$$

where ω_{mn} is the mn^{th} natural frequency of the shell; ζ_{mn} is the damping ratio of the mn^{th} vibration mode; and $N_{mn} = \int_0^{\beta^*} \int_0^L U_{mn}^2 R dx d\beta$.

9.1.2.3 State-space Equations

Assuming that the first $N=m \times n$ vibration modes are taken into account and introducing the state vector $\chi = [\eta_1, \eta_2, \dots, \eta_N, \dot{\eta}_1, \dot{\eta}_2, \dots, \dot{\eta}_N]^T$, the sensing and actuating equations can be transformed into the state-space equation as

$$\begin{cases} \dot{\chi} = A\chi + BV^a \\ \phi^s = C\chi \end{cases} \tag{9.14}$$

where

$$A = \begin{bmatrix} \mathbf{0}_{N \times N} & \mathbf{I}_{N \times N} \\ -A\Omega^2 & -2\zeta\Omega \end{bmatrix}, \quad B = \begin{bmatrix} \mathbf{0}_{N \times N_p} \\ \bar{B}_{N \times N_p} \end{bmatrix}, \quad C = [\bar{C}_{N_p \times N} \quad \mathbf{0}_{N_p \times N}] \tag{9.15}$$

$$\bar{B} = \begin{bmatrix} B_{11} & B_{12} & \cdots & B_{1N_p} \\ B_{21} & B_{22} & \cdots & B_{2N_p} \\ \vdots & \vdots & \ddots & \vdots \\ B_{N1} & B_{N2} & \cdots & B_{NN_p} \end{bmatrix}, \quad V^a = \begin{bmatrix} V_1^a \\ V_2^a \\ \vdots \\ V_{N_p}^a \end{bmatrix} \tag{9.16}$$

$$\bar{C} = \begin{bmatrix} C_{11} & C_{12} & & C_{1N} \\ C_{21} & C_{22} & & C_{2N} \\ \vdots & \vdots & \dots & \vdots \\ C_{Np1} & C_{Np2} & & C_{NpN} \end{bmatrix}, \quad \boldsymbol{\varphi}^s = \begin{bmatrix} \phi_1^s \\ \phi_2^s \\ \vdots \\ \phi_{Np}^s \end{bmatrix} \quad (9.17)$$

$$B_{ki} = \frac{-e_{31}}{\rho h N_{pq}} \cdot \int_{\beta_{i1}}^{\beta_{i2}} \int_{\alpha_{i1}}^{\alpha_{i2}} \left[r_a \left(\frac{\partial^2 U_{pq}}{\partial x^2} + \frac{1}{R^2} \frac{\partial^2 U_{pq}}{\partial \beta^2} \right) - \frac{U_{pq}}{R} \right] R dx d\beta \quad (9.18)$$

$$C_{ik} = \frac{h^s e_{31}}{S_i^e \epsilon_{33}} \cdot \int_{\beta_{i1}}^{\beta_{i2}} \int_{\alpha_{i1}}^{\alpha_{i2}} \left[\frac{U_{pq}}{R} - r^s \left(\frac{\partial^2 U_{pq}}{\partial x^2} + \frac{\partial^2 U_{pq}}{R^2 \partial \beta^2} \right) \right] R dx d\beta \quad (9.19)$$

in which $i=1,2,\dots,Np$; $k=n(p-1)+q$; $p=1,2,\dots,m$; $q=1,2,\dots,n$;

$$\boldsymbol{\Omega} = \begin{bmatrix} \omega_1 & & & \\ & \omega_2 & & \\ & & \ddots & \\ & & & \omega_N \end{bmatrix}; \quad \boldsymbol{\varsigma} = \begin{bmatrix} \varsigma_1 & & & \\ & \varsigma_2 & & \\ & & \ddots & \\ & & & \varsigma_N \end{bmatrix} \quad (9.20)$$

in which $\omega_k = \omega_{pq}$; $k=n(p-1)+q$; $p=1,2,\dots,m$; $q=1,2,\dots,n$; ς_k is the damping ratio of the k^{th} vibration mode of the shell; and the natural frequency ω_{pq} is the smallest value of the solutions of the following equation

$$\begin{vmatrix} \rho h \omega^2 - \gamma_{11} & \gamma_{12} & \gamma_{13} \\ \gamma_{12} & \rho h \omega^2 - \gamma_{22} & \gamma_{23} \\ \gamma_{13} & \gamma_{23} & \rho h \omega^2 - \gamma_{33} \end{vmatrix} = 0 \quad (9.21)$$

where

$$\begin{aligned} \gamma_{11} &= \gamma \cdot \left[\left(\frac{p\pi}{L} \right)^2 + \frac{1-\mu}{2R^2} \left(\frac{q\pi}{\beta^*} \right)^2 \right]; \quad \gamma_{12} = \gamma \cdot \frac{1+\mu}{2R} \frac{pq\pi^2}{L\beta^*}; \quad \gamma_{13} = -\frac{\mu p\pi}{RL} k \\ \gamma_{22} &= \left[\left(\frac{1-\mu}{2} + \frac{h^2(1-\mu)}{24R^2} \right) \left(\frac{p\pi}{L} \right)^2 + \left(\frac{1}{R^2} + \frac{h^2}{12R^4} \right) \left(\frac{q\pi}{\beta^*} \right)^2 \right] \cdot \gamma; \\ \gamma_{23} &= -\gamma \left[\frac{h^2}{12R^2} \cdot \left(\frac{p\pi}{L} \right)^2 \cdot \frac{q\pi}{\beta^*} + \frac{h^2}{12R^4} \cdot \left(\frac{q\pi}{\beta^*} \right)^3 + \frac{q\pi}{R^2 \beta^*} \right]; \\ \gamma_{33} &= \gamma \cdot \left\{ \frac{1}{R^2} + \frac{h^2}{12} \left[\left(\frac{p\pi}{L} \right)^2 + \frac{q^2 \pi^2}{R^2 \beta^{*2}} \right]^2 \right\}; \quad \gamma = Eh/(1-\mu^2) \end{aligned} \quad (9.22)$$

• Simplification for Smart Plates

Consider the smart plate model shown in Fig. 9.4. The collocated piezoelectric patches, polarized along the z -axis, are bonded to the lower and upper surfaces of the plate as the S/As. Because the i^{th} sensor is bonded to the lower surface of the plate, which cannot be visually seen from the angle of view, it has not been shown in this figure.

The differential vibration equations of the plate can be derived from those of the cylindrical shell by the simplifications of $R \rightarrow \infty$ and $y = R\beta$. Substituting the above expressions into the equations of motion of the cylindrical shell, *i.e.*, Eq. (9.10), we obtain the vibration equations of the plate as:

$$\begin{aligned} \frac{\partial^2 u_x}{\partial x^2} + \frac{1-\mu}{2} \frac{\partial^2 u_x}{\partial y^2} + \frac{1+\mu}{2} \frac{\partial^2 u_y}{\partial x \partial y} + \frac{1-\mu^2}{Eh} \sum_{i=1}^{Np} F_{1i}^a &= \frac{1-\mu^2}{E} \rho \ddot{u}_x \\ \frac{1+\mu}{2} \frac{\partial^2 u_x}{\partial x \partial y} + \frac{1-\mu}{2} \frac{\partial^2 u_y}{\partial x^2} + \frac{\partial^2 u_y}{\partial y^2} + \frac{(1-\mu^2)}{Eh} \sum_{i=1}^{Np} F_{2i}^a &= \frac{1-\mu^2}{E} \rho \ddot{u}_y \quad (9.23) \\ \frac{h^2}{12} \left(\frac{\partial^4 u_3}{\partial x^4} + 2 \frac{\partial^4 u_3}{\partial x^2 \partial y^2} + \frac{\partial^4 u_3}{\partial y^4} \right) - \frac{(1-\mu^2)}{Eh} \sum_{i=1}^{Np} F_{3i}^a &= -\frac{1-\mu^2}{E} \rho \ddot{u}_3 \end{aligned}$$

Similarly, the transverse oscillation of the plate is of primary interest in this study. The output voltage of the i^{th} sensor, ranging from x_{i1} to x_{i2} in the x -direction, and from y_{i1} to y_{i2} in the y -direction, can be expressed as

$$\phi_i^s = \frac{h^s e_{31}}{S_i^e \epsilon_{33}} \sum_{m=1}^{\infty} \sum_{n=1}^{\infty} \eta_{mn}(t) \int_{y_{i1}}^{y_{i2}} \int_{x_{i1}}^{x_{i2}} \left[-r^s \left(\frac{\partial^2 U_{mn}}{\partial x^2} + \frac{\partial^2 U_{mn}}{\partial y^2} \right) \right] dx dy \quad (9.24)$$

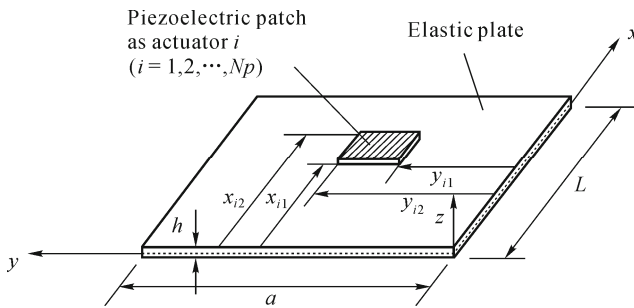


Fig. 9.4 Plate model with sensors and actuators

Also, the transverse modal vibration equations with distributed actuators can be expressed as

$$\begin{aligned}
 & \ddot{\eta}_{mn}(t) + 2\zeta_{mn}\omega_{mn}\dot{\eta}_{mn}(t) + \omega_{mn}^2\eta_{mn}(t) \\
 &= \frac{1}{\rho h N_{mn}} \sum_{i=1}^{N_p} \int_0^a \int_0^L -r_a d_{31} E_p \left(\frac{\partial^2 V_i^a}{\partial x^2} + \frac{\partial^2 V_i^a}{\partial y^2} \right) U_{mn} dx dy \\
 &= \frac{-r_a e_{31}}{\rho h N_{mn}} \sum_{i=1}^{N_p} \left[\int_{y_{i1}}^{y_{i2}} \left(\frac{\partial U_{mn}}{\partial x} \Big|_{x=y_{i2}} - \frac{\partial U_{mn}}{\partial x} \Big|_{x=y_{i1}} \right) dy \right. \\
 & \quad \left. + \int_{x_{i1}}^{x_{i2}} \left(\frac{\partial U_{mn}}{\partial y} \Big|_{y=y_{i2}} - \frac{\partial U_{mn}}{\partial y} \Big|_{y=y_{i1}} \right) dx \right] \cdot V_i^a(t) \\
 &= \frac{-r_a e_{31}}{\rho h N_{mn}} \sum_{i=1}^{N_p} \int_{y_{i1}}^{y_{i2}} \int_{x_{i1}}^{x_{i2}} \left(\frac{\partial^2 U_{mn}}{\partial x^2} + \frac{\partial^2 U_{mn}}{\partial y^2} \right) dx dy \cdot V_i^a(t)
 \end{aligned} \tag{9.25}$$

where $N_{mn} = \int_0^a \int_0^L U_{mn}^2 dx dy$.

Following the same derivation procedures, we obtain the state-space equations of the smart plate in the same form as Eq. (9.14). The difference is that the coefficients in the state matrix have the following forms:

$$B_{ki} = \frac{-r_a e_{31}}{\rho h N_{pq}} \cdot \int_{y_{i1}}^{y_{i2}} \int_{x_{i1}}^{x_{i2}} \left(\frac{\partial^2 U_{pq}}{\partial x^2} + \frac{\partial^2 U_{pq}}{\partial y^2} \right) dx dy \tag{9.26}$$

$$C_{ik} = \frac{-r^s h^s e_{31}}{S_i^e \varepsilon_{33}} \cdot \int_{y_{i1}}^{y_{i2}} \int_{x_{i1}}^{x_{i2}} \left(\frac{\partial^2 U_{pq}}{\partial x^2} + \frac{\partial^2 U_{pq}}{\partial y^2} \right) dx dy \tag{9.27}$$

9.1.3 Energy-Based Approach for Integrated Optimal Design

The most attractive methodology that accounts for transient vibration responses is characterized by the maximization of the dissipation energy extracted by the feedback control system. Lee and Chen (1994) applied this optimization method to a beam model and presented an integrated determination of the S/A locations and feedback gains. In this section, this method is also applied to the cylindrical shell structures.

The crucial consideration of optimal control design is the selection of an appropriate criterion for finding the most desirable performance. This criterion depends on how the system's physical requirements are translated into mathematical formulation. For the vibration suppression of flexible systems, the total energy stored in the system can be considered as a representation of the vibration response. The advantage of this representation is that the phenomenon of vibration can be expressed as a scalar. Clearly, the time behavior of the total

energy is a scalar function with respect to time. This time behavior of the scalar function can be used to evaluate the effectiveness of vibration suppression.

The input control vector can be expressed as follows, when considering a constant negative velocity feedback

$$V^a = -G\dot{\phi}^s = -GC\dot{\chi} \quad (9.28)$$

where G is the feedback gain matrix.

The corresponding closed-loop state-space equation is

$$\dot{\chi} = \bar{A}\chi \quad (9.29)$$

where the closed-loop system matrix \bar{A} is given as

$$\bar{A} = \begin{bmatrix} \mathbf{0}_{N \times N} & I_{N \times N} \\ -\Omega^2 & -\bar{B}G\bar{C} - 2\zeta\Omega \end{bmatrix} \quad (9.30)$$

The objective of optimization is to maximize the energy dissipated by the active controller. The more the energy is dissipated by the control system, the lesser the energy is stored in the system. This can be used to simultaneously optimize the geometry of the S/As and the values of the feedback gains. The integrated total energy stored in the system can be written as

$$W = \int_0^\infty \chi^T \tilde{Q} \chi dt \quad (9.31)$$

where \tilde{Q} is defined as $\tilde{Q} = \begin{bmatrix} \Omega^2 & \mathbf{0} \\ \mathbf{0} & I_{N \times N} \end{bmatrix}$.

Application of the standard state transformation techniques to Eq. (9.31) yields

$$W = -\chi^T(t_0) P \chi(t_0) \quad (9.32)$$

where $\chi(t_0)$ is the initial state and P is the solution of the following Lyapunov equation

$$\bar{A}^T P + P \bar{A} = -\tilde{Q} \quad (9.33)$$

9.1.4 General Formulation and Modified Real-Encoded GA

- *Problem Formulation*

In order to optimize the placement and size of the piezoelectric patches and the feedback control gains, the locations of the N_p pieces of S/As x_{i1} , x_{i2} , β_{i1} , β_{i2} ($i=1,2,\dots,N_p$) and the feedback gain matrix G are defined as the design variables.

In general, this optimization problem can be expressed in the following form

$$\text{Minimize } W(\vec{X}, G) = -\chi^T(t_0) \mathbf{P} \chi(t_0) \quad (9.34)$$

subject to:

(1) variable limits:

$$0 \leq x_{i1}, x_{i2} \leq L, \quad 0 \leq \beta_{i1}, \beta_{i2} \leq \beta^*, \quad 0 \leq G_{ij} \leq G^i; \quad (9.35)$$

(2) static constraints:

$$x_{i1} \leq x_{i2}, \quad \beta_{i1} \leq \beta_{i2}; \quad (9.36)$$

(3) dynamic constraints which avoid overlap of piezoelectric patches, where \vec{X} is the vector of the $4N_p$ design variables x_{i1} , x_{i2} , β_{i1} , and β_{i2} ; G_{ij} is the element in the feedback gain matrix G ; and $i, j=1,2,\dots,N_p$.

In the above formulation, the significance of the variable limits and the static constraints is straightforward. The dynamic constraint means that this kind of constraints will dynamically appear during the computation process. Different from the variable limits and static constraints which will constantly exist during the whole computation process, the dynamic constraints will emerge unpredictably in the offspring generated by the genetic operators, *e.g.*, crossover and mutation. The possible geometric distributions of two piezoelectric patches are illustrated in Fig. 9.5. Assume that the location of Patch i is fixed, a feasible design of Patch j can be located at the region including Locations 1 to 8. However, the region including Location 9 should be avoided to prevent overlap.

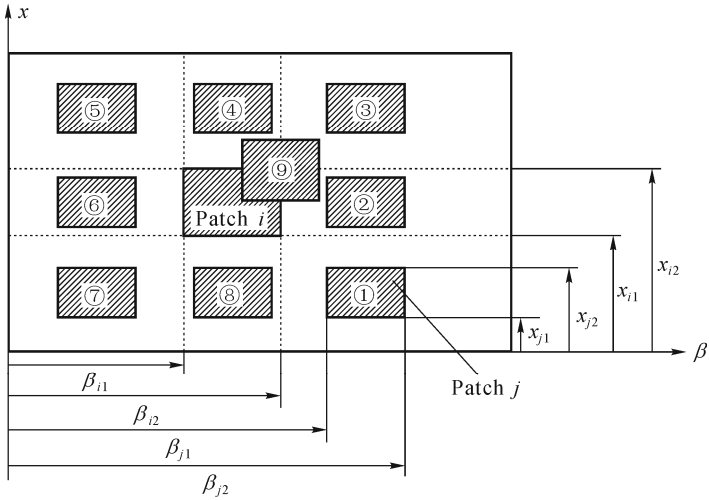


Fig. 9.5 Possible geometric distributions of two piezoelectric patches

To achieve the feasible designs, one or two of the following four constraints must be satisfied:

- (1) $x_{j1} > x_{i2}$, for region including Locations 1, 2 and 3;
- (2) $x_{j2} < x_{i1}$, for region including Locations 5, 6 and 7;
- (3) $\beta_{j1} > \beta_{i2}$, for region including Locations 3, 4 and 5;
- (4) $\beta_{j2} < \beta_{i1}$, for region including Locations 7, 8 and 1.

Since during the computation process, the emergence of infeasible designs, e.g., Patch i and Patch j at Location 9, is inevitable, the dynamic constraints should be imposed to avoid such “illegal” designs. Therefore, the dynamic constraints can be expressed as

$$x_{j1} > x_{i2}, \text{ or } x_{j2} < x_{i1}, \text{ or } \beta_{j1} > \beta_{i2}, \text{ or } \beta_{j2} < \beta_{i1} \quad (i, j = 1, 2, \dots, Np, i \neq j) \quad (9.37)$$

Any feasible design should satisfy one or two of the above constraints. If none of the constraints is satisfied, it implies an infeasible design has been generated with the piezoelectric patches overlapped. For instance, for Location 9, Patches i and j may overlap partially or completely, depending on their sizes and relative positions. A penalty function is introduced to deal with such situation. The details will be discussed in the next section.

• **Constraint Handling and Modified Real-Encoded GA**

A modified real-encoded GA is used to solve the problem formulated in Eqs.

(9.34) – (9.36). The fundamental mechanisms leading the GA search process are the equivalents of natural selection, crossover and mutation. GA deals with a population that is a collection of individuals and the chromosome of each individual represents a candidate solution. For any GA, a chromosome representation is needed to describe each individual in the population of interest. Each individual or chromosome is made up of a sequence of genes from a certain alphabet such as binary digits, floating point numbers, integers, etc. For the present problem, a chromosome in GA population consists of design variables \bar{X} and G , as shown in Fig. 9.6. The length of the chromosome is $4 \times Np + Np \times Np = Np(4 + Np)$.

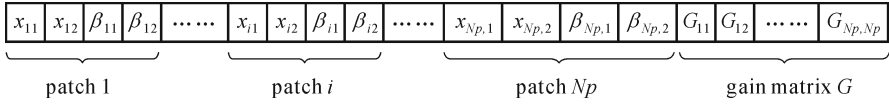


Fig. 9.6 A chromosome in modified real-encoded GA

An option to deal with all the constraints in this problem, *i.e.*, the variable limits, the static constraints and the dynamic constraints, is to adopt the penalty method. However, due to the large quantity of constraints, it is very time-consuming and the efficiency and accuracy cannot be guaranteed. Therefore, a modified GA with specific genetic operators designed to handle the variable limits and the static constraints and a penalty function to deal with the dynamic constraints is developed.

Different from the standard GA, in this study, a whole arithmetical crossover is used and a uniform mutation is modified to make the offspring of the parents satisfy inequalities (9.35) and (9.36). The whole arithmetic crossover produces two complimentary linear combinations of the parents as

$$\tilde{X} = r\bar{X} + (1-r)\bar{Y}, \quad \tilde{Y} = (1-r)\bar{X} + r\bar{Y}, \quad \text{where } r \in (0,1) \tag{9.38}$$

This will always guarantee that the offspring \tilde{X} and \tilde{Y} satisfy all the variable limits and the static constraints if their parents \bar{X} and \bar{Y} do. The mutation operator is also quite different from the traditional ones with respect to the mutation range. A traditional mutation is performed within the static domains for all genes; however, our proposed mutation is performed within the dynamic domains. For a chromosome $s = \langle x_{11}, x_{12}, \dots, x_{i1}, x_{i2}, \dots, G_{11}, \dots, G_{NpNp} \rangle$, if a random gene x_{i1} of the chromosome is selected, the result of this mutation is $s = \langle x_{11}, x_{12}, \dots, x_{i1}^*, x_{i2}, \dots, G_{11}, \dots, G_{NpNp} \rangle$, where x_{i1}^* is a random value in the dynamic range of $[0, x_{i2}]$. If x_{i2} is selected, the result of this mutation is $s = \langle x_{11}, x_{12}, \dots, x_{i1}, x_{i2}^*, \dots, G_{11}, \dots, G_{NpNp} \rangle$, where x_{i2}^* is a random value in the dynamic range of $[x_{i1}, L]$. By these genetic operators, the offspring can satisfy all

the variable limits and the static constraints.

For the dynamic constraints, a penalty function is introduced to penalize the items which violate the constraints appearing with the optimization. For Patches i and j shown in Fig. 9.5, the penalty function can be expressed as

$$P_{ij} = r_{ij} \cdot \frac{A_{overlap}}{A_i + A_j}, \quad i, j = 1, 2, \dots, Np \quad (9.39)$$

where $A_{overlap}$ is the area overlapped between Patches i and j , A_i and A_j are the areas of Patches i and j , respectively, and r_{ij} is the penalty parameters. Thus, evaluation of the objective function can be represented by $\varphi(\vec{X}, G)$ in the following form

$$\varphi(\vec{X}, G) = W(\vec{X}, G) + \sum_{i=1}^{Np} \sum_{\substack{j=1 \\ j \neq i}}^{Np} P_{ij} \quad (9.40)$$

When $r_{ij} \rightarrow \infty$, the solution of Eq. (9.40) tends to be the solution of the original problem defined in Eq. (9.34).

The general process of the modified GA can be briefly described as follows. First, the initial generation comprising the individuals which satisfy all the variable limits and static constraints is randomly generated. The whole arithmetic crossover and the uniform mutation are then applied to generate the next generation with all the individuals satisfying inequalities (9.35) and (9.36). Meanwhile, if applicable, the penalty function will be activated for the dynamic constraints. This will significantly reduce the infeasible individuals which breach the constraints, and avoid spending too much time to evaluate the infeasible individuals. In the procedures of performing genetic operators, better individuals have higher probability to be selected. The above process continues until the maximum number of generations is reached. More details can be found in Yang *et al.* (2006).

9.1.5 Numerical Examples

In this section, the optimal design of vibration control system based on the proposed approach is carried out and the simulation is implemented for a simply supported plate, a simply supported cylindrical shell, and a plate with three edges simply supported and one edge clamped.

• *Simply Supported Plate*

Consider a plate with four edges simply supported onto which collocated S/As are bonded (Fig. 9.4). The material properties and geometric configuration of the system are listed in Table 9.1. The parameters are quoted from Yang *et al.* (2006).

Table 9.1 Plate and piezoelectric patch specifications

Item	Plate	Actuators	Sensors
Mass density (kg/m ³)	7800	7600	1780
Young's modulus (GPa)	210	63	2
Poisson's ration	0.3	0.3	0.3
Piezo-constant d_{31} (m/V)		37×10^{-12}	30×10^{-12}
Piezo-constant e_{31} (N/(V·m))		2.331	0.06
Permittivity constant ϵ_{33} (F/m)			8.85×10^{-9}
Thickness (m)	0.001	0.0004	0.0004
Length (m)	1.0		
Width (m)	2.0		
Damping ratio	0.01		

Substituting the mode shape functions $U_{pq} = \sin(p\pi x/L)\sin(q\pi y/a)$ into Eqs. (9.26) and (9.27), we obtain the coefficients of the simply supported plate in the state matrix as

$$B_{ki} = \frac{4r_a e_{31}}{\rho h} \left(\frac{p}{qL^2} + \frac{q}{pa^2} \right) \cdot T_{pqi} \quad (9.41)$$

$$C_{ik} = \frac{r^s h^s e_{31}}{S_i^e \epsilon_{33}} \left(\frac{pa}{qL} + \frac{qL}{pa} \right) \cdot T_{pqi} \quad (9.42)$$

in which

$$T_{pqi} = [\cos(p\pi x_{i1}/L) - \cos(p\pi x_{i2}/L)][(\cos(q\pi y_{i1}/a) - \cos(q\pi y_{i2}/a))]$$

For simplicity, only the first four vibration modes of the plate and the shell have been taken into account because, generally, the first few vibration modes approximately reflect the exact vibration status. The initial conditions denoted by the generalized coordinate vector are given by:

$$\eta(0) = [0 \ 0 \ 0 \ 0], \quad \dot{\eta}(0) = [0.5 \ 0.4 \ 0.3 \ 0.2].$$

The optimization problem, as previously formulated, is a non-linear optimization with constraints. In this case, besides the geometric constraints, a simple bound is

imposed on the feedback control gain matrix G , i.e., $0 < G_{ij} \leq 100$. In order to ensure the system is asymptotically stable, an additional constraint is needed, $\det(G) \geq 0$, where $\det(G)$ represents the determinant of the matrix G .

Using the modified GA, for the simply supported plate, three cases with one to three pieces of piezoelectric patches are studied. The control parameters for the GA run are as follows. The population size, the crossover probability, the mutation probability and the maximum number of generations are set as 200, 0.8, 0.05 and 300, respectively. The optimization results are shown in Table 9.2. The time behaviors of the vibration modes without control and with control using one to three pieces of piezoelectric patches are shown in Figs. 9.7 – 9.10. From Table 9.2 and Figs. 9.7 – 9.10, it can be observed that the speed of decay of the vibration increases when more patches are used, which implies that the vibration of the structure can be controlled more effectively by using more patches with the optimized placement and size, as well as the feedback control gains.

Table 9.2 Optimal S/As positions and feedback gains for simply supported plate

N_p	Locations of patches		Feedback gain matrix	Objective function $\phi(\bar{X}, G)$
	$x_{i1} - x_{i2}$	$y_{i1} - y_{i2}$		
1	0.0857–0.6925m, 0.1573–1.1902m		[100]	0.1320
2	0.0985–0.4971m, 0.1658–1.3037m	0.4971–0.8821m, 0.1540–1.1062m	$\begin{bmatrix} 100 & 96.74 \\ 40.17 & 100 \end{bmatrix}$	0.0690
	0.0863–0.5021m, 0.1454–1.3409m			
3	0.5021–0.8226m, 0.1322–1.1908m	0.8226–0.8227m, 0.5847–0.6026m	$\begin{bmatrix} 100 & 100 & 12.14 \\ 100 & 100 & 100 \\ 37.91 & 22.74 & 65.40 \end{bmatrix}$	0.0497
	0.8226–0.8227m, 0.5847–0.6026m			
	0.8226–0.8227m, 0.5847–0.6026m			

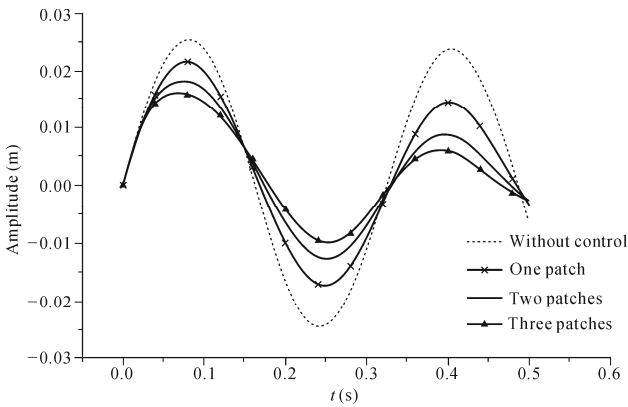


Fig. 9.7 Time response of 1st mode with different numbers of patches for simply supported plate

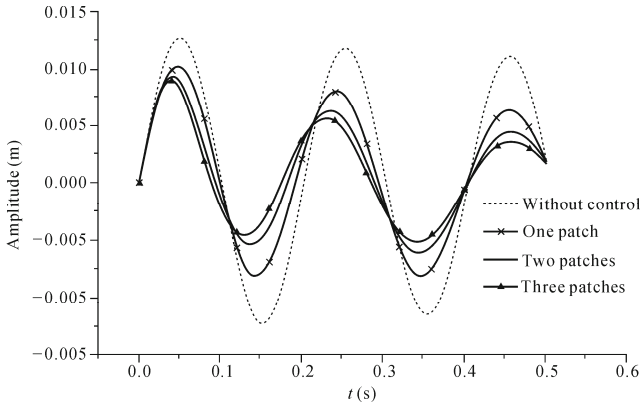


Fig. 9.8 Time response of 2nd mode with different numbers of patches for simply supported plate

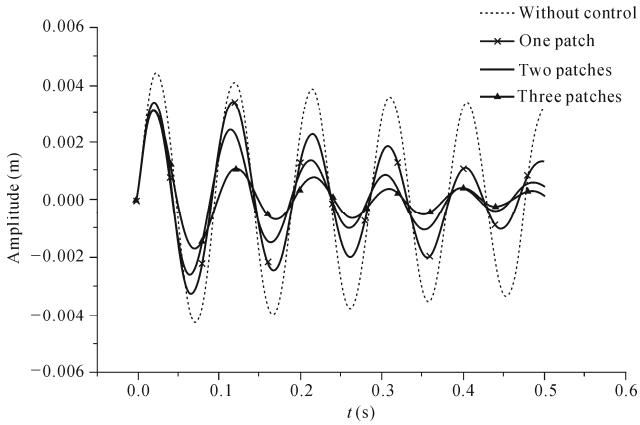


Fig. 9.9 Time response of 3rd mode with different numbers of patches for simply supported plate

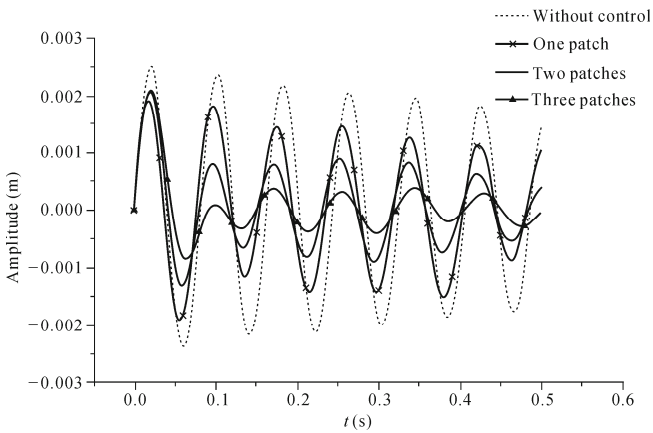


Fig. 9.10 Time response of 4th mode with different numbers of patches for simply supported plate

In order to investigate the distribution of the piezoelectric patches, different cases based on different controlled vibration modes are studied. In these cases, the feedback control gain matrix G is set as a constant 10.0 to emphasize the optimal distribution of the piezoelectric patches. The first six vibration modes are considered with the initial conditions $\eta(0)^T = [0 \ 0 \ 0 \ 0 \ 0 \ 0]$ and $\dot{\eta}(0)^T = [0.5 \ 0.4 \ 0.3 \ 0.2 \ 0.2 \ 0.1]$. The optimal geometric distributions of the piezoelectric patches are shown in Table 9.3. The schematic illustration of Table 9.3 is graphically shown in Fig. 9.11, in which the dashed line denotes the nodal line of the vibration modes and the areas filled with diagonals represent the piezoelectric patches bonded to the plate. In Table 9.3 and Fig. 9.11, the case of $m=i, n=j, (i=1,2, j=1,2,3)$ means that $i \times j$ vibration modes are simultaneously considered. From the results, we can find that, for specific controlled vibration modes, the optimal distribution of piezoelectric S/As is located in the areas separated by the nodal lines to achieve optimal control effect. This implies that, for specific controlled modes, certain number of piezoelectric patches is needed to achieve optimal control effect. For example, for the case of $m=1, n=1, i.e.,$ only the first vibration mode is considered, one patch is adequate as the number of areas formed by the nodal lines is one; and for the case of $m=2, n=3, i.e.,$ 6 vibration modes are considered, eight patches are required as there are eight areas formed by the nodal lines. The above finding is hereafter referred to as “nodal line separating patch.”

In order to show that it is better to position the piezoelectric patches within the areas separated by the nodal lines and support the above two explanation points, a design with two pieces of piezoelectric patches which are asymmetric and located across the nodal line, is investigated to compare the control effect with the case of $m=2$ and $n=1$. Assume the x coordinates of the edges of the two patches are $x_{11}=0.1130$ m, $x_{12}=0.7$ m, and $x_{21}=0.7$ m, $x_{22}=0.8871$ m, respectively. The y coordinates are the same as those obtained using the optimization method shown in Table 9.3. These two patches are schematically shown in Fig. 9.12. The objective function value for the case with piezoelectric patches located across the nodal line is 0.3117. However, for the case with piezoelectric patches located within the areas separated by nodal lines, the objective function value is 0.2982. From the objective function values, it is apparent that the latter is better. The time behaviors of the second vibration mode with the two piezoelectric patch designs are shown in Fig. 9.13. It can be seen that the vibration can be suppressed more effectively when the piezoelectric patches are located within the area separated by the nodal lines compared with the design that the piezoelectric patches are located across the nodal lines.

Table 9.3 Optimal S/A positions with various controlled modes for simply supported plate

n	$m=1$	$m=2$
	$x_{i1} - x_{i2}, y_{i1} - y_{i2}$	$x_{i1} - x_{i2}, y_{i1} - y_{i2}$
1	0.1290–0.8710 m, 0.2580–1.7420 m	0.1130–0.5017 m, 0.2580–1.7420 m 0.5017–0.8871 m, 0.2580–1.7420 m
2	0.1290–0.8710 m, 0.1919–1.0141 m 0.1290–0.8710 m, 1.0141–1.8087 m	0.1189–0.5015 m, 0.1908–1.0056 m 0.1189–0.5015 m, 1.0056–1.8075 m 0.5015–0.8811 m, 0.1908–1.0056 m 0.5015–0.8811 m, 1.0056–1.8075 m
3	0.1290–0.8710 m, 0.1503–0.6807 m 0.1290–0.8710 m, 0.6807–1.0667 m 0.1290–0.8710 m, 1.0667–1.3948 m 0.1290–0.8710 m, 1.3948–1.8568 m	0.1150–0.5089 m, 0.1354–0.6578 m 0.1150–0.5089 m, 0.6578–0.9894 m 0.1150–0.5089 m, 0.9894–1.3263 m 0.1150–0.5089 m, 1.3263–1.8540 m 0.5089–0.8844 m, 0.1354–0.6578 m 0.5089–0.8844 m, 0.6578–0.9894 m 0.5089–0.8844 m, 0.9894–1.3263 m 0.5089–0.8844 m, 1.3263–1.8540 m

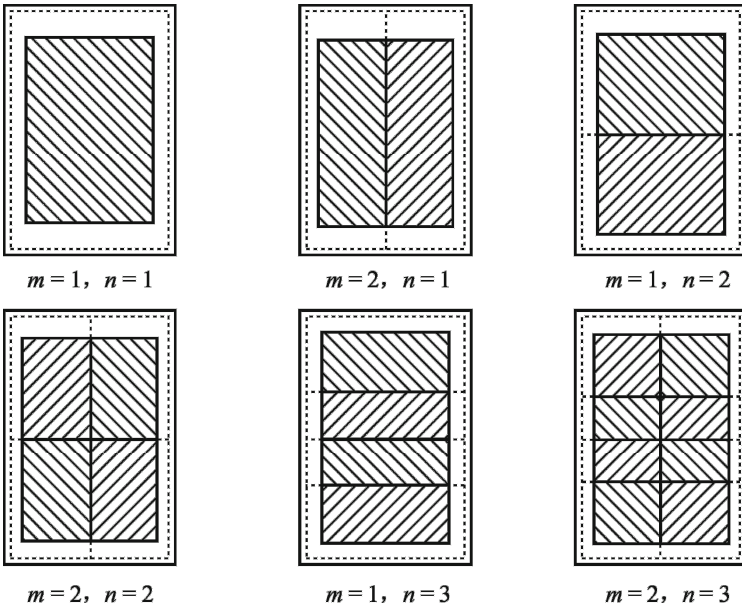


Fig. 9.11 Optimal geometric distributions of piezoelectric patches for different vibration modes of simply supported plate

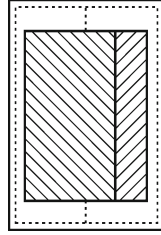


Fig. 9.12 Two pieces of piezoelectric patches which are asymmetric and located across the nodal line ($m = 2$ and $n = 1$)

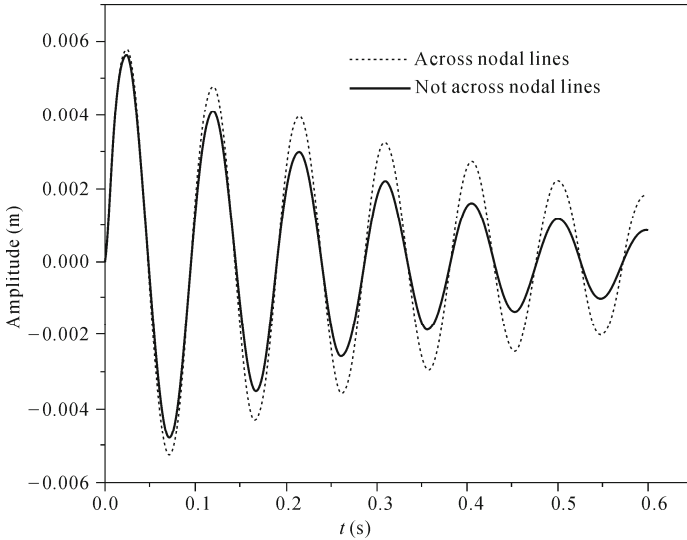


Fig. 9.13 Time response of the second vibration mode of the simply supported plate for the two piezoelectric patch designs

• *Simply Supported Cylindrical Shell*

Consider the cylindrical shell shown in Fig. 9.2 with four edges simply supported. The material properties and dimensions of the system are listed in Table 9.4, which are cited from Yang *et al.* (2006).

Substituting the mode shape functions $U_{pq}(x, \beta) = \sin(p\pi x / L)\sin(q\pi\beta / \beta^*)$ into Eqs. (9.18) and (9.19), we obtain the coefficients of the simply supported cylindrical shell in the state matrix as

$$B_{ki} = \frac{4e_{31}}{\rho h} \cdot \left\{ \frac{1}{pq\pi^2 R} + r_a \left[\frac{p}{qL^2} + \frac{q}{p(R\beta^*)^2} \right] \right\} \cdot T_{pqi} \quad (9.43)$$

$$C_{ik} = \frac{h^s e_{31}}{S_i^e \epsilon_{33}} \left[\frac{\beta^* L}{p q \pi^2} + r^s \left(\frac{p R \beta^*}{q L} + \frac{q L}{p R \beta^*} \right) \right] \cdot T_{pqi} \quad (9.44)$$

in which $T_{pqi} = [\cos(p\pi x_{i1} / L) - \cos(p\pi x_{i2} / L)][\cos(q\pi \beta_{i1} / \beta^*) - \cos(q\pi \beta_{i2} / \beta^*)]$.

Table 9.4 Cylindrical shell and piezoelectric patch specifications

Item	Shell	Actuators	Sensors
Mass density (kg/m ³)	7800	7600	1780
Young's modulus (GPa)	210	1.6	1.6
Poisson's ration	0.3	0.3	0.3
Piezo-constant d_{31} (m/V)		6×10^{-12}	30×10^{-12}
Piezo-constant e_{31} (N/(V·m))		0.0096	0.048
Permittivity constant ϵ_{33} (F/m)			8.85×10^{-9}
Thickness (m)	0.001		
Length (m)	1.0		
Curvature angle (rad)	$\pi/3$	0.0004	0.0004
Radius (m)	1.2		
Damping ratio	0.01		

Similar to the simply supported plate model, the first four modes are considered to be the controlled modes. The initial conditions and the control parameters for the modified GA are the same as those for the plate model.

Again, three cases with one to three pieces of piezoelectric patches are studied. The optimization results are shown in Table 9.5. The time behaviors of the vibration modes without control and with control using one to three pieces of piezoelectric patches are shown in Figs. 9.14–9.17. From Table 9.5 and Figs. 9.14–9.17, similar conclusion can be drawn that the control effect can be significantly enhanced when more pieces of patches are used.

Table 9.5 Optimal S/A positions and feedback gains for simply supported cylindrical shell

N_p	Location of the patches		Feedback gain matrix	Objective Function $\varphi(\bar{X}, G)$
	$x_{i1} - x_{i2}$,	$\beta_{i1} - \beta_{i2}$		
1	0.0879–0.7185 m, 0.0767–0.5514 rad		[100]	0.0052
2	0.0866–0.7045 m, 0.0851–0.5130 rad 0.3514–0.9175 m, 0.5130–0.9615 rad		$\begin{bmatrix} 100 & 1.68 \\ 0 & 100 \end{bmatrix}$	0.0034
3	0.0962–0.7660 m, 0.0870–0.5035 rad 0.3769–0.8042 m, 0.5036–0.9880 rad 0.8042–0.8693 m, 0.5606–0.8623 rad		$\begin{bmatrix} 100 & 0.19 & 0.58 \\ 0.17 & 100 & 100 \\ 1.27 & 98.8 & 99.98 \end{bmatrix}$	0.0027

Optimal geometric distributions of the piezoelectric patches for specific controlled vibration modes are also calculated. The results are listed in Table 9.6 and plotted in Fig. 9.18. It is observed that, similar to the simply supported plate model, for specific controlled vibration modes the optimal distribution of piezoelectric S/As is located in the areas separated by the nodal lines to achieve optimal control effect; that is, the conclusion of “nodal line separating patch” is applicable.

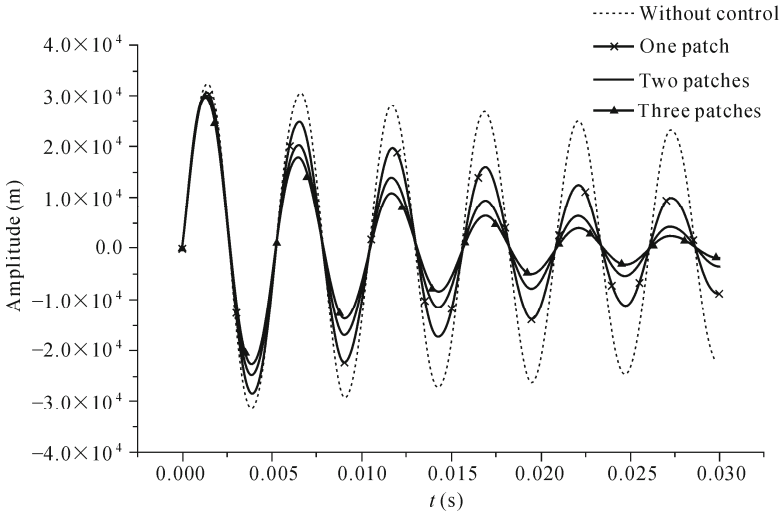


Fig. 9.14 Time response of 1st mode with different numbers of patches for simply supported cylindrical shell

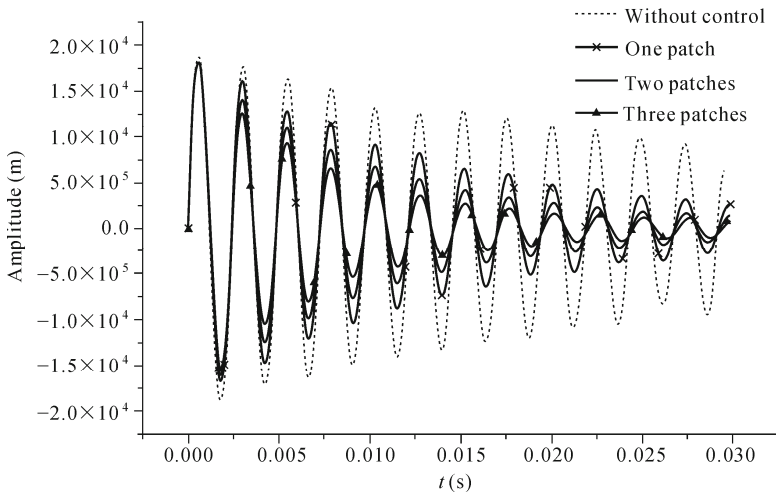


Fig. 9.15 Time response of 2nd mode with different numbers of patches for simply supported cylindrical shell

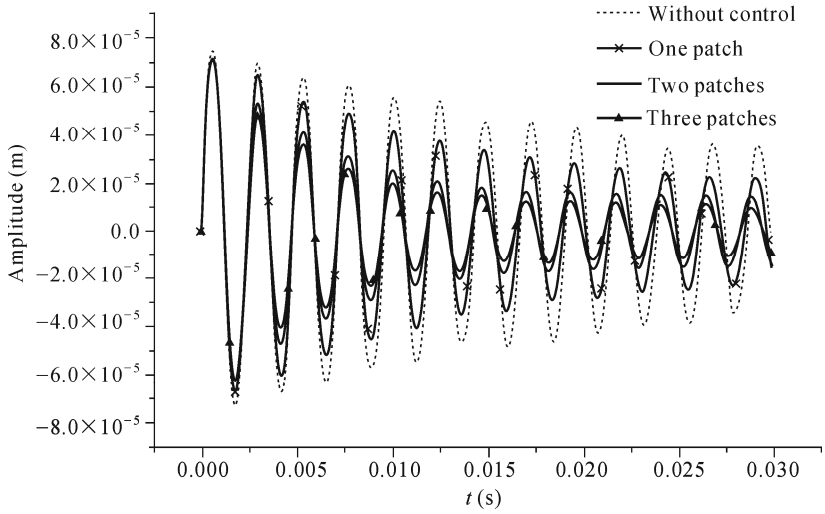


Fig. 9.16 Time response of 3rd mode with different numbers of patches for simply supported cylindrical shell

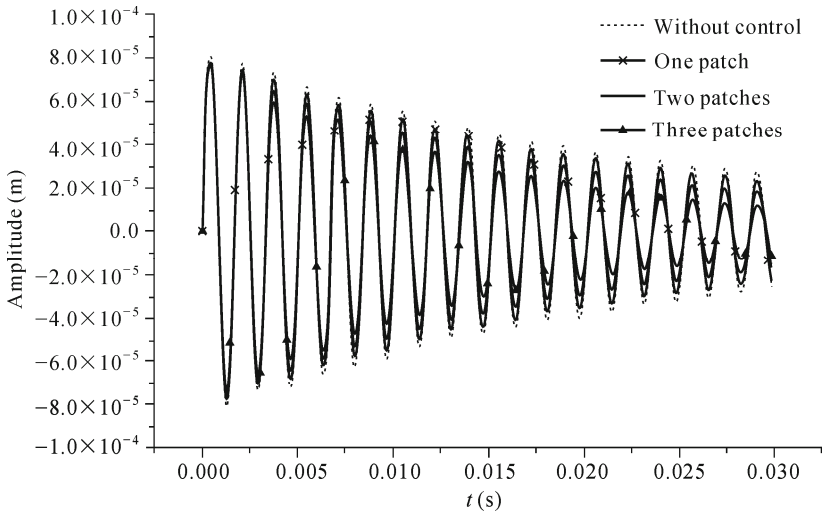


Fig. 9.17 Time response of 4th mode with different numbers of patches for simply supported cylindrical shell

Table 9.6 Optimal S/A positions with various controlled modes for simply supported cylindrical shell

n	$m=1$	$m=2$
	$x_{i1} - x_{i2}, \beta_{i1} - \beta_{i2}$	$x_{i1} - x_{i2}, \beta_{i1} - \beta_{i2}$
1	0.1290–0.8710 m, 0.1352–0.9121 rad	0.0992–0.5000 m, 0.1351–0.9121 rad 0.5000–0.9009 m, 0.1351–0.9121 rad
2	0.1290–0.8710 m, 0.0741–0.5221 rad 0.1290–0.8710 m, 0.5252–0.9731 rad	0.1133–0.5005 m, 0.0751–0.5237 rad 0.5005–0.8866 m, 0.0751–0.5237 rad 0.1133–0.5005 m, 0.5237–0.9721 rad 0.5005–0.8866 m, 0.5237–0.9721 rad
3	0.1290–0.8715 m, 0.0787–0.3564 rad 0.1290–0.8715 m, 0.3564–0.5585 rad 0.1290–0.8715 m, 0.5585–0.7303 rad 0.1290–0.8715 m, 0.7303–0.9722 rad	0.1190–0.4967 m, 0.0418–0.3346 rad 0.4967–0.8832 m, 0.0418–0.3346 rad 0.1190–0.4967 m, 0.3346–0.5190 rad 0.4967–0.8832 m, 0.3346–0.5190 rad 0.1190–0.4967 m, 0.5190–0.6897 rad 0.4967–0.8832 m, 0.5190–0.6897 rad 0.1190–0.4967 m, 0.6897–0.9638 rad 0.4967–0.8832 m, 0.6897–0.9638 rad

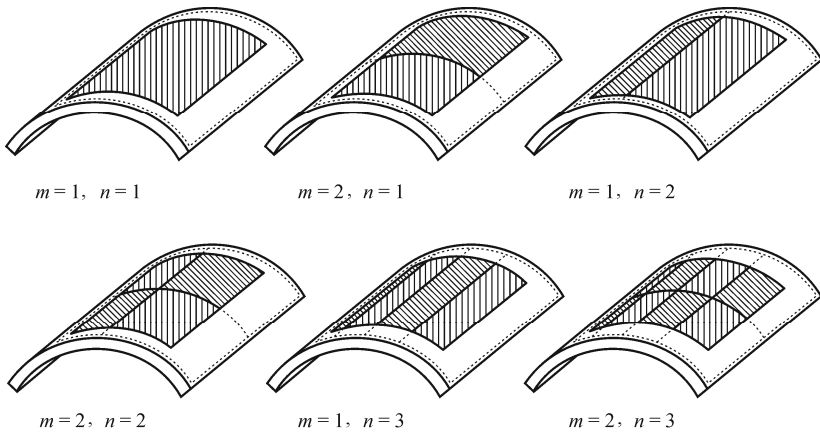


Fig. 9.18 Optimal geometric distributions of piezoelectric patches with different vibration modes of simply supported cylindrical shell

9.1.5.3 Clamped-Simply Supported Plate

One similarity of the previous two examples is that the boundary conditions are symmetric. In this example, un-symmetric boundary conditions are considered to examine whether the above finding of “nodal line separating patch” is still applicable.

Consider a plate with un-symmetric boundary conditions, *i.e.*, three edges simply supported and one edge clamped (Fig. 9.4) where the edge $y=a$ is clamped.

The material properties and dimensions of the system are identical with the simply supported plate, as listed in Table 9.1.

In order to investigate the optimal geometric distributions of the piezoelectric patches for specific vibration modes, the first six vibration modes with the following initial conditions are considered:

$$\begin{aligned}\eta(0)^T &= [0 \ 0 \ 0 \ 0 \ 0 \ 0] \\ \dot{\eta}(0)^T &= [0.1 \ 0.2 \ 0.2 \ 0.3 \ 0.4 \ 0.5]\end{aligned}$$

The feedback control gain matrix G is set as a constant 100.0 to emphasize the optimal distribution of the piezoelectric patches.

The mode shape function U_{pq} of the clamped-simply supported plate can be expressed as:

$$U_{pq} = [\sin(\lambda_{pq}y) - r_{pq} \cdot \sinh(v_{pq}y)] \cdot \sin(p\pi x / L), \quad (9.45)$$

where $\lambda_{pq}^2 = \beta_{pq}^2 - p^2\pi^2 / L^2$; $r_{pq} = \sin(\lambda_{pq} \cdot a) / \sinh(v_{pq} \cdot a)$; $v_{pq}^2 = \beta_{pq}^2 + p^2\pi^2 / L^2$; $\beta_{pq}^2 = \omega_{pq} \sqrt{\rho h / D_0}$; $D_0 = Eh^3 / [12(1 - \mu^2)]$; and β_{pq} satisfies the following frequency equation:

$$\frac{\tan(\lambda_{pq}a)}{\lambda_{pq}} = \frac{\tanh(v_{pq}a)}{v_{pq}} \quad (9.46)$$

Substituting Eq. (9.45) into Eqs. (9.26) and (9.27), the coefficients in the state matrix are obtained as:

$$B_{ki} = \frac{-r_a e_{31}}{\rho h N_{pq}} \cdot T_{pqi} \quad \text{and} \quad C_{ik} = \frac{r^s h^s e_{31} L}{S_i^e \epsilon_{33}} \cdot T_{pqi} \quad (9.47)$$

where

$$\begin{aligned}N_{pq} &= r_{pq} [v_{pq} \cdot \cosh(v_{pq}a) \sin(\lambda_{pq}a) - \lambda_{pq} \\ &\quad \cdot \cos(\lambda_{pq}a) \sinh(v_{pq}a)] / (\lambda_{pq}^2 + v_{pq}^2) \\ &\quad + \sin(2a\lambda_{pq}) / (8\lambda_{pq}) - r_{pq}^2 \sinh(2av_{pq}) / (8v_{pq}) + a(r_{pq}^2 - 1) / 4\end{aligned} \quad (9.48)$$

$$\begin{aligned}T_{pqi} &= \beta_{pq}^2 / (p\pi) \cdot [\cos(p\pi x_{i1} / L) - \cos(p\pi x_{i2} / L)] \\ &\quad \cdot \{ [\cos(\lambda_{pq}y_{i1}) - \cos(\lambda_{pq}y_{i2})] / \lambda_{pq} \\ &\quad - r_{pq} [\cosh(v_{pq}y_{i1}) - \cosh(v_{pq}y_{i2})] / v_{pq} \}\end{aligned} \quad (9.49)$$

Using the above coefficients, optimal geometric distributions of the piezoelectric patches for specific controlled vibration modes are calculated. The results are

listed in Table 9.7 and plotted in Fig. 9.19. Similar to the simply supported plate and shell models, it is found that the conclusion of “nodal line separating patch” is still applicable to the un-symmetric boundary conditions studied in this example.

Table 9.7 Optimal S/A positions with various controlled modes for clamped-simply supported plate

<i>n</i>	<i>m</i> =1	<i>m</i> =2
	$x_{i1} - x_{i2}, y_{i1} - y_{i2}$	$x_{i1} - x_{i2}, y_{i1} - y_{i2}$
1	0.1290–0.8710 m, 0.2324–1.5421 m	0.0678–0.4679 m, 0.2415–1.6184 m
		0.5322–0.9322 m, 0.2415–1.6184 m
2	0.1290–0.8710 m, 0.1246–0.8585 m 0.1290–0.8710 m, 0.9832–1.6828 m	0.0695–0.4852 m, 0.1301–0.9072 m
		0.0695–0.4852 m, 0.9733–1.7294 m
		0.5148–0.9305 m, 0.1301–0.9072 m
		0.5148–0.9305 m, 0.9733–1.7294 m
3	0.1290–0.8710 m, 0.0996–0.6230 m 0.1290–0.8710 m, 0.6230–0.9140 m 0.1290–0.8710 m, 0.9140–1.2396 m 0.1290–1.8710 m, 1.2396–1.7293 m	0.0668–0.4579 m, 0.0990–0.6179 m
		0.0668–0.4579 m, 0.6179–0.9121 m
		0.0668–0.4579 m, 0.9121–1.2531 m
		0.0668–0.4579 m, 1.2531–1.7842 m
		0.5423–0.9332 m, 0.0990–0.6179 m
		0.5423–0.9332 m, 0.6179–0.9121 m
		0.5423–0.9332 m, 0.9121–1.2531 m
		0.5423–0.9332 m, 1.2531–1.7842 m

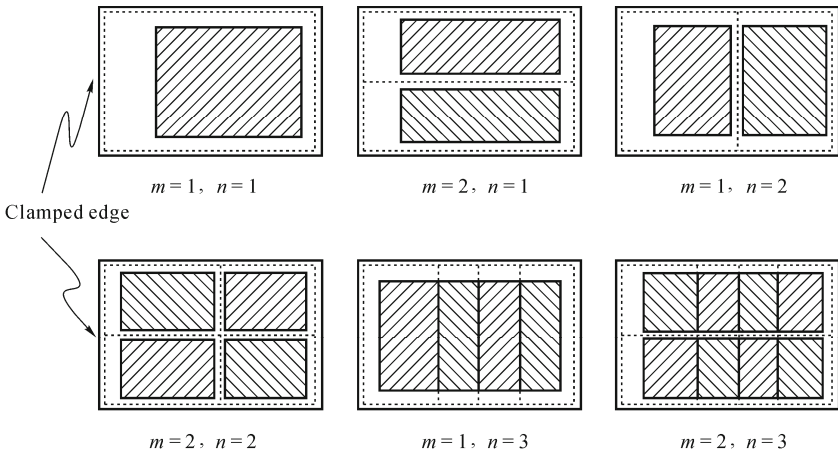


Fig. 9.19 Optimal geometric distributions of piezoelectric patches with different vibration modes of clamped-simply supported plate

This phenomenon could be physically explained by the following two points. First, at both sides of the nodal line, the signs of the strains of the vibration mode are opposite (the strain is related to the second order derivative of the vibration mode). Fig. 9.20 illustrates the second mode shapes of the simply supported plate, simply supported cylindrical shell and clamped-simply supported plate, and the

corresponding second order derivatives with respect to y (or β) which are related to the strains at the y (or β) direction. It can be observed that at both sides of the nodal line, the signs of the strains are opposite for all these structures. If a piezoelectric sensor locates across the nodal line, the output voltage which depends on the integration of strain over the surface of the sensor will decrease because the two sides of the nodal line will generate opposite charges over the sensor, which counteract each other. Thus, the sensor signal fed back to the actuator will decrease or even become nil. Accordingly, the control force generated by the actuator will become smaller and the control effect will be impaired. Second, at both sides of the nodal line, the vibration of the structure has opposite directions (Fig. 9.20). If a piezoelectric actuator locates across the nodal line, the control force generated by the actuator will suppress the vibration at one side, but accelerate the vibration at the other side. Thus the entire control effect contributed by the control force is weakened.

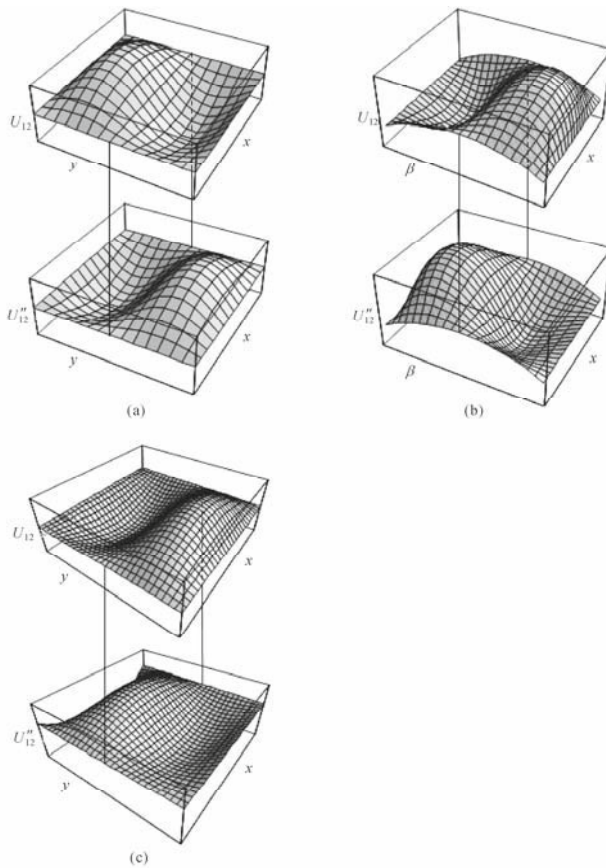


Fig. 9.20 2nd modal shapes and corresponding 2nd order derivatives with respect to y (β). (a) Simply supported plate; (b) Simply supported cylindrical shell; (c) clamped-simply supported plate

The conclusion that the optimal distribution of piezoelectric S/As is located in the region separated by the vibration nodal lines for the simply supported plate, simply supported cylindrical shell and clamped-simply supported plate structures provides a meaningful and referable criterion for practical positioning of piezoelectric patches. However, applicability of the above conclusion for other types of plates/shells with different boundary conditions needs further investigation.

9.2 Optimal Excitation of Piezoelectric Plates and Shells

9.2.1 Introduction

The applications of piezoelectric materials are usually associated with a host structure, such as beam or plate. Several analytical and numerical models have been introduced in the literature to describe the behaviors of structures with piezoelectric actuators. In addition to the extensive studies on the interactions between S/As and host structures, an important issue is how to optimally place the sensors and actuators on the host structures. Appropriate placement of actuators would promote system efficiency, improve controllability and observability, as well as save material and energy. As mentioned in Section 9.1.1, several researchers have studied the optimal placement of piezoelectric S/As from the vibration control perspective.

In many engineering applications, due to the assembly process, plates are placed on elastic media which act as elastic foundations, and subjected to in-plane forces. Furthermore, previous researches on optimal placement of sensors and actuators have focused on beam and plate vibration control. In certain applications, excitation of vibration is desirable. Therefore, it is meaningful to study the optimal placement of actuators from the perspective of maximizing the plate/shell vibration. However, in the literature, this kind of optimal placement of PZT actuators has received little attention.

In this section, an analytical model of a simply supported rectangular plate subjected to in-plane forces, resting on an elastic foundation and actuated by a PZT actuator, is introduced. The formulation and solution procedures are then applied to a simply supported cylindrical shell on an elastic foundation actuated by a pair of collocated PZT actuators. Based on the analytical solutions obtained, the optimal placement of PZT actuator in terms of maximizing the plate/shell deflection is calculated and discussed. A simple yet general procedure to determine the optimal excitation locations of the PZT actuator is presented.

9.2.2 Piezoelectric Actuated Plates

• Problem Formulation

Fig.9.21 shows a rectangular plate with length a , width b and thickness h , bonded on an elastic foundation. The plate is bonded with a PZT actuator of thickness h_p on the surface. The PZT actuator is assumed to be perfectly bonded and its stiffness is neglected due to its limited contribution to the dynamic behavior of the plate. x, y and z are the global coordinates defined in the mid-plane of the plate, and ξ and η are the normalized coordinates in the xy plane.

Under plane stress condition, the constitutive relations of the plate are

$$\begin{bmatrix} \sigma_{xx} \\ \sigma_{yy} \\ \sigma_{xy} \end{bmatrix} = \frac{E}{1-\nu^2} \begin{bmatrix} 1 & \nu & 0 \\ \nu & 1 & 0 \\ 0 & 0 & 1-\nu \end{bmatrix} \begin{bmatrix} \varepsilon_{xx} \\ \varepsilon_{yy} \\ \varepsilon_{xy} \end{bmatrix} \quad (9.50)$$

where σ_{xx}, σ_{yy} and σ_{xy} are the normal stress in the x direction, normal stress in the y direction and shear stress in the xy plane, respectively; $\varepsilon_{xx}, \varepsilon_{yy}$ and ε_{xy} are the corresponding normal and shear strains; E is the Young's modulus of the plate; and ν is the Poisson's ratio of the plate.

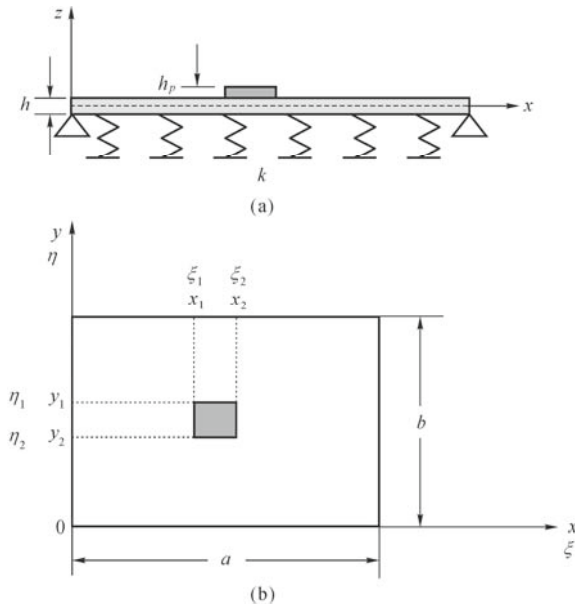


Fig. 9.21 (a) Plate and PZT actuator system; (b) Plate and PZT actuator coordinate system

The strain-displacement relations of von Karman's plate theory are

$$\begin{bmatrix} \varepsilon_{xx} \\ \varepsilon_{yy} \\ \varepsilon_{xy} \end{bmatrix} = \begin{bmatrix} \frac{\partial u}{\partial x} - z \frac{\partial^2 w}{\partial x^2} + \frac{1}{2} \left(\frac{\partial w}{\partial x} \right)^2 \\ \frac{\partial v}{\partial y} - z \frac{\partial^2 w}{\partial y^2} + \frac{1}{2} \left(\frac{\partial w}{\partial y} \right)^2 \\ \frac{\partial u}{\partial y} + \frac{\partial v}{\partial x} - 2z \frac{\partial^2 w}{\partial x \partial y} + \frac{\partial w}{\partial x} \frac{\partial w}{\partial y} \end{bmatrix} \quad (9.51)$$

where u , v and w are the displacements of mid-plane of the plate in the x , y and z directions, respectively.

Using the Hamilton's principle, the governing equations of the plate can be derived as (Yang and Zhang, 2006)

$$-\frac{Eh}{1-\nu^2} \frac{\partial^2 u}{\partial x^2} - \frac{Eh}{2(1+\nu)} \frac{\partial^2 u}{\partial y^2} - \frac{Eh}{2(1-\nu)} \frac{\partial^2 v}{\partial x \partial y} + \rho h \frac{\partial^2 u}{\partial t^2} = -q_1(x, y, t) \quad (9.52)$$

$$-\frac{Eh}{1-\nu^2} \frac{\partial^2 v}{\partial y^2} - \frac{Eh}{2(1+\nu)} \frac{\partial^2 v}{\partial x^2} - \frac{Eh}{2(1-\nu)} \frac{\partial^2 u}{\partial x \partial y} + \rho h \frac{\partial^2 v}{\partial t^2} = -q_2(x, y, t) \quad (9.53)$$

$$D \nabla^4 w - \frac{\partial}{\partial x} \left(N_x \frac{\partial w}{\partial x} \right) - \frac{\partial}{\partial y} \left(N_y \frac{\partial w}{\partial y} \right) - \frac{\partial}{\partial y} \left(N_{xy} \frac{\partial w}{\partial x} \right) + \frac{\partial}{\partial x} \left(N_{xy} \frac{\partial w}{\partial y} \right) + \rho h \frac{\partial^2 w}{\partial t^2} + c \frac{\partial w}{\partial t} + kw = -q_3(x, y, t) \quad (9.54)$$

where ρ is the material density of the plate; c is the plate damping per unit area; k is the stiffness of elastic foundation; $D = Eh^3 / [12(1-\nu^2)]$ is the bending rigidity of the plate; $N_x = \int_{-h/2}^{h/2} \sigma_{xx} dz$, $N_y = \int_{-h/2}^{h/2} \sigma_{yy} dz$ and $N_{xy} = \int_{-h/2}^{h/2} \sigma_{xy} dz$ are the stress resultants in the x , y directions and the xy plane, respectively. The in-plane forces $q_1(x, y, t)$ and $q_2(x, y, t)$ applied by the PZT actuator are

$$q_1(x, y, t) = -E_p d_{31} V(t) [\delta(x-x_1) - \delta(x-x_2)] \cdot [H(y-y_1) - H(y-y_2)] \quad (9.55)$$

$$q_2(x, y, t) = -E_p d_{31} V(t) [H(x-x_1) - H(x-x_2)] \cdot [\delta(y-y_1) - \delta(y-y_2)] \quad (9.56)$$

where E_p is the Young's modulus of the PZT actuator; d_{31} is the piezoelectric constant; $V(t)$ is the voltage applied on the PZT actuator; x_1 , x_2 , y_1 and y_2 are the coordinates of the four corners of the PZT actuator (Fig.9.21); $\delta(\cdot)$ is the Dirac

delta function and $H(\cdot)$ is the Heaviside function; $q_3(x, y, t) = \frac{\partial^2 M_{px}}{\partial x^2} + \frac{\partial^2 M_{py}}{\partial y^2}$

with M_{px} and M_{py} being the moments applied by the PZT actuator which can be expressed as

$$M_{px} = -E_p d_{31} V(t) \frac{h_p + h}{2} [H(x - x_1) - H(x - x_2)] \cdot [H(y - y_1) - H(y - y_2)] \quad (9.57)$$

$$M_{py} = -E_p d_{31} V(t) \frac{h_p + h}{2} [H(y - y_1) - H(y - y_2)] \cdot [H(x - x_1) - H(x - x_2)] \quad (9.58)$$

Since the transverse vibration is the main concern of this study, by assuming that the plate is subjected to constant in-plane forces $N_x = N_x^0$, $N_y = N_y^0$ and $N_{xy} = 0$, Eq.(9.54) can be simplified as:

$$D \nabla^4 w - N_x^0 \frac{\partial^2 w}{\partial x^2} - N_y^0 \frac{\partial^2 w}{\partial y^2} + \rho h \frac{\partial^2 w}{\partial t^2} + c \frac{\partial w}{\partial t} + kw = -q_3(x, y, t) \quad (9.59)$$

The above equation can be normalized by letting $\xi = \frac{x}{a}$, $\eta = \frac{y}{b}$ and $\beta = \frac{a}{b}$,

$$\begin{aligned} & \frac{\partial^4 w}{\partial \xi^4} + 2\beta^2 \frac{\partial^4 w}{\partial \xi^2 \partial \eta^2} + \beta^4 \frac{\partial^4 w}{\partial \eta^4} - a^2 \frac{N_x^0}{D} \frac{\partial^2 w}{\partial \xi^2} - a^2 \beta^2 \frac{N_y^0}{D} \frac{\partial^2 w}{\partial \eta^2} \\ & + a^4 \frac{\rho h}{D} \frac{\partial^2 w}{\partial t^2} + a^4 \frac{c}{D} \frac{\partial w}{\partial t} + a^4 \frac{k}{D} w = -a^4 \frac{q_3(\xi, \eta, t)}{D} \end{aligned} \quad (9.60)$$

where

$$\begin{aligned} q_3(\xi, \eta, t) &= \frac{\partial^2 M_{p\xi}}{a^2 \partial \xi^2} + \frac{\beta^2 \partial^2 M_{p\eta}}{a^2 \partial \eta^2} \\ &= \frac{-E_p d_{31} V(t) (h_p + h)}{2a^2} \{ [\delta'(\xi - \xi_1) - \delta'(\xi - \xi_2)] \cdot [H(\eta - \eta_1) - H(\eta - \eta_2)] \\ & \quad + \beta^2 [\delta'(\eta - \eta_1) - \delta'(\eta - \eta_2)] \cdot [H(\xi - \xi_1) - H(\xi - \xi_2)] \} \end{aligned} \quad (9.61)$$

ξ_1, ξ_2, η_1 and η_2 are the normalized coordinates of the four corners of the PZT actuator (Fig. 9.21); and $\delta'(\cdot)$ is the derivative of the Dirac delta function.

The governing equation of Eq. (9.60) is applicable to all thin plates regardless of the boundary conditions. Eq. (9.60) can be solved by the method of separation of variables. In this method, the solution can be assumed to be the product of a function of position $\Phi(\xi, \eta)$ and a function of time $f(t)$. For a simply supported plate, the solution can be expressed as

$$w(\xi, \eta, t) = \sum_{n=1}^{\infty} \sum_{m=1}^{\infty} \sin(m\pi\xi) \sin(n\pi\eta) f_{mn}(t) \quad (9.62)$$

Substituting the solution into Eq. (9.60), multiplying both sides with $\int_0^1 \int_0^1 \sin(m^* \pi \xi) \sin(n^* \pi \eta) d\xi d\eta$ and using the mode orthogonality, we get

$$\begin{aligned} & \ddot{f}_{m^*n^*}(t) + \frac{c}{\rho h} \dot{f}_{m^*n^*}(t) \\ & + \frac{ka^4 + (D \cdot (m^{*4} \pi^4 + 2\beta^2 m^{*2} n^{*2} \pi^4 + \beta^4 n^{*4} \pi^4) + a^2 N_x^0 m^{*2} \pi^2 + a^2 \beta^2 N_y^0 n^{*2} \pi^2)}{a^4 \rho h} \quad (9.63) \\ & \times f_{m^*n^*}(t) = -\frac{4}{\rho h} \int_0^1 \int_0^1 q_3(\xi, \eta, t) \sin(m^* \pi \xi) \sin(n^* \pi \eta) d\xi d\eta \end{aligned}$$

Letting $m = m^*, n = n^*, \Omega = \frac{c}{2\rho h}$,

$$\begin{aligned} \omega_{mm}^2 = & \frac{1}{a^4 \rho h} [ka^4 + D \cdot (m^4 \pi^4 + 2\beta^2 m^2 n^2 \pi^4 + \beta^4 n^4 \pi^4) \\ & + (a^2 N_x^0 m^2 \pi^2 + a^2 \beta^2 N_y^0 n^2 \pi^2)] \quad (9.64) \end{aligned}$$

and

$$Q_{mn}(\xi, \eta, t) = -\frac{4}{\rho h} \int_0^1 \int_0^1 q_3(\xi, \eta, t) \sin(m\pi\xi) \sin(n\pi\eta) d\xi d\eta \quad (9.65)$$

Eq. (9.63) can be rewritten in a simple form as

$$\ddot{f}_{mn}(t) + 2\Omega \dot{f}_{mn}(t) + \omega_{mn}^2 f_{mn}(t) = Q_{mn}(\xi, \eta, t) \quad (9.66)$$

where ω_{mn} is the natural frequency of the plate and $Q_{mn}(\xi, \eta, t)$ represents the excitation force provided by the PZT actuator.

The homogeneous solution to Eq.(9.66) is

$$f_{mn}^h(t) = \begin{cases} C_1 e^{(-\Omega - \sqrt{\Omega^2 - \omega_{mn}^2})t} + C_2 e^{(-\Omega + \sqrt{\Omega^2 - \omega_{mn}^2})t} & \Omega^2 - \omega_{mn}^2 \neq 0 \\ (C_1 + C_2 t) e^{-\Omega t} & \Omega^2 - \omega_{mn}^2 = 0 \end{cases} \quad (9.67)$$

If the PZT actuator is driven by a sinusoidal voltage, *i.e.*, $V(t) = V_0 \sin(\omega t)$ and $Q_{mn}(\xi, \eta, t) = Q_{mn}(\xi, \eta) \sin(\omega t)$, the particular solution can be written as:

$$f_{mn}^p(t) = C_3 \sin(\omega t) + C_4 \cos(\omega t) \quad (9.68)$$

where ω is the angular driving frequency of the PZT actuator.

Substituting Eq. (9.68) into Eq. (9.66), we obtain

$$f_{nn}^p(t) = R_{nn} \sin \omega t + \frac{2R_{nn}\Omega\omega}{\omega^2 - \omega_{nn}^2} \cos \omega t \tag{9.69}$$

where

$$R_{nn} = \frac{Q_{nn}(\xi, \eta)}{\omega_{nn}^2 - \omega^2 + 4\Omega^2\omega^2 / (\omega_{nn}^2 - \omega^2)} \tag{9.70}$$

Substituting $f_{nn}(t) = f_{nn}^h(t) + f_{nn}^p(t)$ into Eq. (9.66) and incorporating the initial conditions of the problem shown below:

$$f_{nn}|_{t=0} = 0, \quad \frac{df_{nn}}{dt}|_{t=0} = 0 \tag{9.71}$$

C_1 and C_2 become

$$C_1 = \frac{-\omega Q_{nn}(\xi, \eta)}{2\sqrt{\Omega^2 - \omega_{nn}^2} (2\Omega^2 + \omega^2 - \omega_{nn}^2 + 2\Omega\sqrt{\Omega^2 - \omega_{nn}^2})} \tag{9.72}$$

$$C_2 = \frac{\omega Q_{nn}(\xi, \eta)}{2\sqrt{\Omega^2 - \omega_{nn}^2} (2\Omega^2 + \omega^2 - \omega_{nn}^2 - 2\Omega\sqrt{\Omega^2 - \omega_{nn}^2})} \tag{9.73}$$

Thus, the final solution $f_{nn}(t) = f_{nn}^h(t) + f_{nn}^p(t)$ can be obtained from Eqs. (9.67), (9.69), (9.70), (9.72) and (9.73).

If the damping of plate is negligible, *i.e.*, $c=0$, we have $\Omega=0$; thus $\Omega^2 - \omega_{nn}^2 < 0$. For this case, the plate deflection is

$$w = \sum_{n=1}^{\infty} \sum_{m=1}^{\infty} \sin(m\pi\xi) \sin(n\pi\eta) \frac{Q_{nm}(\xi, \eta)}{\omega_{nm}^2 - \omega^2} \left[\sin \omega t - \frac{\omega}{\omega_{nm}} \sin \omega_{nm} t \right] \tag{9.74}$$

The steady-state response of the deflection is

$$w = \sum_{n=1}^{\infty} \sum_{m=1}^{\infty} \sin(m\pi\xi) \sin(n\pi\eta) \frac{Q_{nm}(\xi, \eta)}{\omega_{nm}^2 - \omega^2} \sin \omega t \tag{9.75}$$

From Eq. (9.65), $Q_{nm}(\xi, \eta)$ in Eq.(9.75) is

$$\begin{aligned}
Q_{mn}(\xi, \eta) = & \frac{-4M_0}{a^2 \rho h} \int_0^1 \int_0^1 \{ [\delta'(\xi - \xi_1) - \delta'(\xi - \xi_2)] \cdot [H(\eta - \eta_1) - H(\eta - \eta_2)] \\
& + \beta^2 [\delta'(\eta - \eta_1) - \delta'(\eta - \eta_2)] \cdot [H(\xi - \xi_1) - H(\xi - \xi_2)] \} \\
& \times \sin(m\pi\xi) \sin(n\pi\eta) d\xi d\eta
\end{aligned} \quad (9.76)$$

where $M_0 = -E_\nu d_{31} V_0 (h_p + h) / 2$.

After integration, we obtain

$$Q_{mn}(\xi, \eta) = \frac{4M_0}{a^2 \rho h} \left(\frac{m}{n} + \frac{n\beta^2}{m} \right) (\cos(m\pi\xi_2) - \cos(m\pi\xi_1)) (\cos(n\pi\eta_2) - \cos(n\pi\eta_1)) \quad (9.77)$$

By using the trigonometric formulas, the expression of the modal force can be transformed into

$$Q_{mn}(\xi, \eta) = \frac{16M_0}{a^2 \rho h} \left(\frac{m}{n} + \frac{n\beta^2}{m} \right) \sin(m\pi\xi_0) \sin(n\pi\eta_0) \sin(m\pi \cdot r_\xi) \sin(n\pi \cdot r_\eta) \quad (9.78)$$

where $\xi_0 = (\xi_1 + \xi_2) / 2$, $\eta_0 = (\eta_1 + \eta_2) / 2$, $r_\xi = (\xi_2 - \xi_1) / 2$ and $r_\eta = (\eta_2 - \eta_1) / 2$. ξ_0 and η_0 are the coordinates of the center of the PZT actuator in the $\xi - \eta$ plane, and r_ξ and r_η are the half dimensions of the PZT actuator in the ξ and η directions, respectively.

Therefore, the steady-state solution to Eq. (9.60) with negligible plate damping is

$$\begin{aligned}
w = & \sum_{n=1}^{\infty} \sum_{m=1}^{\infty} \frac{16M_0}{a^2 \rho h} \frac{\sin \omega t}{\omega_{mn}^2 - \omega^2} \left(\frac{m}{n} + \frac{n\beta^2}{m} \right) \sin(m\pi\xi_0) \sin(n\pi\eta_0) \\
& \times \sin(m\pi \cdot r_\xi) \sin(n\pi \cdot r_\eta) \sin(m\pi\xi) \sin(n\pi\eta)
\end{aligned} \quad (9.79)$$

If $N_x^0 = N_y^0 = 0$ and $k = 0$, Eq. (9.79) remains unchanged in form, which is the steady solution to the forced vibration of a simply supported plate without in-plane forces and elastic foundation. However, the natural frequency in Eq. (9.79) becomes $\omega_{mn}^2 = D(m^4\pi^4 + 2\beta^4 m^2 n^2 \pi^2 + \beta^4 n^4 \pi^4) / (a^4 \rho h)$, which is identical with Leissa's formula (Leissa, 1973). This result implicitly validates our solution.

• Illustrative Example

With the solution given in Eq. (9.79), we can obtain the plate deflection at any specified time. Figs. 9.22 and 9.23 depict the deflections of a rectangular plate

with $a=0.15m$ and $\beta=1.5$ excited by one PZT actuator at two different locations on the plate. The upper limits of m and n in Eq. (9.79) are set to be $m=150$ and $n=50$. The upper limits are chosen according to the convergence study as shown in Fig. 9.24. Figs. 9.22 and 9.23 are plotted for the time when the sinusoidal electric potential reaches its maximum value of 10 volts. The in-plane tensile force is $N_x^0 = N_y^0 = 10 \text{ N/m}$ and the foundation stiffness is $k = 7 \times 10^9 \text{ N/m}^3$. The material properties used in the calculation are listed in Table 9.8.

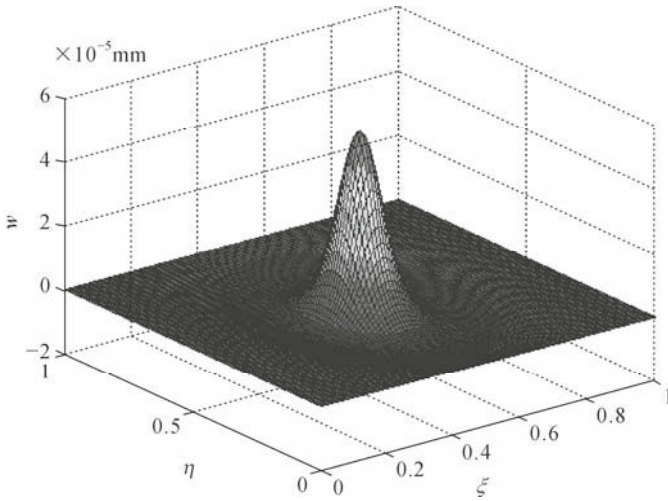


Fig. 9.22 Deflection of rectangular plate actuated by one PZT actuator at center ($\omega=18849.6 \text{ rad/s}$)

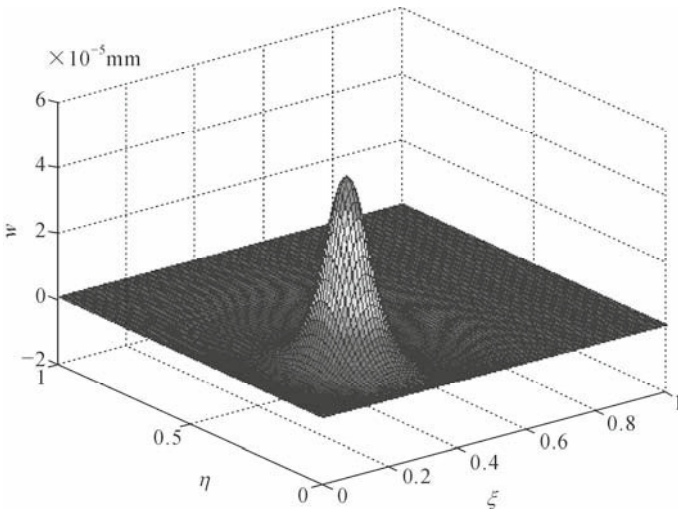


Fig. 9.23 Deflection of rectangular plate actuated by one PZT actuator at $\xi=\eta=0.3$ ($\omega=18849.6 \text{ rad/s}$)

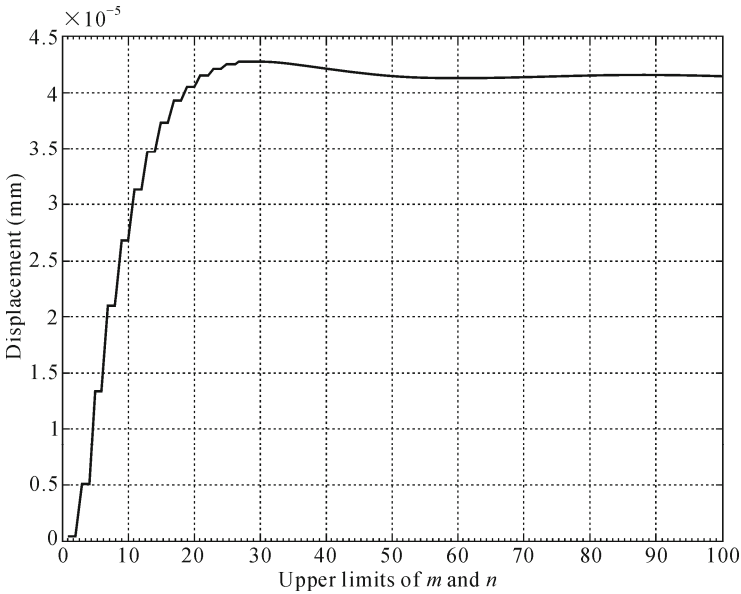


Fig. 9.24 Convergence of Eq. (9.79) vs. m and n

Table 9.8 Material properties and constants for plate and PZT

	Young's modulus (N/m ²)	Material density (kg/m ³)	Poisson's ratio	Dimension (mm)	Electric potential (V)	d_{31} (m/V)
Plate	7.03×10^{10}	2700	0.34	$a = 150$ $h = 2$	N.A.	N.A.
PZT	7.94×10^{10}	N.A.	0.30	$l_{px} = 0.1a$ $l_{pz} = 0.1a\beta$ $h_p = 0.2$	10	-1.3×10^{-10}

Note: N.A. means “not applicable”

9.2.3 Piezoelectric Actuated Cylindrical Shell

After solving the vibration problem of piezoelectric actuated plate, the formulation and solution procedure can be readily extended to piezoelectric actuated shell structures. Consider a thin cylindrical shell segment of length L , radius R , total cutout angle Φ and thickness h . The shell is bonded on an elastic foundation with stiffness k , and bonded with a pair of collocated PZT actuators with length l_p , width $R\theta_p$ and thickness h_p , which are driven by equal but opposite electric fields. The PZT actuators are assumed to be small and perfectly bonded, and thus their stiffness can be neglected.

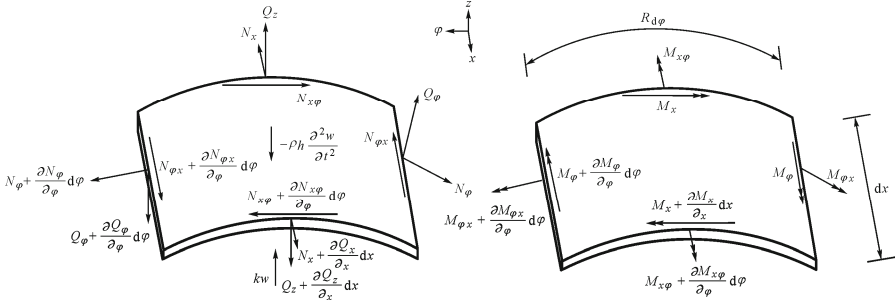


Fig. 9.25 Stress resultants on a shell element

Fig.9.25 illustrates the stress resultants acting on a differential element of the cylindrical shell, where Q_x and Q_ϕ are the shear force resultants of shear stresses τ_{xz} and $\tau_{\phi z}$, respectively; N_x , N_ϕ and $N_{x\phi}$ are the membrane forces in the x , ϕ directions and the $x\phi$ plane, respectively; w is the transverse displacement of the shell; ρ is the material density; t is time; and M_x , $M_{x\phi}$ and M_ϕ are the bending moments in the ϕz plane, twisting moment in the $x\phi$ plane and bending moment in the xz plane, respectively.

According to equilibrium of the shell element in the radial direction, we have

$$R \frac{\partial Q_x}{\partial x} + \frac{\partial Q_\phi}{\partial \phi} + N_\phi - R\rho h \frac{\partial^2 w}{\partial t^2} - Rkw = 0 \quad (9.80)$$

$$Q_x = \frac{\partial M_x}{\partial x} + \frac{1}{R} \frac{\partial M_{\phi x}}{\partial \phi} \quad (9.81)$$

$$Q_\phi = -\frac{\partial M_{x\phi}}{\partial x} + \frac{1}{R} \frac{\partial M_\phi}{\partial \phi} \quad (9.82)$$

Substituting Eqs. (9.81) and (9.82) into Eq. (9.80), and considering that the moments M_x and M_ϕ and the force N_ϕ should include the contribution of the PZT actuators bonded on the shell, we obtain

$$\begin{aligned} R \frac{\partial^2 (M_x - M_x^a)}{\partial x^2} + 2 \frac{\partial^2 M_{\phi x}}{\partial \phi \partial x} + \frac{1}{R} \frac{\partial^2 (M_\phi - M_\phi^a)}{\partial \phi^2} + N_\phi - N_\phi^a \\ - R\rho h \frac{\partial^2 w}{\partial t^2} - Rkw = 0 \end{aligned} \quad (9.83)$$

where M_x^a , M_ϕ^a and N_ϕ^a are the bending moments and in-plane force provided

by the PZT actuators. Since the PZTs are collocated and driven by equal but opposite electric fields, the membrane force $N_\varphi^a = 0$.

Using the Donnell-Mushtari's shell theory and considering the displacement relations for pure bending, $u = -z \frac{\partial w}{\partial x}$ and $v = -\frac{z}{R} \frac{\partial w}{\partial \varphi}$, the motion equation can be obtained from Eq. (9.83) as

$$\begin{aligned} R^2 \frac{\partial^4 w}{\partial x^4} + 2 \frac{\partial^4 w}{\partial x^2 \partial \varphi^2} + \frac{1}{R^2} \frac{\partial^4 w}{\partial \varphi^4} - \frac{\nu}{2} \frac{\partial^2 w}{\partial x^2} + \frac{6}{h^2} w + \frac{R^2}{2D} \rho h \frac{\partial^2 w}{\partial t^2} + \frac{R^2}{2D} k w \\ = -\frac{R^2}{2D} F_r \end{aligned} \quad (9.84)$$

where $F_r = \frac{\partial^2 M_x^a}{\partial x^2} + \frac{1}{R^2} \frac{\partial^2 M_\varphi^a}{\partial \varphi^2}$; $D = \frac{E h^2}{12(1-\nu^2)}$; and E and ν are the Young's modulus and Poisson's ratio of the shell, respectively.

Letting $x = \xi L$ and $\varphi = \theta \Phi$, Eq. (9.84) can be normalized as

$$\begin{aligned} \frac{R^2}{L^4} \frac{\partial^4 w}{\partial \xi^4} + \frac{2}{L^2 \Phi^2} \frac{\partial^4 w}{\partial \xi^2 \partial \theta^2} + \frac{1}{R^2 \Phi^4} \frac{\partial^4 w}{\partial \theta^4} - \frac{2\nu}{L^2} \frac{\partial^2 w}{\partial \xi^2} + \frac{6}{h^2} w + \frac{R^2}{2D} \rho h \frac{\partial^2 w}{\partial t^2} + \frac{R^2}{2D} k w \\ = -\frac{R^2}{2D} \bar{F}_r \end{aligned} \quad (9.85)$$

where

$$\bar{F}_r = \frac{\partial^2 M_\xi^a}{L^2 \partial \xi^2} + \frac{1}{R^2 \Phi^2} \frac{\partial^2 M_\theta^a}{\partial \theta^2} \quad (9.86)$$

and

$$M_\xi^a = 2M_\xi^* [H(\xi - \xi_1) - H(\xi - \xi_2)] \cdot [H(\theta - \theta_1) - H(\theta - \theta_2)] e^{i\omega t} \quad (9.87)$$

$$M_\theta^a = 2M_\theta^* [H(\theta - \theta_1) - H(\theta - \theta_2)] \cdot [H(\xi - \xi_1) - H(\xi - \xi_2)] e^{i\omega t} \quad (9.88)$$

M_ξ^* and M_θ^* are the amplitudes of distributed moments in the x and φ directions, respectively, and can be expressed as $M^a = M_\xi^* = M_\theta^* = E_p d_{31} V (h_p + h) / 2$, where E_p is the Young's modulus of PZT actuators; d_{31} is the piezoelectric constant; V is the voltage applied on the PZT actuators; ω is the angular frequency of the electric field; and ξ_1 , ξ_2 , θ_1 and θ_2 are the normalized coordinates of the four corners of the PZT actuators.

Eq. (9.85) can also be solved by the method of separation of variables. For simply supported shell, the solution can be expressed as

$$w = \sum_{m=1}^{\infty} \sum_{n=1}^{\infty} C_{mn} \sin(m\pi\xi) \sin(n\pi\theta) e^{i\omega t} \tag{9.89}$$

Substituting Eq. (9.89) into Eq. (9.85), multiplying both sides by $\sin(m^*\pi\xi) \sin(n^*\pi\theta)$ and integrating on the shell domain, the solution to Eq. (9.85) is obtained as:

$$w = \sum_{m=1}^{\infty} \sum_{n=1}^{\infty} \frac{4B_{mn} \sin(n\pi\theta_0) \sin(m\pi\xi_0)}{\omega_{mn}^2 - \omega^2} \sin(m\pi\xi) \sin(n\pi\theta) e^{i\omega t} \tag{9.90}$$

where $\omega_{mn}^2 = \frac{2D}{\rho h} \left[\left(\frac{m^2\pi^2}{L^2} + \frac{n^2\pi^2}{R^2\Phi^2} \right)^2 + \frac{2\nu m^2\pi^2}{R^2L^2} + \frac{6}{R^2h^2} + k \right]$ is the natural frequency

of the shell; $B_{mn} = \frac{4M^a}{\rho h} \left(\frac{m}{nL^2} + \frac{n}{mR^2\Phi^2} \right) \sin\left(m\pi \frac{l_\xi}{2}\right) \sin\left(n\pi \frac{\theta_p}{2}\right)$; $\xi_0 = (\xi_1 + \xi_2) / 2$;

$\theta_0 = (\theta_1 + \theta_2) / 2$; $l_\xi = \xi_2 - \xi_1$; and $\theta_p = \theta_2 - \theta_1$.

Eq. (9.90) is the solution of the radial displacement of the cylindrical shell actuated by a pair of collocated piezoelectric actuators. It is evident that Eq. (9.90) has the same form as Eq. (9.79).

Fig. 9.26 shows the deformation of a cylindrical shell actuated by a pair of collocated PZT actuators located at the center of the shell. The radial displacement is in the order of 10^{-3} mm.

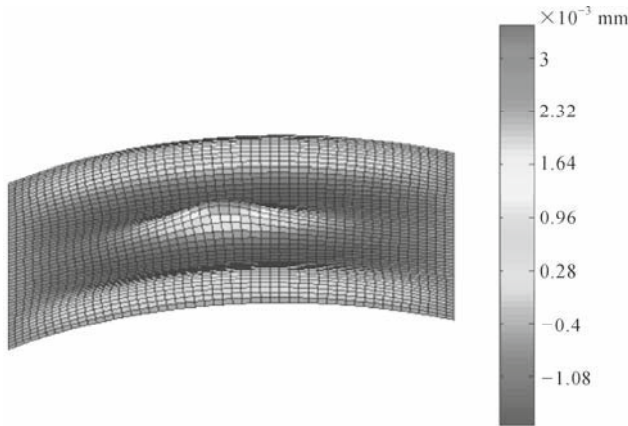


Fig. 9.26 Deformation of cylindrical shell segment actuated by a pair of PZT actuators at center ($\omega = 5,155$ rad/s)

9.2.4 Optimal Placement of PZT Actuator on Plate

In this section, the optimal placement of PZT actuator in terms of maximizing the plate deflection is studied. When the electric potential reaches its maximum value, the maximum plate deflection may be positive or negative. To eliminate this effect, the absolute value of plate deflection $|w|$ is considered. A computer program is implemented to calculate the plate deflection according to Eq. (9.79). In the calculation, a 19×19 grid is used to represent the PZT locations. The PZT actuator can be located at any of the grid node, and at each location, the maximum plate deflection is calculated. After obtaining the maximum deflections corresponding to all the 361 PZT actuator locations, the relationship between the maximum plate deflection and PZT actuator locations is revealed. The parameters used in the calculation are listed in Table 9.8.

- *Driving Frequencies Close to Natural Frequencies*

Numerical Results of PZT Optimal Locations

Fig. 9.27 shows the results when the driving frequencies are close to the resonant/natural frequencies of the first nine vibration modes. The driving frequencies are set to be 5 Hz less than the natural frequencies. The contour plots in Fig. 9.27 illustrate the relationship between the maximum plate deflection and the PZT actuator location. This relationship is associated with the optimal location pattern of the PZT actuator. For a specific PZT actuator location, the maximum plate deflection is represented by the color of this location which can be read from the color bar. Fig. 9.28 shows the first nine vibration mode shapes with the absolute values of mode shapes being adopted. Comparing Fig. 9.27 with Fig. 9.28, it can be observed that the pattern of optimal location of the PZT actuator with driving frequency close to the natural frequency of mode (m,n) is identical with the vibration mode shape (m,n) , for $m,n \in \{1,2,3\}$.

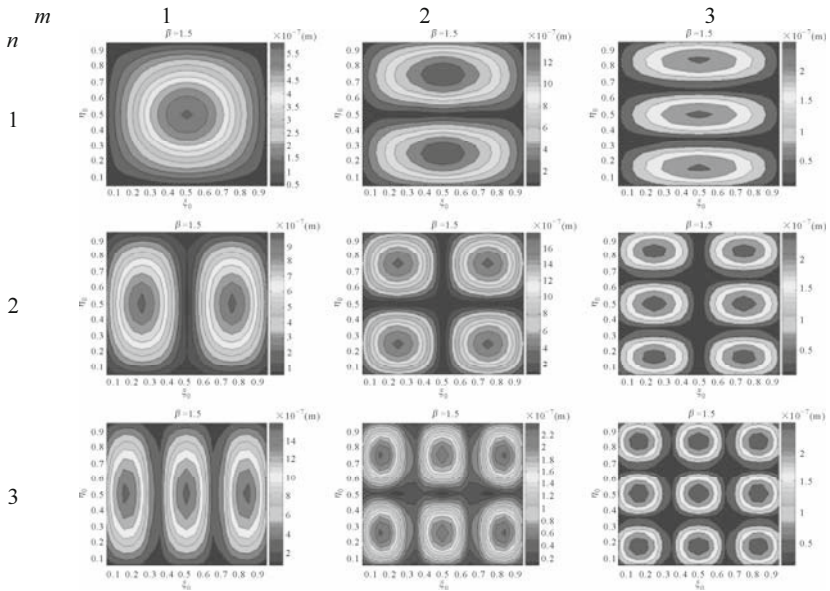


Fig. 9.27 Optimal location patterns of a PZT actuator on a rectangular plate with $\beta = 1.5$ at driving frequencies close to natural frequencies

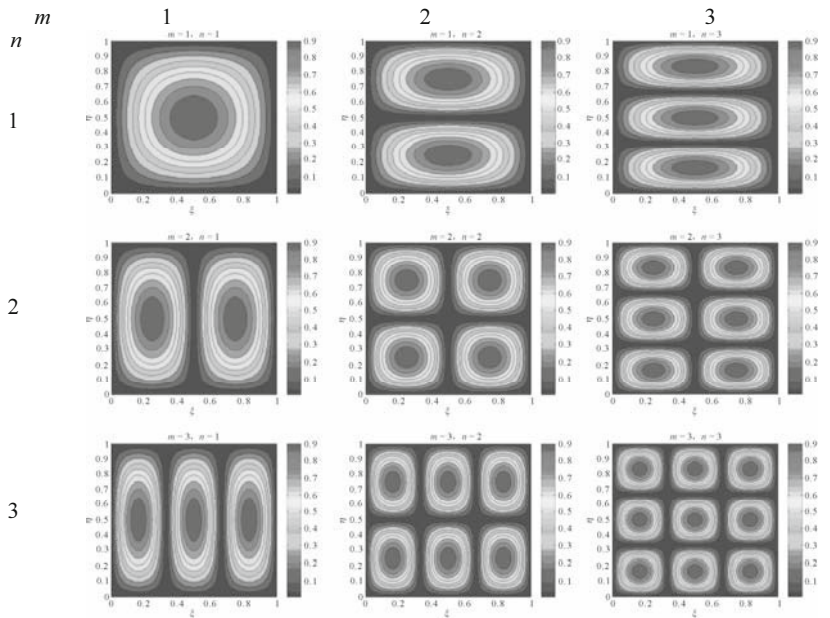


Fig. 9.28 First nine mode shapes of rectangular plate

Combined Position Mode Function (CPMF)

The process of finding the optimal locations of the PZT actuator is essentially equivalent to maximizing the plate deflection $|w|$ by altering the four variables ξ_0, η_0, ξ and η , the values of which can be determined from the following equations:

$$\frac{\partial w}{\partial \xi_0} = \sum_{n=1}^{\infty} \sum_{m=1}^{\infty} A_{mn} m \pi \cos(m \pi \xi_0) \sin(n \pi \eta_0) \sin(m \pi \xi) \sin(n \pi \eta) = 0 \quad (9.91)$$

$$\frac{\partial w}{\partial \eta_0} = \sum_{n=1}^{\infty} \sum_{m=1}^{\infty} A_{mn} n \pi \sin(m \pi \xi_0) \cos(n \pi \eta_0) \sin(m \pi \xi) \sin(n \pi \eta) = 0 \quad (9.92)$$

$$\frac{\partial w}{\partial \xi} = \sum_{n=1}^{\infty} \sum_{m=1}^{\infty} A_{mn} m \pi \sin(m \pi \xi_0) \sin(n \pi \eta_0) \cos(m \pi \xi) \sin(n \pi \eta) = 0 \quad (9.93)$$

$$\frac{\partial w}{\partial \eta} = \sum_{n=1}^{\infty} \sum_{m=1}^{\infty} A_{mn} n \pi \sin(m \pi \xi_0) \sin(n \pi \eta_0) \sin(m \pi \xi) \cos(n \pi \eta) = 0 \quad (9.94)$$

where $A_{mn} = \frac{16M_0}{a^2 \rho h} \frac{\sin \alpha t}{\omega_{mn}^2 - \omega^2} \left(\frac{m}{n} + \frac{n\beta^2}{m} \right) \sin(m\pi \cdot r_\xi) \sin(n\pi \cdot r_\eta)$.

Subtracting Eq. (9.91) from Eq. (9.93), and Eq. (9.92) from Eq. (9.94), we obtain

$$\sum_{n=1}^{\infty} \sum_{m=1}^{\infty} A_{mn} m \pi \sin(n \pi \eta_0) \sin(n \pi \eta) \sin(m \pi (\xi - \xi_0)) = 0 \quad (9.95)$$

$$\sum_{n=1}^{\infty} \sum_{m=1}^{\infty} A_{mn} n \pi \sin(m \pi \xi_0) \sin(m \pi \xi) \sin(n \pi (\eta - \eta_0)) = 0 \quad (9.96)$$

Since $\sin(n\pi\eta_0)$ and $\sin(n\pi\eta)$ should not be zero when $|w|$ reaches maximum, it is evident that, for any A_{mn} , Eq. (9.95) holds only for $\xi - \xi_0 = K_m / m$, where K_m is an integer in domain $(-m, m)$. From Eq. (9.96), $\eta - \eta_0 = K_n / n$ can also be concluded, where K_n is an integer in domain $(-n, n)$. By adding Eq. (9.91) to Eq. (9.93), and Eq. (9.92) to Eq. (9.94), another set of relations can be obtained as $\xi + \xi_0 = K'_m / m$ and $\eta + \eta_0 = K'_n / n$, where K'_m and K'_n are integers in domains $(0, 2m)$ and $(0, 2n)$, respectively. The two sets of relations result in four combinations of possible values of (ξ, η) , which are $(K_m / m + \xi_0, K_n / n + \eta_0)$, $(K_m / m + \xi_0, K'_n / n - \eta_0)$, $(K'_m / m - \xi_0, K_n / n + \eta_0)$ and $(K'_m / m - \xi_0, K'_n / n - \eta_0)$.

Substituting these relationships into $|w|$, the maximum plate deflection can be expressed as

$$|w_M| = \left| \sum_{n=1}^{\infty} \sum_{m=1}^{\infty} A_{mn} (-1)^{K_m + K_n} \sin^2(m\pi\xi_0) \sin^2(n\pi\eta_0) \right| \quad (9.97)$$

$$|w_M| = \left| \sum_{n=1}^{\infty} \sum_{m=1}^{\infty} A_{mn} (-1)^{K_m + K_n - 1} \sin^2(m\pi\xi_0) \sin^2(n\pi\eta_0) \right| \quad (9.98)$$

$$|w_M| = \left| \sum_{n=1}^{\infty} \sum_{m=1}^{\infty} A_{mn} (-1)^{K_m + K_n - 1} \sin^2(m\pi\xi_0) \sin^2(n\pi\eta_0) \right| \quad (9.99)$$

$$|w_M| = \left| \sum_{n=1}^{\infty} \sum_{m=1}^{\infty} A_{mn} (-1)^{K_m + K_n - 2} \sin^2(m\pi\xi_0) \sin^2(n\pi\eta_0) \right| \quad (9.100)$$

The maximum of Eqs. (9.97) to (9.100) is the equation that the optimal locations of PZT actuator should satisfy. Since Eqs. (9.97) to (9.100) also satisfy the inequality of

$$|w_M| \leq \sum_{n=1}^{\infty} \sum_{m=1}^{\infty} |A_{mn}| \sin^2(m\pi\xi_0) \sin^2(n\pi\eta_0) \quad (9.101)$$

where the equal sign holds only when all coefficients of $\sin^2(m\pi\xi_0) \sin^2(n\pi\eta_0)$ in Eqs. (9.97) to (9.100) have the same sign. Thus, the optimal locations of PZT actuator is governed by

$$|w_M| = \sum_{n=1}^{\infty} \sum_{m=1}^{\infty} |A_{mn}| \sin^2(m\pi\xi_0) \sin^2(n\pi\eta_0) \quad (9.102)$$

The PZT actuator location (ξ_0, η_0) which maximizes Eq. (9.102) is the optimal locations of the PZT actuator. Since the term $\chi_{mn} = \sin^2(m\pi\xi_0) \sin^2(n\pi\eta_0)$ in Eq. (9.102) is a function of locations of the PZT actuator, it is hereby named as the “position mode function” (PMF).

For a rectangular plate, a natural frequency ω_{mn} generally corresponds to a unique vibration mode (m, n) . Thus, when the PZT driving frequency ω approaches ω_{mn} , only one PMF $\chi_{mn} = \sin^2(m\pi\xi_0) \sin^2(n\pi\eta_0)$ is amplified. Neglecting all the other terms that are not amplified in Eq. (9.102), the optimal locations of PZT actuator can be found by

$$\frac{\partial \chi_{mn}}{\partial \xi_0} = 0 \quad \text{and} \quad \frac{\partial \chi_{mn}}{\partial \eta_0} = 0 \tag{9.103}$$

in the conditions of
$$\left| \begin{array}{cc} \frac{\partial^2 \chi_{mn}}{\partial \xi_0 \partial \eta_0} & \frac{\partial^2 \chi_{mn}}{\partial \xi_0^2} \\ \frac{\partial^2 \chi_{mn}}{\partial \eta_0^2} & \frac{\partial^2 \chi_{mn}}{\partial \xi_0 \partial \eta_0} \end{array} \right| < 0, \quad \frac{\partial^2 \chi_{mn}}{\partial \xi_0^2} < 0 \quad \text{and} \quad \frac{\partial^2 \chi_{mn}}{\partial \eta_0^2} < 0.$$

The solutions are $\xi_0 = \frac{4N \pm 1}{2m}$ and $\eta_0 = \frac{4N \pm 1}{2n}$, where $N=0,1,2,\dots$, and $0 < \xi_0, \eta_0 < 1$. These solutions coincide with the optimal locations shown in Fig.9.27. For example, if the driving frequency is close to the natural frequency of vibration mode (1,2), the optimal locations of the PZT actuator are (1/2,1/4) and (1/2,3/4), which are consistent with the results shown in Fig. 9.27.

The optimal locations are actually identical with the anti-nodes of the respective vibration modes. This observation agrees with the FE analysis results of optimal positions of a piezoelectric patch on a simply supported rectangular plate obtained by Ip and Tse (2001). Their optimal locations were obtained from the controllability perspective, in which the objective function of controllability was equivalent to maximizing the maximum transverse vibration of plate, which is also the focus of this section. The difference lies in the methods used. Ip and Tse used FEM to study this problem while in this section an analytical method is employed.

For certain rectangular plates, two or more different vibration modes, $(m_1, n_1), (m_2, n_2), \dots, (m_N, n_N)$, may have the same or very close natural frequency. When the driving frequency approaches this natural frequency, all these vibration modes will be amplified. For this case, the optimal locations of PZT can be found through a combination of PMFs of these vibration modes, *i.e.*, $\Psi = |A_{m_1 n_1}| \chi_{m_1 n_1} + |A_{m_2 n_2}| \chi_{m_2 n_2} + \dots + |A_{m_N n_N}| \chi_{m_N n_N}$, which is named as the combined position mode function (CPMF). The optimal locations of the PZT actuator can be obtained by

$$\frac{\partial \Psi}{\partial \xi_0} = 0 \quad \text{and} \quad \frac{\partial \Psi}{\partial \eta_0} = 0 \tag{9.104}$$

in the conditions of
$$\left| \begin{array}{cc} \frac{\partial^2 \Psi}{\partial \xi_0 \partial \eta_0} & \frac{\partial^2 \Psi}{\partial \xi_0^2} \\ \frac{\partial^2 \Psi}{\partial \eta_0^2} & \frac{\partial^2 \Psi}{\partial \xi_0 \partial \eta_0} \end{array} \right| < 0, \quad \frac{\partial^2 \Psi}{\partial \xi_0^2} < 0 \quad \text{and} \quad \frac{\partial^2 \Psi}{\partial \eta_0^2} < 0.$$

Generally, the analytical solution to Eq. (9.104) is not attainable. However, the CPMF can be plotted in the $\xi_0 \eta_0$ -plane, through which the PZT optimal locations can be identified.

Fig. 9.29 illustrates an example for such a case. The natural frequency of vibration mode (2,2) is equal to that of vibration mode (4,1), which is 45294.85 rad/s. It is observed that the optimal location patterns are neither similar to vibration mode (2,2) nor vibration mode (4,1). Nevertheless, the plot of CPMF, $\Psi = \chi_{22} + \chi_{41}$, as shown in Fig. 9.30, agrees well with the pattern obtained by the computer program when $A_{22} = A_{41}$, as shown in Fig. 9.29.

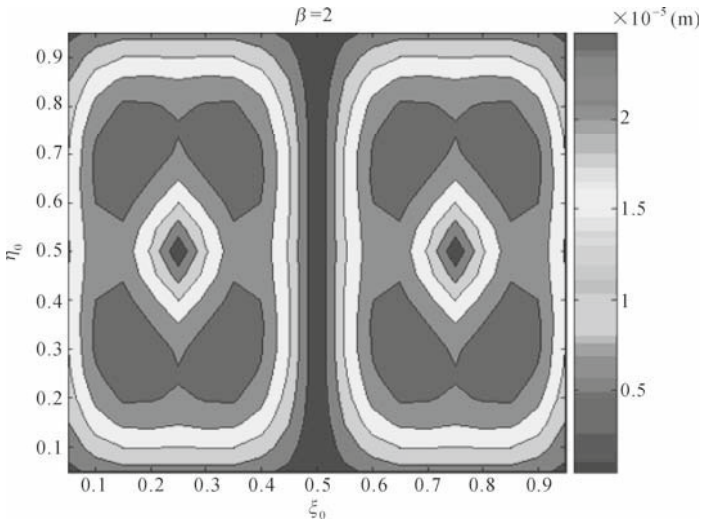


Fig. 9.29 Optimal locations of a PZT actuator on rectangular plate with driving frequency close to natural frequency of vibration modes (2,2) and (4,1)

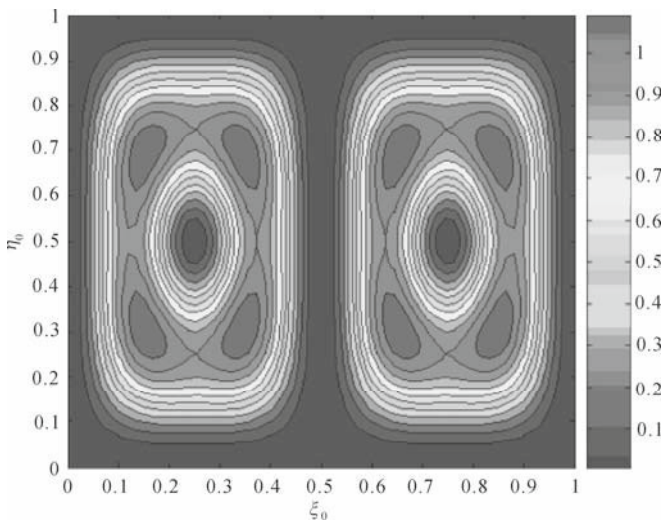


Fig. 9.30 Plot of CPMF $\Psi = \chi_{22} + \chi_{41}$

As a special case of rectangular plate, any two symmetric vibration modes of a square plate share the same natural frequency. Therefore, the CPMF for a square plate can be expressed as $\Psi = |A_{mn}|\chi_{mn} + |A_{nm}|\chi_{nm}$. Since $r_\zeta = r_\eta$ and $\omega_{mn} = \omega_{nm}$ for the square plate, $A_{mn} = A_{nm}$. Thus, the CPMF can be simplified as $\Psi = \chi_{mn} + \chi_{nm}$. Fig. 9.32 shows the contour plots of the CPMFs for $m, n \in \{1, 2, 3\}$. Compared with the results from the computer program (Fig. 9.31), it is evident that the patterns indicated in Fig. 9.32 are almost the same as those in Fig. 9.31 and the optimal locations in Fig. 9.32 are exactly the same as those determined from Fig. 9.31. This means that the CPMFs can be used to determine the optimal placement of the PZT actuator.

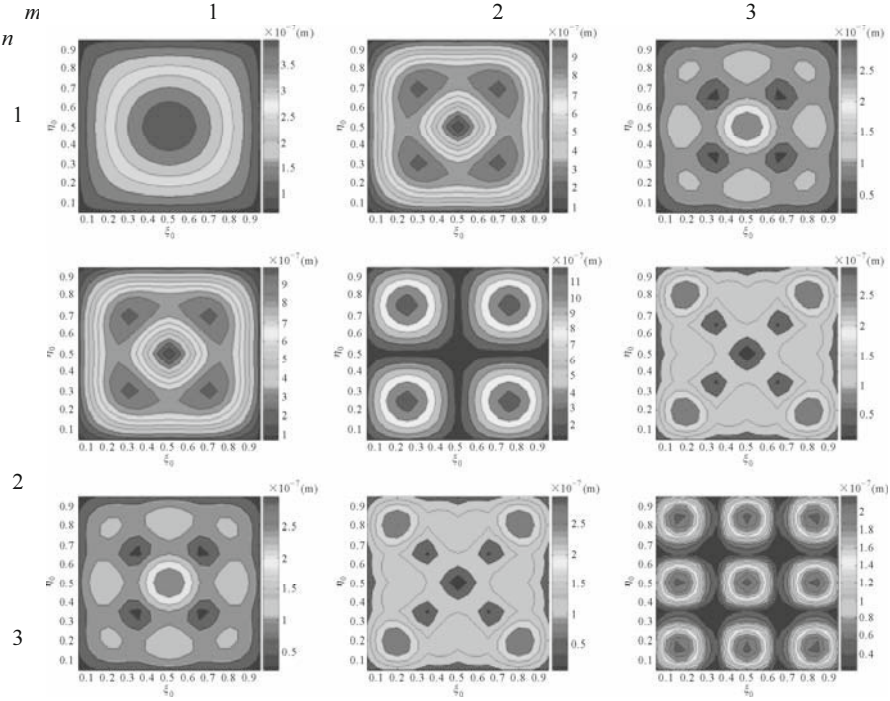


Fig. 9.31 Optimal location patterns of a PZT actuator on a square plate at driving frequencies close to natural frequencies

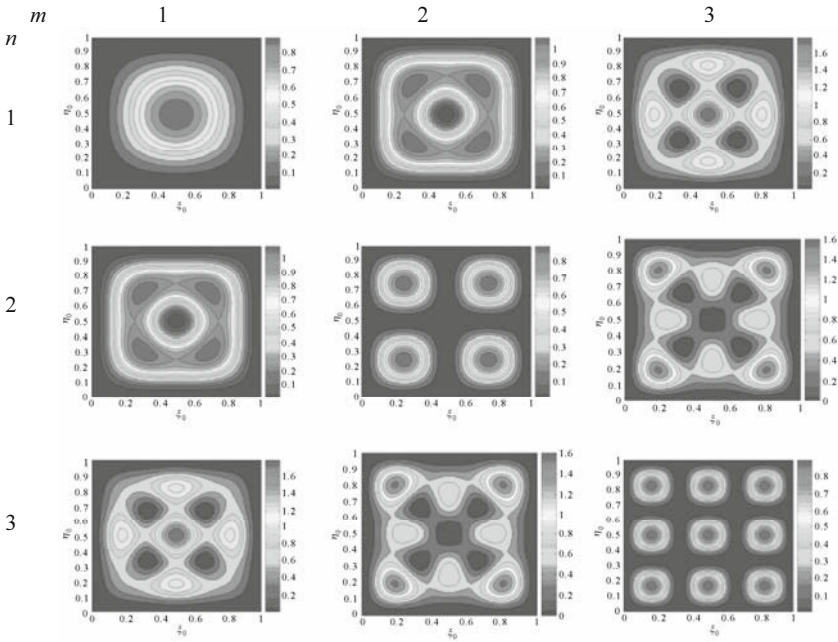


Fig. 9.32 Plots of CPMFs for square plate

For the square plate, the mode shapes are identical to those shown in Fig. 9.28. It is worth noting that, for a vibration mode (m,n) , the optimal location pattern in Fig. 9.31 or Fig. 9.32 is different from the mode shape in Fig.9.28 for $m \neq n$, and they are the same for $m=n$, unlike the rectangle plate where the optimal location patterns are always identical with their corresponding mode shapes (Figs. 9.27 and 9.28). This observation can be explained as follows. For the rectangular plate, the optimal location pattern can be determined from a single PMF $\chi_{mn} = \sin^2(m\pi\xi_0)\sin^2(n\pi\eta_0)$ which has the same plot as the mode shape (m,n) . However, for the square plate, the optimal location pattern is determined by the CPMF $\Psi = \chi_{nm} + \chi_{mn} = \sin^2(m\pi\xi_0)\sin^2(n\pi\eta_0) + \sin^2(n\pi\xi_0)\sin^2(m\pi\eta_0)$ which has different plot from the mode shape (m,n) when $m \neq n$, and has the same as the mode shape when $m=n$.

- *Driving Frequencies Not Close to Natural Frequencies*

In most situations, the driving frequencies may not be close to any natural frequency. In order to study the optimal locations of PZT actuator on rectangular plate for such situations, three frequencies within the interval of two adjacent natural frequencies are selected to be the driving frequencies. These three

driving frequencies are $\omega_1 = \omega_{m_1 n_1} + (\omega_{m_2 n_2} - \omega_{m_1 n_1}) / 4$, $\omega_2 = (\omega_{m_1 n_1} + \omega_{m_2 n_2}) / 2$ and $\omega_3 = \omega_{m_1 n_1} + 3(\omega_{m_2 n_2} - \omega_{m_1 n_1}) / 4$, where $\omega_{m_1 n_1}$ and $\omega_{m_2 n_2}$ are the two adjacent natural frequencies and $\omega_{m_1 n_1} < \omega_{m_2 n_2}$.

From Eq. (9.102), when the driving frequency ω is not close to any natural frequency and $\omega_{m_1 n_1} < \omega < \omega_{m_2 n_2}$, where $\omega_{m_1 n_1}$ and $\omega_{m_2 n_2}$ are the two adjacent natural frequencies, the two adjacent PMFs $\chi_{m_1 n_1}$ and $\chi_{m_2 n_2}$ will have the largest weights and contribute the most to the deflection. Thus, the pattern of optimal locations can be approximately determined by the CPMF, $\Psi = |A_{m_1 n_1}| \chi_{m_1 n_1} + |A_{m_2 n_2}| \chi_{m_2 n_2}$.

Fig. 9.33 shows the results of optimal locations of the PZT actuator for these three driving frequencies. For a specific mode in Fig. 9.33, the first row shows the optimal location patterns calculated by the computer program while the second row presents the predictions obtained from the CPMFs. It is apparent from Fig. 9.33 that the patterns of optimal locations are similar to each other within two adjacent natural frequencies. Transitions can be observed with driving frequencies changing from ω_1 to ω_3 . The optimal patterns of ω_1 are similar to the previous resonance patterns while the optimal patterns of ω_3 are similar to the next resonance patterns. It can also be observed that, in the second row of each vibration mode, the optimal locations predicted by the CPMFs match well with those obtained by the computer program. Although the patterns are not exactly the same, the major optimal locations are quite similar. The same conclusion can be drawn for the square plate, where the results are shown in Fig. 9.34. Both Figs. 9.33 and 9.34 indicate that the CPMFs can successfully identify the optimal locations of the PZT actuator driven by non-resonant frequencies.

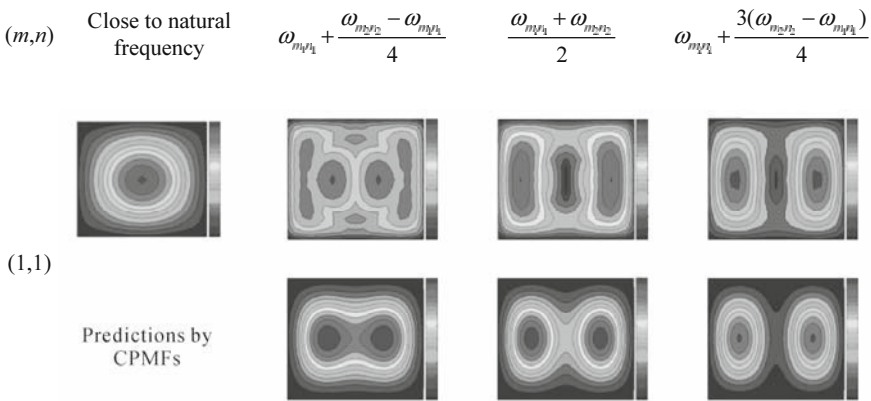


Fig. 9.33 Optimal location patterns of a PZT actuator on a rectangular plate with driving frequencies not close to natural frequencies (Non-dimensional scales are used as in Figs. 9.31 and 9.32)

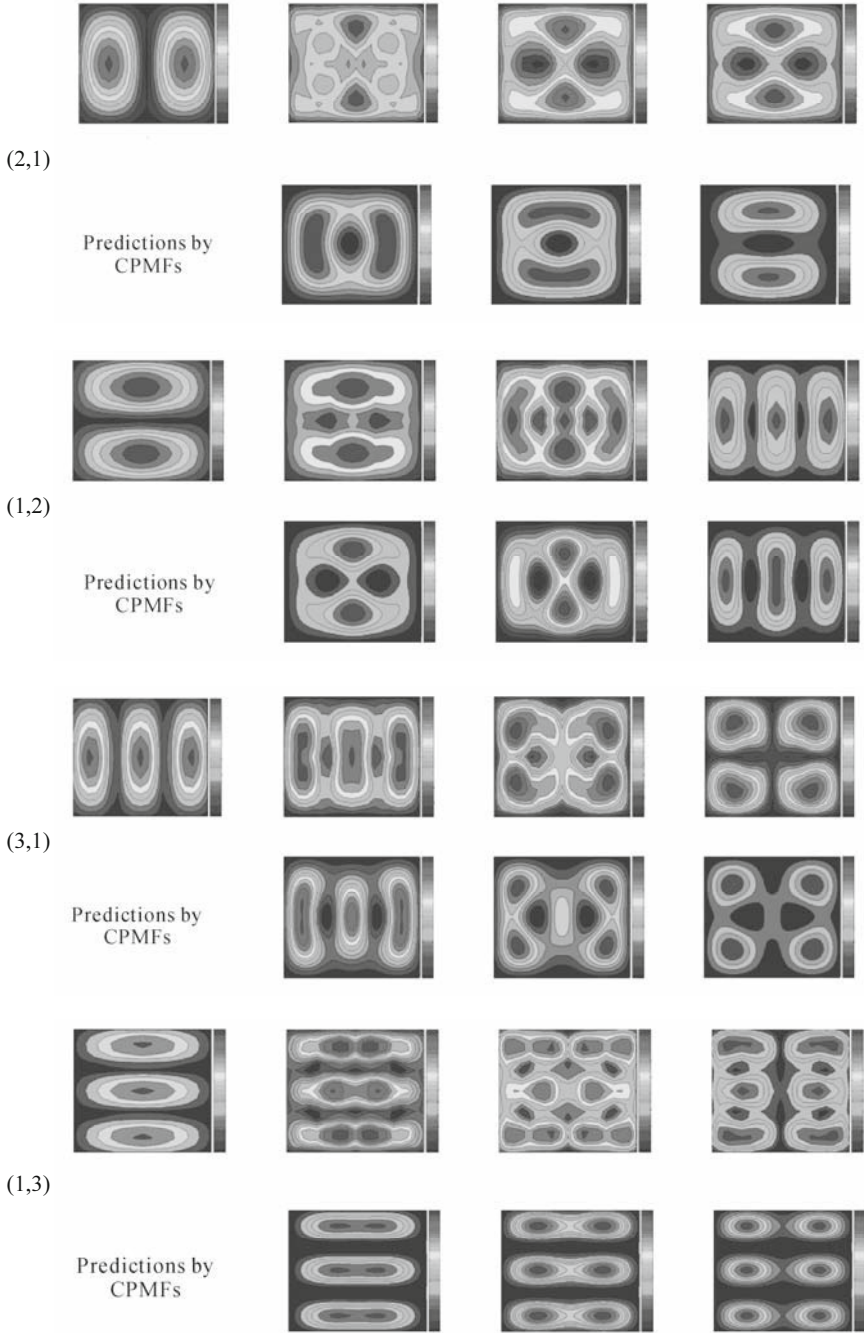


Fig. 9.33 Continued

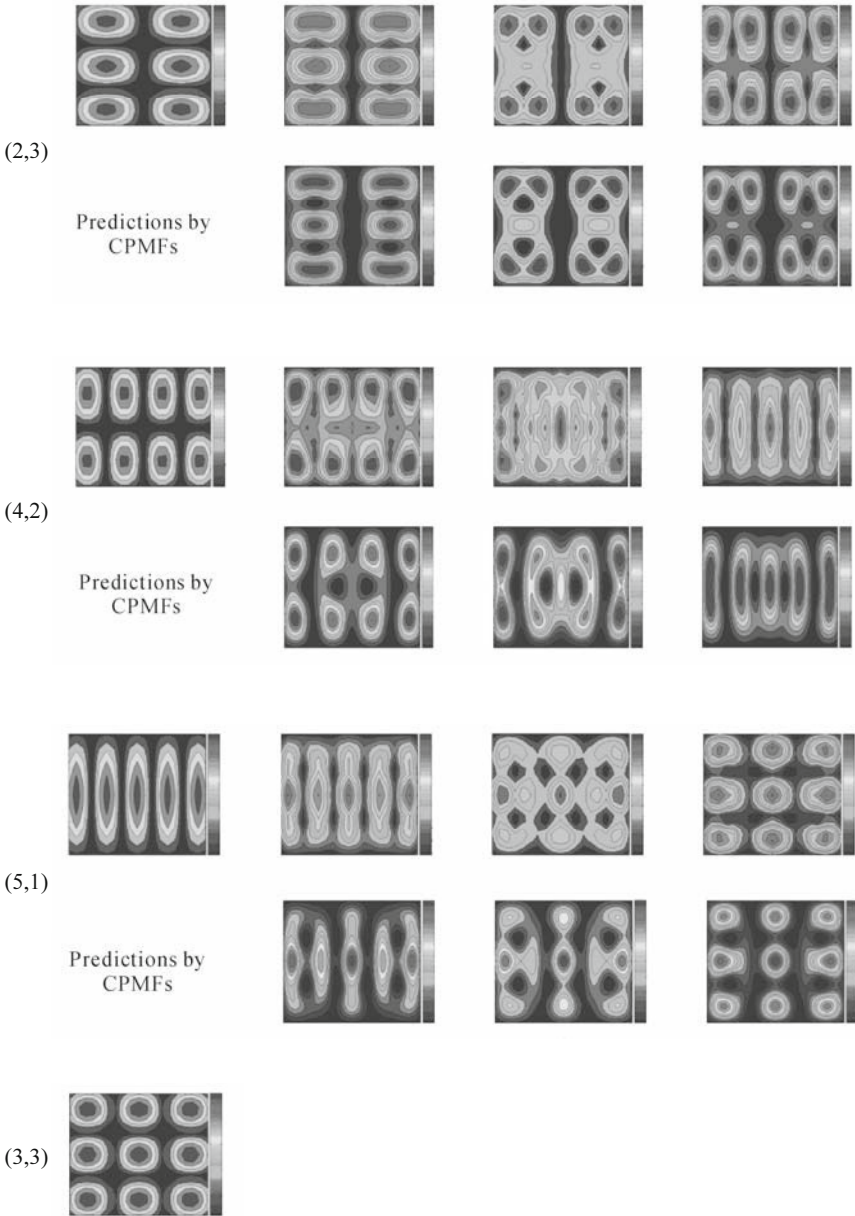


Fig. 9.33 Continued

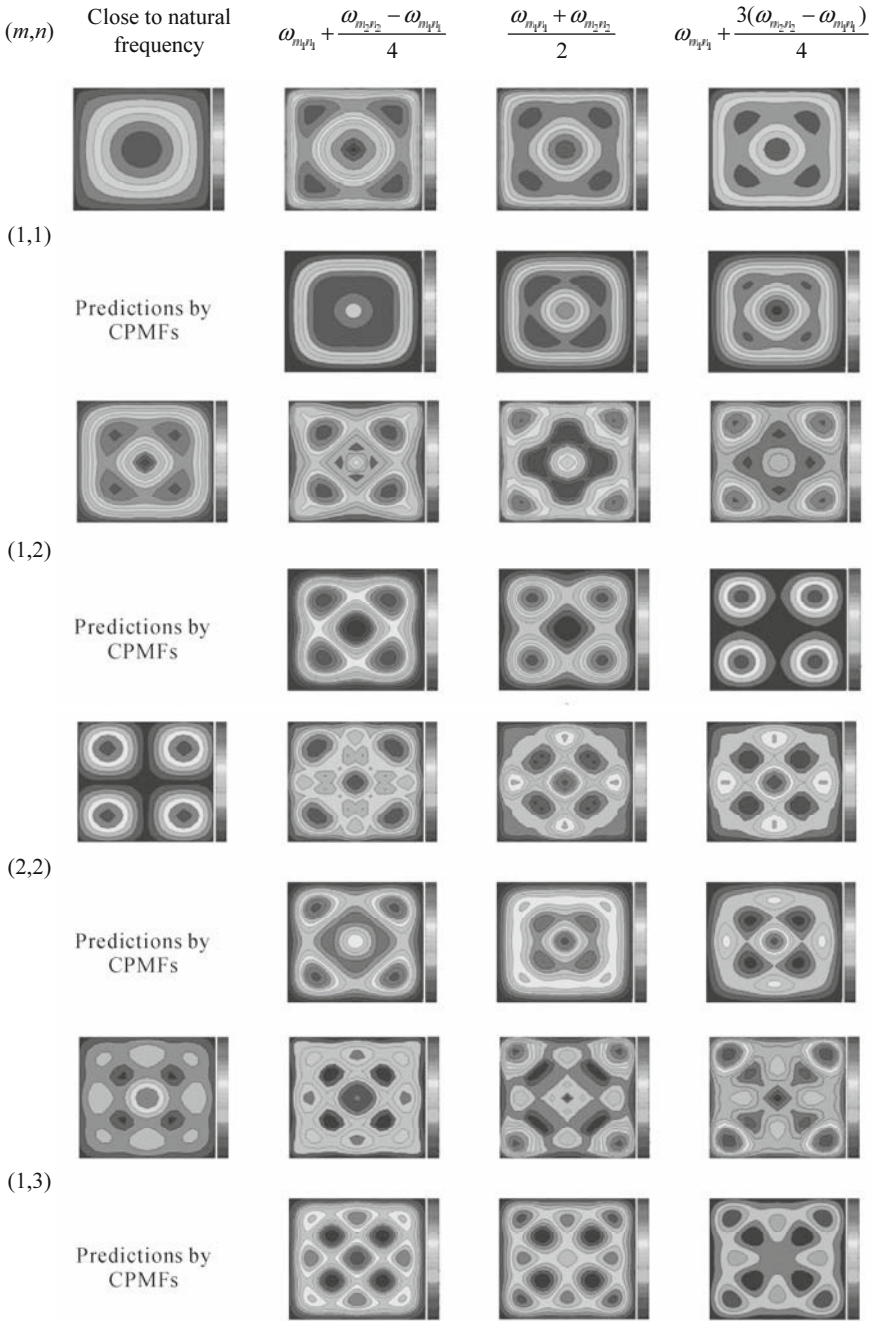


Fig. 9.34 Optimal location patterns of a PZT actuator on a square plate with driving frequencies not close to natural frequencies (Non-dimensional scales are used as in Figs. 9.31 and 9.32)

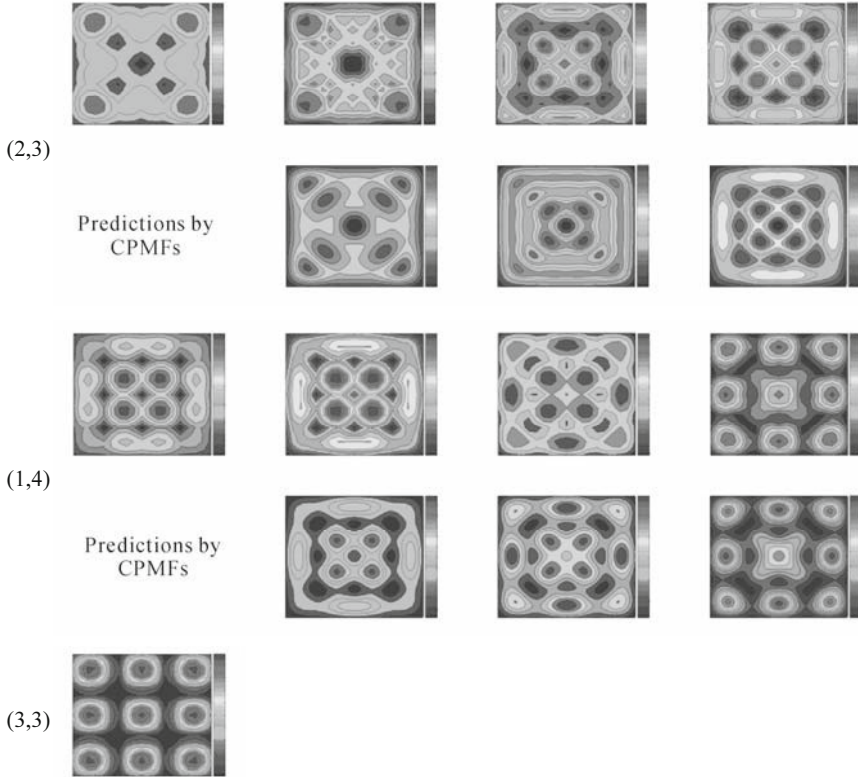


Fig. 9.34 Continued

• *General Procedure to Determine PZT Optimal Locations via CPMF*

In summary, the optimal location pattern of the PZT actuator can be represented by the CPMF, $\Psi = |A_{m_1 n_1}| \chi_{m_1 n_1} + |A_{m_2 n_2}| \chi_{m_2 n_2} + \dots + |A_{m_N n_N}| \chi_{m_N n_N}$. When the driving frequency is close to a natural frequency, the CPMF is the sum of all PMFs at resonance. When the driving frequency is not close to any natural frequency, the CPMF is composed of two PMFs whose corresponding natural frequencies are adjacent to the driving frequency. If more than one vibration modes share the same natural frequency, the corresponding PMFs should be added in the CPMF. Therefore, the general procedure to determine the optimal locations of a PZT actuator on a rectangular/ square plate can be summarized as follows.

- (1) Determine the natural frequencies of the plate by using Eq. (9.64), and find whether there are more than one vibration modes that share the same natural frequency.

(2) Construct the CPMF. If the driving frequency ω is close to a natural frequency $\omega_{m_1 n_1}$, the CPMF will consist of the corresponding PMF, *i.e.*, $\Psi = \chi_{m_1 n_1}$. If two or more different vibration modes, $(m_1, n_1), (m_2, n_2), \dots, (m_N, n_N)$ share the same natural frequency, the CPMF can be expressed as $\Psi = |A_{m_1 n_1}| \chi_{m_1 n_1} + |A_{m_2 n_2}| \chi_{m_2 n_2} + \dots + |A_{m_N n_N}| \chi_{m_N n_N}$. If the driving frequency ω is not close to any natural frequency, *i.e.*, $|\omega - \omega_{ij}| > \Delta$, where i, j are arbitrary natural numbers and Δ is an empirical quantity, say 31.4 (10 Hz) for the examples in this section, and $\omega_{m_1 n_1} < \omega < \omega_{m_2 n_2}$, where $\omega_{m_1 n_1}$ and $\omega_{m_2 n_2}$ are the two adjacent natural frequencies, then the CPMF is $\Psi = |A_{m_1 n_1}| \chi_{m_1 n_1} + |A_{m_2 n_2}| \chi_{m_2 n_2}$. If there are other modes sharing the same natural frequency as $\omega_{m_1 n_1}$ or $\omega_{m_2 n_2}$, the corresponding PMFs should be added in the CPMF.

(3) Finally, plot the CPMF in the $\xi_0 \eta_0$ -plane, and the locations with the maximum values on the CPMF plot are the optimal locations of the PZT actuator on the plate.

The computer program mentioned earlier in this chapter uses Eq. (9.79) to calculate the plate deflections for all the possible PZT locations, where the natural frequencies must be obtained beforehand. Using the proposed general procedure, which only requires calculation of the natural frequencies of the plate and the CPMF, the computational cost can be significantly reduced.

9.2.5 Optimal Placement of PZT Actuator on Shell

After determining the optimal locations of PZT actuator on plate, the procedure developed in Section 9.2.4 can be readily used for the optimal placement of PZT actuator on shell. The radial vibration solution of a simply-supported cylindrical shell actuated by a pair of collocated PZT actuators has been obtained in Eq. (9.90). This solution is similar in form to the solution of plate vibration. Thus, the following relationship can be used,

$$|w|_{\max} = \sum_{m=1}^{\infty} \sum_{n=1}^{\infty} |A_{mn}| \sin^2(n\pi\theta_0) \sin^2(m\pi\xi_0) e^{i\omega t} \quad (9.105)$$

where $\omega_{mn}^2 = \frac{2D}{\rho h} \left[\left(\frac{m^2\pi^2}{L^2} + \frac{n^2\pi^2}{R^2\Phi^2} \right)^2 + \frac{2\nu m^2\pi^2}{R^2L^2} + \frac{6}{R^2h^2} \right]$ is the natural frequency of

the shell; $A_{mn} = \frac{16M^a}{\omega_{mn}^2 - \omega^2 \rho h} \left(\frac{m}{nL^2} + \frac{n}{mR^2\Phi^2} \right) \sin\left(m\pi \frac{l_\xi}{2}\right) \sin\left(n\pi \frac{\theta_p}{2}\right)$; $\xi_0 = (\xi_1 + \xi_2) / 2$;

$\theta_0 = (\theta_1 + \theta_2) / 2$; $l_\xi = \xi_2 - \xi_1$; and $\theta_p = \theta_2 - \theta_1$.

The CPMF for shell vibration is

$$\Psi = |A_{m_1 n_1}| \chi_{m_1 n_1} + |A_{m_2 n_2}| \chi_{m_2 n_2} \tag{9.106}$$

By plotting Eq. (9.106), the optimal locations of the PZT pair can be determined. An example is calculated for illustration. The parameters used are listed in Table 9.9.

Table 9.9 Material properties and constants for shell and PZT

	Young's modulus (N/m ²)	Material density (kg/m ³)	Poisson's ratio	Dimension (mm)	Electric potential (V)	<i>d</i> ₃₁ (m/V)
Shell	7.03×10 ¹⁰	2700	0.34	<i>L</i> = 500 <i>R</i> = 1,000 $\Phi = \pi/3$ <i>h</i> = 2	N.A.	N.A.
PZT	7.94×10 ¹⁰	N.A.	0.30	<i>l</i> _{<i>p</i>} = 50 $\theta_p = \pi/30$ <i>h</i> _{<i>p</i>} = 0.5	10	-1.3×10 ⁻¹⁰

Figs. 9.35 and 9.36 show the optimal locations of the PZT pair on the cylindrical shell determined by the computer program and the CPMF, respectively. It is evident that all the six optimal locations determined by the computer program are also identified by the CPMF with reasonable accuracy. These results indicate that the CPMF is valid to be used to determine the optimal placement of PZT actuators on shell structures.

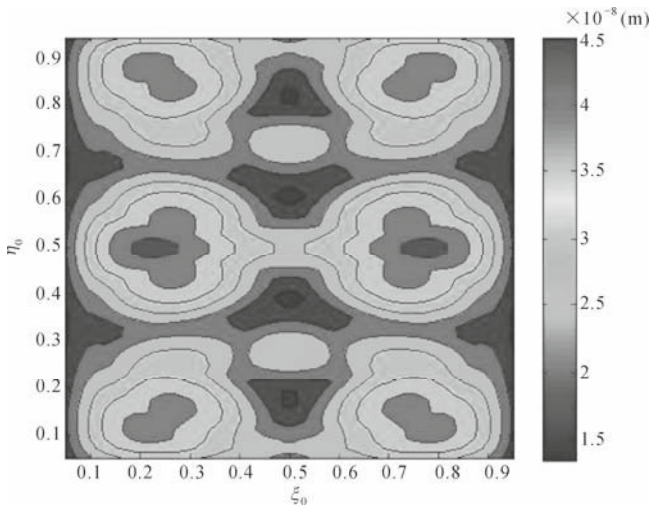


Fig. 9.35 Numerical results of optimal location pattern of a pair of collocated PZTs when $\omega = 5,155$ rad/s

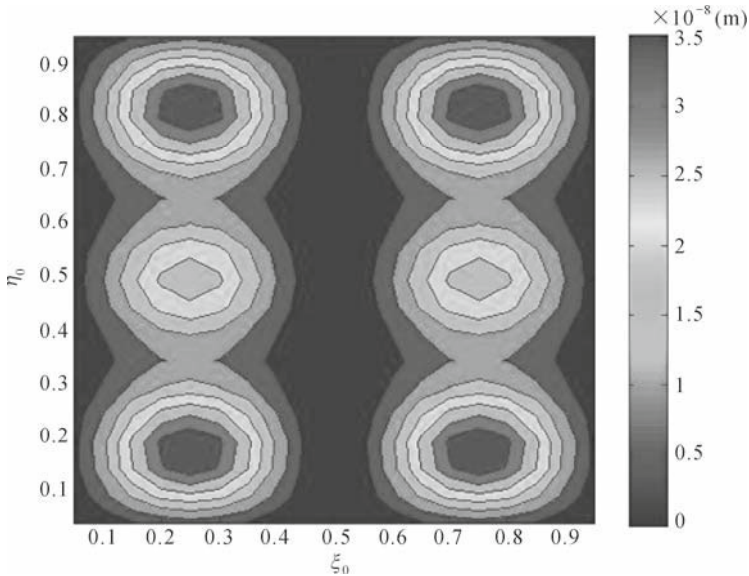


Fig. 9.36 Optimal location pattern of a pair of collocated PZTs when $\omega = 5,155$ rad/s determined by Eq. (9.106)

9.2.6 Discussions

- *Driving Frequency Lower than the First Natural Frequency*

When the driving frequency is lower than the natural frequency of the first vibration mode, the optimal location pattern at very low driving frequency, *i.e.*, near static condition, should be considered. Fig. 9.37 shows the optimal locations of PZT when the driving frequency is 0.01 Hz. It can be seen that the optimal locations of the PZT are located near the boundaries. Fig.9.38 shows the optimal location pattern of a PZT actuator when the driving frequency is 4,000 Hz. It can be observed that the two figures are similar. However, it can also be observed that in most regions of the plate, the maximum plate deflection is not very sensitive to the location of the PZT actuator. The changes of maximum plate deflection with different PZT actuator locations are limited in a very small range.

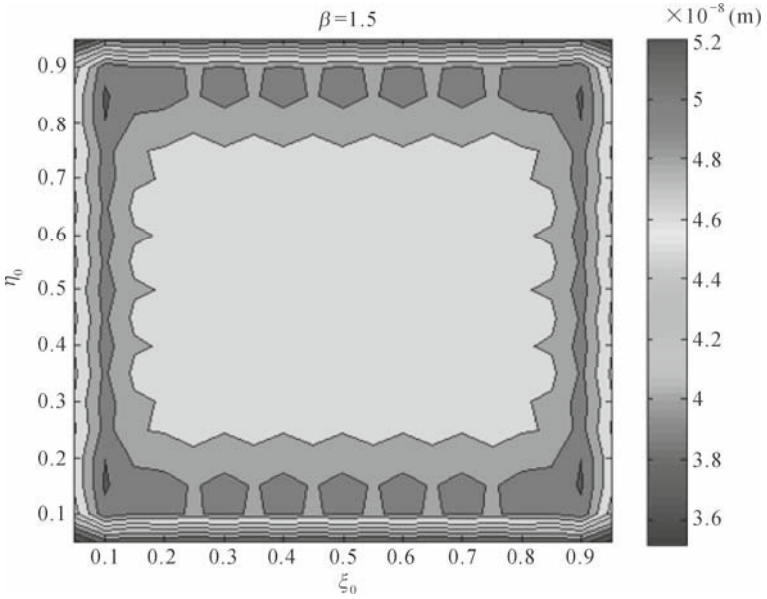


Fig. 9.37 Optimal locations when driving frequency is near zero ($\omega = 0.0628$ rad/s)

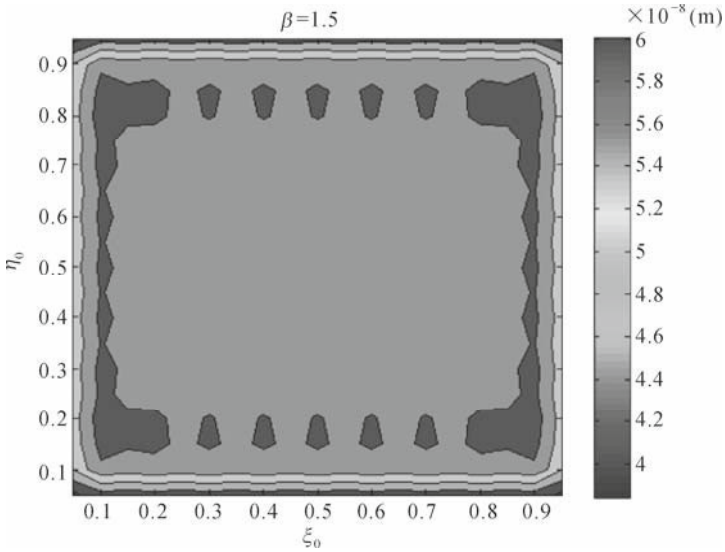


Fig. 9.38 Optimal locations when driving frequency lower than the first natural frequency ($\omega = 25,133$ rad/s)

- *Effect of PZT Size*

According to the solution of Eq. (9.79), when the dimensions of the PZT actuator are set at certain values, some vibration modes will vanish; that is, certain vibration modes can be suppressed by varying the size of the PZT actuator. For example, when $r_\xi = \frac{N}{m}$ and/or $r_\eta = \frac{N}{n}$, the deflection of mode $(m,*)$ or $(n,*)$ becomes zero, where $N=1,2,3,\dots$, and “*” stands for any positive integer. Similar observation was reported by Dimitriadis *et al.* (1991), who drew the conclusion from some numerical examples. This finding may be useful for vibration control with PZT actuators.

- *Effects of Material Properties, Foundation Stiffness and In-plane Forces*

From the above discussion, it is observed that the key factors determining the optimal locations of a PZT actuator on a rectangular plate are the driving frequency of PZT and the natural frequencies of plate. Since the natural frequencies of plate are determined by the material properties, foundation stiffness as well as the in-plane forces, as indicated in Eq. (9.64), variations in these parameters will cause changes in the natural frequencies. However, because the general procedure is based on the relations between the driving frequency and the natural frequencies, these variations will not affect the applicability of the proposed general procedure to determine the optimal locations of the PZT actuator. Thus, the proposed general procedure is applicable to any plate with given material properties, foundation stiffness and in-plane stresses based on the von Karman’s plate theory where the general procedure is derived.

9.2.7 Summary

In this section, optimal placements of a PZT actuator in terms of maximizing the plate and shell vibration are discussed. It has been found that the optimal locations of the PZT actuator are dependent on the driving frequency of the actuator and the natural frequencies of the plate. The optimal locations of the actuator could be identified by the CPMF no matter whether the driving frequency is close to the natural frequencies or not. It has also been found that the geometry of PZT actuator has the capacity of suppressing certain vibration modes. These findings provide guidelines for exciting plates and shells on elastic foundations by PZT actuators. It is worth mentioning that the solution procedure presented in this section is not only applicable to the simply supported plates or cylindrical shells but also to the plates and shells with other boundary conditions, such as clamped plates and cantilevered plates provided that the mode shape functions in the derivation are changed accordingly.

References

- Aldraihem, J., Singh, T., and Wetherhold, R.C. (2000). "Optimal size and location of piezoelectric actuator/sensors: practical considerations", *AIAA Journal of Guidance, Control, and Dynamics*, 23(3): 509-515.
- Bailey, T., and Hubbard, J.E. (1985). "Distributed piezoelectric-polymer active vibration control of a cantilever beam", *AIAA Journal of Guidance, Control, and Dynamics*, 8(5): 605-611.
- Baz, A., and Poh, S. (1988). "Performance of an active control system with piezoelectric actuators", *Journal of Sound and Vibration*, 126(2): 327-343.
- Chandrashekara, K., and Agarwal, A.N. (1993). "Active vibration control of laminated composite plates using piezoelectric devices: a finite element approach", *Journal of Intelligent Material Systems and Structures*, 4(4): 496-508.
- Chee, C., Tong, I. and Steven, G.P. (1998). "A review on the modeling of piezoelectric sensors and actuators incorporated in intelligent structures", *Journal of Intelligent Material Systems and Structures*, 9: 3-19.
- Crawley, E.F. and de Luis, J. (1987). "Use of piezoelectric actuators as elements of intelligent structures", *AIAA Journal*, 25(10): 1373-1385.
- Devasia, S., Meressi, T., Paden, B. and Bayo, E. (1993). "Piezoelectric actuator design for vibration suppression: placement and sizing", *AIAA Journal of Guidance, Control, and Dynamics*, 16 (5): 859-864.
- Dimitriadis, E.K., Fuller, C.R. and Rogers, C.A. (1991). "Piezoelectric actuators for distributed vibration excitation of thin plates", *Journal of Vibration and Acoustics*, 113(1): 100-107.
- Han, J. and Lee, I. (1999). "Optimal placement of piezoelectric sensors and actuators for vibration control of a composite plate using genetic algorithms", *Smart Materials and Structures*, 8: 257-267.
- Henry, J.K. and Clark, R.I. (1999). "A curved piezo-structures model: implications and active structural acoustic control", *Journal of the Acoustical Society of America*, 106: 1400-1407.
- Ip, K.H. and Tse, P.C. (2001). "Optimal configuration of a piezoelectric patch for vibration control of isotropic rectangular plates", *Smart Materials and Structures*, 10: 395-403.
- Kumar, K.R. and Narayanan, S. (2007). "The optimal location of piezoelectric actuators and sensors for vibration control of plates", *Smart Materials and Structures*, 16: 2680-2691.
- Lee, A.C. and Chen, S.T. (1994). "Collocated sensor/actuator positioning and feedback design in the control of flexible structure system", *ASME Journal of Vibration and Acoustics*, 116(4): 146-154.
- Leissa, A.W. (1973). "The free vibration of rectangular plates." *Journal of Sound and Vibration*, 31: 257-93.
- Qiu, J. and Tani, J. (1995). "Vibration control of a cylindrical shell using distributed piezoelectric sensors and actuators", *Journal of Intelligent Material*

- Systems and Structures*, 6(3): 474-481.
- Qiu, Z., Zhang, X., Wu, H. and Zhang, H. (2007). "Optimal placement and active vibration control for piezoelectric smart flexible cantilever plate", *Journal of Sound and Vibration*, 301: 521-543.
- Song, G., Qiao, P.Z., Binienda, W.K. and Zou, G.P. (2002). "Active vibration damping of composite beam using smart sensors and actuators", *Journal of Aerospace Engineering*, 7: 97-103.
- Sun, D. and Tong, L. (2001). "Modal control of smart shells by optimized discretely distributed piezoelectric transducers", *International Journal of Solids and Structures*, 38: 3281-3299.
- Tzou, H.S. and Bao, Y. (1996). "Parametric study of segmented transducers laminated on cylindrical shells, part 1: sensor patches", *Journal of Sound and Vibration*, 197(2): 207-224.
- Wang, B.T. and Rogers, C.A. (1991). "Modeling of finite-length spatially-distributed induced strain actuators for laminated beams and plate", *Journal of Intelligent Material Systems and Structures*, 2(1): 38-58.
- Yang, Y.W. and Zhang, L. (2006). "Optimal excitation of a rectangular plate resting on an elastic foundation by a piezoelectric actuator", *Smart Materials and Structures*, 15(4): 1063-1078.
- Yang, Y.W., Jin, Z.L. and Soh, C.K. (2006). "Integrated optimization of control system for smart cylindrical shells using modified GA", *Journal of Aerospace Engineering*, 19(2): 68-79.
- Zhang, H.W., Lennox, B., Goulding, P.R. and Leung, A.Y.T. (2000). "A float-encoded genetic algorithm technique for integrated optimization of piezoelectric actuator and sensor placement and feedback gains", *Smart Materials and Structures*, 9: 552-557.

Cylindrical Shells with Piezoelectric Shear Actuators

H. Y. Li*, Y. W. Yang

Department of Engineering Mechanics, Shanghai Jiao Tong University, Shanghai 200030, P.R. China.

Tel: (86)-21-3420-6197; Fax: (86)-21-3420-6197

Email: hyli@sjtu.edu.cn

10.1 Introduction

Due to the advantage of having properties such as rapid response, high resolution, low power consumption and large bandwidth, piezoelectric materials have in recent years been employed as actuators and sensors in many structures for noise reduction, vibration control, shape control and health monitoring. In the applications of piezoelectric actuators, the electromechanical interactions between them and their host structures must be fully understood. Generally, the piezoelectric actuators bonded to the surface of an adaptive structure are thin elements which have been poled in the thickness direction. When an electric field is applied in the thickness direction of a piezoelectric actuator, longitudinal strains are induced in the actuator, forcing the host structure to deform. Such actuation mechanism of piezoelectric actuators is known as extensional actuation. So far, the majority of research work on the applications of piezoelectric actuators in smart structures is based on such extensional mechanism (Rao and Sunar, 1999).

In order to achieve the most effective actuation and control, extensional piezoelectric actuators are usually placed on the surface of a structure at selected optimal locations (Jin *et al.*, 2005; Yang and Zhang, 2006). However, this subjects the actuators to high longitudinal stresses which may be detrimental to the actuators as they are made of brittle piezoceramics. To avoid such problems, Sun and Zhang (1995) proposed a laminated structure incorporating an axially poled piezoelectric core sandwiched between two elastic layers. The application of an electric field along the thickness direction will induce transverse shear

deformation of the core, which in turn will deform the structure. The piezoelectric actuators poled in such a way, where the polarization direction is perpendicular to the electric field in the thickness direction to generate transverse shear deformation, are called *shear actuators*. Presently, various piezoelectric shear actuators (PSAs) are commercially available, for example from Morgan Matroc (2006).

Zhang and Sun (1996) presented an analytical model to predict the static behavior of an adaptive sandwich beam with a shear-mode actuator. Benjeddou *et al.* (1997) developed an FE model for a sandwich beam with extension and shear mode piezoelectric patches. Benjeddou *et al.* (2001a, 2001b) also proposed a theoretical formulation and its FE implementation for an adaptive sandwich shell of revolution that uses the transverse shear response of a piezoelectric core sandwiched between two elastic layers. Khdeir and Aldraihem (2001) presented solutions for deflections of first-order and higher-order beams with one PSA. They also developed the exact solutions for beams with multiple PSAs (Aldraihem and Khdeir, 2003). Raja *et al.* (2002) developed a control scheme based on the linear quadratic regulator and the independent modal space control method, and utilized it to estimate the active stiffness and damping induced by the shear and extension-bending actuators. Baillargeon and Vel (2005) discussed the active damping of composite plates with PSAs. They also studied the static deformation and active damping of simply supported hybrid cylindrical shells with embedded PSAs (Vel and Baillargeon, 2005). Li *et al.* (2004) obtained the static solutions for multilayered cylindrical shells with embedded PSAs. Trindade and Benjeddou (2008) studied the refined sandwich model for vibration of beams with embedded shear piezoelectric actuators and sensors. Kant and Shiyekar (2008) used a higher order shear and normal deformation theory to study cylindrical bending of piezoelectric laminates.

In this chapter, exact solutions are presented for the dynamic response of a fully coupled hybrid piezo-elastic cylindrical shell with PSAs. Section 10.2 develops the governing equations of a multi-laminated cylindrical shell. Section 10.3 presents a set of eight first-order homogeneous ordinary differential equations with variable coefficients obtained through expanding the response quantities of each layer into the double Fourier series and using the state-space approach. Solutions to the differential equations derived by the Frobenius method are also discussed. Section 10.4 describes an active vibration control model for a simply supported laminated cylindrical shell with piezoelectric shear sensor and actuator layers established using the negative velocity feedback control method. The detailed derivations can be found in Li and Yang (2007). Numerical results of responses are presented in Section 10.5 to illustrate the effects of thickness ratio and location of PSAs on the shell response for both mechanical and electric loadings. Other numerical examples are also included in Section 10.5 to verify the feasibility of the control model. Finally, summary and conclusions are given in Section 10.6.

10.2 Governing Equations

Fig. 10.1 shows a piezo-elastic laminated cylindrical shell. Each lamina of the N -layer laminated shell is either an orthotropic piezoelectric layer or an orthotropic elastic layer. The global cylindrical coordinate system (x, θ, r) and the local coordinate system for each layer (x, θ, r) ($0 \leq z \leq h^{(i)}$) are related by $r = r_i + z$, where r_i and $h^{(i)}$ are the radius of the inner surface and the thickness of the i^{th} layer, respectively. As indicated in Fig. 10.1, L, R and H are the length, the radius of the middle surface and the total thickness of the shell, respectively. The principal material directions are assumed to coincide with the coordinate axes, and the poling direction of the piezoelectric layers is along the x axis.

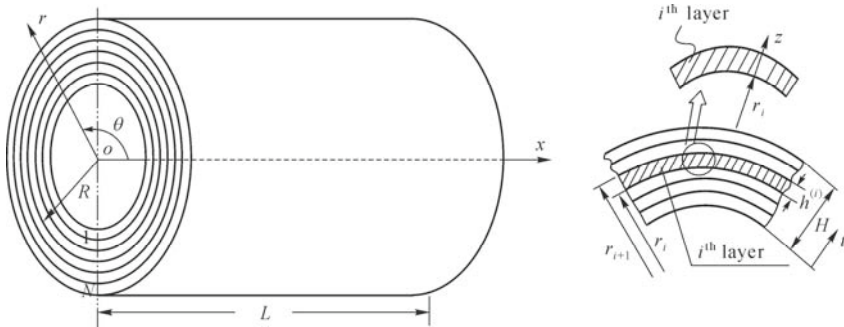


Fig. 10.1 A piezo-elastic laminated cylindrical shell

The constitutive relationships for the i^{th} lamina in the local coordinate system (x, θ, z) are

$$\begin{Bmatrix} \sigma_x \\ \sigma_\theta \\ \sigma_z \\ \tau_{\theta z} \\ \tau_{xz} \\ \tau_{x\theta} \end{Bmatrix}^{(i)} = \begin{bmatrix} c_{11} & c_{12} & c_{13} & 0 & 0 & 0 \\ c_{12} & c_{22} & c_{23} & 0 & 0 & 0 \\ c_{13} & c_{23} & c_{33} & 0 & 0 & 0 \\ 0 & 0 & 0 & c_{44} & 0 & 0 \\ 0 & 0 & 0 & 0 & c_{55} & 0 \\ 0 & 0 & 0 & 0 & 0 & c_{66} \end{bmatrix}^{(i)} \begin{Bmatrix} s_{xx} \\ s_{\theta\theta} \\ s_{zz} \\ s_{\theta z} \\ s_{xz} \\ s_{x\theta} \end{Bmatrix}^{(i)} - \begin{bmatrix} e_{11} & 0 & 0 \\ e_{12} & 0 & 0 \\ e_{13} & 0 & 0 \\ 0 & 0 & 0 \\ 0 & 0 & e_{35} \\ 0 & e_{26} & 0 \end{bmatrix}^{(i)} \begin{Bmatrix} E_x \\ E_\theta \\ E_z \end{Bmatrix}^{(i)} \quad (10.1)$$

$$\begin{Bmatrix} D_x \\ D_\theta \\ D_z \end{Bmatrix}^{(i)} = \begin{bmatrix} e_{11} & e_{12} & e_{13} & 0 & 0 & 0 \\ 0 & 0 & 0 & 0 & 0 & e_{26} \\ 0 & 0 & 0 & 0 & e_{35} & 0 \end{bmatrix}^{(i)} \begin{Bmatrix} s_{xx} \\ s_{\theta\theta} \\ s_{zz} \\ s_{\theta z} \\ s_{xz} \\ s_{x\theta} \end{Bmatrix}^{(i)} + \begin{bmatrix} \epsilon_{11} & 0 & 0 \\ 0 & \epsilon_{22} & 0 \\ 0 & 0 & \epsilon_{33} \end{bmatrix}^{(i)} \begin{Bmatrix} E_x \\ E_\theta \\ E_z \end{Bmatrix}^{(i)} \quad (10.2)$$

where $\{\sigma_x, \sigma_\theta, \sigma_z, \tau_{\theta z}, \tau_{xz}, \tau_{x\theta}\}^{(i)}$, $\{s_{xx}, s_{\theta\theta}, s_{zz}, s_{\theta z}, s_{xz}, s_{x\theta}\}^{(i)}$, $\{D_x, D_\theta, D_z\}^{(i)}$ and $\{E_x, E_\theta, E_z\}^{(i)}$ are the stress, strain, electric displacement and electric field components of the i^{th} lamina, respectively; and $c_{jk}^{(i)}$, $e_{jk}^{(i)}$ and $\epsilon_{jj}^{(i)}$ are the elastic stiffness constants, piezoelectric stress constants and dielectric constants, respectively. For brevity, the superscript i , signifying quantities for the i^{th} lamina, is omitted in the following derivations.

The mechanical strain and the displacements $\{u, v, w\}$, as well as the electric field components and the electric potential ϕ , are related by the following equations.

$$\begin{aligned} s_{xx} &= \frac{\partial u}{\partial x}, \quad s_{\theta\theta} = \frac{1}{r_i + z} \frac{\partial v}{\partial \theta} + \frac{w}{r_i + z}, \quad s_{zz} = \frac{\partial w}{\partial z}, \quad s_{\theta z} = \frac{1}{r_i + z} \frac{\partial w}{\partial \theta} + \frac{\partial v}{\partial z} - \frac{v}{r_i + z}, \\ s_{xz} &= \frac{\partial u}{\partial z} + \frac{\partial w}{\partial x}, \quad s_{x\theta} = \frac{1}{r_i + z} \frac{\partial u}{\partial \theta} + \frac{\partial v}{\partial x} \end{aligned} \quad (10.3)$$

$$E_x = \frac{\partial \phi}{\partial x}, \quad E_\theta = \frac{1}{r_i + z} \frac{\partial \phi}{\partial \theta}, \quad E_z = \frac{\partial \phi}{\partial z} \quad (10.4)$$

The motion equations are

$$\frac{\partial \sigma_x}{\partial x} + \frac{1}{r_i + z} \frac{\partial \tau_{x\theta}}{\partial \theta} + \frac{\partial \tau_{xz}}{\partial z} + \frac{\tau_{xz}}{r_i + z} = \rho \frac{\partial^2 u}{\partial t^2} \quad (10.5a)$$

$$\frac{\partial \tau_{x\theta}}{\partial x} + \frac{1}{r_i + z} \frac{\partial \sigma_\theta}{\partial \theta} + \frac{\partial \tau_{\theta z}}{\partial z} + \frac{\tau_{x\theta}}{r_i + z} = \rho \frac{\partial^2 v}{\partial t^2} \quad (10.5b)$$

$$\frac{\partial \tau_{xz}}{\partial x} + \frac{1}{r_i + z} \frac{\partial \tau_{\theta z}}{\partial \theta} + \frac{\partial \sigma_z}{\partial z} + \frac{\sigma_z - \sigma_\theta}{r_i + z} = \rho \frac{\partial^2 w}{\partial t^2} \quad (10.5c)$$

where ρ represents the mass density of the material.

The charge equation of electrostatics is

$$\frac{\partial D_x}{\partial x} + \frac{1}{r_i + z} \frac{\partial D_\theta}{\partial \theta} + \frac{\partial D_z}{\partial z} + \frac{D_z}{r_i + z} = 0 \quad (10.6)$$

10.3 Non-Damping Vibration of Simply Supported Shell

To obtain meaningful solutions, the two ends of the cylindrical shell $x=0$ and L are assumed to be mechanically simply supported and electrically insulated, that is

$$v = w = \sigma_x = 0, \quad D_x = 0 \quad (10.7)$$

The steady response solutions satisfying the above boundary conditions are expanded in the following double Fourier series:

$$[u, \phi, \tau_{xz}, D_z] = \sum_{m=0} \sum_{n=1} [U, \Phi, \bar{\tau}_{xz}, \bar{D}_z]_{mn} (\cos \alpha_m x \sin n\theta) e^{j\alpha x} \quad (10.8a)$$

$$[v, \tau_{\theta z}] = \sum_{m=1} \sum_{n=0} [V, \bar{\tau}_{\theta z}]_{mn} (\sin \alpha_m x \cos n\theta) e^{j\alpha x} \quad (10.8b)$$

$$[w, \sigma_x, \sigma_\theta, \sigma_z, D_x] = \sum_{m=1} \sum_{n=1} [W, \bar{\sigma}_x, \bar{\sigma}_\theta, \bar{\sigma}_z, \bar{D}_x]_{mn} (\sin \alpha_m x \sin n\theta) e^{j\alpha x} \quad (10.8c)$$

$$[\tau_{x\theta}, D_\theta] = \sum_{m=1} \sum_{n=1} [\bar{\tau}_{x\theta}, \bar{D}_\theta]_{mn} (\cos \alpha_m x \cos n\theta) e^{j\alpha x} \quad (10.8d)$$

where $\alpha_m = m\pi/L$; ω is the excitation frequency of the external force or the applied electric field; and U_{mn} , V_{mn} , W_{mn} , $\bar{\sigma}_{xmn}$, $\bar{\sigma}_{\theta mn}$, $\bar{\sigma}_{zmn}$, $\bar{\tau}_{\theta zmn}$, $\bar{\tau}_{xzmn}$, $\bar{\tau}_{x\theta mn}$, \bar{D}_{xmn} , $\bar{D}_{\theta mn}$, \bar{D}_{zmn} and Φ_{mn} are the unknown amplitudes which are only dependent on z .

The vector of fundamental unknowns \mathbf{R} , which consists of amplitudes of response quantities associated with the i^{th} layer and a pair of harmonics (m, n) , is defined as

$$\mathbf{R}(z) = [\{U(z), V(z), W(z), \Phi(z), \bar{\sigma}_z(z), \bar{\tau}_{xz}(z), \bar{\tau}_{\theta z}(z), \bar{D}_z(z)\}_{mn}]^T \quad (10.9)$$

where the superscript T denotes transposition.

Using the constitutive relationships Eqs. (10.1) and (10.2) to eliminate σ_x , σ_θ , $\tau_{x\theta}$, D_x and D_θ from the equations of motion and the electric charge equation, *i.e.*, Eqs. (10.5) and (10.6), eight state-space equations associated with a pair of harmonics (m, n) for each layer are obtained and expressed in the below vector-matrix differential equation:

$$A(z)\frac{dR(z)}{dz} + B(z)R(z) = 0 \quad (10.10)$$

where $A(z)=A_0+A_1z+A_2z^2$ and $B(z)=B_0+B_1z+B_2z^2$. The expressions of matrices A_j and B_j ($j=0,1,2$) are given in Appendix F. Eq. (10.10) represents a set of homogeneous ordinary differential equations with variable coefficients, which can be solved by the Frobenius method.

The continuous conditions at the interface between the outer surface of the i^{th} layer and the inner surface of the $(i+1)^{\text{th}}$ layer can be specified as follows.

(1) If the interface is just a mechanical interface between the two laminas, the continuous conditions can be written in the following form:

$$R^{(i+1)}(0) = R^{(i)}(h^{(i)}) \quad (10.11)$$

(2) If the interface is electroded, the electric potential can be assumed to be a known function Φ_{0mn} . The normal component of the electric displacement \bar{D}_{zmn} need not be continuous across this interface; thus, the continuous conditions are

$$\begin{aligned} & [U(0), V(0), W(0), \sigma_z(0), \tau_{\theta z}(0), \tau_{xz}(0)]_{mn}^{(i+1)} \\ &= [U(h^{(i)}), V(h^{(i)}), W(h^{(i)}), \sigma_z(h^{(i)}), \tau_{\theta z}(h^{(i)}), \tau_{xz}(h^{(i)})]_{mn}^{(i)} \\ & \Phi_{mn}^{(i)}(h^{(i)}) = \Phi_{mn}^{(i+1)}(0) = \Phi_{0mn} \end{aligned} \quad (10.12)$$

Using the Frobenius method, the solution to Eq. (10.10) can be expressed as

$$R(z) = \left(\sum_{k=0}^{\infty} F_k z^k \right) y_0 \quad (10.13)$$

where $F_{k+1} = -\frac{1}{k+1} A_0^{-1} \{ (B_0 + kA_1)F_k + [B_1 + (k-1)A_2]F_{k-1} + B_2F_{k-2} \}$, $k = 0, 1, 2, \dots$; $F_{-1} = F_{-2} = \mathbf{0}$; F_0 is the identity matrix; and y_0 is a constant vector to be determined by the boundary conditions and the interface continuous conditions.

Eq. (10.13) consists of a set of 8 simultaneous linear algebraic equations in terms of the 8 unknown amplitudes y_{0j} ($j=1, \dots, 8$) for each layer. Considering $8(N-1)$ continuous conditions and a total of 8 boundary conditions at the outer and inner surfaces of the shell, a total of $8N$ unknown amplitudes $y_{0j}^{(i)}$ ($i=1, 2, \dots, N$; $j=1, \dots, 8$) can be determined. After these amplitudes are obtained, the responses of displacement, stress, electric potential and electric displacement can be computed at any location within the laminate.

The in-plane components of response quantities for the i^{th} layer can be defined

as

$$\mathbf{P}(z) = \left[\left\{ \bar{\sigma}_x(z), \bar{\sigma}_\theta(z), \bar{\tau}_{x\theta}(z), \bar{D}_x(z), \bar{D}_\theta(z) \right\}_{mn} \right]^T \quad (10.14)$$

Vector $\mathbf{P}(z)$ can be expressed in terms of vector $\mathbf{R}(z)$ as:

$$\mathbf{P}(z) = \mathbf{TR}(z) \quad (10.15)$$

where the explicit form of matrix \mathbf{T} is given in Appendix F.

10.4 Active Vibration Control of Cylindrical Shell with PSAs

The closed-loop control method is employed to control the transverse vibration of the shell-PSA system. Based on the negative velocity feedback control, the active vibration control model shown in Fig. 10.2 is proposed. To dampen the response of the system, the potential applied to the actuator is used as the control variable.

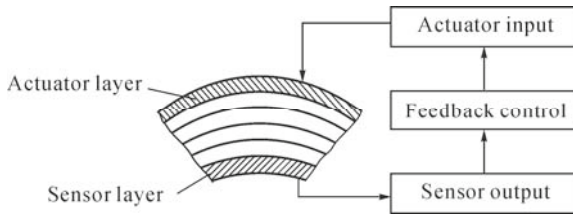


Fig. 10.2 An active control model of cylindrical shell

For sensing purpose, there exist two conditions for the piezoelectric laminae: the close circuit (Lee and Moon, 1990) and the open circuit (Tzou, 1993) conditions. Here, the open circuit condition is considered where the electric displacement D_z on the boundaries is zero. Thus, the output voltage V across the top and bottom electroded surfaces of the sensor are obtained by integrating the electric field over the thickness of the piezoelectric sensor layer as

$$\begin{aligned} V &= \int_{h^{(s)}} E_z^{(s)} dz = \frac{1}{\epsilon_{33}^{(s)}} \int_{h^{(s)}} \left(D_z^{(s)} - e_{35}^{(s)} s_{xz}^{(s)} \right) dz \\ &= -\frac{e_{35}^{(s)}}{\epsilon_{33}^{(s)}} \int_{h^{(s)}} s_{xz}^{(s)} dz = -\frac{e_{35}^{(s)}}{\epsilon_{33}^{(s)}} \int_{h^{(s)}} \left(\frac{\partial u}{\partial z} + \frac{\partial w}{\partial x} \right)^{(s)} dz \end{aligned} \quad (10.16)$$

where the superscript s denotes the components associated with the sensor layer. The above equation depicts the relationship between the output voltage of the sensor with the vibration of the laminate. According to the negative velocity feedback control method, the control voltage ϕ_a is calculated as

$$\phi_a = -\kappa \frac{dV}{dt} = \frac{\kappa \epsilon_{33}^{(s)}}{\epsilon_{33}^{(s)}} \frac{d}{dt} \left(\int_{h^{(s)}} \left(\frac{\partial u}{\partial z} + \frac{\partial w}{\partial x} \right)^{(s)} dz \right) \quad (10.17)$$

where κ is the gain of feedback. Substituting the expressions of the displacements in Eq. (10.8) into Eq. (10.17), the following is obtained

$$\phi_a = \sum_{m=0} \sum_{n=1} \Phi_{amn} (\cos \alpha_m x \sin n\theta) e^{i\omega t} \quad (10.18)$$

where

$$\Phi_{amn} = \frac{i\omega \kappa \epsilon_{33}^{(s)}}{\epsilon_{33}^{(s)}} \left(U_{mn}^{(s)} \Big|_0^{h^{(s)}} + \alpha_m \int_0^{h^{(s)}} W_{mn}^{(s)} dz \right).$$

The above expression can be regarded as the equivalent active damping. Hence, the solutions for other active vibration control problems can be similarly solved using the method presented in Section 10.3, with the electric potential on the surface of the piezoelectric actuator replaced by the control voltage ϕ_a .

10.5 Numerical Results and Discussions

The cylindrical shell studied has four graphite-epoxy layers as host structure and two piezoelectric layers, one as sensor and the other as actuator (Fig. 10.3). A total of three different configurations are considered. The graphite-epoxy is assumed to be orthotropic. The piezoelectric layer, PZT-5A, is transversely isotropic with the x axis as the axis of transverse isotropy and the poling direction. The material properties of graphite-epoxy and PZT-5A are listed in Table 10.1.

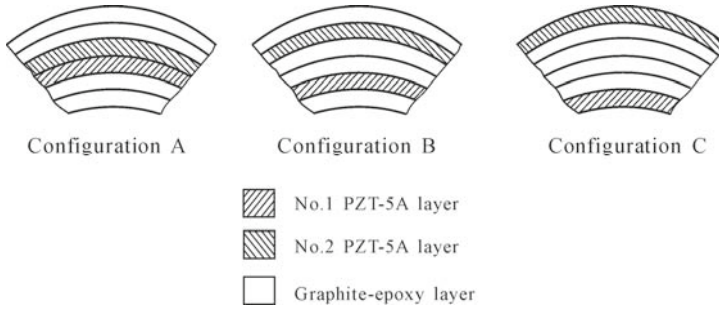


Fig. 10.3 Three different shell configurations

Table 10.1 Material properties of graphite-epoxy layer and PZT-5A shear actuator

Property	Graphite-epoxy	Shear PZT-5A
C_{11} (GPa)	183.443	86.856
C_{22} (GPa)	11.662	99.201
C_{33} (GPa)	11.662	99.201
C_{12} (GPa)	4.363	50.778
C_{13} (GPa)	4.363	50.778
C_{23} (GPa)	3.918	54.016
C_{44} (GPa)	2.870	22.593
C_{55} (GPa)	7.170	21.100
C_{66} (GPa)	7.170	21.100
e_{11} (cm^{-2})	0	15.118
e_{12} (cm^{-2})	0	-7.209
e_{13} (cm^{-2})	0	-7.209
e_{26} (cm^{-2})	0	12.322
e_{35} (cm^{-2})	0	12.322
ϵ_{11} (10^{-10} F/m)	153.0	153.0
ϵ_{22} (10^{-10} F/m)	153.0	153.0
ϵ_{33} (10^{-10} F/m)	153.0	153.0
ρ (kg/m^3)	1,590	7,750

The radius of the middle surface and the length of the shell are $R=1$ m and $L=1$ m, respectively. Each graphite-epoxy layer has the same thickness and the total thickness of four layers is $h_e=0.4$ m. The two PZT-5A layers also have the same thickness, with h_p denoting their total thickness.

10.5.1 Steady-State Response Analysis

An example is used to illustrate the effects of thickness ratio h_p/h_e and the position of the piezoelectric layer on the steady-state response of the shell. Two

different loads are applied to the shell: (1) the transverse mechanical load $q_0 \sin(\pi x/L) \sin \theta e^{i\omega t}$ on the outer surface of the shell, and (2) the electric potentials $\phi_0 \cos(\pi x/L) \sin \theta e^{i\omega t}$ on the inner surface of No. 1 PZT-5A layer and $-\phi_0 \cos(\pi x/L) \sin \theta e^{i\omega t}$ on the outer surface of No. 2 PZT-5A layer. The excitation frequency ω is set as 1 kHz. The mechanical displacement, stress, electric displacement and electric potential are normalized as $[\hat{U}, \hat{V}, \hat{W}] = [u, v, w]C_0/Lq_0$, $[\hat{D}_x, \hat{D}_\theta, \hat{D}_z] = [D_x, D_\theta, D_z]C_0/(e_0q_0)$, $\hat{\phi} = \phi e_0/(Lq_0)$, $[\hat{\sigma}_x, \hat{\sigma}_\theta, \hat{\sigma}_z, \hat{\tau}_{\theta z}, \hat{\tau}_{xz}, \hat{\tau}_{x\theta}] = [\sigma_x, \sigma_\theta, \sigma_z, \tau_{\theta z}, \tau_{xz}, \tau_{x\theta}]/q_0$ for the applied mechanical load, and $[\hat{U}, \hat{V}, \hat{W}] = [u, v, w]C_0/(e_0\phi_0)$, $[\hat{D}_x, \hat{D}_\theta, \hat{D}_z] = [D_x, D_\theta, D_z]LC_0/(e_0^2\phi_0)$, $\hat{\phi} = \phi/\phi_0$, $[\hat{\sigma}_x, \hat{\sigma}_\theta, \hat{\sigma}_z, \hat{\tau}_{\theta z}, \hat{\tau}_{xz}, \hat{\tau}_{x\theta}] = [\sigma_x, \sigma_\theta, \sigma_z, \tau_{\theta z}, \tau_{xz}, \tau_{x\theta}]L/(e_0\phi_0)$ for the applied electric load. $C_0=22.583$ GPa and $e_0=12.322$ cm⁻² are the typical values of the elastic and piezoelectric moduli for PZT-5A, respectively.

Fig. 10.4 compares the amplitude of transverse response \hat{w} along the thickness direction of the shell, under mechanical loading, for all three configurations and for two different thickness ratios, $h_p/h_e=0.02$ and $h_p/h_e=0.2$. It is apparent that, for the small thickness ratio $h_p/h_e=0.02$, the distributions of displacement responses \hat{w} in the thickness direction for the three configurations are almost the same. However, for the large thickness ratio $h_p/h_e=0.2$, the displacement responses for the three configurations are significantly different, where the amplitude for Configuration A is the smallest and that for Configuration C the largest.

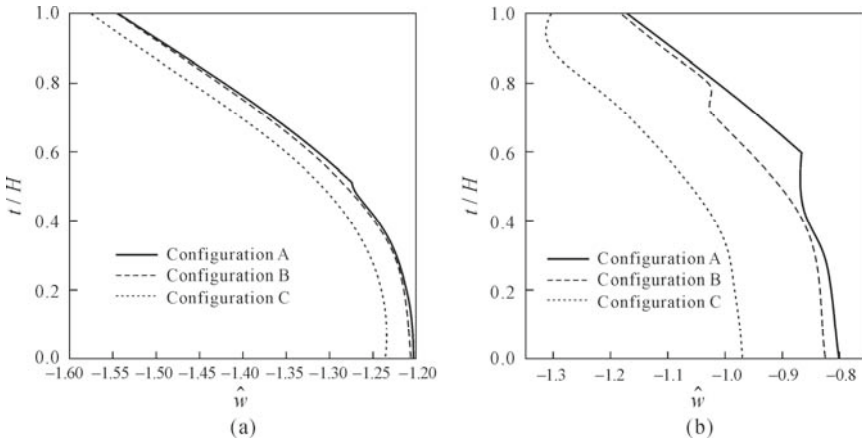


Fig. 10.4 Amplitude of transverse response under mechanical loading. (a) $h_p/h_e = 0.02$; (b) $h_p/h_e = 0.2$

The above observation could be explained as follows. When the shell is only subjected to mechanical loading, the mechanical properties are the dominant parameters affecting the response. For the small thickness ratio, the total structural stiffnesses are almost the same for all three configurations, resulting in marginal differences in their responses. For the large thickness ratio, the stiffnesses of the three configurations are quite different from one another. Since PZT-5A is stiffer than graphite-epoxy, the configuration with PZT-5A layers closer to the middle surface of the shell is stiffer than those with PZT-5A further away. Thus, Configuration A has the largest stiffness and Configuration C has the smallest resulting in Configuration A with the smallest absolute value of deformation and Configuration C with the largest.

Figs. 10.5 and 10.6 compare the transverse responses of the three shell configurations under electric loading. From Fig. 10.5, it is apparent that for both thickness ratios, the response of Configuration A is the largest and that of Configuration C is the smallest. These results are established on the shear actuation mechanism of piezoelectric materials, where the application of electric potential produced transverse shear deformation in the piezoelectric layers which in turn caused the structure to deflect in the transverse direction. The closer are the two piezoelectric layers, the greater is the shear strain. Therefore, the response of Configuration A is greater than those of the other two configurations.

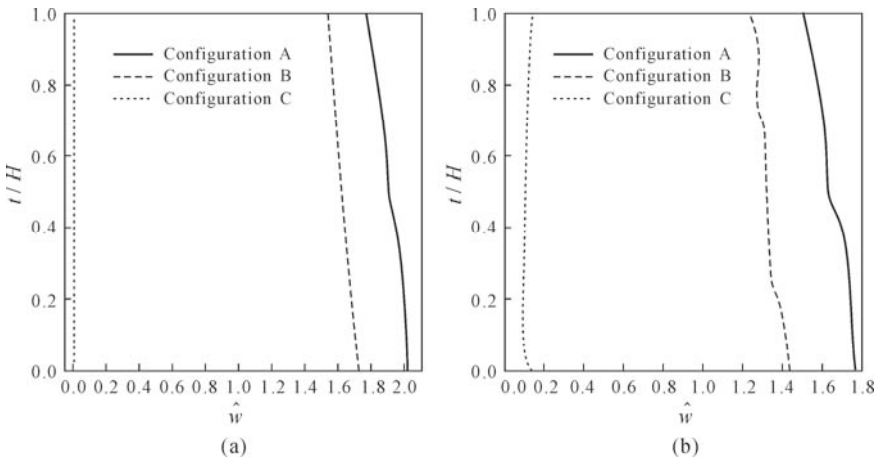


Fig. 10.5 Amplitude of transverse response under electrical loading. (a) $h_p/h_c = 0.02$; (b) $h_p/h_c = 0.2$

The above results are different from those of a hybrid shell with extension piezoelectric layers, where the extension-mode actuators provided the longitudinal strains and supplied the bending load. The nearer are the two piezoelectric layers, the smaller is the bending load and the smaller is the response induced in the shell.

Therefore, if large transverse deformation of the shell is desired by applying electric potential on the PSAs, the PSAs should be arranged close to each other. Conversely, if the extension piezoelectric actuators are used, they should be arranged as far as possible from each other to generate large transverse deformation in the shell.

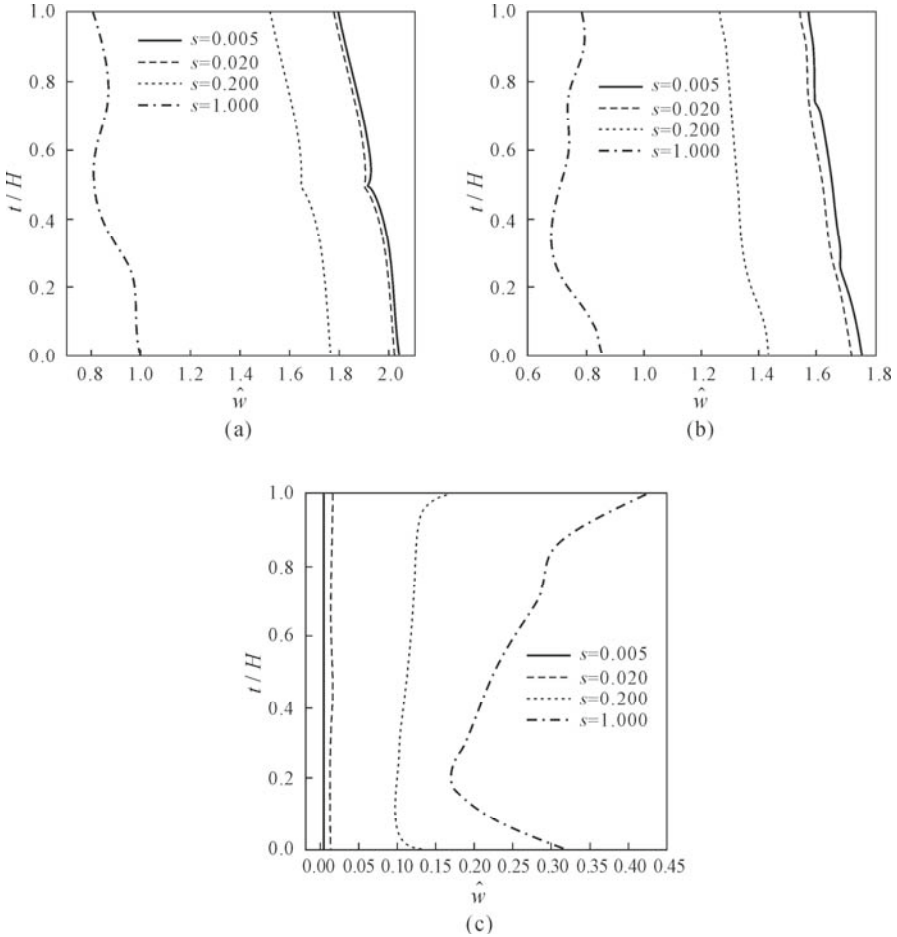


Fig. 10.6 Distribution of transverse response for different thickness ratios under electrical loading. (a) Configuration A; (b) Configuration B; (c) Configuration C

Fig. 10.6 depicts the distribution of transverse responses for different thickness ratios for the three shell configurations subjected to electric loading, where $s = h_p/h_e$ represents the thickness ratio. It can be seen that when the thickness of piezoelectric layer increases, the deformation of the entire composite shell

decreases for both Configurations A and B (Figs. 10.6a and 10.6b), but that of Configuration C increases (Fig. 10.6c). The phenomenon for Configurations A and B can be explained as follows. The shear strain induced by the electric potential is proportional to the derivative of electrical potential with respect to thickness. Therefore, for a given electric load, a thinner piezoelectric layer generated larger shear strain, subsequently inducing larger deformation of the shell.

However, the situation is different for Configuration C because the shear strain is affected not only by the electric potential, but also by the shear stress. In Configuration C, the piezoelectric layers are placed on the outer and inner surfaces of the shell. To satisfy the free shear stress boundary condition, the level of shear stress in the piezoelectric layers is low because they are in the vicinity of the boundaries. Therefore, the shear strain is smaller when the piezoelectric layer is thinner, thus inducing smaller response of the shell.

10.5.2 Active Vibration Control

When no load is applied on the shell, Eq. (10.13) can be used to calculate the natural frequencies of the shell. Again, Configurations A, B and C with two different thickness ratios are considered. Table 10.2 lists their natural frequencies that are below 10 kHz.

Table 10.2 Natural frequencies of three shell configurations

h_p/h_e	Configuration A	Configuration B	Configuration C
0.02	5,303.85	5,294.19	5,241.50
	7,572.16	7,566.77	7,540.63
0.2	4,839.40	4,754.75	4,415.30
	7,169.40	7,145.41	6,971.28
		9,844.22	8,659.90

The control model shown in Fig. 10.2 is used. For all three configurations, No.1 PZT-5A layer functioned as a sensor and No.2 PZT-5A layer as an actuator. All the three configurations are subjected to the transverse mechanical loading $q_0 \sin(\pi x/L) \sin \theta e^{j\alpha t}$ on their outer surfaces. Figs. 10.7 and 10.8 show the amplitude of response \hat{w} versus the excitation frequency under different feedback gains. It is obvious from both figures that the response can be effectively reduced by increasing the feedback gain κ in the vicinity of the natural frequencies. However, when the excitation frequency is not close to any natural frequencies, the reduction in response by increasing κ is very small.

Fig. 10.9 plots the control voltage versus the excitation frequency under different feedback gains for the control shown in Fig. 10.8(a), *i.e.*, Configuration

A. The control voltage for the other two configurations is similar to that for Configuration A and thus not shown. It is obvious from Fig. 10.9 that, as expected, large feedback gain κ corresponds to high control voltage and that the control voltage increases rapidly near the natural frequencies in order to suppress the resonant responses.

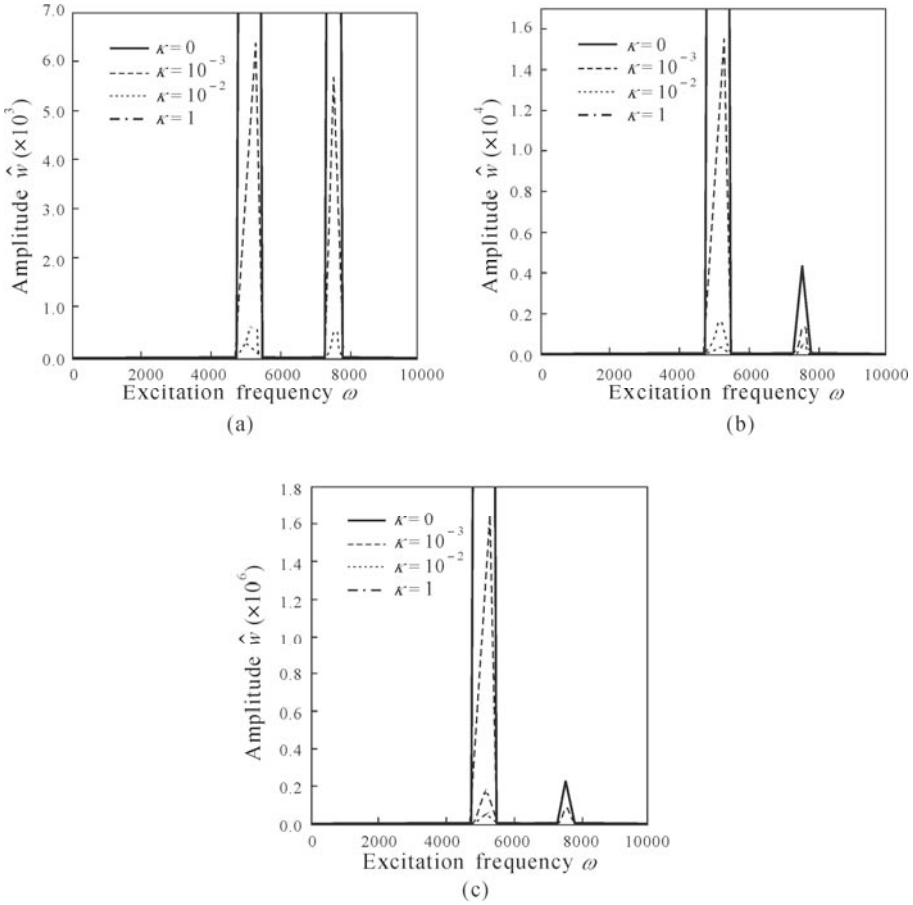


Fig. 10.7 Amplitude of transverse response under different feedback gains, for thickness ratio $h_p/h_e = 0.02$. (a) Configuration A; (b) Configuration B; (c) Configuration C

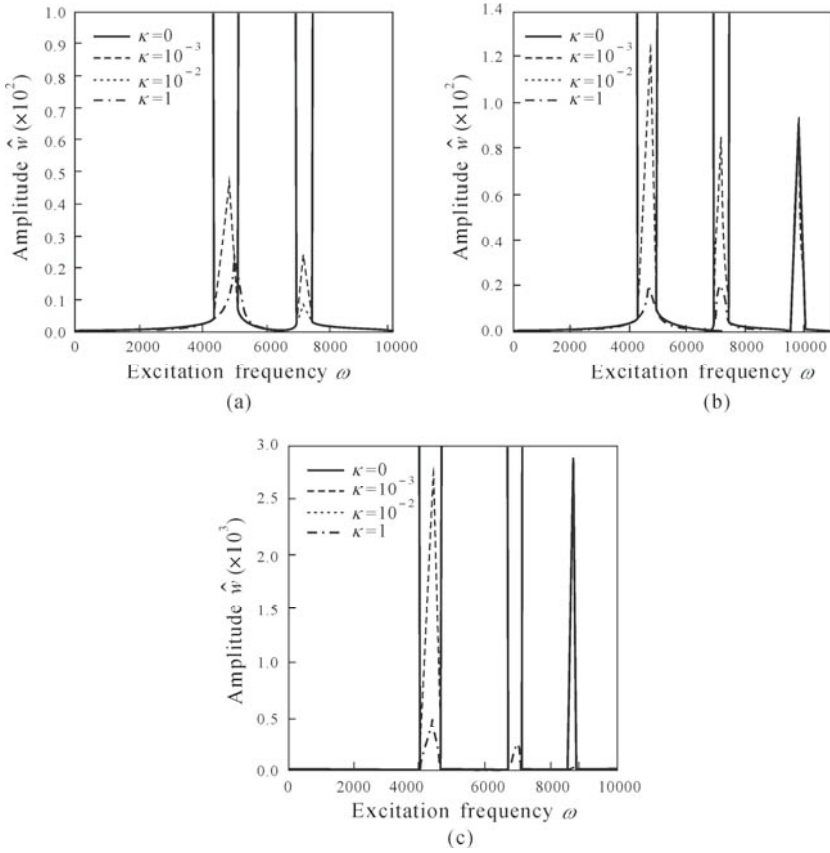


Fig. 10.8 Amplitude of transverse response under different feedback gains, for thickness ratio $h_p/h_e = 0.2$: (a) Configuration A; (b) Configuration B; (c) Configuration C

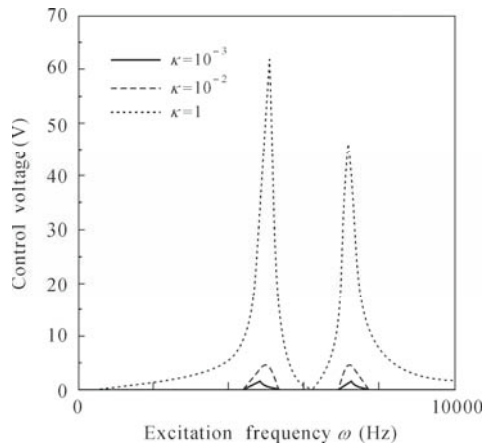


Fig. 10.9 Control voltage under different feedback gains for Configuration A

10.6 Summary

The analysis of dynamic response of a fully coupled piezo-elastic cylindrical shell with embedded PSAs is presented in this chapter. Numerical examples are used to illustrate the effects of thickness ratio and location of PSAs on the transverse response for both the mechanical and electric loadings. It is observed that the response of the shell subjected to mechanical loading is mainly determined by the mechanical properties of the structure. For the electric loading, the response of shell with embedded PSAs is larger than that of the shell with surface-mounted PSAs. Furthermore, for the shell with embedded PSAs, thinner piezoelectric layer rendered larger response, and for the shell with surface-mounted PSAs, thicker piezoelectric layer generated larger response.

Based on the negative velocity feedback control method, an active vibration control model for a simply supported cylindrical shell with piezoelectric shear sensor and actuator layers is presented. The numerical results showed that the vibration of the shell can be effectively suppressed in the vicinity of the resonant zone by increasing the feedback gain. This presents a possible way for PSAs to actively reduce the harmful effect of resonance in the cylindrical shells.

References

- Aldraihem, O.J. and Khdeir, A.A. (2003). "Exact deflection solutions of beams with shear piezoelectric actuators", *International Journal of Solids and Structures*, 40(1): 1-12.
- Baillargeon, B.P. and Vel, S.S. (2005). "Exact solution for the vibration and active damping of composite plates with piezoelectric shear actuators", *Journal of Sound and Vibration*, 282: 781-804.
- Benjeddou, A., Trindade, M.A. and Ohayon, R. (1997). "A unified beam finite element model for extension and shear piezoelectric actuation mechanisms", *Journal of Intelligent Material Systems and Structures*, 8 (12): 1012-1025.
- Benjeddou, A., Gorge, V. and Ohayon, R. (2001a). "Use of piezoelectric shear response in adaptive sandwich shells of revolution—part 1: theoretical formulation", *Journal of Intelligent Material Systems and Structures*, 12 (4): 235-245.
- Benjeddou, A., Gorge, V. and Ohayon, R. (2001b). "Use of piezoelectric shear response in adaptive sandwich shells of revolution—part 2: finite element implementation", *Journal of Intelligent Material Systems and Structures*, 12 (4): 247-257.
- Jin, Z.L., Yang, Y.W. and Soh, C.K. (2005). "Application of fuzzy GA for optimal vibration control of smart cylindrical shells", *Smart Materials and Structures*, 14 (6): 1250-1264.
- Kant, T. and Shiyekar, S.M. (2008). "Cylindrical bending of piezoelectric

- laminates with a higher order shear and normal deformation theory”, *Computers and Structures*, 86: 1594-1603.
- Khdeir, A.A. and Aldraihem, O.J. (2001). “Deflection analysis of beams with extension and shear piezoelectric patches using discontinuity functions”, *Smart Materials and Structures*, 10(2): 212-220.
- Lee, C.K. and Moon, F.C. (1990). “Modal sensors/actuators”, *Journal of Applied Mechanics*, 57: 434-441.
- Li, H.Y., Sun, Y. and Liu, Z.X. (2004). “Three-dimensional analytical solutions for multilayered cylindrical shells with embedded piezoelectric shear actuators”, *Key Engineering Materials*, 274-276: 1125-1130.
- Li, H.Y. and Yang, Y.W. (2007). “Dynamic response and active control of a composite cylindrical shell with piezoelectric shear actuators”, *Smart Materials and Structures*, 16(3): 909-918.
- Morgan Matroc (2006). Electro ceramic Div., Bedford, OH, http://www.morganelectroceramics.com/piezo_products.html.
- Rao, S.S. and Sunar, M. (1999). “Recent advances in sensing and control of flexible structures via piezoelectric material technology”, *Applied Mechanics Reviews*, 52: 1-16.
- Raja, S., Prathap, G. and Sinha, P.K. (2002). “Active vibration control of composite sandwich beams with piezoelectric extension-bending and shear actuators”, *Smart Materials and Structures*, 11(1): 63-71.
- Sun, C.T. and Zhang, X.D. (1995). “Use of thickness shear mode in adaptive sandwich structures”, *Smart Materials and Structures*, 4(3): 202-206.
- Trindade, M.A. and Benjeddou, A. (2008). “Refined sandwich model for the vibration of beams with embedded shear piezoelectric actuators and sensors”, *Computers and Structures*, 86: 859-869.
- Tzou, H.S. (1993). *Piezoelectric Shells—Distributed Sensing and Control of Continua*. Dordrecht: Kluwer Academic Publishers.
- Vel, S.S. and Baillargeon, B.P. (2005). “Analysis of static deformation, vibration and active damping of cylindrical composite shells with piezoelectric shear actuators”, *Journal of Vibration and Acoustics*, 127(4): 395-407.
- Yang, Y.W. and Zhang, L. (2006). “Optimal excitation of a rectangular plate resting on an elastic foundation by a piezoelectric actuator”, *Smart Materials and Structures*, 15(4): 1063-1078.
- Zhang, X.D. and Sun, C.T. (1996). “Formulation of an adaptive sandwich beam”, *Smart Materials and Structures*, 5(6): 814-823.

Fiber Bragg Grating

R. Suresh*, S. C. Tjin and J. Hao

*Department of Physics, S.V.College, University of Delhi,
Dhaura Kuan, New Delhi 110021, India
Tel: 91-11-2411-2196; Fax: 91-11-2411-8535
Email: rsuresh.assoc@ntu.edu.sg

11.1 Introduction

Fiber optics has emerged as a promising sensing technology over the past two decades. Fiber optic sensors (FOS) have generated great interest due to their small size, immunity to electro-magnetic interference and radio frequency (RF) interference, inherent safety, and accuracy. A sensor based on intensity modulation of light propagating in an optical fiber was first reported in the early 1980's (Giallorenzi *et al.*, 1982). Soon after, sensors based on phase modulation were also reported (Mellberg, 1983). However, both the intensity-modulated and the phase-modulated FOSs are susceptible to changes in the light intensity received by the detector. The change in light intensity could be a result of fiber loss due to scattering, absorption or bending, losses at fiber couplers or source intensity fluctuations. The intensity losses in the fiber caused by external force variations often require time averaging to assess and map the spatial changes in the loss or scattering coefficients along the fiber. As a result, the induced noise of the received signal increases, thus complicating the signal processing of the system. On the other hand, a FOS using fiber Bragg grating (FBG) provides an absolute wavelength measurement that is independent of the overall system light levels and dependent only upon the strain and temperature effects acting on the sensor. In this chapter, FBG sensor technology, which provides an absolute measurement, is described. This technique is wavelength encoded to avoid problems with scale resetting and signal intensity variation that plague the intensity and phase modulated sensors. FBG is a

wavelength modulated element, making the signal immune to losses. This chapter presents the fundamental concept of FBG and dwells upon FBG-based pressure/strain and shear force sensors.

11.2 History of FBG

Hill *et al.* (1978) first reported the photosensitivity of germanosilicate optical fiber and its application for fabrication of reflection filters. These filters were formed by exposure of the photosensitive core of the fiber to intense contra-directionally propagating coherent beams. The resulting standing wave pattern in the fiber core formed a periodic perturbation that comprised the filter. Subsequently, Lam and Garside (1981) found that the grating strength increases as the square of the writing power (*i.e.* the laser power), indicating a two-photon phenomenon involved in grating formation.

Meltz *et al.* (1989) reported the transverse holographic method for fabrication of grating. In this technique, the Bragg grating was written in germanosilicate optical fibers, by exposing the core through the side of the cladding, to a coherent ultra-violet (UV) two-beam interference pattern. Later, Hill *et al.* (1993) reported the fabrication of fiber grating by the phase mask technique, where the interference pattern formed between the beams diffracted in the ± 1 order, is exposed to the fiber core through the side of the cladding. This technique is now widely used and has been found to be a very efficient and quick way of fabricating FBGs.

Fiber Bragg grating is essentially a wavelength-selective filter. A fiber Bragg grating will reflect light that has a wavelength corresponding to twice its period, multiplied by the effective refractive index of the fiber that the propagating mode observes. This is called the Bragg condition, given by (Kersey *et al.*, 1997),

$$\lambda_b = 2n_{eff} \Lambda \quad (11.1)$$

where λ_b is the Bragg wavelength that will be reflected back, n_{eff} the effective refractive index of the fiber core, and Λ the period of the grating. Light at other wavelengths will be transmitted without significant attenuation. In other words, the grating operates as a narrow-band wavelength notch filter. The transmission and reflection spectra of a FBG are shown in Fig. 11.1 (Hao *et al.*, 2003).

The fundamental cause of grating inscription in the fiber core is the photosensitivity of the material (Salik *et al.*, 2000; Zhang and Raghavachari, 1997; Nagamo *et al.*, 1991; Williams *et al.*, 1993; Kashyap, 1999; Malo *et al.*, 1993a). Initially, special photosensitive fiber such as high concentration germanium-doped or boron-codoped fibers were used for grating fabrication. Later, Lemaire *et al.*

(1993) reported a simple and cost-effective process of photosensitizing the communication fibers. In this technique, hydrogen molecules are diffused into the fibers at high pressure (Atkins *et al.*, 1993; Poumellec *et al.*, 2003; Lou *et al.*, 2003). This technique ensures higher photosensitivity with cost effectiveness. The stability issue (Guan *et al.*, 2000; Atkins and Espindola, 1997) of the gratings written in both the doped and hydrogenated fibers (Riant and Poumellec, 1998) has been discussed by Patrick *et al.* (1995) and it is found that annealing the gratings written in hydrogenated fiber could lead to a much longer FBG lifetime (Limberger and Varelas, 1999). Later, Kohnke *et al.* (1999) and Canning (2000) reported enhancement of photosensitivity of hydrogen loaded, germanium or phosphor doped fiber by pre-UV treatment. Chen and Herman (2003) reported photosensitivity locking in standard telecom fiber, where a strong and permanent UV photosensitivity enhancement was locked into standard optical fiber pre-treated with above-bandgap, 157-nm F2-laser radiation.

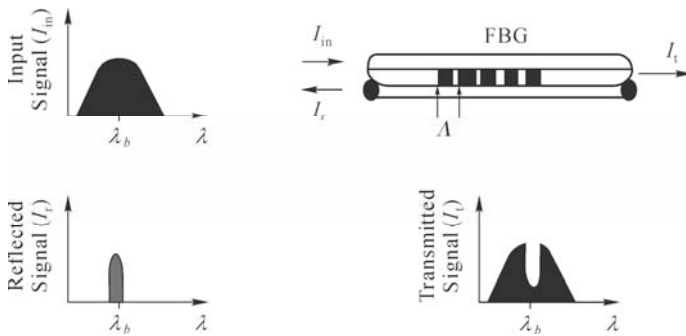


Fig. 11.1 Transmission and reflection spectra of FBG (Hao *et al.*, 2003)

FBG is now extensively used in optical communication (Giles, 1997; Yankov *et al.*, 2003) and covers the major part of the fiber optic sensing technology. The following section discusses the characteristic of FBG as a sensor and its advantages over other sensors.

11.3 Fabrication of FBG

FBGs can be formed by exposing a photosensitive optical fiber to a 3D fringe pattern created by two interfering high-energy UV beams, which is known as the holographic technique (Meltz *et al.*, 1989); or by the transmission pattern from an appropriate diffractive optical element, which is called the phase mask technique (Malo *et al.*, 1993 b). The phase mask technique involves the use of a +1/-1 order phase mask (Fig. 11.2). Irradiation of the silica fiber with bright portions of the UV pattern, spurred by the presence of defect centers, creates a permanent modulation of refractive index of the core.

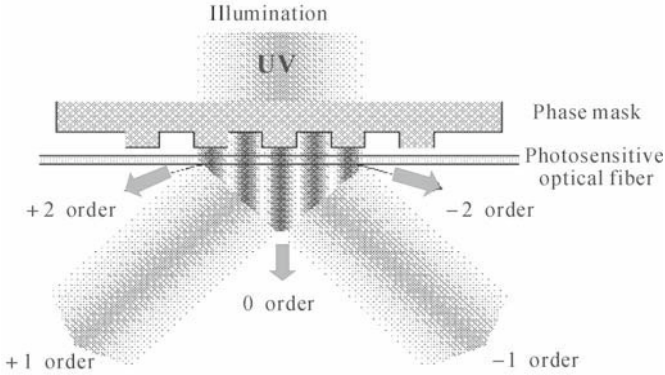


Fig. 11.2 Phase mask photo- imprinting of fiber Bragg grating (Hao, 2001)

The phase mask is optimized to diffract the UV light equally into the ± 1 order. Self-interference between these two orders creates an interference pattern into the core of the photosensitive fiber with the grating period at half the pitch size of the phase mask. Additional zeroth order and higher order noises are highly suppressed by the phase mask. A typical phase mask is shown in Fig. 11.3.

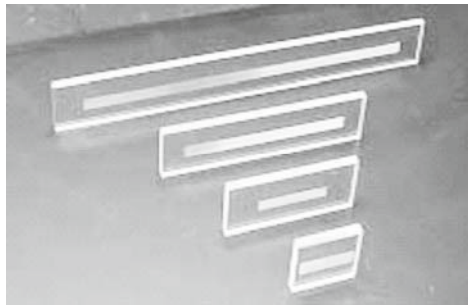


Fig. 11.3 A typical phase mask (picture reproduced with permission from <http://www.qpscom.com/pages/phasemask-1.htm>)

Fiber can be rendered photosensitive by doping the core with germanium, phosphorous or boron during fabrication. The photosensitivity of all fibers can be boosted by loading them with hydrogen under temperature and/or pressure, that is, by putting them in a chamber filled with hydrogen gas (Juma, 1996, Lemaire *et al.*, 1993). Another technique known as “flame brushing” is also sometimes used (Bilodeau *et al.*, 1993). The highly germanium-doped fiber is able to reduce the magnitude of short wavelength loss commonly observed in FBGs. It has similar numerical aperture (0.11 ± 0.02) and mode field diameter ($10.5 \pm 1.5 \mu\text{m}$ @1550 nm) as the standard single mode communication fiber at 1550 nm. High reflectivity gratings (at least 20 dB) without hydrogen loading can be easily fabricated in less than two minutes (SpecTran, 2001). The UV-induced refractive index change (Δn)

is found to exhibit temperature dependent decay of Δn with time after inscription. Erdogan *et al.* (1994) reported the measurement of thermally induced decay of gratings fabricated in erbium co-doped germanosilicate fibers. The decay in reflectivity is characterized by the power law, which is a function of time, exhibiting a rapid initial decay followed by a decreasing rate of decay. Briefly, this behavior is consistent with the thermal depopulation of the trapped states occupied by carriers that are photo excited from their original band locations by the UV irradiation. Thermally exciting carriers out of shallow traps cause the observed decay in the refractive index, and residual carriers that are not excited out of the traps lead to the “stable” portion of the index change.

Canning and Sceats (1995) demonstrated photosensitivity at 193-nm in phosphosilicate fibers fabricated by the flash condensation technique (Cater *et al.*, 1992). Strasser *et al.* (1995) showed for the first time that strong (>3 nm spectral width) UV-induced Bragg gratings could also be written in phosphorus-doped silica material. This grating was produced by a 10-minute exposure at 30 Hz and 90 mJ/cm² pulse. Thermal erasure of a grating written in a phosphosilicate channel waveguide at 193-nm has been demonstrated by Malo *et al.* (1994). The immediate advantages of using 193-nm channel waveguide are (1) a reduction of laser-induced damage to the fiber when using a phase mask and (2) a higher spatial resolution in diffraction-limited applications, such as point-by-point writing. Also, Bragg gratings fabricated at 193 nm irradiation appear to develop much stronger reflectivity than at 248 nm under similar excitation conditions. Dong *et al.* (1996) also observed that the grating growth is much faster at 193 nm than at 248 nm.

11.4 Optical Properties of Grating

The optical properties of a fiber grating are essentially determined by the variation of the induced index change along the fiber axis. The types of gratings include uniform, chirped, discrete phase-shifted, superstructure, short period, long period, symmetric, tilted, cladding-mode and radiation-mode coupling gratings. Uniform FBG is commonly used for most sensor applications. Therefore, only the optical behavior of uniform FBG is discussed in this chapter.

A fiber grating is simply an optical diffraction grating inscribed in the core of an optical fiber. It is well established that the effect of light incident on a diffraction grating at an angle θ_1 can be described by grating equation (Erdogan, 1997)

$$n \sin \theta_2 = n \sin \theta_1 + m \frac{\lambda}{\Lambda} \quad (11.2)$$

where θ_2 is the angle of the diffracted wave, n stands for the refractive index of the

fiber core, the integer m determines the diffraction order, λ is the wavelength, and Λ is the grating period (see Fig. 11.4). Eq. (11.2) not only predicts the direction θ_2 into which the constructive interference occurs, but is also capable of determining the wavelength at which the fiber grating couples light between the two modes efficiently.

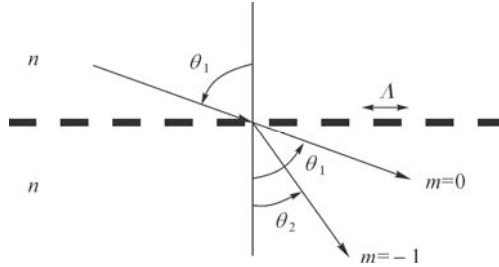


Fig. 11.4 The diffraction of a light wave by a grating (Erdogan, 1997, ©1997 IEEE)

In general, fiber gratings can be broadly classified into two types:

- (1) Bragg gratings: Reflection grating or short period grating, in which coupling occurs between contra-propagating modes; and
- (2) Transmission gratings: Long period grating, where coupling occurs between modes propagating co-directionally.

Fig. 11.5 illustrates the reflection of a mode by a grating with a reflection angle θ_1 into the same mode travelling in the opposite direction with a reflection angle of $\theta_2 = -\theta_1$.

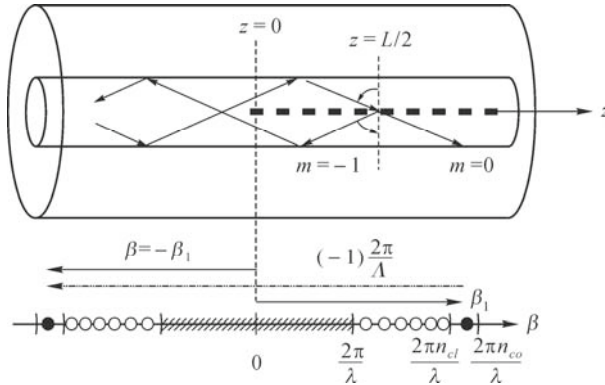


Fig. 11.5 Ray-optic illustration of a core-mode Bragg reflection by an FBG (Erdogan, 1997, ©1997 IEEE)

The mode propagation constant β is given by

$$\beta = \left(\frac{2\pi}{\lambda} \right) n_{eff} \tag{11.3}$$

where n_{eff} is the effective index given by

$$n_{eff} = n_{co} \sin \theta \quad (11.4)$$

where n_{co} is the refractive index of the fiber core. We may rewrite Eq. (11.2) for the guided mode as

$$\beta_2 = \beta_1 + m \frac{2\pi}{\Lambda} \quad (11.5)$$

For the first order diffraction, which usually dominates in a fiber grating, $m = -1$. This condition is illustrated on the β axis shown below the fiber in Fig. 11.5. The solid circles represent the bound core modes ($n_{cl} < n_{eff} < n_{co}$), the open circles represent the cladding modes ($1 < n_{eff} < n_{cl}$) while the hatched regions represent the continuum of radiation modes. Here, n_{cl} is the refractive index of the cladding. Negative values of β signify modes propagating in the $-z$ direction. Using Eq. (11.5) and $\beta_2 < 0$ (*i.e.* a negative value of β_2 , which indicates propagation in the $-z$ direction) the resonant wavelength for reflection of a mode of index $n_{eff,1}$ into a mode of index $n_{eff,2}$ can be obtained as:

$$-\left(\frac{2\pi}{\lambda_b}\right)n_{eff,2} = \left(\frac{2\pi}{\lambda_b}\right)n_{eff,1} - 1\left(\frac{2\pi}{\Lambda}\right) \quad (11.6)$$

$$\frac{2\pi}{\Lambda} = \frac{2\pi}{\lambda_b}(n_{eff,1} + n_{eff,2}) \quad (11.7)$$

which implies

$$\lambda_b = (n_{eff,1} + n_{eff,2})\Lambda \quad (11.8)$$

If the two modes are identical, *i.e.*, $n_{eff,1} = n_{eff,2}$, Eq. (11.8) is reduced to

$$\lambda_b = 2n_{eff}\Lambda \quad (11.9)$$

This forms the basic governing equation for FBG. The grating reflectivity for a given mode at the centre wavelength is given by (Morey *et al.*, 1989),

$$R = \tanh^2 \left[\pi L \Delta n \frac{\eta(V)}{\lambda_b} \right] \quad (11.10)$$

where L is the length of the grating, Δn is the magnitude of the index perturbation

and $\eta(V)$ is a function of the fiber V parameter, which represents the fraction of the integrated mode intensity contained in the core.

11.5 Thermal Properties of FBG

FBGs are periodic structures that couple light from one fiber mode to another. A change in the grating period will result in a change in the reflected wavelength. For this reason, FBGs are susceptible to any externally applied thermal-mechanical loads that affects the grating period.

Strain shifts the Bragg wavelength through expansion or contraction of the grating periodicity and the strain-optic effect, which is attributed to the strain-optic tensors and the Poisson ratio of the grating fiber. In addition, temperature change affects the Bragg response through thermal expansion and contraction of the grating periodicity and the thermo-optic effect (the thermal modulation of the refractive index of the fiber core). These effects are well understood and, when adequately modeled, provide a means for predicting these changes. The shift in Bragg wavelength $\Delta\lambda_B$, with strain and temperature can be expressed as (Kersey *et al.*, 1997):

$$\Delta\lambda_B = 2n\Lambda \left(\left\{ 1 - \left(\frac{n^2}{2} \right) [P_{12} - \nu(P_{11} + P_{12})] \right\} \varepsilon + \left[\alpha + \frac{\left(\frac{dn}{dT} \right)}{n} \right] \Delta T \right) \quad (11.11)$$

where n is the refractive index of the core, ε is the applied strain, P_{ij} are the Pockel's (piezo) coefficients of the stress-optic tensor, ν is the Poisson's ratio, α is the coefficient of thermal expansion (CTE) of the fiber material (*e.g.*, silica), and ΔT is the temperature change. The factor $\{(n^2/2)[P_{12} - \nu(P_{11} + P_{12})]\}$ is found to have a numerical value of about 0.22 (Kersey *et al.*, 1997).

The measured strain response at constant temperature can be reduced to

$$\frac{1}{\lambda_B} \frac{\delta\lambda_B}{\delta\varepsilon} = 0.78 \times 10^{-6} \mu\varepsilon^{-1} \quad (11.12)$$

This responsivity gives a “rule-of-thumb” measure of Bragg wavelength shift with strain equals to 1 nm per 1000 $\mu\varepsilon$ at 1.3 μm wavelength. In silica fibers, the thermal response is dominated by the $\frac{dn}{dT}$ effect (change of refractive index with temperature), which accounts for nearly 95% of the observed shift. The normalized thermal responsivity at constant strain is (Kersey *et al.*, 1997)

$$\frac{1}{\lambda_B} \frac{\delta \lambda_B}{\delta T} = 6.67 \times 10^{-6} \text{ } ^\circ\text{C}^{-1} \quad (11.13)$$

Typical values of the dependence of Bragg wavelength on fiber strain and temperature are 1.15 pm/ $\mu\epsilon$ and 13 pm/ $^\circ\text{C}$, respectively for FBG at 1550 nm (Morey *et al.*, 1991).

11.6 Mechanical Properties of FBG

Since FBGs are essentially optical fibers made of silica (glass), they should not be subjected to mechanical stress in excess of the limit that could cause them to be permanently deformed and damaged. The mechanical and strength properties of FBGs are determined using identical characterization techniques associated with grating fibers. Failure test performed on Bragg gratings manufactured by 3M (1996) showed the mean failure strength to be in excess of 1.38 GPa (200 ksi).

When mechanical pressure is applied to an FBG, the internal microstructure of the FBG is disturbed. As a result, there is a variation of the refractive index determined by the pressure distribution in the FBG. The strain response of the grating arises from the physical elongation of the sensor, leading to a fractional change in the grating pitch, with a corresponding change in the fiber index because of the photoelastic effect.

A pressure change of ΔP leads to a corresponding wavelength shift $\Delta \lambda_p$ (Othonos and Kalli, 1999),

$$\frac{\Delta \lambda_p}{\lambda_B} = \frac{\Delta(n\Lambda)}{n\Lambda} = \left(\frac{1}{\Lambda} \frac{\partial \lambda}{\partial P} + \frac{1}{n} \frac{\partial n}{\partial P} \right) \Delta P \quad (11.14)$$

In the case of a single-mode fiber, the fractional change in the fiber diameter resulting from the applied pressure is negligible as compared to the change in the physical length and refractive index, for which

$$\frac{\Delta L}{L} = - \frac{(1-2\nu)P}{E} \quad (11.15)$$

and

$$\frac{\Delta n}{n} = \frac{n^2 P}{2E} (1-2\nu)(2\rho_{12} + \rho_{11}) \quad (11.16)$$

where E is the Young's modulus and ν the Poisson's ratio. ρ_{ij} are the strain-optic

constants. Given that $\Delta L/L = \Delta\Lambda/\Lambda$, the normalized pitch pressure and the index-pressure coefficients are given by

$$\frac{1}{\Lambda} \frac{\partial \Lambda}{\partial P} = -\frac{(1-2\nu)}{E} \quad (11.17)$$

and

$$\frac{1}{n} \frac{\partial n}{\partial P} = \frac{n^2}{2E} (1-2\nu)(2\rho_{12} + \rho_{11}) \quad (11.18)$$

Therefore, the wavelength-pressure sensitivity is given by

$$\Delta\lambda_P = \lambda_B \left[-\frac{(1-2\nu)}{E} + \frac{n^2}{2E} (1-2\nu)(2\rho_{12} + \rho_{11}) \right] \Delta P \quad (11.19)$$

11.7 Maximun Reflectivity of Bragg Grating

The reflectivity of a uniform fiber grating of length L can be found by assuming a forward-going wave incident from $z = -\infty$ and requiring that no backward-going wave exist for $z \geq L/2$, as given by

$$r = \frac{\sinh^2\left(\sqrt{k^2 - \hat{\sigma}^2} L\right)}{\cosh^2\left(\sqrt{k^2 - \hat{\sigma}^2} L\right) - \frac{\hat{\sigma}^2}{k^2}} \quad (11.20)$$

where $\hat{\sigma}$ is a general “ dc ” (period-averaged) - coupling coefficient, k is the “AC” coupling coefficient and N is the total number of grating periods ($N=L/\Lambda$, chosen here to be $N=10000$).

Typical example of power reflectivity r for uniform gratings with $kL=2$ and $kL=8$ are shown in Fig. 11.6, where the reflectivity is plotted against the normalized wavelength. λ_{max} is the wavelength at which maximum reflectivity occurs. It may also be noted that the normalized wavelength is given by

$$\frac{\lambda}{\lambda_{max}} = \frac{1}{1 + \frac{\hat{\sigma}L}{\pi N}} \quad (11.21)$$

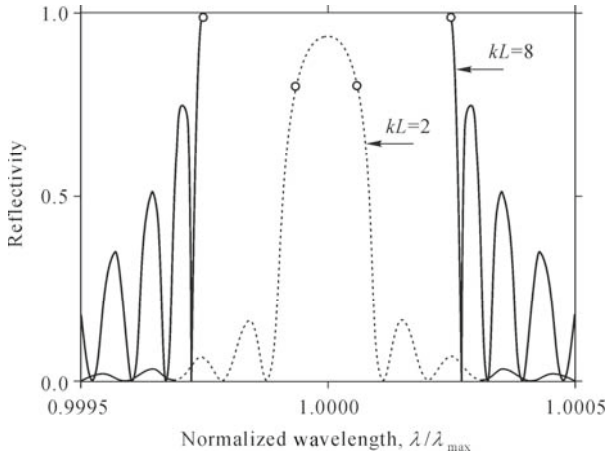


Fig. 11.6 Reflection spectra versus normalized wavelength for Bragg reflection in uniform grating $kL=2$ (dashed line) and $kL=8$ (solid line) (Erdogan, 1997, ©1997 IEEE)

If N is varied, *i.e.*, larger or smaller, the reflection bandwidth would be narrower or broader, respectively. For a given value of coupling constant kL , the maximum reflectivity r_{\max} for a Bragg grating is

$$r_{\max} = \tanh^2(kL) \quad (11.22)$$

and it occurs when $\hat{\sigma} = 0$, or at the wavelength given by

$$\lambda_{\max} = \left(1 + \frac{\overline{\delta n_{\text{eff}}}}{n_{\text{eff}}} \right) \lambda_D \quad (11.23)$$

where $\lambda_D \equiv 2n_{\text{eff}}A$ is the “design wavelength” for Bragg scattering resulting from an infinitesimally weak grating ($\overline{\delta n_{\text{eff}}} \rightarrow 0$) with a period A .

11.8 Full Width at Half Maximum

The spectra width of a light source is measured by its full-width at half-maximum (FWHM). As the term implies, FWHM is defined as the bandwidth of the signal at half the power (-3 dB) of the peak wavelength. For weak gratings or low reflectivity gratings, Erdogan (1997) found that

$$\frac{\Delta\lambda_o}{\lambda} \rightarrow \frac{v\overline{\delta n_{\text{eff}}}}{n_{\text{eff}}} \quad (v\overline{\delta n_{\text{eff}}} \gg \frac{\lambda_D}{L}) \quad (11.24)$$

where $v\bar{\delta}n_{eff}$ is simply the “AC” part of the induced index change. The bandwidth of weak grating is said to be “length limited”, and the $\Delta\lambda$ (or FWHM) for weak gratings with $kL < 2.3$ can be approximated by (Archambault, 1994),

$$\Delta\lambda = \frac{0.44\lambda_b^2}{n_{eff}L} \sqrt{1 + 0.7(kL)^2} \quad (11.25)$$

On the other hand, for strong gratings,

$$\frac{\Delta\lambda_o}{\lambda} \rightarrow \frac{\lambda_D}{n_{eff}L} = \frac{2}{N} \quad (v\bar{\delta}n_{eff} \ll \frac{\lambda_D}{L}) \quad (11.26)$$

For this case, light does not penetrate the full length of the grating. The bandwidth is thus independent of length and directly proportional to the induced index changes (Erdogan, 1997).

11.9 FBG Sensors

Since FBGs are sensitive to both strain and temperature, it becomes logical to use them as either strain sensors or temperature sensors or both, depending on the need. Indeed, these are the two most common uses of FBG sensors to date. This section describes the use of a bare FBG for force sensing which is termed as “direct sensing” as compare to “indirect sensing” where the FBG is embedded between layers of suitable materials.

11.9.1 Direct Sensing Using FBG

For direct sensing, the perturbation is applied directly onto the bare FBG. For experimental demonstration (Hao *et al.*, 2003), the effect of the normal force (perpendicular to the fiber axis) on bare FBG was taken into account. The measured wavelength shift was converted into axial strain based on the information that $1 \mu\epsilon$ strain corresponds to 1.2 pm wavelength shift. The deduced axial strain and the standard deviation are plotted against the applied force as shown in Fig. 11.7. The graph shows a non-linear response of axial strain with respect to the applied normal/perpendicular force.

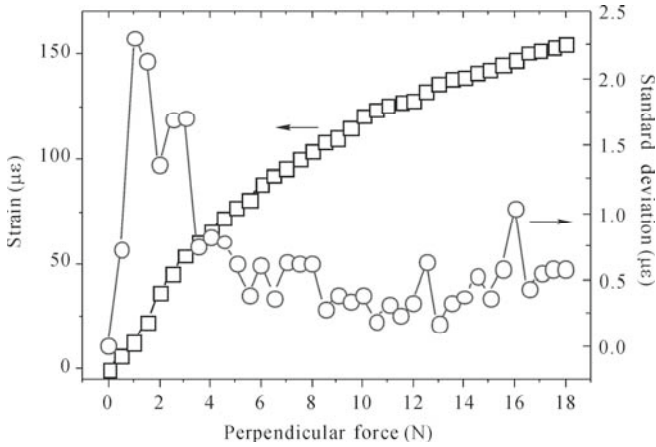


Fig. 11.7 Axial strain versus perpendicular force applied on a bare FBG (Hao *et al.*, 2003)

The non-linearity between the axial strain and the perpendicular force may be due to changes in polarization as a result of stress-induced birefringence. The non-linearity may also be due to the heterogeneity of the FBG material, the varying environmental effects such as temperature drifts, typically around $13 \text{ pm}/^\circ\text{C}$ at $1.55 \text{ }\mu\text{m}$ gratings, instability of the applied force or changes in the contact position (Morey *et al.*, 1991; Grattan and Meggitt, 1995; Hao *et al.*, 2003; Burger, 1987; Sirkis, 1993; Morey *et al.*, 1989; Melle *et al.*, 1991).

From visual inspection and repeated experiments, it was found that permanent deformation of the FBG occurs when the applied force exceeded 10 N. This can also be seen from the detected non-recoverable Bragg wavelength, which shifted to 1550.06 nm as measured from the optical spectrum analyzer (OSA), which is equivalent to a wavelength shift of 144 pm. Fractures started to occur at approximately 18 N and no reflected signal could be detected beyond that, suggesting that the FBG is permanently damaged. In summary, the non-linear response and the limited force sensing range makes direct sensing using bare FBGs impractical.

11.9.2 Indirect Sensing by Embedded FBG

To minimize problems faced by the direct sensing technique, grating fiber embedded into carbon/epoxy composite material (to form a reinforced laminate) is employed for sensing. This technique is known as indirect sensing. A force applied on the laminate is transferred from the composite matrix to a longitudinal strain onto the fiber. The laminate used in our experiment is a carbon epoxy laminate called Fiberdux (913C-XAS) available in prepreg form. It comprised a modified epoxy resin pre-impregnated into unidirectional carbon fibers. The longitudinal Young's modulus of the carbon fiber is 147.5 GPa and the Poisson's ratio is 0.306.

Since the optical fiber has considerably larger diameter than the composite reinforcements, the physical dimension of the grating fiber in comparison with the thickness of the composite ply is important. It has been known that small diameter (smaller than the thickness of the composite ply) fibers will actually disrupt the adjacent layers of the composite to a lesser degree than the larger diameter (larger than the thickness of the composite ply) fibers (Leka and Bayo, 1989). Less ply disruption occurs when the optical fiber runs in parallel with the reinforcement, as compared to when the optical fiber is oriented in any other direction (Davidson, 1990). Early work (Jensen and Pascual, 1990) also suggested that acrylate-coated fibers can seriously degrade the mechanical properties of the Carbon-Fiber Reinforced Plastic (CFRP).

For indirect sensing, an FBG with 10 μm polyimide coating was employed. The polyimide-coated FBG not only provided an excellent interface to glass (bare FBG) but also bonded well with the epoxies. It also gave an added advantage of minimizing the chemical or mechanical degradation during the epoxy curing process. The FBG used was 1 cm in length, with a peak reflectivity of 85% at a center wavelength of 1539.62 nm. It was embedded rectilinearly between layers of unidirectional carbon-epoxy laminate with grating fiber parallel to the carbon fibers. This structure is commonly termed as 0° uni-ply laminate.

In order to measure the performance of the embedded FBG, a range of normal force from 0 N up to 60 N were applied to the sensor (Hao *et al.*, 2003). It can be seen from Fig. 11.8 that excellent linear relationship exists between the axial strain and the applied normal force. The regression coefficient, R , is equal to 0.999. The embedded FBG sensor remained in an excellent state all the way up to an applied force of 60 N. Hence, the indirect sensing ensures a larger force sensing range as well as excellent linearity.

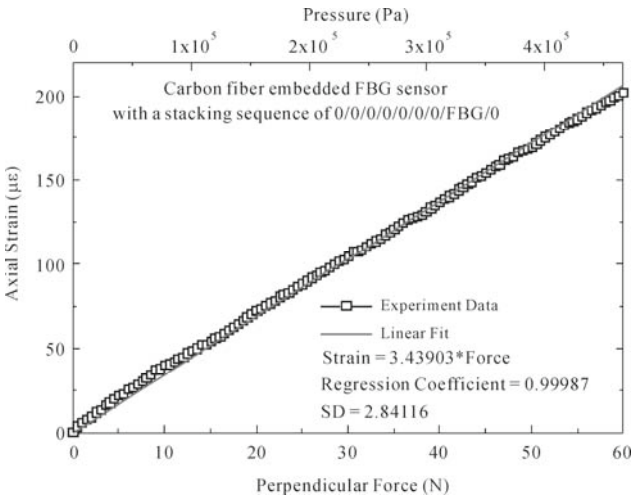


Fig. 11.8 Axial strain performance when the FBG is embedded within layers of composite material (Hao *et al.*, 2003)

In the following section, a detailed discussion of FBG sensors based on indirect sensing technique is presented.

11.10 FBG-based Pressure/Strain Sensor

The effect of the position of rectilinearly embedded FBG within composite material, such as that shown in Fig. 11.9, can be explained using simple mechanics. With rectilinearly embedded FBG, when a normal force is applied, the layers above the neutral layer are compressed. Hence, when the FBG is embedded above the neutral layer, the period of grating decreases, resulting in a blue-shift of the reflected spectrum. On the other hand, the layers below the neutral layer will be under tension. Thus, when FBG is embedded below the neutral layer, it will be under tension resulting in an elongation of the fiber and hence a red-shift of the reflected wavelength. The experimental results are shown in Fig. 11.10. It can be seen that when the FBG is embedded above the neutral layer, the FBG is compressed and exhibits a sensitivity of -1.61 pm/N, whereas when it is embedded below the neutral layer, the FBG is elongated and exhibits a sensitivity of 3.96 pm/N. Therefore, for force sensing, the FBG should be embedded below the neutral layer for higher force sensitivity.

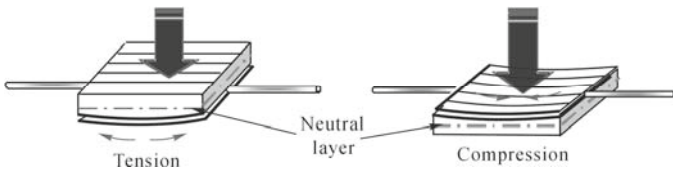


Fig. 11.9 Effect of FBG position on sensor performance (Hao *et al.*, 2003)

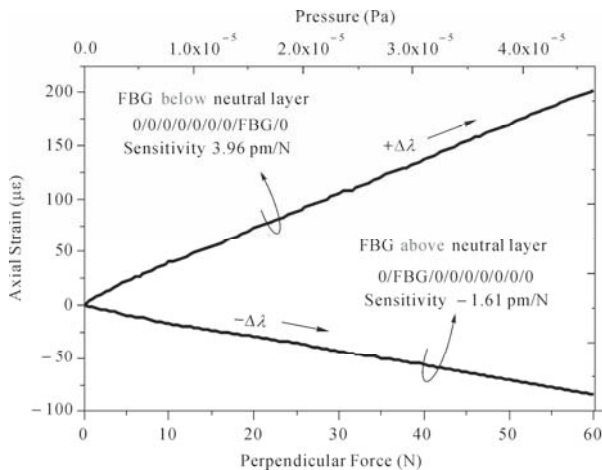


Fig. 11.10 Axial strain performance of the embedded sensor when FBG is embedded above/below the neutral layer (Hao *et al.*, 2003)

For the embedded FBG sensor, the polyimide-coated grating fiber bonds well with the parallel-aligned carbon fibers after curing. Moreover, the grating fiber is too small to degrade the mechanical properties of the laminate. The grating fiber described here was embedded within eight layers of unidirectional carbon-epoxy laminate. Since the FBG is located between layers 7 and 8 (which is below the neutral layer, which lies between layers 4 and 5), tension is developed along the carbon fibers when a perpendicular force is applied on the top layer. The carbon fibers adjacent to the FBG transfer the tensile strain to the FBG in the longitudinal direction causing the grating period to increase.

An important feature of the carbon fiber materials of high-modulus or high strength types is that they have very large range of elastic linearity (Gill, 1972). Therefore, the shift in wavelength is linearly proportional to the axial strain for an embedded FBG before it deforms, which explains the linear response obtained between axial strain and perpendicular force. The birefringent effect resulting from lateral and radial strain on the FBG is considered to be negligible. It is also reasonable to ignore small temperature fluctuations due to comparably low thermal expansion coefficient ($0.73 \times 10^{-6} \text{ } ^\circ\text{C}$) of the carbon fiber laminates.

By comparing the performances of direct sensing (using bare FBG) and indirect sensing (using embedded FBG), the indirect sensing method provides better linearity, stability and wider force sensing range. By using different types and configurations of embedding materials, it is possible to extend the sensing range of the sensor. As mentioned before, in our experiment, the grating fiber was embedded within eight layers of unidirectional carbon-epoxy laminate with the FBG oriented parallel to the carbon fibers at layers 7 and 8. With this combination, a linear force sensing range from 0 to 60 N (pressure from 0 to $4.66 \times 10^5 \text{ N/m}^2$) is obtained with a resolution of 0.5 N (3885.6 N/m^2). It may be noted that the resolution of 0.5 N is limited due to the noise during the experiment, and does not represent the resolution of the fiber optic pressure sensor. As mentioned before, the FBG should be embedded below the neutral layer in order to achieve higher sensitivity. Furthermore, the response of the embedded fiber shows better stability with respect to time as compared to the bare FBG used in the direct sensing technique.

Since the FBG is embedded away from the neutral layer of the laminates, the FBG undergoes either tension or compression, depending on the direction of the applied force. Hence, by tracking the change of FBG wavelength from zero force condition, the sensor is able to determine both the magnitude and direction (force applied from which side) of the applied force. This property proves to be critical in assessing structural deformation as will be explained in more detail in the next chapter.

11.11 FBG-based Shear Force Sensor

For shear force measurement, the FBG is embedded at a small angle between the

upper and lower layers of carbon composite material (CCM) with a deformable layer of silicon rubber between them. This embedding technique is known as non-rectilinear embedding (Suresh *et al.*, 2004). With this embedding technique, a relative motion between the upper and lower layers occurs when shear force is applied to the upper layer of CCM. The upper layer will move in the direction of the applied shear force with respect to the lower layer. This relative motion will stretch the fiber embedded in between. Hence, the applied shear force results in a change of fiber length and thus changing the reflected Bragg wavelength. Therefore, this embedding technique ensures the transformation of shear strain to the axial strain of the fiber.

Fig. 11.11 schematically explains the concept of the sensor. Fig. 11.11(a) shows the sensor when no shear force is applied, and Fig. 11.11(b) shows the sensor under an applied shear force. The solid line shows the unstrained fiber and the dashed line shows the stretched fiber under the applied shear force (Tjin *et al.*, 2004).

An analytical model of this sensor is also developed (Fig. 11.12), which leads to an explicit relationship between the applied shear force and wavelength shift. (Tjin *et al.*, 2004; Suresh *et al.*, 2004; Suresh and Tjin, 2005). The main parameters taken into consideration for this model are the applied shear force, the induced axial strain in the fiber and the reflected wavelength. It is assumed that the fiber is embedded along the diagonal of the deformable layer matrix. This approximation is justified since the horizontal length (length of the fiber embedded directly in the CCM layer at opposite sides) of the fiber (shown as x_h in Fig. 11.12) is small compared to the overall length of the fiber.

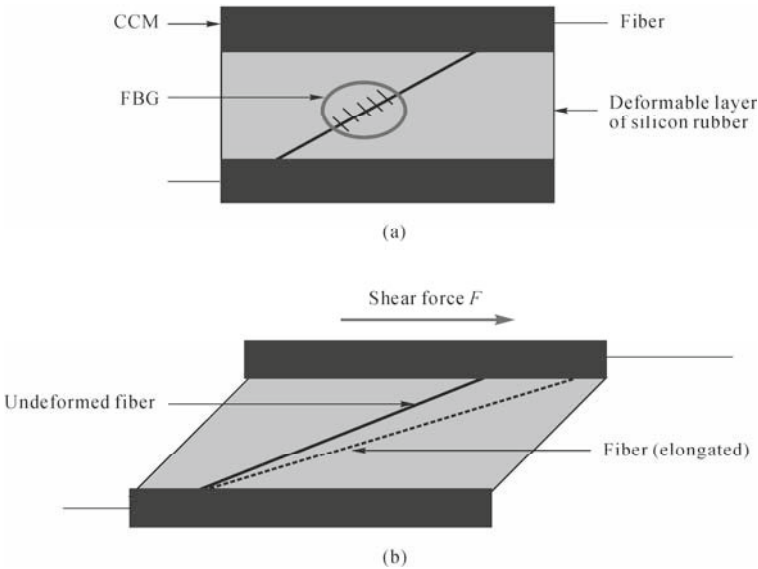


Fig. 11.11 Basic sensor structure and sensing concept (a) in absence of applied shear force and (b) with applied shear force (Tjin *et al.*, 2004, © 2004 IEEE)

Besides this assumption, the CCM layer has been ignored and only the silicon rubber matrix of the deformable layer has been considered in this model. This assumption is realistic taking into consideration the very high stiffness of CCM layer as compared to that of the deformable layer matrix. Only the part of the sensor with the fiber embedded in the silicon rubber matrix is taken into consideration for this model (see Fig. 11.12(a)). The dimension of the sensor has also been reduced accordingly. The reduced dimensions of the sensor are termed as the “*effective dimensions*”. The idealized model of the sensor is shown in Fig. 11.12(b).

It should be noted that the length is much greater than the thickness of the sensor. However, for the sake of clarity, the thicknesses are exaggerated in the figures. Also, the dependence of the reflected Bragg wavelength on temperature has been neglected in the present model as the experiments were performed under temperature-controlled laboratory conditions.

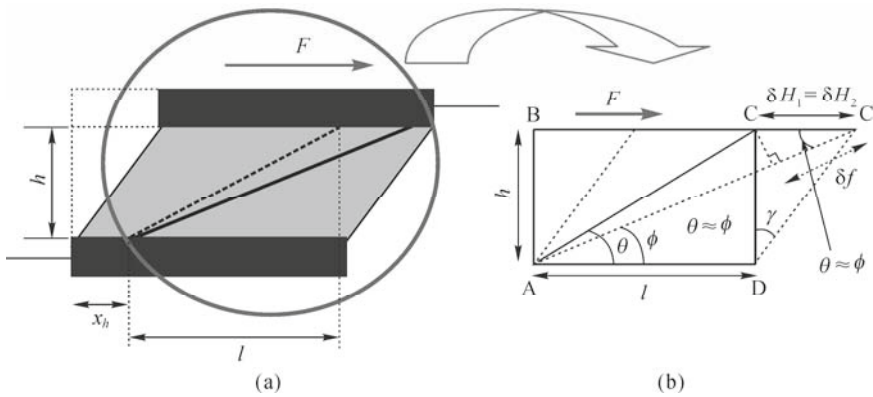


Fig. 11.12 Theoretical model of the sensor. (a) Part of the sensor taken into consideration; (b) Extended view (Tjin *et al.*, 2004, © 2004 IEEE)

For the sensor shown in Fig. 11.12, let the total applied shear force be F , the force carried by the deformable layer matrix be F_1 and the force carried by the fiber be F_2 . In this analysis, the fiber and the deformable layer matrix are considered individually and the individual effects are then superimposed. This is reasonable since both the matrix and the fiber are considered linearly elastic in nature. Let δH_1 and δH_2 be the horizontal deformation in the deformable layer matrix and the fiber respectively, as shown in Fig. 11.12(b). The effective sensor dimensions are length l , width b and thickness h . By definition, shear stress for deformable layer is

$$\tau = \frac{\text{Force}}{\text{Area}} = \frac{F_1}{l \times b} \tag{11.27}$$

where $l \times b$ is the surface area.

For the deformable layer matrix, the shear strain is

$$\gamma = \frac{\tau}{G} = \frac{F_1}{l \times b \times G} \quad (11.28)$$

where G is the shear modulus of the deformable layer. It is known that

$$\gamma = \frac{\delta H_1}{h} \quad (11.29)$$

Thus, equating Eqs. (11.27) and (11.28), we get

$$\frac{\delta H_1}{h} = \frac{F_1}{b \times l \times G} \quad (11.30)$$

We know that the shear modulus can be written as

$$G = \frac{E_m}{2(1 + \nu_m)} \quad (11.31)$$

where E_m and ν_m are the Young's modulus and Poisson's ratio of the deformable layer matrix, respectively. Solving Eqs. (11.30) and (11.31), we can obtain the horizontal elongation of the matrix as

$$\delta H_1 = \frac{F_1}{k_m} \quad (11.32)$$

where k_m denotes the stiffness of the deformable layer matrix, which can be expressed as

$$k_m = \frac{b \times l \times E_m}{2 \times h \times (1 + \nu_m)} \quad (11.33)$$

If δf is the elongation of fiber along the diagonal, then it can be written in terms of the horizontal elongation of the fiber, δH_2 , as (Fig. 11.12b)

$$\delta H_2 \cos \theta = \delta f \quad (11.34)$$

The horizontal force shared by the fiber is F_2 . This force component can be written in terms of the diagonal force F_f as

$$F_f \cos \theta = F_2 \quad (11.35)$$

Although the angle θ changes with the applied force, we have assumed θ to be a constant since the change in value of cosine of the angle θ is very small (a change of even 10 times in the angle θ shows negligible change in the cosine value for small values of θ used in the fabrication of the sensor). Thus, the cosine value is assumed constant (*i.e.* $\theta \approx \phi$, see Fig. 11.12(b)), which is true only when $l \gg h$; *i.e.* the thickness is very small compared to the length, as is in the present case. Elongation along the diagonal can thus be written as

$$\delta f = \frac{F_f}{k_f} \quad (11.36)$$

where k_f denotes the longitudinal stiffness of the fiber, and can be expressed as

$$k_f = \frac{E_f A_f}{\sqrt{l^2 + h^2}} \quad (11.37)$$

where E_f and A_f are the Young's modulus and cross-sectional area of the fiber, respectively. Solving Eqs. (11.34), (11.35), and (11.36), the horizontal elongation of the fiber can be derived as

$$\delta H_2 = \frac{F_2}{k_f \cos^2 \theta} \quad (11.38)$$

As we know from the compatibility condition, the horizontal elongation of the fiber δH_2 (shown as length CC' in Fig. 11.12(b)) and the deformable layer matrix δH_1 should be the same (*i.e.*, $\delta H_1 = \delta H_2$). Thus, from Eqs. (11.32) and (11.38)

$$\frac{F_1}{k_m} = \frac{F_2}{k_f \cos^2 \theta} \quad (11.39)$$

The total applied force F is the sum of the forces carried by the matrix F_1 , and the force carried by the fiber F_2 , *i.e.*,

$$F_1 + F_2 = F \quad (11.40)$$

Solving Eqs. (11.38) to (11.40), we can obtain the horizontal elongation of the fiber as:

$$\delta H_2 = \frac{F}{(k_m + k_f \cos^2 \theta)} \quad (11.41)$$

Thus, the elongation of the fiber along the diagonal is given by

$$\delta f = \delta H_2 \cos \theta = \frac{F \cos \theta}{(k_m + k_f \cos^2 \theta)} \quad (11.42)$$

Now, the axial strain in the fiber (ε = elongation/original length) is given as

$$\varepsilon = \frac{\delta f}{\sqrt{l^2 + h^2}} \quad (11.43)$$

Hence,

$$\varepsilon = \frac{F \cos \theta}{\sqrt{l^2 + h^2} (k_m + k_f \cos^2 \theta)} \quad (11.44)$$

From Eqs. (11.33), (11.37) and (11.44), we obtain

$$\varepsilon = \frac{\frac{F \times l}{\sqrt{l^2 + h^2}}}{\sqrt{l^2 + h^2} \left(\frac{b \times l \times E_m}{2h \times (1 + \nu_m)} + \frac{E_f A_f}{\sqrt{l^2 + h^2}} \left(\frac{l}{\sqrt{l^2 + h^2}} \right)^2 \right)} \quad (11.45)$$

As we know, the wavelength shift with the strain can be expressed as

$$\frac{\Delta \lambda_b}{\lambda_b} = \varepsilon \times \left[1 - 0.5 n_{eff}^2 \{P_{12} - \nu_f (P_{11} + P_{12})\} \right] \quad (11.46)$$

Using Eqs. (11.45) and (11.46), the variation of the Bragg wavelength with the applied shear force is given by

$$\frac{\Delta \lambda_b}{\lambda_b} = \frac{\frac{F \times l}{\sqrt{l^2 + h^2}} \left[1 - 0.5 n_{eff}^2 \{P_{12} - \nu_f (P_{11} + P_{12})\} \right]}{\sqrt{l^2 + h^2} \left(\frac{b \times l \times E_m}{2h \times (1 + \nu_m)} + \frac{E_f A_f}{\sqrt{l^2 + h^2}} \left(\frac{l}{\sqrt{l^2 + h^2}} \right)^2 \right)} \quad (11.47)$$

This can be further simplified as

$$\frac{\Delta\lambda_b}{\lambda_b} = K_s \times F \tag{11.48}$$

where

$$K_s = \frac{\frac{l}{\sqrt{l^2 + h^2}} \left[1 - 0.5n_{eff}^2 \{P_{12} - \nu_f (P_{11} + P_{12})\} \right]}{\sqrt{l^2 + h^2} \left(\frac{b \times l \times E_m}{2h \times (1 + \nu_m)} + \frac{E_f A_f}{\sqrt{l^2 + h^2}} \left(\frac{l}{\sqrt{l^2 + h^2}} \right)^2 \right)} \tag{11.49}$$

It should be noted that K_s has the unit of N^{-1} . Eqs. (11.47) to (11.49) show that the wavelength shift depends on the sensor dimensions (l, b, h) and the material properties of the deformable layer matrix (E_m, ν_m). The material parameter values of silicon rubber used in this model are listed in Table 11.1 (RS Components, 2003).

Table 11.1 Key specification of silicon rubber used in this study (RS Components, 2003)

Parameter	Value
Young’s modulus, E_m	$1.5 \times 10^6 \text{ N/m}^2$
Poisson’s ratio, ν_m	0.48
Temperature range	$-50 \text{ }^\circ\text{C}$ to $+250 \text{ }^\circ\text{C}$

An experiment was performed to verify the above theoretical model. The silicon rubber parameters given in Table 11.1 were used. We considered the fiber parameters as: cross sectional area $A_f = 1.23 \times 10^{-8} \text{ m}^2$; Young’s modulus $E_f = 7.245 \times 10^{10} \text{ N/m}^2$; effective index of core $n_{eff} = 1.448$; strain-optic coefficients P_{12} and P_{11} are 0.270 and 0.121, respectively, and Poisson’s ratio $\nu_f = 0.17$ (Seo and Kim, 1999). Considering the effective dimensions of the sensor as length $l = 4.15 \text{ cm}$, width $b = 2.162 \text{ cm}$ and thickness $h = 1 \text{ mm}$, the value of K_s is obtained as $0.000039787 \text{ N}^{-1}$. Thus, Eq. (11.48) can be written as

$$\Delta\lambda = (0.000039787) F \lambda_b \tag{11.50}$$

The reference Bragg wavelength for this sensor was $1553.83 \pm 0.001 \text{ nm}$, and the FBG was fabricated using the phase mask technique. The experimental setup consisted of a tunable laser source (TLS, ANDO) with center wavelength 1554 nm and span (tuning or scanning range) 10 nm , an optical spectrum analyzer (ANDO 6317) with a wavelength accuracy of $\pm 0.001 \text{ nm}$, a circulator and a shear force device. Analytical and experimental results of this sensor are shown in Fig. 11.13,

where it can be observed that good agreement between the experimental and theoretical model is obtained. The analytical model shows a sensitivity of 62 pm/N whereas the experimental result shows a sensitivity of 67 pm/N, which are comparable.

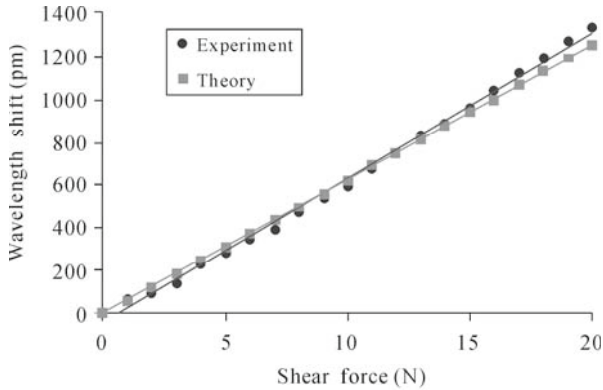


Fig. 11.13 Comparison of analytical and experimental results of the sensor

Using the experimental results as a reference, the difference between the experimental and theoretical results is found to be only 7%, which is in good agreement; thus verifying the analytical model. This small difference may be attributed to the experimental errors as well as the idealized assumptions made in the theoretical model. As expected, the theoretical results show a linearity of 100% (with a regression coefficient of $R=1$). However, the experimental plot shows small non-linearity ($R=0.998$, indicating a non-linearity of 0.2%). This can be attributed to two causes: (1) the friction of the device used to apply shear force, which is unavoidable and; (2) the slight non-linear nature of the deformable layer matrix. The elastomeric silicon rubber, which was used as the deformable layer matrix, shows small non-linearity of less than 5% (Panek and Cook, 1984). It should be noted that due to the assumptions of linear elastic behavior of the fiber and the matrix, this model fits well in the linear region only and cannot explain the failure point of the sensor. This can be done by non-linear material modeling, which is however beyond the scope of present treatment.

References

- 3M (1996). *Fiber Bragg Gratings Application Note – The Mechanical and Optical Reliability of Fiber Bragg Gratings*.
- Archambault, J.L. (1994). “Photorefractive gratings in optical fibers”, *PhD thesis*, university of Southampton, UK.
- Atkins, R.M., Lemaire, P.J., Erdogan, T. and Mizrahi V. (1993). “Mechanics of

- enhanced UV photosensitivity via hydrogen loading in germanosilicate glasses”, *Electronics Letters*, 29: 1234-1235.
- Atkins, R.M. and Espindola, R.P. (1997). “Photosensitivity and grating writing in hydrogen loaded germanosilicate core optical fibers at 325 and 351 nm”, *Applied Physics Letters* 70: 1068-1069.
- Bilodeau, F., Malo, B., Albert, J., Johnson, D.C., Hill, K.O., Hibino, Y., Abe, M. and Kawachi M. (1993). “Photosensitization of optical fiber and silica-on-silicon/silica waveguides”, *Optics Letters*, 18: 953-955.
- Burger, C.P. (1987). “Photoelasticity”, *Handbook on Experimental Mechanics*, edited by A.S. Kobayashi, Prentice-Hall, Englewood Cliffs, N.J.
- Canning, J. and Sceats, M.G. (1995). “Transient gratings in rare-earth doped phosphosilicate optical fibers through periodic population inversion”, *Electronics Letters*, 31: 576-578.
- Canning, J. (2000). “Photosensitization and photostabilization of laser-induced index change in optical fiber”, *Optical Fiber Technology*, 6: 275-289.
- Cater, A.L.G., Sceat, M.G. and Poole, S.B. (1992). “Flash condensation technique for the fabrication of high phosphorous-content rare earth doped fibers”, *Electronics Letters*, 28: 2009-2010.
- Chen, K.P. and Herman, P.R. (2003). “Photosensitization of Standard Fibers with Deep UV Laser Radiation”, *IEEE Journal of Lightwave Technology*, 21(9): 1958-1968.
- Davidson, R. (1990). “The current status and future prospects of smart composites”, *Proceedings of ESA Symposium on Space Applications of Advanced Structural Materials*, ESTEC, March, Noordwijk, 21-23.
- Dong, L., Liu, W.F. and Reekie, L. (1996). “Negative-index gratings formed by a 193-nm excimer laser”, *Optics Letters*, 21: 2032-2034.
- Erdogan, T. (1997). “Fiber Grating Spectra”, *IEEE Journal of Lightwave Technology*, 15(8): 1277-1294.
- Erdogan, T., Mizrahi, V. Lemaire, P.J. and Monroe, D. (1994). “Decay of Ultraviolet Induced Fiber Bragg Gratings”, *Journal of Applied Physics*, 76: 73-80.
- Giallorenzi, T.G., Bucaro, J.A., Dandridge, A., Sigel, Jr G.H., Cole, J.H., Rashleigh, S.C. and Priest, R.G. (1982). “Optical fiber sensor technology”, *IEEE Journal of Quantum Electronics*, 18: 626-665.
- Giles, C.R. (1997). “Lightwave applications of fiber Bragg gratings”, *IEEE Journal of Lightwave Technology*, 15(8): 1391-1404.
- Gill, R.M. (1972). *Carbon Fibers in Composite Materials*, London: Iliffe Books, 69-73.
- Grattan, K.T.V. and Meggitt, B.T. (1995). *Optical Fiber Sensor Technology: Optical and Quantum Electronics Series*, Chapman and Hall, London: 37-39 & 224-225.
- Guan, B.O., Tam, H.Y., Tao, X.M. and Dong, X.Y. (2000). “Highly stable fiber Bragg grating written in hydrogen- loaded fiber”, *IEEE Photonics Technology Letters*, 12:1349-1351.
- Hao, J. (2001), “Design and Fabrication of a fiber optic pressure sensor”, *Ph.D.*

- Thesis*, Nanyang Technological University, Singapore.
- Hao, J.Z., Tjin, S.C., Chaudhuri, P.R., Liaw, C.Y., Guo, X. and Lu, C. (2003). "Realization of an embedded fiber Bragg grating-based pressure sensor in fiber-reinforced composites: embedding techniques and performance characteristics", *Proceeding of SPIE APOC'2003*, 2-6 November, 111-125.
- Hill, K.O., Fujii, F., Johnson, D.C. and Kawasaki, B.S. (1978). "Photosensitivity on optical fibre waveguides: application to reflection filter fabrication", *Applied Physics Letters*, 32: 647-649.
- Hill, K.O., Malo, B., Bilodeau, F., Johnson, D.C. and Albert, J. (1993). "Bragg gratings fabricated in monomode photosensitive optical fiber by UV exposure through a phase mask", *Applied Physics Letters*, 62: 1035-1037.
<http://www.qpscom.com/pages/phasemask-1.htm>
- Jensen, D.W. and Pascual, J. (1990). "Degradation of graphite/bismaleimide laminates with multiple embedded fiber-optic sensors", *Proceedings of SPIE - Fiber Optic Smart Structures and Skins III*, 1370: 228-237.
- Juma, S. (1996). "Bragg gratings boost data transmission rates", *Laser Focus World*, November: 55.
- Kashyap, R. (1999), *Fibre Bragg Grating*, Academic Press.
- Kersey, A.D., Davis, M.A., Patric, H.J., LeBlanc, M., Koo, K.P., Askins, C.G., Putnam, M.A. and Friebele, E.J. (1997). "Fiber grating sensors", *IEEE Journal of Lightwave Technology*, 15(8): 1442-1463.
- Kohnke, G.E., Nightingale, D.W., Wigley, P.G. and Pollock, C.R. (1999). "Photosensitization of optical fiber by UV exposure of hydrogen loaded fiber", *Optical Fiber Communication Conference*, Post Deadline paper, PD-20:PD 20/1-PS 20/3.
- Lam, D.K.W. and Garside, B.K. (1981). "Characterization of single-mode optical fiber filters", *Applied Optics*, 20: 440-445.
- Leka, L.G. and Bayo, E. (1989). "A close look at the embedment of optical fibers into composite structures", *Journals of Composites Technology and Research*, 11: 106-112.
- Lemaire, P.J., Atkins, R.M., Mizrahi, V. and Reed, W.A. (1993). "High pressure H₂ loading as a technique for achieving ultrahigh UV photosensitivity in GeO₂ doped optical fibers", *Electronics Letters*, 29: 1191-1193.
- Limberger, H.G. and Varelas, D. (1999). "Advances in fibre gratings: technology, applications, and reliability of optical fibers and optical fibre systems", *Proceedings of SPIE*, 73:341-374.
- Lou, V., Sato, R. and Tomozawa, M. (2003). "Hydrogen diffusion in fused silica at high temperatures", *Non-Crystalline Solids* 315: 13-19.
- Malo, B., Bilodeau, F., Albert, J., Johnson, D.C., Hill, K.O., Hibino, Y. and Abe, M. (1993a). "Photosensitivity in optical fiber and silica-on-substrate waveguides", *Proceeding of SPIE Conference on Photosensitivity and Self-Organization in Optical Fibers and Waveguides*, 2044: 42-54.
- Malo, B., Johnson, D.C., Bilodeau, F., Albert, J. and Hill, K.O. (1993b). "Single-excimer-pulse writing of fiber gratings by use of a zero-order nulled phase mask: grating spectral response and visualization of index perturbations",

- Optics Letters*, 18:1277-1279.
- Malo, B., Albert, J., Bilodeau, F., Kitagawa, T., Johnson, D.C., Hill, K.O., Hattori, K., Hibino, Y. and Gujrathi, S. (1994). "Photosensitivity in phosphorus-doped silica glass and optical waveguides", *Applied Physics Letters*, 65: 394-396
- Mellberg, R.S. (1983). "Fiber Optic Sensors", *SRI International*, Research Report No. 684.
- Melle, S.M., Liu, K. and Measures, R.M. (1991). "Strain sensing using fiber Bragg gratings", *Proceedings of SPIE*, 1588: 225-263.
- Meltz, G., Morey, W.W. and Glenn, W.H. (1989). "Formation of Bragg gratings in optical fibers by a transverse holographic method", *Optics Letters*, 14: 823-825.
- Morey, W.W., Meltz, G. and Glen, W.H. (1989). "Fiber optic Bragg grating sensors", *Proceedings of SPIE*, 1169:98-106.
- Morey, W.W., Dunphy, J.R. and Meltz, G. (1991). "Multiplexed fiber Bragg grating sensors", *Proceedings of SPIE*: 1586, paper 22.
- Nagano, N., Saito, M., Baba, N. and Sawanobori, N. (1991). "Refractive indices of SiO₂- and GeO₂-based glasses near the infrared absorption peaks", *Journal of Non-Crystalline Solids*, 135: 114-121.
- Othonos, A. and Kalli, K. (1999). *Fiber Bragg Grating: Fundamentals and Applications in Telecommunications and Sensing*, Boston: Artech House
- Panek, J. R. and Cook, P. (1984). *Construction Sealants and Adhesives*, 2nd Edition, John Wiley and Sons, Inc., USA.
- Patrick, H., Gilbert, S.L., Lidgard, A. and Gallagher, M.D. (1995). "Annealing of Bragg gratings in hydrogen- loaded optical fiber", *Journal of Applied Physics*, 78: 2940-2945.
- Poumellec, B., Douay, M., Krupa, J.C., Garapon, J. and Niay, P. (2003). "Comparison of UV optical absorption and UV excited luminescence behaviors in Ge doped silica under H₂ loading or CW UV laser irradiation", *Non-Crystalline Solids*, 317: 319-334
- Riant, I. and Poumellec, B. (1998). "Thermal decay of grating written in hydrogen- loaded germanosilicate fibers", *Electronics Letters*, 34: 1603-1604.
- RS Components Product Catalogue (2003). <http://www.rs-components.com>
- Salik, E., Starodubov, D.S., Grubsky, V. and Feinberg, J. (2000). "Increase of photosensitivity in ge- doped fibers under strain", *OSA Technical Digest Series*, Paper number TuH5.
- Seo, C and Kim, T. (1999). "Temperature sensing with different coated metals on fiber Bragg grating sensors", *Microwave Optical Technology Letters*, 21: 162-165.
- Sirkis, J.S. (1993). "Unified approach to phase-strain-temperature models for smart structure", *Interferometric optical fiber sensors part I: development*, *Optical Engineering*, April.
- SpecTran Specialty optics Company (2001). *Photosensitive Fiber Data Sheet*, Ct, USA.
- Strasser, T.A., White, A.E., Yan, M.F., Lemaire, P.J. and Erdogan, T. (1995). "Strong Bragg phase gratings in phosphorus-doped fiber by ArF excimer

- radiation”, *Proceedings of Conference of Optical Fiber Communication*, San Jose 159.
- Suresh, R., Tjin, S.C. and Ngo, N. Q. (2004). “Shear force sensing by strain transformation using non-rectilinearly embedded fiber Bragg grating”, *Sensors and Actuators A: Physical*, 116: 107-118.
- Suresh, R. and Tjin, S.C. (2005). “Effects of dimensional and material parameters and cross coupling on FBG based shear force sensor”, *Sensors and Actuators A: Physical*, 120: 26-36.
- Tjin, S.C., Suresh, R. and Ngo, N.Q. (2004). “FBG based shear force sensor: modeling and testing”, *IEEE/ OSA Journal of Lightwave Technology*, 22(7): 1728-1733.
- Williams, D.L., Ainslie, B.J., Kashyap, R., Maxwell, G.D., Armitage, J.R., Campbell, R.J. and Wyarr, R. (1993). “Photosensitive index changes in germania doped silica glass fibers and waveguides”, *SPIE Proceedings of SPIE Conference on Photosensitivity and Self-Organization in Optical Fibers and Waveguides*, 2044:55-68.
- Yankov, V., Babin, S., Ivonin, I., Goltsov, A., Morozov, A., Polonskiy, L., Spector, M., Talapov, A., Kley, E.B. and Schmidt, H. (2003). “Multiwavelength Bragg gratings and their application to optical MUX/DEMUX devices”, *IEEE Photonics Technology Letters*, 15: 410-412.
- Zhang, B.L. and Raghavachari, K. (1997). “Photoabsorption and photoluminescence of divalent defects in silicate and germanosilicate glasses: first-principles calculations”, *Physical Review B*, 55: 993-996.

Applications of Fiber Bragg Grating Sensors

R. Suresh*, S. C. Tjin and J. Hao

*Department of Physics, S.V.College, University of Delhi,
Dhaura Kuan, New Delhi 110021, India
Tel: 91-11-2411-2196; Fax: 91-11-2411-8535
Email: rsuresh.assoc@ntu.edu.sg

12.1 Introduction

The basic concepts and fabrication of optical FBG-based strain, directional force or pressure, and shear force sensors have been presented in Chapter 11. It is noted that the response to external stimulus is non-linear when direct sensing technique is applied to the FBG. However, excellent linearity and larger sensing range are observed with indirect sensing technique, where the FBG is embedded within layers of composite materials. In this Chapter, the applications of these FBG-based sensors are covered.

12.2 Pressure Monitoring at Foot Sole of Diabetic Patients

Foot is an important part of human anatomy as it supports the entire body weight and provides leverage for walking, running and standing. It consists of several bones connected together in the form of an arch. This provides the flexibility to adapt to uneven surfaces. In addition, the foot also serves as a resilient spring to absorb shocks during activities like running and jumping.

There are many bones that make up a foot, but the bones that experience the most pressure when standing, walking or running are the first to fifth metatarsals (the balls behind toe) and the calcaneum (the heel bone). In addition to bones, the foot is also made up of four layers of muscles, nerves and blood vessels (Basil and Wilson, 1988). Fig. 12.1 shows the pressure distribution on a normal foot (symbol ⊗

indicates the pressure points).

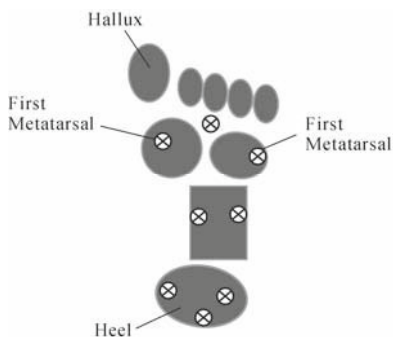


Fig. 12.1 Pressure distribution on a normal foot

Research conducted by Simoneau *et al.* (1994) on diabetic patients confirmed that the control of posture is mainly contributed by the somatosensory system, and the loss of sensory perception secondary to diabetic distal symmetrical sensory neuropathy has a markedly detrimental effect on postural stability. People with diabetes are more likely to experience foot problems because of nerve damage and circulatory problems caused by this chronic disease. As a result, the patient may not be aware of excessive pressure exerted on a particular area of their feet in the course of their normal daily activities. This may result in inflammation and erosion of the fibers connecting the muscles to the bones and hence damaging the plantar of the heels. In particular, patients with incorrect posture while standing, walking or running are prone to ulcerations at the sole which may lead to amputation if the condition is not treated timely. Hence, a foot pressure sensor will be useful for orthopedic surgeons to map the pressure distribution on the patient's plantar surface through the gait cycle and provide a dynamic measurement that takes into account the influence of the leg. With FBG pressure sensor, the orthopedic surgeons and doctors can determine the actual force exerted at the key pressure points under the patients' feet as well as the total applied force along with its center (Hao *et al.*, 2003). These tests will also assist the doctors to study the posture of a patient, hence correcting the patient's way of walking and standing. A customized orthopedic shoe suitable for the individual patient can then be designed, thus enabling proper rehabilitative programs to be carried out. Orthopedic surgeons, doctors in sports medicine and shoe manufacturers can benefit substantially from this kind of foot pressure sensor system.

Based on the performance of the embedded FBG sensor mentioned in the previous chapter, it is possible to make a foot pressure sensor in the shape of an insole by embedding a single strand of grating fiber into carbon/epoxy laminates. FBGs with different wavelengths can be written onto a single strand of fiber for monitoring pressure at different points. A simplified pressure distribution on the planar surface of a normal foot is depicted in Fig. 12.2(a), where five FBGs with five different Bragg wavelengths (1,536.96 nm, 1,541.47 nm, 1,546.69 nm, 1,550.77 nm and 1,556.36 nm) are employed. Fig. 12.2(b) shows the reflection spectrum of the five FBGs used in the experiment.

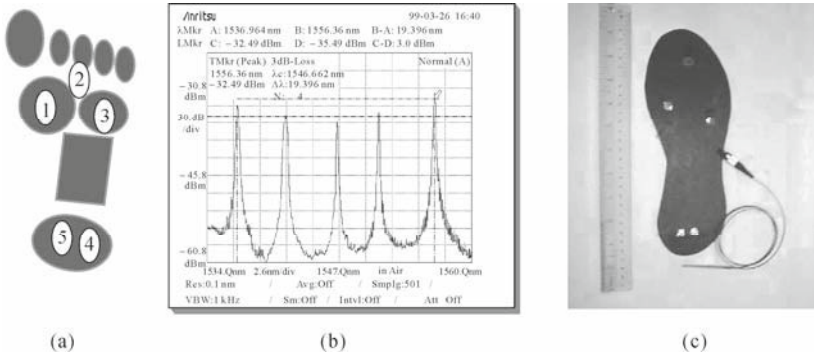


Fig. 12.2 (a) A simplified pressure distribution on a normal foot; (b) The reflection spectrum of the five FBG sensors; (c) An overview of a foot pressure sensor pad (Hao *et al.*, 2003)

The FBGs were embedded between ten layers of carbon/epoxy laminate, cut into the shape of a footpad, with eight layers at the top, *i.e.* the FBGs were below the neutral layer. The five FBGs were spatially placed at the five main pressure points and orientated parallel to the carbon fiber to avoid any delamination or warping that could significantly affect the sensors' performance.

An overview of the footpad, with a thickness of 1.25 mm and weighs merely 30 g, is shown in Fig. 12.2(c). Locations of the five FBGs are clearly marked in the figure.

To use the FBG-based pressure sensor, the normal applied force of the FBG sensor must be properly calibrated against the axial strain. For this purpose, normal force was applied onto each of the embedded FBG one at a time, leaving the rest of the four FBGs to be force-free. Fig. 12.3 shows a typical calibration graph for one of the FBG sensors, with a linear regression coefficient of 0.99. From the slope, the sensitivity of the sensor is determined to be approximately 700 pm/MPa.

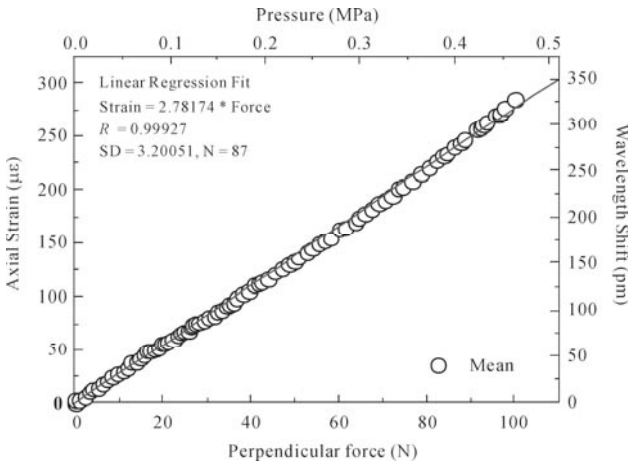


Fig. 12.3 Calibration of the foot pressure sensor

From the linear fitting coefficient obtained for the calibration results, the following relations are obtained

$$Force (N) = 0.36 * Strain (\mu\epsilon) \quad (Strain \geq 0 \mu\epsilon) \tag{12.1}$$

$$pressure (Pa) = 166.09 * Strain (\mu\epsilon) \quad (Strain \geq 0 \mu\epsilon) \tag{12.2}$$

Thus, by measuring the force induced strain, we are able to determine the amount of force or pressure exerted on each of the five pressure points beneath the foot. Using this FBG foot pressure sensor pad, we conducted few simple tests on a 26-year-old male subject with a body weight of 60 kg. The pressure distribution of the normal standing gait (with both feet firmly on the ground and carrying the total body weight) and the abnormal standing gait (an unbalanced standing posture with only one foot bearing most of the body weight) are depicted in Figs. 12.4 and 12.5 respectively.

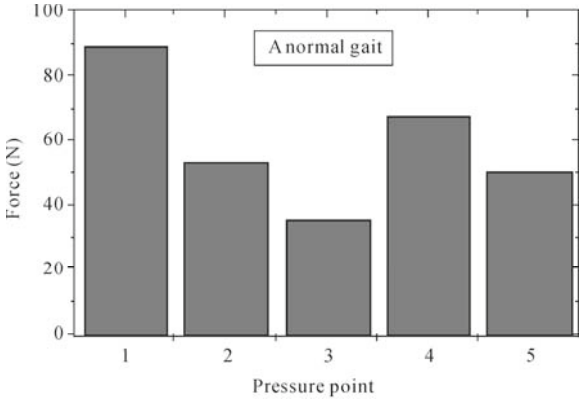


Fig. 12.4 Foot pressure distribution of a normal standing gait

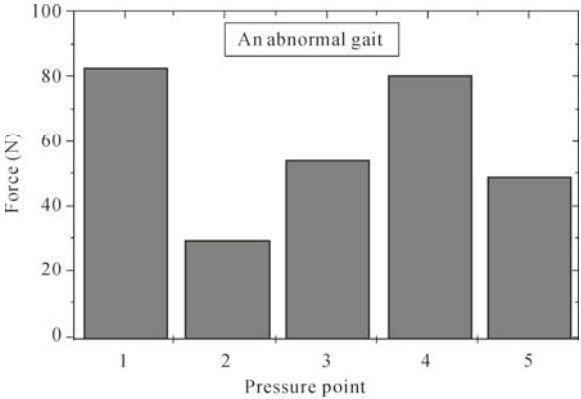


Fig. 12.5 Foot pressure distribution of an abnormal standing gait

With the normal standing gait, it is observed that the first metatarsal near hallux (big toe, great toe, or thumb toe) seems to experience most of the pressure, while the fifth metatarsal head appears to experience the least pressure (Fig. 12.4). For the abnormal standing gait, the pressure distribution deviates from a typical distribution pattern as depicted in Fig. 12.5. Initial tests were also performed on some other volunteers and a statistical force distribution of a normal standing gait is plotted in Fig. 12.6. This could provide useful diagnostic references for orthopedic surgeons. The resolution of the foot pressure sensor is measured by sampling the data over a period of 1 hour. The average standard deviation of each sensor is around 5.35 pm at a data acquisition rate of 33 Hz. This gives a resolution of 0.93 pm/ $\sqrt{\text{Hz}}$ (equivalent to 0.40 N/ $\sqrt{\text{Hz}}$ or 3108 Pa/ $\sqrt{\text{Hz}}$). The sensitivity of the foot pressure sensor is 5.44 pm/N or 700 pm/MPa (Hao *et al.*, 2003).

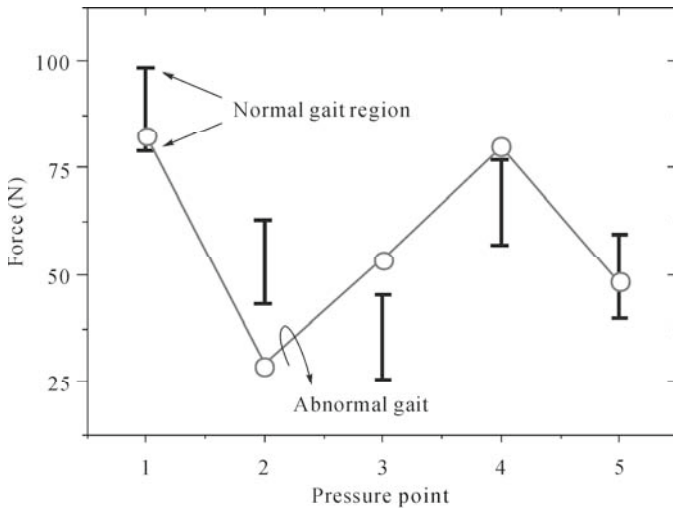


Fig. 12.6 Force distribution of a normal standing gait and measurement obtained from an abnormal standing gait

12.3 Pressure and Temperature Monitoring in a Dental Splint

Sleep apnea, defined as repeated episodes of obstructive apnea and hypopnea during sleep, together with daytime sleepiness or altered cardiopulmonary function, is a common condition that plagues many adults (Strollo and Rogers, 1996). The most common form of sleep apnea is known as obstructive sleep apnea, which involves an obstruction or occlusion of the upper airway during sleep. This is mainly a result of an anatomical abnormality, which could be either a narrow airway or excessive tissue in the upper airway that causes a blockage during the deeper stages of sleep when the body is most relaxed. Instead of a partial collapse of the air passage in the throat associated with snoring, patients suffering from

sleep apnea experience a complete or near complete obstruction to the airflow through the windpipe during their sleep. This phenomenon causes great discomfort or even choking while the patient is asleep. The more serious and adverse cases can be fatal when the obstructed airway cannot recover itself. Several techniques have since been developed to help patients suffering from sleep apnea in reducing the likelihood of snoring. One such technique is to use a device known as a splint, which the patient can wear during his/her sleep. This device helps to hold the tongue back to prevent it from collapsing into the airway and hence keep the air passage open. The purpose of our application is to develop a sensor system that helps doctors monitor the proper use of splint by sampling the pressure exerted on the dental splint as it is worn.

Since FBG is sensitive to both temperature and strain, we can embed two FBGs into the splint to carry out the sensory functions. One FBG is used as a pressure sensor while the other as a temperature sensor. The reading obtained from the temperature sensor will be subtracted from that of the pressure sensor to obtain the temperature compensated pressure reading.

12.3.1 Structure of FBG-based Splint Sensor

The two FBGs (one for pressure sensing and another for temperature sensing) were first embedded in glass fiber composite material to protect the FBGs and also to linearly transfer the normal load into axial strain in the fiber. All the FBG sensors were calibrated individually. Fig. 12.7 shows the schematic of the splint with embedded FBG sensors (Tjin *et al.*, 2001a).

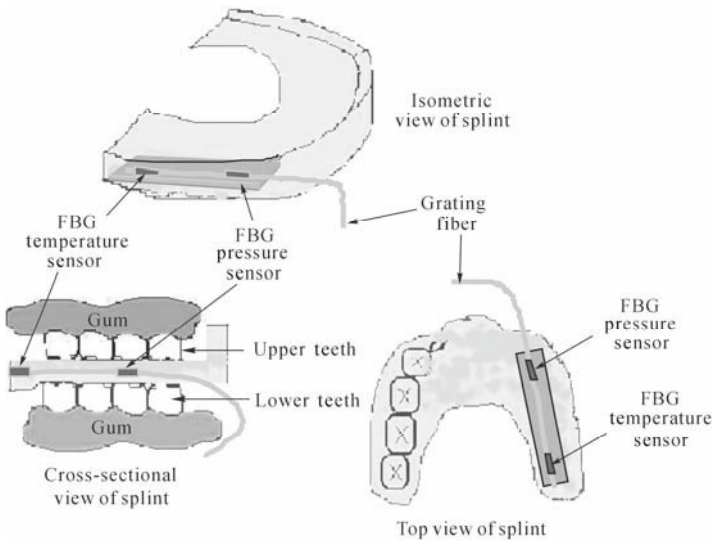


Fig. 12.7 Schematic diagram of splint with embedded FBG sensors (Tjin *et al.*, 2001a)

The FBG pressure sensor is placed in between the upper jaw and the lower jaw, as illustrated in the cross-sectional view of the splint. The FBG temperature sensor is placed away from the FBG pressure sensor to prevent the former from picking up pressure disturbances. The layout of the FBG splint sensor is shown in Fig. 12.8.

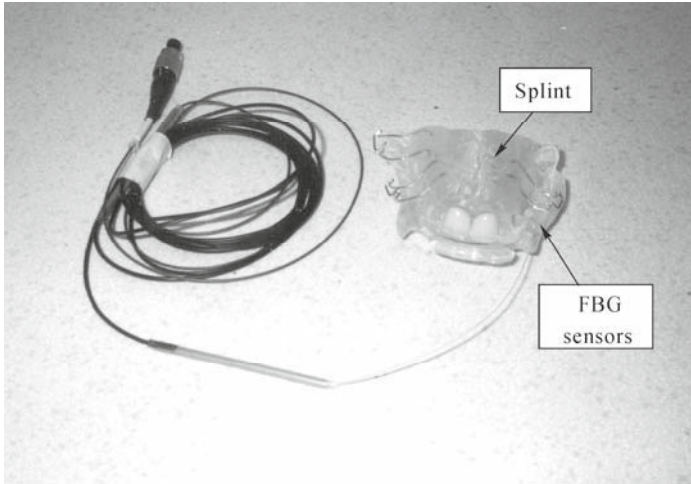


Fig. 12.8 Outlook of the splint with embedded FBG sensors (Hao, 2001)

12.3.2 Experimental Results and Discussions

Experiments were carried out on four patients with each patient wearing the dental splint for approximately 45 minutes per session. Within this period, the temperature and pressure measurements were constantly acquired by the interrogation system at a rate of 30 readings per second. The wavelength of the FBG after the splint material was fully cured was taken as the reference wavelength or the “zero” wavelength. After the experiments, the recorded pressure and temperature data were plotted against time, as shown in Fig. 12.9, to illustrate their relationship. These graphs also reflect the monitoring ability of the sensor system.

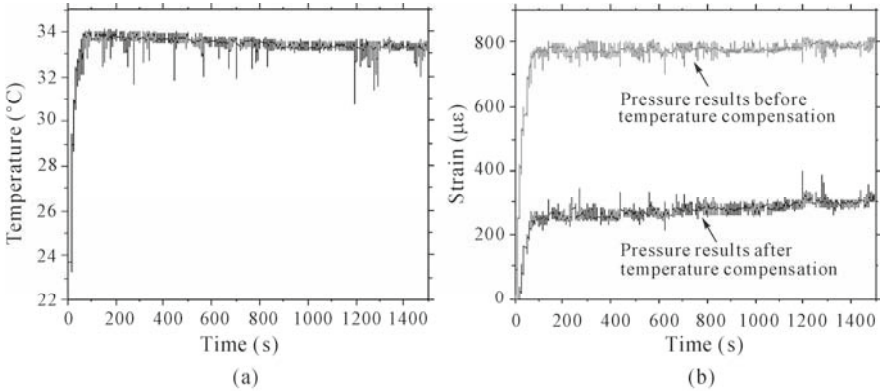


Fig. 12.9 Measurements on Patient 1 (Tjin *et al.*, 2001a). (a) Temperature results; (b) Pressure results

Fig. 12.9(a) shows the temperature results of Patient 1. It was observed that the temperature in the mouth did not vary much once it has stabilized. Hence, as long as the splint remains in the mouth, the temperature remains somewhat constant. The pressure results of Patient 1 are shown in Fig. 12.9 (b). One graph shows the pressure results before temperature compensation and the other the temperature-compensated pressure results. When the splint is not in the mouth, no force is exerted on the sensor, and the FBG sensor reflects a low strain value. The pressure data indicates a rise when the splint is positioned in the mouth. This is because as the patient’s teeth grip on to the splint, force is exerted on the FBG sensors.

For the entire trial period, the changes in pressure were monitored closely. The data are important and relevant for doctors in monitoring the usage and effectiveness of the splint. The same conclusion was drawn for the other three patients. Figs. 12.10(a) and (b) respectively show the temperature and pressure results of Patient 2.

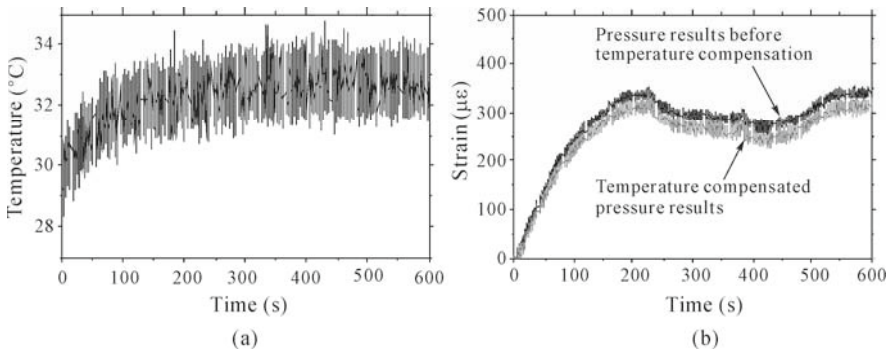


Fig. 12.10 (a) Temperature results of Patient 2; (b) Pressure results of Patient 2 (Tjin *et al.*, 2001a)

The above results show that the pressure exerted on the splint can be monitored continuously over a long period. Therefore, the FBG sensor monitoring system used in the dental application successfully proved to be a novel idea.

12.4 Monitoring Civil Structures

12.4.1 Sensing Approach

Reinforced concrete (RC) is a ubiquitous construction material that is formed from several components, such as cement, aggregate, steel reinforcement and various chemical additives. As a result, it exhibits complex processes, most of which are initiated or occur beneath the surface. When a bare FBG is embedded in the concrete, the alkali nature of concrete may damage the silicon in the glass. The FBG sensor must therefore be protected by some inert material before being embedded in the concrete. The laminated FBG will become part of the structure and serves to monitor any premature failure in the concrete. The embedded FBG sensor is reliable due to its good linearity, high sensitivity and wide load sensing range.

In the experiments, a series of full field load tests on concrete beams were performed. The FBG sensors were either surface mounted or embedded in the concrete beams using the approaches described in the following sections.

12.4.2 Symmetrically Bonded FBG Sensor Arrays on Rebars

The FBG sensor arrays are symmetrically bonded onto the top surface of the RC beam's reinforcement bar (rebar) prior to pouring and curing of the concrete. This allows the reaction of the structure to the external loads to be measured. Fig. 12.11 (a) illustrates a rebar that is placed below the neutral layer of the RC beam. When a load is applied perpendicularly to the top surface of the beam, a bending induced tension will cause the grating period to increase and hence a red shift in the spectrum of the reflected light. However, when the rebar is above the neutral layer, as shown in Fig. 12.11(b), an application of load perpendicularly to the top surface of the beam causes a bending induced compression on the FBG and hence a blue shift of the reflection spectrum (Hao, 2001). In the following, two cases are covered: surface bonded sensors and embedded sensors.

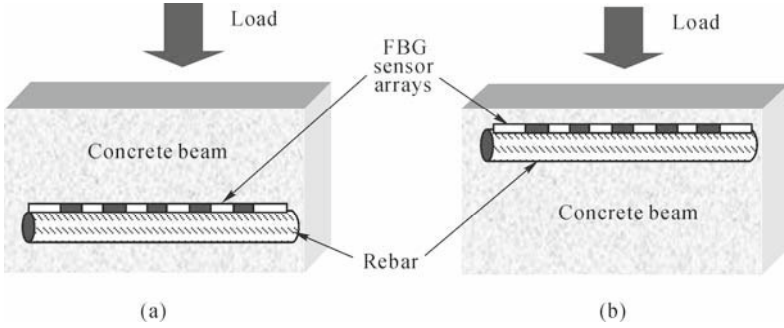


Fig. 12.11 FBG sensor array embedded on (a) bottom rebar; (b) top rebar

• *Surface Mounted FBG Sensor Array*

The FBG sensors can be mounted on the surface of the structure using suitable epoxies, as illustrated in Fig. 12.12. This configuration was tested and compared with the case where the sensors were embedded within the concrete. For the test, the load was gradually applied onto the RC beams all the way to failure whereby physical cracking of the concrete occurred. It was observed that as long as cracking does not occur, the reflected wavelengths from each sensor are linearly proportional to the applied load, but with different gradients. The closer the sensor is from the load point, the steeper is the response, and vice versa. These results are expected since when the sensor is placed in close proximity to the load, the bending stresses are higher, and the resulting change in the grating period is maximum. By further increasing the load, the response becomes nonlinear since permanent deformation occurs in the sensor region due to the crack. As the crack becomes more severe, the bending induced strain disappears because the sensor detaches from the concrete surface and the FBG wavelength returns to its original wavelength value. The behavior of the wavelength shift versus applied load follows the same trend as the stress-strain curve of concrete. The detailed experimental results are discussed in Section 12.4.2 (c).

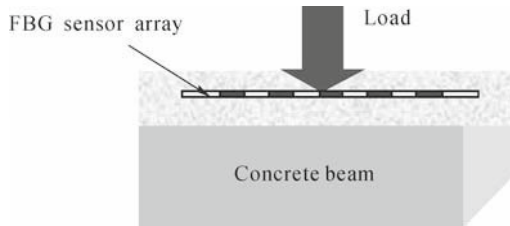


Fig. 12.12 FBG sensor arrays attached onto the surface of the concrete beam

- *Embedded FBG Sensor Array*

Two cascaded carbon fiber laminated FBG sensor arrays were embedded in two separate 5 meter long RC beams to monitor the strain at different locations along the rebar during the loading test. Since the load was applied on top of the beam, the effect was symmetrical on both sides of the beam. Hence, only one side of the beam was monitored. Fig. 12.13 schematically shows the structure of the beam. The rebars are in groups of 4, placed inside the wooden formwork before the concrete was poured in.

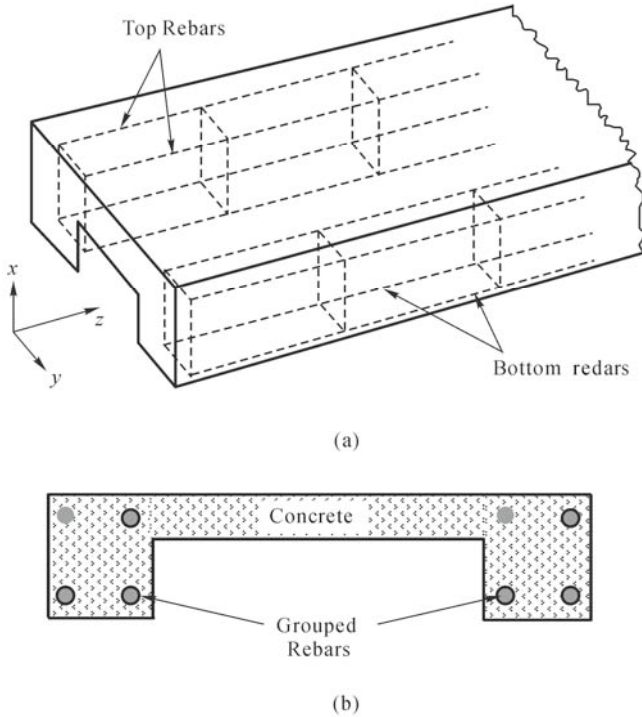


Fig. 12.13 The concrete beam. (a) Isometric view; (b) Cross-sectional view

Fig. 12.14 depicts the layout of the two cascaded FBG sensor arrays embedded in the two beams with one on the top rebar and another on the bottom rebar. Each sensor array consisted of four FBGs spatially distributed along a single strand of optical fiber, which was well protected by heat shrinkable sleeves. These FBGs were sandwiched within 10 layers of uni-ply carbon/epoxy laminates, with a dimension of 20 mm×5 mm×1.25 mm, with a stacking sequence of 0/0/0/0/0/0/0/0/FBG/0. The grating fiber was attached to a 25 mm long polished surface of the rebar in the longitudinal direction, as shown in Fig. 12.14. Similarly, two conventional strain gauges were also embedded in the top and bottom of the beam to collect strain readings for comparison with the readings obtained by the FBGs.

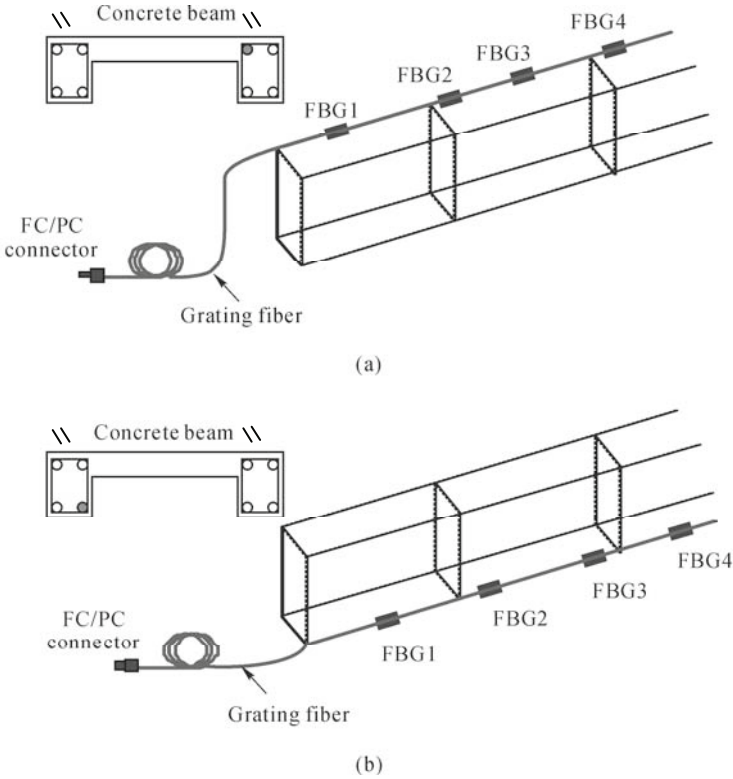


Fig. 12.14 FBG sensor array mounted in RC beam on the (a) top rebar; (b) bottom rebar

• Experiments

The experimental setup is shown in Fig. 12.15. The RC beam was supported on both ends and secured by two holders. The load was applied at the center of the beam to cause bending in the $x-z$ plane. Due to the two holders at the ends of the beam, the strain distribution along the rebar was much more complicated than that with the two ends free. The RC beam experienced compression or expansion at different location along the z -axis. The internal and external strains of the beam were monitored during the loading and unloading stages. An FBG interrogation system was used to acquire and process the reflected Bragg wavelength from the FBG sensor array. A computer was connected to the interrogation system enabling the measured readings to be displayed and saved as data files for post-processing (Wang *et al.*, 2000).

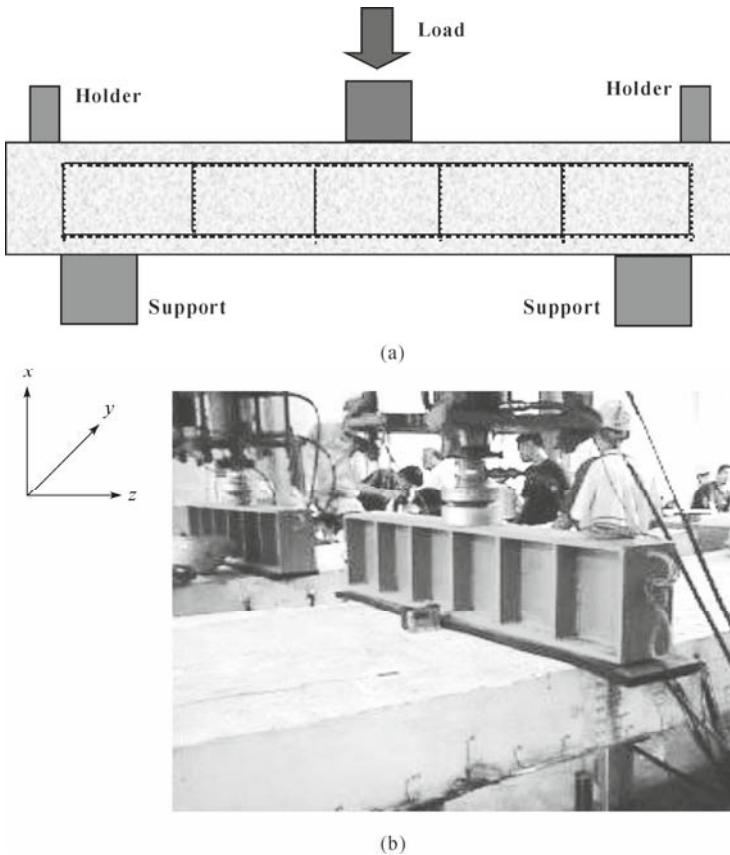


Fig. 12.15 Setup of the load test on RC beam. (a) Schematic drawing; (b) Application of loading on the beam (Hao, 2001)

The loading and unloading tests were performed in two parts, *i.e.* cyclic test and failure test. In the cyclic test, a relatively small force was applied on the beam and this force was gradually increased to ensure a recoverable deformation in the RC beam (Jensen and Koharchik, 1991). For small forces, the deformation undergone can be assumed to be elastic and linear. The corresponding force range is dependent on the structure of the beam. Cracks appearing on the beam set the maximum force for the linear region. When maximum force was reached, the unloading process was initiated to complete the test cycle of loading and unloading. The second part of the load test was the failure test. In order to perform the failure test, the forces were increased beyond the linear range. This maximum force was also gauged visually by the number of cracks appearing on the surfaces of the beam. After it reached a significant number, the beam was deemed to have failed, *i.e.* in an unrecoverable state.

Results of the load tests are presented in Fig. 12.16 to Fig. 12.18 (Hao, 2001). The maximum applied force was 40 kN. The strain readings in Fig. 12.16 and

Fig. 12.17 have comparable values but opposite signs. This shows that the FBGs on the top rebar were compressed, while the FBGs at the bottom were stretched. Although the data points obtained from the unloading process shows that after removal of the loads, the beam was trying to recover to the initial state, they do not overlap completely with the data points obtained during the loading process. This hysteresis profile in the curves implies that there is permanent deformation in the concrete beam. The strain distribution obtained along the top surface of the beam is shown in Fig. 12.18.

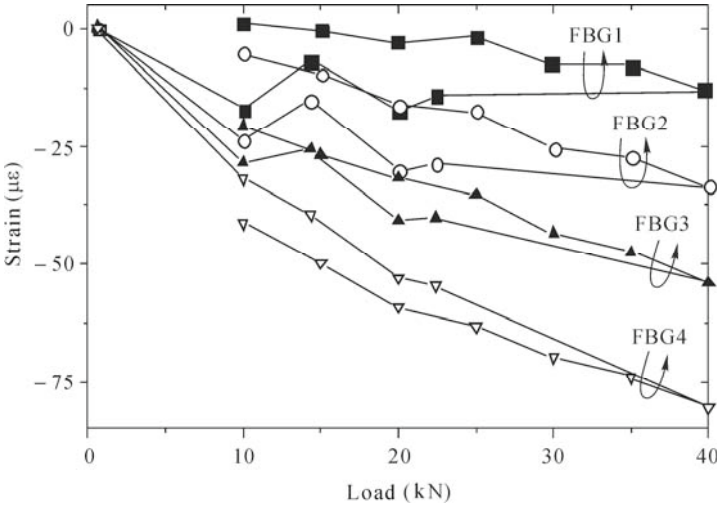


Fig. 12.16 Strain distribution along the top rebar under cyclic test

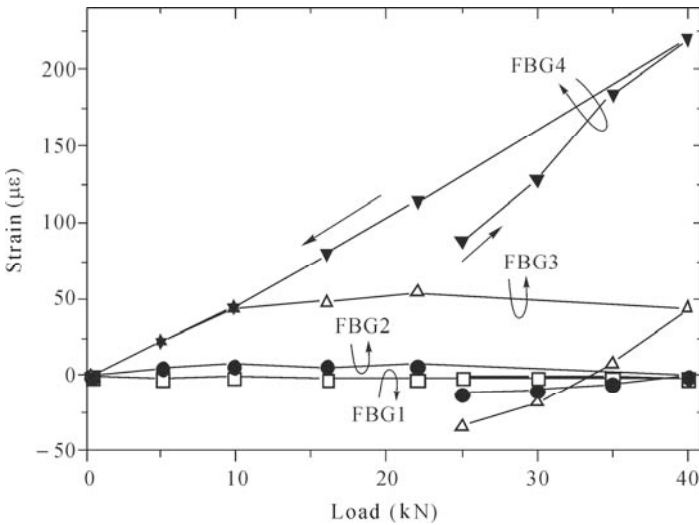


Fig. 12.17 Strain distribution along bottom rebar under cyclic test

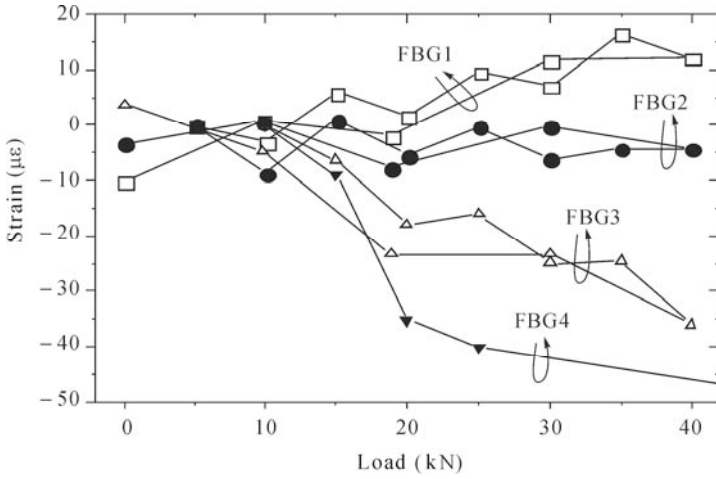


Fig. 12.18 Strain distribution on surface of the concrete beam under cyclic test

Comparison of the strain readings obtained from FBG1 to FBG4 shows that FBG4 was picking up most of the strain reading whereas FBG1 was picking up the least strain. The results are in agreement since FBG1 was closer to the end where minimum bending occurred in the beam, whereas FBG4 was closer to the loading bar where the maximum bending occurred. Fig. 12.19 shows the strain measured by the electrical resistive strain gauges.

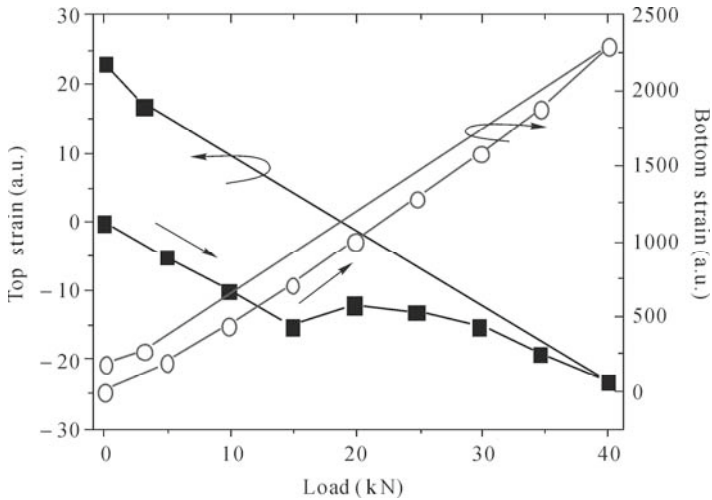


Fig. 12.19 Strain readings obtained from conventional resistive strain gauges mounted on the top and bottom surface of concrete beam during cyclic test

From the strain readings obtained by the FBG (Fig. 12.16) mounted on the top rebar and the strain readings obtained using the conventional resistive strain

gauges mounted on the top surface of the RC beam (Fig. 12.19), we can conclude that a contraction occurred in the position of FBG4. Furthermore, comparing the bottom strain readings from the FBG mounted at the bottom rebar (Fig. 12.17) with the conventional strain gauge mounted on the bottom surface of the beam (Fig. 12.19), a similar trend is observed suggesting that the strain readings obtained from the embedded FBGs are reliable.

Results of the failure test are shown in Fig. 12.20 to Fig. 12.22 (Hao, 2001). Fig. 12.20 shows that the strain reading saturated at a threshold force of about 50 kN. We termed this force range as the “saturation” region. When the loading force increased beyond 80 kN, the strain readings started to rise as the number of cracks on the beam increases steeply, and this region is termed the “failure” region. When the loading force exceeded 110 kN, Fig. 12.20 (top rebar) shows an abrupt change in the strain reading which may be due to a major crack within the RC beam, reaching the “breakdown” region. When the loading force was totally removed, the strain readings did not return to the original state. This implies a permanent deformation in the beam, and hence the region is termed the “deformed” region.

Hence, as depicted in Fig. 12.20, the entire loading can be divided into regions classified as “Safe”, “Saturation”, “Failure” and “Breakdown”. Broadly speaking, a structure can be considered as “healthy” if the measured strain readings are well within the “Safe” region. On the other hand, when the strain readings approach the “Failure” and “Breakdown” regions, the structure is considered to be “unhealthy” and dangerous. The ability to assess the “state of health” of the structure requires regular strain measurements to be taken to identify sudden changes in trends.

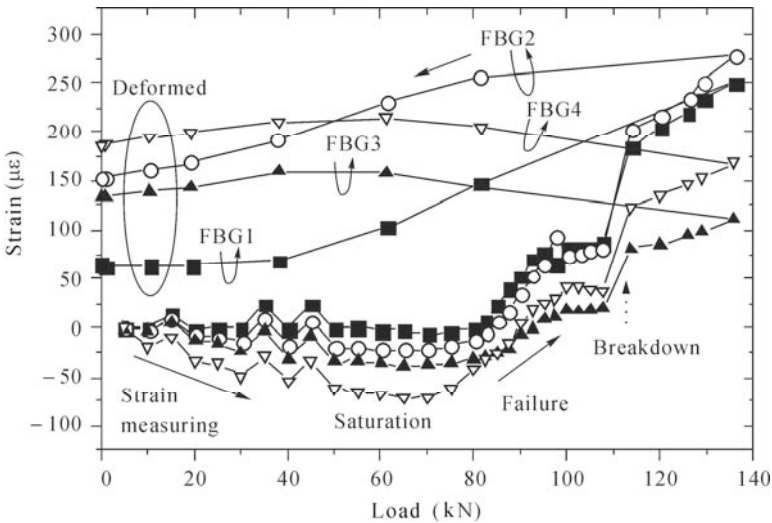


Fig. 12.20 Strain distribution along top rebar under failure test

There was however no indication of major abrupt change in the strain readings in Fig. 12.21 (bottom rebar) and Fig. 12.22 (surface) even though the applied load exceeded the 110 kN limit. A possible explanation for this is that the beam broke into two parts at 110 kN, causing the bottom rebar to bounce back to the initial strain-free condition, resulting in a sudden “hop back” to the initial strain-free state as shown in Fig. 12.21 and Fig. 12.22. This is supported by the physical observation that when the applied load reached 110 kN, the concrete in the middle section already gave way and could no longer provide resistance to the applied force. Based on the plot from Fig. 12.20 to Fig. 12.22, it can be confirmed that the concrete beam broke when loaded to around 110 kN.

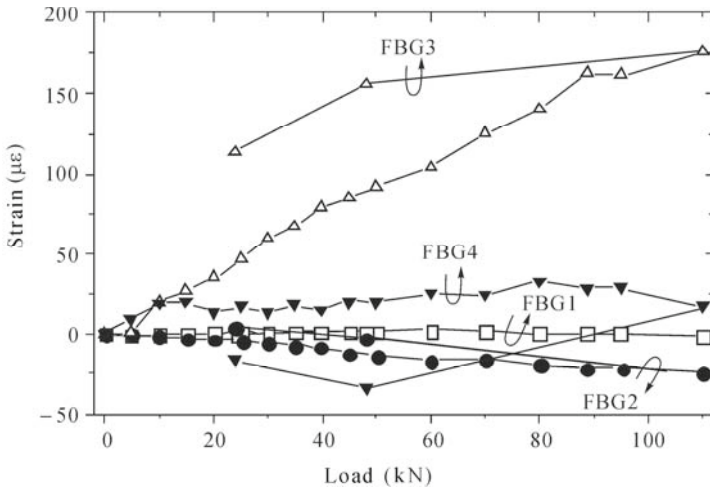


Fig. 12.21 Strain distribution along bottom rebar under failure test

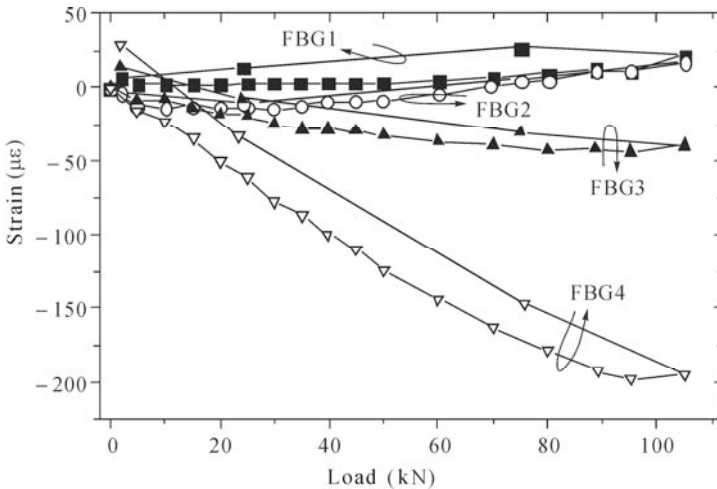


Fig. 12.22 Strain distribution on top surface of RC beam under failure test

Fig. 12.23 shows the top and bottom strain readings obtained from the conventional resistive strain gauges during the failure test. The bottom strain readings indicate a steady strain measurement until failure started to occur at about 90 kN. At about 110 kN, the bottom strain readings “hop back” to the load-free state with an unrecoverable offset from the initial strain value. This offset could be caused by a permanent deformation in the RC beam. For the top strain gauge, the strain readings indicate a steady strain measurement until failure started to occur at about 80 kN. At about 110 kN, the top strain readings “hop back” to the load-free state with an offset from the initial strain reading. Similarly, this offset could be caused by a permanent deformation in the RC beam. Nevertheless, for both cases, it was shown from the strain gauge measurement that the beam broke at about 110 kN.

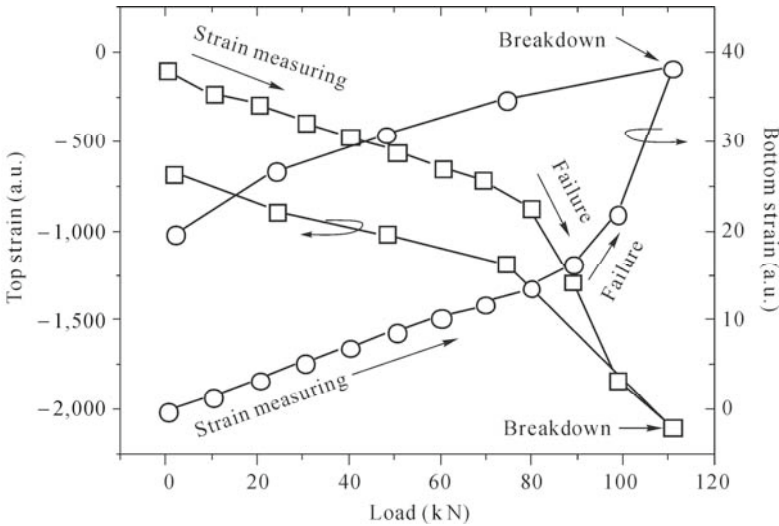


Fig. 12.23 Strain readings obtained from conventional resistive strain gauges mounted on the top and the bottom surfaces of the RC beam during failure test

12.4.3 Contact Force Measurement at Beam-Column Joint

In the design of any structure, the structure needs to be analyzed for different load conditions such as dead loads, superimposed loads, earthquake/wind loads and their possible load combinations. In such an analysis and design, the shear force between different structural components also needs to be considered. Furthermore, after construction, forces in the structure need to be monitored for verification of the design assumptions and also for the purpose of structural health monitoring (Soh *et al.*, 2000; Bhalla and Soh, 2004). Shear force measurement is an important

aspect of structural health monitoring. In this study, FBG-based shear force sensor have been used for contact force measurement between different structural components. A beam-column joint was fabricated by connecting a 160 mm long concrete beam between two concrete cubes (Suresh *et al.*, 2005). At the interfaces of the beam and the cubes, shear force sensors (fabrication covered in Chapter 11) were embedded. The sensors were first embedded between two aluminum plates and these plates were attached at the beam-column interface using epoxy (RS 850-940). Fig. 12.24 shows the schematic layout of this model. Fig. 12.25 depicts the complete experimental setup (Suresh *et al.*, 2005, © IOP).

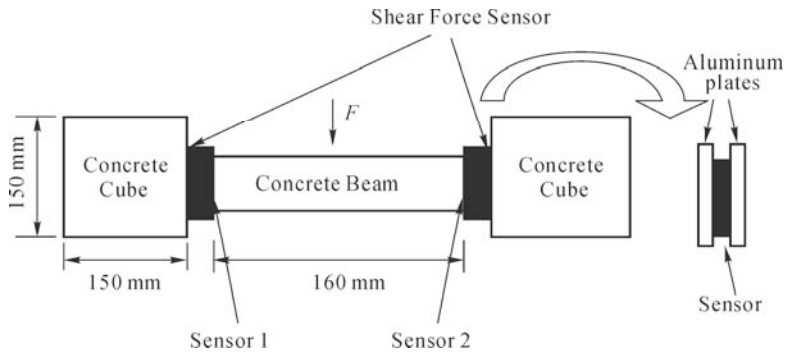


Fig. 12.24 Schematic arrangement of the experimental model for the measurement of contact force at two different structural components (Suresh *et al.*, 2005, © IOP)

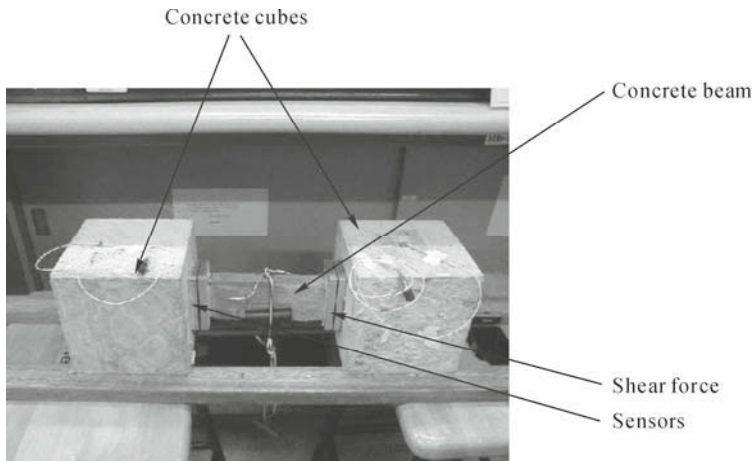


Fig. 12.25 Experimental model of beam-column joint (Suresh *et al.*, 2005, © IOP)

A force in the range of 0 – 25 N was applied at approximately the midpoint of the beam. The responses of the sensors at the ends were recorded. The responses obtained at the two sensors are shown in Fig. 12.26. This data was used for calibration of the two sensors. Later, an unknown force was applied at an

unknown position along the length of the beam and using the reference calibration data, the magnitude as well as the location of the applied force was determined. Table 12.1 provides a comparison between the experimentally measured magnitude and location with the actual values.

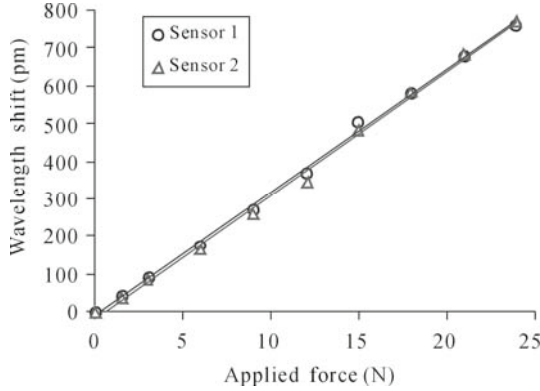


Fig. 12.26 Calibration of shear force sensors (Suresh *et al.*, 2005)

Table 12.1 Measurement of unknown applied force and location (Suresh *et al.*, 2005, © IOP)

S. No.	Applied force (N)	Measured force (N)	Error in measured force (%)	Location of applied force (cm)	Calculated location (cm)	Error in calculated location (%)
1	9	8.75	2.7	5	6.24	7.94
2	9	9	0	6	6.93	5.98
3	9	9	0	7.8	7.8	0
4	9	9	0	9.6	8.23	4.9
5	12	11.75	2.08	5	5.97	6.24
6	12	11.5	2.16	6	6.68	5.01
7	12	12	0	7.8	7.8	0
8	15	14	6.6	4	5.2	8.2
9	15	14.5	3.3	6	6.7	4.6
10	15	14	6.6	9.6	8.07	9.7

From the table, the applied force is determined with an average error of 2.5% and the location of force application is monitored within an average error of 5%. The small error, which is in acceptable range, is attributed to experimental error such as slight non-prismatic nature of the cast beam.

12.5 Multi-Component Force Measurement

Multi-component force measurement is important in several engineering applications such as robotic gripper, where information is needed about the normal and shear forces at the contact surfaces between the gripper and the object for secure

grasping (Chappell and Elliott, 2003). Another example of multi-components existing together is in the foot sole, where simultaneous measurement of the shear and pressure components will provide complete information of 3D stress distribution at discrete points along a diabetic patient's foot sole, so as to enable suitable rehabilitative programs to be adopted (Thomas *et al.*, 2004).

Although the concept of multi-component force measurement is important, very few sensors have been fabricated so far (Kim and Lee, 2003; Kang, 2001; Liu and Tzo, 2002; Kim *et al.*, 1999; Peiyu *et al.*, 2005; Aiquo *et al.*, 2007). Most of these sensors are prone to electromagnetic interference, which may lead to inaccuracy in the measurement. Using FBG for multi-component force measurement will make the sensor system immune to electromagnetic interference. Fernandez *et al.* (2001) reported a FBG strain sensor based multi-component force sensor, which was based on Maltese cross-shaped transducer, for measurement of the three components of a force. Although a linear response was obtained in the sensor, a large number of FBG strain sensors (8 FBG-based strain sensors) were needed and rigorous analysis is required to determine the various components.

In the previous chapter, FBG-based pressure and shear force sensors have been presented. The two concepts are utilized together to form a sensor that simultaneously measures the two components of force, namely the normal force and the shear force. This sensor structure is further modified to measure all the three components of the applied force: (i) the normal force (and hence, pressure) (ii) the longitudinal shear force, and (iii) the transverse shear force.

The following sections discuss the basic structure and the test results of a FBG-based multi-component force sensor.

12.5.1 Basic Concept

FBG-based shear and pressure sensors have been discussed in the previous chapter. It is explained that for pressure measurement, the FBG is embedded rectilinearly (parallel), above or below the neutral layer, within the layers of composite material. When embedded at the neutral layer, the FBG is immune to the applied pressure. However, for shear force measurement, the FBG is embedded at the neutral layer non-rectilinearly. Hence, shear force sensor should be immune to the applied pressure while pressure sensor should be immune to the applied shear force.

Experiments were carried out to study the response of shear force sensor under pressure. The results of these experiments are shown in Fig. 12.27. The maximum wavelength shift under a normal force of 20 N is found to be 10 pm (compared to approximately 1500 pm in the case of applied shear force of 20 N), which is still within the error range of the interrogation system (OSA: Optical spectrum analyzer; accuracy ± 10 pm). Resolution of the OSA used was 10 pm. Thus, the sensor shows negligible response to applied pressure. Under uniform pressure, the

fiber, which is embedded at a very small angle, becomes slightly more horizontal. The force component along the fiber is likely to be very small and hence, the axial strain in the fiber is also expected to be very negligible. This configuration thus becomes similar to embedding the fiber at the neutral layer (Suresh and Tjin, 2005a). As it is known, if the fiber is embedded at the neutral layer, there is no effect of the applied pressure on the sensor and hence no noticeable wavelength shift was observed under uniform pressure (Fig. 12.27(a)). This is consistent with what is expected.

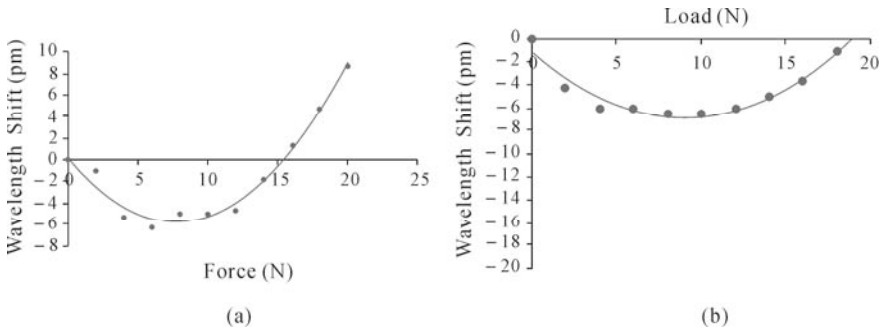


Fig. 12.27 Response of shear FBG to pressure. (a) Uniform pressure; (b) Localized pressure for small sensor thickness

When the thickness of the shear force sensor is small (≈ 1 mm), the embedded FBG becomes more horizontal under applied localized pressure as well. This is similar to embedding the FBG at the neutral layer and hence immune to the applied pressure (Fig. 12.27(b)). However, if the thickness of the sensor is large, the shear FBG will not be completely immune to pressure. In this case, it does not resemble embedding at the neutral layer and hence, it will show pressure sensitivity. In the experiments, small sensor thicknesses were used to ensure that the shear FBG is immune to the applied pressure.

Based on this observation, two-component and eventually three-component force sensors are fabricated for the measurement of magnitude and direction of the applied force in 2D and 3D space. The following sections describe the two- and three-component force sensors (Suresh and Tjin, 2005b; Suresh *et al.*, 2009).

12.5.2 Two-Component Force Measurement

As discussed above, the layers of embedding material show deformation under applied pressure. However, for small sensor thickness, the FBG embedded non-rectilinearly in the deformable layer remains insensitive to pressure. In this situation, if another FBG is embedded rectilinearly in the upper layer of the CCM, axial strain will be transferred to this FBG. Hence, this FBG can measure the

applied normal force and hence, pressure. Thus, both the shear and normal forces can be measured simultaneously. The resultant of the normal and shear forces gives the magnitude of the applied force in 2D plane, and the direction of application of this force can thus be obtained. Hence, for two components force measurement (*i.e.* one shear and one normal), two FBGs are embedded (one in the deformable layer which is the shear FBG and one in the CCM layer which is the normal force/pressure FBG) as shown in Fig. 12.28.

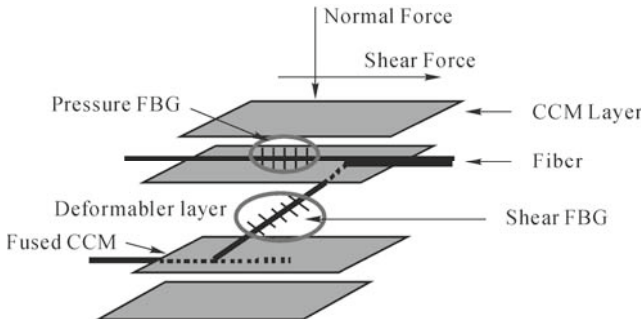


Fig. 12.28 Schematic of the embedding technique for two-component force sensor (Suresh *et al.*, 2009)

The shear FBG is embedded within the deformable layer non-rectilinearly with the CCM layer, and the normal force FBG is embedded rectilinearly within the upper layer of CCM. The working principle of this sensor is illustrated in Fig. 12.29.

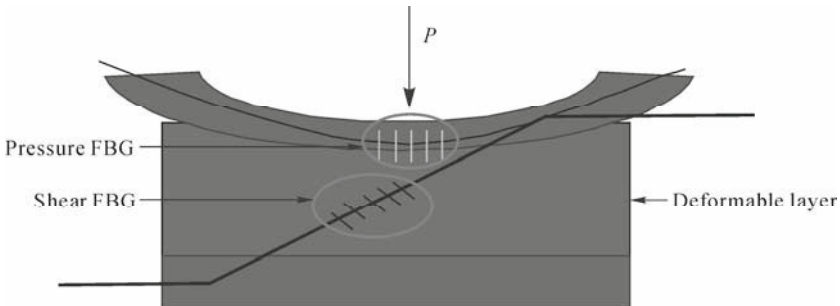


Fig. 12.29 Schematic diagram of the two-component force sensor under applied normal force (Suresh *et al.*, 2009)

Under applied pressure, the CCM will deform since it is not at the neutral layer. This deformation of CCM will cause stretching/compression of the pressure FBG (which is embedded in the CCM). This stretching/compression will eventually cause the Bragg wavelength to shift, which is a measure of the applied pressure. Under applied pressure, the shear FBG (which is embedded non-rectilinearly in the deformable layer) will become almost horizontal resembling

the embedding of FBG at the neutral layer, and thus is immune to the applied pressure.

Under applied shear force, the normal force FBG is unaffected, since in this case, the horizontal movement of the upper layer will displace the pressure sensing fiber without any stretching or compression (rigid body motion of the normal force FBG). Thus, the wavelength of the normal force FBG will remain unaffected whereas the shear FBG will be stretched and will undergo a wavelength shift proportional to the applied shear force. Hence, this two-component force sensor is able to measure both the shear and pressure components simultaneously.

For experimental verification of this sensor, two sets of reference data were collected; one set under applied shear force and the other under applied pressure. Fig. 12.30 shows the response characteristic of the sensor under applied shear force.

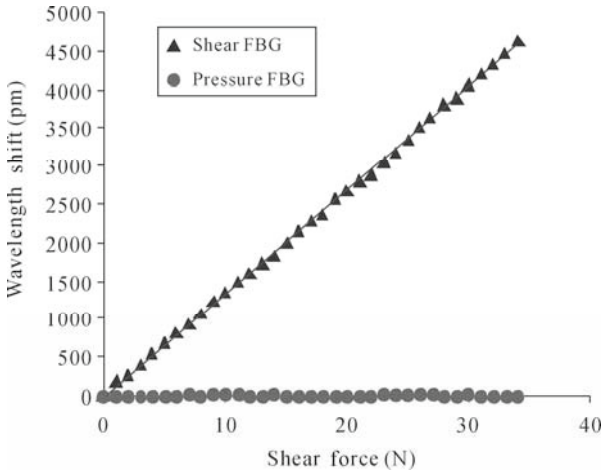


Fig. 12.30 Response characteristic of two-component force sensor under applied shear force (Suresh *et al.*, 2009)

From the measurements, a shear force sensitivity of 135 pm/N was obtained. It is apparent that the pressure FBG was not affected by the applied shear force, which is in agreement with the above discussion. Similarly, the response characteristic of the sensor under applied normal force (both under compression and tension) was also evaluated. The result of this experiment is shown in Fig. 12.31, which shows that the shear FBG was immune to the applied pressure.

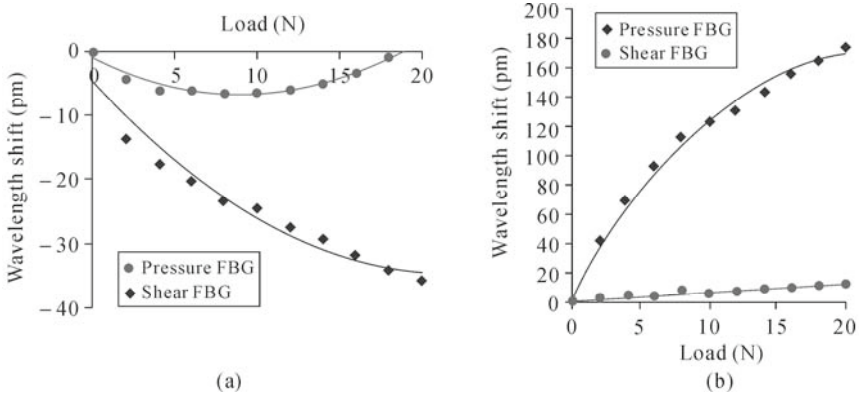


Fig. 12.31 Response characteristic of sensor under applied pressure. (a) pressure FBG under compression (b) pressure FBG under tension (Suresh *et al.*, 2009)

The normal force FBG shows a higher shift in the Bragg wavelength while only a small negligible shift was observed in the wavelength of the shear FBG as the FBG is embedded almost at the neutral layer.

It should be noted that the normal force FBG displays a non-linear shift in the wavelength since the deformable layer may have borne part of the applied force; thus the applied pressure may not be transferred fully to the pressure FBG. Another possible reason for the non-linearity could be due to the non-linear characteristics of the silicon rubber under compression as well as the associated geometric non-linearity. In the first experiment, the normal force was applied from the top so that the normal force FBG was under compression; thus showing a blue shift in the reflected wavelength (Fig. 12.31(a)). Another experiment was performed to obtain the response curve of the sensor when the pressure was applied from the bottom so that the pressure FBG was under tension. The result is shown in Fig. 12.31(b)). In this case, the pressure FBG shows a red shift in the wavelength as explained in Chapter 11. The response is again found to be non-linear due to factors explained above. Under both conditions, similar magnitudes of wavelength shift are expected since the embedding is at the same location above and below the neutral layer under pure bending. However, under point load/non-uniform load, where the stress distribution is complex, lesser compressive strain is observed as compared to the tensile strain at corresponding location below the neutral layer.

From Fig. 12.31, we observed that the shear FBG is almost insensitive to the applied pressure (the small shift obtained is negligible). The results of these experiments serve as a reference calibration data for the measurement of the unknown applied force. The following is the description of 2D force measurements.

12.5.3 2D Force Measurement

From the measured shear (S) and normal force (P), the unknown applied force or the resultant force can be obtained as

$$F = \sqrt{S^2 + P^2} \tag{12.3}$$

The direction of the applied force (w.r.t sensor orientation) can be measured as

$$\theta = \arctan\left(\frac{P}{S}\right) \tag{12.4}$$

Based on the above analysis, experiments were performed for the 2D force sensor. A digital force gauge was employed to determine the magnitude of the applied force in the vertical direction, while a metal stage of different orientation in 2D was used to keep the sensor at different angles with respect to the force gauge.

Forces of different magnitudes were applied at different angles. The results of this experiment are summarized in Tables 12.2 and 12.3. The measured forces and angles are calculated using Eqs. (12.3) and (12.4) respectively.

Table 12.2 shows the measurement of the direction of the applied force, and Table 12.3 shows the magnitude of the applied force.

Table 12.2 Measurement of direction of the applied force in 2D (Suresh *et al.*, 2009)

S. No.	Applied angle (Degree)	Measured angle (Degree)	Normalized error (%)
1	90.0	90.0	0.0
2	88.0	85.7	2.6
3	80.0	79.1	1.1
4	75.0	71.5	4.6

Table 12.3 Measurement of magnitude of the applied force (Suresh *et al.*, 2009)

S. No.	Applied force (N)	Measured force (N)	Normalized error (%)
1	0.0	0.0	0.0
2	5.0	5.4	8.2
3	10.0	9.2	8.2
4	15.0	13.7	8.6

The results show that the applied angle can be measured within an average error of about 2%, and the magnitude can be measured within an average error of about 6%. This 2D force measurement can be extended for measuring 3D forces, as detailed in the following section.

12.5.4 3D Force Measurement

An arbitrarily applied force in space can be resolved into three mutually orthogonal components. Out of the three components, two components (longitudinal and transverse shear components) always fall in the same plane but at mutually perpendicular directions, with the third component (normal force/pressure component) being perpendicular to the corresponding plane. Thus, the longitudinal and transverse shear forces correspond to the mutual orthogonal shear component of the force.

It has been explained earlier that, for small sensor thickness, the FBG which is embedded non-rectilinearly in the deformable layer is insensitive to the applied normal force and hence, pressure. Another experiment was carried out to determine the response of the longitudinal shear FBG under applied transverse shear force. The result of this experiment is shown in Fig. 12.32 (Suresh and Tjin, 2005a, 2005b; Suresh *et al.*, 2009). It was observed that the FBG in the shear force sensor shows highest sensitivity to the longitudinal applied shear force and negligible sensitivity to the transverse shear force since the component of the applied transverse shear force along the fiber is small. Hence, the transverse shear force has little effect on the fiber.

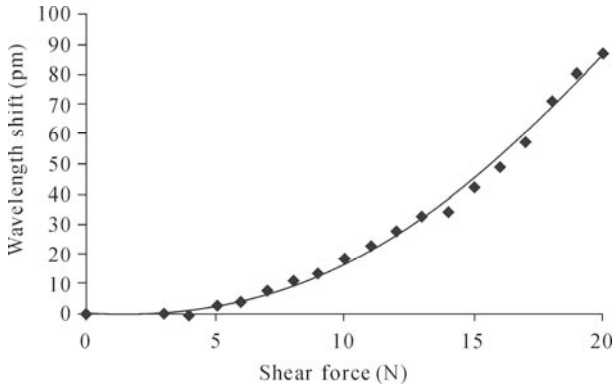


Fig. 12.32 Response of longitudinal shear FBG under transverse shear force (Suresh *et al.*, 2009)

A wavelength shift of around 80 pm under a transverse shear force of 20 N is observed. On the other hand, under longitudinal shear force of 20 N, a wavelength shift of 1500 pm is observed. Thus, it is verified that the transverse shear FBG shows high sensitivity to longitudinal shear force but low sensitivity to transverse shear force. In the two-component sensor structure, if another FBG is embedded in the deformable layer in the transverse direction, this will be sensitive to the transverse shear force and almost insensitive to the longitudinal shear force. Based on this principle, a three-component force sensor can be fabricated. The schematic design of this sensor is shown in Fig. 12.33. For measurement of the three force components, another FBG is embedded non-rectilinearly within the deformable

layer (which is shown as transverse FBG in Fig. 12.33) in the orthogonal direction of the longitudinal shear FBG. The pressure FBG is embedded in the CCM layer.

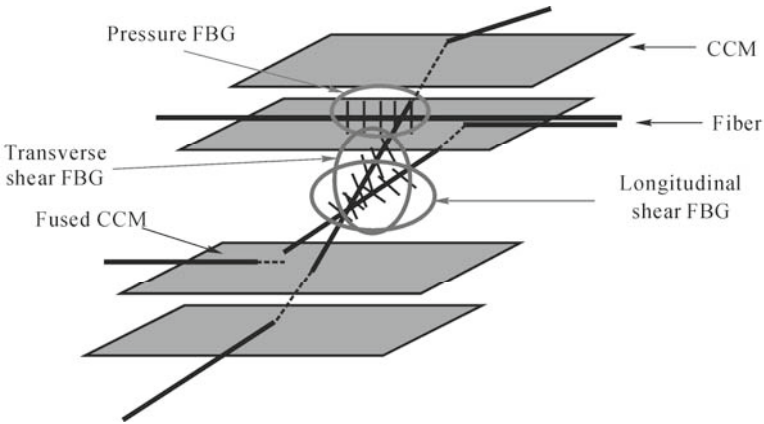


Fig. 12.33 Schematic diagram of 3D force sensor (Suresh *et al.*, 2009)

The applied force in 3D can be resolved in three mutually orthogonal components, namely (i) the normal force, (ii) the longitudinal horizontal (longitudinal shear) force and (iii) the transverse horizontal (transverse shear) force. The longitudinal shear FBG will show highest sensitivity to the longitudinal shear component of the applied force. Similarly, the transverse shear FBG will show highest sensitivity to the transverse shear component since the transverse shear component will appear in the longitudinal direction of this FBG. The normal force FBG will be sensitive only to the normal component of the applied force. Thus, under the applied normal force, only the normal force FBG would be responding, whereas under the applied longitudinal or transverse shear force, the corresponding FBG will show large wavelength shift; the other two will be almost immune (though not completely) to the orthogonal components.

For experimental verification of this sensor, three sets of reference data were recorded; one under the applied normal force and the other two under the applied co-planar shear forces (longitudinal and transverse shear). The following section discusses the experiments in detail.

From here on, the normal force FBG will be addressed as P, the longitudinal shear FBG as S_1 and the transverse shear FBG as S_2 .

● *Effect of Applied Normal Force*

Experiments were carried out to investigate the response of the three FBGs under applied pressure. A normal force of 0 – 20 N was applied on the sensor, such that the upper layer of the CCM was under compressive stress. The response of the

three FBGs is shown in Fig. 12.34. Here, the term “sensor” refers to the composite structure containing CCM, the deformable layer and the three FBGs.

The result in Fig. 12.34(a) shows that only the normal force FBG responded to the applied normal force, which is in agreement with the earlier discussions. This result will be used as reference for measurement of the magnitude and direction of the unknown applied force.

In this experiment, the normal force was applied from the top, so that the corresponding FBG was under compression, thereby showing a blue shift in the reflected wavelength. Another experiment was performed to obtain the response curve of the sensor when the normal force was applied from the bottom where the corresponding FBG was under tension. The result is shown in the Fig. 12.34(b), which again verifies that under normal force, only the corresponding FBG (P) shows noticeable wavelength shift. The sensors S_1 and S_2 show negligible shifts.

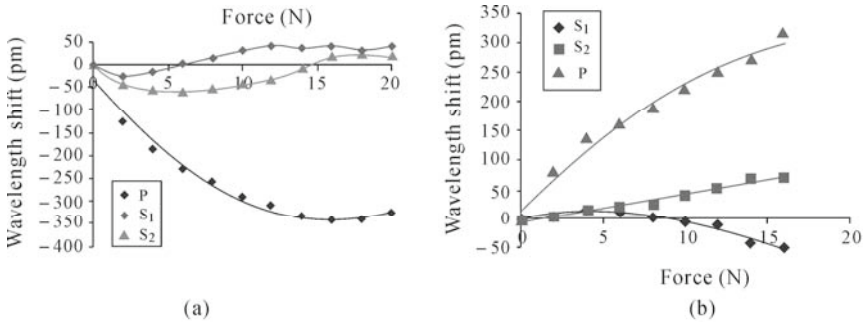


Fig. 12.34 Response of S_1 , S_2 and P FBGs of three-component force sensor under applied normal force. (a) Normal force FBG under compression; (b) Normal force FBG under tension (Suresh *et al.*, 2009)

It is observed that the two shear FBGs (S_1 and S_2) show negligible sensitivity to the applied normal force, which is again in agreement with the earlier discussions. Small shift in the wavelength was obtained for the two shear FBGs since the shear FBGs were not embedded exactly at the neutral layer. Under applied normal force, the two FBGs will become more horizontal but not completely, so they will not be exactly at the neutral layer, hence will only exhibit negligible wavelength shift. This small sensitivity can be further reduced either by reducing the thickness of the deformable layer or by increasing the stiffness of the deformable layer (Suresh and Tjin, 2005a).

In a similar way, the responses of the FBGs to the longitudinal and transverse shear forces were investigated. The results of the experiments are discussed in the following sections.

• Effect of Applied Longitudinal Shear Force

The response characteristic of the three-component force sensor under applied

longitudinal shear force is shown in Fig. 12.35. It was found that S_1 shows the highest sensitivity to the applied longitudinal shear force. P and S_2 show negligible sensitivity, which is in agreement with the theoretical prediction that only S_1 will be sensitive to the applied shear force in the longitudinal direction.

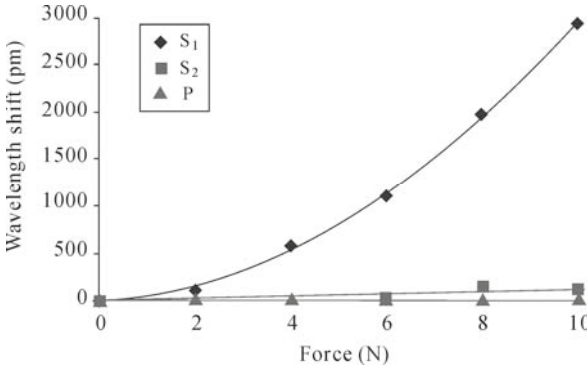


Fig. 12.35 Response of S_1 , S_2 and P FBGs of three-component force sensor under applied longitudinal shear force (Suresh *et al.*, 2009)

• *Effect of Applied Transverse Shear Force*

The response characteristic of the sensor under applied shear force in the transverse direction is shown in Fig. 12.36 (Suresh and Tjin, 2005b; Suresh *et al.*, 2009).

It is found that only S_2 shows sensitivity to the applied transverse shear force. The pressure (P) and the longitudinal FBG (S_1) show negligible sensitivity, which is again found to be in agreement with the theoretical conclusion that only the transverse shear FBG (S_2) will be sensitive to the applied transverse shear force.

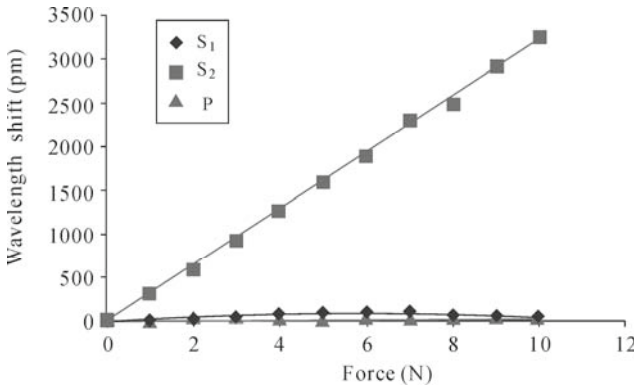


Fig. 12.36 Response of three-component force sensor under applied transverse shear force (Suresh *et al.*, 2009)

The results obtained in these basic characterization experiments were then used for actual measurement of the three force components. The wavelength shifts of the three FBGs will give the respective force component and hence, the resultant force can be determined. The resultant of the three components measures the actual force applied in 3D. In the experiment conducted, as a simplification, instead of changing the direction of the applied force, the surface on which the sensor was mounted was adjusted (with resolution 0.5 degrees). Forces of various magnitudes were applied (measured using a digital force gauge with resolution of 0.5 N). A 3D stage was used to secure the sensor so that the force can be applied to the sensor in various directions.

The results of this experiment are summarized in Table 12.4, which shows the measurement of the magnitude as well as the direction of the applied force in 3D.

Table 12.4 Measurement of magnitude and direction of applied force in 3D (Suresh *et al.*, 2009)

Parameter	Actual value	Experimentally measured value	Normalized Error (%)
Force (N)	2.0	1.8	9.0
	4.0	3.7	6.5
	6.0	5.9	1.6
Angle at horizontal plane (ϕ) (Degree)	38.4	37.5	2.3
	35.0	31.4	10.4
	37.0	32.0	13.5
Angle from horizontal (θ) (Degree)	8.0	7.0	12.5
	10.5	9.2	12.3
	11.6	12.2	5.4

It was found that the sensor could measure the magnitude and direction of the applied force within an average error of 10%. Although the error is apparently large, this work demonstrates the feasibility of using FBGs for determining 3D forces. Part of this error is attributed to experimental error, which includes measurement of the actual angles at which the force was applied.

The magnitude and direction of the applied force characterize the applied force vector completely in 3D. Hence, two- and three-component force sensors have been successfully fabricated and tested. The two-component force sensor measures the normal force/pressure and the longitudinal shear force and hence, measures the magnitude and direction of the applied force in 2D. For the three-component force sensor, three FBGs are embedded within the CCM layer. This sensor measures the normal force/pressure, longitudinal shear and transverse shear components of the force and hence, measures the magnitude and direction of the applied force in 3D. From Tables 12.2, 12.3 and 12.4, it may be noted that the accuracy of measurement increases with the angle as well as magnitude. Presently, the cross-coupling effects are present, though in small magnitude. So far, sensor with thickness approximately 1 mm has been found to be insensitive to normal force (Suresh and Tjin, 2005a). To minimize cross-coupling between the transverse and the longitudinal shear FBGs, highly orthotropic material may be used for embedding. Although, carbon composites is one such material, however no

complete immunity to orthogonal shear component has been achieved so far.

The advantage of this multi-component force sensor over other reported sensor is that, in this sensor, only 3 FBGs are required (as compared to 8 FBGs reported by Fernandez *et al.*, 2001). Hence, less signal processing is needed. For shear force sensor, the sensitivity dependence on the sensor parameters has been well established (Suresh and Tjin, 2005a). The dependence of sensitivity/accuracy/force sensing range on the sensor parameters such as sensor dimension and material parameters is apparent. Hence, based on the requirement of practical applications, such as higher sensitivity or larger sensing range, sensor for particular applications can be fabricated. As the FBGs are embedded within the CCM layers, the whole sensor may be embedded within composite structures for strain monitoring, if required. However, this sensor has not been tested for such applications. For practical application, advanced signal processing is required as well.

12.6 Simultaneous Measurement of Pressure and Temperature

In general, all strain sensors, including FBG-based sensors, are subjected to both pressure and temperature simultaneously. For FBG-based strain sensors, measurement of the reflected wavelength shift obtained from a single grating does not facilitate discrimination of the sensor's response to the two perturbations. Thus, special technique is required to separate the information corresponding to the two measured parameters. This section presents an FBG-based sensor which is configured in such a way that the pressure and temperature can be measured simultaneously and independently. Along with the inherent temperature independent measurement of the pressure, this sensor is also able to indicate the direction of the applied pressure, which is the added advantage of this sensor over the other reported sensors (Jincheng *et al.*, 2008; Liu *et al.*, 2007; Tian *et al.*, 2005; Huang *et al.*, 2003).

12.6.1 Sensor Configuration and Working Principle

The sensor consists of two FBGs which are embedded within the layers of CCM. One FBG is embedded above while the other below the neutral layer at equal distances, as shown in Fig. 12.37(a). The reflection spectra of the FBGs are sufficiently separated as shown in Fig. 12.37(b) (Tjin *et al.*, 2009).

For ease of explanation, we have embedded the FBG with lower Bragg wavelength above the neutral layer while the other FBG with a higher Bragg wavelength is embedded below the neutral layer. When pressure is applied from the top, the FBG embedded above the neutral layer is compressed and the FBG below the neutral layer is stretched. The reflected Bragg wavelengths shift towards

the shorter and longer wavelengths for the compressed and the stretched FBGs, respectively. Under this condition, the separation between the two FBG spectra increases. This shift of the separation of the FBG spectra is a function of the applied pressure. Fig. 12.37(b) shows the spectra of the FBGs when no pressure is applied. With the application of pressure, the FBGs show shifts toward the shorter/longer wavelengths as shown in Fig. 12.37(c). When pressure is applied from the bottom, the peak wavelength of the FBG embedded above the neutral layer (which is the FBG with lower Bragg wavelength) shifts toward longer wavelength while the peak wavelength of the FBG embedded below the neutral layer shifts toward shorter wavelength. In other words, the separation between the two peak wavelengths decreases (Fig. 12.37(c)). Thus, an increase or decrease of the spectral separation indicates the direction of the applied pressure while the magnitude of the separation is proportional to the magnitude of the applied pressure.

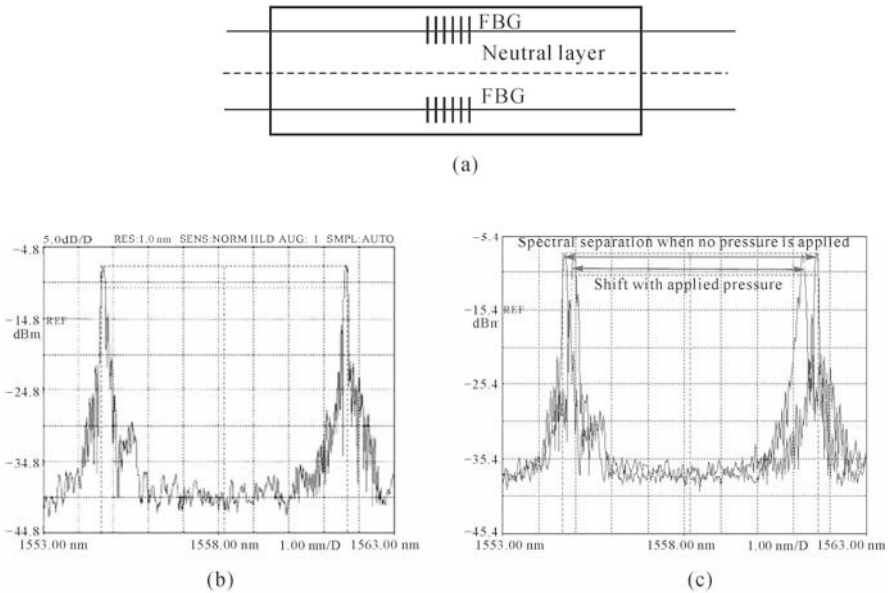


Fig. 12.37 Sensor structure for measurement of temperature and pressure. (a) Block diagram; (b) FBG spectra; (c) Variation of the shift of two spectra with pressure (Tjin *et al.*, 2009)

When the temperature varies, both the FBGs spectra shift either towards longer wavelengths (for increase in temperature) or shorter wavelengths (for decrease in temperature) in equal amounts since both FBGs are exposed to the same temperature variation and have the same temperature sensitivity. The separation between the two spectra peaks remains unchanged. Fig. 12.38 shows the behavior of the sensor with increasing temperature, where the spectra of the two FBGs at room temperature and at increased temperature are shown.

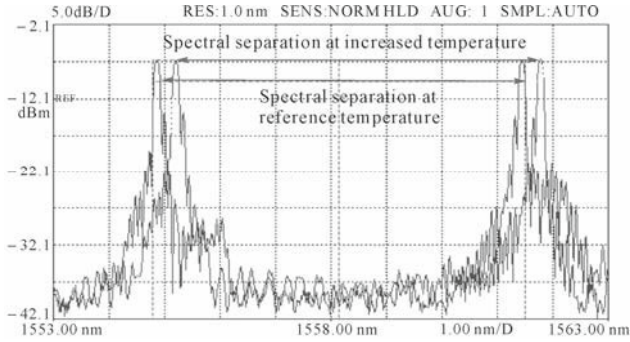


Fig. 12.38 Sensor under increasing temperature: Separation of the spectra remains unchanged (Tjin *et al.*, 2009)

With the variation of temperature, the two spectral peaks will shift by equal magnitudes, while the peak separation will remain the same. Though the shift of individual peak gives a measure of the temperature, the shift of both the spectra should be measured so that the average of the two can be used to determine the temperature. When the sensor is exposed to both temperature and pressure, the separation between the two FBG spectra gives a measure of the applied pressure while the average of the shift of individual peak gives a measure of the temperature (Fig. 12.39).

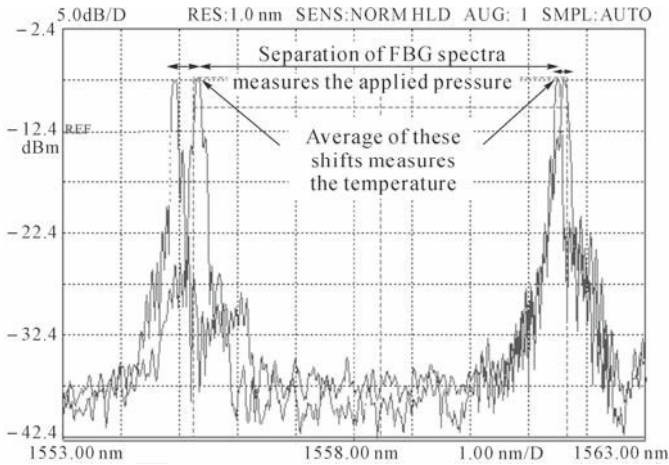


Fig. 12.39 Simultaneous measurement of temperature and pressure (Tjin *et al.*, 2009)

12.6.2 Sensor Fabrication and Experimental Procedure

Two FBGs with Bragg wavelengths 1554.754 nm and 1561.700 nm were used for sensor fabrication. The FBGs were written using the phase mask technique, and have reflectivity of more than 90%. The FBGs were embedded within the CCM. Tunable laser source (TLS) was used as the light source and optical spectrum analyzer (OSA) was used to analyze the FBG spectra. The experiments were performed in three stages. Following is a discussion of the various steps.

(a) Response of Sensor at Variable Temperatures Under Constant Pressure

As discussed earlier, with temperature variations, the individual FBG peak shifts while the separation between the two FBG spectra remains unchanged. An experiment was performed to verify this concept. The sensor was placed in an oven, and the temperature was varied between 20 °C to 60 °C with pressure kept constant at 5 MPa. The individual Bragg wavelengths and the separation between the two spectra were measured. The results of this experiment are shown in the Fig. 12.40. Fig. 12.40(a) shows the shift of individual peaks whereas Fig. 12.40(b) shows the change in separation between the two spectra with temperature.

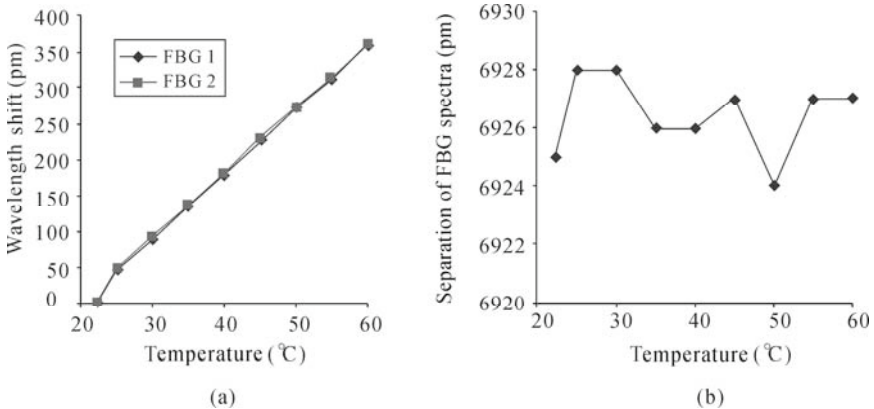


Fig. 12.40 Response of the sensor under temperature. (a) Shift of individual peak; (b) Shift of separation of the two FBG spectra (Tjin *et al.*, 2009)

Note that the individual wavelength changes linearly with temperature while the separation of the two spectra remains approximately constant. The separation of the two spectra was approximately 6,925 pm at a temperature of 22 °C and a pressure of 5 MPa. A shift of the spectral separation of approximately 3 pm was obtained with increasing temperature of up to 60 °C. This shift is small as compared to the 10 pm accuracy of the OSA. Hence, this shift of spectral separation can be considered as negligible.

(b) Response of Sensor at Constant Temperature Under Variable Pressure

Another experiment was carried out to verify that the change of separation between the two FBG spectra gives a measure of the applied pressure. Pressure in the range of 0 to 10 MPa was applied from the top/bottom of the sensor with the temperature kept constant at 20 °C. The reflected Bragg wavelengths of the two FBGs were measured, and the separation of the spectra was determined. The result of this experiment is shown in Figs. 12.41 and 12.42.

Fig 12.41 shows the shift of individual wavelength. Figs. 12.42(a) and 12.42(b) show the shift of separation between the two spectra for the pressure applied from the top and from the bottom. It can be observed that separation of the two spectra increases/decreases when the pressure is applied from the top/bottom respectively. The magnitude of shifts of the two spectra gives a measure of the magnitude of applied pressure. The increase/decrease of the spectral shift represents the direction of application of pressure.

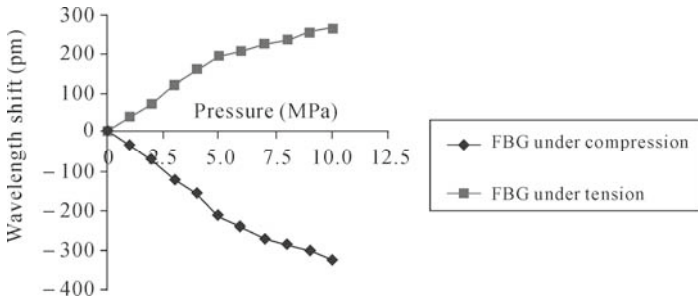


Fig. 12.41 Response of the sensor under applied pressure: wavelength shift of the two FBGs (Tjin *et al.*, 2009)

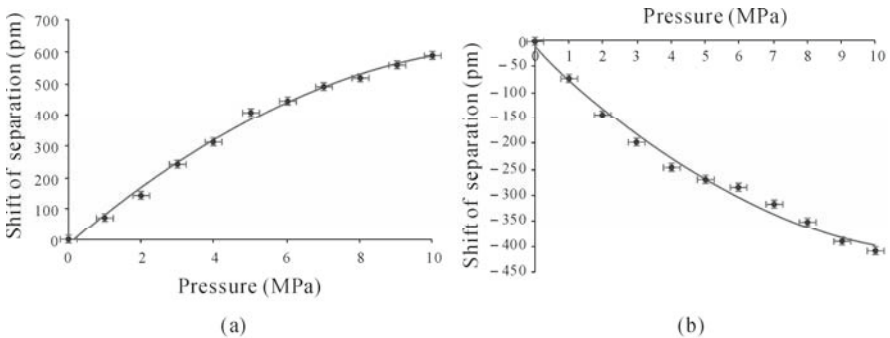


Fig.12.42 Separation of spectra when pressure is applied from (a) top and (b) bottom (Tjin *et al.*, 2009)

- *Simultaneous Measurement of Pressure and Temperature*

Based on the individual temperature and pressure measurements obtained so far, the feasibility of simultaneous measurement of temperature and pressure was experimentally verified. The sensor was placed in an oven, and pressures of various amplitudes were applied. The oven temperature was also varied. The results of this experiment are summarized in Tables 12.5 and 12.6.

Table 12.5 Measurement of pressure (Tjin *et al.*, 2009)

Actual applied pressure (MPa)	Measured pressure (MPa)	Normalized error (%)
2	2	0
5	4.65	7
10	10.2	2

Table 12.6 Measurement of temperature (Tjin *et al.*, 2009)

Actual temperature (°C)	Measured temperature (°C)	Normalized error (%)
35.2	36	2.2
45	46.4	3.1
55	54.25	1.4

Tables 12.5 and 12.6 show the results for the measurement of pressure and temperature, respectively. It was observed that using the proposed embedding technique, the temperature and pressure can be measured simultaneously within acceptable error limits. The average of the individual shifts gives a measure of the temperature with error within 5%, while the shift of the separation of the two FBG spectra gives a measure of the magnitude and direction of the applied pressure within an error of 7%. This embedding technique allows simultaneous measurement of the magnitude and direction of the applied pressure as well as the temperature.

12.7 Summary

Several applications of embedded FBG sensor array are described in this chapter. In biomedical applications, the development of a foot pressure sensor to monitor the foot pressure distribution of patients suffering from diabetics was covered. The lost of sensory feedback as a result of illness may cause the patients to exert excessive pressure on a particular area of their foot unknowingly. Over prolonged period of time, if the condition is left untreated, the nerves may get damaged and the potential of developing gangrene and later amputation of the limb increases. Hence, the foot pressure sensor serves as an external sensory feedback system to both patients and doctors, providing them information that can help correct the patients' gait.

Another biomedical application of FBG sensors described in this chapter is its

use for recording compliance of dental splint in obstructive sleep apnea through the measurement of pressure and temperature. The sensors fabricated using FBGs have advantages over the conventional force and temperature monitoring sensors in that they do not carry any electrical current and hence, pose no risk to the patient. In addition, the two sensors were fabricated on the same optical fiber, with both working independently of the other. The sensors are also much flatter than most conventional sensors and, hence more appropriate for sensing within a confined area (Tjin *et al.*, 2001b).

In civil engineering applications, “smart structures” are structures which provide information on the “state of health” of the structure much like our body’s nervous system providing pain signals to warn us of possible internal ailments. In an experiment to demonstrate the concept of “smart structures” using FBGs, two separate sensor arrays, comprising four FBGs each, were embedded in an RC beam. The beam was supported on both sides and a perpendicular force was gradually applied to the center of the beam. The strain readings obtained from the sensor arrays show a contraction on the top and an expansion at the bottom of the concrete beam. The FBGs that are closer to the center of the beam were more sensitive to the applied force, while the FBGs closer to the supported end were less sensitive to the applied force. When the applied loading on the beam exceeded the damage threshold, the strain readings from the sensors went in the reverse direction even though the applied pressure was increased. The plot in Fig. 12.21 illustrates different regions of measurement. This is useful when the “health” of the structure is to be classified into “healthy” or “unhealthy” state, based on the strain readings obtained from the embedded sensors.

Fabrication and testing of two- and three-component force sensors has also been covered. The two-component force sensor measures the normal force/pressure and the longitudinal shear force. The three-component force sensor measures the normal force/pressure, and the longitudinal and transverse shear forces. Hence, it can measure the magnitude as well as the direction of the applied force in 3D space. This sensor has potential applications in fields such as aerospace, defense and robotics.

Finally, the embedding technique for simultaneous measurement of temperature and pressure is presented. A proof of concept has also been performed to demonstrate that the temperature and pressure can be measured simultaneously within acceptable error limits. It is also found that along with the magnitude, this sensor also determines the direction of the applied pressure, which is an advantage compared with the other reported sensors.

References

- Aiquo, S., Juan, W., Gang, Q. and Huang, W.Y. (2007). “A novel self-decoupled four degree of freedom wrist force/torque sensor”, *Measurement* 40: 883-891.
- Basil, H. and Wilson, D. (1988). *The foot*, UK, Longmann.

- Bhalla, S. and Soh, C.K. (2004). "High frequency piezoelectric signatures for diagnosis of seismic/blast induced structural damages", *NDT&E International*, 37: 23-33.
- Chappell, P.H. and Elliott, J.A. (2003). "Contact force sensor for artificial hands with a digital interface for a controller", *Measurement Science and Technology* 14: 1275-1279.
- Fernandez, A.F., Berghmans, F., Brichard, B., Mégret, P., Decréton, M., Blondel, M. and Delchambre, A. (2001). "Multi-component force sensor based on multiplexed fiber Bragg grating strain sensors", *Measurement Science and Technology*, 12: 810-813.
- Hao, J. (2001). "Design and Fabrication of a fiber optic pressure sensor", *Ph.D. Thesis*, Nanyang Technological University, Singapore.
- Hao, J.Z., Tan, K.M., Tjin, S.C., Liaw, C.Y., Chaudhuri, P.R., Guo, X. and Lu, C. (2003). "Design of a foot-pressure monitoring transducer for diabetic patients based on FBG sensors", *Lasers and Electro-Optics Society, LEOS 2003, The 16th Annual Meeting of the IEEE*, 27-28 October: 23-24.
- Huang, Y., Li, J., Kai, G., Yuan, S. and Dong, X. (2003). "Temperature compensation package for fiber Bragg gratings", *Microwave and Optical Technology Letters*, 39:70-72.
- Jincheng, P., Yang, X., Zhan, Y., Zhu, R. and Xiang, S. (2008). "On a fiber grating sensor system with the capacity of cross- sensitivity discrimination", *Optik*, 119: 565-570.
- Jensen, D.W. and Koharchik, M.J. (1991). "Cyclic loading of composite-embedded fiber-optic strain sensors", *Proceedings of Spring Conference Society of Experimental Mechanics*, Milwaukee, Wisconsin, 233-238.
- Kim, G.S. and Lee, H.D. (2003). "Development of a six-axis force/moment sensor and its control system for an smart materials and structures intelligent robot's gripper", *Measurement Science and Technology*, 14: 1265-1274.
- Kang, C.G. (2001). "Closed-form force sensing of a 6-axis force transducer based on the stewart platform", *Sensors and Actuators A: Physical*, 90: 31-37.
- Kim, G.S., Kang, D.L. and Rhee, S.H. (1999). "Design and fabrication of a six-component force/moment sensor", *Sensors and Actuators A: Physical*, 77: 209-220.
- Liu, S.A. and Tzo, H.L. (2002). "A novel six- component force sensor of good measurement isotropy and sensitivities", *Sensors and Actuators A: Physical*, 100: 223-230.
- Peiyu, L., Tan, D., Liu, D., Liu, G. and Ying, M. (2005). "Six component force sensor and its calibration system", *China Mechanical Engineering*, 16: 1523-1526.
- Liu, L., Zhang, H., Zhao, Q., Liu, Y. and Li, F. (2007). "Temperature independent FBG pressure sensor with high sensitivity", *Optical Fiber Technology*, 13: 78-80.
- Soh, C.K., Tseng, K.K.H., Bhalla, S. and Gupta, A. (2000). "Performance of smart piezoceramic patches in health monitoring of a RC bridge", *Smart Materials and Structures*, 9: 533-542.

- Strollo, P.J. and Rogers, R.M. (1996). "Current Concepts: Obstructive Sleep Apnea", *New England Journal of Medicine*, 334: 99-104.
- Simoneau, G.G., Ulbrecht, J.S., Derr, J.A., Becker, M.B. and Cavanagh, P.R. (1994). "Postural instability in patients with diabetic sensory neuropathy", *Diabetes Care*, 17: 1411-1421.
- Suresh, R. and Tjin, S.C. (2005a). "Effects of dimensional and material parameters and cross coupling on FBG based shear force sensor", *Sensors and Actuators A: Physical*, 20: 26-36.
- Suresh, R. and Tjin, S.C. (2005b). "Application of fiber Bragg grating for multi component force measurement", *Proceeding of the Fourth International Conference on Smart Materials, Structures and Systems*, July 28-30, Bangalore, India, SD- 10: 70-76.
- Suresh, R., Tjin, S.C. and Ngo, N.Q. (2005). "Application of a new fiber Bragg grating based shear force sensor for monitoring civil structural components", *Smart Materials and Structures*, 14: 982-988.
- Suresh, R., Tjin, S.C. and Bhalla, S. (2009). "Multi-component force measurement using FBG sensor", *Optics and Laser Technology* 41(4): 431-440.
- Tian, K., Liu, Y. and Wang, Q. (2005). "Temperature-independent fiber Bragg grating strain sensor using bimetal cantilever", *Optical Fiber Technology*, 11: 370-377.
- Tjin, S.C., Suresh, R. and Bhalla, S. (2009). "Simultaneous and independent measurement of pressure and temperature", *International Journal of COMADEM*, 12.
- Tjin, S.C., Tan, Y.K., Yow, M., Lam, Y.Z. and Hao, J. (2001a). "Recording compliance of dental splint use in obstructive sleep apnoea patients by force and temperature modeling", *Medical and Biological Engineering and Computing*, 39: 182-184.
- Tjin, S.C., Hao, J., Lam, Y.Z., Ho, Y.C. and Ng, B.K. (2001b). "A pressure sensor using fiber Bragg grating", *Fiber and Integrated Optics*, 20: 59-69.
- Thomas, V.S., Patil, K.M. and Radhakrishnan, S. (2004). "Three dimensional stress analysis for the mechanics of plantar ulcers in diabetic neuropathy", *Medical and Biological Engineering and Computing*, 42: 230-235.
- Wang, Y., Tjin, S.C., Hao, J.Z., Lim, T.K., Tan, K.B., Chan, K.M., Moyo, P. and Brownjohn, J.M.W. (2000). "Determination of load-strain characteristics of concrete slabs by using embedded fiber Bragg grating sensors", *Proceedings of SPIE International Symposium on Applied Photonics*, 22-25 May, Glasgow, UK.

Monitoring of Rocks and Underground Structures Using PZT and FBG Sensors

S. Bhalla^{*}, Y. W. Yang, C. K. Soh

^{*}Department of Civil Engineering, Indian Institute of Technology Delhi,
Hauz Khas, New Delhi 110016, India
Tel: 91-11-2659-1040; Fax: 91-11-2658-1117
Email: sbhalla@civil.iitd.ac.in

13.1 Introduction

This chapter discusses the feasibility of employing the new generation fiber optic and piezoelectric sensor systems for comprehensive monitoring of rocks, covering load history monitoring/retrieval as well as damage assessment. In several major cities across the world, city planners are paying serious attention to the development of usable underground space in the form of caverns and tunnels due to continuously depleting land availability (Zhao *et al.*, 1999). In addition, underground structures are considered safer compared to surface structures against earthquakes and hurricanes, and are less prone to noise pollution (Goel, 2001). However, they demand huge resources for construction and maintenance, and any collapse could be detrimental to the nation's economy in terms of lives and properties. This necessitates their comprehensive monitoring on a regular basis to check the onset of damages. Damages might occur due to environment-induced degradation, fatigue, excessive/unpredicted loads, and underground blasts. In addition, instrumentation and monitoring of the underground structures during construction and operation can facilitate validation of key design assumptions. This is especially pertinent to the underground structures, since quite often, many geotechnical and environmental complexities cannot be accurately considered at the design stage. Comprehensive instrumentation can pave the way for long-term monitoring of external loads, stress distributions and deflections, which can be

useful for comparing the predicted and the actual responses as well as detecting the occurrence of structural damage in real-time, thereby ensuring a high level of safety. In addition, the database generated could economize future constructions.

In general, structural monitoring should cater for two requirements in the underground structures: (i) monitoring external loads (due to construction, vehicle movement, blasts, shocks and environmental effects) and corresponding deflections/strains, which can be termed as load history retrieval (LHR); and (ii) monitoring the occurrence of damages, that is, SHM. This chapter illustrates, using rock specimens, how PZT transducers can be utilized for SHM and FBG-based sensors for LHR simultaneously.

13.2 Conventional Versus Smart Material Based Sensor Systems for LHR and SHM of Underground Structures

Strain gauges are the most widely used sensors for LHR. The conventional strain gauges are based on vibrating wire or electrical resistance principle. Vibrating wire strain gauges (VWSGs) involve measuring the frequency of vibration of a pre-tensioned wire (whose ends are fixed to the monitored component) from which strain in the component is deduced. They are considered reliable for long-term strain monitoring, as demonstrated by Bakker (2000) on tunnels and Moyo (2002) on bridges. However, they are suitable for measuring static strains only, and are highly susceptible to mechanical noise from ambient vibrations. In addition, they are bulky and expensive. The electrical strain gauges (ESGs), which are based on stress dependence of a conductor's resistance, offer a low-cost alternative to VWSGs. On the other hand, the ESGs tend to be unstable over long periods of time due to decay, and hence are suitable for short-term monitoring only. Furthermore, they can be easily deteriorated by water and hence can be problematic if employed for monitoring underground rock structures such as caverns where damp conditions commonly occur. In general, both VWSGs and ESGs warrant separate cables from each sensing unit, which implies many wires for handling. At the same time, for long distance monitoring, these cables suffer from electro-magnetic interference and electrical noise, which further contaminates the measured strains.

In addition to strain gauges, extensometers are commonly employed for measuring displacements in underground structures, especially in newly constructed rock caverns. Generally, two types of extensometers are employed—tape extensometers and multiple point borehole extensometers. A tape extensometer consists of a telescopic rod, an invar bar, and a tape under constant tension placed between two measuring points, such as on the surface of a rock cavern. Hence, it measures relative displacements (convergence/divergence) between the two points. Multiple point borehole extensometers work on similar principle but can measure relative displacements between several points, such as

at various depths along a borehole. Both types of extensometers have been extensively employed for monitoring large caverns in Singapore (Zhao *et al.*, 2002). However, the main limitation of the conventional extensometers is that they entail manual recording of data, which can be tedious. In tape extensometers, slight loosening of the convergence pins can severely affect the accuracy of the measurement since the displacements to be measured are in the range of a few millimeters. In addition, they tend to obstruct the usable area of the cavern. A more detailed review of sensors available for SHM can be found in Bhalla *et al.* (2005).

As far as SHM is concerned, several local and global techniques are currently under practice or are being investigated in several parts of the world, as explained in Part 1 of this book. However, these have so far not been applied on any underground structures. Similarly, not much research has been devoted to applying these materials to LHR and SHM of rocks. Following sections describe our study on the application of smart optical fiber and smart piezo-electric ceramic materials on LHR and SHM of rocks, respectively.

13.3 Experimental Investigations on Rocks

The experimental tests were performed by Yang *et al.* (2007) on three cylindrical specimens, each 50 mm in diameter and 100 mm in length, cored out from the Bukit Timah granite site in Singapore. Fig. 13.1 shows the instrumentation details of these specimens. Specimens 1 and 2 were instrumented with two ESGs (of a gauge length of 60 or 3 mm), two multiplexed FBG sensors (one for sensing strain and the other for temperature) and one PZT patch. Specimen 3 was instrumented with a PZT patch only. The ESGs were manufactured by Tokyo Sokki Kenkyujo Co, Ltd. (TML, 2004). They were bonded to the rock surface using quick set RS 850-940 epoxy adhesive (RS Components, 2004).

The two FBG-based strain gauges, manufactured by the Institute of Infocomm Research (I²R) Singapore, had a length of 50 mm each. One of them was employed to record surface strain and the other for temperature compensation. The strain sensing FBG and the temperature sensing FBG were multiplexed. Temperature compensation is essential because FBG has relatively high sensitivity to temperature, measuring about 13 pm/°C against 1 pm for a micro-strain. Accordingly, the strain measuring FBG sensor was physically bonded to the specimen surface whereas the temperature measuring sensor was kept mechanically free. High strength epoxy adhesive RS 159-3957 (RS Components, 2004) was used for bonding the strain measuring FBG sensor for specimen 1 and quick set epoxy adhesive RS 850-940 was utilized for specimen 2. The PZT patches bonded to the specimens were 10 mm×10 mm×0.3 mm in size, conformed to grade PIC 151 (PI Ceramic, 2004), and were bonded to the rock specimens using the quick set epoxy adhesive RS 850-940.

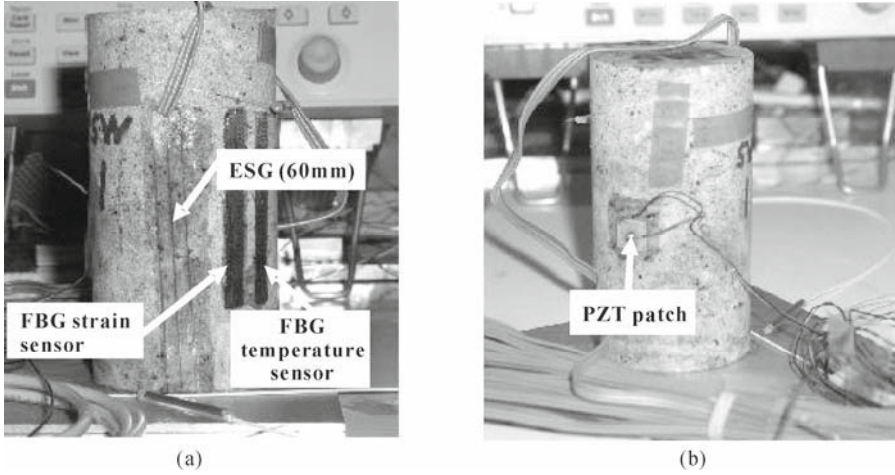


Fig. 13.1 Typical installation details of ESGs, FBG sensors and PZT patches on rock specimens. (a) ESG and FBG sensors; (b) PZT transducer

Fig. 13.2 shows the experimental setup for loading the test specimens and for measuring the responses of the ESG sensors and the PZT transducers. The PZT patch instrumented on the rock specimen was wired to a HP 4192A impedance analyzer (Hewlett Packard, 1996), which was controlled by a personal computer. The ESG sensors were wired to a strain recording data logger. The FBG sensors were wired to a micron-optics interrogator that was controlled by a notebook computer, as shown in Fig. 13.3.

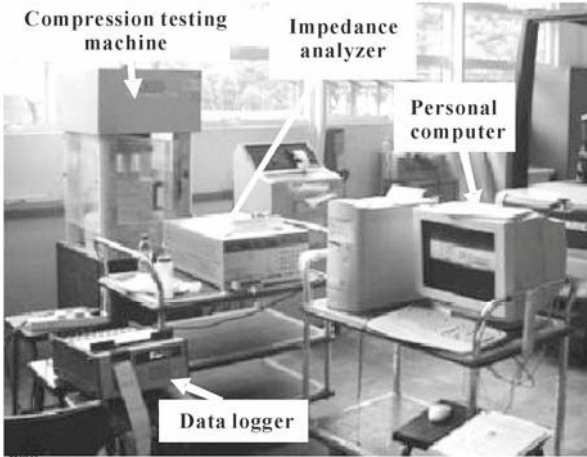


Fig. 13.2 Experimental setup showing compression testing machine, data logger (for ESGs) and impedance analyzer (for PZT transducers)

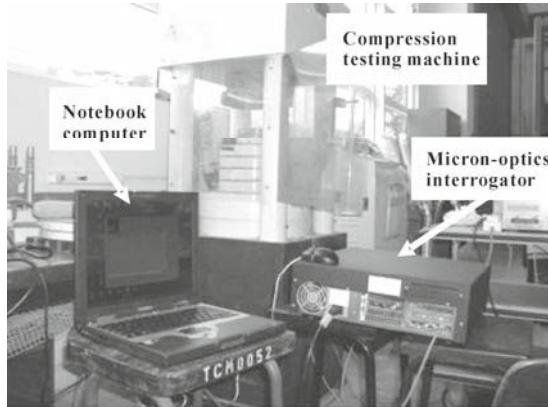


Fig. 13.3 Experimental setup showing compression testing machine and micron-optics interrogator (for interrogating FBG sensor)

Each rock specimen was compressed at a rate of 330 kN/min until the first predetermined load. It was then unloaded to zero load level at the same rate. Readings from the ESGs and FBGs were both recorded during loading and unloading at fixed intervals. After complete unloading, the conductance and susceptance signatures (real and imaginary components of admittance \bar{Y}) were acquired from the bonded PZT patch. In the next cycle, the specimen was compressed to the next higher level of load and the signatures of the PZT patch were acquired after unloading, as in the first cycle. This loading, unloading and signature acquisition process was repeated until failure. Thus, damage was induced to the rock specimens in a cyclic fashion.

13.4 LHR by ESG and FBG Sensors

13.4.1 Specimen 1

Fig. 13.4 shows the stress-strain history of specimen 1 obtained using the 3-mm ESG, the 60-mm ESG and the FBG-based strain sensors. From this figure, it is evident that the strain history retrieved by the 60-mm ESG (Fig. 13.4(b)) is similar to that by the FBG strain sensor (Fig. 13.4c). However, the strain measured by the 3-mm ESG is quite different from the other two strain gauges. This is because the 3-mm strain gauge tends to measure the local surface strain due to its small gauge length. The 60-mm ESG and 50-mm long FBG strain sensors, on the other hand, measure the overall surface strain and hence exhibit similar stress-strain plots. Fig. 13.5 compares the recordings from the 60-mm ESG and 50-mm FBG strain gauge for each load cycle. The load histories match quite well for cycles III, IV and V.

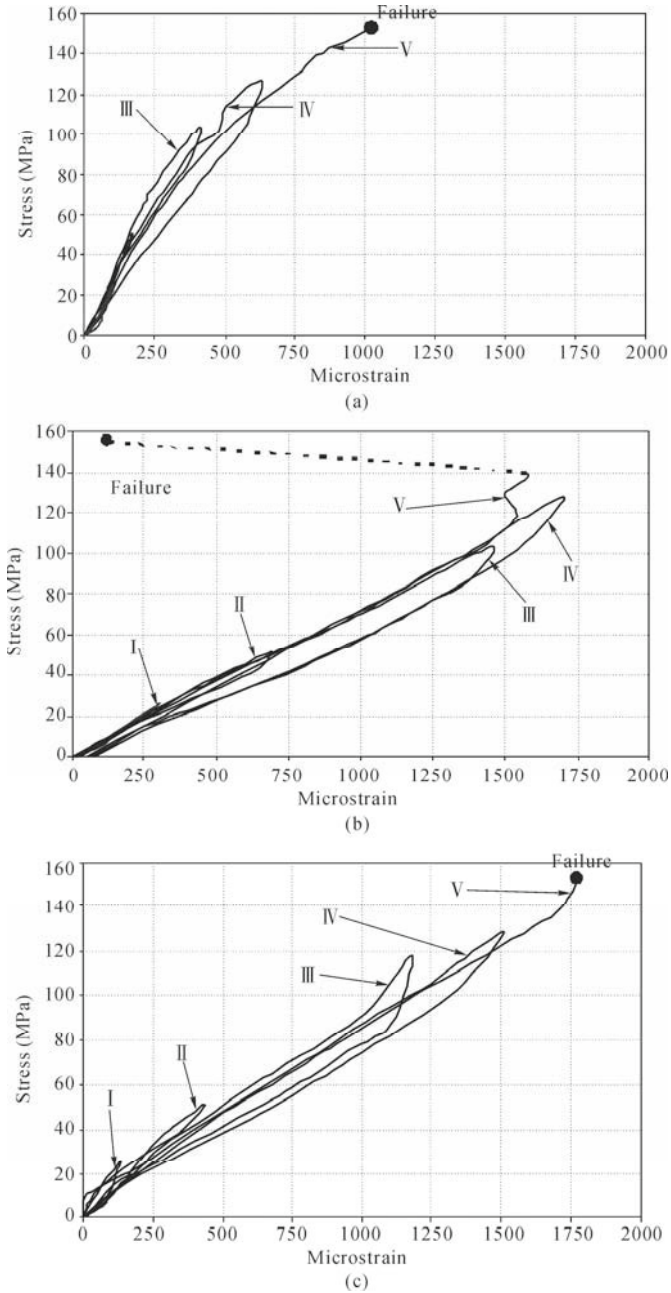


Fig. 13.4 Stress-strain histories for specimen 1 obtained using: (a) 3-mm ESG, (b) 60-mm ESG; (c) FBG based strain gauge

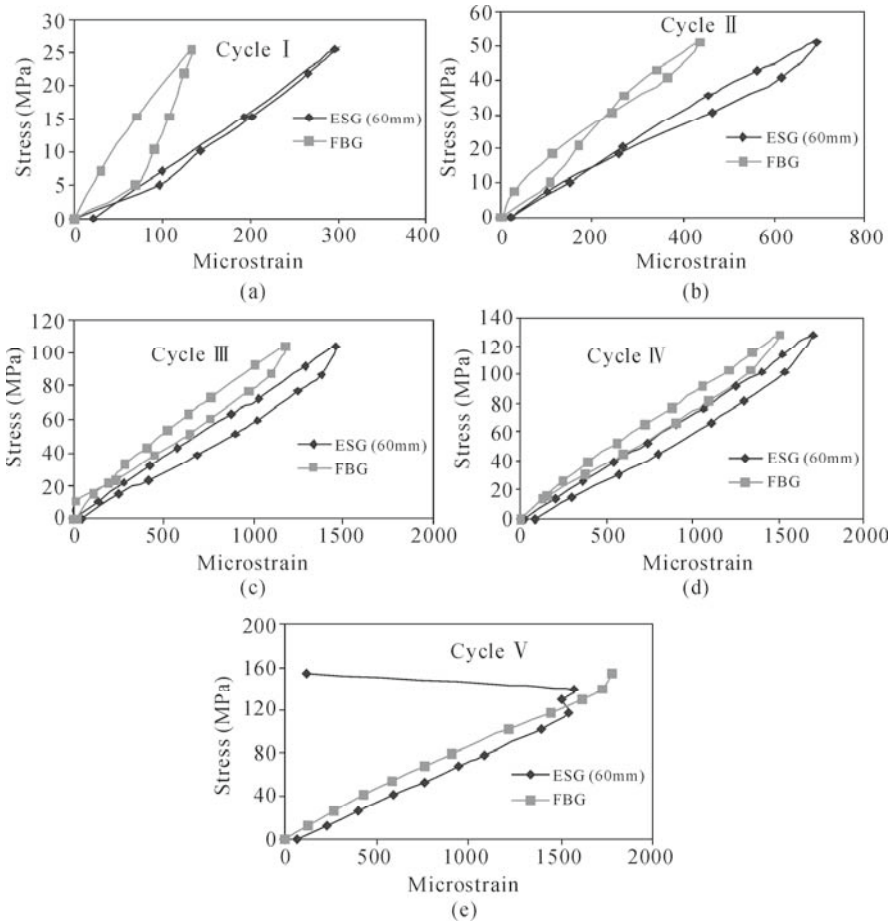


Fig. 13.5 Measurements of ESG (60 mm) and FBG (50 mm) sensor for each cycle for specimen 1. (a) Cycle I; (b) Cycle II; (c) Cycle III; (d) Cycle IV; (e) Cycle V

13.4.2 Specimen 2

Fig. 13.6 shows the stress-strain histories for specimen 2 obtained from the 3-mm ESG, the 60-mm ESG and the FBG-based strain sensors. Again, as in the case of specimen 1, strain history retrieved by the 60-mm ESG (Fig. 13.6(b)) is similar to that for the FBG strain sensor (Fig. 13.6(c)) but quite different from that for the 3-mm ESG (Fig. 13.6(a)). Fig. 13.7 compares the recordings of the 60-mm ESG and 50-mm FBG strain gauge for each load cycle. The load histories match very well for cycles IV, V and VI. Incidentally, both the 60-mm ESG and the FBG-based strain sensors failed prematurely during Cycle VI, well before failure of the specimen, which occurred during Cycle VIII.

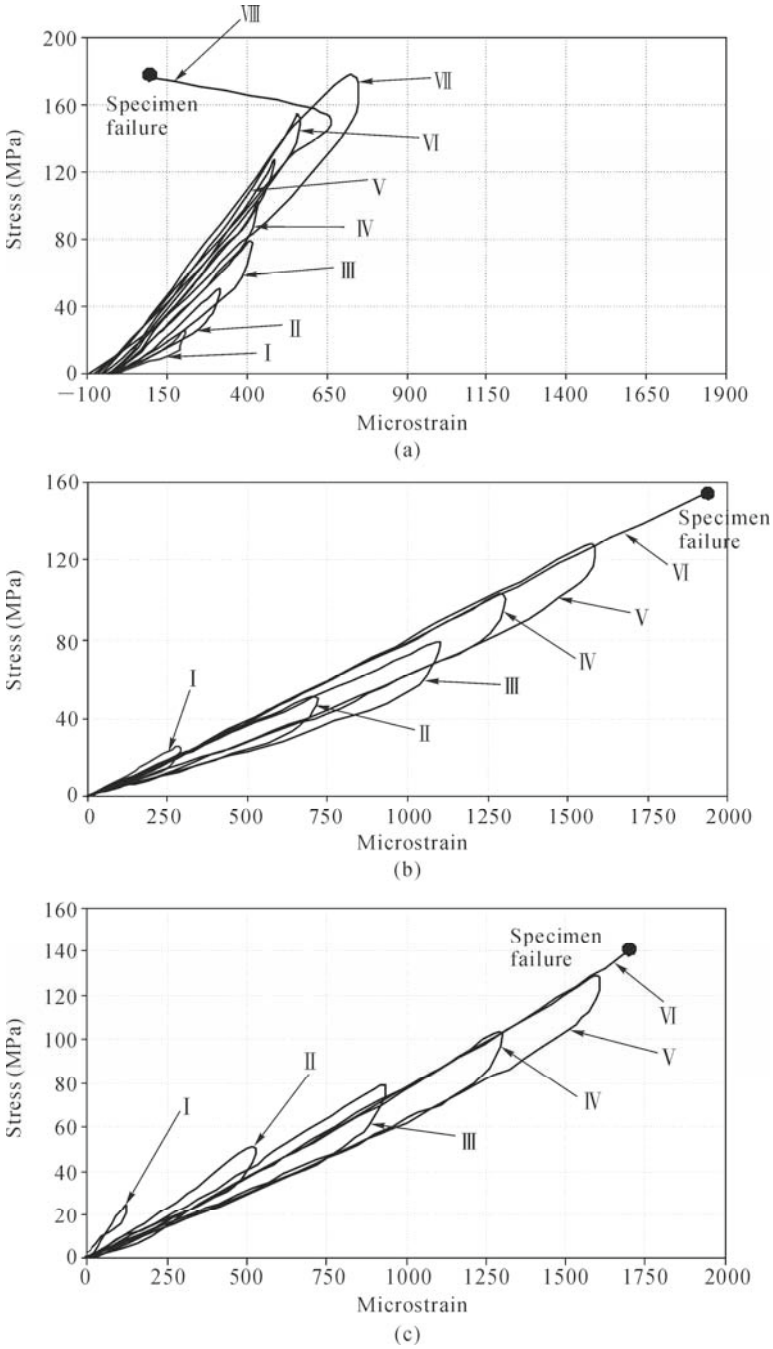


Fig. 13.6 Stress-strain histories for specimen 2 obtained using (a) 3-mm ESG; (b) 60-mm ESG; (c) FBG based strain gauge

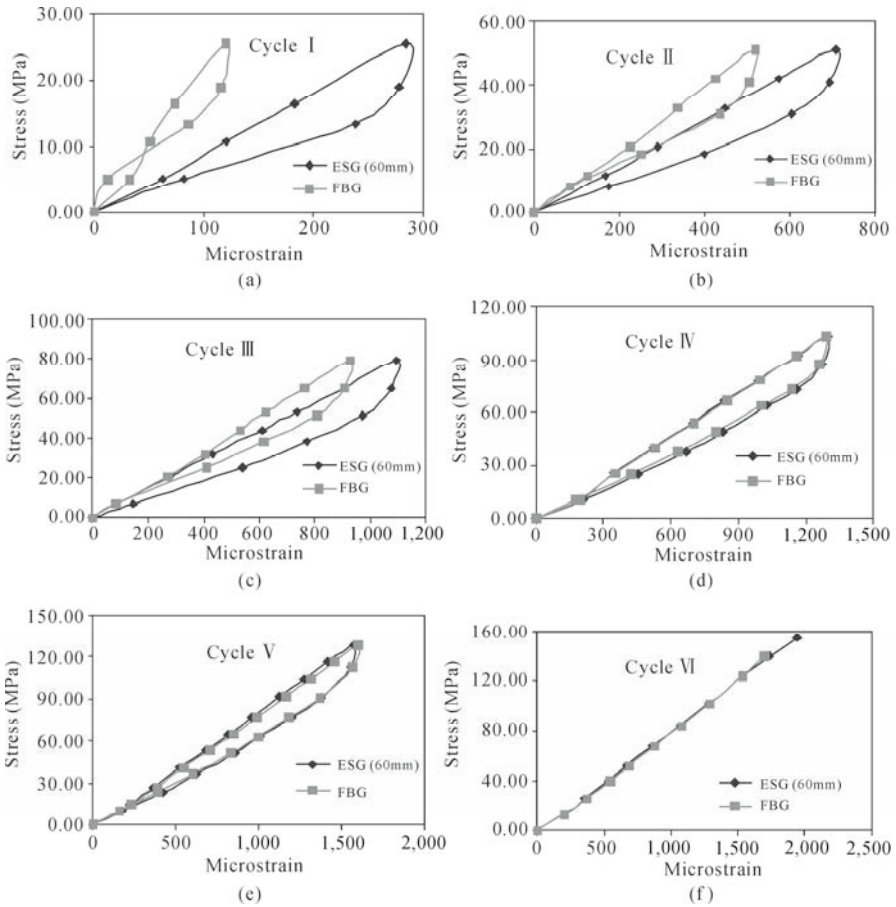


Fig. 13.7 Measurements of ESG (60 mm) and FBG (50 mm) sensor for each cycle for specimen 2. (a) Cycle I; (b) Cycle II; (c) Cycle III; (d) Cycle IV; (e) Cycle V; (f) Cycle VI

13.5 SHM by PZT Transducers

13.5.1 Specimen 1

Fig. 13.8 shows the conductance signatures acquired by the PZT patch bonded to specimen 1 at various stages during the loading process (in unloaded condition, after loading it to a specific load and then unloading). The signatures were acquired in a frequency range of 60 – 100 kHz at an interval of 100 Hz. In this figure, “load ratio” refers to the stress imposed on the specimen divided by the

ultimate stress (recorded at failure of the specimen). As shown in Fig. 13.4, the specimen was subjected to five load cycles and it failed during Cycle V, after withstanding a maximum stress of 154.3 MPa (corresponding to a load ratio = 1.0). During the loading process, when loaded up to load ratios of 0.33 and 0.66, the conductance plot underwent upward shifts. At the same time, major peaks shifted to the left, as shown in Fig. 13.9 for a frequency range of 90 – 100 kHz for load ratios of 0.0 and 0.33.

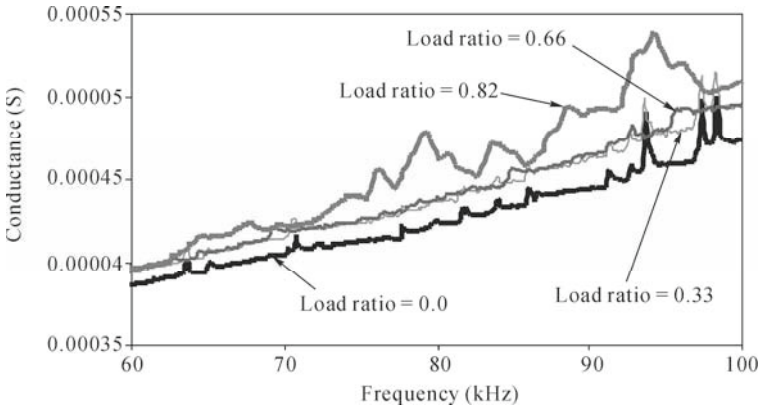


Fig. 13.8 Conductance signatures of PZT patch bonded to specimen 1 at various loading stages

Although the damage was incipient at a load ratio of 0.33, the conductance peaks underwent noticeable leftward shifts. Since the peaks represent structural resonance, leftward shifting of the peaks indicates loss of structural stiffness. Although visually no detectable damage was observed until a load ratio of 0.66, clear indication was however provided by the piezo-impedance signatures at a load ratio of 0.33. Furthermore, as apparent from Fig. 13.8, at a load ratio of 0.82, there is a very significant shift in the conductance signature indicating the occurrence of severe damage in the specimen. Careful examination of the specimen revealed the presence of a vertical crack running longitudinally across the specimen. Thus, by carefully observing the raw conductance signatures, it is possible to qualitatively infer the nature and magnitude of damage occurring in the host structure. Rigorous calibration for quantitative prediction is carried out in the next section. The PZT patch was found broken at the failure load, so conductance signature could not be recorded at a load ratio of 1.0.

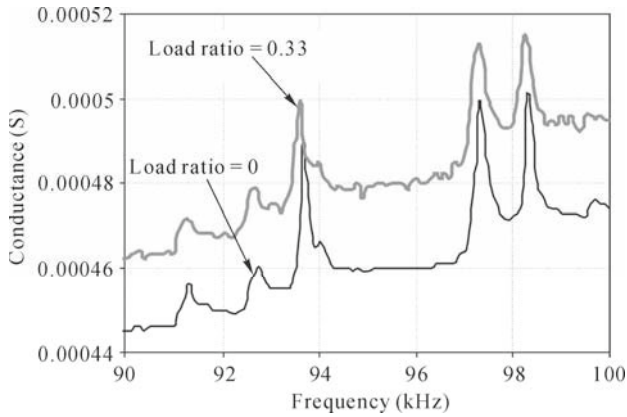


Fig. 13.9 Shifting of peaks of conductance signatures for PZT patch on specimen 1

13.5.2 Specimen 2

Fig. 13.10 shows the conductance signatures of the PZT patch bonded to specimen 2. As clearly observed from the figure, the conductance signature underwent consistent drifts with increasing load ratios. Fig. 13.11 shows the shifts in the peaks with damage progression in the frequency range of 92 – 93 kHz. These figures demonstrate that it is possible to detect both incipient and severe damages using PZT transducers. The PZT patch was able to sustain high strains of up to 2,000 micro-strain and was functioning well even after failure of the specimen.

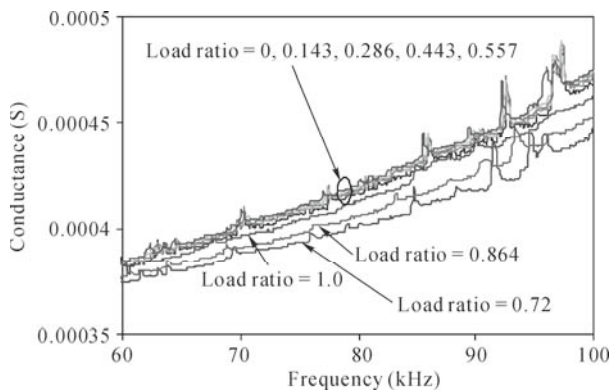


Fig. 13.10 Conductance signatures of PZT patch bonded to specimen 2 at various loading stages

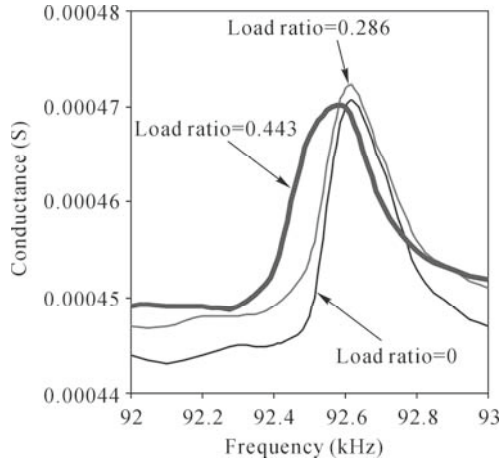


Fig. 13.11 Shifting of peaks of conductance signatures for PZT patch on specimen 2

13.5.3 Specimen 3

Fig. 13.12 shows the conductance signatures acquired by the PZT patch bonded to specimen 3 at various loading stages. Leftward shift of the resonance peaks (and hence indication of stiffness loss) is clearly evident from the figure. Similar to specimens 1 and 2, the results of specimen 3 also confirm the high sensitivity of the PZT transducers to the occurrence of damage. This specimen withstood a stress of 101.9 MPa (load ratio = 1.0) during Cycle VI. During Cycle VII, it failed at a stress of 50.9 MPa (corresponding signature marked as “after failure” in Fig. 3.12).

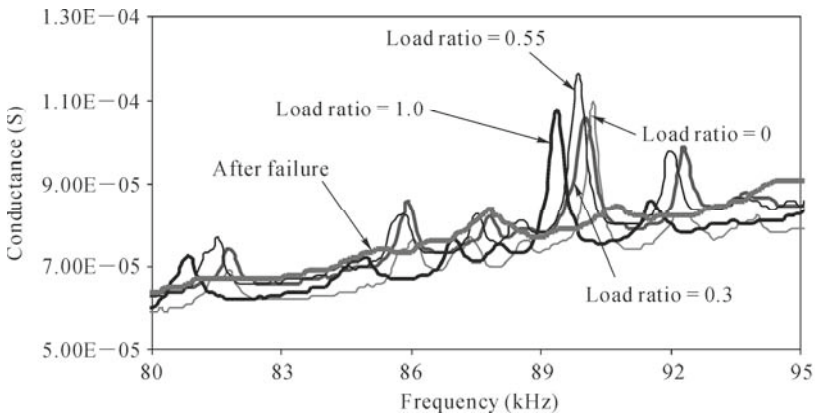


Fig. 13.12 Conductance signatures of PZT patch bonded to specimen 3 at various loading stages

13.5.4 Extraction of Structural Mechanical Impedance

Although it is possible to detect and qualitatively predict the level of damage from raw conductance signatures, as shown in Chapter 4, the real and imaginary components of the admittance signature can together be utilized to identify the host structural system as well as quantify damage more realistically. The first step is to extract the host structure's mechanical impedance from the admittance signatures, as outlined in Chapter 4. A close look at the variations of “ x ” and “ y ” (real and imaginary components of the extracted mechanical impedance) indicates a system behavior similar to a series combination of spring, damper and mass (system 7 of Table 4.1), for which the following relations hold true (Hixon, 1988)

$$x = \frac{c^{-1}}{c^{-2} + (\omega/k - 1/(\omega m))^2} \quad \text{and} \quad y = \frac{-(\omega/k - 1/(\omega m))}{c^{-2} + (\omega/k - 1/(\omega m))^2} \quad (13.1)$$

In addition, at frequency $\omega = \omega_o$, at which $y = 0$

$$k = m\omega_o^2 \quad (13.2)$$

Solving Eqs. (13.1) and (13.2) simultaneously, the system parameters k , c and m are derived at any frequency as

$$c = \frac{x^2 + y^2}{x} \quad (13.3)$$

$$m = \frac{cy(\omega^2 - \omega_o^2)}{(x - c)\omega\omega_o^2} \quad (13.4)$$

and

$$k = \frac{cy(\omega^2 - \omega_o^2)}{x(x - c)\omega} \quad (13.5)$$

Using these equations, the system parameters are derived at each measurement point within the frequency range and the average values then obtained. For specimen 1, the average parameters were found to be: $c = 46.8813$ N·s/m, $k = 2.8776 \times 10^7$ N/m and $m = 1.7851 \times 10^{-4}$ kg. Fig. 13.13 compares the experimental plots of x and y with those of the equivalent system based on the computed average values of the parameters k , c and m . Reasonable agreement can be observed from the figure. The parameters were similarly worked out at various load ratios for specimen 1 as well as specimen 2.

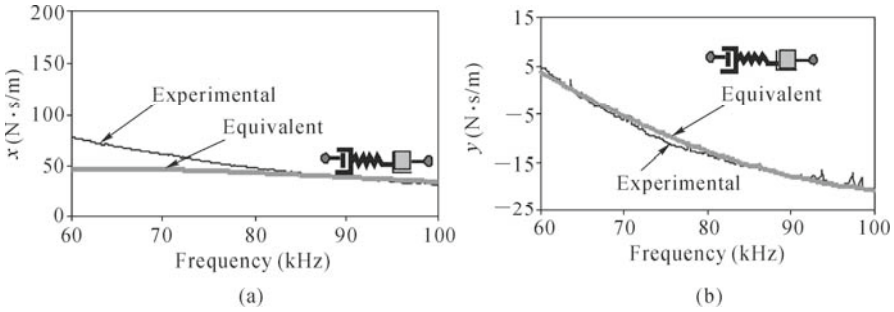


Fig. 13.13 Comparison between experimental and equivalent system impedance plots for specimen 1. (a) x vs. frequency; (b) y vs. frequency

13.5.5 Calibration of Extracted Parameters for Damage Quantification

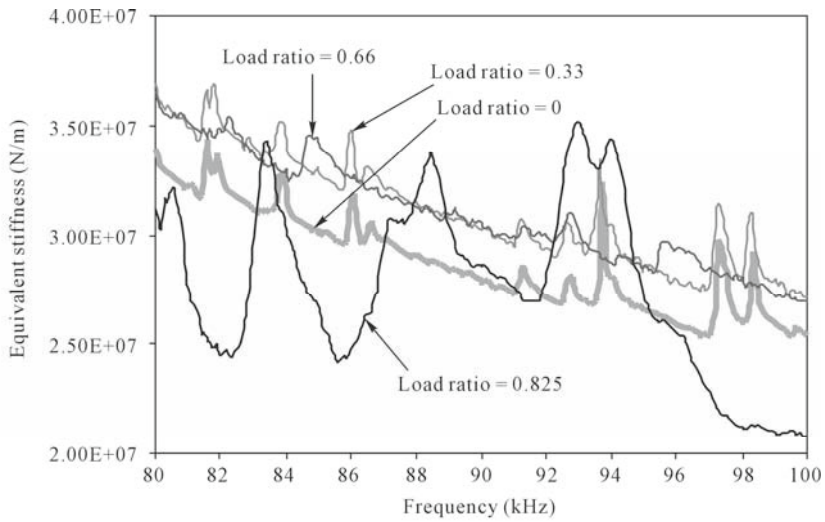
Chapter 5 establishes an impedance-based damage model for concrete based on the identified stiffness parameter k . In the frequency range 60 – 100 kHz, concrete essentially behaves as a parallel spring-damper combination. On the other hand, in the case of rock specimens, the PZT patches identified the structure as a series combination of m , k and c (Fig. 13.13). A similar trend with respect to k is observed for the rock specimens. The identified stiffness is found to gradually reduce with damage. This is evident from the plots of k shown in Fig. 13.14, corresponding to different load ratios, for specimens 1 and 2. For specimen 1, there is slight increase at small load ratios but at higher load ratio, there is an overall reduction. For specimen 2, on the other hand, a very consistent reduction is observed.

At j^{th} frequency, a damage variable, D_j , can be defined in terms of the identified stiffness, similar to the case of concrete (Chapter 5), as

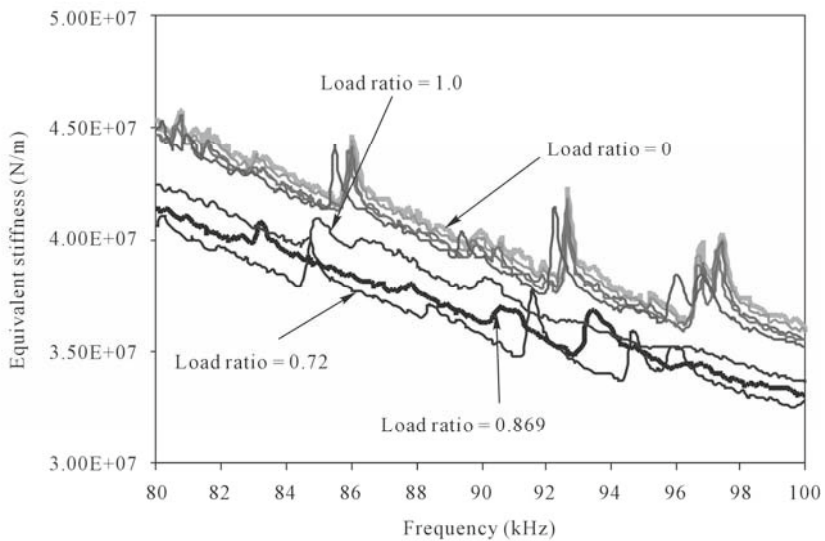
$$D_j = 1 - \frac{k_{dj}}{k_{oj}} \quad (0 < D_j < 1) \tag{13.6}$$

where k_{oj} is the equivalent spring stiffness at the j^{th} measurement point in the pristine state, and k_{dj} represents the corresponding value after damage. From the theory of continuum damage mechanics, an element can be deemed to fail if $D > D_c$. However, it is not possible to define a unique value of D_c due to unavoidable uncertainties related to rock and PZT patches. The damage variable is computed at each frequency in the interval 80 – 100 kHz, corresponding to each load ratio for specimens 1 and 2. Statistical examination of the data indicates that the damage variable follows a normal probability distribution. This is evident in Fig. 13.15, which shows the empirical cumulative probability distribution of D and also the theoretical normal probability distribution for specimens 1 and 2 at or near failure.

The normal distribution is found to be acceptable under 85% confidence limit for both specimens.



(a)



(b)

Fig. 13.14 Variation of identified spring stiffness with damage progression. (a) Specimen 1; (b) Specimen 2

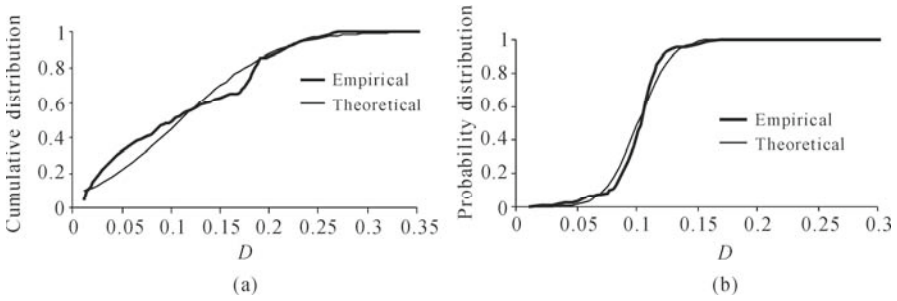


Fig. 13.15 Theoretical and empirical cumulative probability distributions near failure. (a) Specimen 1; (b) Specimen 2

Using the fuzzy set theory, a fuzzy region may be defined in the interval (D_L, D_U) . $D > D_U$ represents a failure region with 100% failure possibility and $D < D_L$ represents a safe region with 0% failure possibility. Within the fuzzy or the transition region, that is, $D_L < D < D_U$, the failure possibility could vary between 0 and 100%. A characteristic or a membership function f_m can be defined ($0 < f_m(D) < 1$) to express the grade of failure possibility within the region (D_L, D_U) . The fuzzy failure probability (FFP) can then be determined by Eq. (5.12) as in the case of concrete. Based on observations made during the tests, D_L and D_U were chosen as 0.0 and 0.12, respectively. Furthermore, the sinusoidal membership function given by Eq. (5.14) is adopted as in the case of concrete.

Using this membership function, the fuzzy failure probability (FFP) was worked out for the two specimens at each load ratio. At a load ratio of 0.7, which can be regarded as a state of severe damage, both specimens exhibited a fuzzy failure probability of greater than 70%. Fig. 13.16 shows the FFP of the specimens at various stages during the tests.

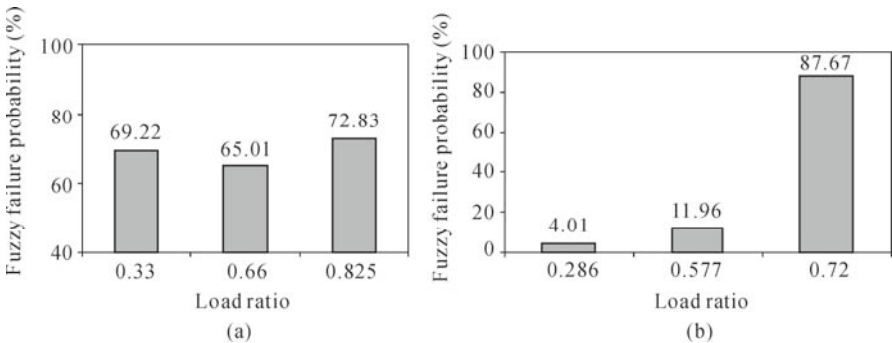


Fig. 13.16 Fuzzy failure probability of specimens 1 and 2 at various load ratios. (a) Specimen 1; (b) Specimen 2

Based on minute observations made during the tests on rock specimens, the following classification of damage is recommended based on FFP.

- (1) $FFP < 30\%$ Incipient Damage (Micro-cracks);

- | | |
|--------------------------------|---------------------------------------|
| (2) $30\% < \text{FFP} < 50\%$ | Moderate damage (Cracks opening up); |
| (3) $50\% < \text{FFP} < 70\%$ | Severe damage (large visible cracks); |
| (4) $\text{FFP} > 70\%$ | Failure imminent. |

Thus, the fuzzy probabilistic approach quantifies the extent of damage on a uniform 0 – 100% scale, which can be employed to evaluate damage in real-life rock structures, such as caverns and tunnels.

13.6 Robustness of PZT Transducers and FBG-based Strain Gauges

In our experimental study, three types of sensors were evaluated for their application on rocks, namely, PZT transducers, ESGs and FBG-based strain sensors. Fig. 13.17 shows close-up views of the three specimens after failure. The PZT patches were found to be intact and functioning well in specimens 2 and 3. However, the PZT patch bonded to specimen 1 broke at a load ratio of 0.826 because the failure crack passed directly through the location of the PZT patch, as shown in Fig. 13.17(a). In spite of this fracture, no debonding was observed between the PZT patch and the host rock surface. Hence, RS 840-950 epoxy adhesive is suitable for bonding PZT patches on rock surfaces. As observed from Figs. 13.17(c) and (e), the PZT patch was intact in both specimens 2 and 3.

The 60 mm long ESGs worked well until failure in specimen 1 (Fig. 13.17(a)), but failed prematurely at a load ratio of 0.868 in the case of specimen 2 (Fig. 13.17(d)). However, some debonding was noticed between the specimen and the sensor in the case of both specimens 1 and 2, as seen in Figs. 13.17(b) and 13.17(d).

The FBG sensors performed well at low loads in the case of specimen 1, but failed prematurely during Cycle VI (somewhere prior to failure of the ESG) in the case of specimen 2. As noticed from Figs. 13.17(b) and 13.17(d), significant debonding occurred between the rock surface and the FBG sensor prior to specimen failure. Hence, future tests need to be conducted to find a more robust adhesive for these sensors.

13.7 Potential Applications of Smart Sensors on Rock Structures

This chapter has demonstrated the feasibility of employing smart piezo-impedance transducers for SHM and FBG-based strain sensors for LHR of rock structures. PZT transducers show long-term durability and fast dynamic response, have low cost, exhibit negligible aging, and are immune to ambient noise. They facilitate direct estimation of damage without warranting analytical/numerical modeling. They can be used for wide ranging applications on rock structures such as assessing the condition of rocks after underground blasts, detection of cracks in caverns during the convergence period, monitoring the condition of rock bolts,

rock quality/strength assessment and measurement of dynamic strains. The results confirm that they are reliable damage indicators, and can warn of any imminent damage before it could be physically visible. The fuzzy probabilistic damage model quantifies damage realistically, and could be employed for damage diagnosis of real-life rock structures such as caverns and tunnels.

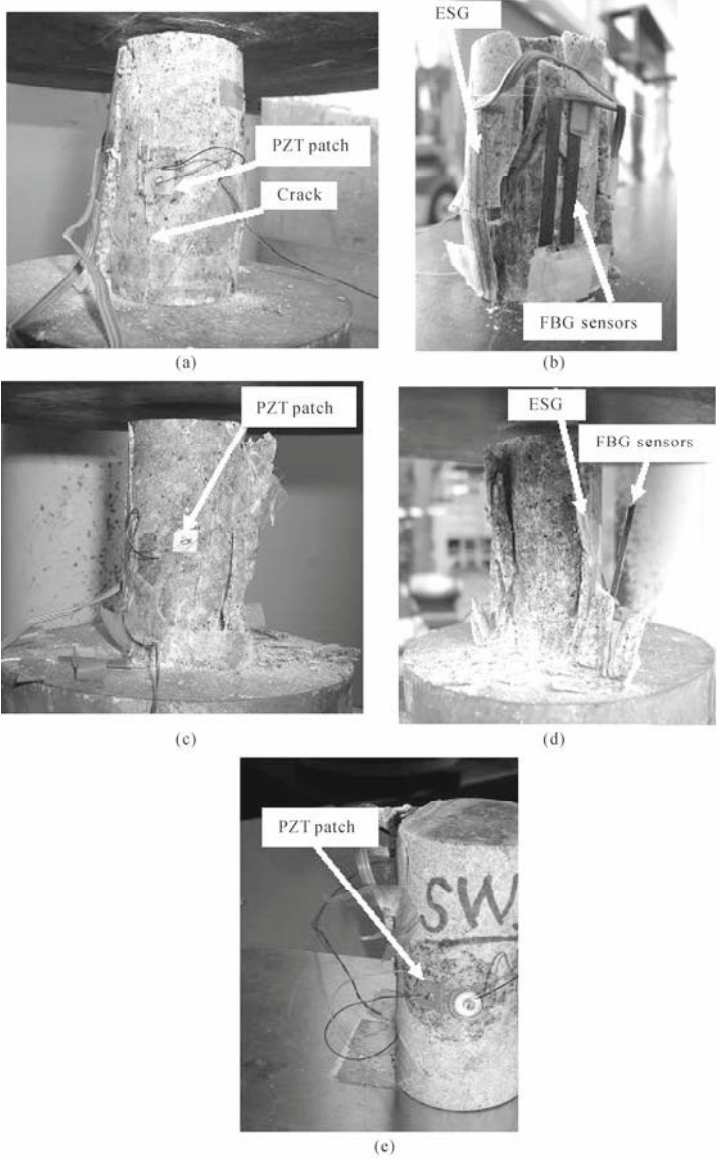


Fig. 13.17 Condition of specimens after failure. (a) Specimen 1: PZT patch; (b) Specimen 1: FBG and ESG; (c) Specimen 2: PZT patch; (d) Specimen 2: FBG and ESG; (e) Specimen 3: PZT patch

FBG sensors are characterized by long-term stability, are chemically inert and small sized, and carry the potential of eliminating cables that are troublesome in data transmission and retrieval. In rock structures, in addition to monitoring the static and dynamic strains in tunnels, caverns and rock bolts, these could be employed for precise measurement of cavern deflections/convergence, and long-term soil/rock movements. Thus, as PZT patches can perform SHM well and FBG sensors can facilitate LHR, they complement each other in structural monitoring.

References

- Bakker, K. J. (2000). "Soil retaining structures: development of models for structural analysis", *Ph.D. Thesis*, Delfts University of Technology, Netherlands.
- Bhalla, S., Yang, Y.W., Zhao, J. and Soh, C.K. (2005). "Structural health monitoring of underground facilities—technological issues and challenges", *Tunnelling and Underground Space Technology*, 20: 487-500.
- Goel, R.K. (2001). "Status of tunnelling and underground construction activities and technologies in India", *Tunnelling and Underground Space Technology*, 16:63-75.
- Hixon, E.L. (1988). "Mechanical impedance", *Shock and Vibration Handbook*, edited by C. M. Harris, 3rd ed., Mc Graw Hill Book Co., New York.
- Hewlett Packard (1996). *HP LF 4192A impedance analyzer*, Operation manual, Japan.
- Moyo, P. (2002). "Structural performance monitoring and health assessment of highway bridges", *Ph.D. Thesis*, Nanyang Technological University, Singapore.
- PI Ceramic (2004). *Product Information Catalogue*, Lindenstrabe, Germany, <http://www.piceramic.de>.
- RS Components (2004). Northants, UK, <http://www.rs-components.com>.
- TML (2004). *Tokyo Sokki Kenkyujo Co. Ltd.*, Tokyo.
- Yang, Y.W., Bhalla, S., Wang, C., Soh, C.K. and Zhao, J. (2007). "Monitoring of rocks using smart sensors", *Tunnelling and Underground Space Technology*, 22: 206-221.
- Zhao, J., Liu, Q., Lee, K.W., Choa, V. and Teh, C.I. (1999). "Underground cavern development in the Jurong sedimentary rock formation", *Tunnelling and Underground Space Technology*, 14: 449-459.
- Zhao, J., Cai, J.G., Tunbridge, L., Song, H.W., Zhang, X.H. and Zhao, X.B. (2002). "Results of rock cavern monitoring and assessment of cavern stability", *Technical report for NTU-DSTA Joint R&D Project on instrumentation and monitoring of rock caverns during construction and operation*.

Ionic Polymer-Metal Composite and its Actuation Characteristics

Y. W. Yang^{*}, L. Zhang, C. K. Soh

School of Civil and Environmental Engineering, Nanyang Technological University,
50 Nanyang Avenue, Singapore 639798

Tel: (65)-6790-4057, Fax: (65)-6791-0676

Email: cywyang@ntu.edu.sg

14.1 Introduction

14.1.1 History and Characterizations

Compared to piezoelectric materials and fiber optics, ionic polymer-metal composite (IPMC) is a relatively new smart material. IPMC, also known as ionic conducting polymer gel film (ICPF), was initially found in fuel cell research. In the early 1990's, Sadeghipour *et al.* (1992) found the sensing ability of ionic polymer. Later, the converse process of charge storage mechanism associated with fuel cell, *i.e.*, actuation capacity, was found by Oguro *et al.* (1992). Ever since then, ionic polymer has been attracting more and more attention from researchers.

IPMC is a type of wet electro-active polymers (EAPs) in that salt solution is required for its actuation. As shown in Fig. 14.1, an IPMC consists of a thin polyelectrolyte membrane and a type of noble metal, such as platinum and gold, chemically plated on both sides of the membrane. The typical polyelectrolyte membranes used in IPMC are Nafion, Flemion and Aciplex.

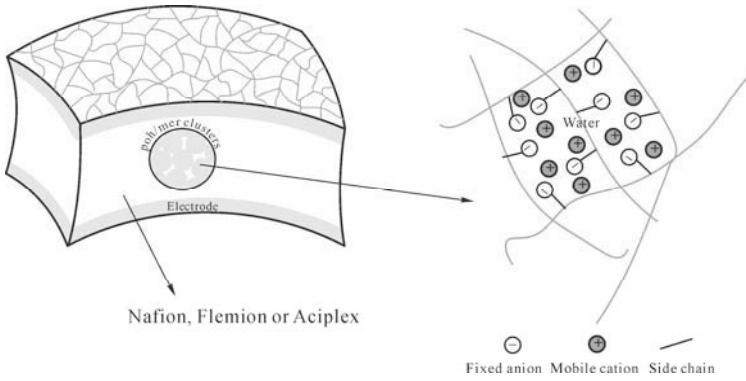


Fig. 14.1 Structure of a typical IPMC sample

Fig. 14.2 illustrates the microstructure of a platinum electrode surface, and Fig. 14.3 shows the chemical structures of the three types of membranes.

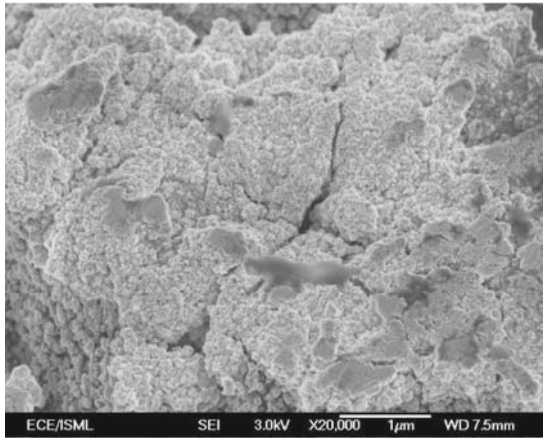


Fig. 14.2 Microstructure of platinum electrode surface

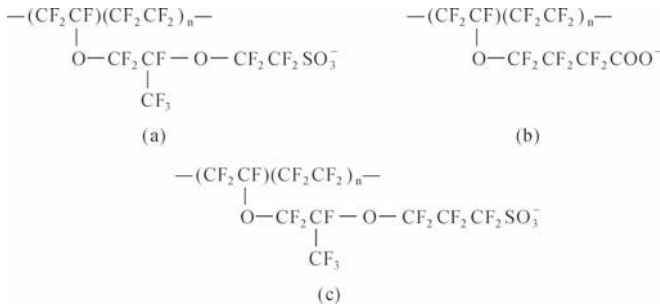


Fig. 14.3 Chemical structures of polyelectrolyte membrane used in IPMC. (a) Nafion; (b) Flemion; (c) Aciplex

As shown in Fig. 14.1, the microstructures of IPMC membrane are in the form of interconnected clusters in which the anions are covalently fixed to the backbone of the polymers while the cations and their associated solvent molecules are free to move within or out of the clusters. Thus, when an electric potential is applied to the electrode, the free cations and the associated solvent molecules will migrate under electric field from anode to cathode. As illustrated in Fig. 14.4, due to the charge redistribution process, two layers near the electrodes are formed, *i.e.*, the cation dominant cathode boundary layer and the anion dominant anode boundary layer. Due to the imbalance of electrostatic stresses and other chemical stresses developed within the two layers, IPMC will bend under electric potential.

IPMC can undergo a fast and large bending motion when a low electric potential is applied to its electrodes. Conversely, IPMC can generate a measurable electric potential when it is subjected to sudden bending. Thus, IPMC can serve as both actuators and sensors. When IPMC is subjected to a constant voltage, IPMC's fast bending motion is generally followed by a slow relaxation. The relaxation direction is dependent on the membrane type. For Nafion, the relaxation direction is reverse to the initial bending direction, while for Flemion, the relaxation is in the same direction as that of the initial bending. The phenomenon can be explained by the cation charge redistribution and the following solvent diffusion within the polyelectrolyte membrane.

14.1.2 Experimental Study and Physical Modeling

One of the common questions asked, when considering a smart material for certain applications, is how much effect the material can provide. For IPMC materials, the bending capacity of IPMC is usually a first concern when they are used as actuators. Thus, the actuation mechanism of IPMC materials should be studied. Some models have been developed based on experiments and/or theoretical analyses. These researches provide a basis for further understanding of IPMC materials.

Asaka *et al.* (1995) experimentally studied the bending response of a solid polymer electrolyte membrane-platinum (SPM-Pt) under various electric stimuli waveforms. They represented the bending response of SPM-Pt as a function of current flow between two electrodes. Asaka and Oguro (2000a) proposed a kinetic model of SPM-Pt bending response. Comparisons were made between their experimental and theoretical results. Their theoretical model included the effect of interfacial stress between the Pt electrode and the membrane. The bending behavior after the characteristic time was explained successfully by this model, including the interfacial effect. Asaka and Oguro (2000b) reported the oscillatory bending responses of SPM-Pt. The oscillations took place when the anodic oxidations of formaldehyde or sodium formate in aqueous sulfuric acid solutions happened on a plated Pt electrode. The frequency and the waveform of the

oscillations were dependent on the concentration of the organic compounds and the direct current applied. Shahinpoor and Kim (2001, 2004, 2005) and Kim and Shahinpoor (2003) presented a series of review papers on the fundamental properties and characteristics of IPMC, manufacturing techniques, phenomenological modeling of actuation and sensing mechanism, and potential applications. Nemat-Nasser and Li (2000) presented a micromechanical model based on electrostatic interaction of ion transport. Central to their theory was the recognition that the interaction between an imbalanced charge density and the backbone polymer could be represented by an eigenstress field. Their theory was able to explain IPMC bending under electric field and also generative charges when bent. Their comparisons showed a good match between theoretical predictions and experimental results. Later, Nemat-Nasser (2002) studied the micromechanics of IPMC materials and proposed a nano-scale hybrid model incorporating electrostatic, osmotic and elastic effects in the actuation process. This model is able to account for both the static and dynamic behaviors of IPMC. Newbury and Leo (2002) presented a linear, two-port model to represent the electromechanical (EM) transduction in ionic polymer actuators. The model parameters were determined by fitting the simulated responses of Laplace domain transfer functions to experimental data of Nafion-based actuator. Shahinpoor and Kim (2002) investigated the mass transfer induced actuation of IPMC, and developed a technique to minimize water leakage and to increase the force density of IPMC.

Tamagawa *et al.* (2002) proposed a simple method to estimate the time-dependent nominal Young's moduli and generated force of IPMC. IPMC cantilevered beams were tested and numerically simulated to validate the proposed method. Taking into account the viscoelastic property of polymer material, Newbury and Leo (2003a) developed a linear EM model based on equivalent circuit for IPMC transducers. A series of experimental tests were conducted to verify the model (Newbury and Leo, 2003b). Nemat-Nasser and Wu (2003) carried out extensive experimental studies on IPMC with different backbone ionomers and various cation forms. Experimental results on both Nafion and Flemion-based IPMC with alkali-metal or alkyl-ammonium cations were reported. It was observed that Flemion-based IPMC with fine dendritic gold electrodes had higher ion-exchange capacity, better surface conductivity, higher hydration capacity and higher longitudinal stiffness than Nafion-based IPMC. Under the same voltage, Flemion-based IPMC displayed greater bending actuation. Yagasaki and Tamagawa (2004) studied the viscoelastic properties of IPMC. An experimental method was proposed to estimate the general time-dependent elastic moduli of IPMC. A viscoelastic model for IPMC beam was presented and validated by experimental tests. Farinholt and Leo (2004) presented a model for charge sensing due to imposed deformation in IPMC. An expression for charge density, electric field and electric potential under short-circuit conditions was developed from the electrostatic field equations. This model predicted that the induced stress would produce a capacitive discharge in the polymer. Experimental results verified the basic form of the model, and also demonstrated that the geometric scaling predicted in the model agreed with the measured data. Two of

the primary limitations of IPMC are unstable operation in air due to vaporizing solvent and low solvent breakdown voltage. To overcome these limitations, Bennett and Leo (2004) proposed using highly stable ionic liquids to serve as solvent of IPMC instead of the commonly used water. Ionic liquids have certain advantages over water such as low vapor pressure and greater electrochemical stability. A 1-ethyl-3-methylimidazolium trifluoromethanesulfonate ionic liquid was used in their study. Their experimental results indicated that the use of ionic liquid improved the stability of Nafion transducers. The major limitation associated with the use of ionic liquid was the slow speed of response as compared to the case of water as solvent. Later, Akle *et al.* (2006) studied the electrode composition for IPMC with ionic liquid as solvent. The electrode composition was studied as a function of the surface to volume ratio and conductivity of the metal particulates. Their results showed that the surface to volume ratio of the metal particulate was critical to increasing the capacitance of the IPMC transducer. Increased conductivity of the metal particulates improved the IPMC response at frequencies higher than 10 Hz. By increasing the capacitance of IPMC, more than 2% strain can be achieved at voltage level of 3 V. More recently, Bennett *et al.* (2006) examined the mechanism of EM transduction in ionic liquid-swollen Nafion-based IPMC. The morphology and relevant ion associations within the membranes were investigated by using small angle X-ray scattering, Fourier transform infrared spectroscopy and nuclear magnetic resonance spectroscopy. Their results indicated that ionic liquid interacted with the membrane in very much the same way as water did, and the counter ions of the Nafion membrane were the primary charge carriers in the ionic liquid-swollen transducers. Bonomo *et al.* (2005) developed a system to experimentally characterize IPMC membranes as motion sensors. Their system was built to study the IPMC reaction under mechanical bending in a wide frequency range. Toi and Kang (2005) presented a 2D FE formulation based on Galerkin method to model the electrochemical-mechanical behaviors of IPMC beams with two pairs of electrodes. The electrochemical solutions for the case of unidirectional voltages agreed well with that of the 1D solutions by finite difference method. The 2D electrochemical response and 3D deformation for bidirectional voltage were qualitatively reasonable. Akle and Leo (2005) studied the relationship between ion conduction and EM coupling of IPMC through a series of experiments on three types of ionomeric materials. An approximate linear correlation between the strain response of the ionomeric transducer and the capacitance of the transducer was found. This correlation was independent of the polymer composition and the plating parameters. A strong relationship between surface charge accumulation and mechanical deformation in ionomeric actuators was concluded from this correlation. Weiland and Leo (2005a) developed a computational micromechanics model to assess the impact of uniform ion distribution on spherical clusters of IPMC ionomer. They also employed a Monte Carlo approach to study the effects of pendant chain stiffness and charge balance of the equilibrium state of a single cluster in ionic polymer (Weiland and Leo, 2005b). Matthews *et al.* (2006) presented a multiscale modeling approach for the prediction of material stiffness

of Nafion polymer. The simulation model was developed by combination of traditional rotational isomeric state theory and Monte Carlo method. The probability density function was estimated and used as an input parameter to enhance the existing energetics-based models. Nemat-Nasser and Wu (2006) presented novel methods to tailor the EM response of IPMC to optimize the actuation performance. Optimal actuation activities were identified by introducing various monovalent or multivalent cations and cation combinations. Their experimental results showed a good accord with the nano-scaled physical model. It was found that the bending motion could be tailored by proper changing of the time-variation function of the applied potential. For Nafion-based IPMC, the initial bending towards the anode could be controlled and eliminated by linearly increasing the electric potential at certain rate. The tip displacement of Flemion-based IPMC was found to be always linearly related to the cation charge accumulation at the cathode. Nemat-Nasser and Zanami (2006a, 2006b) studied the effect of various solvent on the behavior of IPMC. A series of tests were conducted on both Nafion- and Flemion-based IPMC with various organic solvents such as ethylene glycol, glycerol and crown ethers (Nemat-Nasser and Zanami, 2006a). By employing these solvents, higher operational voltages and hydration rate were obtained compared with the condition with water as solvent. They could work in air for longer time and at low temperature environment. Their slow responses allowed better observation of physical characteristics of the actuation process. Nemat-Nasser and Zanami (2006b) applied the nano-scale hybrid actuation model proposed by Nemat-Nasser (2002) to model the initial fast motion and subsequent relaxation of Nafion-based IPMC under various solvents. The model successfully matched the experimental observations both qualitatively and quantitatively. Bufalo *et al.* (2008) presented a mixture theory framework for the mechanical actuation of IPMC materials where the IPMC was viewed as a mixture of backbone polymer matrix, solvent and mobile ions.

Although much effort has been devoted to understanding the actuation and sensing mechanism of IPMC materials, the actuation mechanism of IPMC has not yet been fully understood. Nevertheless, the existing models have already cast important insights into the mechanism research. Of all the first principle models developed, Nemat-Nasser (2002)'s hybrid model has been proven to be useful for IPMC with different cation and solvent types (Nemat-Nasser and Zamini, 2006b). The model parameters can be determined through experiments. This hybrid model has set up the framework of mechanism research towards a complete understanding of IPMC's working mechanism. However, Nemat-Nassar's hybrid model does not provide an explicit bending moment expression. A computer program is generally required to perform the calculations. The inconvenience of computation hinders the practical application of this model. In view of this, in this chapter, Nemat-Nasser's hybrid actuation model is studied and simplified. Explicit bending moment expressions are derived based on this model by certain simplifications. The obtained bending moment expressions are applicable for both static and dynamic electric potentials.

14.1.3 *Implemented and Potential Applications*

Although the mechanism of IPMC has not yet been fully understood, research on applications of IPMC has attracted considerable attention from various disciplines. IPMC offers many advantages over the conventional EAP materials, such as compliance, light weight, low operation voltage and capability of working in aqueous environments. These properties make it promising for numerous applications in biomedical, naval, robotic and microelectromechanical system (MEMS) engineering. Shahinpoor (1992) proposed using ionic polymer gel for autonomous swimming robotic structures. A conceptual design for such structures was presented followed by a discussion on the kinematics and dynamics of such structures. Shahinpoor and Kim (2005) presented many potential applications of IPMC such as heart compression band, four-finger gripper and artificial fish. Paquette and Kim (2004) investigated potential applications of IPMC for naval applications. Comparisons were made between IPMC and other smart materials for biomimetic propulsor applications. Yamakita *et al.* (2004) developed an artificial muscle linear actuator using IPMC for biped walking robot application. The linear actuator effectively transforms bending motion of IPMC into longitudinal motion. Zhang and Yang (2007) and Yang and Zhang (2008) investigated the actuation characteristics of IPMC as beams and rings on human tissues, respectively. More applications can be found in references Bar-Cohen (2004, 2006) and the WorldWide Electroactive Polymer Webhub established by Dr. Bar-Cohen at <http://ndea.jpl.nasa.gov/nasa-nde/lommas/eap/EAP-web.htm>.

14.2 Bending Moment Capacity of IPMC

14.2.1 *Charge Redistribution*

Although the mechanism of IPMC remains unclear, it is known that the cation motion under applied electric field is the key issue. The microstructure of the polyelectrolyte membrane of an IPMC sample is in the form of interconnected nano-scale clusters as shown in Fig. 14.1. The nano-scale clusters are composed of the backbone perfluorinated copolymer of polytetrafluoroethylene with perfluorinated vinyl ether sulfonate pendants for Nafion-based IPMC, and perfluorinated propyl ether carboxylate pendants for Flemion-based IPMC. When an IPMC sample is solvated, the cations are free to move within or out of the clusters while the anions are covalently fixed to the clusters. Thus, when an electric potential is applied to the electrodes of IPMC, the cations will migrate to the cathode while the anions remain stationary as shown in Fig. 14.4. Two boundary layers will form due to the cation movement, characterized as the anion dominant anode boundary layer

(ABL) and the cation dominant cathode boundary layer (CBL) (Nemat-Nasser, 2002). The two boundary layers will effectively balance the electric field applied, resulting in the region between the two layers being shielded. Stresses will develop in the two layers, leading to the deformation of the IPMC material. It is the ABL and CBL that primarily contribute to the bending motion of IPMC. Therefore, it is essential to determine the thickness of the ABL and CBL prior to calculating the bending moment. To achieve this, the cation redistribution under an electric field should be considered first.

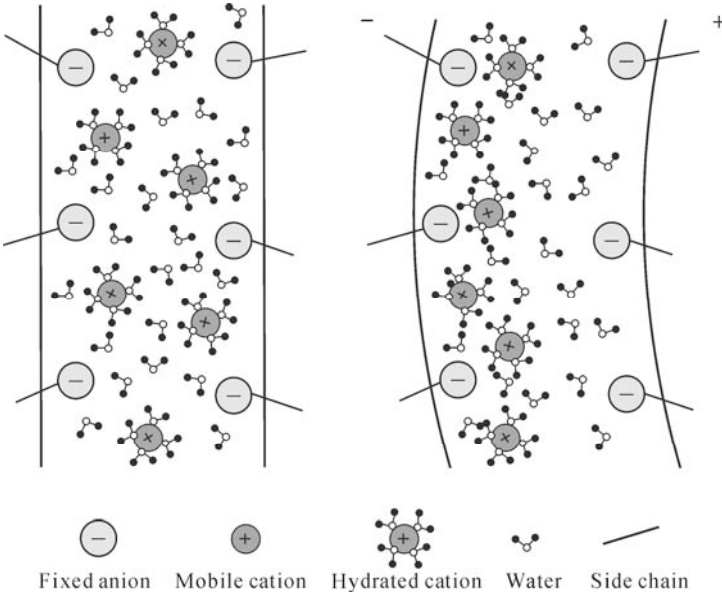


Fig. 14.4 IPMC under electric potential

Consider an IPMC sample with thickness H and length L , as shown in Fig. 14.5. The thickness of membrane part is h . The IPMC sample is driven by time-dependent electric potentials applied at the electrodes. It is assumed that the top electrode is the cathode and the bottom electrode is the anode. The electric potentials applied at the cathode and the anode are $\varphi_1(t)$ and $\varphi_2(t)$, respectively. When electric potentials are on, due to the cation movement within the IPMC membrane, the IPMC will vibrate at the driving frequency with certain phase lag.

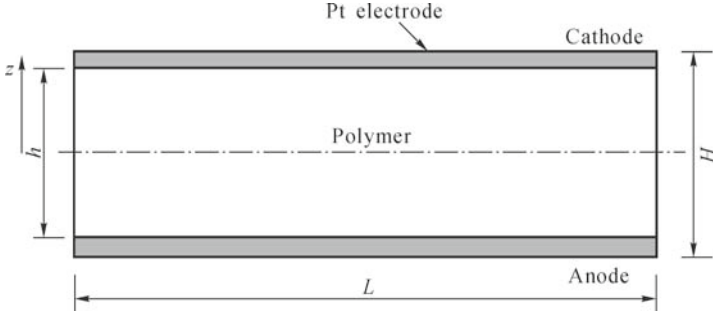


Fig.14.5 Schematic cross-section of an IPMC sample

The cation flux $J_i^+(z,t)$ of ion species i due to diffusion, migration and convection is determined by the Nernst-Planck equation as

$$J_i^+(z,t) = -D_i^+ \left[\frac{\partial C_i^+(z,t)}{\partial z} + \frac{v_i^+ C_i^+(z,t) F}{RT} \frac{\partial \varphi(z,t)}{\partial z} \right] + C_i^+(z,t) v \quad (14.1)$$

where the species i refers to a particular type of ion in the membrane, such as Na^+ or K^+ , marked as the i^{th} type ion; D_i^+ is the cation diffusivity coefficient of species i ; v_i^+ is the valence of cations of species i ; $\varphi(z,t)$ is the electric potential; F is the Faraday's constant; R is the gas constant; T is the temperature and v is the solvent velocity. The solvent velocity v can be determined by the Darcy's Law as

$$v = D_h [v^- C^- F E(z,t) - \frac{\partial p}{\partial z}] \quad (14.2)$$

where D_h is the hydraulic permeability coefficient, v^- and C^- are the valence and density of anions, respectively, $E(z,t)$ is the electric field and p is the fluid pressure. C^- is approximately considered as constant since anions are fixed to the polymer backbone.

Since only one type of cations is considered, the subscript i in Eq.(14.1) can be dropped. Rewriting Eq. (14.1), we obtain,

$$J^+(z,t) = -D^+ \left[\frac{\partial C^+(z,t)}{\partial z} - \frac{v^+ C^+(z,t) F}{RT} \frac{\partial \varphi(z,t)}{\partial z} \right] + C^+(z,t) v \quad (14.3)$$

The time variation of cation concentration can be described by the continuity equation, which is

$$\frac{\partial C^+(z,t)}{\partial t} = -\frac{\partial J^+(z,t)}{\partial z} \quad (14.4)$$

Substituting Eq. (14.3) into Eq. (14.4), the following equation is obtained,

$$\frac{\partial C^+(z,t)}{\partial t} = D^+ \frac{\partial^2 C^+(z,t)}{\partial z^2} - D^+ \frac{v^+ F}{RT} \left[\frac{\partial C^+(z,t)}{\partial z} \frac{\partial \varphi(z,t)}{\partial z} + C^+(z,t) \frac{\partial^2 \varphi(z,t)}{\partial z^2} \right] \quad (14.5)$$

The basic electrostatic equations associated with the problem are

$$E(z,t) = -\frac{\partial \varphi(z,t)}{\partial z} \quad (14.6)$$

$$D = \kappa_e E(z,t) \quad (14.7)$$

$$\frac{\partial D}{\partial z} = \rho_c \quad (14.8)$$

$$\rho_c = (v^+ C^+(z,t) - v^- C^-(z,t)) F \quad (14.9)$$

where κ_e is the electric permittivity; D is the electric displacement; and ρ_c is the net charge density.

The relationship between cation concentration and electric potential can be derived from Eqs. (14.6) to (14.9), which is the Poisson's equation, as

$$\frac{\partial^2 \varphi(z,t)}{\partial z^2} = -\frac{F}{\kappa_e} (v^+ C^+(z,t) - v^- C^-(z,t)) \quad (14.10)$$

Eqs. (14.5) and (14.10) are the governing equations of the cation transportation within the IPMC membrane. Integrating Eq. (14.10) with respect to z , the electric field due to charge concentration can be obtained as

$$\frac{\partial \varphi(z,t)}{\partial z} = \int^z -\frac{F}{\kappa_e} (v^+ C^+(z,t) - v^- C^-(z,t)) dz + A(t) \quad (14.11)$$

The time-dependent function A in Eq. (14.11) can be viewed as the electric field induced by the electric potential applied on the IPMC membrane. Thus, Eq. (14.11) can be rewritten as

$$\frac{\partial \varphi(z, t)}{\partial z} = \frac{\varphi_1(t) - \varphi_2(t)}{h} + \int_{-h/2}^z -\frac{F}{\kappa_c} (v^+ C^+(z, t) - v^- C^-) dz \quad (14.12)$$

Substituting Eq. (14.12) into Eq. (14.5), we obtain

$$\begin{aligned} \frac{\partial C^+(z, t)}{\partial t} = & D^+ \frac{\partial^2 C^+(z, t)}{\partial z^2} + \frac{D^+}{\ell^2} \left\{ \frac{\varepsilon}{v^- C^- F} \frac{\varphi_1(t) - \varphi_2(t)}{h} \right. \\ & \left. - \int_{-h/2}^z \left(\frac{v^+ C^+(z, t)}{v^- C^-} - 1 \right) dz \right\} \frac{\partial C^+(z, t)}{\partial z} - \frac{D^+}{\ell^2} C^+(z, t) \left(\frac{v^+ C^+(z, t)}{v^- C^-} - 1 \right) \end{aligned} \quad (14.13)$$

where $\ell = \sqrt{\frac{\varepsilon RT}{v^+ v^- n^- F^2}}$ is a natural length scale.

The boundary and initial conditions for the problem are

$$\int_{-h/2}^{h/2} \rho_c dz = 0 \quad (14.14)$$

$$\varphi(h/2, t) = \varphi_1(t), \quad \varphi(-h/2, t) = \varphi_2(t) \quad (14.15)$$

$$J^+(\pm h/2, t) = 0 \quad (14.16)$$

$$\varphi_1(0) = 0, \varphi_2(0) = 0, \rho_c(z, 0) = 0 \quad (14.17)$$

Passing t and z to the new variables t and $z^* = z + D^+ \frac{v^+ F}{RT} \int \frac{\varphi_1(t) - \varphi_2(t)}{h} dt$, a simpler equation can be obtained as

$$\begin{aligned} \frac{\partial C^+(z^*, t)}{\partial t} = & D^+ \frac{\partial^2 C^+(z^*, t)}{\partial z^{*2}} - \frac{D^+}{\ell^2} \int_{-h/2}^{z^*} \left(\frac{v^+ C^+(z^*, t)}{v^- C^-} - 1 \right) dz^* \frac{\partial C^+(z^*, t)}{\partial z^*} \\ & - \frac{D^+}{\ell^2} C^+(z^*, t) \left(\frac{v^+ C^+(z^*, t)}{v^- C^-} - 1 \right) \end{aligned} \quad (14.18)$$

Introducing the normalized charge density, which is

$$Q(z^*, t) = \frac{v^+ C^+(z^*, t)}{v^- C^-} - 1 \quad (14.19)$$

Eq. (14.18) can be written as an equation of $Q(z^*, t)$ as

$$\frac{\partial Q(z^*, t)}{\partial t} = D^+ \frac{\partial^2 Q(z^*, t)}{\partial z^{*2}} - \frac{D^+}{\ell^2} \int_{-h/2}^z Q(z^*, t) dz^* \frac{\partial Q(z^*, t)}{\partial z^*} - \frac{D^+}{\ell^2} [1 + Q(z^*, t)] Q(z^*, t) \quad (14.20)$$

Assuming $n(z^*, t) = \int_{-h/2}^z Q(z^*, t) dz^*$,

$$\frac{\partial}{\partial z^*} \left(\frac{\partial n(z^*, t)}{\partial t} \right) = \frac{\partial}{\partial z^*} \left\{ D^+ \frac{\partial^2 n(z^*, t)}{\partial z^{*2}} - \frac{D^+}{\ell^2} n(z^*, t) \frac{\partial n(z^*, t)}{\partial z^*} - \frac{D^+}{\ell^2} n(z^*, t) \right\} \quad (14.21)$$

Eq. (14.21) can be solved using numerical method. Thus, the normalized charge density $Q(z, t)$ can be finally determined, and the thicknesses of ABL and CBL can be calculated as (Nemat-Nasser, 2002)

$$L_A = \int_{-h/2}^0 Q(z, t) dz \quad (14.22)$$

$$L_C = 2 \left(\frac{h}{2} - \frac{\int_0^{h/2} z \cdot Q(z, t) dz}{L_A} \right) \quad (14.23)$$

With Eqs. (14.22) and (14.23), the bending moment due to the electric potential can subsequently be derived. In the following section, explicit bending moment solutions are obtained based on Nemat-Nasser's (2002) hybrid actuation model.

14.2.2 Bending Moment

Since the axial strain of IPMC is related to the water uptake in the membrane clusters, the bending moment rate can be expressed as a function of water uptake as (Nemat-Nasser, 2002)

$$\dot{M}^e(t) = \int_{-h/2}^{h/2} Y_b \dot{\epsilon}_x \cdot z dz = \frac{1}{3} \int_{-h/2}^{h/2} Y_b \frac{\dot{w}(z, t)}{1 + w(z, t)} \cdot z dz \quad (14.24)$$

where Y_b is the effective Young's modulus of boundary layers in IPMC, *i.e.*, the Young's modulus of polyelectrolyte membrane; ϵ_x is the axial strain in the x direction; $w(z, t)$ is the function accounting for the water uptake in the clusters; and

the dot above all symbols denotes the first derivative with respect to time.

Completing the integration at the right hand side of Eq. (14.24) by considering the thickness of ABL and CBL and neglecting the small terms, the bending moment rate can be written as

$$\dot{M}^e(t) = -\frac{Y_b h}{6} \left(\frac{\dot{w}_A(z,t)}{1+w_A(z,t)} L_A - \frac{\dot{w}_C(z,t)}{1+w_A(z,t)} L_C \right) \quad (14.25)$$

where w_A and w_C are the water uptakes at ABL and CBL, respectively.

Integrating both sides of Eq. (14.25) over time and considering the initial condition $M^e(0)=0$ when $w_A(z,0)=w_C(z,0)=w_0$, where w_0 is the initial water uptake before the application of electric potential, the bending moment for the beam with width b is obtained as:

$$M^e = -\frac{Y_b b h L_A}{6} \{ \ln[1+w_A(z,t)] - \beta \ln[1+w_C(z,t)] + (1-\beta) \ln(1+w_0) \} \quad (14.26)$$

where $\beta = L_C / L_A$.

Since the bending strain is small, the change of water uptake in the clusters is also small. Thus, the bending moment can be approximated by expanding the right hand side of Eq. (14.26) at w_0 using Taylor's series with the higher-order terms neglected, as

$$M^e = -\frac{Y_b b h L_A}{6(1+w_0)} [(w_A(t) - \beta w_C(t)) - (1-\beta)w_0] \quad (14.27)$$

Once the water uptakes w_A and w_C are obtained, the bending moment due to electric potential can be determined by Eq. (14.27). The water uptakes at ABL and CBL are governed by the following two equations (Nemat-Nasser, 2002)

$$\frac{\dot{w}_A(z,t)}{1+w_A(z,t)} = D_A t_A \quad (14.28)$$

$$\frac{\dot{w}_C(z,t)}{1+w_C(z,t)} = D_C \bar{t}_C \quad (14.29)$$

where D_A and D_C are the constant coefficients accounting for the diffusion in ABL and CBL, respectively; t_A and \bar{t}_C are the pressure in the clusters in ABL and CBL, respectively, which are defined as

$$t_A = \Pi_A + p_{AA} + p_{AED} + \sigma_r(a_0, t) \quad (14.30)$$

$$\bar{t}_C = \bar{\Pi}_C + \bar{p}_{DC} + \bar{p}_{CDD} + \bar{\sigma}_r(a_0, t) \quad (14.31)$$

where $\Pi_A(t)$, p_{AA} , p_{ADD} and $\sigma_r(a_0, t)$ are the osmotic pressure, anion-anion electrostatic stress, dipole-dipole interaction stress and elastic stress in the polymer matrix in ABL, respectively; and $\bar{\Pi}_C$, \bar{p}_{DC} , \bar{p}_{CDD} and $\bar{\sigma}_r(a_0, t)$ are the average values of osmotic pressure, dipole-cation interaction stress, dipole-dipole interaction stress and elastic stress in the polymer matrix in CBL, respectively. They are defined as follows

$$\Pi_A(t) = \frac{\phi Q_B^- K_0}{w_A(t)} [2 - g(t)] \quad (14.32)$$

$$p_{AA} = \frac{g(t) (Q_B^-)^2 R_0^2}{18\kappa_A [w_A(t)]^2} \quad (14.33)$$

$$p_{AED} = \frac{1 - g(t) \pm [\alpha_A(t)]^2}{3\kappa_A [w_A(t)]^2} (Q_B^-)^2 \quad (14.34)$$

$$\bar{\Pi}_C(t) = \frac{\phi Q_B^- K_0}{w_C(t)} [2 + \frac{g(t)}{\beta}] \quad (14.35)$$

$$\bar{p}_{DC} = \frac{2(Q_B^-)^2 R_0 \alpha_C(t)}{9\kappa_C [w_C(t)]^{5/3}} g(t) \quad (14.36)$$

$$\bar{p}_{CDD} = \frac{(Q_B^-)^2 \pm [\alpha_C(t)]^2}{3\kappa_C [w_C(x, t)]^2} [1 - g(t)] \quad (14.37)$$

and

$$\sigma_r(a_0, t) = -p_0 + K(w/w_i)^{-4/3} \quad (14.38)$$

where

$$p_0 = K \left(\frac{w_0}{w_i} \right)^{-4/3} + p_c \quad (14.39)$$

$$K = p_c \frac{1+w}{w_i I_n - \left(\frac{w_i}{w}\right)^{4/3}} \quad (14.40)$$

$$p_c = \frac{v\phi Q_B^- K_0}{w} + \frac{\pm[\alpha_A(t)]^2 (Q_B^-)^2}{3k_e w^2} \quad (14.41)$$

$$w_i = \frac{n_0}{1-n_0}, \quad I_n = \frac{1+2An_0}{n_0(1+An_0)^{1/3}} - \frac{1+2A}{(1+A)^{1/3}}, \quad A = \frac{w}{w_i} - 1 \quad (14.42)$$

ϕ is the osmotic factor; $g(t)$ is the time variation function; and Q_B^- is the anion charge density of the dry bare membrane defined as

$$Q_B^- = \frac{\rho_B F}{EW_{ion}} \quad (14.43)$$

where ρ_B is the density of bare membrane and EW_{ion} is the equivalent weight of ion content,

$$EW_{ion} = \frac{EW_{H^+} - 1.008 + FW_{ion}}{SF} \quad (14.44)$$

EW_{H^+} is the equivalent weight of the dry ionomer in proton form, FW_{ion} is the formula weight of the cation used and SF is a scaling factor accounting for added electrode mass; $K_0 = \frac{RT}{F}$; R_0 is the initial cluster size in dry condition; κ_A and κ_C are the effective electric permittivity of the cluster in ABL and CBL respectively; $\alpha_A(t)$ and $\alpha_C(t)$ are the effective dipole length at ABL and CBL, respectively, which are governed by the following equation:

$$\pm[\alpha(t)]^2 = \begin{cases} a_1 w + a_2 & m_w \leq CN \\ \pm\left(\frac{7+6f}{7-6f}\right)^2 (a_1 w + a_2) & m_w > CN \end{cases} \quad (14.45)$$

where a_1 and a_2 are coefficients; w is the water uptake; m_w is the number of mole water per mole ion within a cluster defined as:

$$m_w = \frac{EW_{ion} w}{18v\rho_B} \quad (14.46)$$

and

$$f = \frac{m_w - CN}{m_w} \tag{14.47}$$

where CN is the coordination number; N_0 is the initial porosity of dry membrane; and $\nu = 2$. Detailed definitions of the above notations can be found in (Nemat-Nasser, 2002).

It is difficult to solve Eqs. (14.28) and (14.29) due to their nonlinearity. By transferring $[1 + w_A(z, t)]$ and $[1 + w_C(z, t)]$ to the right hand sides of Eqs. (14.28) and (14.29), respectively, and expanding their right hand sides at w_0 using Taylor’s series with higher order terms neglected, two linear partial differential equations can be obtained,

$$\frac{\partial w_A(z, t)}{\partial t} = F_A(w_0, t) + F_{A1}(w_0, t) \cdot (w_A - w_0) \tag{14.48}$$

$$\frac{\partial w_C(z, t)}{\partial t} = F_C(w_0, t) + F_{C1}(w_0, t) \cdot (w_C - w_0) \tag{14.49}$$

where $F_A(w_0, t) = D_A(1 + w_0)t_A(w_0, t)$; $F_{A1}(w_0, t) = \frac{\partial F_A(w_A, t)}{\partial w_A} \Big|_{w_A=w_0}$;

$F_C(w_0, t) = D_C(1 + w_0)t_C(w_0, t)$; and $F_{C1}(w_0, t) = \frac{\partial F_C(w_C, t)}{\partial w_C} \Big|_{w_C=w_0}$.

The solutions of w_A and w_C can be obtained from Eqs. (14.48) and (14.49) as

$$w_A(z, t) = e^{\left(\int F_{A1} dt\right)} \cdot \left(C_1 + \int e^{\left(-\int F_{A1} dt\right)} \cdot (F_A - F_{A1}w_0) dt\right) \tag{14.50}$$

$$w_C(z, t) = e^{\left(\int F_{C1} dt\right)} \cdot \left(C_2 + \int e^{\left(-\int F_{C1} dt\right)} \cdot (F_C - F_{C1}w_0) dt\right) \tag{14.51}$$

where C_1 and C_2 are the integration constants. After simplification, the solutions of water uptakes are

$$w_A(z, t) = \left[C_1 \bar{h}_A(t) - \frac{f_A}{f_{A1}} - \frac{f_A f_{A2}}{f_{A1}} \bar{h}_A(t) \int \frac{1}{\bar{h}_A(t)} dt \right] + w_0 \tag{14.52}$$

$$w_C(z, t) = \left[C_2 \bar{h}_C(t) - \frac{f_C}{f_{C1}} - \frac{f_C f_{C2}}{f_{C1}} \bar{h}_C(t) \int \frac{1}{\bar{h}_C(t)} dt \right] + w_0 \tag{14.53}$$

where

$$f_A = D_A(1+w_0) \left[-\frac{\phi Q_B^- K_0}{w_0} + \frac{(Q_B^-)^2}{18\kappa_A} \frac{R_0^2}{w_0^{4/3}} - \frac{(Q_B^-)^2 \pm (\alpha_A(w_0))^2}{3\kappa_A w_0^2} \right] \quad (14.54)$$

$$f_{A1} = D_A \left\{ (1+w_0) \left[\frac{\phi Q_B^- K_0}{w_0^2} - \frac{2(Q_B^-)^2}{27\kappa_A} \frac{R_0^2}{w_0^{7/3}} + \frac{2(Q_B^-)^2 \pm [\alpha_A(w_0)]^2}{3\kappa_A w_0^3} - \frac{(Q_B^-)^2}{3\kappa_A w_0^2} \frac{d \pm [\alpha_A(w_A)]^2}{dw_A} \Big|_{w_A=w_0} \right] + t_A(w_0, t) \right\} \quad (14.55)$$

$$f_{A2} = D_A(1+w_0) \left[-K \frac{4}{3w_i} \left(\frac{w_0}{w_i} \right)^{-7/3} \right] \quad (14.56)$$

$$f_C = D_C(1+w_0) \left\{ \frac{\phi Q_B^- K_0}{\beta w_0} + \frac{2(Q_B^-)^2}{9\kappa_C} \frac{R_0 \alpha_C(w_0)}{w_0^{5/3}} - \frac{(Q_B^-)^2 \pm (\alpha_C(w_0))^2}{3\kappa_C w_0^2} \right\} \quad (14.57)$$

$$f_{C1} = D_C \left\{ (1+w_0) \left(-\frac{\phi Q_B^- K_0}{\beta w_0^2} - \frac{10}{3} \frac{(Q_B^-)^2}{9\kappa_C} \frac{R_0 \alpha_C(w_0)}{w_0^{7/3}} + \frac{2(Q_B^-)^2}{9\kappa_C} \frac{R_0}{w_0^{5/3}} \frac{d \alpha_C(w_A)}{dw_A} \Big|_{w_A=w_C} + \frac{2(Q_B^-)^2 \pm [\alpha_C(w_0)]^2}{3\kappa_C w_0^3} - \frac{(Q_B^-)^2}{3\kappa_C w_0^2} \frac{d \pm [\alpha_C(w_A)]^2}{dw_A} \Big|_{w_A=w_C} \right) + t_C(w_0, t) \right\} \quad (14.58)$$

$$f_{C2} = D_C(1+w_0) \left[-K \frac{4}{3w_i} \left(\frac{w_0}{w_i} \right)^{-7/3} \right] \quad (14.59)$$

$$\hat{h}_{(\bullet)}(t) = e^{\int [f_{1\bullet}(t) + f_{2\bullet}] dt} \quad (14.60)$$

where the dot in the subscript stands for either A or C .

As $f_{2\bullet}$ is negative, with the increase of time, $\hat{h}_{(\bullet)}(t)$ will diminish. For the steady state, *i.e.*, when t is sufficiently large, the following relation stands,

$$\hat{h}_{(\bullet)}(t) \int \frac{1}{\hat{h}_{(\bullet)}(t)} dt = -e^{\frac{f_{1\bullet}(\Omega t - \pi/2)}{\Omega}} / f_{2\bullet} \quad (14.61)$$

Using the approximation of Eq. (14.61), Eqs. (14.52) and (14.53) can be further simplified as

$$w_A(z, t) = C_1 \tilde{h}_A(t) + \frac{f_A}{f_{A1}} \left[e^{\left(\frac{f_{A1}}{\Omega} e^{j(\Omega t - \pi/2)}\right)} - 1 \right] + w_0 \quad (14.62)$$

$$w_C(z, t) = C_2 \tilde{h}_C(t) + \frac{f_C}{f_{C1}} \left[e^{\left(\frac{f_{C1}}{\Omega} e^{j(\Omega t - \pi/2)}\right)} - 1 \right] + w_0 \quad (14.63)$$

Considering the initial conditions:

$$w_A(z, 0) = w_0, \quad w_C(z, 0) = w_0, \quad \text{and} \quad g(0) = 0 \quad (14.64)$$

the coefficients C_1 and C_2 can be obtained from Eqs. (14.47) and (14.48) as

$$C_1 = -\frac{f_A}{f_{A1}} \left[e^{\left(\frac{f_{A1}}{\Omega} e^{-j\pi/2}\right)} - 1 \right] / \tilde{h}_A(0) \quad (14.65)$$

$$C_2 = -\frac{f_C}{f_{C1}} \left[e^{\left(\frac{f_{C1}}{\Omega} e^{-j\pi/2}\right)} - 1 \right] / \tilde{h}_C(0) \quad (14.66)$$

As $\tilde{h}_{(\bullet)}(t)$ will diminish with time, for the steady state vibration, $C_1 \tilde{h}_A(t)$ and $C_2 \tilde{h}_C(t)$ will eventually vanish. Finally, the solutions of water uptake functions are

$$w_A(z, t) = \frac{f_A}{f_{A1}} \left[e^{\left(\frac{f_{A1}}{\Omega} e^{j(\Omega t - \pi/2)}\right)} - 1 \right] + w_0 \quad (14.67)$$

$$w_C(z, t) = \frac{f_C}{f_{C1}} \left[e^{\left(\frac{f_{C1}}{\Omega} e^{j(\Omega t - \pi/2)}\right)} - 1 \right] + w_0 \quad (14.68)$$

Since the time variation of $w_A(z, t)$ and $w_C(z, t)$ should be $e^{j(\Omega t - \pi/2)}$, Eqs. (14.67) and (14.68) can be approximated as

$$w_A(z, t) = \frac{f_A}{f_{A1}} (e^{\frac{f_{A1}}{\Omega}} - 1) e^{j(\Omega t - \pi/2)} + w_0 \quad (14.69)$$

$$w_C(z, t) = \frac{f_C}{f_{C1}} (e^{\frac{f_{C1}}{\Omega}} - 1) e^{j(\Omega t - \pi/2)} + w_0 \quad (14.70)$$

Using the solutions of water uptake in Eqs. (14.69) and (14.70), the bending moment generated by the IPMC can be obtained from Eq. (14.27).

$$M^e = -\frac{Y_b b h L_A}{6(1+w_0)} \left[\frac{f_A}{f_{A1}} (e^{\frac{f_{A1}}{\Omega}} - 1) - \frac{\beta f_C}{f_{C1}} (e^{\frac{f_{C1}}{\Omega}} - 1) \right] e^{j(\Omega t - \pi/2)} \quad (14.71)$$

It is worth noting that Eq. (14.71) is an explicit expression of bending moment which includes the effects of osmotic, electrostatic and elastic stresses of IPMC. This equation provides a convenient way to estimate the bending moment of IPMC at a given hydration rate. The frequency of the applied electric potential Ω appears in the expression of bending moment. It is evident that, with the increase of driving frequency Ω , the generative bending moment and therefore the vibration amplitude of IPMC decreases. This conclusion agrees with the experimental observations by Shahinpoor and Kim (2001). In addition, a phase lag between the bending moment and the input signal is observed, *i.e.*, $\delta_0 = \pi/2$. It is noted that this phase lag is obtained without considering the viscous properties of solvent. For different solvent, the phase lag should vary. To include the effect of viscous property of solvent in the IPMC, Eqs. (14.24), (14.28) and (14.29) need modifications. The effect of viscosity of solvent can also be reflected in the overall damping coefficient of an IPMC sample, which can be evaluated through experiments.

Since the thicknesses of ABL and CBL are derived from the condition of static electric potential and multiplied by the time variation function, they may be inaccurate for a high frequency electric field, especially for the CBL. This may result in an overestimation of bending moment from Eq. (14.70) since the time required for cation redistribution is neglected. However, as the time required for cation redistribution is very short, for low driving frequency, the cations should have ample time to achieve a quasi-equilibrium state. Thus, Eq. (14.71) is more accurate for low frequency electric fields.

When Ω is very small; *e.g.*, when a direct current (DC) signal is applied, Eq. (14.71) is not applicable anymore. However, the bending moment for this case can be easily obtained by setting the time variation function $g(t)$ in Eqs. (14.48) and (14.49) to unity. The bending moment under a DC signal is

$$M^e = -\frac{Y_b b h L_A}{6(1+w_0)} \left[\frac{f_A}{f_{A1} + f_{A2}} (e^{(f_{A1} + f_{A2})t} - 1) - \frac{\beta f_C}{f_{C1} + f_{C2}} (e^{(f_{C1} + f_{C2})t} - 1) \right] \quad (14.72)$$

For the transverse vibration of an IPMC beam, Eq. (14.71) should be used. For static signal input, the bending moment can be calculated from Eq. (14.72).

14.3 Validation and Discussions

In Section 14.2, small strain is assumed in the actuation process of IPMC to reduce the nonlinearity of Eqs. (14.28) and (14.29). Analytical solutions are obtained based on this assumption through the Taylor's series expansion. Therefore, it is important to compare the results of the analytical solutions with the numerical solutions of Eqs. (14.28) and (14.29), and verify whether the assumption is valid. As Eqs. (14.28) and (14.29) have the same format, so do Eqs. (14.69) and (14.70); hence, only Eqs. (14.28) and (14.69) are calculated and compared. The numerical solution of Eq. (14.28) is obtained by using the MATLAB function ode45. Fig. 14.6 shows the results of water uptakes obtained from Eqs. (14.69) and (14.28). The parameters considered are listed in Table 14.1. It is evident that the analytical solution of Eq. (14.69) and the numerical solution of Eq. (14.28) match well, except that the peak values are slightly different. A lag of $\pi/2$ is also observed by comparing the driving signal and the water uptake solution. This result indicates that the simplification procedure is valid.

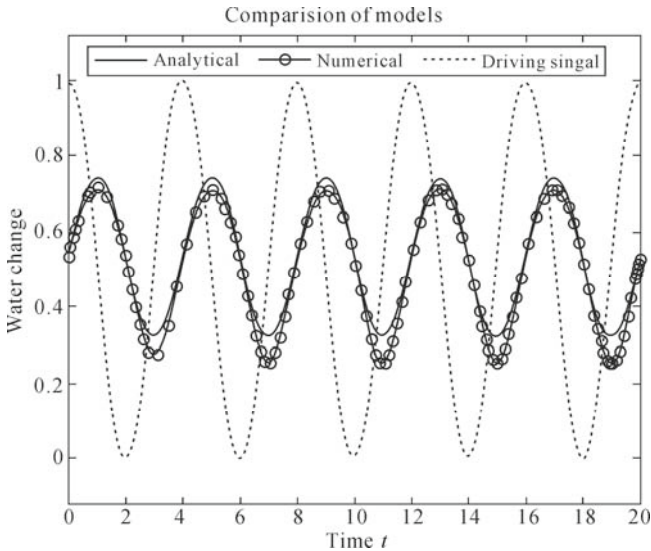


Fig. 14.6 Comparison between analytical and numerical solutions

Before the above solutions can be used, the bending moment solution obtained in Section 14.2 should first be validated by comparing the tip displacement of a cantilevered beam with the results obtained by Nemat-Nasser (2002). Consider a Nafion-based cantilevered IPMC beam in Li^+ form with a length of 18 mm, a width of 2 mm and a thickness of 224 μm (Fig. 14.7). The plating metal is platinum, and the thickness of electrode is 6 μm for both the top and bottom surfaces of the IPMC beam. Assume that the initial water uptake of IPMC is $w_0 = 0.533$ and the electric potential is a 1-V DC signal. For simplicity, the

viscous damping of the IPMC is set as zero. Other material properties considered in the calculation are listed in Table 14.1. All the above parameters are the same as in (Nemat-Nasser, 2002).

Table 14.1 Parameters, symbols and values for an IPMC sample with Li^+ as cation

Parameter	Symbol	Value	Parameter	Symbol	Value
IPMC density	ρ	3,385 kg/m ³	Temperature	T	300 K
Gas constant	R	8.3143 J/(mol·K)	Initial porosity	n_0	0.01
Faraday's constant	F	96,485 C/mol	Inner radius of cluster at w_0	a	1.6×10^{-9} m
Bare membrane density	ρ_B	2.01×10^3 kg/m ³	Capacitance per unit area	Cap	12 F/m ²
Platinum density	ρ_p	21.45×10^3 kg/m ³	Effective permittivity at ABL	κ_A	1.7852×10^{-10} F/m
Effective permittivity at CBL	κ_C	5.31×10^{-11} F/m	Osmotic coefficient	ϕ	1
Coordination Number of Li^+	CN	6	Equivalent weight of bare Nafion in proton form	EW_{H^+}	1,100 g/mol
Formula weight of Li^+	FW_{Li^+}	6.94 g/mol	Effective dipole length coefficient	a_1	1.728×10^{-20}
Effective dipole length coefficient	a_2	-0.0778×10^{-20}	Concentration factor	A_B	0.5
Coefficient	D_A	1.0×10^{-8}	Solvation number	SN	0
Young's modulus of platinum	Y_M	1.50×10^{11} N/m ²	Mass scaling factor	SF	0.623

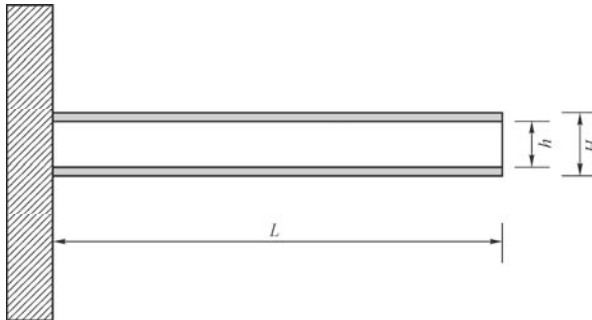


Fig. 14.7 Configuration of an IPMC cantilevered beam

Since the signal is DC, the bending moment can be obtained from Eq. (14.72). The normalized tip displacement of the cantilevered beam can be expressed as

$$\frac{u_3}{L} = \frac{M^e L}{2YI}, \tag{14.73}$$

where Y is the Young’s modulus of the IPMC beam and I is the moment of inertia.

Fig. 14.8 compares the normalized tip displacements obtained using Eqs. (14.72) and (14.73) with the results given in Nemat-Nasser (2002). It can be seen that the present model is in accordance with the data given in Nemat-Nasser (2002) at the initial deformation stage. The final displacements after a long time span also closely match each other. Since Eq. (14.72) does not take into account the relaxation of the IPMC beam, the relaxation stage does not match well, but this does not affect the accuracy of Eq. (14.71) as it accounts for the continuous vibration of IPMC beam where the relaxation effect is negligible.

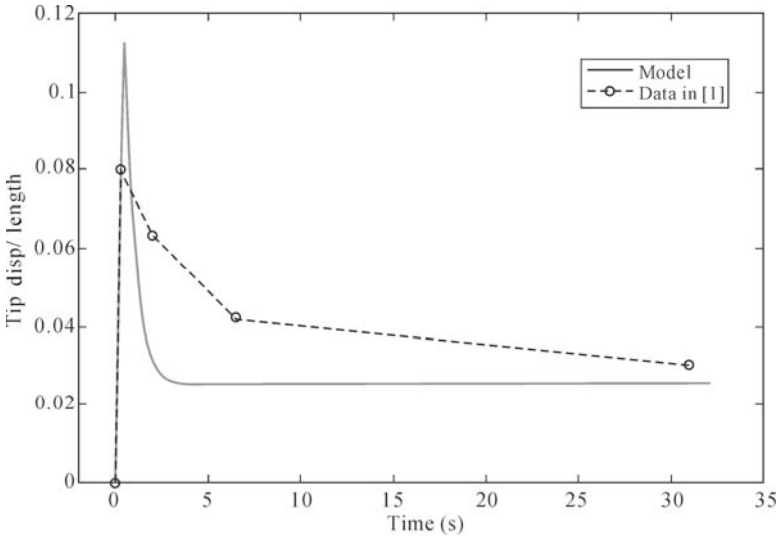


Fig. 14.8 Comparison between calculated displacement and data in Nemat-Nasser (2002)

Besides the tip displacement of an IPMC cantilevered beam, the blocked force is another parameter of interest to evaluate the actuation performance of IPMC. The blocked force can be defined as a force required to prevent any deflection. The blocked force for an IPMC cantilevered beam can be estimated by considering the beam subjected to a point force at the tip. The blocked force will balance the bending moment caused by the electric field such that the tip displacement will be zero. Using Castigliano’s theorem, the blocked force can be derived as

$$F_b = \frac{3M^e}{2L} \quad (14.74)$$

For the 1-V DC potential, the maximum blocked force is equivalent to 0.033 g, which is about 1.211 times the self-weight of the IPMC beam. When the electric potential increases to 5 V, the ratio of the blocked force to the beam weight is 4.37. This ratio is comparable with the experimental result obtained by Shahinpoor and Kim (2005) for the thin gold electrode IPMC. In their experiment, a 2 mm thick IPMC strip with a weight of 0.24 g developed a 1.2-g force under 5-V potential, where the force-weight ratio is 5.0. This comparison indicates that the results obtained are reasonable.

The above calculation validates the bending moment expression for static electric potential. To validate the bending moment expression for dynamic condition, consider a Nafion-based IPMC cantilevered beam with a length of 30 mm and a thickness of 224 μm . The applied electric potential is a 1-V sinusoidal signal with a frequency of 0.25 Hz. The cation type is Na^+ and the solvent is water. The damping ratio c is set as zero. The other parameters considered are shown in Table 14.2.

Table 14.2 Parameters, symbols and values for an IPMC sample with Na^+ as cation

Parameter	Symbol	Value	Parameter	Symbol	Value
Young's modulus of hydrated polymer	Y_b	89 MPa	Temperature	T	300 K
Young's modulus of IPMC	Y	0.186 Gpa	Initial porosity	n_0	0.01
IPMC Density	ρ	3385 kg/m^3	Radius of cluster	a	1.65 nm
Gas constant	R	8.3143 J/mol K	Capacitance per unit area	Cap	15 F/m^2
Faraday's constant	F	96485 C/mol	Effective permittivity at anode boundary	κ_A	2.1462×10^{-10} F/m
Effective permittivity at cathode boundary layer	κ_C	5.31×10^{-11} F/m	Formula weight of Na^+	FW_{Na^+}	23 g/mol
Bare membrane density	ρ_B	2010 kg/m^3	Equivalent weight of proton	FW_{H^+}	1100 g/mol
Osmotic coefficient	ϕ	1	Diffusion coefficient	D_A	10^{-2}
Effective dipole length coefficient	a_1	1.5234×10^{-20}	Effective dipole length coefficient	a_2	-0.0703×10^{-20}
Coordination number	CN	4.5	Solvation number	SN	0

The transverse vibration of a cantilevered beam is governed by the following motion equation:

$$YI \frac{\partial^4 w}{\partial x^4} + \rho A \frac{\partial^2 w}{\partial t^2} + c \frac{\partial w}{\partial t} = f(x, t) \quad (14.75)$$

where ρ is the material density; A is the cross section area; c is the damping ratio and $f(x, t)$ is the load effect due to IPMC actuation which is

$$f(x, t) = M_0 [\delta'(x-0) - \delta'(x-L)] e^{j\Omega t}, \quad (14.76)$$

where M_0 is the time independent part of Eq. (14.71).

Eq. (14.75) can be solved by the method of separation of variables. It is assumed that the solution is in the following form:

$$w = \sum_{n=1}^{\infty} A_n X_n(x) e^{j\Omega t}, \quad (14.77)$$

where $X_n(x) = [\cos(k_n x) - \cosh(k_n x)] - \sigma_n [\sin(k_n x) - \sinh(k_n x)]$;

$\sigma_n = \frac{\cos(k_n L) + \cosh(k_n L)}{\sin(k_n L) + \sinh(k_n L)}$ and k_n is determined by the frequency equation

$$\cos(k_n L) \cosh(k_n L) = -1 \quad (14.78)$$

Substituting Eq. (14.77) into Eq. (14.75) and using the orthogonal properties of normal mode, the solution to the IPMC cantilever beam vibration can be obtained as

$$w = \sum_{n=1}^{\infty} \frac{M_0}{L} \frac{2 \cdot (-1)^n + k_n [-\sin(k_n L) - \sinh(k_n L) + \sigma_n (\cos(k_n L) - \cosh(k_n L))]}{(YIk_n^4 - \rho A \Omega^2 + j\Omega c)} X_n(x) e^{j\Omega t} \quad (14.79)$$

Fig. 14.9 shows the deflection curves of the IPMC cantilever beam at three different time points, $t = 1/(12f)$, $t = 1/(6f)$ and $t = 1/(4f)$, where f is the driving frequency which is 0.25 Hz. It is observed that the maximum tip displacement is 4.2% of the beam length. In Nemat-Nasser and Wu (2006), the experimental test showed that the maximum tip displacement of a cantilever beam of the same dimension under the same electric potential is 3.6% of the beam length. Considering the length of beam, the difference in vibration amplitude is only 0.18 mm. As the experimental data of IPMC generally vary a lot from case to case, the calculated result can be viewed as acceptable and thus validates the proposed model.

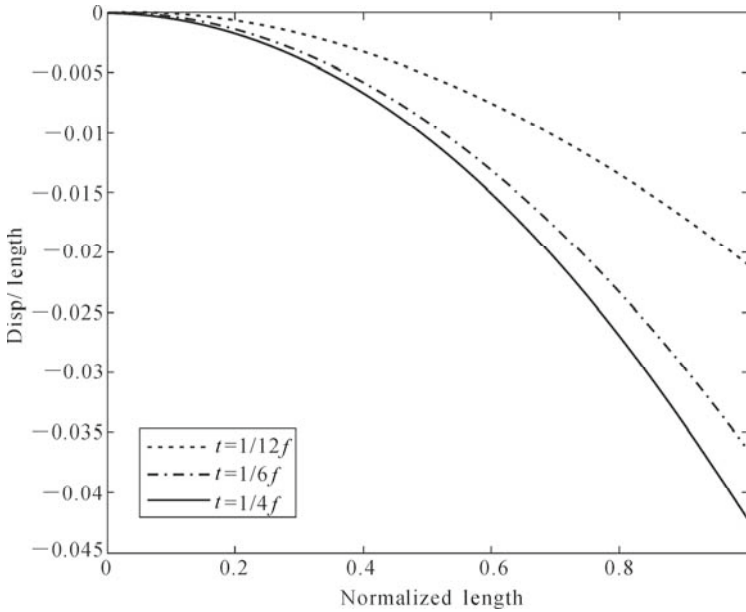


Fig. 14.9 IPMC cantilever beam deflections at $t = 1/(12f)$, $t = 1/(6f)$ and $1/(4f)$

14.4 Frequency Dependent Characteristics

After validating the theoretical model presented in Section 14.2, the dynamic characteristics of IPMC can be investigated. One of the significant characteristics of IPMC is their frequency-dependent behaviors. Although it has been widely observed in experimental studies (Shahinpoor and Kim, 2001; 2004; Nemat-Nasser and Wu, 2006) that, with increase in driving frequency, the vibration amplitude of an IPMC sample would decrease even though the electric potential was kept unchanged, the effect of driving frequency on the actuation characteristics of IPMC has not been investigated theoretically. In this section, the effect of driving frequency on the actuation characteristics of IPMC is investigated using the model presented in Section 14.2.

Consider a Nafion-based IPMC cantilevered beam with a length of 18 mm and a thickness of 224 μm . The thickness of membrane part is 212 μm . The applied electric potential is 1-V sinusoidal signal with frequency varying from 0.15 to 1 Hz. The cation type is Na^+ and the solvent is water. The damping ratio c is also set as zero. The other parameters used are shown in Table 14.2.

Using Eqs. (14.71) and (14.79), vibration of the IPMC sample in frequency domain can be calculated. Fig. 14.10 shows the relationship between the normalized tip displacements of the IPMC cantilevered beam and the driving frequency. It is evident that, with increase in driving frequency, the vibration

amplitude decreases dramatically. The experimental data presented in Fig. 14.10 are extracted from Nemat-Nasser and Wu (2006). It can be seen that the results obtained by the model match reasonably well with the experimental data. The difference between the model and experimental data may be due to the limited frequency-dependent variables considered in the model. Several parameters used in the model are actually not constant but frequency-dependent on the actuation process. However, it is difficult to assign frequency-dependent values to these parameters due to their complicated or unclear relationships with frequencies.

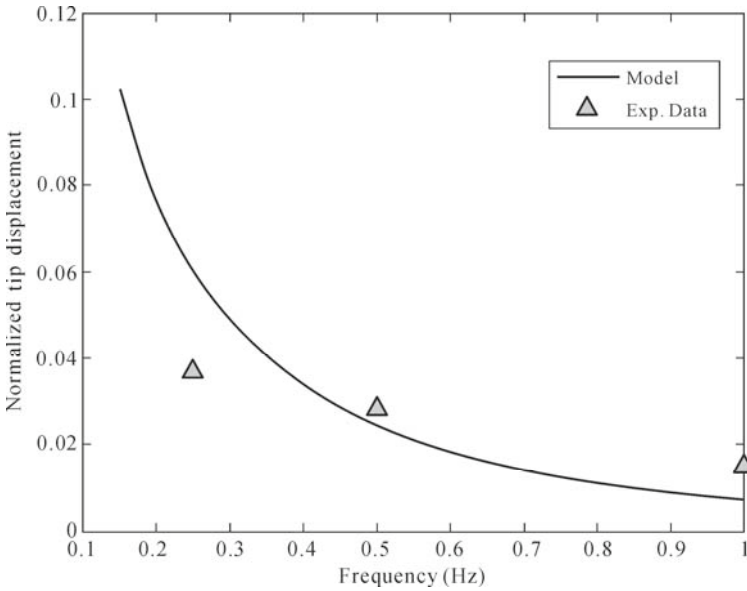


Fig. 14.10 Normalized tip displacement of IPMC beam vs. frequency

Fig. 14.11 shows the decrease of axial strains with increase of frequency in ABL and CBL. Fig. 14.12 illustrates the reduction of actuation stresses in ABL and CBL against driving frequency. It can be observed that both the strains and stresses decrease dramatically with increase in driving frequency. Hence, Figs. 14.10–14.12 demonstrate the strong frequency-dependent characteristics of IPMC material under actuation.

When the range of driving frequency is further expanded to 1–10 Hz, resonance of the IPMC cantilevered beam can be observed. By comparing with the experimental results, the material properties, especially the damping ratio of IPMC can be calibrated.

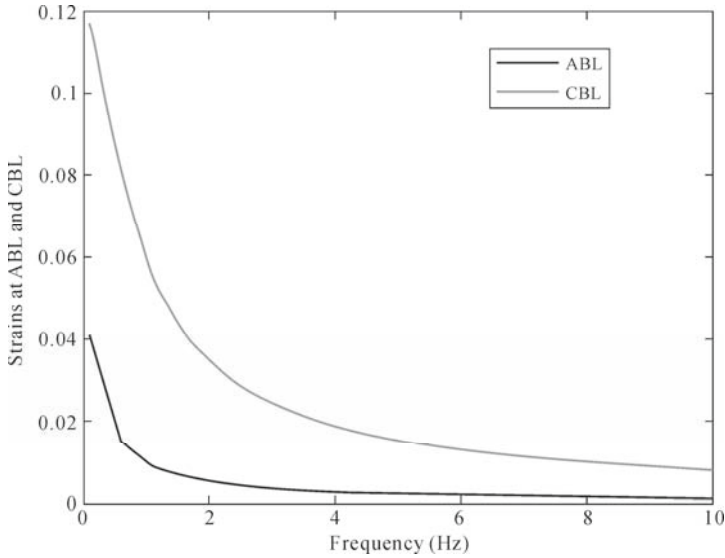


Fig. 14.11 Strains at ABL and CBL vs. frequency

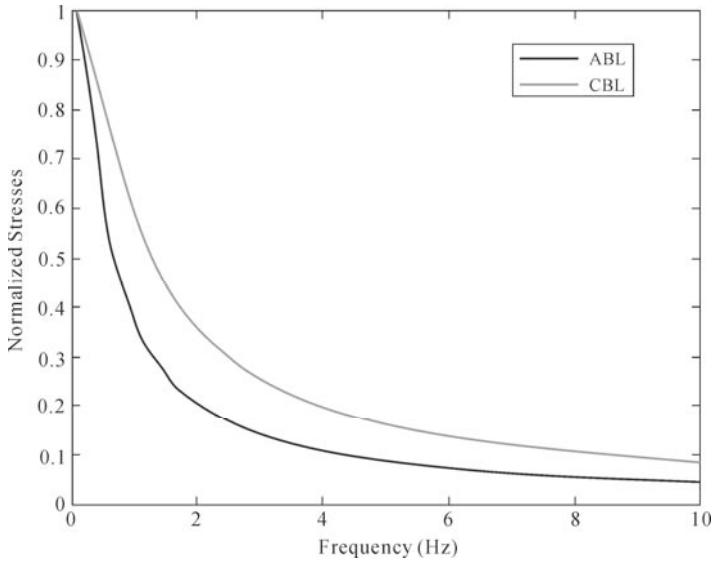


Fig. 14.12 Stress reduction at ABL and CBL vs. frequency

Experimental tests are also conducted on an IPMC cantilevered beam excited by sinusoidal signals. The IPMC sample is a Nafion-based IPMC with sodium as counter ions. The dimensions of the sample are 50 mm long, 7.5 mm wide and 0.3 mm thick. The equipments used are a Polytec scanning laser vibrometer, model 0FV-056, with a function generator and a computer with Polytec measurement

software (Fig. 14.13). The scanning laser vibrometer can scan from 1 to 10 Hz, with a resolution of 0.01 Hz, and records the vibration amplitudes at the tip of the cantilevered beam for each frequency point. After scanning, the results are plotted in a diagram (Fig. 14.14) to show the dynamic responses of the IPMC cantilevered beam under 1- and 2-V signals in frequency domain, respectively. It is evident that the first resonance occurs at around 6.72 Hz. This information is used to determine the damping ratio c , which is set as $-0.174j$. By using the parameters given in Table 14.2, the vibration of the IPMC cantilevered beam in frequency domain can be calculated using Eq. (14.79).

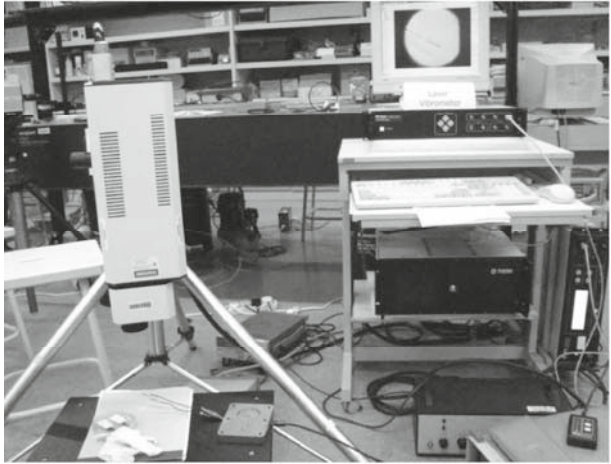


Fig. 14.13 Experimental setup for dynamic tests of IPMC

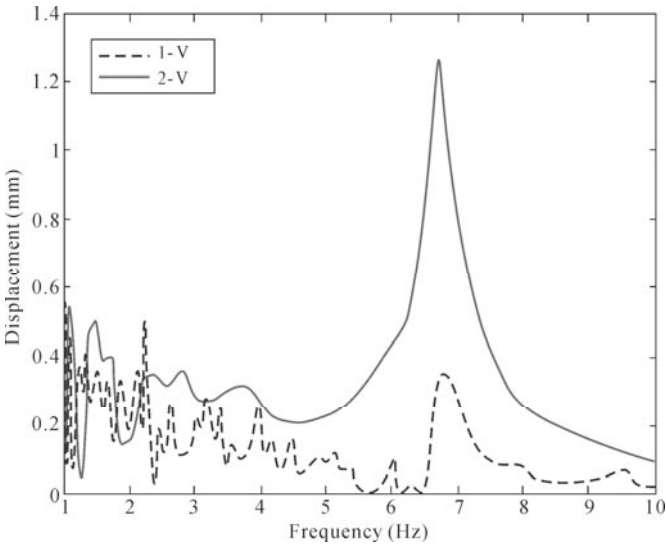


Fig. 14.14 Vibrations of an IPMC cantilever beam in frequency domain

Fig. 14.15 compares the model predictions with the experimental results. It can be observed that the model predictions and the experimental results for 1-V signal match well in most regions of the frequency domain except for the peak values at resonant frequency. However, for the 2-V signal, the peak values at the resonant frequency match well but have large discrepancies at the non-resonant regions. This implies the existence of some frequency-dependent parameters, which were considered as frequency-independent values in the model. However, given the large variation of experimental tests on IPMC materials from case to case, the model predictions are deemed acceptable.

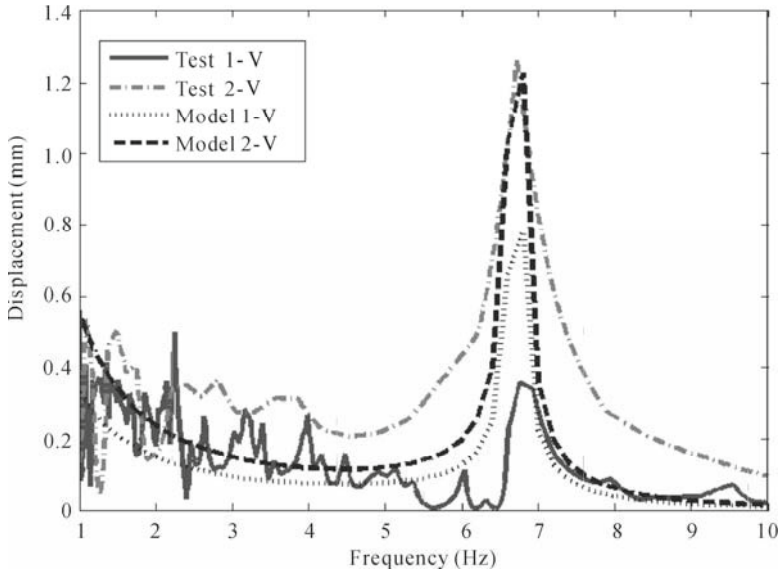


Fig. 14.15 Comparisons of model predictions and experimental results

14.5 Summary

In this chapter, explicit bending moment expressions are derived from the Nemat-Nasser's hybrid actuation model for both dynamic and static electric potentials. Comparisons with the numerical solutions and the experimental results available in the literature show that our derived model is reasonably accurate. By using the bending moment expressions, the frequency dependent characteristics of IPMC samples are investigated and discussed. It is found that the model presented in this chapter is capable of modeling the dynamic behaviors of IPMC in frequency domain. The bending moment expressions derived in this chapter provide an easy way to estimate the bending capacity of IPMC materials at a given hydration rate. These expressions are used in the next chapter to model IPMC-based structures for biomedical applications.

References

- Akle, B.J. and Leo, D.J. (2005). "Correlation of capacitance and actuation in ionomeric polymer transducers", *Journal of Materials Science*, 40: 3715-3724.
- Akle, B.J., Bennett, M.D. and Leo, D.J. (2006). "High-strain ionomeric-ionic liquid electroactive actuators", *Sensors and Actuators A: Physical*, 126: 173-181.
- Asaka, K. and Oguro, K. (2000a). "Bending of polyelectrolyte membrane platinum composites by electric stimuli II: response kinetics", *Journal of Electroanalytical Chemistry*, 480(1-2): 186-198.
- Asaka, K. and Oguro, K. (2000b). "bending of polyelectrolyte membrane platinum composites by electric stimuli III: self-oscillation", *Electrochimica Acta*, 45: 4517-4523.
- Asaka, K., Oguro, K., Nishimura, Y., Mizuhata, M. and Takenaka, H. (1995). "Bending of polyelectrolyte membrane platinum composites by electric stimuli I: response characteristics to various waveforms", *Polymer Journal*, 27: 436-440.
- Bar-Cohen, Y. (Editor) (2004). *Electroactive polymer (EAP) Actuators as Artificial Muscles, Reality, Potential, and Challenges*, 2nd Edition, Washington: SPIE Press.
- Bar-Cohen, Y. (Editor) (2006). *Biomimetics: Biologically Inspired Technologies*, New York: CRC/Taylor & Francis.
- Bennett, M.D. and Leo, D.J. (2004). "Ionic liquids as stable solvents for ionic polymer transducers", *Sensors and Actuators A: Physical*, 115:79-90.
- Bennett, M.D., Leo, D.J., Wilkes, G.L., Beyer, F.L. and Pechar, T.W. (2006). "A model of charge transport and electromechanical transduction in ionic liquid-swollen nafion membranes", *Polymer*, 47: 6782-6796.
- Bonomo, C., Fortuna, L., Giannone, P. and Graziani, S. (2005). "A method to characterize the deformation of an IPMC sensing membrane", *Sensor and Actuators A Physical*, 123-124: 146-154.
- Bufalo, G.D., Placidi, L. and Porfiri, M. (2008). "A mixture theory framework for modeling the mechanical actuation of ionic polymer metal composites", *Smart Materials and Structures*, 17: 045010.
- Farinholt, K. and Leo, D.J. (2004). "Modeling of electromechanical charge sensing in ionic polymer transducers", *Mechanics of Materials*, 36: 421-433.
- Kim, K.J. and Shahinpoor, M. (2003). "Ionic polymer-metal composites: II. manufacturing techniques", *Smart Materials and Structures*, 12: 65-79.
- Matthews, J.L., Lada, E.K., Weiland, L.M., Smith, R.C. and Leo, D.J. (2006). "Monte Carlo simulation of a solvated ionic polymer with cluster morphology", *Smart Materials and Structures*, 15: 187-199.
- Nemat-Nasser, S. (2002). "Micromechanics of actuation of ionic polymer-metal composites", *Journal of Applied Physics*, 92: 2899-2915.
- Nemat-Nasser, S. and Li, J.Y. (2000). "Electromechanical response of ionic polymer-metal composites", *Journal of Applied Physics*, 87: 3321-3331.

- Nemat-Nasser, S. and Wu, Y. (2003). "Comparative experimental study of the ionic polymer-metal composites with different backbone ionomers and in various cation forms", *Journal of Applied Physics*, 93: 5255-5267.
- Nemat-Nasser, S. and Wu, Y. (2006). "Tailoring the actuation of ionic polymer-metal composites", *Smart Materials and Structures*, 15: 1-15.
- Nemat-Nasser, S. and Zamani, S. (2006a). "Effect of solvents on the chemical and physical properties of ionic polymer-metal composites", *Journal of Applied Physics*, 99: 104902.
- Nemat-Nasser, S. and Zamani, S. (2006b). "Modeling of electrochemomechanical response of ionic polymer-metal composites with various solvents", *Journal of Applied Physics*, 100: 064310.
- Newbury, K.M. and Leo, D.J. (2002). "Electromechanical modeling and characterization of ionic polymer benders", *Journal of Intelligent Material Systems and Structures*, 13: 51-60.
- Newbury, K.M. and Leo, D.J. (2003a). "Linear electromechanical model of ionic polymer transducers-part I: model development", *Journal of Intelligent Material Systems and Structures*, 14: 333-342.
- Newbury, K.M. and Leo, D.J. (2003b). "Linear electromechanical model of ionic polymer transducers-part II: experimental validation", *Journal of Intelligent Material Systems and Structures*, 14: 343-357.
- Oguro, K., Kawami, Y. and Takenaka, H. (1992). "Bending of an ion-conducting polymer film-electrode composite by an electric stimulus at low voltage", *Trans. Journal of Micromachine Society*, 5: 27-30.
- Paquette, J.W. and Kim, K.J. (2004). "Ionomeric electroactive polymer artificial muscle for naval applications", *IEEE Journal of Ocean Engineering*, 29: 729-737.
- Sadeghipour, K., Salomon, R. and Neogi, S. (1992). "Development of a novel electrochemically active membrane and 'smart' material based vibration sensor/damper", *Smart Materials and Structures*, 1: 172-179.
- Shahinpoor, M. (1992). "Conceptual design, kinematics and dynamics of swimming robotic structures using ionic polymer gel muscles", *Smart Materials and Structures*, 1: 91-94.
- Shahinpoor, M. and Kim, K.J. (2001). "Ionic polymer-metal composites: I. fundamentals", *Smart Materials and Structures*, 10: 819-833.
- Shahinpoor, M. and Kim, K.J. (2002). "Mass transfer induced hydraulic actuation in ionic polymer-metal composites", *Journal of Intelligent Material Systems and Structures*, 13: 369-376.
- Shahinpoor, M. and Kim, K.J. (2004). "Ionic polymer-metal composites: III. modeling and simulation as biomimetic sensors, actuators, transducers, and artificial muscles", *Smart Materials and Structures*, 13: 1362-1388.
- Shahinpoor, M. and Kim, K.J. (2005). "Ionic polymer-metal composites: IV. industrial and medical applications", *Smart Materials and Structures*, 14: 197-214.
- Tamagawa, H., Yagasaki, K. and Nogata, F. (2002). "Mechanical characteristics of ionic polymer-metal composite in the process of self-bending", *Journal of*

- Applied Physics*, 92: 7614-7618.
- Toi, Y. and Kang, S.S. (2005). "Finite element analysis of two-dimensional electrochemical-mechanical response of ionic conducting polymer-metal composite beams", *Computers and Structures*, 83: 2573-2583.
- Weiland, L.M. and Leo, D.J. (2005a). "Computational analysis of ionic polymer cluster energetics", *Journal of Applied Physics*, 97: 013541.
- Weiland, L.M. and Leo, D.J. (2005b). "Ionic polymer cluster energetics: computational analysis of pedant chain stiffness and charge imbalance", *Journal of Applied Physics*, 97: 123530.
- Yagasaki, K. and Tamagawa, H. (2004). "Experimental estimate of viscoelastic properties for ionic polymer-metal composites", *Physical Review E* 70: 052801.
- Yamakita, M., Kamamichi, N., Kaneda, Y., Asaka, K. and Luo, Z.W. (2004). "Development of an artificial muscle linear actuator using ionic polymer-metal composites", *Advanced Robotics*, 18: 383-399.
- Yang, Y.W. and Zhang, L. (2008). "Modeling of ionic polymer-metal composite ring", *Smart Materials and Structures*, 17: 015023.
- Zhang, L. and Yang, Y.W. (2007). "Modeling of ionic polymer-,metal composite beam on human tissues", *Smart Materials and Structures*, 16: S197-S207.

IPMC-Based Biomedical Applications

L. Zhang^{*}, Y. W. Yang, C. K. Soh

Institute of Materials Research and Engineering, A*STAR (Agency for Science, Technology and Research), 3 Research Link, Singapore 117602

Tel: (65)-6874-5199; Fax: (65)-6872-7744

Email: zhangl@imre.a-star.edu.sg

15.1 Introduction

Ionic polymer-metal composite (IPMC) as an ionic electro-active polymer (EAP) offers many advantages over the conventional smart materials, such as good compliance, light weight, low operation voltage and capability of working in aqueous environments. These properties make IPMC promising for numerous applications in biomedical, naval, robotic and microelectromechanical system (MEMS) engineering (Paquette and Kim, 2004; Shahinpoor and Kim, 2005; Yamakita *et al.*, 2004; Bar-Cohen, 2006; Zhang and Yang, 2006; 2007; Yang and Zhang, 2008). One of the important applications of IPMC is in the biomedical related instruments which come in contact with human organs or tissues, such as artificial ventricular muscles, surgical tools and active scleral bands. The configurations of IPMC materials for such applications could be in various forms including bands, rings or shells.

In this chapter, possible applications of IPMC materials for biomedical engineering are explored. Three prototype models, *i.e.*, an IPMC beam on human tissues, an IPMC ring with elastic medium and an IPMC cylindrical shell with flowing fluid, are developed. The explicit bending moment expressions obtained in Chapter 14 are used in the modeling process. Examples are presented for illustration.

15.2 IPMC Beam on Human Tissues

One of the important applications of smart materials in biomedical engineering is the minimally invasive surgical (MIS) tools which come in contact with human tissues or organs. These surgical tools are generally expected to apply forces on tissues and organs, or change shapes to adapt to small incisions. Many of the MIS tools are in the form of strips or beams, and operated in dynamic electric potentials.

In this section, an analytical model is developed to depict the vibration response of a simply-supported IPMC beam bonded to an elastic foundation under an alternative electric field. Elastic foundation is employed to simulate the effect of human tissues. Eq. (14.71) is incorporated into the motion equation to account for the applied alternative electric field. A closed-form solution is obtained to describe the transverse vibration of the IPMC beam subjected to the applied electric field. Based on this solution, the pressure generated on human tissue is calculated by numerical integration. To maximize the beam deflection and the total pressure generated, the optimal location and length of the single electrode on the IPMC beam are discussed. To increase the flexibility of the IPMC beam and the variety of beam motion, multiple-electrodes on the IPMC beam are also considered. The deflection curve and generative pressure of the IPMC beam with multiple electrodes are obtained. The developed model is useful not only for the biomedical devices that employ IPMC materials but also for any other applications that utilize the vibration of IPMC materials.

15.2.1 Modeling of IPMC Beam on Human Tissues

As shown in Fig. 15.1, a Nafion-based IPMC beam of length L , thickness H and width b is studied. The IPMC beam is chemically plated with platinum electrode on both sides, and x_1 and x_2 are the coordinates of the two ends of the electrode. The thickness of the Nafion part of IPMC is denoted as h . The IPMC beam is assumed to be simply supported on the human tissue. The effect of the tissue is modeled as a Winkler foundation with stiffness k . Assume that the alternative electric potentials at the top and bottom surfaces are $-\varphi_0 e^{i\Omega t}/2$ and $\varphi_0 e^{i\Omega t}/2$, respectively, where φ_0 is the time-independent magnitude of electric potential, Ω is the angular frequency and j is the imaginary unit. Due to the redistribution of cations and associated water under the applied electric field, the IPMC beam will vibrate at a frequency equal to that of the applied electric potential.

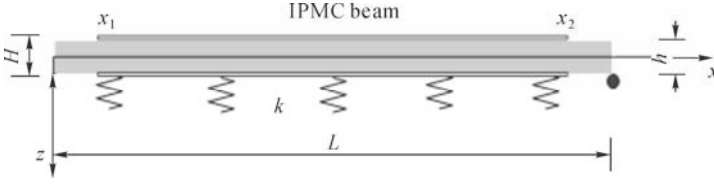


Fig. 15.1 Configuration of an IPMC beam on human tissue

The motion equation of the beam can be obtained from Euler-Bernoulli's beam theory as (Soedel, 2004)

$$\frac{\partial^2 [M(x,t) - M^e(x,t)]}{\partial x^2} + \rho A \frac{\partial^2 u_3(x,t)}{\partial t^2} + c_v \frac{\partial u_3(x,t)}{\partial t} + k \cdot u_3(x,t) = 0 \quad (15.1)$$

where $M(x,t)$ is the bending moment in the IPMC beam; $M^e(x,t)$ is the bending moment due to the electric field; ρ is the material density of the IPMC beam; A is the cross-sectional area of the beam; c_v is the viscous damping coefficient of the IPMC beam; and $u_3(x,t)$ is the transverse displacement of the beam.

Transferring the term due to electric field to the right hand side and utilizing the strain-stress and strain-displacement relationships, the following equation can be obtained

$$YI \cdot \frac{\partial^4 u_3}{\partial x^4} + \rho A \frac{\partial^2 u_3}{\partial t^2} + c_v \frac{\partial u_3}{\partial t} + k u_3 = \frac{\partial^2 M^e(x,t)}{\partial x^2} \quad (15.2)$$

where Y and I are the Young's modulus and moment of inertia of the beam, respectively.

Since the IPMC beam will undergo pure bending at the frequency of the applied electric potential, $M^e(x,t)$ can be expressed as

$$M^e(x,t) = M_0 \cdot [H(x-x_1) - H(x-x_2)] e^{j(\Omega t - \delta_0)} \quad (15.3)$$

where $H(\cdot)$ is the Heaviside function; M_0 is the time-independent amplitude of bending moment; and $\delta_0 = \pi/2$ is the phase difference between bending moment and applied electric potential which can be determined using Eq. (14.71).

Using the method of separation of variables, the solution of Eq. (15.2) can be derived as

$$u_3(x,t) = \sum_{m=1}^{\infty} -\frac{2m\pi M_0^e [\cos(\frac{m\pi x_1}{L}) - \cos(\frac{m\pi x_2}{L})]}{\rho A L^2 \omega_m^2 \sqrt{(1 - \Omega^2 / \omega_m^2)^2 + [c_v \Omega / (\rho A \omega_m^2)]^2}} \sin(\frac{m\pi x}{L}) e^{j(\Omega t - \delta_m)} \quad (15.4)$$

where $\omega_m = \sqrt{(YI \cdot (m^4 \pi^4) / L^4 + k) / \rho A}$ is the natural frequency of the beam for zero damping; and $\delta_m = \delta_0 + \tan^{-1} \frac{c_v \Omega / \rho A}{\omega_m^2 - \Omega^2}$ is the phase lag due to viscous damping.

With the solution of Eq. (15.4), the total force generated by the IPMC beam can be readily obtained by

$$p = k \cdot \int_0^L u_3 H(u_3) dx. \quad (15.5)$$

Computation of the total pressure can be implemented by numerical integration.

15.2.2 Illustrative Examples and Discussions

• Illustrative Examples

Consider a Nafion-based IPMC beam in Li^+ form with a length of 18 mm, a width of 2 mm and a thickness of 224 μm . The plating metal is platinum and the electrode thickness is 6 μm for both the top and bottom surfaces of the IPMC beam. Assume that the initial water uptake of IPMC is $w_0 = 0.533$ and the electric potential is a 1-V AC signal. For simplicity, viscous damping of the IPMC is set as zero. The other material properties used are as listed in Table 14.1.

The AC signal is a 1-volt sinusoidal potential with a frequency of 0.25 Hz. The stiffness of tissue is set as 15 kPa, which is within the range of experimental data of the passive stiffness of hamster trabecula (Abe *et al.*, 1996). Using Eq. (15.4), the beam deflection curve at any time can be obtained. The total terms of summation used in Eq. (15.4) is $m = 100$. Fig. 15.2 and Fig. 15.3 respectively illustrate the IPMC beam deflection and the pressure distribution on human tissue when the electric potential is at its maximum. It can be observed that the maximum deflection of IPMC beam is in the order of 0.01 mm and the maximum pressure is around 120 Pa. The total pressure can be evaluated by Eq. (15.5), which is 0.2298 gram for the pressure distribution in Fig. 15.3. This pressure is equivalent to 0.4693 mmHg on the human tissue beneath the beam. Fig. 15.4 and Fig. 15.5 show the beam deflection and pressure distribution for the tissue stiffness varying from 0 to 20 kPa. It is evident that the displacement reduces with increase of stiffness. The maximum deflection of beam for zero foundation stiffness is about 0.45 mm. However, for the pressure distribution, the higher the tissue stiffness, the larger the maximum pressure value. It is also noted that the displacement curve of beam for low stiffness (0 and 1 kPa) is different from that of high stiffness (above 5 kPa).

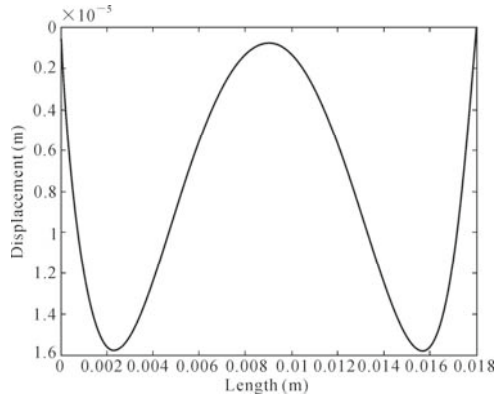


Fig. 15.2 Deflection of IPMC beam under 1-V sinusoidal potential ($k=15$ kPa)

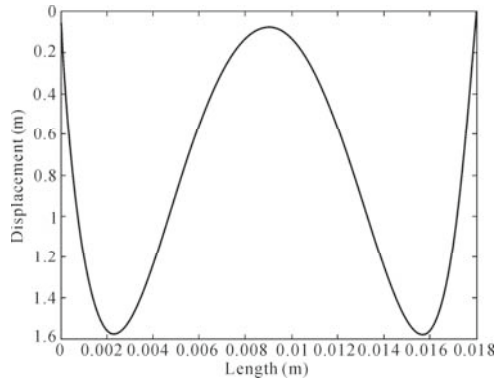


Fig. 15.3 Pressure distribution on human tissue under 1-V sinusoidal potential ($k=15$ kPa)

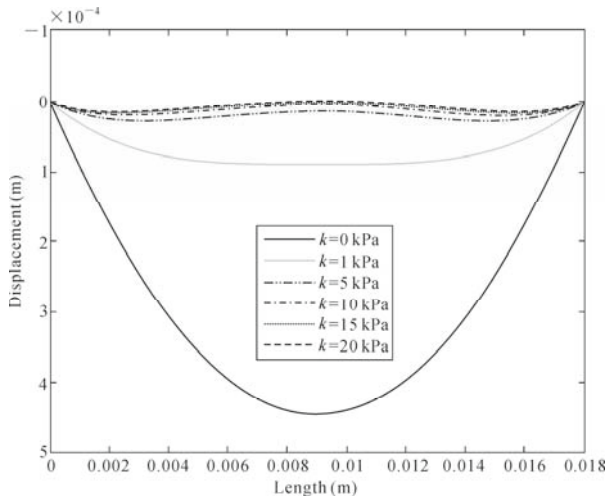


Fig. 15.4 Displacements vs. tissue stiffness

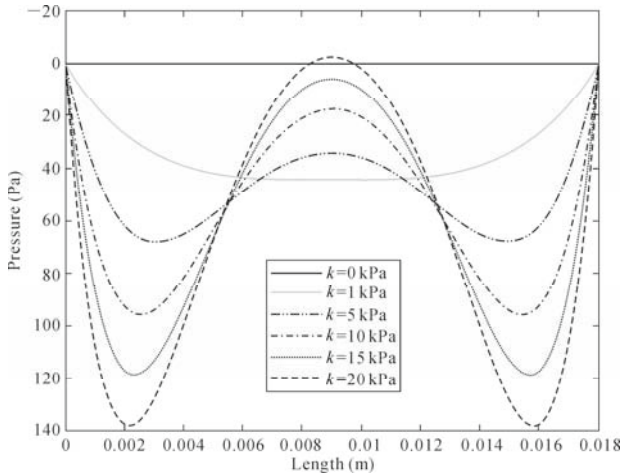


Fig. 15.5 Pressure vs. tissue stiffness

• *Optimal Electrode Length*

It is evident from Eq. (15.4) that, for different values of x_1 and x_2 , which determine the position and length of the electrode, the maximum transverse displacement and therefore the generative pressure is different. For biomedical applications of IPMC, maximum deflection and maximum generative pressure may be required for different purposes. For examples, maximum pressure is needed for heart compression bands and maximum deflection is sometime necessary for surgical tools. To generate the maximum deflection or pressure, optimal values of coordinates of x_1 and x_2 can be calculated using the developed model. For ease of computation, we assume that the stiffness of beam does not change due to changes in the electrode location and length. In Chapter 9, the optimal placement of a PZT actuator on a rectangular plate in terms of maximizing vibration amplitude has been studied. The natural frequency is used as a measure to determine the optimal location of PZT actuator. As IPMC is generally actuated at low frequency, far below the first natural frequency of the beam, the predominant vibration mode is the first mode. Therefore, to maximize the first vibration mode, the values of x_1 and x_2 should maximize the absolute value of $\left[\cos\left(\frac{\pi x_1}{L}\right) - \cos\left(\frac{\pi x_2}{L}\right) \right]$, where $x_1 \neq x_2$, and $x_1, x_2 \in [0, L]$. It is obvious that the solutions are $x_1=0$ and $x_2=L$ or vice versa.

However, when the elastic foundation beneath the IPMC beam is stiff, all vibration modes will have similar, small contributions to the overall vibration. In this condition, the first mode may not appear to be dominant, such as the deflection curve in Fig. 15.2. Fig. 15.6 shows the influence of the electrode coordinates x_1 and x_2 on the maximum beam deflection for the case of Fig. 15.2.

The maximum beam deflection of any (x_1, x_2) combination is denoted by the color of the point, which can be read from the color bar at the right. It is observed that the optimal location of the electrode is at either end of the beam with the electrode lengths of $0.25L$ to $0.39L$, *i.e.*, 4.5 to 7.0 mm. For higher foundation stiffness, say 40 kPa, the value of optimal length reduces. Fig. 15.7 shows the relationship between the electrode coordinates and the maximum beam deflection for this case. The optimal electrode position is also close to either end of the beam with electrode lengths of $0.22L$ to $0.27L$. Fig. 15.8 shows the optimal electrode coordinates for the IPMC beam with foundation stiffness of 0.9 kPa. It is obvious that the optimal length of electrode is equal to the length of beam.

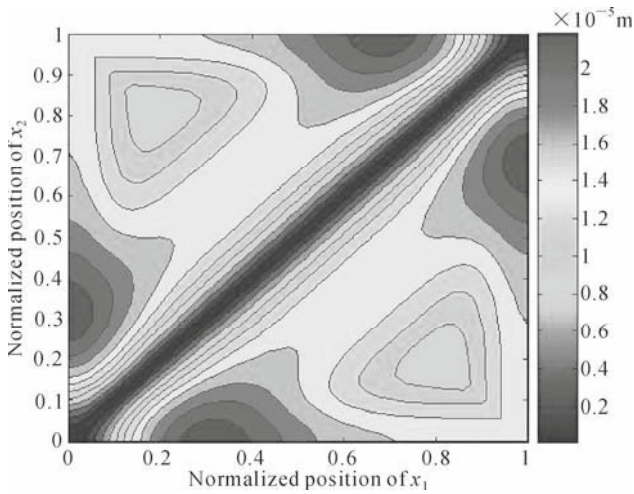


Fig. 15.6 Relationship between electrode coordinates and maximum beam deflection ($k=15$ kPa)

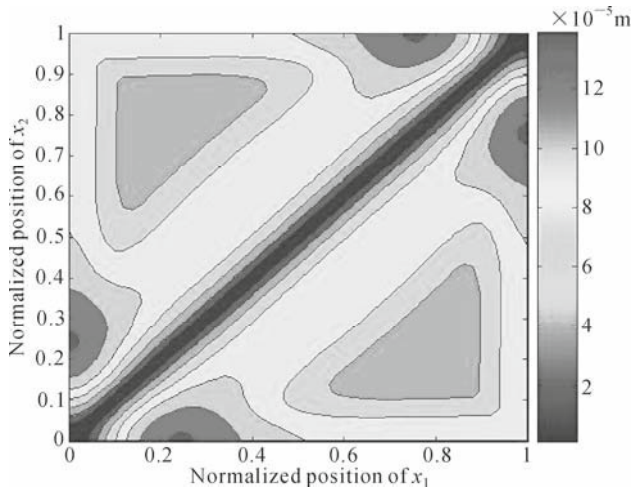


Fig. 15.7 Relationship between electrode coordinates and maximum beam deflection ($k=40$ kPa)

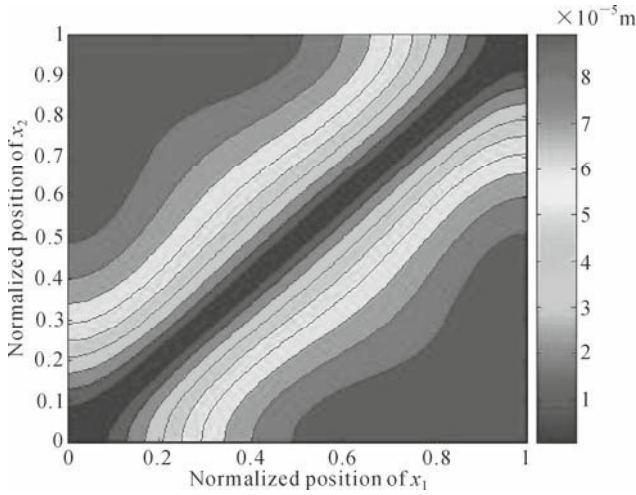


Fig. 15.8 Relationship between electrode coordinates and maximum beam deflection ($k=0.9 \text{ kPa}$)

Therefore it can be concluded that, for soft foundations, the electrode should cover the entire beam surface; while for stiff foundations, the electrode should be located near either end of the beam but the length of the electrode need not necessarily cover the entire beam.

Another issue is the optimal location and length of the electrode in terms of maximizing the total pressure. Figs. 15.9 – 15.11 illustrate the relationships between the electrode coordinates and the generative pressure for foundation stiffnesses of 0.9, 15 and 40 kPa, respectively. All the results indicate that the optimal electrode length is equal to the length of the beam. Thus, IPMC beam with fully covered electrode will generate the largest force compared with the other electrode configuration for the simply supported condition.

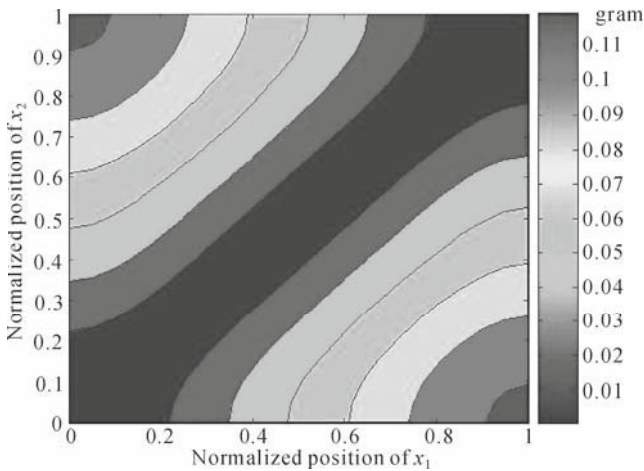


Fig. 15.9 Relationship between electrode coordinates and pressure ($k=0.9 \text{ kPa}$)

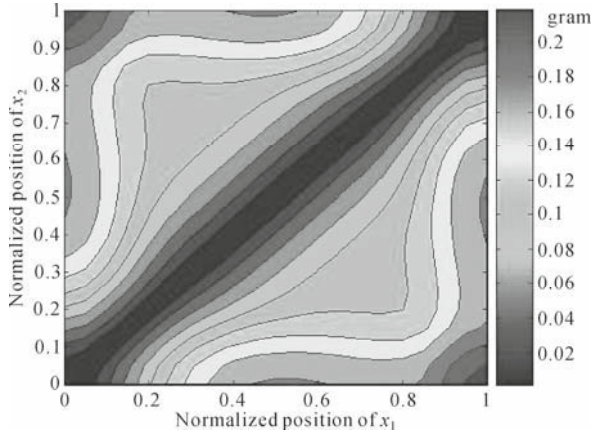


Fig. 15.10 Relationship between electrode coordinates and pressure ($k=15$ kPa)

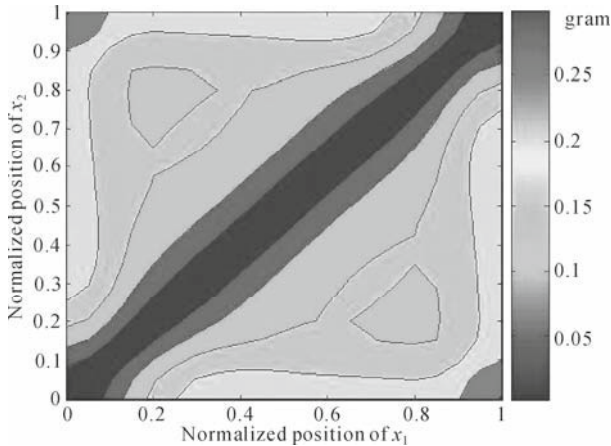


Fig. 15.11 Relationship between electrode coordinates and pressure ($k=40$ kPa)

15.2.3 Multiple Electrodes

If the IPMC beam is discretely plated with multiple electrodes and the applied electric potentials are different for each electrode, the IPMC beam will be more flexible. In such situation, the IPMC beam will be able to produce larger pressure or displacement on the human tissue. For this case, Eq. (15.4) should be modified as

$$u_3(x, t) = \sum_{n=1}^s \sum_{m=1}^{\infty} - \frac{2m\pi M_0^e \left[\cos\left(\frac{m\pi x_{n1}}{L}\right) - \cos\left(\frac{m\pi x_{n2}}{L}\right) \right]}{\rho A L^2 \omega_m^2 \sqrt{(1 - \Omega^2 / \omega_m^2)^2 + [c_v \Omega / (\rho A \omega_m^2)]^2}} \sin\left(\frac{m\pi x}{L}\right) f_n(t) \quad (15.6)$$

where s is the total number of discrete electrodes and $f_n(t)$ is the time variation function of the electric potential applied to the n^{th} electrode. From Eq. (15.6), it can be deduced that larger transverse displacement can be achieved by multiple electrodes. However, multiple electrodes imply complexity and difficulty in operating the control system.

A 2-electrode IPMC beam is studied (Fig. 15.12). The two electrodes with the same length of $0.35L$ are located at the two ends of the beam. To avoid computational difficulty due to change of beam stiffness, the region in between the electrodes is also considered to be plated with platinum but is isolated from the electrodes by a negligible small interval. This can be achieved by chemical etching. The foundation stiffness is set as 15 kPa. Figs. 15.13 and 15.14 illustrate deflections of the beam under identical and opposite electric potentials, respectively. It is found that opposite electric potential can produce larger transverse displacement. However, calculation shows that the generative pressure for Figs. 15.13 and 15.14 are 0.2935 g and 0.1895 g, respectively. This means that, when the two electrodes are controlled by identical potentials, greater pressure will be generated on the human tissue.

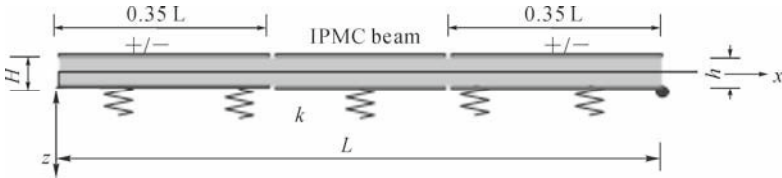


Fig. 15.12 Configuration of two discrete electrodes

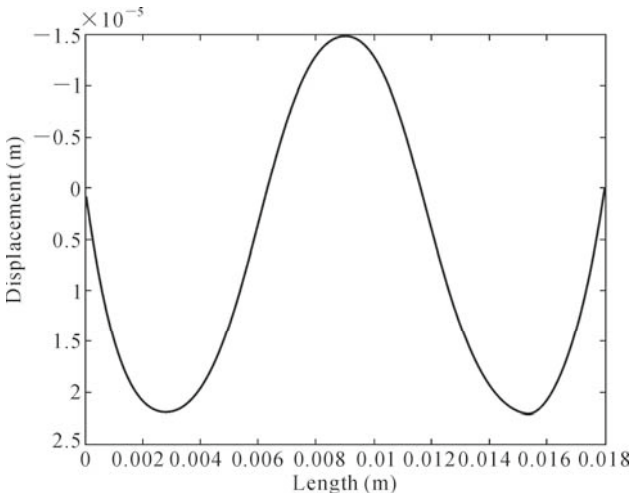


Fig. 15.13 Deflection of beam with two electrodes under identical potentials

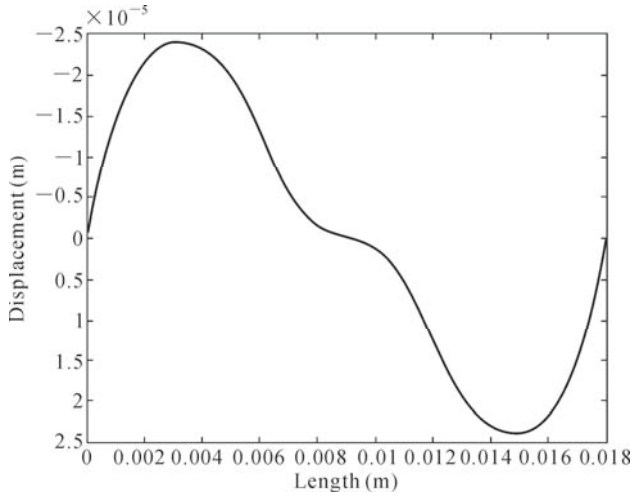


Fig. 15.14 Deflection of beam with two electrodes under opposite potentials

15.3 IPMC Ring with Elastic Medium

Shahinpoor and Kim (2005) proposed using an IPMC ring structure to serve as a heart compression band and scleral band to apply supplementary pressure to human organs. In this section, an IPMC ring filled with elastic medium is investigated. An analytical model is developed for an IPMC circular ring filled with elastic medium, where the elastic medium is used to model human tissues or organs. A closed-form solution is obtained to depict the vibration response of the IPMC ring. Based on this solution, the characteristics of vibration are discussed. To increase the flexibility of the IPMC ring, a segmented IPMC ring is also considered.

15.3.1 Problem Formulation

Consider a thin IPMC circular ring with outer radius R , inner radius r and width b (Fig. 15.15). The electrode is located between θ_1 and θ_2 . The motion equation for a circular ring can be deduced from Love's shell theory as (Soedel, 2004)

$$\frac{1}{R} \frac{\partial(N_{\theta\theta} - N_{\theta\theta}^e)}{\partial\theta} + \frac{1}{R^2} \frac{\partial(M_{\theta\theta} - M_{\theta\theta}^e)}{\partial\theta} - \rho h \frac{\partial^2 u_\theta}{\partial t^2} = 0 \quad (15.7)$$

$$\frac{1}{R^2} \frac{\partial^2 (M_{\theta\theta} - M_{\theta\theta}^e)}{\partial \theta^2} - \frac{N_{\theta\theta} - N_{\theta\theta}^e}{R} - kw - \rho h \frac{\partial^2 u_3}{\partial t^2} = 0 \quad (15.8)$$

where $N_{\theta\theta}$ and $N_{\theta\theta}^e$ are the membrane force resultants in the circumferential direction; and $M_{\theta\theta}$ and $M_{\theta\theta}^e$ are the corresponding bending moments. The superscript e denotes the membrane force or bending moment due to the applied electric potential; ρ is the material density of IPMC; $H=R-r$ is the thickness of the IPMC ring; u_θ and u_3 are the displacements in the circumferential and radial directions, respectively; k is the elastic foundation stiffness; and t is time.

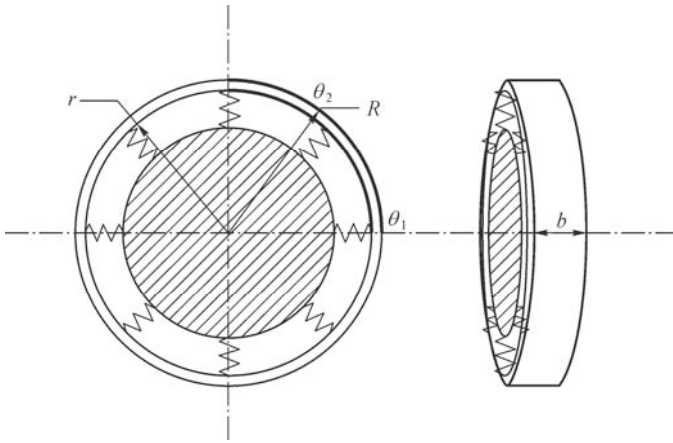


Fig. 15.15 A circular IPMC ring filled with elastic medium

Transferring the terms due to electric field to the right hand side, Eqs. (15.7) and (15.8) can be converted to

$$\frac{1}{R} \frac{\partial N_{\theta\theta}}{\partial \theta} + \frac{1}{R^2} \frac{\partial M_{\theta\theta}}{\partial \theta} - \rho H \frac{\partial^2 u_\theta}{\partial t^2} = \frac{1}{R} \frac{\partial N_{\theta\theta}^e}{\partial \theta} + \frac{1}{R^2} \frac{\partial M_{\theta\theta}^e}{\partial \theta} \quad (15.9)$$

$$\frac{1}{R^2} \frac{\partial^2 M_{\theta\theta}}{\partial \theta^2} - \frac{N_{\theta\theta}}{R} - ku_3 - \rho H \frac{\partial^2 u_3}{\partial t^2} = \frac{1}{R^2} \frac{\partial^2 M_{\theta\theta}^e}{\partial \theta^2} - \frac{N_{\theta\theta}^e}{R} \quad (15.10)$$

The membrane forces and the corresponding bending moments in Eqs. (15.9) and (15.10) are defined by

$$N_{\theta\theta} = \int_{-H/2}^{H/2} \sigma_{\theta\theta} \cdot dz \quad (15.11)$$

$$M_{\theta\theta} = \int_{-H/2}^{H/2} \sigma_{\theta\theta} \cdot z dz \quad (15.12)$$

where $\sigma_{\theta\theta}$ is the normal stress in the circumferential direction.

For a thin circular ring, the stress-strain relation under plain stress condition is

$$\sigma_{\theta\theta} = Y \cdot \varepsilon_{\theta\theta} \quad (15.13)$$

where Y and $\varepsilon_{\theta\theta}$ are the Young's modulus and the normal strain in the circumferential direction, respectively. The strain-displacement relation can be expressed as

$$\varepsilon_{\theta\theta} = \frac{1}{R} \left(\frac{\partial u_{\theta}}{\partial \theta} + u_3 \right) + \frac{z}{R^2} \left(\frac{\partial u_{\theta}}{\partial \theta} - \frac{\partial^2 u_3}{\partial \theta^2} \right) \quad (15.14)$$

Substituting Eqs. (15.13) and (15.14) into Eqs. (15.9) to (15.12), the motion equation can be written in a matrix form as

$$\begin{bmatrix} L_{11} & L_{12} \\ L_{21} & L_{22} \end{bmatrix} \cdot \begin{bmatrix} u_{\theta} \\ u_3 \end{bmatrix} = \begin{bmatrix} f_{\theta} \\ f_r \end{bmatrix} \quad (15.15)$$

where

$$L_{11} = \left(\frac{K}{R^2} + \frac{D}{R^4} \right) \frac{\partial^2}{\partial \theta^2} - \rho H \frac{\partial^2}{\partial t^2} \quad (15.16)$$

$$L_{12} = -\frac{D}{R^4} \frac{\partial^3}{\partial \theta^3} + \frac{K}{R^2} \frac{\partial}{\partial \theta} \quad (15.17)$$

$$L_{21} = \frac{D}{R^4} \frac{\partial^3}{\partial \theta^3} - \frac{K}{R^2} \frac{\partial}{\partial \theta} \quad (15.18)$$

$$L_{22} = -\frac{D}{R^4} \frac{\partial^4}{\partial \theta^4} - \frac{K}{R^2} - \rho H \frac{\partial^2}{\partial t^2} - k \quad (15.19)$$

$$\begin{bmatrix} f_{\theta} \\ f_r \end{bmatrix} = \begin{bmatrix} \frac{1}{R} \frac{\partial N_{\theta\theta}^e}{\partial \theta} + \frac{1}{R^2} \frac{\partial M_{\theta\theta}^e}{\partial \theta} \\ \frac{1}{R^2} \frac{\partial^2 M_{\theta\theta}^e}{\partial \theta^2} - \frac{N_{\theta\theta}^e}{R} \end{bmatrix} \quad (15.20)$$

$$K = YHb, \quad D = Y \cdot H^3b / 12 \quad (15.21)$$

The governing equation Eq. (15.15) can be solved by the method of modal expansion.

Since the IPMC ring vibrates in a pure bending mode when actuated, $N_{\theta\theta}^e = 0$ can be assumed. Considering that the bending moment of IPMC is uniform within the regions of the electrodes, the moment distribution of IPMC ring can be expressed as

$$M_{\theta\theta}^e = M_0 [H(\theta - \theta_1) - H(\theta - \theta_2)] e^{j\Omega t} \quad (15.22)$$

where M_0 is the time independent part of Eq. (14.71), expressed as

$$M_0 = -\frac{Y_b b h L_A}{6(1 + w_0)} \left\{ \frac{f_A}{f_{A1}} \left[\exp\left(\frac{f_{A1}}{\Omega}\right) - 1 \right] - \frac{\beta f_C}{f_{C1}} \left[\exp\left(\frac{f_{C1}}{\Omega}\right) - 1 \right] \right\} \quad (15.23)$$

According to Eq. (15.20), the force vector is

$$\begin{bmatrix} f_\theta \\ f_r \end{bmatrix} = \begin{bmatrix} \frac{1}{R^2} M_0 [\delta(\theta - \theta_1) - \delta(\theta - \theta_2)] \\ \frac{1}{R^2} M_0 [\delta'(\theta - \theta_1) - \delta'(\theta - \theta_2)] \end{bmatrix} e^{j\Omega t} \quad (15.24)$$

15.3.2 Displacement Solutions

For a closed circular ring, the solution can be found in below form:

$$u_\theta(\theta, t) = \sum_{n=1}^{\infty} A_n \sin(n\theta + \varphi) e^{j\Omega t} \quad (15.25)$$

$$u_r(\theta, t) = \sum_{n=1}^{\infty} B_n \cos(n\theta + \varphi) e^{j\Omega t} \quad (15.26)$$

where φ is a phase angle.

When $\varphi = 0$, the natural modes of the ring can be expressed as

$$U_{\theta n1} = A_{n1} \sin(n\theta) e^{j\Omega t} \quad (15.27)$$

$$U_{3n1} = B_{n1} \cos(n\theta) e^{i\Omega t} \quad (15.28)$$

For a complete solution, another orthogonal mode should be taken into account.

When $\varphi = \pi/(2n)$,

$$U_{\theta n2} = A_{n2} \cos(n\theta) e^{i\Omega t} \quad (15.29)$$

$$U_{3n2} = B_{n2} \sin(n\theta) e^{i\Omega t} \quad (15.30)$$

For $\varphi = 0$, the modal force vector is

$$\mathbf{F}_{n1} = \begin{bmatrix} -\frac{M_0}{R^2\pi} [\sin(n\theta_2) - \sin(n\theta_1)] \\ \frac{nM_0}{R^2\pi} [\sin(n\theta_2) - \sin(n\theta_1)] \end{bmatrix} e^{i\Omega t} \quad (15.31)$$

The coefficients in Eqs. (15.27) and (15.28) can be obtained as:

$$\begin{bmatrix} A_{n1} \\ B_{n1} \end{bmatrix} = \begin{bmatrix} \rho H \Omega^2 - s_{11} & s_{12} \\ s_{21} & \rho H \Omega^2 - s_{22} \end{bmatrix}^{-1} \begin{bmatrix} -\frac{M_0}{R^2\pi} [\sin(n\theta_2) - \sin(n\theta_1)] \\ \frac{nM_0}{R^2\pi} [\cos(n\theta_2) - \cos(n\theta_1)] \end{bmatrix} \quad (15.32)$$

where

$$s_{11} = \left(\frac{K}{R^2} + \frac{D}{R^4} \right) n^2 \quad (15.33)$$

$$s_{12} = s_{21} = -\frac{D}{R^4} n^3 - \frac{K}{R^2} n \quad (15.34)$$

$$s_{22} = \frac{D}{R^4} n^4 + \frac{K}{R^2} + k \quad (15.35)$$

Similarly, for $\varphi = \pi/(2n)$, the coefficients in Eqs. (15.29) and (15.30) are

$$\begin{bmatrix} A_{n2} \\ B_{n2} \end{bmatrix} = \begin{bmatrix} \rho H \Omega^2 - s_{11} & -s_{12} \\ -s_{21} & \rho H \Omega^2 - s_{22} \end{bmatrix}^{-1} \begin{bmatrix} -\frac{M_0}{R^2\pi} [\cos(n\theta_2) - \cos(n\theta_1)] \\ -\frac{nM_0}{R^2\pi} [\sin(n\theta_2) - \sin(n\theta_2)] \end{bmatrix} \quad (15.36)$$

Using Eqs. (15.32) and (15.36), the final solution of the IPMC ring vibration can be expressed as:

$$\begin{bmatrix} u_\theta(\theta, t) \\ u_3(\theta, t) \end{bmatrix} = \sum_{n=1}^{\infty} \begin{bmatrix} \sin(n\theta) & 0 \\ 0 & \cos(n\theta) \end{bmatrix} \begin{bmatrix} A_{n1} \\ B_{n1} \end{bmatrix} e^{i\Omega t} + \sum_{n=1}^{\infty} \begin{bmatrix} \cos(n\theta) & 0 \\ 0 & \sin(n\theta) \end{bmatrix} \begin{bmatrix} A_{n2} \\ B_{n2} \end{bmatrix} e^{i\Omega t} \quad (15.37)$$

The corresponding total force generated on the elastic medium inside the ring can be calculated as:

$$p_3(t) = \int_0^{2\pi} k \cdot u_3(\theta, t) \cdot H(u_3) d\theta \quad (15.38)$$

More detailed derivation of the above formulation can be found in Yang and Zhang (2008).

15.3.3 Illustrative Examples

Assume a Nafion-based IPMC ring in Na^+ form with mean radius of 50 mm and thickness of 0.224 mm. The IPMC ring consists of Nafion membrane and platinum electrodes. The thickness is 212 μm for the Nafion membrane and 6 μm for the electrode on each surface. The applied electric potential is a 1.5-V sinusoidal signal with a frequency of 0.25 Hz. The calculated thicknesses of anode boundary and cathode boundary are $L_A = 9.78\ell$ and $L_C = 2.84\ell$, respectively, where $\ell = 0.862 \mu\text{m}$. The other model parameters considered are listed in Table 14.2.

Figs. 15.16 – 15.22 show the deformations of the IPMC ring for different electrode area with zero stiffness of elastic medium. As the elastic deformation of the IPMC ring is of interest, the rigid body motion due to the first vibration mode is not included in the calculation, *i.e.*, the lower limit of the summation in Eq. (15.37) is $n = 2$. It is observed that the maximum deformation of the IPMC ring varies for different electrode areas. As shown in Fig. 15.18 and Fig. 15.20, the IPMC ring has the largest deformation for electrode areas of $\pi/2$ and $3\pi/2$. In Fig. 15.22, when the IPMC is fully plated with electrodes, the deformation is zero. This is true because the bending moment cancels each other at each point. By changing the area of electrode, larger deformation can be achieved. This conclusion is meaningful for reducing the cost of IPMC materials.

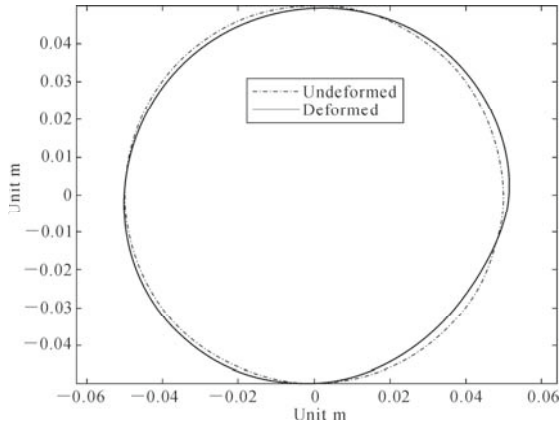


Fig. 15.16 Deformation of IPMC ring with electrode area of $\pi/6$

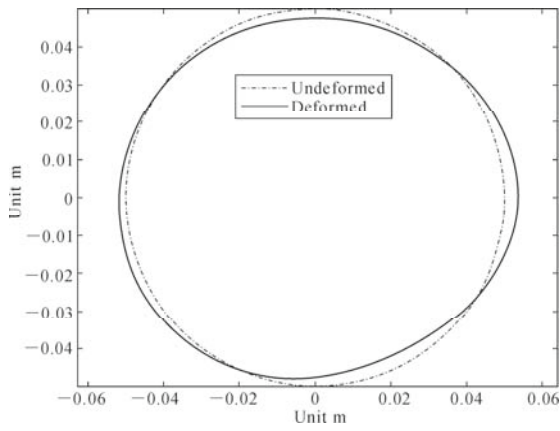


Fig. 15.17 Deformation of IPMC ring with electrode area of $\pi/3$

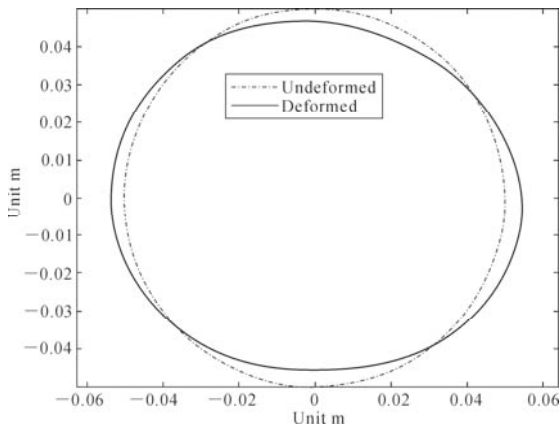


Fig. 15.18 Deformation of IPMC ring with electrode area of $\pi/2$

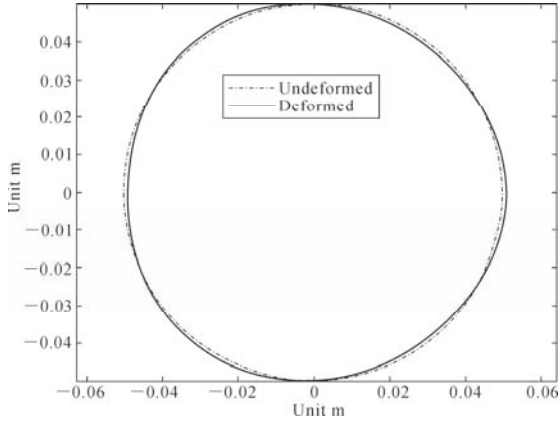


Fig. 15.19 Deformation of IPMC ring with electrode area of π

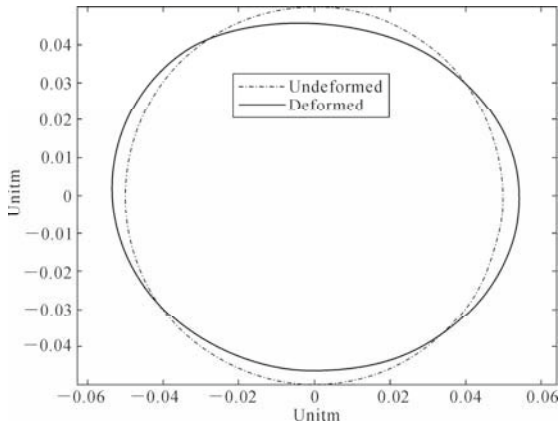


Fig. 15.20 Deformation of IPMC ring with electrode area of $3\pi/2$

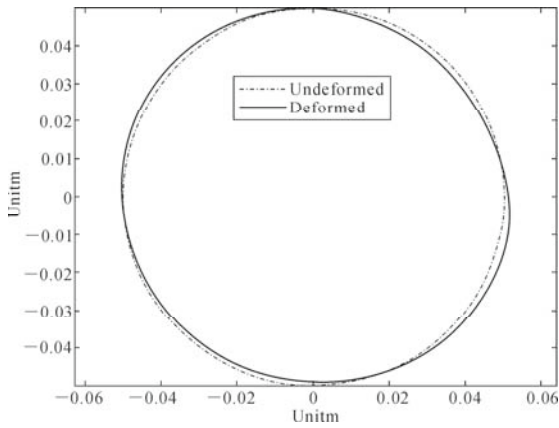


Fig. 15.21 Deformation of IPMC ring with electrode area of 1.9π

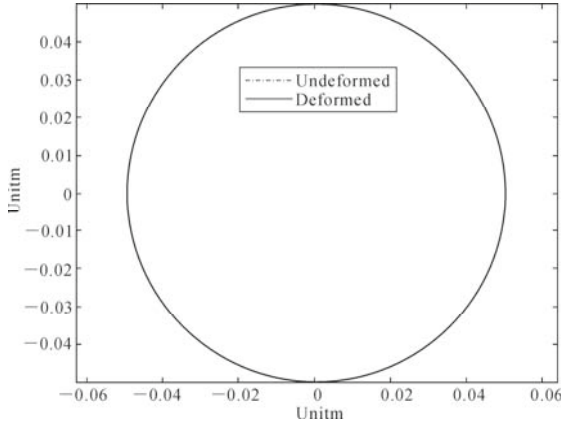


Fig. 15.22 Deformation of IPMC ring with electrode area of 2π

Table 15.1 summarizes the largest deformation of the IPMC ring for different electrode areas. It is evident that the largest radial displacement occurs when the electrode area is around $\pi/2$ and 1.5π . To further identify the electrode area corresponding to the largest radial deformation, a computer program is developed to find the relation between the electrode area and the maximum radial displacement. This computer program calculates the maximum radial displacement of the ring with different length of electrode. A figure is plotted for the maximum radial displacements vs. the length of electrode (Fig. 15.23). It is observed that, when the electrode area is around $\pi/2$ or $3\pi/2$, maximum radial displacement can be achieved.

Table 15.1 Maximum radial displacements for different electrode areas

Electrode area	$\pi/6$	$\pi/3$	$\pi/2$	π	1.5π	1.9π	2π
Maximum deformation (m)	0.0019	0.0037	0.0047	0.0011	0.0045	0.0019	0

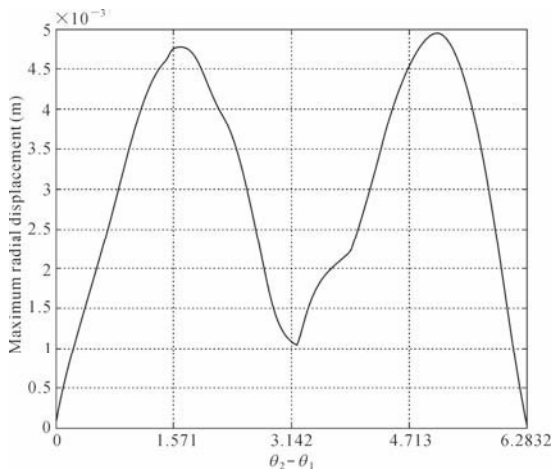


Fig. 15.23 Electrode areas vs. maximum radial displacements

If the ring is assembled by two or more IPMC strips and electric potentials are applied independently to the electrodes, the vibration of the ring will vary significantly. The solution for this case can be obtained by the superposition of Eq. (15.37) for different coordinates of electrodes. Fig. 15.24 illustrates an IPMC ring with segmented electrodes. Of the four segments, two opposite segments are set to be the electrodes. Both electrode areas are $\pi/2$.

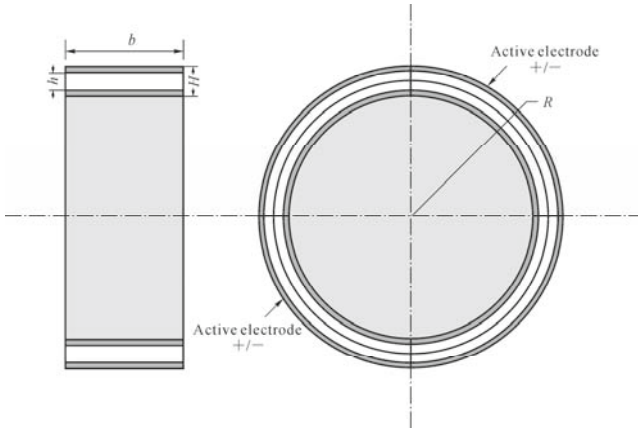


Fig. 15.24 Configuration of two active electrode areas of IPMC ring

Fig. 15.25 illustrates the IPMC ring deformation with two electrodes. Compared to the deformation of one electrode with area of $\pi/2$ (Fig. 15.18) the deformation is increased. The maximum radial displacement is 0.0082 m, which is 1.74 times the maximum radial displacement for single electrode.

The stiffness of the elastic medium in the above examples is set to zero. When the stiffness is not zero, the displacements are small as compared to the scale of the ring. The total pressure generated on the elastic medium by the ring can be evaluated by Eq. (15.38).

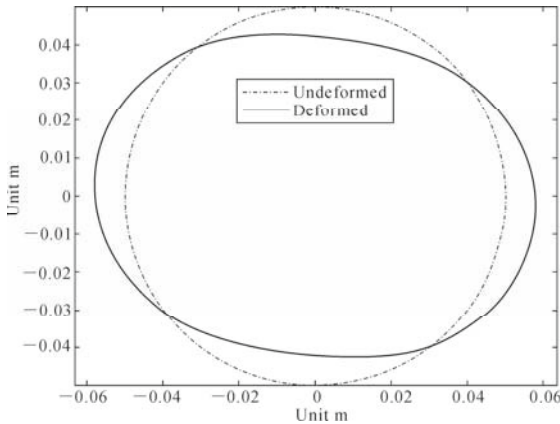


Fig. 15.25 Deformation of IPMC ring with two electrodes

Fig. 15.26 shows the relationship between the maximum radial displacement of the IPMC ring and the electrode area for six different elastic media. The stiffnesses of these elastic media are 0.3, 0.5, 1.0, 1.5, 2.33 and 3 kPa. It is found that, to achieve the largest displacement, the optimal electrode area is around 0.2-0.4 radian for the elastic media concerned. The higher the stiffness of the elastic medium, the smaller should be the active electrode area so as to achieve the largest displacement. Fig. 15.27 illustrates the pressure distribution of the IPMC ring for the two electrodes, as configured in Fig. 15.24, for the six different media. The pressure distribution (in N/m) is the distribution of generated pressure (in Pa) along the circumference of the ring, which is obtained by integrating the generated pressure along the width of the ring. It is observed that with the increase of stiffness of the elastic medium, the peak value of pressure also increases. For the elastic medium with stiffness of 2.33 kPa, the peak value of pressure distribution is 0.0707 N/m. Using Eq. (15.38), the overall force is calculated to be 0.0312 N, which is equivalent to 3.18 g of weight.

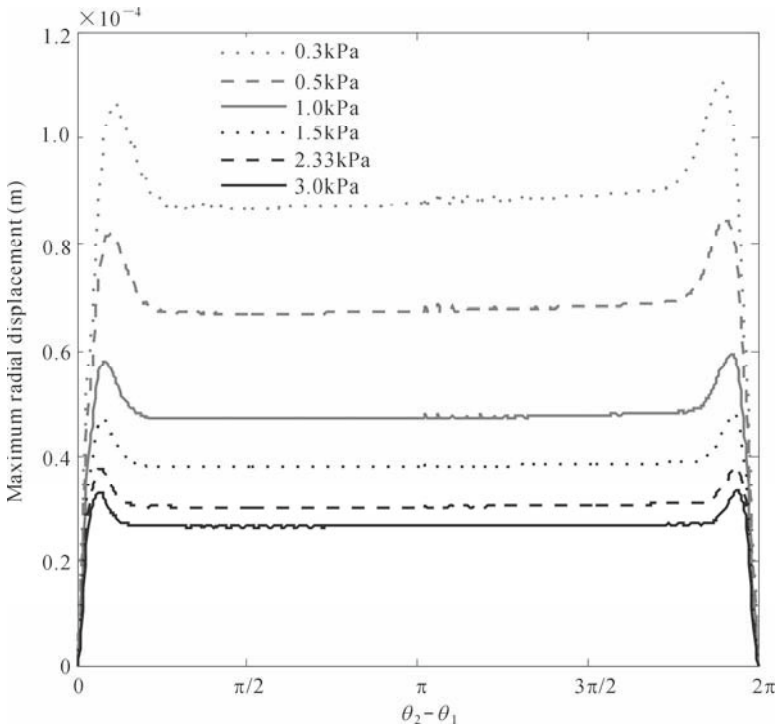


Fig. 15.26 Electrode area vs. maximum radial displacement for different elastic media

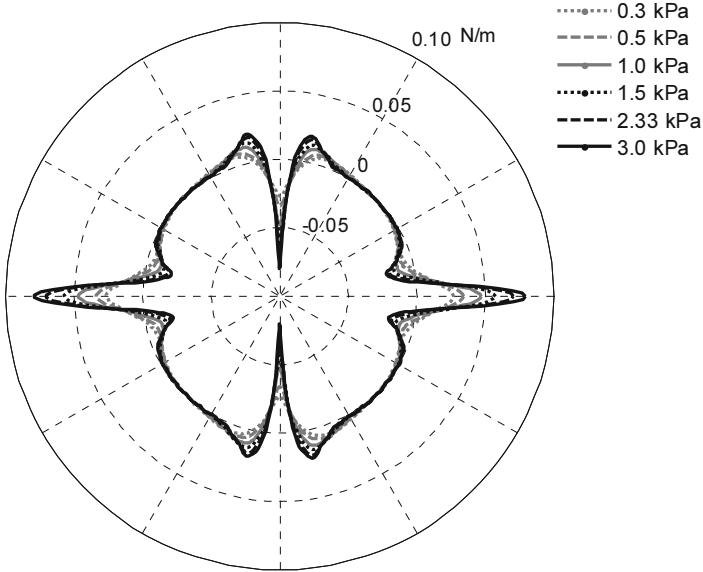


Fig. 15.27 Pressure distribution of IPMC ring with two electrodes

15.4 IPMC Shell with Flowing Fluid

In some applications, the IPMC may be fabricated in the form of cylindrical shell. This kind of IPMC structure can function as artificial vessels which are useful for biomedical practices. This section presents a study on an infinite IPMC cylindrical shell filled with steady-flow fluid. Vibrations of the shell-fluid coupled system occur when an electric potential is applied onto the electrodes of the IPMC. Analytical solutions are derived using the wave propagation method for the displacement of the cylindrical shell, the pressure in the liquid and the axial velocity of the liquid due to the electric potential excitation. The developed model will be useful for devices using IPMC cylindrical shell structures with or without contained fluid.

15.4.1 Problem Formulation

- *Motion Equation of Cylindrical Shell*

Consider a segment of an infinite IPMC cylindrical shell with a discrete electrode

(Fig. 15.28). The mean radius of the shell is R , the thickness of the shell wall is H and the thickness of the polyelectrolyte membrane part is h . The electrode of the shell covers the entire circumferential direction and locates between x_1 and x_2 in the axial direction.

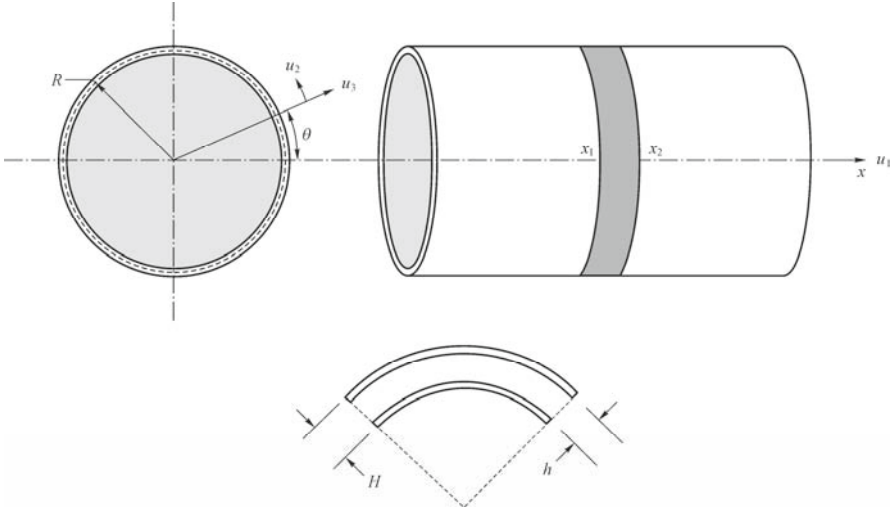


Fig. 15.28 Configuration of IPMC cylindrical shell filled with fluid

Assume that the IPMC cylindrical shell is completely filled with an inviscid and incompressible fluid, and an alternative electric potential is applied to the electrode on the IPMC shell. Due to the internal cation movement under electric field, the IPMC shell will vibrate at a frequency same as that of the applied electric potential, resulting in the contained fluid being disturbed. According to the thin shell theory, the following equations can be derived (Soedel, 2004),

$$\frac{\partial(N_{xx} - N_{xx}^e)}{\partial x} + \frac{1}{R} \frac{\partial N_{\theta x}}{\partial \theta} - c_v \frac{\partial u_1}{\partial t} - \rho H \frac{\partial^2 u_1}{\partial t^2} = 0 \quad (15.39)$$

$$\begin{aligned} \frac{\partial N_{x\theta}}{\partial x} + \frac{1}{R} \frac{\partial(N_{\theta\theta} - N_{\theta\theta}^e)}{\partial \theta} + \frac{1}{R} \frac{\partial M_{x\theta}}{\partial x} \\ + \frac{1}{R^2} \frac{\partial(M_{\theta\theta} - M_{\theta\theta}^e)}{\partial \theta} - c_v \frac{\partial u_2}{\partial t} - \rho H \frac{\partial^2 u_2}{\partial t^2} = 0 \end{aligned} \quad (15.40)$$

$$\begin{aligned} \frac{\partial^2(M_{xx} - M_{xx}^e)}{\partial x^2} + \frac{2}{R} \frac{\partial^2 M_{x\theta}}{\partial x \partial \theta} + \frac{1}{R^2} \frac{\partial^2(M_{\theta\theta} - M_{\theta\theta}^e)}{\partial \theta^2} - \frac{N_{\theta\theta} - N_{\theta\theta}^e}{R} \\ - c_v \frac{\partial u_3}{\partial t} - \rho H \frac{\partial^2 u_3}{\partial t^2} - p_p = 0 \end{aligned} \quad (15.41)$$

where N_{xx} , $N_{\theta x}$, $N_{x\theta}$, $N_{\theta\theta}$, M_{xx} , $M_{x\theta}$ and $M_{\theta\theta}$ are the membrane force resultants and bending moments in their respective directions; the superscript e denotes the effect due to electric potential; c_v is the damping coefficient of the IPMC shell; ρ is the material density of the shell; u_1 , u_2 and u_3 are the displacements of middle surface of the shell in the axial, circumferential and radial directions, respectively; and p_p is the perturbation pressure of fluid on the inner shell surface, which will be determined in Section 15.4.1.2.

Using the strain-stress and strain-displacement relationships of Flügge's shell theory (Soedel, 2004), the equation of motion can be obtained as

$$\begin{bmatrix} L_{11} & L_{12} & L_{13} \\ L_{21} & L_{22} & L_{23} \\ L_{31} & L_{32} & L_{33} \end{bmatrix} \begin{bmatrix} u_1 \\ u_2 \\ u_3 \end{bmatrix} = \gamma \begin{bmatrix} f_1 \\ f_2 \\ f_3 \end{bmatrix} \quad (15.42)$$

where L_{pq} ($p=1,2,3$ and $q=1,2,3$) are the differential operators defined as

$$\begin{aligned} L_{11} &= R^2 \frac{\partial^2}{\partial x^2} + (1+k) \frac{(1-\mu)}{2} \frac{\partial^2}{\partial \theta^2} - \frac{(1-\mu^2)R^2 c_v}{EH} \frac{\partial}{\partial t} - \frac{(1-\mu^2)\rho_s R^2}{E} \frac{\partial^2}{\partial t^2} \\ L_{12} &= L_{21} = R \frac{1+\mu}{2} \frac{\partial^2}{\partial x \partial \theta} \\ L_{13} &= L_{31} = R \mu \frac{\partial}{\partial x} + k(-R^3 \frac{\partial^3}{\partial x^3} + R \frac{1-\mu}{2} \frac{\partial^3}{\partial x \partial \theta^2}) \\ L_{22} &= R^2 \frac{(1-\mu)}{2} \frac{\partial^2}{\partial x^2} + \frac{\partial^2}{\partial \theta^2} + kR^2 \frac{3(1-\mu)}{2} \frac{\partial^2}{\partial x^2} - \frac{(1-\mu^2)R^2 c_v}{EH} \frac{\partial}{\partial t} - \frac{\rho_s(1-\mu^2)R^2}{E} \frac{\partial^2}{\partial t^2} \\ L_{23} &= L_{32} = \frac{\partial}{\partial \theta} - kR^2 \frac{(3-\mu)}{2} \frac{\partial^3}{\partial x^2 \partial \theta} \\ L_{33} &= 1+k+k\nabla^4 + 2k \frac{\partial^2}{\partial \theta^2} - \frac{(1-\mu^2)R^2 c_v}{EH} \frac{\partial}{\partial t} - \frac{\rho_s(1-\mu^2)R^2}{E} \frac{\partial^2}{\partial t^2} - \frac{(1-\mu^2)R^2 p_p}{EH} \end{aligned} \quad (15.43)$$

where $k = \frac{H^2}{12R^2}$ is a non-dimensional thickness parameter; μ is the Poisson's ratio; $\gamma = \frac{R^2(1-\mu^2)}{EH}$ and f_1 , f_2 and f_3 are the external loads in the axial, circumferential and radial directions, respectively, which can be expressed as

$$f_1 = \frac{\partial N_{xx}^e}{\partial x} \quad (15.44)$$

$$f_2 = \frac{1}{R} \frac{\partial N_{\theta\theta}^e}{\partial \theta} + \frac{1}{R^2} \frac{\partial M_{\theta\theta}^e}{\partial \theta} \quad (15.45)$$

$$f_3 = \frac{\partial^2 M_{xx}^e}{\partial x^2} + \frac{1}{R^2} \frac{\partial^2 M_{\theta\theta}^e}{\partial \theta^2} - \frac{N_{\theta\theta}^e}{R} \quad (15.46)$$

• *Fluid Perturbation*

Consider the fluid contained in the infinite cylindrical shell. Assume that the initial axial flow velocity is v_0 . When the IPMC shell vibrates due to the electric potential, the fluid inside the shell will be disturbed. The disturbed velocity field of the contained fluid is composed of two parts, the steady axial flow v_0 and the perturbation velocity due to the oscillation of the shell. Expressing the perturbation velocity as a function of perturbation potential Φ , the total velocity field can be written as

$$\begin{bmatrix} v_1 \\ v_2 \\ v_3 \end{bmatrix} = \begin{bmatrix} v_0 + \frac{\partial \Phi}{\partial x} \\ \frac{1}{r} \frac{\partial \Phi}{\partial \theta} \\ \frac{\partial \Phi}{\partial r} \end{bmatrix} \quad (15.47)$$

The governing equation of the irrotational potential flow can be described by the Laplace equation (Paidoussis, 2004) as

$$\frac{\partial^2 \Phi}{\partial r^2} + \frac{1}{r^2} \frac{\partial^2 \Phi}{\partial \theta^2} + \frac{\partial^2 \Phi}{\partial x^2} + \frac{1}{r} \frac{\partial \Phi}{\partial r} = 0 \quad (15.48)$$

The impermeability condition of the shell surface requires that the radial velocity of the fluid on the shell surface matches the instantaneous rate of change of the shell displacement in the radial direction. This boundary condition implies a permanent contact between the shell surface and the fluid boundary layer, which can be expressed as

$$v_3 \Big|_{r=R} = \frac{\partial \Phi}{\partial r} \Big|_{r=R} = \frac{\partial u_3}{\partial t} + v_0 \frac{\partial u_3}{\partial x} \quad (15.49)$$

The dynamic condition on the interface of the fluid and shell can be determined by the Bernoulli's equation for the disturbed motion as

$$\rho_f \frac{\partial \Phi}{\partial t} + \rho_f \frac{v_1^2 + v_2^2 + v_3^2}{2} + p_p = 0 \quad (15.50)$$

where ρ_f is the density of the contained liquid.

With Eqs. (15.47) and (15.50), the perturbation pressure on the fluid-shell interface can be obtained as

$$p_p = -\rho_f \left(\frac{\partial \Phi}{\partial t} + v_0 \frac{\partial \Phi}{\partial x} \right) \quad (15.51)$$

Note that the higher order terms in Eq. (15.51) can be neglected. The velocity potential Φ can be expressed as

$$\Phi(r, x, \theta, t) = \Lambda(r) e^{j(\lambda x/R + n\theta + \Omega t)} \quad (15.52)$$

where $\Lambda(r)$ is a function to be determined; j is the imaginary unit; λ is a complex coefficient; n is the circumferential wave number; Ω is the angular frequency and t is time.

Substituting Eq. (15.52) into Eq. (15.48), the following equation can be obtained

$$\frac{d^2 \Lambda}{dr^2} + \frac{1}{r} \frac{d\Lambda}{dr} - \left(\frac{n^2}{r^2} + \frac{\lambda^2}{R^2} \right) \Lambda = 0 \quad (15.53)$$

Eq. (15.53) can be solved in terms of the modified Bessel functions of the first and second kind:

$$\Lambda(r) = D_1 I_n(\lambda r/R) + D_2 K_n(\lambda r/R) \quad (15.54)$$

where D_1 and D_2 are coefficients; and I_n and K_n are the n^{th} order modified Bessel functions of the first and second kind, respectively. To derive a finite solution, D_2 should be zero for the internal flow as $K_n(\lambda r/R)$ is singular at $r = 0$. Similarly, D_1 should be zero for the external flow as $I_n(\lambda r/R)$ approaches infinity when $r \rightarrow \infty$.

From Eqs. (15.51), (15.52) and (15.54), the perturbation pressure can be obtained as

$$p_p = p_i - p_e, \quad (15.55)$$

where p_i is the internal pressure on the inner surface and p_e is the external pressure on the outer surface.

$$p_i = -\rho_i \frac{R}{n + \lambda I_{n+1}(\lambda) / I_n(\lambda)} \left(\frac{\partial}{\partial t} + v_0 \frac{\partial}{\partial x} \right)^2 u_3 \quad (15.56)$$

$$p_e = -\rho_e \frac{R}{n - \lambda K_{n+1}(\lambda) / K_n(\lambda)} \left(\frac{\partial}{\partial t} + v_0 \frac{\partial}{\partial x} \right)^2 u_3 \quad (15.57)$$

where ρ_i and ρ_e are the density of internal and external flow, respectively.

As the IPMC shell is in pure bending deformation under the electric potential, assumptions can be made that $N_{xx}^e = N_{\theta\theta}^e = 0$, and the bending moments in the two orthogonal direction are identical, *i.e.*, $M_{xx}^e = M_{\theta\theta}^e$, due to the homogeneous nature of IPMC. Consider that the bending moments are developed uniformly within the region of electrode,

$$M_{xx}^e = M_0 \cdot [H(x - x_1) - H(x - x_2)][H(\theta - 0) - H(\theta - 2\pi)]e^{j(\Omega t - \pi/2)} \quad (15.58)$$

$$M_{\theta\theta}^e = M_0 \cdot [H(\theta - 0) - H(\theta - 2\pi)][H(x - x_1) - H(x - x_2)]e^{j(\Omega t - \pi/2)} \quad (15.59)$$

where M_0 is the time-independent part of Eq. (14.71). Thus, the force vector in Eq. (15.42) can be determined as

$$\begin{bmatrix} f_1 \\ f_2 \\ f_3 \end{bmatrix} = \begin{bmatrix} 0 \\ 0 \\ M_0 [\delta'(x - x_1) - \delta'(x - x_2)] \end{bmatrix} \quad (15.60)$$

where $\delta'(\cdot)$ is the derivative of Dirac-delta function with respect to x .

15.4.2 Wave Propagation Solutions

The solution of displacement field to Eq. (15.42) can be written in the below form of traveling wave:

$$\begin{bmatrix} u_1 \\ u_2 \\ u_3 \end{bmatrix} = \begin{bmatrix} A \\ B \\ C \end{bmatrix} e^{j(\lambda x/R + n\theta + \Omega t)} \tag{15.61}$$

where A , B and C are complex coefficients.

Substituting Eq. (15.61) into Eq. (15.42) and equating the left-hand side to zero, a linear homogeneous equation can be obtained for free vibration as

$$\begin{bmatrix} a_{11} & a_{12} & a_{13} \\ a_{21} & a_{22} & a_{23} \\ a_{31} & a_{32} & a_{33} \end{bmatrix} \cdot \begin{bmatrix} A \\ B \\ C \end{bmatrix} = \begin{bmatrix} 0 \\ 0 \\ 0 \end{bmatrix} \tag{15.62}$$

where $a_{11} = \lambda^2 + \frac{1-\mu}{2} n^2(1+k) + j(\bar{c}_v \bar{\Omega}) - \bar{\Omega}^2$

$$a_{12} = a_{21} = \frac{1+\mu}{2} \lambda n$$

$$a_{13} = -j a_{31} = -j \lambda [\mu + k(\lambda^2 - \frac{1-\mu}{2} n^2)]$$

$$a_{22} = n^2 + \frac{1-\mu}{2} \lambda^2(1+3k) + j(\bar{c}_v \bar{\Omega}) - \bar{\Omega}^2$$

$$a_{23} = -j a_{32} = -j(n + \frac{3-\mu}{2} \lambda^2 n k)$$

$$a_{33} = -j \{ 1 + k[(\lambda^2 + n^2)^2 - 2n^2 + 1] + j(\bar{c}_v \bar{\Omega}) - \bar{\Omega}^2 - \frac{(R/h)(\rho_i / \rho_f)(\bar{\Omega} + \bar{U}_i \lambda)^2}{n + \lambda I_{n+1}(\lambda) / I_n(\lambda)} + \frac{(R/h)(\rho_e / \rho_f)(\bar{\Omega} + \bar{U}_e \lambda)^2}{n + \lambda K_{n+1}(\lambda) / K_n(\lambda)} \}$$

$$\bar{\Omega} = R \Omega \left[\frac{\rho(1-\mu^2)}{E} \right]^{1/2}$$

$$\bar{U}_i = v_0 \left[\frac{\rho(1-\mu^2)}{E} \right]^{1/2}$$

$$\bar{U}_e = 0$$

and

$$\bar{c}_v = c_v R \left[\frac{\rho(1-\mu^2)}{E} \right]^{1/2}$$

For non-trivial solution, the determinant of the coefficient matrix in Eq. (15.62) should be zero, *i.e.*,

$$\det \begin{bmatrix} a_{11} & a_{12} & a_{13} \\ a_{21} & a_{22} & a_{23} \\ a_{31} & a_{32} & a_{33} \end{bmatrix} = 0 \quad (15.63)$$

Through Eq. (15.63), the coefficient λ can be obtained for a given circumferential wave number n . Due to the transcendental nature of λ , there are infinite roots of λ for Eq. (15.63). Therefore, the complete solution of displacement field can be expressed as

$$\begin{bmatrix} u_1 \\ u_2 \\ u_3 \end{bmatrix} = \sum_{i=1}^{\infty} \begin{bmatrix} \alpha_i C_i \\ \gamma_i C_i \\ C_i \end{bmatrix} e^{i(\lambda_i x / R + n\theta + \Omega t)} \quad (15.64)$$

where the coefficients α_i and γ_i can be determined from Eq.(15.62) with the eigenvalue λ_i . However, since the available boundary conditions are generally not infinite, it is impossible to include infinite λ_i in Eq. (15.64). Moreover, the values of λ_i that contribute most to the modal shapes are those with small modulus. Thus, it is possible to use truncated set of λ_i , say four or eight, to represent the displacement field with acceptable accuracy. In this section, only eight λ_i are used for the calculation.

The values of C_i can be determined through the boundary conditions. There are four internal forces in the shell wall in the axial direction, which are the axial force N_{xx} , the bending moment M_{xx} , the transverse shear force S_{xx} and the torsional shear force T_{xx} , expressed as

$$N_{xx} = R \frac{\partial u_1}{\partial x} + \mu \frac{\partial u_2}{\partial \theta} + \mu u_3 - \frac{H^2}{12} \frac{\partial^2 u_3}{\partial x^2} z \quad (15.65)$$

$$M_{xx} = R^2 \frac{\partial^2 u_3}{\partial x^2} + \mu \frac{\partial^2 u_3}{\partial \theta^2} - \mu \frac{\partial u_2}{\partial \theta} - R \frac{\partial u_1}{\partial x} \quad (15.66)$$

$$S_{xx} = R^3 \frac{\partial^3 u_3}{\partial x^3} + (2 - \mu) R \frac{\partial^3 u_3}{\partial x \partial \theta^2} - \frac{3 - \mu}{2} R \frac{\partial^2 u_2}{\partial x \partial \theta} + \frac{1 - \mu}{2} \frac{\partial^2 u_1}{\partial \theta^2} - R^2 \frac{\partial^2 u_1}{\partial x^2} \quad (15.67)$$

$$T_{xx} = \frac{\partial u_1}{\partial \theta} + R \frac{\partial u_2}{\partial x} + \frac{H^2}{4R} \left(\frac{\partial u_2}{\partial x} - \frac{\partial^2 u_3}{\partial x \partial \theta} \right). \quad (15.68)$$

At x_1 and x_2 , the following boundary conditions apply

$$N_{xx}(x = x_1, x_2) = 0 \tag{15.69}$$

$$M_{xx}(x = x_1, x_2) = -M_0 \tag{15.70}$$

$$S_{xx}(x = x_1, x_2) = 0 \tag{15.71}$$

$$T_{xx}(x = x_1, x_2) = 0 \tag{15.72}$$

Substituting Eq. (15.64) into Eqs. (15.69) to (15.72) and utilizing Eqs. (15.65) to (15.68), the following equation can be obtained,

$$\begin{bmatrix} b_{11} & b_{12} & b_{13} & b_{14} & 0 & 0 & 0 & 0 \\ b_{21} & b_{22} & b_{23} & b_{24} & 0 & 0 & 0 & 0 \\ b_{31} & b_{32} & b_{33} & b_{34} & 0 & 0 & 0 & 0 \\ b_{41} & b_{42} & b_{43} & b_{44} & 0 & 0 & 0 & 0 \\ 0 & 0 & 0 & 0 & b_{55} & b_{56} & b_{57} & b_{58} \\ 0 & 0 & 0 & 0 & b_{65} & b_{66} & b_{67} & b_{68} \\ 0 & 0 & 0 & 0 & b_{75} & b_{76} & b_{77} & b_{78} \\ 0 & 0 & 0 & 0 & b_{85} & b_{86} & b_{87} & b_{88} \end{bmatrix} \cdot \begin{bmatrix} C_1 \\ C_2 \\ C_3 \\ C_4 \\ C_5 \\ C_6 \\ C_7 \\ C_8 \end{bmatrix} = \begin{bmatrix} 0 \\ -M_0 \\ 0 \\ 0 \\ 0 \\ -M_0 \\ 0 \\ 0 \end{bmatrix} \tag{15.73}$$

where

$$\begin{aligned} b_{1s} &= (j\alpha_s \lambda_s + j\mu\gamma_s n + \mu + k\lambda_s^2) e^{j(\lambda_s x_1 / R + n\theta)} \\ b_{2s} &= (-\lambda_s^2 - \mu n^2 - j\mu\gamma_s n - j\alpha_s \lambda_s) e^{j(\lambda_s x_1 / R + n\theta)} \\ b_{2s} &= (-\lambda_s^2 - \mu n^2 - j\mu\gamma_s n - j\alpha_s \lambda_s) e^{j(\lambda_s x_1 / R + n\theta)} \\ b_{3s} &= [-j\lambda_s^3 - j(2 - \mu)\lambda_s n^2 + (3 - \mu)\gamma_s \lambda_s n / 2 - (1 - \mu)\alpha_s n^2 / 2 + \alpha_s \lambda_s^2] e^{j(\lambda_s x_1 / R + n\theta)} \\ b_{4s} &= [j\alpha_s n + j\gamma_s \lambda_s n^2 + 3k(j\gamma_s \lambda_s + \lambda_s n)] e^{j(\lambda_s x_1 / R + n\theta)}, \quad s = 1, 2, 3, 4 \end{aligned}$$

and

$$\begin{aligned} b_{5m} &= (j\alpha_m \lambda_m + j\mu\gamma_m n + \mu + k\lambda_m^2) e^{j(\lambda_m x_2 / R + n\theta)} \\ b_{6m} &= (-\lambda_m^2 - \mu n^2 - j\mu\gamma_m n - j\alpha_m \lambda_m) e^{j(\lambda_m x_2 / R + n\theta)} \\ b_{7m} &= [-j\lambda_m^3 - j(2 - \mu)\lambda_m n^2 + (3 - \mu)\gamma_m \lambda_m n / 2 - (1 - \mu)\alpha_m n^2 / 2 + \alpha_m \lambda_m^2] e^{j(\lambda_m x_2 / R + n\theta)} \\ b_{8m} &= [j\alpha_m n + j\gamma_m \lambda_m n^2 + 3k(j\gamma_m \lambda_m + \lambda_m n)] e^{j(\lambda_m x_2 / R + n\theta)}, \quad m = 5, 6, 7, 8 \end{aligned}$$

The coefficient $C_i, i = 1, 2, \dots, 8$, can be solved from Eq. (15.73) as

$$\begin{bmatrix} C_1 \\ C_2 \\ C_3 \\ C_4 \\ C_5 \\ C_6 \\ C_7 \\ C_8 \end{bmatrix} = \begin{bmatrix} b_{11} & b_{12} & b_{13} & b_{14} & 0 & 0 & 0 & 0 \\ b_{21} & b_{22} & b_{23} & b_{24} & 0 & 0 & 0 & 0 \\ b_{31} & b_{32} & b_{33} & b_{34} & 0 & 0 & 0 & 0 \\ b_{41} & b_{42} & b_{43} & b_{44} & 0 & 0 & 0 & 0 \\ 0 & 0 & 0 & 0 & b_{55} & b_{56} & b_{57} & b_{58} \\ 0 & 0 & 0 & 0 & b_{65} & b_{66} & b_{67} & b_{68} \\ 0 & 0 & 0 & 0 & b_{75} & b_{76} & b_{77} & b_{78} \\ 0 & 0 & 0 & 0 & b_{85} & b_{86} & b_{87} & b_{88} \end{bmatrix}^{-1} \begin{bmatrix} 0 \\ -M_0 \\ 0 \\ 0 \\ 0 \\ -M_0 \\ 0 \\ 0 \end{bmatrix} \quad (15.74)$$

Therefore, for eight eigenvalues of λ , the displacement field is

$$\begin{bmatrix} u_1 \\ u_2 \\ u_3 \end{bmatrix} = \sum_{i=1}^8 \begin{bmatrix} \alpha_i C_i \\ \gamma_i C_i \\ C_i \end{bmatrix} e^{j(\lambda_i x / R + n\theta + \Omega t)} \quad (15.75)$$

The corresponding velocity field of the contained fluid can be obtained from Eqs. (15.75), (15.52) and (15.49) as

$$\begin{bmatrix} v_1 \\ v_2 \\ v_3 \end{bmatrix} = \begin{bmatrix} \sum_{i=1}^8 \frac{C_i \lambda_i (\Omega R + \lambda_i v_0) I_n(\lambda_i r / R)}{R(nI_n(\lambda_i) + \lambda_i I_{n+1}(\lambda_i))} e^{j(\lambda_i x / R + n\theta + \Omega t)} + v_0 \\ \sum_{i=1}^8 \frac{C_i n (\Omega R + \lambda_i v_0) I_n(\lambda_i r / R)}{r(nI_n(\lambda_i) + \lambda_i I_{n+1}(\lambda_i))} e^{j(\lambda_i x / R + n\theta + \Omega t)} \\ \sum_{i=1}^8 \frac{j C_i (\Omega R + \lambda_i v_0) (\lambda_i I_{n+1}(\lambda_i r / R) + n R I_n(\lambda_i r / R) / r)}{R(nI_n(\lambda_i) + \lambda_i I_{n+1}(\lambda_i))} e^{j(\lambda_i x / R + n\theta + \Omega t)} \end{bmatrix} \quad (15.76)$$

15.4.3 Illustrative Example and Discussion

To illustrate how the calculation procedure is carried out, assume a Nafion-based IPMC cylindrical shell in Na^+ form with mean radius of 15 mm and thickness of 224 μm . The IPMC cylindrical shell is composed of Nafion membrane and platinum electrode. The thickness of Nafion membrane is 212 μm and the thickness of electrode is 6 μm on each surface. The contained fluid is water with a density of 10^3 kg/m^3 , and the initial axial velocity is assumed to be 0.9 m/s. The applied electric potential is a 1.5-V sinusoidal signal with a frequency of 0.25 Hz. The coordinates of electrode are $x_1 = -0.005 \text{ m}$ and $x_2 = 0.005 \text{ m}$. The calculated thickness of anode boundary and cathode boundary are $L_A = 9.78 \ell$ and $L_C = 2.84 \ell$, respectively, where $\ell = 0.862 \mu\text{m}$. The damping coefficient c_v is set to zero to

ease the computation. The other model parameters used are as listed in Table 14.2.

Fig. 15.29 shows the deformation of the IPMC shell when the electric potential is at its maximum. The radial deformation of the shell is amplified 10 times for clearer illustration. It is observed that the waves are propagating symmetrically away from the electrode. The maximum axial velocity for this case is 0.9195 m/s, which is 2.17% larger than the initial flow. For v_2 and v_3 , the maximum velocities are 0.0592 and 0.0055 m/s, respectively. It is evident that the velocity components v_2 and v_3 are negligible for this case. The maximum shell deformation is about 0.4 mm.

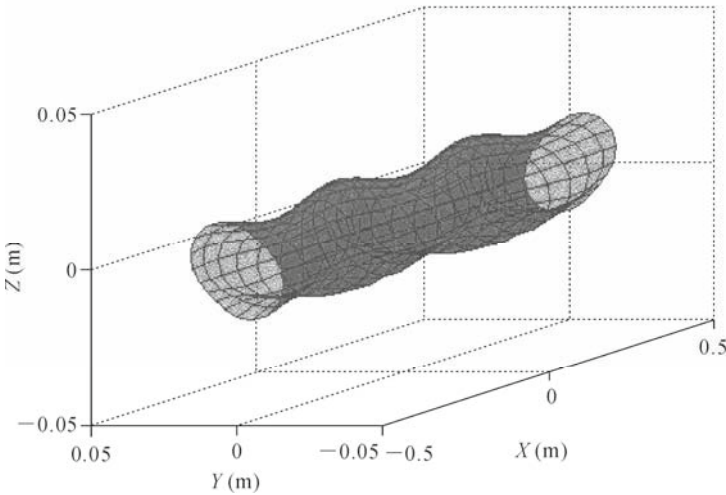


Fig. 15.29 Amplified shell deformation at electric signal of 1.5 V/0.25 Hz (10 times)

Compared to the initial axial velocity, the change in axial velocity is quite small for 1.5-V electric potential. However, the axial velocity can be increased by applying larger electric potential. For a 3-V signal, the maximum axial velocity is calculated to be 1.236 m/s, which is about 37.3% increase of the initial flow. This increase of axial flow is significant as compared to that under 1.5-volt signal. Fig. 15.30 shows the shell deformation in this condition without amplification. The maximum deformation of the shell is around 4.992 mm. It is worth mentioning that under such large deformation, Eq. (15.42) may not be valid. In addition, the IPMC material has become unstable under such high voltage. However, this example provides the approximate order of magnitude of shell deformation and maximum increase of axial flow, which is meaningful for future study.

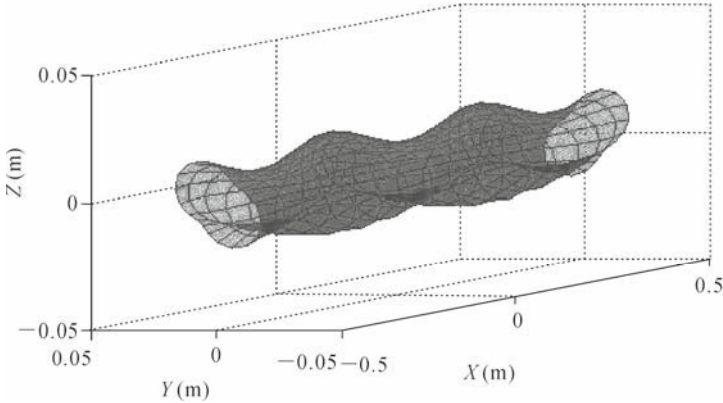


Fig. 15.30 Shell deformation at electric signal of 3 V/0.25 Hz

Due to the limitation of solvent electrolysis, the applied electric potential generally cannot be too high for IPMC, *e.g.*, 3 volts (electrolysis begins beyond 1.23 V) for water as solvent. Alternatively, the axial velocity can be increased by utilizing multiple electrodes as shown in Fig. 15.31. By individually exciting the different electrodes, it is possible to generate a wave that could significantly amplify the axial velocity of flow. The solutions for multiple electrodes can be obtained by the superposition of the results of single electrode obtained in this section. For other special cases, the developed model can be reduced to the solutions of IPMC shell with quiescent fluid or without fluid.

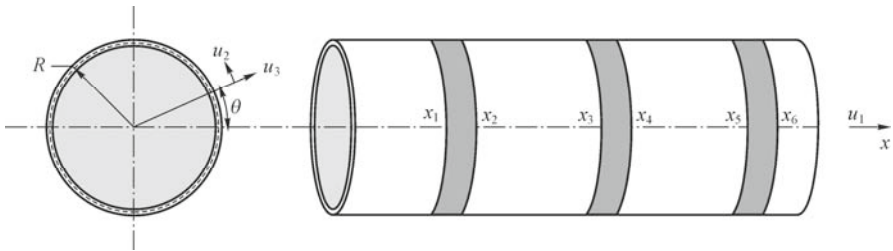


Fig. 15.31 Cylindrical shell with multiple electrodes

15.5 Summary

In this chapter, three models of IPMC-based structures, *i.e.*, an IPMC beam on human tissues, an IPMC ring with elastic medium and a fluid-filled IPMC cylindrical shell, are developed for possible biomedical applications. Analytical solutions are derived to account for the effect of IPMC actuation. The characteristics of structural response under IPMC actuation are presented and

discussed, with examples solved for illustration.

For the IPMC beam on human tissues, the beam deflection curve and the pressure distribution generated on human tissue are calculated. The optimal electrode location and length in terms of maximizing the deflection and generative pressure are discussed. It is found that, to achieve maximum deflection, the electrode should be located at either end of the beam, and to achieve higher total pressure, full length electrode should be used. The deflection curve and generative pressure for a multiple discrete electrode IPMC beam are also obtained. The developed model is useful not only for IPMC-related biomedical instruments interacting with human tissues but also for any other devices that utilize IPMC materials.

For the IPMC ring with elastic medium, the deformation of IPMC ring under different electrode areas and the pressure generated on elastic medium inside the ring are calculated. Multiple electrodes are also considered for the IPMC ring. From the results given in the illustrative examples, it is found that the largest radial displacement is dependent on the stiffness of the elastic medium. For zero stiffness, the largest ring displacement occurred when the electrode area was around $\pi/2$ and 1.5π for the IPMC with single electrode. While for the stiffness of elastic medium ranging from 0.3 to 3 kPa, the optimal electrode area was within $0.2 - 0.4$ rad. The peak value of the pressure generated on the elastic medium is found to increase with the stiffness of the elastic medium. The IPMC ring with multiple electrodes is shown to be capable of producing larger deformation and pressure than the IPMC ring with single electrode. This model provides a general procedure for modeling the dynamic behavior of IPMC ring structure with elastic medium.

For the fluid-filled IPMC shell, the vibration response of the shell and the velocity field of the contained fluid under applied electric potential are obtained by the wave propagation method. An illustrative example is presented and the results show that the flow velocity could be enhanced by the application of electric potential on the IPMC shell. It is also possible to further increase the axial flow by multiple electrodes, and the solutions obtained can be extended to multiple electrode analysis.

By examining the modeling results, it is found that the bending capacity of IPMC materials is not sufficient to be used directly for biomedical applications. The force generation capacity of IPMC materials needs to be improved by nano or chemical fabrication methods. Another alternative is to replace the IPMC materials with other stronger EAPs to generate sufficient force or bending moment for practical use. The results obtained in this chapter provide guidelines for further modeling and experimental tests of these models.

References

- Abe, H., Hayashi K and Sato, M. (1996). *Data Book on Mechanical Properties of Living Cells, Tissues, And Organs*, Tokyo: Springer-Verlag.
- Bar-Cohen, Y. (Editor) (2006). *Biomimetics: Biologically Inspired Technologies*, New York: CRC/Taylor & Francis.
- Paidoussis, M.P. (2004). *Fluid-Structure Interactions: Slender Structure and Axial Flow*, Vol. II, New York: Elsevier Academic Press.
- Paquette, J.W. and Kim, K.J. (2004). "Ionomeric electroactive polymer artificial muscle for naval applications," *IEEE Journal of Ocean Engineering* 29: 729-737.
- Shahinpoor, M. and Kim, K.J. (2005). "Ionic polymer-metal composites: IV. industrial and medical applications", *Smart Materials and Structures*, 14:197-214.
- Soedel, W. (2004). *Vibrations of Shells and Plates*, 3rd Edition, New York: Marcel Dekker.
- Yamakita, M., Kamamichi, N., Kaneda, Y., Asaka, K. and Luo, Z.W. (2004). "Development of an artificial muscle linear actuator using ionic polymer-metal composites", *Advanced Robotics*, 18: 383-399.
- Yang, Y.W. and Zhang, L. (2008). "Modeling of ionic polymer-metal composite ring", *Smart Materials and Structures*, 17: 015023.
- Zhang, L. and Yang, Y.W. (2006). "Modeling of a fluid-filled ionic polymer-metal composite cylindrical shell", *SPIE International Symposium on Smart Materials, Nano- and Micro-Smart Systems cum Smart Structures, Devices, and Systems III, Proceedings of SPIE 6414*, 64140E, 11-13 Dec. Adelaide, Australia.
- Zhang, L. and Yang, Y.W. (2007). "Modeling of ionic polymer-metal composite beam on human tissues", *Smart Materials and Structures*, 16: S197-206.

Bone Characterization Using Piezo-Transducers as Bio-Medical Sensors

S. Bhalla*

Department of Civil Engineering, Indian Institute of Technology Delhi,
Hauz Khas, New Delhi 110016, India
Tel: 91-11-2659-1040; Fax: 91-11-2658-1117
Email: sbhalla@civil.iitd.ac.in

16.1 Introduction

Bones form the main load carrying structure of the human body. Their well being is vital for our functionality at a satisfactory level. However, no direct techniques are available to characterize the mechanical properties of bones *in situ* in a non-destructive manner. The mechanical properties of bones undergo changes after an injury and during the healing phase. They also change during diseased conditions, such as osteoporosis, which shows incidence in middle aged women and older men, and is a leading cause of functional loss among the elderly. This chapter demonstrates the possibility of employing miniaturized PZT patches as bio-medical sensors to assess the condition of bones by detecting changes occurring in them. The previous chapters of the book have mainly focused on the use of piezo-impedance transducers as “damage sensors”. This chapter, on the other hand, explores their application to monitor the reverse phenomenon, that of healing, in the case of bones.

Recently, there has been a growing interest in the bio-medical community to utilize the direct and converse effects of PZT patches for clinical applications. Bender *et al.* (2006) reported the use of embedded PZT patches to monitor capsule formation around soft tissue implants in Sprague-Dawley rats, via the EMI technique. Interestingly, their observations are similar to those of Soh and Bhalla (2005), who demonstrated the use of piezo-impedance transducers for monitoring

strength, damage and curing of concrete. Christopoulou *et al.* (2006) reported the measurement of modal damping of bones of adult female Wistar rats using accelerometers. However, compared to accelerometers, the PZT patches, as will be demonstrated in this chapter, have several advantages such as low-cost, negligible weight and the ability to be permanently implanted in bone-like structures. Additionally, they are also not likely to alter the subject’s dynamic properties by their own added mass. Special interest has been associated with the mechanical properties of bones since the condition of bones can be easily determined from their mechanical properties (Ritchie *et al.*, 2006). Bones undergo slow but continuous restructuring as a normal biological process as well as under diseased conditions, such as osteoporosis, which is accompanied by the loss of bone density, especially near the ends.

Bhalla and Bajaj (2008) successfully demonstrated PZT patches as actuator-sensor pair to detect changes in the mechanical properties of bones by conducting an experiment on a 12.5 cm long fresh chicken femur, as shown in Fig. 16.1(a). The actuator patch was excited into vibrations using a sinusoidal voltage signal of 5 V amplitude by means of a function generator, and the voltage response across the sensor patch was measured using the Agilent 34411A digital multimeter (Agilent Technologies, 2009). The frequency was varied from 0.5 kHz to 23 kHz at small intervals, and the measurements made at each frequency. A plot of voltage gain (voltage sensed by the sensor patch divided by the voltage applied across the actuator) as a function of frequency, shown in Fig. 16.1(b), served as a frequency response function (FRF). From this plot, the first two modal frequencies are identified as 4.95 kHz and 14.3 kHz.

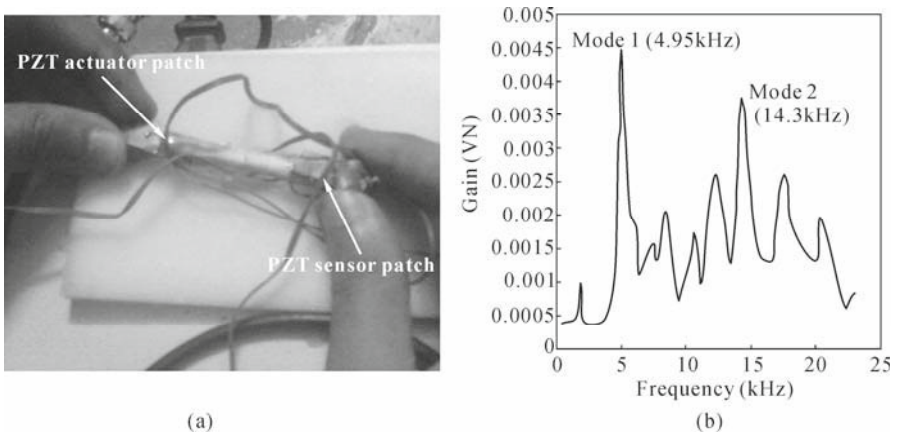


Fig. 16.1 Experiment by Bhalla and Bajaj (2008). (a) Chicken femur instrumented with PZT actuator-sensor pair; (b) FRF in form of gain vs frequency

Considering axial vibrations, the natural frequencies of the bone can be determined as (Mukhopadhyay, 2006)

$$f_n = \frac{(2n-1)}{4l} \sqrt{\frac{E}{\rho}} \quad (16.1)$$

where E represents the Young's modulus of the bone, ρ the density, n the mode number and l the distance of the nodal point (here, the centre of the PZT actuator patch) from the farther end of the bone. Note that the use of the distance from the centre of the PZT patch to the nearer end will also determine peaks, but of proportionally higher frequencies.

With the substitution of $E = 20$ GPa, $\rho = 2000$ kg/m³ (Erickson *et al.*, 2002) and $l = 0.1$ m, the first two natural frequencies resulted as 7.91 kHz and 23.72 kHz respectively, which are somewhat higher than the experimental frequencies, indicating difference in the mechanical properties from the assumed values. Thereafter, the bone was allowed to dry for one week, after which a small incision was made in between the actuator-sensor pair. Fig. 16.2 compares the FRF of the pristine bone with that after these changes. The overall effect was an increase in the natural frequencies.

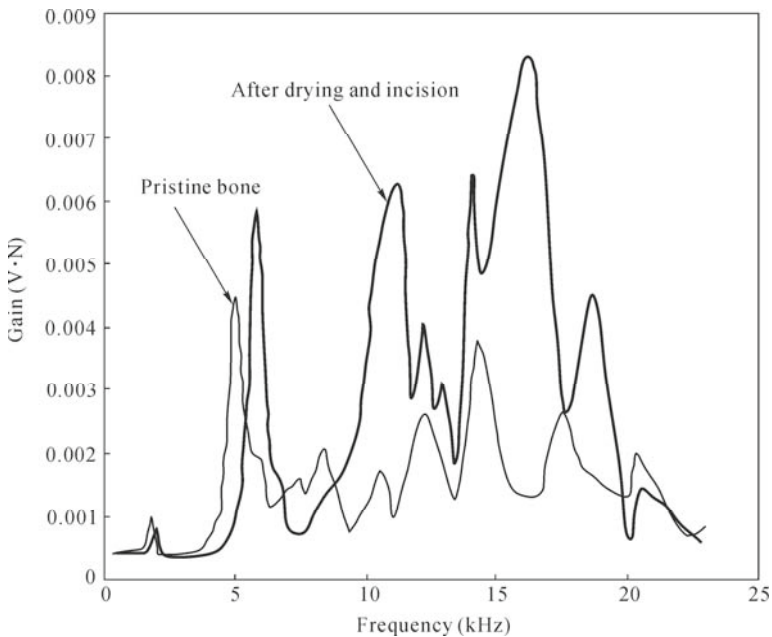


Fig. 16.2 Effect of change in condition of bone on FRF

In addition to natural frequencies, damping can also be determined from the FRF. In the SHM community, modal damping has been shown to be suitable for damage detection and localization (Kawiecki, 2001). In the bio-medical community, Christophoulou *et al.* (2006) demonstrated its use in detecting bone related ailments. Bhalla and Bajaj (2008) determined the modal damping of their test bone as 0.04

from the FRF, which is of the typical order reported by Christopoulou *et al.*, who determined it using an accelerometer. Furthermore, the damping ratio reduced from 0.04 to 0.035 (a reduction of 12.5%) as a result of the process of drying. These initial results prompted systematic studies reported in the following sections. The next sections highlight studies on the possibility of employing the EMI technique to detect changes in bone density, monitoring their healing process, and their FE modeling as reported by Bhalla and Suresh (2011).

16.2 Monitoring Changes in Bone Density

A 403 mm long human femur was chosen to conduct a specific study on the possibility of detecting changes in bone density by means of surface-bonded PZT patches. Two PZT patches were bonded approximately in the middle, as shown in Fig. 16.3; the patch marked “A” using two part epoxy araldite (Huntsman International, 2010) and the patch marked “C” using cynoacrylate (CN) adhesive (TML, 2009). Both PZT patches were covered with silicon rubber manufactured by Pidilite Industries Ltd. (2010) so as to safeguard them from moisture.

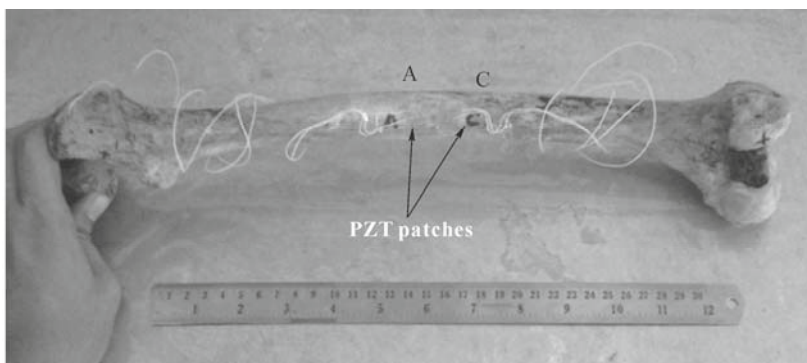


Fig. 16.3 Test bone for study on detecting changes in bone density

Signatures of the two patches were recorded using the Agilent E4980 LCR meter (Agilent Technologies, 2009). The bone was then made to absorb moisture so as to increase its density, by covering its ends with wet clothes for a period of two days. Care was taken that water does not come in direct contact with the PZT patches (even though covered with silicon rubber). The act of wetting the bone for two days increased its density by 6.2%. The signatures were then recorded in the wet state. The bone was thereafter dried for a period of two days in open air, which reduced its density to 1.01% of the density in the original dry state, after which, the signatures were again recorded. This was followed by the final drying for three additional days, which also included periodic use of a lamp for mild heating, which restored the bone’s density to 0.288% of the original value, after

which, the final signatures were recorded.

Fig. 16.4 shows the conductance signatures of the bone for the four conditions: dry, wet, dried for two days and dried for five days, for the PZT patch bonded using the araldite adhesive. It can be observed from the figure that marked changes are induced in the signature due to increase in density. At the same time, as the density restores back to the original value, the signature also restores back to the original. Similarly, Fig. 16.5 shows the corresponding signatures for the PZT patch bonded using the CN adhesive. For this patch, results similar to the patch bonded with araldite adhesive are observed, except that the additional drying pushes the signature further downwards, which is unexpected and calls for exploration of susceptibility to check for debonding.

Fig. 16.6 shows the pattern of RMSD variation with change in bone density. The RMSD index went up by more than 30% after the bone absorbed moisture causing 6.2% increment in density. As the density restored back to the normal value, the RMSD index also gradually fell back reaching a value of less than 5% after five days of drying. However, the final RMSD index for the PZT patch bonded using the CN adhesive provides a misleading signal, contrary to physical effect. Careful physical examination of this particular patch revealed debonding. This is also confirmed by the large variation of the imaginary component, as shown in Fig. 16.7 for the PZT patches corresponding to the two adhesives. Whereas the patch bonded using araldite exhibits very small variations of B , the patch bonded using the CN adhesive shows large variations, indicative of debonding and degradation, in accordance with the diagnostic test recommended by Park *et al.* (2006). Hence, CN adhesive does not form good bonding between bone and PZT patch.

Overall, the results of this experiment show that even small variations in bone's density can be detected using the EMI technique. The PZT patches, therefore, could possibly aid in the detection of the condition of osteoporosis in bones.

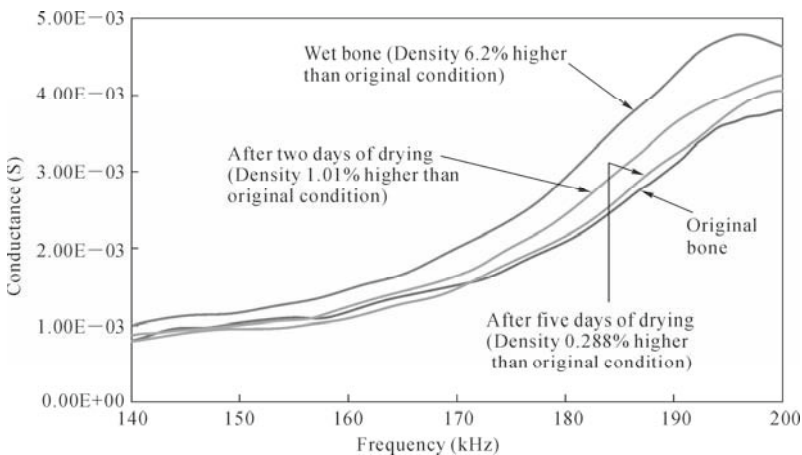


Fig. 16.4 Effect of bone density on conductance signature of PZT patch bonded with araldite

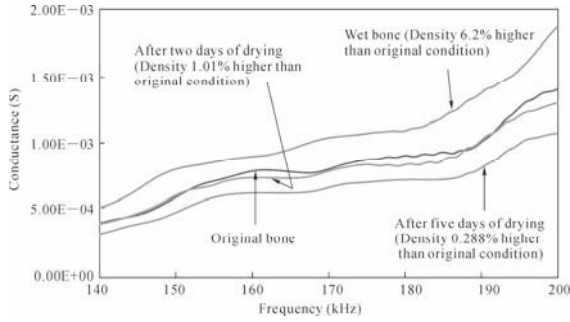


Fig. 16.5 Effect of bone density on conductance signature of PZT patch bonded with CN adhesive

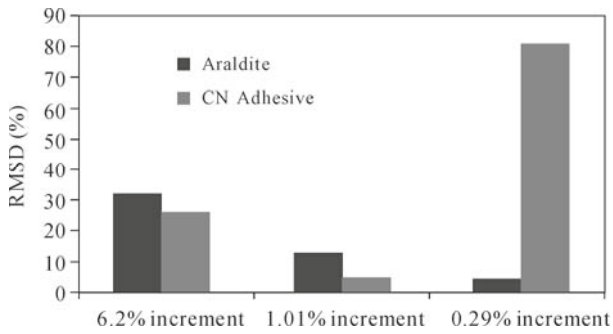


Fig. 16.6 Variation of RMSD (%) with bone density

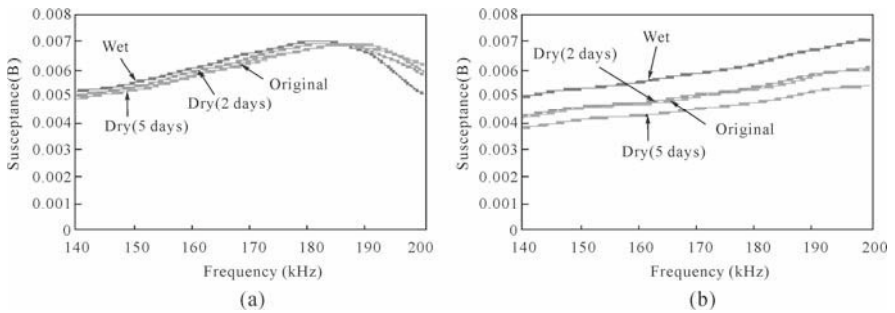


Fig.16.7 Variation of susceptance (B). (a) PZT patch bonded using araldite; (b) PZT patch bonded using CN adhesive

16.3 Monitoring Healing Process in Bones

This section explores the possibility of employing the EMI technique to monitor healing process in bones after fracture. In order to experimentally simulate the phenomenon, three rabbit bones were utilized. Each bone was instrumented with a PZT patch using the araldite adhesive. After acquiring the baseline signature, the bones were fractured by an impact and the signatures were re-acquired. The parts of the fractured bones were joined back using araldite epoxy adhesive and cured for over 24 hours under room temperature. Finally, the signatures of the rejoined bones were acquired. Figs. 16.8 to 16.10 show the concerned bones as well as the signatures in the three states, namely the intact, fractured and rejoined states. From the signatures, it is apparent that after the fracture, the signature underwent change. However, after the parts were joined back, the signature changed again, this time shifting towards the original intact state.

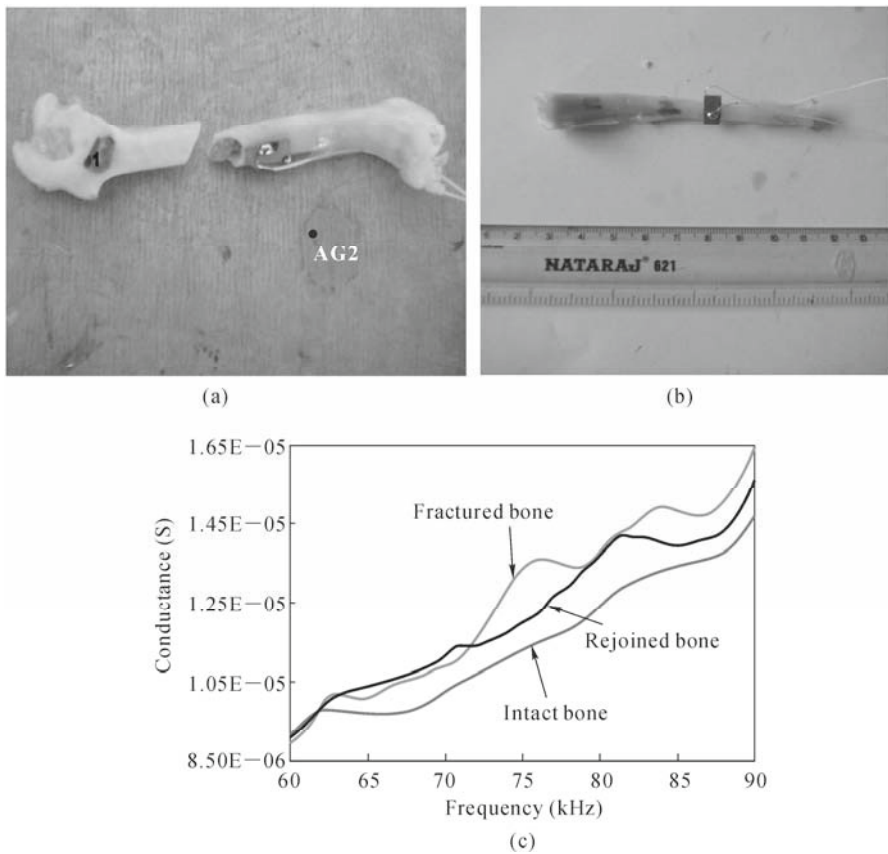


Fig. 16.8 Results for first rabbit bone. (a) Fractured bone; (b) Rejoined bone; (c) Conductance signatures for three states

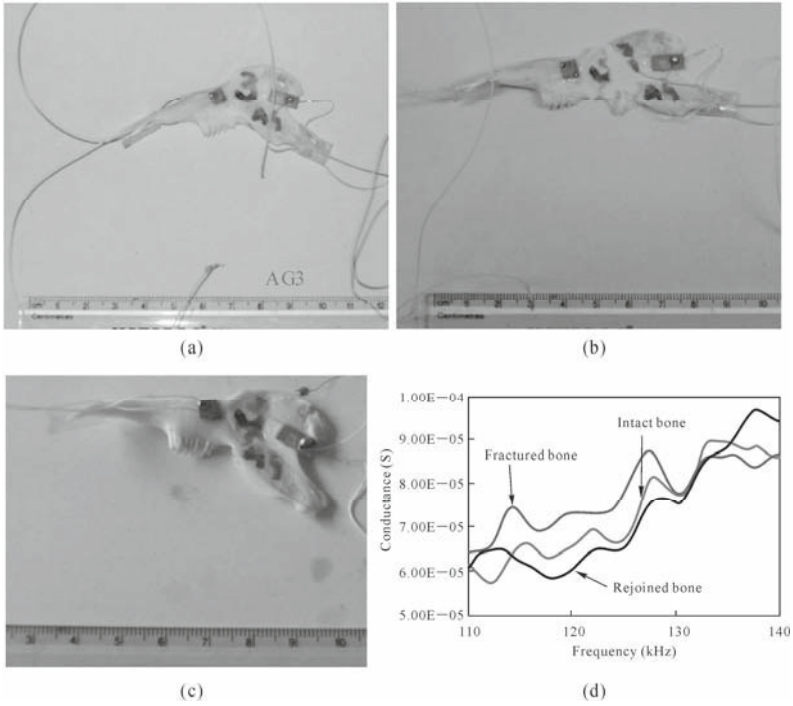


Fig. 16.9 Results for second rabbit bone. (a) Intact bone; (b) Fractured bone; (c) Rejoined bone; (d) Conductance signatures for three states

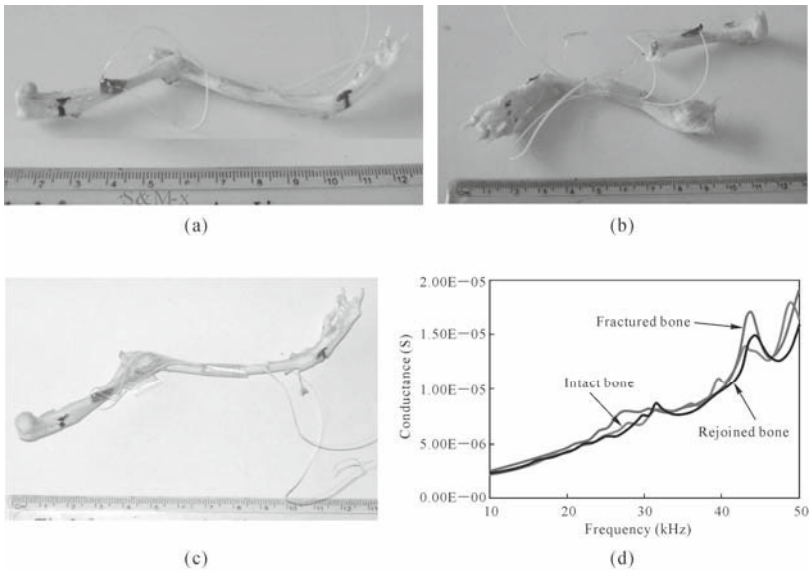


Fig. 16.10 Results for third rabbit bone. (a) Intact bone; (b) Fractured bone; (c) Rejoined bone; (d) Conductance signatures for three states

Fig. 16.11 shows the variation of the RMSD index for the three bones for the two cases—fractured and rejoined. The reduction in RMSD index provides a clear indication of the healing process. It may be noted that the restoration of signatures to that of the original intact state is not one hundred percent since the healing process simulated in the present context is grossly crude in nature, adopted only due to ease of experimentation. Much better results are expected in the case of natural healing where the joining is normally more perfect. This is however, beyond the scope of the study reported here.

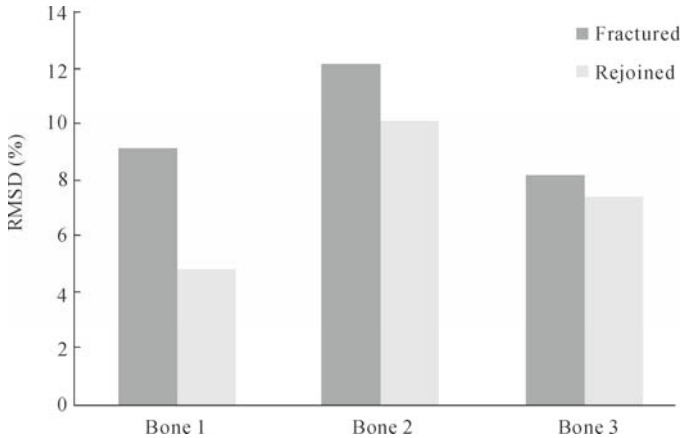


Fig. 16.11 Variation of RMSD (%) with fracture and rejoining

16.4 FE Simulation of EMI Technique on Bones

This section outlines simulating the signatures of the PZT patches bonded on bones using finite element (FE) approach and detecting occurrence of cracks and fracture using EMI technique. For this purpose, the 403 mm long human femur (covered in Section 16.2), with “free-free” boundary condition, as shown in Fig. 16.12(a), was chosen. Fig. 16.12(b) shows the 2D FE model of the femur generated using plane 42 elements of ANSYS 12 FE software, considering Young’s modulus as 12 GPa (Erickson *et al.*, 2002) and density as 1600 kg/m³. The conductance signature of the bone was obtained using the 1D impedance model covered in Chapter 2 (see also Appendix A). For this purpose, the mechanical impedance Z of the bone was determined by applying a pair of equal and opposite harmonic forces F on the bone at the points of attachment of the PZT patch, determining the displacement response u through dynamic harmonic FE analysis, and computing the mechanical impedance Z through the relation

$$Z = \frac{F}{\dot{u}} = \frac{F}{j\omega u} \quad (16.2)$$

From Z , the EM admittance was computed using Eq. (2.31). Fig. 16.13 shows a comparison of conductance signature obtained using the Agilent E4980 LCR meter (Agilent Technologies, 2009) with that derived through the FE approach in the frequency range 0 – 200 kHz. Due to the use of 2D modelling, the magnitudes of the experimental and the FE derived signatures do not match. However, the general trend is similar. In order to gain a deeper insight, active components of the signature were determined, since it is well established (see Chapter 2), that active components have higher sensitivity to damage. The active conductance signatures are compared in Fig. 16.14. Contrary to the raw conductance, both the experimental and the FE signatures are agreeable to a greater degree, capturing well the first axial mode of vibrations. The magnitudes of the conductance are not comparable due to 2D nature of the FE modeling. The raw conductance signature (Fig. 16.13) in itself is not able to capture the essence of the structure, since it is camouflaged by the passive component.

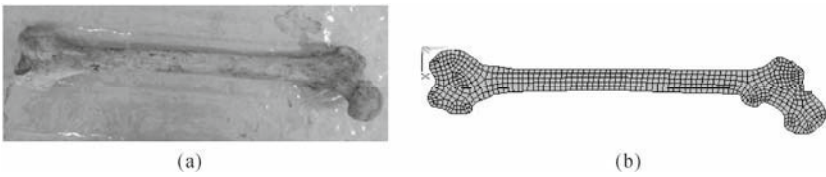


Fig. 16.12 (a) Real bone; (b) FE model

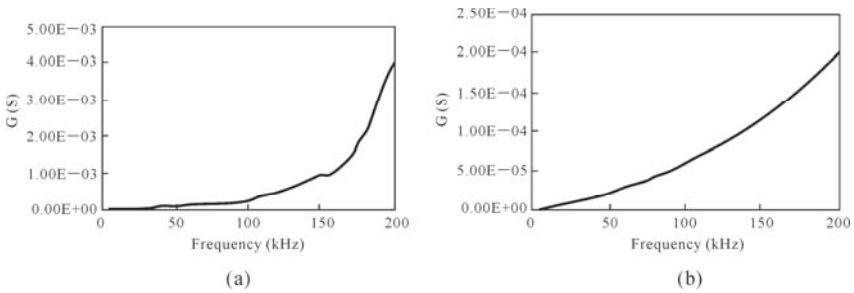


Fig. 16.13 (a) Experimental signature; (b) Numerical signature

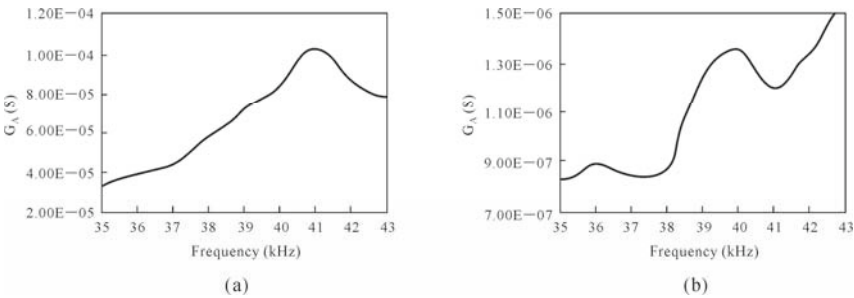


Fig. 16.14 (a) Experimental active-conductance signatures; (b) Numerical active-conductance signatures.

In order to induce damage, a cut was made through the bone as shown in Fig. 16.15(a). This cut was then extended throughout the bone to generate fracture, as shown in Fig. 16.15(b). The same phenomenon was also simulated numerically, by reducing the Young's modulus of elasticity of the elements along crack to negligibly small values, as shown in Fig. 16.15(c). Fig. 16.16 shows the active conductance signatures- both experimental as well as numerical for the three states- intact bone, bone with cut and fractured bone. The effect of crack and fracture is also comparable for the two cases- experiment and numerical simulation. The major peak tends to shift to the left after damage, which matches with expectations. Detection of crack/fracture, as illustrated here, is not unexpected taking into view the already established high sensitivity of the EMI technique to damage. The major new outcome is the successful demonstration of the fact that FE approach can suitably model the dynamic phenomenon of bone-PZT interaction. The FE modelling could possibly substitute experiments and could aid in preliminary studies related to the application of the EMI technique to bones.

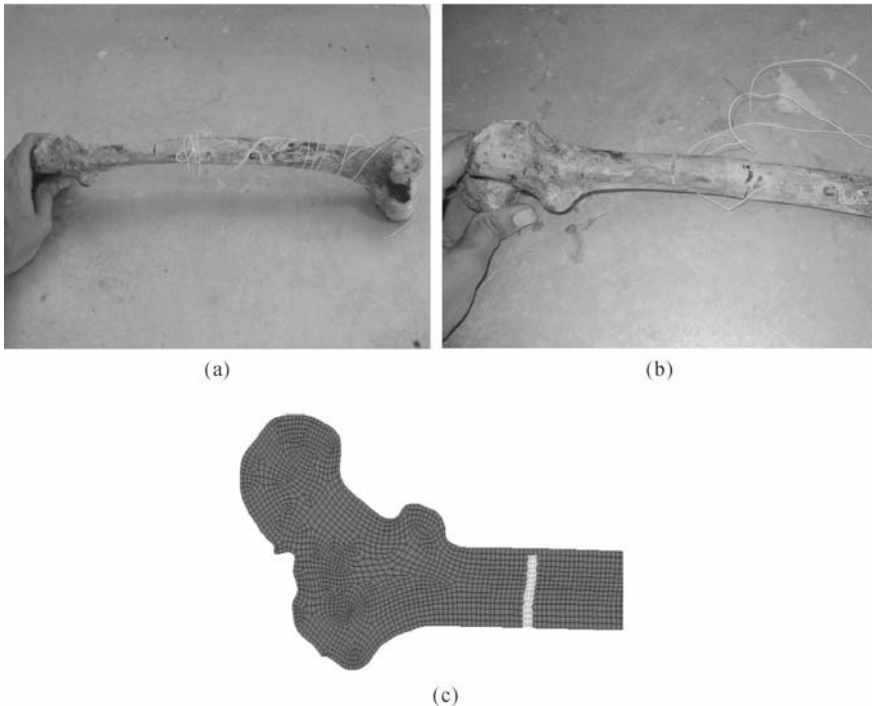


Fig. 16.15 (a) Bone with crack; (b) Bone with fracture; (c) Simulation of crack

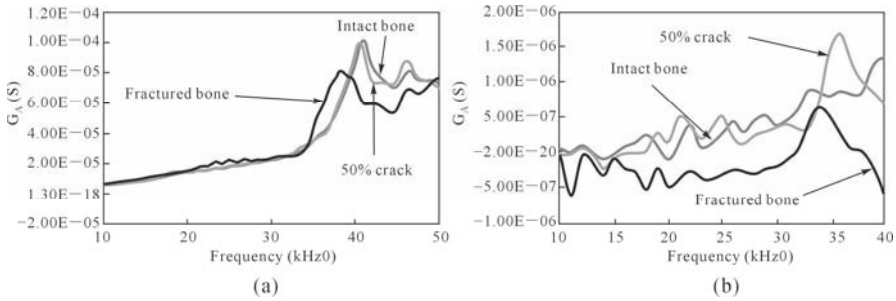


Fig. 16.16 (a) Experimental active-conductance signatures; (b) Numerical active-conductance signatures

In a nutshell, this chapter illustrates the potential of the EMI technique (which is conventionally employed for SHM) for monitoring the condition of bones, including the healing process. However, before the EMI technique could be used in the field, several questions remain to be answered, such as what kind of PZT patches could be potentially bonded to the bone, the bio compatibility of the sensor, and the acquisition of the signatures. Through the recent advances in nanotechnology, it could be possible to implant nano-sized PZT patches on bones requiring monitoring. The advances in wireless telemetry could further facilitate remote signature acquisition, without necessitating the wires. The authors are also exploring the possibility of a piezo-fibre band, which could be tied on the limb externally, without necessitating surgical intervention. The chapter only provides a proof-of-concept. Clinical trials need to follow so as to further establish the technique in real-life subjects.

References

- Agilent Technologies (2009). <http://www.agilent.com>.
- Bhalla, S. and Bajaj, S. (2008). "Bone characterization using piezo-transducers as bio-medical sensors", *Strain*, 44: 475-478.
- Bhalla, S. and Suresh, R. (2011). "Monitoring condition of bones using piezo-transducers", *Strain*, in press.
- Bender, J.W., Friedman, M.D., Giurgiutiu, V., Watson, C., Fitzmaurice, M. and Yost, M.L. (2006). "The use of biomedical sensors to monitor capsule formation around soft tissue implants", *Annals of Plastic Surgery*, 56: 72-77.
- Christopoulou, G.E., Stavropoulou, A., Anastassopoulos, G., Panteiou, S.D., Papadaki, E., Karamanos, N.K. and Panagiotopoulos, E. (2006). "Evaluation of modal damping factor as a diagnostic tool for osteoporosis and its relation with serum osteocalcin and collagen I N-Telopeptide for monitoring the efficacy of alendronate in ovariectomized rats", *Journal of Pharmaceutical and Biomedical Analysis*, 41: 891-897.

- Erickson, G.M., Catanese, J. and Keaveny, T.M. (2002). "Evaluation of the biomechanical material properties of the femur", *Anatomical Record*, 268: 115-124.
- Huntsman International LLC (2010) <http://www.huntsman.com>.
- Kawiecki, G. (2001). "Modal damping measurement for damage detection," *Smart Materials and Structures* 10: 466-471.
- Liang, C., Sun, F.P. and Rogers, C.A. (1994). "Coupled electro-mechanical analysis of adaptive material systems—determination of the actuator power consumption and system energy transfer", *Journal of Intelligent Material Systems and Structures*, 5: 12-20.
- Mukhopadhyay, M. (2006). *Structural Dynamics*, Ane Books India, New Delhi.
- PI ceramic (2007). <http://www.piceramic.de>
- Pidilite Industries Ltd. (2010). <http://www.pidilite.net>
- Park, G., Farrar, C.R., di Scalia, F.L. and Coccia, S. (2006). "Performance assessment and validation of piezoelectric active-sensors in structural health monitoring", *Smart Materials and Structures*, 15: 1673-1683.
- Ritchie, R.O., Nalla, R.K., Kruzic, J.J., Ager III, J.W., Balooch, G. and Kinney, J.H. (2006). "Fracture and ageing in bone: toughness and structural characterization", *Strain*, 42: 225-232.
- Soh, C.K. and Bhalla, S. (2005). "Calibration of piezo-impedance transducers for strength prediction and damage assessment of concrete", *Smart Materials and Structures*, 14: 671-684.
- TML (2009). Tokyo Sokki Kenkyujo Co. Ltd., Tokyo.

Future of Smart Materials

Y. W. Yang*, S. Bhalla, L. H. Tang, L. Zhang, C. K. Soh

School of Civil and Environmental Engineering, Nanyang Technological University,
50 Nanyang Avenue, Singapore 639798

Tel: (65)-6790-4057, Fax: (65)-6791-0676

Email: cywyang@ntu.edu.sg

17.1 Past and Future Developments of IPMC

The success of a new material is usually dependent on its applications. When ionic polymer-metal composites (IPMC) were first invented, the potential application areas were identified as biomedical and robotics, due to their resemblance to biological muscles in both properties and performances. Thus, IPMC is sometimes referred to as artificial muscles. Throughout the years, a large number of biomedical applications have been proposed, including the applications presented in Chapter 15. Recent developments in the applications of IPMC include Braille displays (Kato *et al.*, 2007), active guide-wire system for cardiac catheterization (Fang *et al.*, 2010) and biomimetic micro-collector for collection of particles in chronic total occlusion disease (Cho and Lee, 2009). However, continuous improvement on the controllability, stability and actuation effects of IPMC are still essential for their future applications in solving practical engineering problems.

In 1999, Dr. Yoseph Bar-Cohen of the Jet Propulsion Lab posed a scientific challenge to the worldwide research and engineering community to develop a robotic arm, actuated by electroactive polymers (EAP), to wrestle with a human arm (Fig. 17.1). However, humans have been winning in all the competitions so far, implying that continuous efforts are still needed for the practical applications of EAP, including IPMC.



Fig. 17.1 Grand challenge for EAP arm wrestling with human arm
 (Web: <http://ndeaa.jpl.nasa.gov/nasa-nde/lommas/eap/EAP-armwrestling.htm>;
 Courtesy of Yoseph Bar-Cohen, Jet Propulsion Laboratory/Caltech/NASA)

In addition to the applications that have been implemented so far, it is envisioned that IPMC could also contribute to the following areas due to their characteristic strength as both sensors and actuators.

Energy Harvesting in Aqueous Environments

Like most other smart materials, IPMC is also a natural energy transducer which is capable of energy conversion between mechanical and electrical domains. The unique property of IPMC, which needs solvent for both sensing and actuating, makes them ideal for energy harvesting in aqueous environments. The fluctuations in aqueous environments, ranging from sea waves to blood flows, provide a wide arena for energy harvesting with IPMC for various applications. A recent paper by Aureli *et al.* (2010) advocated the possibility of using IPMC in aqueous environments to harvest vibration energy.

MEMS Actuators

IPMC is usually fabricated either by casting dispersing solution and evaporating the solvent, or by hot molding. Thus, IPMC can be easily fabricated in any shape and dimension. By miniaturization of the IPMC-based components, they can be employed as MEMS actuators. Their low operational voltage, large deformation and compliance property make them good candidates as actuators in MEMS devices, especially those devices which work with solvents.

Humanoid and Underwater Bionic Robots

As a type of artificial muscles, IPMC has attracted much attention in robotic engineering (Bar-Cohen, 2001; Kim and Tadokoro, 2007). IPMC has been used in both humanoid robots and underwater bionic robots. It is expected that great developments in human-like robots and miniaturized bionic robots with IPMC and other EAP can be seen in the coming decade.

17.2 PZT/ MFC in Energy Harvesting

The concept of capturing the ambient energy surrounding a system and converting it into electrical energy is termed energy harvesting. Different energy sources from residual heat to mechanical vibration are available in the environment. For an environment where a thermal gradient or a varying temperature exists, thermoelectric or pyroelectric materials are best options for energy harvesting. One successful implementation of thermoelectric energy harvesting is a wrist watch developed by Seiko (Kishi *et al.*, 1999), capable of operating from skin thermal gradients. For vibration energy harvesting, piezoelectric materials are prevalently used as the conversion mechanism for their high energy density compared with the other conversion mechanisms (Roundy *et al.*, 2003). Interest in the application of piezoelectric energy harvesters has increased dramatically in recent years (Anton and Sodano, 2007). A great amount of work published in the literature focuses on the maximum achievable power by theoretical modeling and laboratory tests. Although some prototypes of piezoelectric energy harvesters are available, several limitations still exist, such as limited bandwidth, hindering their way to practical deployment.

17.2.1 *Current Research in Energy Harvesting using Piezoelectric Materials*

Since mechanical vibration is ubiquitous in the environment, from low-frequency human motions to machinery and vehicles, a great amount of research interest is attracted on vibration energy harvesting using piezoelectric materials. Current efforts in this field can be divided into two groups, accurate modeling of piezoelectric energy harvesters and developing efficiency improvement approaches.

- *Modeling Issues*

In the past few years, theoretical modeling of piezoelectric energy harvesters is approaching higher accuracy, from single degree-of-freedom systems to distributed-parameter models, from uncoupled models to electromechanical (EM) coupled models and from analytical derivations to the Rayleigh-Ritz scheme (Sodano *et al.*, 2004; duToit *et al.*, 2005; Chen *et al.*, 2006; Erturk and Inman, 2008). Besides, numerical approach for modeling piezoelectric energy harvesters, such as the FEM, has been established in literature, which is capable of dealing with energy harvester with complicated profiles (De Marqui *et al.*, 2009). However, both the theoretical and FE methods predict achievable power by attaching a pure resistor. To consider the practical energy storage and conditioning

circuits, some researchers devoted their efforts to developing the equivalent circuit model (ECM) of piezoelectric transducer (Elvin and Elvin, 2009; Yang and Tang, 2009), so that the entire energy harvesting system could be modeled in an electric simulator, such as SPICE (2010). It should be mentioned that, although the above models or approaches are validated by experiments or by each other, they were derived based on the linear piezoelectricity and linear deformation assumptions.

- *Efforts in Efficiency Improvement*

Besides the modeling issues in piezoelectric energy harvesting, several researchers have attempted to develop schemes for efficiency improvement. Although the power consumption is decreasing dramatically with the advancement of circuitry technologies, the efficiency of piezoelectric energy harvesting is still required to improve so as to match the power requirement of most current electronics. Generally, the efforts in improving energy harvesting efficiency can be divided into two groups: (1) optimization of piezoelectric configuration and structural configuration, and (2) development of adaptive energy harvesting circuits for charge extraction.

Optimal Piezoelectric and Structural Configuration

Various piezoelectric materials can be used for energy harvesting, such as the quick pack (QP) actuators or the macro-fiber composites (MFC) rather than the traditional PZT (Sodano *et al.*, 2005; Yang *et al.*, 2009). Besides, various structural configurations have been proposed by the researchers to improve their efficiency, such as the initial curved PZT (Danak *et al.*, 2003), the increasing-trapezoidal shaped cantilever (Roundy *et al.*, 2005) and the piezoelectric “cymbal” (Kim *et al.*, 2004). Furthermore, another potential way to improve energy harvesting capability is to utilize multiple pieces of piezoelectric element or to stack a large number of piezoceramic wafers together, termed as multilayer or stack configuration. It was found that both the voltage output and the matching load are much more manageable for a PZT stack than a monolithic configuration, making the stack configuration a more attractive option in energy harvesting applications (Platt *et al.*, 2005).

Adaptive Energy Harvesting Circuit for Charge Extraction

Rather than the standard energy harvesting circuit in which the battery is charged directly, the adaptive circuit developed by Ottman *et al.* (2002) maximized the power flow from the piezoelectric energy harvester. A switch-mode DC-DC converter was added to the standard circuit and an adaptive control algorithm was developed to continuously implement optimal power transfer by tuning the duty cycle of DC-DC converter. The basis of such circuit is to tune the load impedance

to match the internal impedance of the piezoelectric harvester. Recently, techniques such as “synchronous electric charge extraction” (SECE) (Lefeuvre *et al.*, 2005) and “synchronous switch harvesting on inductor” (SSHI) (Lefeuvre *et al.*, 2006) were proposed by researchers from electrical engineering. Different from the control circuit in the impedance adaptation, SECE and SSHI focus on synchronizing the charge extraction with the mechanical vibrations of the system. It was claimed that the maximum available power by SECE is nearly 400% of that by the impedance adaptation standard circuit, and the maximum available power by SSHI is even up to 17 times of the standard circuit.

17.2.2 Main Concerns for Future Practical Applications

Although energy harvesting using smart materials, especially piezoelectric materials for harnessing vibration energy, has evoked tremendous research interests and some evaluation prototypes have been developed, practical deployment of the energy harvesting technologies using piezoelectric materials for autonomous sensing systems is still far from ready.

- ***Bandwidth for Energy Harvesting***

One main concern for piezoelectric energy harvester is the frequency bandwidth. Although many efforts have sought to increase the power output, most of the developed energy harvesters can only exploit the vibrations occurring very near their resonance frequencies. If the vibration does not occur at the right resonance frequency, the power output will dramatically decrease and it will be useless in powering the sensor. Unfortunately, the vibrations existing in the environment are random or frequency variable. Hence, in practice, the energy harvesting devices have to be designed to operate over a wide range of frequency. This will be the next research hotspot in the field of energy harvesting.

Multi-Modal Energy Harvesting

In order to effectively harvest energy from the ambient environment, the concept of multi-modal energy harvesting is being pursued, *i.e.*, different energy harvesting schemes are combined into one system. A suitable example of multi-modal energy harvesting device is a system that combines both electromagnetic and piezoelectric mechanisms (Priya and Inman, 2009), as shown in Fig. 17.2. The advantage of this design is that, at constant acceleration, the output power from electromagnet is much higher at lower frequencies (first transversal resonance mode), whereas the output from piezoelectric is higher at higher frequencies (second transversal resonance mode). Since the frequency content of a random

vibration is wide, such a device can utilize multiple frequency spectra, making energy harvesting more effective. However, such design still requires further investigation on its feasibility. The electromagnetic energy harvesting induces additional damping effect, which in turn affects the vibration and the efficiency of piezoelectric energy harvesting. The form factor of such device may also be a limitation in small-scale applications.

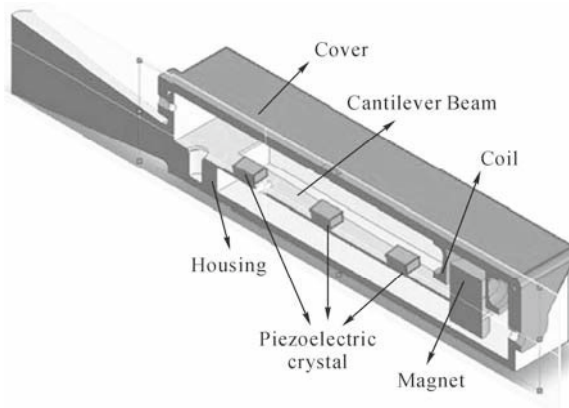


Fig. 17.2 Handheld multi-modal energy harvester (Copyright: Springer; Priya and Inman, 2009)

Resonance Tuning

Another idea to broaden the bandwidth is to tune the resonant frequency of a piezoelectric harvester to match the frequency of the ambient vibrations. Leland and Wright (2006) developed a novel tunable-resonance vibration energy harvester. In this device, a compressive axial preload is used to alter the structure's stiffness and hence the resonance could be adjusted straightforwardly. It was determined that a compressive axial preload could reduce the resonance frequency of a vibration energy harvester by up to 24%. Challa *et al.* (2008) proposed a magnetic force technique in which the applied magnetic force alters the effective stiffness of the harvester (Fig. 17.3). Four magnets are used in this device, and placed such that attractive and repulsive magnetic forces can be applied on the beam. The distance between the magnets can be controlled to alter the magnetic force, which induces additional stiffness on the vibrating beam and in turn alters its resonance frequency. However, since these designs do not include the actuator and closed-loop controller, the frequency tuning is achieved manually. Hence, such devices cannot be tagged as "smart harvester". The ideal piezoelectric energy harvester should be self-tuning, and it is expected that "self-tuning harvester" will attract more research attention in the future. The main concern for developing self-tuning technique is that the power required to tune the frequency should not outweigh the increase in power output.

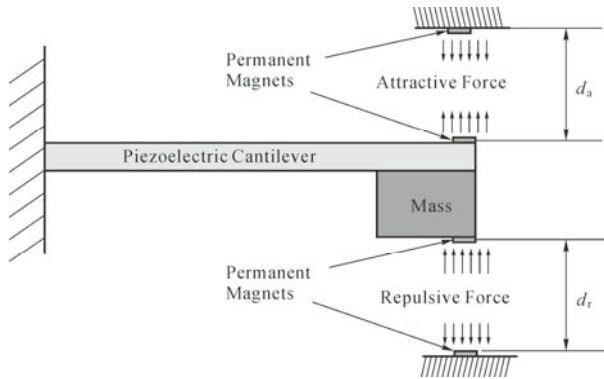


Fig. 17.3 Schematic of resonance frequency tunable energy harvesting device (Copyright: IOPP; Challa *et al.*, 2008)

Energy Harvester with Cantilever Array

Rather than resonance tuning, using multiple piezoelectric cantilevers (*i.e.* cantilever array) is another idea for broadband energy harvesting. Shahruz (2006) designed such a completely passive energy harvesting system. The device consists of multiple piezoelectric cantilevers with various lengths and tip masses attached to a common base, thereby capable of resonating at various frequencies without the need for any adjustment. Each cantilever has a unique resonant frequency, the combination of which into a single device creates the so-called “mechanical band-pass filter” (Fig. 17.4(a)). By properly selecting the length and tip mass of each beam, the overall device is designed to provide voltage response over a wider frequency range (Fig. 17.4(b)). However, such design results in significant increase in both size and cost. Moreover, the power density is sacrificed since most of the cantilever beams are inactive at a given point of time. Hence, the number of cantilevers, the tip masses and the other parameters of such device should be carefully selected according to vibration sources and the form factor requirements. Additionally, a more complex electric circuit is needed to extract energy from each piezoelectric beam.

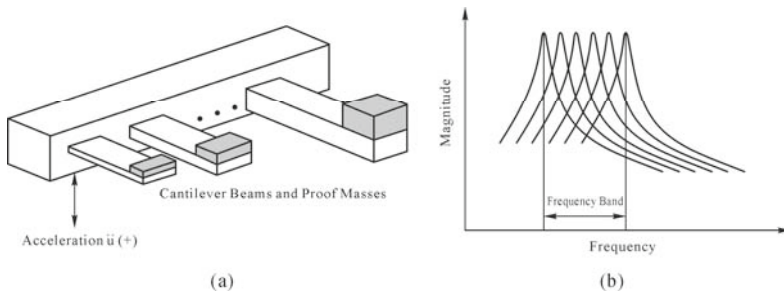


Fig. 17.4 (a) band-pass filter (dimension of the beams and tip masses are chosen appropriately) and (b) its transfer function (Copyright: Elsevier, Shahruz, 2006)

- *Nonlinear Effects*

Current research efforts, as discussed in the previous sections, are based on the assumption of linearity, *i.e.*, linear deformation and linear piezoelectric theory. However, in some scenarios with low vibration frequency (<10 Hz) and large vibration amplitude, the deformation of the harvester at resonance could be too large to apply the linear deformation assumption. This is especially so for some piezoelectric materials such as MFC and PVDF which are characterized by their flexibility and bearability. In addition, nonlinearity exists in the piezoelectric material properties, as illustrated in Fig. 17.5, which shows the experimental values of the piezoelectric constant d_{31} by Crawley and Anderson (1990). It is noted that d_{31} exhibits significant dependence on the induced strain in the material. However, only few previous works considered the nonlinear piezoelectric constitutive relations in the modeling. These non-linear phenomena and their effects on energy harvesting performance are worth more investigation in the future.

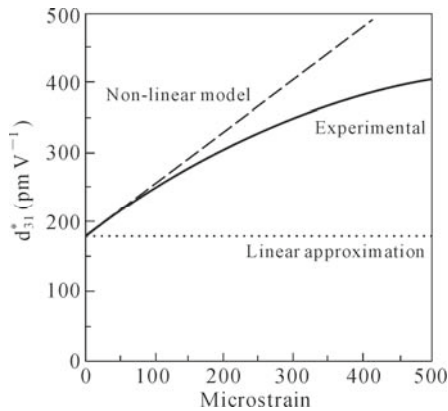


Fig. 17.5 Dependence of d_{31} on induced strain by linear approximation-nonlinear model by Triplett and Quinn (2009) and experimental test by Crawley and Anderson (1990) (Copyright: SAGE)

- *Storage and Power Conditioning Circuit*

The energy generated by smart materials is usually insufficient to directly power a sensor or other electronics. Therefore, the fragment energy captured should firstly be accumulated or stored for later use. Developing efficient methods for storing energy will continue to be one of the main issues in energy harvesting. In practical applications, the storage medium, electronics and other parameters should be selected and designed carefully to ensure that the time required to store sufficient energy for one operation (for example, transmitting signal once by a sensor) can match with the operation duty cycle.

Furthermore, in the SECE and SSHI techniques for piezoelectric energy harvesting, the key issue is the voltage peak searching for synchronization. When the peak is found, the charge will be suddenly released from the piezo element. However, this process will generate a pulse force because of the EM coupling, which will in turn affect the beam's original vibration and cause difficulty in peak searching. In the setup of Lefeuvre *et al.* (2005, 2006), the beam was clamped at one end and the force or displacement loading was applied at the other end. Such configuration can suppress the extra vibration induced by EM coupling. However, in practical application, the cantilever setup is more favorable. In such case, the feasibility of these nonlinear circuit techniques is worth further investigation in the future.

17.3 Futuristic Applications of Smart Materials

It is envisaged that smart materials will have enormous potential applications in our day-to-day lives in the future. With active research in energy harvesting underway worldwide, some day, the energy harvesting devices would become an indispensable part of our daily lives. It could be a reality in the near future that we use piezo-based devices embedded in our shoes to harvest energy associated with our daily movements to power personal devices such as mobile phones, watches, i-pods and even laptop computers. These could also become an essential part of bridges by harvesting generated energy to power the diagnostic systems for bridge's health. Such a self-sufficient low-maintenance system would substantially increase the infrastructures' overall performance. Such energy harvesting devices could even provide sufficient energy to power light emitting diode (LED) based lighting systems for bridges and streets. In addition, piezo materials have potential to be part of the diagnostic systems for assessment of the condition of bones after an injury or during their healing, as illustrated in the preceding chapter. Micro-sized piezo-based devices could be permanently implanted on diseased persons to do real time diagnosis of several ailments, similar to the concept of SHM of structures. Piezo-actuators could also enable near actual movements to artificial limbs in the persons suffering from various kinds of disabilities.

The fiber optic sensors, which can transmit light over long distances, could possibly tap sunlight, transmit it to the interiors of buildings, and emit it just like bulbs. This could be the most environment friendly lighting system posing no risk of global warming. The advances in shape memory alloys (SMA) could enable retractable structures for day-to-day uses. These could be sort of packaged structures, which could be initially confined to small spaces/enclosures. When needed, they may be simply heated to erect temporary light weight structures for multiple purposes such as gatherings, expositions and other events. After use, they may simply be collapsed and packed back into small volumes. SMA could also

enable self-healing in structures in synergy with the piezo-transducers. Whereas the piezo-transducers could aid in detecting and locating damages, SMA could be activated to close existing cracks. In principle, crack mitigation by SMA has already been investigated by Song *et al.* (2006) on lab sized reinforced concrete structures. It could be a reality that all the reinforcement bars in RC structures may be based on SMA, paving way for structural control, diagnostics and self repair. In a nutshell, there is no end to contemplating about the future use of smart materials.

References

- Anton, S.R. and Sodano, H.A. (2007). "A review of power harvesting using piezoelectric materials (2003-2006)", *Smart Materials and Structures*, 16: R1-R21.
- Aureli, M., Prince, C., Porfiri, M. and Peterson, S.D. (2010). "Energy harvesting from base excitation of ionic polymer metal composites in fluid environments", *Smart Materials and Structures*, 19: 015003.
- Bar-Cohen, Y. (Editor) (2001). *Electroactive Polymer (EAP) Actuators as Artificial Muscles, Reality, Potential, and Challenges*, Washington: SPIE Press.
- Challa, V.R., Prasad, M.G., Shi, Y. and Fisher, F.T. (2008). "A vibration energy harvesting device with bidirectional resonance frequency tunability", *Smart Materials and Structures*, 17: 015035.
- Chen, S.N., Wang, G.J. and Chien, M.C. (2006). "Analytical modeling of piezoelectric vibration-induced micro power generator", *Mechatronics* 16: 379-387.
- Cho, S.M. and Lee, D.W. (2009). "A biomimetic micro-collector based on an ionic polymer metal composite", *Microelectronic Engineering*, 86: 916-919.
- Crawley, E.F. and Anderson, E.H. (1990). "Detailed models of piezoceramic actuation of beams", *Journal of Intelligent Material Systems and Structures*, 1: 4-25.
- Danak, A.D., Yoon, H.S. and Washington, G.N. (2003). "Optimization of electrical output in response to mechanical input in piezoceramic laminated shells", *Proceedings of ASME International Mechanical Engineering Congress and Exposition, IMECE 2003*: 43185.
- De Marqui, C., Erturk, A. and Inman, D.J. (2009). "An electromechanical finite element model for piezoelectric energy harvester plates", *Journal of Sound and Vibration*, 327: 9-25.
- duToit, N.E., Wardle, B.L. and Kim, S.G. (2005). "Design considerations for MEMS-scale piezoelectric mechanical vibration energy harvesters", *Integrated Ferroelectrics*, 71: 121-160.
- Elvin, N.G. and Elvin, A.A. (2009). "A general equivalent circuit model for piezoelectric generators", *Journal of Intelligent Material Systems and*

- Structures*, 20: 3-9.
- Erturk, A. and Inman, D.J. (2008). "Issues in mathematical modeling of piezoelectric energy harvesters", *Smart Materials and Structures*, 17: 065016.
- Fang, B.K., Lin, C.C.K. and Ju, M.S. (2010). "Development of sensing/actuating ionic polymer-metal composite (IPMC) for active guide-wire system", *Sensors and Actuators, A* 158: 1-9.
- Kato, Y., Sekitani, T., Takamiya, M., Doi, M., Asaka, K., Sakurai, T. and Someya, T. (2007). "Sheet-type Braille displays by integrating organic field-effect transistors and polymeric actuators", *IEEE Transactions on Electron Devices* 54: 202-209.
- Kim, H.W., Batra, A., Priya, S., Uchino, K., Markley, D., Newnham, R.E. and Hofmann, H.F. (2004). "Energy harvesting using a piezoelectric 'cymbal' transducer in dynamic environment", *Japanese Journal of Applied Physics*, 43: 6178-6183.
- Kim, K.J. and Tadokoro, S. (Editors) (2007). *Electroactive Polymers for Robotic Applications: Artificial Muscles and Sensors*, London: Springer-Verlag.
- Kishi, M., Nemoto, H., Hamao, T., Yamamoto, M., Sudou, S., Mandai, M. and Yamamoto, S. (1999). "Micro thermoelectric modules and their application to wristwatches as an energy source", *Proceedings of 18th International Conference on Thermoelectrics*, 301-307.
- Lefevre, E., Badel, A., Richard, C. and Guyomar, D. (2005). "Piezoelectric energy harvesting device optimization by synchronous electric charge extraction", *Journal of Intelligent Material Systems and Structures*, 16:865-876.
- Lefevre, E., Badel, A., Richard, C., Petit, L. and Guyomar, D. (2006). "A comparison between several vibration-powered piezoelectric generators for standalone systems", *Sensors and Actuators A Physical*, 126: 405-416.
- Leland, E.S. and Wright, P.K. (2006). "Resonance tuning of piezoelectric vibration energy scavenging generators using compressive axial preload", *Smart Materials and Structures*, 15:1413-1420.
- Ottman, G.K., Hofmann, H.F., Bhatt, A.C. and Lesieutre, G.A. (2002). "Adaptive piezoelectric energy harvesting circuit for wireless remote power supply", *IEEE Transactions on Power Electronics*, 17: 669-676.
- Platt, S.R., Farritor, S. and Haider, H. (2005). "On low-frequency electric power generation with PZT ceramics", *IEEE/ASME Transactions on Mechatronic*, 10: 240-252.
- Priya, S. and Inman, D.J. (Editors) (2009). *Energy harvesting technologies*. Boston: Springer-Verlag.
- Roundy, S., Leland, E.S., Baker, J., Carleton, E., Reilly, E., Lai, E., Otis, B., Rabaey, J.M., Wright, P.K. and Sundararajan, V. (2005). "Improving power output for vibration-based energy scavengers", *IEEE Pervasive Computing*, 4: 28-36.
- Roundy, S., Wright, P.K. and Rabaey, J. (2003). "A study of low level vibrations

- as a power source for wireless sensor nodes”, *Computer Communications*, 26: 1131-1144.
- Shahruz, S.M. (2006). “Design of mechanical band-pass filters for energy scavenging”, *Journal of Sound and Vibration*, 292: 987-998.
- SPICE (2010). <http://en.wikipedia.org/wiki/SPICE>.
- Sodano, H.A., Inman, D.J. and Park, G. (2005). “Comparison of piezoelectric energy harvesting devices for recharging batteries”, *Journal of Intelligent Material Systems and Structures*, 16: 799-807.
- Sodano, H.A., Park, G. and Inman, D.J. (2004). “Estimation of electric charge output for piezoelectric energy harvesting”, *Strain*, 40: 49-58.
- Song, G., Mo, Y.L., Otero, K. and Gu, H. (2006). “Health monitoring and rehabilitation of a concrete structure using intelligent materials”, *Smart Materials and Structures*, 15: 309-314.
- Triplett, A. and Quinn, D.D. (2009). “The effect of non-linear piezoelectric coupling on vibration-based energy harvesting”, *Journal of Intelligent Material Systems and Structures*, 20: 1959-1967.
- Yang, Y.W. and Tang, L.H. (2009). “Equivalent circuit modeling of piezoelectric energy harvesters”, *Journal of Intelligent Material Systems and Structures*, 20: 2223-2235.
- Yang, Y.W., Tang, L.H. and Li, H.Y. (2009). “Vibration energy harvesting using macro-fiber composites”, *Smart Materials and Structures*, 18: 115025.

Appendix

(A)

MATLAB program to derive conductance and susceptance plots from results of dynamic harmonic analysis using any commercial finite element software, such as ANSYS. This program is based on 1D impedance model of Liang *et al.* (1994), covered in Chapter 2. Input file should be a text file, each line should have frequency (Hz), real part of applied force (Fr), imaginary part of applied force (Fi), real part of displacement (Ur) and imaginary part of displacement (Ui), separated by tab, and the file to be named as “input.txt”.

All units in the SI system

% Definition of constants (user may set these according to the specification of the PZT patch available from

% the manufacturer)

LA = 0.005	%Length of PZT patch'
WA = 1.0	%Width of PZT patch (considered unit value normal to plane of excitation)
HA = 0.0002	%Thickness of PZT patch'
RHO = 7650	%Density of PZT'
D31 = -0.000000000166	%Piezoelectric strain coefficient'
Y11E = 63000000000	%Young's modulus of PZT'
E33T = 0.000000015	%Electric permittivity of PZT'
ETA = 0.001	%Mechanical loss factor'
DELTA = 0.012	%Electric loss factor'

% Definition of key variables

% f	'Frequency in Hz'
% k_real	'Real component of wave number'
% k_imag	'Imaginary component of wave number'
% x, y	'Real and imaginary components of structural mechanical impedance'

```

% xa, ya      'Real and imaginary components of PZT mechanical impedance'
% r, t       'Real and imaginary components of tankl/kl'
% G, B       'Real and imaginary components of admittance'
% Fr, Fi, Ur, Ui 'Real and imaginary components of force and displacement'

```

%Main program

```
data=dlmread('input.txt','t'); %Data-matrix, stores the input to the program
```

```

f = data(:,1);          %Frequency in Hz
Fr = data(:,2);        %Real component of effective force
Fi = data(:,3);        %Imaginary component of effective force
Ur = data(:,4);        %Real component of effective displacement
Ui = data(:,5);        %Imaginary component of effective displacement

```

```
N=size(f);            %No of data points
```

```
for I = 1:N,
```

%Calculation of structure impedance

```

div(I) = 2 * 3.14 * f(I); %Temporary variable
Big_U(I) = Ur(I) * Ur(I) + Ui(I) * Ui(I);
x(I) = (Fi(I)*Ur(I)-Fr(I)*Ui(I))/(div(I) * Big_U(I));
y(I) = (-1.0) * (Fr(I) * Ur(I)+ Fi(I) * Ui(I)) / (div(I) * Big_U(I));

```

%Calculation of wave number kl

```

w(I) = 2.0 * 3.14 * f(I); % Angular frequency in rad/s
cons = sqrt(RHO/(Y11E * (1 + ETA * ETA))); %Temporary constant
rl(I)= cons * w(I)*LA;
im(I) = cons * w(I) * (-0.5 * ETA)*LA;

```

%Calculation of (tankl/kl)

```
% Temporary variables a, b, c, d, u, v, q
```

```

a(I) = (exp(-im(I)) + exp(im(I))) * sin(rl(I));
b(I) = (exp(-im(I)) - exp(im(I))) * cos(rl(I));
c(I) = (exp(-im(I)) + exp(im(I))) * cos(rl(I));
d(I) = (exp(-im(I)) - exp(im(I))) * sin(rl(I));
u(I) = c(I) * rl(I) - d(I) * im(I);
v(I) = d(I) * rl(I) + c(I) * im(I);
h(I) = u(I)^2 + v(I)^2;
r(I) = (a(I) * u(I) - b(I) * v(I)) / h(I);
t(I) = (-1.0) * (a(I) * v(I) + b(I) * u(I)) / h(I);

```

%Calculation of actuator impedance

```
multia(I) = (WA * HA * Y11E) / (2 * 3.14 * LA * f(I)); %Temporary
```

```

variable
Big_rt(I) = r(I) * r(I) + t(I) * t(I);           %Temporary variable
xa(I) = multia(I) * (ETA * r(I) - t(I)) / Big_rt(I); %Temporary variable
ya(I) = multia(I) * (-1.0) * (r(I) + ETA * t(I)) / Big_rt(I); %Temporary variable

%Calculation of complex admittance
% p, q, Big_p, Big_q, Big_R, Big_T, Big_pq;      %Temporary variables
% temp_r, temp_i;                               %Temporary variables
p(I) = x(I) + xa(I);
q(I) = y(I) + ya(I);
Big_p(I) = xa(I) * p(I) + ya(I) * q(I);
Big_q(I) = ya(I) * p(I) - xa(I) * q(I);
Big_R(I) = r(I) - ETA * t(I);
Big_T(I) = ETA * r(I) + t(I);
Big_pq(I) = p(I) * p(I) + q(I) * q(I);
temp_r(I) = (Big_p(I) * Big_T(I) + Big_q(I) * Big_R(I)) / Big_pq(I);
temp_i(I) = (Big_p(I) * Big_R(I) - Big_q(I) * Big_T(I)) / Big_pq(I);
t_r(I) = ETA - temp_r(I);                       %Temporary variables
t_i(I) = temp_i(I) - 1;                         %Temporary variables
multi(I) = (WA * LA * 2.0 * 3.14 * f(I)) / HA;
G(I)=2* multi(I) * (DELTA * E33T + t_r(I) * D31 * D31 * Y11E);
                                                    %Conductance
B(I)=2* multi(I) * (E33T + t_i(I) * D31 * D31 * Y11E);
                                                    %Susceptance

end;

% Plotting of final result
subplot(2,1,1);
plot(f,G);
subplot(2,1,2);
plot(f,B);

```

(B)

MATLAB program to derive conductance and susceptance plots from results of dynamic harmonic analysis using any commercial finite element software, such as ANSYS. This program is based on 2D effective impedance model of Bhalla and Soh (2004a), but without any correction factor for the PZT patch. Input file should be a text file, each line should have frequency (Hz), real part of applied effective force (F_r), imaginary part of applied effective force (F_i), real part of effective displacement (U_r) and imaginary part of effective displacement (U_i), separated by tab, and the file to be named as “input.txt”

All units in the SI system

```
data=dlmread('input.txt','t'); %Data-matrix, stores ANSYS output
```

% The symbols declared below carry same meaning as in Appendices A
% User may set these according to the specification of the PZT patch
available from % the manufacturer

```
LA=0.005; HA= 0.0003; RHO=7800; D31= -0.00000000021;mu=0.3;  
Y11E= 66700000000; E33T=1.7919e-8; ETA= 0.035; DELTA= 0.0238;
```

```
f = data(:,1); %Frequency in Hz  
Fr = data(:,2); %Real component of effective force  
Fi = data(:,3); %Imaginary component of effective force  
Ur = data(:,4); %Real component of effective displacement  
Ui = data(:,5); %Imaginary component of effective  
%displacement
```

```
N=size(f); %No of data points
```

```
for I = 1:N,
```

%Calculation of structural impedance

```
omega(I) = 2* pi * f(I); %Angular frequency in rad/s  
Big_U(I)= Ur(I)*Ur(I) + Ui(I)*Ui(I);  
x(I) = 2*(Fi(I) * Ur(I) - Fr(I) * Ui(I)) / (omega(I) * Big_U(I));  
y(I) = 2*(-1.0) * (Fr(I)*Ur(I)+Fi(I)*Ui(I))/(omega(I) * Big_U(I));
```

%Calculation of wave number

```
cons = (RHO *(1-mu*mu)/ (Y11E * (1 + ETA * ETA)))^0.5;  
k_real(I) = cons * omega(I);  
k_imag(I) = cons * omega(I) * (-0.5 * ETA);  
rl(I) = k_real(I) * LA;  
im(I) = k_imag(I) * LA;
```

%Calculation of tan(kl)/kl

```
a(I) = (exp(-im(I)) + exp(im(I))) * sin(rl(I));  
b(I) = (exp(-im(I)) - exp(im(I))) * cos(rl(I));  
c(I) = (exp(-im(I)) + exp(im(I))) * cos(rl(I));  
d(I) = (exp(-im(I)) - exp(im(I))) * sin(rl(I));  
u(I) = c(I) * rl(I) - d(I) * im(I);  
v(I) = d(I) * rl(I) + c(I) * im(I);  
h(I) = u(I)^2 + v(I)^2;  
r(I) = (a(I) * u(I) - b(I) * v(I)) / h(I);  
t(I) = (-1.0) * (a(I) * v(I) + b(I) * u(I)) / h(I);
```

```

%Calculation of actuator impedance
multia(I) = (HA * Y11E) / (pi * (1-mu)* f(I));
Big_rt(I) = r(I) * r(I) + t(I) * t(I);
xa(I) = multia(I) * (ETA * r(I) - t(I)) / Big_rt(I);
ya(I) = multia(I) * (-1.0) * (r(I) + ETA * t(I)) / Big_rt(I);

%Calculation of conductance and susceptance
p(I) = x(I) + xa(I);
q(I) = y(I) + ya(I);
Big_p(I) = xa(I) * p(I) + ya(I) * q(I);
Big_q(I) = ya(I) * p(I) - xa(I) * q(I);
Big_R(I) = r(I) - ETA * t(I);
Big_T(I) = ETA * r(I) + t(I);
Big_pq(I) = p(I) * p(I) + q(I) * q(I);
temp_r(I) = (Big_p(I)*Big_T(I)+ Big_q(I)* Big_R(I)) / Big_pq(I);
temp_i(I) = (Big_p(I)*Big_R(I)- Big_q(I)* Big_T(I)) / Big_pq(I);
t_r(I) = ETA - temp_r(I);
t_i(I) = temp_i(I) - 1;
multi(I) = (LA * LA * omega(I)) / HA;
K = 2.0 * D31 * D31 * Y11E / (1 - mu);
G(I) = 4*multi(I) * (DELTA * E33T + K * t_r(I));
B(I) = 4*multi(I) * (E33T + K * t_i(I));
end

%Plotting of results
subplot(2,1,1);
plot(f,G);
subplot(2,1,2);
plot(f,B);

```

(C)

MATLAB program to derive conductance and susceptance plots from results of dynamic harmonic analysis using any commercial finite element software, such as ANSYS. This program is based on 2D effective impedance model of Bhalla and Soh (2004a), considering correction factor for the PZT patch (twin-peak case). Input file should be a text file, each line should have frequency (Hz), real part of applied effective force (F_r), imaginary part of applied effective force (F_i), real part of effective displacement (U_r) and imaginary part of effective displacement (U_i), separated by tab, and the file to be named as “input.txt”

NOTE: Single-peak case can also be dealt with by using $cf1 = cf2$

All units in the SI system

%PZT parameters covered below are based on measurement.

data=dlmread('input.txt','t');

%Data-matrix, stores the ANSYS output

%PZT parameters based on updated model derived by experiment

%Symbols for following variables carry same meaning as Appendices A,B

LA=0.005; HA= 0.0003; RHO=7800; D31= -2.1e-10;mu=0.3;

Y11E= 6.67e10; E33T=1.7919e-8; ETA= 0.03; DELTA= 0.0238; K =5.16e-9;

```
f = data(:,1);           %Frequency in Hz
Fr = data(:,2);         %Real component of effective force
Fi = data(:,3);         %Imaginary component of effective force
Ur = data(:,4);         %Real component of effective displacement
Ui = data(:,5);         %Imaginary component of effective displacement
N=size(f);              %No of data points
cf1 = 0.94;             %Correction factors for PZT peaks
cf2 = 0.883;           %For single peak case, Cf1 = cf2
```

for I = 1:N,

%Calculation of structural impedance

omega(I) = 2* pi * f(I); %Angular frequency in rad/s

Big_U(I)= Ur(I)*Ur(I) + Ui(I)*Ui(I);

x(I) = 2*(Fi(I) * Ur(I) - Fr(I) * Ui(I)) / (omega(I) * Big_U(I));

y(I) = 2*(-1.0) * (Fr(I)*Ur(I) + Fi(I)*Ui(I))/(omega(I)* Big_U(I));

%Calculation of wave number

cons = (RHO *(1-mu*mu)/ (Y11E * (1 + ETA * ETA)))^0.5;

k_real(I) = cons * omega(I);

k_imag(I) = cons * omega(I) * (-0.5 * ETA);

%Calculation of tan(kl)/kl

rl(I) = k_real(I) * LA * cf1;

im(I) = k_imag(I) * LA * cf1;

a(I) = (exp(-im(I)) + exp(im(I))) * sin(rl(I));

b(I) = (exp(-im(I)) - exp(im(I))) * cos(rl(I));

c(I) = (exp(-im(I)) + exp(im(I))) * cos(rl(I));

d(I) = (exp(-im(I)) - exp(im(I))) * sin(rl(I));

u(I) = c(I) * rl(I) - d(I) * im(I);

```
v(I) = d(I) * rl(I) + c(I) * im(I);
h(I) = u(I)^2 + v(I)^2;
r1(I) = (a(I) * u(I) - b(I) * v(I)) / h(I);
t1(I) = (-1.0) * (a(I) * v(I) + b(I) * u(I)) / h(I);
```

```
rl(I) = k_real(I) * LA * cf2;
im(I) = k_imag(I) * LA * cf2;
```

```
a(I) = (exp(-im(I)) + exp(im(I))) * sin(rl(I));
b(I) = (exp(-im(I)) - exp(im(I))) * cos(rl(I));
c(I) = (exp(-im(I)) + exp(im(I))) * cos(rl(I));
d(I) = (exp(-im(I)) - exp(im(I))) * sin(rl(I));
u(I) = c(I) * rl(I) - d(I) * im(I);
v(I) = d(I) * rl(I) + c(I) * im(I);
h(I) = u(I)^2 + v(I)^2;
r2(I) = (a(I) * u(I) - b(I) * v(I)) / h(I);
t2(I) = (-1.0) * (a(I) * v(I) + b(I) * u(I)) / h(I);
```

```
r(I) = 0.5 * (r1(I)+r2(I));
t(I) = 0.5 * (t1(I)+t2(I));
```

%Calculation of actuator impedance

```
multia(I) = (HA * Y11E) / (pi * (1-mu) * f(I));
Big_rt(I) = r(I) * r(I) + t(I) * t(I);
xa(I) = multia(I) * (ETA * r(I) - t(I)) / Big_rt(I);
ya(I) = multia(I) * (-1.0) * (r(I) + ETA * t(I)) / Big_rt(I);
```

%Calculation of conductance and susceptance

```
p(I) = x(I) + xa(I);
q(I) = y(I) + ya(I);
Big_p(I) = xa(I) * p(I) + ya(I) * q(I);
Big_q(I) = ya(I) * p(I) - xa(I) * q(I);
Big_R(I) = r(I) - ETA * t(I);
Big_T(I) = ETA * r(I) + t(I);
Big_pq(I) = p(I) * p(I) + q(I) * q(I);
temp_r(I) = (Big_p(I) * Big_T(I) + Big_q(I) * Big_R(I)) / Big_pq(I);
temp_i(I) = (Big_p(I) * Big_R(I) - Big_q(I) * Big_T(I)) / Big_pq(I);
t_r(I) = ETA - temp_r(I);
t_i(I) = temp_i(I) - 1;
multia(I) = (LA * LA * omega(I)) / HA;
G(I) = 4*multia(I) * (DELTA * E33T + K *t_r(I));           %Conductance
B(I) = 4*multia(I) * (E33T + K *t_i(I));                   %Susceptance
```

End

%Plotting of results


```
subplot(2,1,1);
plot(f,G);
subplot(2,1,2);
plot(f,B);
```

(D)

MATLAB program to derive conductance and susceptance plots from results of dynamic harmonic analysis using any commercial finite element software, such as ANSYS. This program is based on 3D effective impedance model of Annamdas and Soh (2007). See Fig 3.21. There should be six faces along three directions: +x, -x, +y, -y, +z and -z. There should be input files for each face: X_100.txt, X_100_E.txt, Y_100.txt, Y_100_E.txt, Z_100.txt and Z_100_E.txt. These input files should be text file, each line should have frequency (Hz), real part of effective displacement (UX_{odd} number) or (EQX_{odd} number) and imaginary part of effective displacement (UX_{even} number) or (EQX_{even} number), separated by tab. Input files should be prepared for all faces. The dimensions and properties of PZT patch can be varied easily. The number of data points on X or Y faces, and Z considered in this program are 6 and 20. These data points can be varied easily.

All units in the SI system

```
L=0.005;           % Half Length of PZT patch, Patch Length = 10 mm = 0.01 m
WD=0.005;         % Half Width of PZT patch (considered unit value normal to
                  % plane of excitation)
H=0.000150;      % Thickness of PZT patch
DELTA=0.015;     % Electric loss factor
EP33 =1.70E-8;   % Electric permittivity of PZT
D31 =-2.1E-10;   % Piezoelectric strain coefficient in Direction X or 1
D32 =-2.1E-10;   % Piezoelectric strain coefficient in Direction y or 2
D33=4.5e-10;     % Piezoelectric strain coefficient in Direction Z or 3
Y11=6.667E+10;  % Young's modulus of PZT
EETA=0.0250;    % Mechanical loss factor
DE=7800;        % (SUPPLIER VALUES) %Density of PZT
```

```
YC11=(1+EETA*j)*Y11; EPC33=(1-DELTA*j)*EP33; DD=D31*D31*YC11;
```

```
MU=0.33;         % Poisson Ratio
```

```
M=dlmread('X_100.txt'); % Input file for Face +X, for considered distributed points
F=M(:,1);
```

%ZX impedance % Data points are 6, hence 6 pairs of displacements (real and imaginary), data can be easily varied by adding or subtracting

```
UX_1=M(:,2);
UX_2=M(:,3);
UX_3=M(:,4);
UX_4=M(:,5);
UX_5=M(:,6);
UX_6=M(:,7);
UX_7=M(:,8);
UX_8=M(:,9);
UX_9=M(:,10);
UX_10=M(:,11);
UX_11=M(:,12);
UX_12=M(:,13);
```

```
EQ=dlmread('X_100_E.txt'); % For Face -X,
```

```
F=EQ(:,1);
```

```
%ZEX impedance
```

```
EQX_1=EQ(:,2);
EQX_2=EQ(:,3);
EQX_3=EQ(:,4);
EQX_4=EQ(:,5);
EQX_5=EQ(:,6);
EQX_6=EQ(:,7);
EQX_7=EQ(:,8);
EQX_8=EQ(:,9);
EQX_9=EQ(:,10);
EQX_10=EQ(:,11);
EQX_11=EQ(:,12);
EQX_12=EQ(:,13);
```

```
M1=dlmread('Y_100.txt'); % For Face +Y,
```

```
%UY impedance
```

```
UY_1=M1(:,2);
UY_2=M1(:,3);
UY_3=M1(:,4);
UY_4=M1(:,5);
UY_5=M1(:,6);
UY_6=M1(:,7);
UY_7=M1(:,8);
UY_8=M1(:,9);
UY_9=M1(:,10);
UY_10=M1(:,11);
UY_11=M1(:,12);
UY_12=M1(:,13);
```

```

EQ1=dlmread('Y_100_E.txt');   % For Face +Y,
%UY impedance
EQY_1=EQ1(:,2);
EQY_2=EQ1(:,3);
EQY_3=EQ1(:,4);
EQY_4=EQ1(:,5);
EQY_5=EQ1(:,6);
EQY_6=EQ1(:,7);
EQY_7=EQ1(:,8);
EQY_8=EQ1(:,9);
EQY_9=EQ1(:,10);
EQY_10=EQ1(:,11);
EQY_11=EQ1(:,12);
EQY_12=EQ1(:,13);

```

%UZ BOTTOM impedance %Z direction

```

M3=dlmread('Z_100.txt');
UZB_1=M3(:,2);
UZB_2=M3(:,3);
UZB_3=M3(:,4);
UZB_4=M3(:,5);
UZB_5=M3(:,6);
UZB_6=M3(:,7);
UZB_7=M3(:,8);
UZB_8=M3(:,9);
UZB_9=M3(:,10);
UZB_10=M3(:,11);
UZB_11=M3(:,12);
UZB_12=M3(:,13);
UZB_13=M3(:,14);
UZB_14=M3(:,15);
UZB_15=M3(:,16);
UZB_16=M3(:,17);
UZB_17=M3(:,18);
UZB_18=M3(:,19);
UZB_19=M3(:,20);
UZB_20=M3(:,21);
UZB_21=M3(:,22);
UZB_22=M3(:,23);
UZB_23=M3(:,24);
UZB_24=M3(:,25);

```

```
UZB_25=M3(:,26);
UZB_26=M3(:,27);
UZB_27=M3(:,28);
UZB_28=M3(:,29);
UZB_29=M3(:,30);
UZB_30=M3(:,31);
UZB_31=M3(:,32);
UZB_32=M3(:,33);
UZB_33=M3(:,34);
UZB_34=M3(:,35);
UZB_35=M3(:,36);
UZB_36=M3(:,37);
UZB_37=M3(:,38);
UZB_38=M3(:,39);
UZB_39=M3(:,40);
UZB_40=M3(:,41);
```

```
EQ3=dlmread('Z_100_E.txt');
EQZB_1=EQ3(:,2);
EQZB_2=EQ3(:,3);
EQZB_3=EQ3(:,4);
EQZB_4=EQ3(:,5);
EQZB_5=EQ3(:,6);
EQZB_6=EQ3(:,7);
EQZB_7=EQ3(:,8);
EQZB_8=EQ3(:,9);
EQZB_9=EQ3(:,10);
EQZB_10=EQ3(:,11);
EQZB_11=EQ3(:,12);
EQZB_12=EQ3(:,13);
EQZB_13=EQ3(:,14);
EQZB_14=EQ3(:,15);
EQZB_15=EQ3(:,16);
EQZB_16=EQ3(:,17);
EQZB_17=EQ3(:,18);
EQZB_18=EQ3(:,19);
EQZB_19=EQ3(:,20);
EQZB_20=EQ3(:,21);
EQZB_21=EQ3(:,22);
EQZB_22=EQ3(:,23);
EQZB_23=EQ3(:,24);
EQZB_24=EQ3(:,25);
EQZB_25=EQ3(:,26);
EQZB_26=EQ3(:,27);
EQZB_27=EQ3(:,28);
```

```

EQZB_28=EQ3(:,29);
EQZB_29=EQ3(:,30);
EQZB_30=EQ3(:,31);
EQZB_31=EQ3(:,32);
EQZB_32=EQ3(:,33);
EQZB_33=EQ3(:,34);
EQZB_34=EQ3(:,35);
EQZB_35=EQ3(:,36);
EQZB_36=EQ3(:,37);
EQZB_37=EQ3(:,38);
EQZB_38=EQ3(:,39);
EQZB_39=EQ3(:,40);
EQZB_40=EQ3(:,41);

```

```
N100=size(F);
```

```
for I = 1:N100
```

```

W(I) = (2*22/7)*F(I);
AFREQ(I)=(W(I)/(1-MU))*W(I)*DE*(1+MU)*(1-2*MU)/YC11;
K(I)=sqrt(AFREQ(I));

```

```

U1(I)=UX_1(I)+j*UX_2(I)+UX_3(I)+j*UX_4(I)+UX_5(I)+j*UX_6(I)+UX_7
(I)+j*UX_8(I)+UX_9(I)+j*UX_10(I)+UX_11(I)+j*UX_12(I);
Z1(I)= 6/ (j*W(I)*U1(I));

```

```

U2(I)=UY_1(I)+j*UY_2(I)+UY_3(I)+j*UY_4(I)+UY_5(I)+j*UY_6(I)+UY_7(I)
+
j*UY_8(I)+UY_9(I)+j*UY_10(I)+UY_11(I)+j*UY_12(I);

```

```
Z2(I)= 6/ (j*W(I)*U2(I));
```

```

U3B(I)=(UZB_1(I)+j*UZB_2(I))+(UZB_3(I)+j*UZB_4(I))+(UZB_5(I)+
j*UZB_6(I))+(UZB_7(I)+j*UZB_8(I))+(UZB_9(I)+j*UZB_10(I))+(UZB_11(
I)+
j*UZB_12(I))+(UZB_13(I)+j*UZB_14(I))+(UZB_15(I)+j*UZB_16(I))+
(UZB_17(I)+j*UZB_18(I))+(UZB_19(I)+j*UZB_20(I))+(UZB_21(I)+
j*UZB_22(I))+(UZB_23(I)+j*UZB_24(I))+(UZB_25(I)+j*UZB_26(I))+
(UZB_27(I)+j*UZB_28(I))+(UZB_29(I)+j*UZB_30(I))+(UZB_31(I)+
j*UZB_32(I))+(UZB_33(I)+j*UZB_34(I))+(UZB_35(I)+j*UZB_36(I))+
(UZB_37(I)+j*UZB_38(I))+(UZB_39(I)+j*UZB_40(I));

```

U3B(I)=(j*W(I)*U3B(I)); %(DISPLACEMENT)

Z3(I)=-20/(U3B(I));

%loop

R=MU/(1-MU) ;

R1(I)=K(I)*L*2*H;

R2(I)=K(I)*WD*2*H;

R3(I)=K(I)*L*WD;

a1(I)=R1(I)*WD* cos(K(I)*WD)-Z1(I)*WD*j*W(I)*sin(K(I)*WD);

a2(I)=R*R1(I)*L*cos(K(I)*L);

a3(I)=R*R1(I)*cos(K(I)*2*H);

a4(I)=R1(I)*(D31+R*(D32+D33));

b1(I)=R*R2(I)* WD*cos(K(I)*WD);

b2(I)=R2(I)* L*cos(K(I)*L)-Z2(I)*j*W(I)*L*sin(K(I)*L);

b3(I)=R*R2(I)*cos(K(I)*2*H);

b4(I)=R2(I)*(D32+R*(D31+D33));

c1(I)=R*R3(I)* WD*cos(K(I)*WD);

c2(I)=R*R3(I)*L*cos(K(I)*L);

c3(I)=R3(I)* cos(K(I)*H)-Z3(I)*j*W(I)*sin(K(I)*2*H);

c4(I)=R3(I)*(D33+R*(D31+D32));

E0num(I)= ((a4(I)*b1(I)-a1(I)*b4(I))*(c1(I)*b2(I)-c2(I)*b1(I))-
((a2(I)*b1(I)-a1(I)*b2(I))*(c1(I)*b4(I)-c4(I)*b1(I)));

E0deno(I)=((c1(I)*b2(I) - c2(I)*b1(I))*(a3(I)*b1(I) - a1(I)*b3(I))-
((c1(I)*b3(I)-c3(I)*b1(I))*(a2(I)*b1(I)-a1(I)*b2(I)));

E0(I)= E0num/E0deno;

C0num(I)= (c1(I)*b4(I)-c4(I)*b1(I))- (c1(I)*b3(I)-c3(I)*b1(I))*E0(I);

C0deno(I)= c1(I)*b2(I) - c2(I)*b1(I);

C0(I)= C0num(I) / C0deno(I);

A0(I)= (a4(I)-a2(I)*C0(I) - a3(I)*E0(I))/ a1(I);

S31(I)=D31*((A0(I)*sin(K(I)*WD)-D31)+R*(C0(I)* sin (K(I)*L)-D32)+
R*(E0(I)*K(I)*cos (K(I)*2*H)-D33));

S32(I)=D32*(R*(A0(I)* sin(K(I)*WD)-D31)+(C0(I)* sin (K(I)*L)-D32)+
R*(E0(I)*K(I)*cos (K(I)*2*H)-D33));

```

S33(I)=D33*(R*(A0(I)* sin(K(I)*WD)-D31)+R*(C0(I)* sin (K(I)*L)-D32)+
(E0(I)*K(I)*cos (K(I)*2*H)-D33));

Y_D=(1+MU)*(1-2*MU);
Y_N=(1-MU);
Y_CONST=Y_N / Y_D;
AA1(I)=(Z1(I)/(Z1(I)+Z2(I)-Z3(I)));
AA2(I)=(Z2(I)/(Z1(I)+Z2(I)-Z3(I)));
AA3(I)=(Z3(I)/(Z1(I)+Z2(I)-Z3(I)));

Y_ADMIT(I)=2*j*W(I)*(L/H)*WD*(EPC33+YC11*Y_CONST*(AA1(I)*S
31(I)+AA2(I)*S32(I)+AA3(I)*S33(I)));

C1(I) = Y_ADMIT(I);

C(I)=real(C1(I));
D(I)=imag(C1(I));

end;
%Plotting of Results
subplot(2,1,1);
plot(F,C); % conductance
subplot(2,1,2);
plot(F,D); % susceptance
dlmwrite('Frequency HZ.txt',F, '\n') ; %stores in a file of same folder
dlmwrite('Conductance S.txt',C, '\n') ; %stores in a file
dlmwrite('Susceptance S.txt',D, '\n') ; %stores in a file

```

(E)

MATLAB program to derive structural mechanical impedance from experimental admittance signatures, using updated PZT model (twin-peak), based on model of Bhalla and Soh (2004a). Input file should be a text file, each line should have frequency (kHz), conductance (G), and susceptance (B), obtained from measurement and separated by tab. The file to be named as “gb.txt”

NOTE: For single-peak case, cf1 = cf2

All units in the SI system

%Inputs: Frequency (kHz), G (S), B (S)

%PZT parameters- based on measurement.

```

data=dlmread('gb.txt','t');           %Data-matrix,

%The symbols for variables carry same meaning as in Appendices A, B and C
LA=0.005; HA= 0.0003; RHO=7800; D31= -2.1e-10; mu=0.3;
Y11E= 6.67e10; E33T=1.7919e-8; ETA= 0.03; DELTA= 0.0238;
cf1 = 0.94; cf2 = 0.883;              %Correction factors for PZT peaks
                                       %For single peak case, cf1 = cf2
f = 1000*data(:,1);                   %Frequency in Hz
G = data(:,2);                         %Conductance
B = data(:,3);                         %Susceptance

K = 5.16e-9;                           %K = 2*D31*D31*Y11E/(1-mu);
no=size(f);                             %No of data points

for I = 1:no,

```

%Calculation of active signatures

```

omega(I) = 2*pi*f(I);
multi(I) = 4*(LA * LA * omega(I)) / HA;
Gp(I) = multi(I) * (E33T * DELTA + K * ETA);
GA(I) = G(I)- Gp(I);
Bp(I) = multi(I) * (E33T - K);
BA(I) = B(I) - Bp(I);

```

%Calculation of M and N

```

M(I) = (BA(I)*HA)/(4*omega(I)*K*LA*LA);
N(I) = (-GA(I)*HA)/(4*omega(I)*K*LA*LA);

```

%Calculation of wave number

```

cons = (RHO * (1-mu*mu) / (Y11E * (1 + ETA * ETA)))^0.5;
k_real(I) = cons * omega(I);
k_imag(I) = cons * omega(I) * (-0.5 * ETA);
rl(I) = k_real(I) * LA;
im(I) = k_imag(I) * LA;

```

%Calculation of tan(kl)/kl

```

rl(I) = k_real(I) * LA * cf1;
im(I) = k_imag(I) * LA * cf1;

a(I) = (exp(-im(I)) + exp(im(I))) * sin(rl(I));
b(I) = (exp(-im(I)) - exp(im(I))) * cos(rl(I));
c(I) = (exp(-im(I)) + exp(im(I))) * cos(rl(I));
d(I) = (exp(-im(I)) - exp(im(I))) * sin(rl(I));

```



```

u(I) = c(I) * rl(I) - d(I) * im(I);
v(I) = d(I) * rl(I) + c(I) * im(I);
h(I) = u(I)^2 + v(I)^2;
r1(I) = (a(I) * u(I) - b(I) * v(I)) / h(I);
t1(I) = (-1.0) * (a(I) * v(I) + b(I) * u(I)) / h(I);

```

```

rl(I) = k_real(I) * LA * cf2;
im(I) = k_imag(I) * LA * cf2;

```

```

a(I) = (exp(-im(I)) + exp(im(I))) * sin(rl(I));
b(I) = (exp(-im(I)) - exp(im(I))) * cos(rl(I));
c(I) = (exp(-im(I)) + exp(im(I))) * cos(rl(I));
d(I) = (exp(-im(I)) - exp(im(I))) * sin(rl(I));
u(I) = c(I) * rl(I) - d(I) * im(I);
v(I) = d(I) * rl(I) + c(I) * im(I);
h(I) = u(I)^2 + v(I)^2;
r2(I) = (a(I) * u(I) - b(I) * v(I)) / h(I);
t2(I) = (-1.0) * (a(I) * v(I) + b(I) * u(I)) / h(I);

```

```

r(I) = 0.5 * (r1(I)+r2(I));
t(I) = 0.5 * (t1(I)+t2(I));

```

%Calculation of actuator impedance

```

multia(I) = (HA * Y11E) / (pi * (1-mu) * f(I));
Big_rt(I) = r(I) * r(I) + t(I) * t(I);
xa(I) = multia(I) * (ETA * r(I) - t(I)) / Big_rt(I);
ya(I) = multia(I) * (-1.0) * (r(I) + ETA * t(I)) / Big_rt(I);

```

%Calculation of structural impedance

```

R(I) = r(I) - ETA * t(I);
S(I) = ETA * r(I) + t(I);
P(I) = xa(I) * R(I) - ya(I) * S(I);
Q(I) = xa(I) * S(I) + ya(I) * R(I);
MN(I) = M(I)^2 + N(I)^2;
x(I) = (P(I)*M(I)+Q(I)*N(I))/MN(I) - xa(I); %Real part of mechanical
impedance
y(I) = (Q(I)*M(I)-P(I)*N(I))/MN(I) - ya(I); %Imaginary part of mechanical
impedance

```

```

end

```

%Plotting of results

```

subplot(2,1,1);
plot(f,x);
subplot(2,1,2);
plot(f,y);

```

(F)

Matrices in the State-Space Equations given in Chapter 10

For a typical layer i , the relations among matrices A_j and B_j ($j=0,1,2$) in Eq. (10.10) are

$$A_1^{(i)} = \frac{dA_0^{(i)}}{dr_i}, \quad A_2^{(i)} = \frac{d^2A_0^{(i)}}{2dr_i^2}, \quad B_1^{(i)} = \frac{dB_0^{(i)}}{dr_i}, \quad B_2^{(i)} = \frac{d^2B_0^{(i)}}{2dr_i^2}$$

where A_0 is a diagonal matrix with non-zero elements $A_0(1,1)=A_0(4,4)=1$, $A_0(2,2)=A_0(3,3)=r_i$, $A_0(5,5)=A_0(6,6)=A_0(7,7)=A_0(8,8)=r_i^2$, and

$$B_0 = \begin{bmatrix} 0 & 0 & \alpha_m & 0 & 0 & b_{16} & 0 & b_{18} \\ 0 & -1 & n & 0 & 0 & 0 & b_{27} & 0 \\ b_{31} & b_{32} & b_{33} & b_{34} & b_{35} & 0 & 0 & 0 \\ 0 & 0 & 0 & 0 & 0 & b_{46} & 0 & b_{48} \\ b_{51} & b_{52} & b_{53} & b_{54} & b_{55} & b_{56} & -nr_i & 0 \\ b_{61} & b_{62} & b_{63} & b_{64} & b_{65} & r_i & 0 & 0 \\ b_{71} & b_{72} & b_{73} & b_{74} & b_{75} & 0 & 2r_i & 0 \\ b_{81} & b_{82} & b_{83} & b_{84} & b_{85} & 0 & 0 & r_i \end{bmatrix}$$

where coefficients b_{ij} are given by

$$b_{16} = -\varepsilon_{33}/g_1, \quad b_{18} = -e_{35}/g_1, \quad b_{27} = -r_i/c_{44}, \quad b_{31} = -c_{13}\alpha_m r_i/c_{33},$$

$$b_{32} = -c_{23}n/c_{33}, \quad b_{33} = c_{23}/c_{33}, \quad b_{34} = -e_{13}\alpha_m r_i/c_{33}, \quad b_{35} = -r_i/c_{33}, \quad b_{46} = b_{16},$$

$$b_{48} = c_{55}/g_1, \quad b_{51} = g_2 r_i, \quad b_{52} = g_3 n, \quad b_{53} = \rho\omega^2 r_i^2 - g_3, \quad b_{54} = g_4 r_i,$$

$$b_{55} = \left(1 - \frac{c_{23}}{c_{33}}\right)r_i, \quad b_{56} = -\alpha_m r_i^2, \quad b_{61} = g_5 r_i^2 - c_{66}n^2, \quad b_{62} = g_6 r_i, \quad b_{63} = g_2 r_i,$$

$$b_{64} = g_7 r_i^2 - e_{26}n^2, \quad b_{65} = c_{13}\alpha_m r_i^2/c_{33}, \quad b_{71} = g_6 r_i, \quad b_{72} = g_8 n^2 + g_9 r_i^2, \quad b_{73} = -g_8 n,$$

$$b_{74} = g_{10} r_i, \quad b_{75} = c_{23}nr_i/c_{33}, \quad b_{81} = g_7 r_i^2 - e_{26}n^2, \quad b_{82} = g_{10} r_i, \quad b_{83} = \rho\omega^2 r_i^2 + g_{11} r_i,$$

$$b_{84} = g_{12} r_i^2 + \varepsilon_{22}n^2, \quad b_{85} = g_{13} r_i^2 \quad \text{with } g_1 = e_{35}^2 + c_{55}\varepsilon_{33}, \quad g_2 = \left(c_{12} - \frac{c_{13}c_{23}}{c_{33}}\right)\alpha_m,$$

$$g_3 = c_{22} - \frac{c_{23}^2}{c_{33}}, \quad g_4 = \frac{e_{13}^2}{c_{33}}\alpha_m^2, \quad g_5 = \left(\frac{c_{13}^2}{c_{33}} - c_{11}\right)\alpha_m^2 + \rho\omega^2,$$

$$g_6 = \left(\frac{c_{13}c_{23}}{c_{33}} - c_{66} - c_{12}\right)\alpha_m n, \quad g_7 = \left(\frac{e_{13}c_{13}}{c_{33}} - e_{11}\right)\alpha_m^2, \quad g_8 = \frac{c_{23}^2}{c_{33}} - c_{22},$$

$$g_9 = \rho\omega^2 - c_{66}\alpha_m^2, \quad g_{10} = \left(\frac{c_{23}e_{13}}{c_{33}} - e_{12} - e_{26}\right)\alpha_m n, \quad g_{11} = \left(e_{12} - \frac{e_{13}c_{23}}{c_{33}}\right)\alpha_m,$$

$$g_{12} = \frac{e_{13}^2}{c_{33}} \alpha_m^2 \text{ and } g_{13} = \frac{e_{13}}{c_{33}} \alpha_m.$$

Matrix T in Eq. (10.15) is

$$T = \begin{bmatrix} t_{11} & t_{12} & t_{13} & t_{14} & t_{15} & 0 & 0 & 0 \\ t_{21} & t_{22} & t_{23} & t_{24} & t_{25} & 0 & 0 & 0 \\ t_{31} & t_{32} & 0 & t_{34} & 0 & 0 & 0 & 0 \\ t_{41} & t_{42} & t_{43} & t_{44} & t_{45} & 0 & 0 & 0 \\ t_{51} & t_{52} & 0 & t_{54} & 0 & 0 & 0 & 0 \end{bmatrix}$$

where $t_{11} = \left(\frac{c_{13}^2}{c_{33}} - c_{11} \right) \alpha_m$, $t_{12} = \left(\frac{c_{13}c_{23}}{c_{33}} - c_{12} \right) n / (r_i + z)$, $t_{13} = \left(c_{12} - \frac{c_{13}c_{23}}{c_{33}} \right) / (r_i + z)$,

$$t_{14} = \left(\frac{e_{13}c_{13}}{c_{33}} - e_{11} \right) \alpha_m, \quad t_{15} = \frac{c_{13}}{c_{33}}, \quad t_{21} = -g_2, \quad t_{22} = g_8 n / (r_i + z), \quad t_{23} = -g_8 / (r_i + z),$$

$$t_{24} = \left(\frac{e_{13}c_{23}}{c_{33}} - e_{12} \right) \alpha_m, \quad t_{25} = \frac{c_{23}}{c_{33}}, \quad t_{31} = c_{66} n / (r_i + z), \quad t_{32} = c_{66} \alpha_m, \quad t_{34} = e_{26} n / (r_i + z),$$

$$t_{41} = t_{14}, \quad t_{42} = \left(\frac{e_{13}c_{23}}{c_{33}} - e_{12} \right) n / (r_i + z), \quad t_{43} = \left(e_{12} - \frac{e_{13}c_{23}}{c_{33}} \right) / (r_i + z),$$

$$t_{44} = \left(\frac{e_{13}^2}{c_{33}} + \varepsilon_{11} \right) \alpha_m, \quad t_{45} = \frac{e_{13}}{c_{33}}, \quad t_{51} = e_{26} n / (r_i + z), \quad t_{52} = e_{26} \alpha_m, \text{ and}$$

$$t_{54} = -\varepsilon_{22} n / (r_i + z).$$

Index

2D effective mechanical impedance 56
2D force measurement 466
3D force measurement 467
3D impedance model 77

A

AC coupling coefficient 422
Acoustic emission 4
Active component 33, 129
Active conductance 34
Active control 301
Active scleral band 533
Active smart material 7
Active structure 6
Active susceptance 34
Active vibration control 401
Actuator-sensor pair 570
Adaptive structure 5
Adaptive template matching (ATM) 39
Adhesive layer 78
Aging rate 276
Ambient noise 497
Angular frequency 18, 23
Anode boundary layer (ABL) 507
Anti-resonance 28
Araldite 572
Artificial ventricular muscle 533
Artificial vessel 554
Aspect ratio 73
Average curvature 237
Axial force 301, 303

Axial strain 424, 433, 446, 462

B

Betti's theorem 226
Binomial distribution 203
Biomimetic micro-collector 583
Bonding film 121
Bonding layer 276, 282
Bone characterization 569
Broadband energy harvesting 589

C

Capsule formation 569
Carbon composite 429, 471
Carbon composite material (CCM) 429
Cathode boundary layer (CBL) 508
Cathode ray oscilloscope 189
Central difference approximation 148
Centrosymmetric crystal 7
Change in flexibility method 2
Change in stiffness method 2
Characteristic function 204
Chicken femur 570
CN adhesive 572
Collective linear impedance 92
Combined position mode function (CPMF) 379
Complex electric permittivity 22, 29
Complex shear modulus 11
Complex Young's modulus 11, 22, 29
Compliance matrix 10

Compression testing machine 485
 Condition assessment 2
 Conductance signature 26
 Convergence test 67
 Converse effect 8, 9, 569
 Corrected actuator effective impedance 75
 Correction factors 74
 Correlation coefficient (CC) 40, 163
 Correspondence principle 255
 Coupled field analysis 108
 Coupled field element 118
 Covariance (Cov) 40, 164
 Cross impedance 55
 Cubic crystal 11
 Cumulative conductance 97
 Cumulative distribution function 202
 Cumulative susceptance 97
 Curie temperature 12
 Curvature mode shape method 2
 Curvature mode shapes 227, 228

D

Damage assessment 187
 Damage growth 208
 Damage index 234, 236, 237
 Damage index method 2
 Damage metric 148
 Damage progression 187, 197, 208
 Damping matrix 226
dc (period-averaged) coupling coefficient 422
 Dental splint 445, 446, 447, 478
 Dielectric loss factor 22, 29
 Dielectric permittivity 9
 Digital meter 189
 Digital multimeter 224, 226
 Direct effect 8, 9
 Direct impedance 55
 Displacement feedback control 306
 Drive point mechanical impedance 56, 107, 132

E

Eddy currents 4
 EDP impedance 132
 Effective drive point (EDP) impedance 58, 63
 Effective force 58, 60
 Effective mechanical impedance 57, 63, 190
 Einbeck pendulum hammer 188
 Elastic compliance tensor 9
 Elastic foundation 363
 Elastic medium 543
 Electrical impedance 44, 45
 Electrical noise 3, 37, 38
 Electrical strain gauge (ESG) 482
 Electro-active polymers (EAPs) 501
 Electromagnetic noise 3, 37, 38
 Electro-mechanical coupling 25
 Electromechanical impedance (EMI) technique 14, 17
 Electromechanical noise 3
 Electro-rheological (ER) fluid 6
 Electrostrictive effect 11
 EM admittance 22, 26, 44
 Embedded PZT patch 210
 EMI technique 230
 Empirical cumulative distribution function 206
 Energy Harvesting 584, 585
 Environmental effect 275
 EP algorithm 173, 174
 Equivalent level of degradation system (ELODS) 39
 Equivalent lumped system parameters 139
 Equivalent spring stiffness 200
 Equivalent system 133, 135, 136, 137, 139, 142, 145, 146, 195
 Experimental impedance spectra 194
 Extensional actuations 77, 81, 82
 Extensometer 482
 Extracted equivalent damping 197

F

FBG sensor 498
 Feasible domain 173
 FFT analyzer 43
 Fiber Bragg Grating 413, 414, 416, 441
 Fiber optic 481
 Fitness function 163, 173, 174
 Flexural stiffness 235
 Foot pressure sensor 442, 443, 444, 445, 477
 Foot sole 441, 461
 Footpad 443
 FOS 413
 Frank spring hammer 188
 Free PZT patch 213
 Frequency response function (FRF) 570
 Full solution method 65
 Function generator 570
 Fuzzy failure probability (FFP) 497

G

Galerkin finite element discretization 64
 Genetic algorithms 334
 Global vibration technique 234
 Goodness-of-fit 203, 206
 Grade of membership 204

H

Harmonic force 18, 64, 103
 High strength epoxy adhesive 483
 Human femur 577
 Human tissues 534
 Hybrid EP algorithm 173, 174, 181, 183, 184
 Hybrid evolutionary programming 164
 Hypergeometric distribution 203

I

Identified equivalent stiffness 208
 Impact echo testing 4

Impedance analyzer 17
 Impedance parameters 187, 194
 Impedance transducers 36
 Impedance-based damage model 201
 Incipient damage 138, 141, 143, 163, 164, 223, 230
 In-situ stresses 265
 Intelligent structure 5
 Ionic polymer-metal composite (IPMC) 501
 IPMC cylindrical shell 554
 IPMC ring 543

K

Kelvin-Voigt model 133, 144, 194, 201, 231
 Kirchhoff plate 179
Kolmogorov-Smirnov 202, 206

L

Laminate/Laminates 425, 426, 428, 442, 443, 449, 451
 LCR meter 17, 231
 Light emitting diode (LED) 591
 Load history monitoring 481
 Load history retrieval (LHR) 481, 482
 Load ratio 197, 205, 206
 Local mutation (LM) 174
 Longitudinal actuators 81, 101, 103
 Longitudinal deformations 148
 Longitudinal mode shapes 151
 Longitudinal vibration mode 148
 Long-term effects 199
 Loss of equivalent spring stiffness 197
 Loss of secant modulus 197

M

Macro fiber composite (MFC) 13, 586
 Macro mutation (MM) 174
 Magnetic field analysis 4
 Magneto-strictive material 6
 Mean absolute percentage deviation (MAPD) 39, 164

- Mechanical impedance 19, 56
 Mechanical impedance of PZT patch 24, 27
 Mechanical impedance of structure 19, 23
 Mechanical loss factor 22, 29
 Mechanical noise 3, 37
 Membership function 204, 497
 Metatarsal 441, 445
 M-Functioning PZT Patches 96
 Microelectromechanical system (MEMS) 12, 108
 Micron-optics interrogator 484
 Miniature aerospace gadgets 143
 Modal approach 163
 Modal damping 570
 Modal frequencies 231
 Modal solution 110
 Mode shape 148, 171, 234, 235
 Mode shape vectors 146, 147
 Modes of vibration 69
 Monoclinic crystal 11
 Multi-component force 460, 461, 472
 Multi-modal energy harvesting 587
 Multiple admittance signatures 106
 Multiple electrodes 541
 Multiple point borehole extensometer 482
- N**
- Natural frequency 226
 Negative velocity feedback control 402
 Non-rectilinear embedding 429
 Non-centrosymmetric crystal 7
 Non-destructive evaluation (NDE) 4
 Normal probability distribution 206
- O**
- One-quarter admittance 102
 Optical spectrum analyzer 425, 434, 461, 475
 Optimal excitation 362
- Orthorhombic crystal 11
 Osteoporosis 570
- P**
- Passive component(s) 33, 129, 131, 133
 Passive control 299
 Passive smart material 7
 Penalty function 348
 Penetrant dye testing 4
 Penetration techniques 188
 Phase mask 414, 415, 416, 417, 434, 475
 Phasor 18
 Photosensitivity 414, 415, 416, 417
 Piezoceramic 11
 Piezoceramic composite actuator 13
 Piezoelectric ceramic 11
 Piezoelectric energy harvester 585
 Piezoelectric material 11
 Piezoelectric polymer 11
 Piezoelectric shear actuator 394
 Piezoelectric strain coefficient 9, 22, 29
 Poisson distribution 203
 polyelectrolyte membrane 507
 Position mode function (PMF) 376
 Prepreg 425
 Pristine state 138
 Probability density function 202
 Pullout test 188
 PZT efficiency factor (PEF) 271
 PZT-adhesive-structure interaction 79
 PZT-structure interaction 29, 80
- Q**
- Quasi-static sensor approximation 26, 71
 Quick set epoxy adhesive 483
- R**
- Random variable(s) 202
 Raw signatures 130

RC bridge 42
 Real-encoded GA 334
 Rebound hammer 188
 Regression coefficient 426, 435, 443
 Relative deviation (RD) 39
 Resonance Tuning 588
 Resonant frequencies 132, 157
 Resonant frequency 28
 Resonant frequency technique 189
 Ritz method, 164, 168, 170
 RMSD 144, 164, 218, 573
 Root mean square deviation (RMSD)
 39, 40, 272

S

Schmidt rebound hammer 188
 Secant modulus 195
 Sensing region 245, 264
 Sensitive modes 150, 159
 Sensory structure 5
 Shape functions 64, 108, 168
 Shape memory alloys (SMA) 591
 Short-term effects 199
 Signal processing 39
 Signature assurance criteria (SAC) 39
 Silicone rubber 277, 572
 Simbi hammer 188
 Single degree of freedom 239
 Smart structure 5
 Smart system 5
 Soniscope 189
 Specific damping capacity 254
 Spit pin hammer 188
 Sprague-Dawley rats 569
 Standard deviation 201, 206
 State-space equation 340
 Static displacement technique 3
 Static response based technique 3
 Static strain measurement technique 3
 Statistical damage quantifiers 41
 Statistical regularity 201
 Strain energy 239
 Strain gauges 482, 498

Strain mode shapes 226
 Structural control 299
 Structural damping 67
 Structural health monitoring (SHM) 1,
 458, 459
 Structural mechanical impedance 129,
 494
 Structural system identification 2
 Surface hardness techniques 188
 Susceptance 26
 Synchronous electric charge extraction
 587
 Synchronous switch harvesting on
 inductor 587
 System parameter identification 132

T

Tape extensometer 482, 483
 Telemetry 45
 Thermoelastic analogy 107
 Thick adhesive bonding 81
 Time domain 225
 Timoshenko beam 246, 255
 Tissue implants 569
 Transmitter 189
 Transverse shear 461, 467, 468, 469,
 470, 471, 478
 Tunable laser source 434, 475
 Turbo machine parts 143
 Two part epoxy 572

U

Ultimate loads 208
 Ultra-low-cost adaptation 45
 Ultrasonic concrete tester 189
 Ultrasonic pulse velocity technique
 189
 Ultrasonic technique 4
 Underground structures 481
 Universal testing machine (UTM) 195
 Updated model 76, 133

V

Velocity feedback control 312
Vibrating wire strain gauge (VWSG)
482
Vibration energy harvesting 585

W

Water uptake 512
Wave functions 88

Wave number 23
Wave propagation 245, 246
Wave propagation approach 43
Waveform chain code (WCC) technique
39
Wavelength analysis 67
William's testing pistol 188
Windsor probe 188